SEDIMENTARY SYSTEM RESPONSES TO EXTERNAL FORCINGS: A PROCESS-BASED PERSPECTIVE

EDITED BY: Brian W. Romans, Julie Fosdick, William Helland-Hansen and Miquel Poyatos Moré

PUBLISHED IN: Frontiers in Earth Science

frontiers Research Topics

frontiers

ISSN 1664-8714
ISBN 978-2-88966-136-7
DOI 10.3389/978-2-88966-136-7

About Frontiers

Frontiers is more than just an open-access publisher of scholarly articles: it is a pioneering approach to the world of academia, radically improving the way scholarly research is managed. The grand vision of Frontiers is a world where all people have an equal opportunity to seek, share and generate knowledge. Frontiers provides immediate and permanent online open access to all its publications, but this alone is not enough to realize our grand goals.

Frontiers Journal Series

The Frontiers Journal Series is a multi-tier and interdisciplinary set of open-access, online journals, promising a paradigm shift from the current review, selection and dissemination processes in academic publishing. All Frontiers journals are driven by researchers for researchers; therefore, they constitute a service to the scholarly community. At the same time, the Frontiers Journal Series operates on a revolutionary invention, the tiered publishing system, initially addressing specific communities of scholars, and gradually climbing up to broader public understanding, thus serving the interests of the lay society, too.

Dedication to Quality

Each Frontiers article is a landmark of the highest quality, thanks to genuinely collaborative interactions between authors and review editors, who include some of the world's best academicians. Research must be certified by peers before entering a stream of knowledge that may eventually reach the public - and shape society; therefore, Frontiers only applies the most rigorous and unbiased reviews.
Frontiers revolutionizes research publishing by freely delivering the most outstanding research, evaluated with no bias from both the academic and social point of view. By applying the most advanced information technologies, Frontiers is catapulting scholarly publishing into a new generation.

What are Frontiers Research Topics?

Frontiers Research Topics are very popular trademarks of the Frontiers Journals Series: they are collections of at least ten articles, all centered on a particular subject. With their unique mix of varied contributions from Original Research to Review Articles, Frontiers Research Topics unify the most influential researchers, the latest key findings and historical advances in a hot research area! Find out more on how to host your own Frontiers Research Topic or contribute to one as an author by contacting the Frontiers Editorial Office: researchtopics@frontiersin.org

SEDIMENTARY SYSTEM RESPONSES TO EXTERNAL FORCINGS: A PROCESS-BASED PERSPECTIVE

Topic Editors:
Brian W. Romans, Virginia Tech, United States
Julie Fosdick, University of Connecticut, United States
William Helland-Hansen, University of Bergen, Norway
Miquel Poyatos Moré, University of Oslo, Norway

Citation: Romans, B. W., Fosdick, J., Helland-Hansen, W., Moré, M. P., eds. (2020). Sedimentary System Responses to External Forcings: a Process-Based Perspective. Lausanne: Frontiers Media SA. doi: 10.3389/978-2-88966-136-7

Table of Contents

frontiers in Earth Science

EDITORIAL
published: 11 September 2020
doi: 10.3389/feart.2020.591420

Editorial: Sedimentary System Response to External Forcings: A Process-Based Perspective

Brian W. Romans[1]*, *Julie C. Fosdick*[2], *Miquel Poyatos-Moré*[3] and *William Helland-Hansen*[4]

[1] Department of Geosciences, Virginia Tech, Blacksburg, VA, United States, [2] Department of Geosciences, University of Connecticut, Storrs, CT, United States, [3] Department of Geosciences, University of Oslo, Oslo, Norway, [4] Department of Earth Science, University of Bergen, Bergen, Norway

Keywords: sedimentology, stratigraphy, geomorphology, tectonics, climate, sea level, source-to-sink

Editorial on the Research Topic

Sedimentary System Response to External Forcings: A Process-Based Perspective

Improving our understanding of how the Earth system responds to change is a critical goal in geoscience. Using the sedimentary record to investigate ancient processes, events, and interactions has contributed to our increasing knowledge of Earth system functioning, yet there is still much to discover. Tectonic activity, climatic conditions and fluctuations, and sea-level change can have substantial impacts on sediment generation, delivery, and accumulation, all of which, in turn, influence the nature of the resulting stratigraphic record. Additionally, the interacting effects of these multiple forcings are complex and, in many cases, compounded by the influence of self-organized dynamics associated with sediment transport processes. Thus, to be able to extract accurate and meaningful information from sedimentary archives we must continue to examine how external (and internal) controls are (or are not) encoded into stratigraphy. All the contributions in this Research Topic touch on the notion of multiple forcings, but span a variety of sedimentary system types, depositional environments, geologic age, tectonic setting, climatic conditions, spatial and temporal scales, and more. Additionally, this Research Topic features a diverse range of methodology and data types, including outcrop characterization, detrital geo- and thermochronology, subsurface mapping, numerical and physical experiments, and other approaches. The 13 contributions to this Research Topic are briefly summarized below and organized in source-to-sink order with upland sedimentary systems (fluvial, alluvial, eolian) listed first, followed by coastal and shelf margin, and ending with the deep sea.

Capaldi et al. employ detrital zircon U-Pb geochronology and sediment mixing models of modern sediments from the continental Andean foreland to show the impact of climate-modulated processes, such as eolian transport and reworking, on sediment provenance signals. Implications for this work bear on how tectonic signals, local storage, and recycling of synorogenic river sediment are reflected in sedimentary archives.

Finzel combines new and pre-existing data to compile an extensive detrital zircon U-Pb geochronologic dataset from modern rivers of the Mesozoic-Cenozoic igneous belts across mountainous regions in south-central Alaska (United States). Finzel uses a recently developed unmixing approach to compare these data to an extensive detrital zircon U-Pb dataset from Lower Cretaceous to Pliocene strata in the forearc basin, in order to investigate the variations in long-term provenance and sediment dispersal patterns in the basin in response to tectonic events. Results reveal a previously undetected sediment recycling source during the Late Cretaceous and Oligocene, linked to specific plate margin events. The unified approach of extensive modern river sampling, comprehensive basin strata characterization and mixture modeling is a valuable approach for

OPEN ACCESS

Edited by:
David Mark Hodgson,
University of Leeds, United Kingdom

Correspondence:
Brian W. Romans
romans@vt.edu

Specialty section:
This article was submitted to Sedimentology, Stratigraphy and Diagenesis, a section of the journal Frontiers in Earth Science

Received: *4 August 2020*
Accepted: *24 August 2020*
Published: *11 September 2020*

Citation:
Romans BW, Fosdick JC, Poyatos-Moré M, Helland-Hansen W (2020) Editorial: Sedimentary System Response to External Forcings: A Process-Based Perspective. Front. Earth Sci. 8:591420. doi: 10.3389/feart.2020.591420

partitioning of widespread and pervasive ages in sediment source terranes with long-lived magmatic histories, and for resolving sedimentary recycling into a basin.

Meek et al. analyze the stratigraphic architecture of two well-exposed ancient alluvial fans in the western United States (Eocene Richards Mountain Conglomerate and Cretaceous Echo Canyon Conglomerate), deposited under relatively similar climate and tectonic regimes, by employing uncrewed aerial vehicle-based photogrammetric models. The authors use a seven-fold hierarchy of bounding surfaces to describe alluvial fan architecture to examine the relative dominance of autogenic and/or allogenic factors. They show that the architectural style of the two alluvial systems is significantly different and link this difference to the mobility of active channels within the fans, attributed to a more seasonal climate, with less vegetation, where increased sediment flux and flood events would have destabilized channels and thus enhanced lateral migration. These results imply that a specific scale of stratigraphic architecture of ancient alluvial fans can provide insight into allogenic controls related to paleoclimate. They also suggest that in regions where anthropogenically induced climate change results in more variable precipitation, alluvial fans may show decreased channel stability, and consequently imply a greater risk to human activity and development on alluvial fans.

Leonard et al. carried out a detailed provenance and sedimentologic study of Oligocene-Miocene foreland basin infill in the Magallanes-Austral Basin to investigate relationships between tectonic activity in sediment source areas and eustatic sea-level. By comparing modal compositions of sandstone and conglomerate with detrital zircon U-Pb geochronology, they suggest a major shift in source area between 27 and 24 Ma that is consistent with rejuvenation of arc magmatism and hinterland fold-and-thrust belt activity. Notably, this provenance change predates a basin margin change in depositional environment from marginal marine to fluvial sedimentation, but the ~2 Myr erosional unconformity beneath the tectonically generated coarse-grained fluvial deposits may be at least partially influenced by a latest Oligocene global regression across this time interval.

Bauer et al. investigate the influence of inherited depositional topography on the evolution of constructional shelf-slope systems, the position of shelf edge zones, and development of phases of coarse-grained sediment delivery to deep water. They combine new outcrop data with published studies of the Cretaceous Tres Pasos and Dorotea Formations, southern Chile, to show that the position and character of abrupt changes in slope from preceding depositional phases impart a significant influence on the position of subsequent shelf-edge zones. With these results, Bauer et al. suggest that the allogenic-autogenic dichotomy is not always so clear, especially in the context of depositional topographic influence that persists through time.

Abatan and Weislogel reconstruct the paleohydrology of Pennsylvanian (~310 Ma) river channels via outcrop characterization coupled with machine learning-assisted methods to examine controls on resulting fluvial stratigraphic architecture. Channel body geometry, sedimentary structures, and grain-size distributions were used to estimate paleoslope and flow velocity. Their results suggest a change from a humid ever-wet climatic regime to a semi-arid, seasonally wet climate during deposition of these fluvial systems and they also discuss the potential effects of tectonic subsidence and sea-level change.

Sømme et al. investigate depositional system response to a short-lived (~0.2 Myr) climatic perturbation superimposed on long-term (~10 Myr) tectonic controls to better understand how these different controls are expressed in the stratigraphic record. They use regional 3D seismic-reflection data combined with borehole and biostratigraphic information to map Paleogene depositional systems and reconstruct sediment supply along the Norwegian margin. They show that the relatively short-lived Paleocene-Eocene Thermal Maximum does not correlate with a discrete peak in sediment supply as it does in depositional systems elsewhere, but may be expressed as a downlap surface recording a base-level rise. Sømme et al. use their results to discuss how tectonic processes and along-strike variability of these multiple interacting controls can potentially be discriminated in stratigraphy.

Straub uses physical experiments to explore how sea-level cycles of varying magnitude and periodicity influence the architecture of linked delta-continental slope sedimentary systems. Results of these state-of-the-art experiments show that, on average, sediment delivery to the slope is promoted during sea-level lowstands. However, smaller magnitude and higher-frequency sea-level cycles lead to greater stochasticity and, therefore, a less predictable response.

Pasquier et al. use strontium isotope geochemistry of Pleistocene deposits in offshore Gulf of Lion, western Mediterranean Sea, to link the proportion of detrital carbonate rocks in the catchment to considerations of source-to-sink flux, which commonly only emphasizes siliciclastic accumulation. Their results indicate a relatively high export of detrital carbonates from the catchment during both glacial and interglacial conditions and suggest that, in analogous systems in the geologic past, detrital carbonate could influence bulk carbonate strontium isotope ratios and their associated chemostratigraphic application.

Ciarletta et al. investigate the dynamics of retreating barrier island systems in the context of sea-level change using a numerical modeling approach. Specifically, they hypothesize that deposits that result from intrinsic (autogenic) processes are linked to higher rates of relative sea-level rise, which could disrupt or mask external signals. Their results suggest that barrier island response to a sea-level pulse is controlled by the magnitude and timing of that pulse, as well as by interactions of shoreface with overwash processes. Additionally, they show that millennial-scale periodicity leads to barrier island systems becoming vulnerable to drowning, even with relatively low rates of relative sea-level rise.

Wei et al. studies two submarine canyon systems in the Inner California Borderlands, offshore Southern California, to investigate how tectonics, shelf width, gradient, and autogenic processes influence turbidite sedimentation. Based on new geophysical imaging, piston and gravity cores, and radiocarbon dating of foraminifera, these authors suggest that Dana Point

Canyon remained active during the most recent sea-level lowstand, transgression, and highstand. In contrast, elsewhere along the shelf, sediment delivery to the San Onofre North and South canyons may have been inhibited by structural growth along the right-lateral Newport Inglewood/Rose Canyon Fault after 8 ka.

Hawie et al. addresses the importance of grain size and discharge as independent controls on submarine fan architecture. They use stratigraphic forward models with variable diffusion coefficients to examine the sensitivity to a range of grain sizes and sediment discharges on submarine fan depositional response. Increasing discharge leads to thicker packages with fewer channel avulsions, coarse-grained sediment build-up at the mouth of the feeder channel, and bypass of fine-grained material. Variable grain-size input experiments show that fine grain sizes result in further basinward transport whereas coarser loads develop compensational stacking.

Hülscher et al. test how four well-known tectonic/erosional events in the European Alps—exhumation of the Tauern Window, Lepontine Dome, visco-elastic relaxation of the European plate, and unroofing and redeposition of the Augenstein Formation—propagated through and into different compartments of the sediment-routing system and how they are recorded in a submarine channel-overbank system. They evaluate the Oligocene-Miocene stratigraphy, biostratigraphy, and chemostratigraphy, along with 3D seismic-reflection data, in the Upper Austrian Molasse Basin and calculate timescale-invariant, spatially averaged sediment-accumulation rates for different time periods and different segments in the basin. Results and interpretations highlight the stratigraphic complexity of a gravity-flow dominated deep-marine channel system and its sedimentological record of these important tectonic/erosional events.

AUTHOR CONTRIBUTIONS

All authors listed have made a substantial, direct and intellectual contribution to the work, and approved it for publication.

Conflict of Interest: The authors declare that the research was conducted in the absence of any commercial or financial relationships that could be construed as a potential conflict of interest.

frontiers in Earth Science

ORIGINAL RESEARCH
published: 28 May 2019
doi: 10.3389/feart.2019.00121

Morphodynamics and Stratigraphic Architecture of Shelf-Edge Deltas Subject to Constant vs. Dynamic Environmental Forcings: A Laboratory Study

*Kyle M. Straub**

Department of Earth and Environmental Sciences, Tulane University, New Orleans, LA, United States

When deltas dock at continental margins they construct thick stratigraphic intervals and activate continental slope sediment routing systems (SRS). Given their thickness, these deposits have the capacity to store detailed paleo-environmental records. Several competing theories describe how SRS comprised of linked deltas-continental slopes respond to sea level cycles of varying magnitude and periodicity. I explore this in a physical experiment where the topography of a coupled delta-slope system was monitored at high resolution. This allows development of process-based theory for the response of SRS to external forcings at the land-ocean interface. Connection between these environments was promoted with input conditions that generated plunging hyperpycnal flows at river mouths. The experiment had three stages, which included: (1) a delta-slope system aggrading with no sea level cycles, (2) a system responding to low magnitude and high frequency sea level cycles, and (3) a system responding to a high magnitude and long period cycle. All stages shared an identical background pseudo-subsidence rate. Here the magnitudes and periods of sea level cycles are discussed relative to key autogenic scales. I find that, on average, sediment transport to the marine is promoted during lowstand conditions in all stages. However, the scale of the sea level cycles with respect to emergent autogenic scales controls the predictability of this response, with greater stochasticity and thus lower predictability for the response to smaller and shorter sea level cycles. Analysis of two SRS suggests that predictable responses can require sea level cycle amplitudes greater than 50 m and periods longer than 200 kyrs, but will vary with system size.

Keywords: shelf-edge delta, autogenics, laboratory experiments, stratigraphy, sea level

OPEN ACCESS

Edited by:
David Mark Hodgson, University of Leeds, United Kingdom

Reviewed by:
Janok Bhattacharya, McMaster University, Canada
Katherine Leigh Maier, National Institute of Water and Atmospheric Research (NIWA), New Zealand

***Correspondence:**
Kyle M. Straub
kmstraub@tulane.edu

Specialty section:
This article was submitted to Sedimentology, Stratigraphy and Diagenesis, a section of the journal Frontiers in Earth Science

Received: *17 February 2019*
Accepted: *07 May 2019*
Published: *28 May 2019*

Citation:
Straub KM (2019) Morphodynamics and Stratigraphic Architecture of Shelf-Edge Deltas Subject to Constant vs. Dynamic Environmental Forcings: A Laboratory Study. Front. Earth Sci. 7:121. doi: 10.3389/feart.2019.00121

INTRODUCTION

Sediment routing systems, which transport sediment from sources to sinks, consist of linked segments within which the dominant morphodynamic processes remain fairly constant (Allen, 2008; Sømme et al., 2009b; Allen, 2017). The coupling of these segments occur at important Earth-surface boundaries which fundamentally alter the method, rate, and variability of sediment

transport. Here I explore the coupling of sediment transport segments that occur at the shoreline, with a specific focus on deltas and their down system environments. In particular, I explore how the magnitude and period of sea level cycles influence the extraction of mass to deposition across the delta-slope transition.

The influence of sea level, or relative sea level (RSL) change in regions with substantial vertical Earth-surface motion due to tectonics, on sediment transport and stratigraphy is not a new question. It has been explored since the time of Gilbert (1890) and ramped up with the advent and examination of hydrocarbon exploration derived seismic surveys, which motivated the development of sequence stratigraphic methods and interpretations (Vail et al., 1977; Van Wagoner et al., 1990; Catuneanu et al., 2009). While the largely qualitative, observational, and conceptual approaches underpinning sequence stratigraphy continue to teach us about continental margin stratigraphy, the approaches championed by the source to sink movement require quantitative data for theory development garnered from field observations and numerical and physical experiments.

In today's icehouse highstand conditions many deltas are separated from the shelf-edge by wide continental shelves (Sweet and Blum, 2016). With these conditions transport of sediment to the deep marine, and in particular coarse sediment, is limited. Icehouse conditions refer to time periods in Earth history when the waxing and waning of continental scale ice sheets result in high amplitude ($\geq$ 100 m) sea level fluctuations, while greenhouse refers to periods with no continental-scale glaciers and thus small-magnitude Milankovitch-forced RSL cycles from the thermal expansion contraction of water. Efficient transport of sediment to the deep marine is currently limited to rivers that link to submarine canyons or fjords (Xu et al., 2004; Vendettuoli et al., 2019). However, analysis of continental margin stratigraphy exposed in outcrop and reflection seismic data suggest that shelf-edge deltas efficiently fed slope systems during recent icehouse lowstand conditions as well as greenhouse periods (Porębski and Steel, 2003; Straub et al., 2012; Sylvester et al., 2012). Here, I present a detailed set of measurements derived from a physical laboratory experiment on the role of RSL in the partitioning of sediment between dominantly terrestrial vs. dominantly marine settings at shelf-edge deltas. In particular, I focus on (A) the sea level cycle characteristics necessary to induce stratigraphic signatures that can clearly be linked to paleo sea level change and (B) the timing and magnitude of sediment delivery to regions past a shelf-edge.

Motivating this experimental study are a suite of results from numerical experiments that explore the impact of RSL variations on sediment dispersal across the shelf-edge during icehouse vs. greenhouse Earth conditions (Harris et al., 2016, 2018). The numerical model used in these studies, Dionisos, simulates sediment transport at basinal length-scales and geological time-scales based off diffusive transport of sediment (Granjeon, 1999). This diffusive algorithm adequately replicates depositional patterns over long spatial and temporal scales. However, over shorter length and time scales morphodyamic processes resulting from the coupling of topography, flow, and sediment transport produce rich stochastic behavior that is not well described by diffusion (Kim et al., 2014; Paola, 2016; Hajek and Straub, 2017). Some of this stochasticity arises due to internal processes within sediment routing systems, for example dune and channel migration and avulsions which are commonly called autogenic processes.

Even with a diffusive description of sediment transport, these models make several predictions that challenge conventional wisdom about the role of RSL change in sediment delivery to the continental slope and beyond due to emergent model autogenic dynamics. These dynamics result from lateral gradients in deposition, which aid occasional channel formation and compensational stacking of lobes. Specifically, I highlight the following results: (1) Harris et al. (2016) found a trivially small difference in cumulative deepwater sand delivery between a model of continental margin evolution with a eustatic history derived from a field compilation and a second model with no eustatic variations. While peak delivery of sand to the deep marine did occur during short periods of sea level fall in the variable eustacy model, similar episodes of sand delivery occur in the constant eustacy model when transport systems occasionally reached and became temporarily locked at the shelf-edge. (2) The delivery of sand to the deep marine is not well correlated to rate or amplitude of sea level fall, which holds regardless of the diffusion coefficients used in the models (Harris et al., 2018).

Motivated by these numerical observations, I conducted a physical experiment to examine the coupling of deltas to the continental slope. Specifically I focus on systems with rivers that spawn hyperpycnal flows downstream of the shoreline. While the diffusion scheme used in Dionisos likely produces muted autogenic dynamics over time scales of delta lobe growth and abandonment, physical experiments are known for self-organization and complex stochastic behavior (Paola et al., 2009).

This work is also motivated and informed by theory which predicts threshold characteristics of sea level cycles necessary to produce geomorphic and stratigraphic signals which can confidently be distinguished from autogenic processes and products (Li et al., 2016; Yu et al., 2017). This theory was recently tested in a set of deltaic experiments, but these experiments lacked a slope downstream of the shoreline and the collection of high resolution bathymetry, both of which are present in this study.

MATERIALS AND METHODS

To study the influence of RSL on the partitioning of sediment between dominantly terrestrial vs. marine environments, I conducted a physical laboratory experiment in the Deepwater Basin housed in the Tulane University Sediment Dynamics and Stratigraphy Laboratory. The basin is 6 m long, 4 m wide, and 2.2 m deep (**Figure 1A**). Sea level is controlled through a weir, which is in hydraulic communication with the basin. The weir is on a computer-controlled vertical slide that allows for sub-millimeter-scale elevation control of sea level. The sea level elevation was monitored and logged once a minute with a transducer to ensure that it matched target elevations.

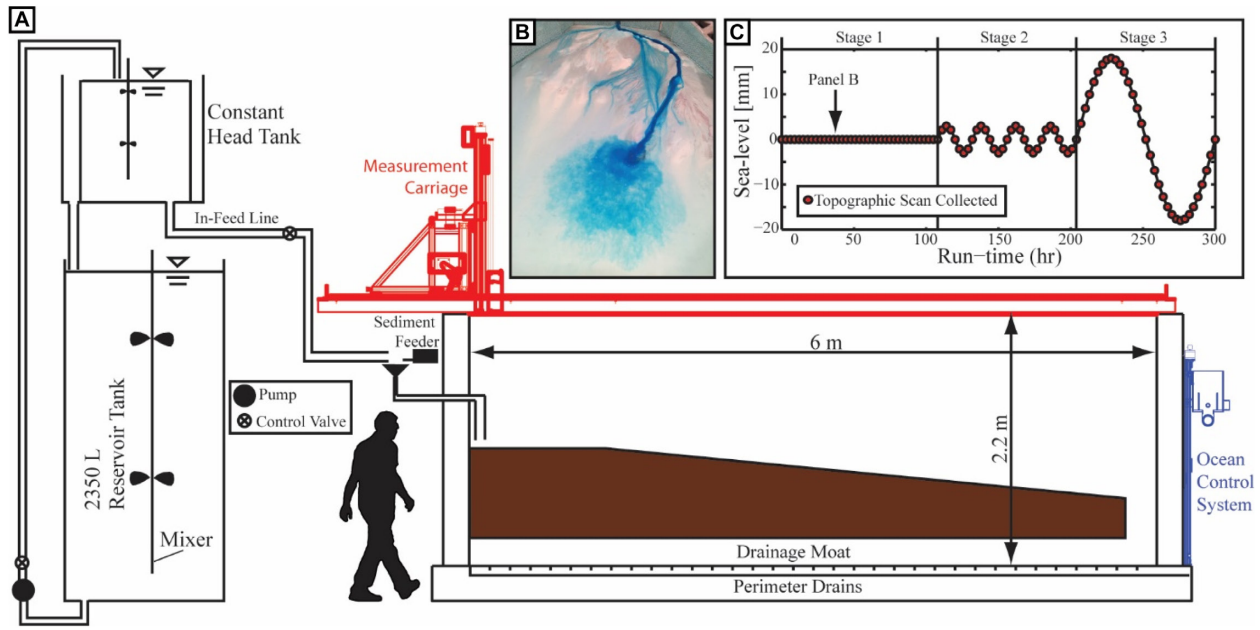

FIGURE 1 | Schematic diagram of the experimental facility and experimental conditions. **(A)** Dip view of the facility and initial topographic form with important basin dimensions noted. A saline mixture was pumped from a reservoir tank to a constant head tank before mixing with sediment in a funnel and then entering the basin. **(B)** Characteristic perspective photo of experimental surface with input flow dyed for visualization. **(C)** Time series of sea-level, minus the long term drift imposed for pseudo-subsidence and referenced to sea level at the start of stage 1 with time of topographic scans noted with red filled circles.

The initial basin topography was characterized in dip by a 1.2 m long flat shelf which connected to a 3.8 m long segment with a 10% slope. Initial topography did not vary in the strike direction. While steeper than typical continental margins, the 10% slope was implemented to match other experimental studies which used distorted Froude scaling to show that increasing the slope for laboratory systems helps better replicate field scale processes (Cantelli et al., 2011).

The input flow to the basin was designed to help facilitate transport of sediment to the deep marine by hyperpycnal flows. Flow was introduced via a constant head tank as a mixture of water and dissolved salt, which gave it a 2% excess density relative to the fresh water of the basin ocean. To keep the density contrast between the input flow and ocean, a system was implemented to extract dense flow at the base of the basin and replace it with fresh water from above at a rate equal to 11 times the saline input. The salinity of our river input and ocean might seem counterintuitive given that deltas constructed at land-ocean interfaces have fresh water in their rivers, which empty into saline oceans. However, this choice was made to promote hyperpycnal plunging of flows in the marine and thus promote transport of sediment to the continental slope. Similar to previous studies, the salt introduced can be thought of as the washload component of a system, which bypasses the region of study (Straub et al., 2008; Hamilton et al., 2017). Once every 3 h the experiment was paused and fresh water was cycled into the basin until no salinity could be detected. The input hydrograph was also designed to include floods to facilitate pumping of sediment to the deep marine. Base flow to the experiment was 1.54×10^{-4} m^3/s. Floods were two-times the base flow and occurred for a continuous 6 min during each run-hour. The ratio of time at base flow to flood was set to mimic seasonal floods on large river deltas. The length of the flood-base flow cycle is set so that a large number of cycles occurred in the time necessary to aggrade, on average, a single channel depth everywhere on the delta top, which has been shown to be an important timescale of autogenic activity (Wang et al., 2011).

Supply of sediment to the basin was controlled through a computer interface. During base flow conditions the sediment delivery rate was 3.53×10^{-4} kg/s and the ratio of sediment to water delivery rate was kept constant for base flow and flood conditions at a volumetric ratio of 1:1000. The input sediment mixture was designed to mimic earlier experimental work (Hoyal and Sheets, 2009; Li et al., 2016) with particle diameters ranging from 1 to 1000 μm with a mean of 67 μm and was dominantly white quartz. One quarter of the coarsest 23.5% of the sediment distribution was commercially dyed red to aid visualization of stratigraphic architecture. A small amount of commercially available polymer (New Drill Plus, distributed by Baker Hughes Inc.) was added to the sediment mixture to enhance sediment cohesion, which aids formation of channels in experiments. I used this sediment mixture as earlier experimental studies found that its fine grain sizes are transported in suspension through the self-organized deep and relatively stable channels and resulted in pumping of substantial volumes of sediment to the marine (Straub et al., 2015). The combination of the saline input flow, fresh water receiving basin, and suspended sediment resulted in continuous plunging of hyperpycnal flows

at river mouths which traversed down the basin slope as turbid underflows (**Figure 1B**).

The experiment included a 120 h build out stage in which sea level was kept constant. The main phase of the experiment followed when I imposed a constant rate of sea level rise ($\overline{r_{SL}}$ = 0.25 mm/h), meant to simulate a constant long term subsidence rate. This pseudo-subsidence resulted in a terrestrial accommodation production rate that matched the average percentage of the volumetric sediment input rate trapped in the terrestrial, determined from earlier experimental work (Straub et al., 2015). As such, long term sea level rise induced a long term deposition rate on the delta-top, $\overline{r_D}$ that matched $\overline{r_{SL}}$. This allowed the mean location of the shoreline to remain constant, with superimposed variations due to autogenic processes and sea level cycles. The main phase of the experiment included three stages: (1) no sea level cycles, (2) small amplitude and short period sea level cycles, and (3) a large amplitude and long period sea level cycle (**Figure 1C**). Stage 1 was 108 h and produced slightly more than two channel depths of stratigraphy over the entire delta-top (maximum autogenic channel depths were ∼12 mm deep).

Following Li et al. (2016), I scale the magnitude and period of sea level cycles in stages 2 and 3 to critical autogenic space and time scales. The magnitude of sea level cycles, M_{RSL}, (i.e., difference in elevation from cycle peak to trough) is compared to the maximum autogenic channel depth, H_c:

$$H^* = \frac{M_{RSL}}{H_C} \tag{1}$$

While the period of a sea level cycle, T_{RSL}, is compared to the average time necessary to deposit one channel depth of stratigraphy over the entire delta-top, which utilizes the long term delta-top deposition rate, $\overline{r_D}$, as:

$$T_C = \frac{H_C}{\overline{r_D}} \text{ (Wang et al., 2011)} \tag{2}$$

Which allows:

$$T^* = \frac{T_{RSL}}{T_C} \tag{3}$$

Stage 2 included four sequential sea level cycles characterized by H^* = 0.5 and T^* = 0.5, and thus were small in comparison to the autogenic scales. Stage 3 included one sea level cycle characterized by H^* = 2 and T^* = 2, and thus was large in comparison to the autogenic scales. Ideally I would run a larger number of sea level cycles for all stages, to allow exploration of statistical variability to forcings. However, results from a similar set of experiments on sea level forcing response of deltas, with no down system slope, indicate a quick adjustment of the deltas to their cycle forcing parameters (Yu et al., 2017).

It is worth noting that T_c does not equal the time scale of avulsion, T_A, as initially defined by Mohrig et al. (2000). T_A is defined as the depth of a system's channels divided by the in-channel, local aggradation rate, measured over one avulsion cycle. The aggradation rate used in the formulation of T_c is the long term or geological rate (i.e., measured over long enough timescales that rates are temporally persistent; Jerolmack and Sadler, 2007). Typically, T_c is several orders of magnitude greater than T_A. As such, T_c does not relate to the average periodicity of any one surface process, but rather estimates the time necessary for even dispersal of sediment across a basin resulting from the full suite of autogenic processes (Wang et al., 2011).

The input current was dyed twice an hour with blue food coloring to aid visualization of morphodynamics. This was done for 1 min of each flood and then 30 min later for 1 min of base flow conditions. Aerial images of the experimental surface were collected at the very end of each dye pulse. Maps of the entire experimental surface were collected every 3 h of run-time with a 1 Khz long range displacement laser connected to a data logger and housed on a measurement carriage capable of movement in all three Cartesian directions. Sequential topographic maps were collected on a common grid with a horizontal grid spacing of 5 mm in the down-basin and cross-basin directions. This produced maps with a vertical resolution of 0.25 mm. For stratigraphic analysis, the topographic maps were used to construct synthetic stratigraphy by stacking all topographic scans and clipping for erosion. Following the completion of the experimental run, the deposit was sectioned along three primarily dip oriented transects and imaged with a digital camera for stratigraphic characterization.

RESULTS

General System Dynamics

I start with a general description of the system dynamics prior to the quantitative analysis of mass partitioning from source to sink. Pseudo-subsidence was turned on at the start of stage 1 with one major river channel located on the river-left side of the basin. This channel and its delta lobe protruded well past the shelf-slope break and remained fixed in position for approximately 70 h before the first large scale lobe avulsion (**Figures 2**, **3**). This time-scale of stability is significantly longer than the compensation time-scale for the stage and longer than any time between avulsions in a previous deltaic experiment that used a very similar setup to that discussed here, but without a coupled slope system (Straub et al., 2015; Li et al., 2017). This might point to enhanced stability of terrestrial channels when their tips reach a shelf-edge, as quantified in previous experiments (Kim et al., 2013). This was followed by several smaller scale avulsion events. As the system reorganized, the long term pseudo-subsidence resulted in drowning of old delta lobes and the construction of a shelf environment. I characterize the shelf in our experiment to be low sloping (S = 0.05 m/m) marine environments that were constructed in terrestrial settings, but later drowned due to the local RSL history.

During stage 1, input flow and sediment was routed to the shoreline through a mixture of channelized and overbanking flow. Coarse sediment was largely confined to the channels while overbanking flow resulted in substantial fine grained deposition on the delta-top. Deposition at the shoreline

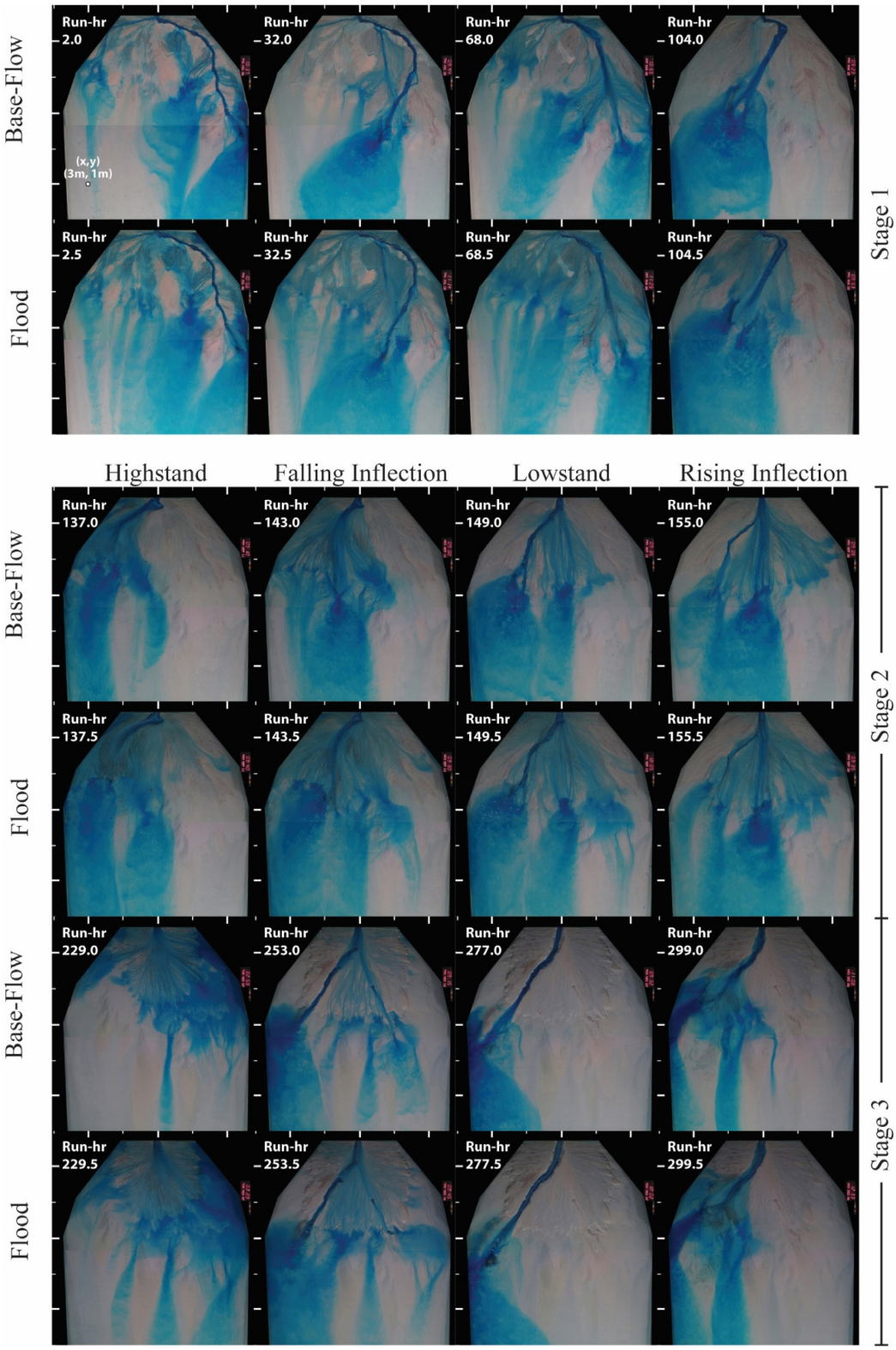

FIGURE 2 | Overhead images of the three experimental stages. Images display transport system at key time periods in sea level cycles (stages 2 and 3), or for key periods in an autogenic channel cycle (stage 1). Photos from base flow conditions and then succeeding flood are shown. Images were taken after 1 full minute of dye release into the basin. Major tick marks on images borders have a 1 m spacing and a reference location is noted in the upper left photo with distances from the proximal basin wall (*x*) and from the river right basin wall (*y*).

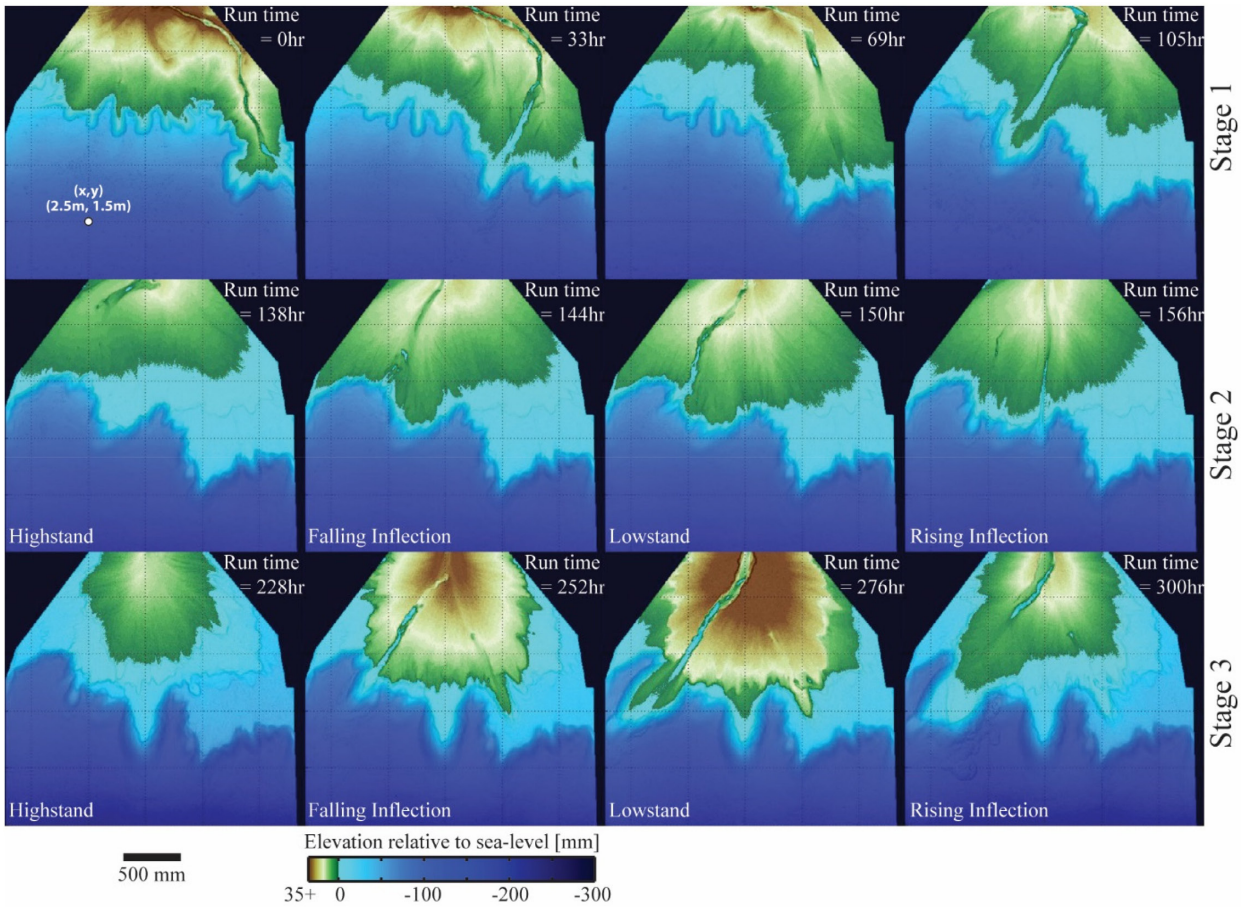

FIGURE 3 | Topographic maps of the three experimental stages. Maps display transport system at key time periods in sea level cycles (stages 2 and 3), or for key periods in an autogenic channel cycle (stage 1). Line spacing of grid over topographic maps is 0.5 m and a reference location is noted in the upper left map with distances from the proximal basin wall (*x*) and from the river right basin wall (*y*).

was dominated by coarse grained delta lobes. Sediment that bypassed the delta foresets in turbid underflows was almost exclusively fine grained. These underflows were sheet-like and lacked any detectable channelization. Underflows traversed the entire length of the basin and plunged into the distal basin moat, but lacked much suspended sediment at this point. The only significant difference between base and flood flow conditions was the amount of terrestrial overbanking flow, which was noticeably higher during flood events.

The small magnitude and short period RSL cycles of stage 2 drove reorganization of channel networks, most of which occurred during highstand conditions when the terrestrial system shrunk in size and the shelf system expanded. However, this was not always the case. Between the second and third RSL cycles a single channel formed down the center of the basin during rising sea level conditions. This channel remained in place during the highstand, pumping high sediment volumes to the marine, and continued to remain open through the succeeding lowstand. Similar to stage 1, a significant amount of the input flow left the terrestrial channels to the overbank during both base and flood flow during the entirety of all stage 2 sea level cycles (**Figures 2**, **3**).

The single RSL cycle of stage 3 produced clear geomorphic responses (**Figures 2**, **3**). Initial rising and then highstand sea level conditions drove a rapid shoreline transgression and wide scale expansion of the experimental shelf. As our experimental setup did not include waves, no large scale erosional ravinement surface formed on the shelf during transgression. During highstand the delta-top system had high lateral mobility and relatively little channelization. During falling sea level conditions channelization occurred that eventually collapsed into a single erosional corridor on the river right side of the basin. This channel was deep and wide enough to contain all flow during base and flood flow conditions. As such, this channel acted as a conveyor belt, transporting all of the input flow and sediment to the marine and the terrestrial overbank was starved of sediment. While the size of the shelf decreased during falling and lowstand conditions, it did not completely disappear as sediment transport and deposition to the marine was laterally constricted to the river right side of the basin.

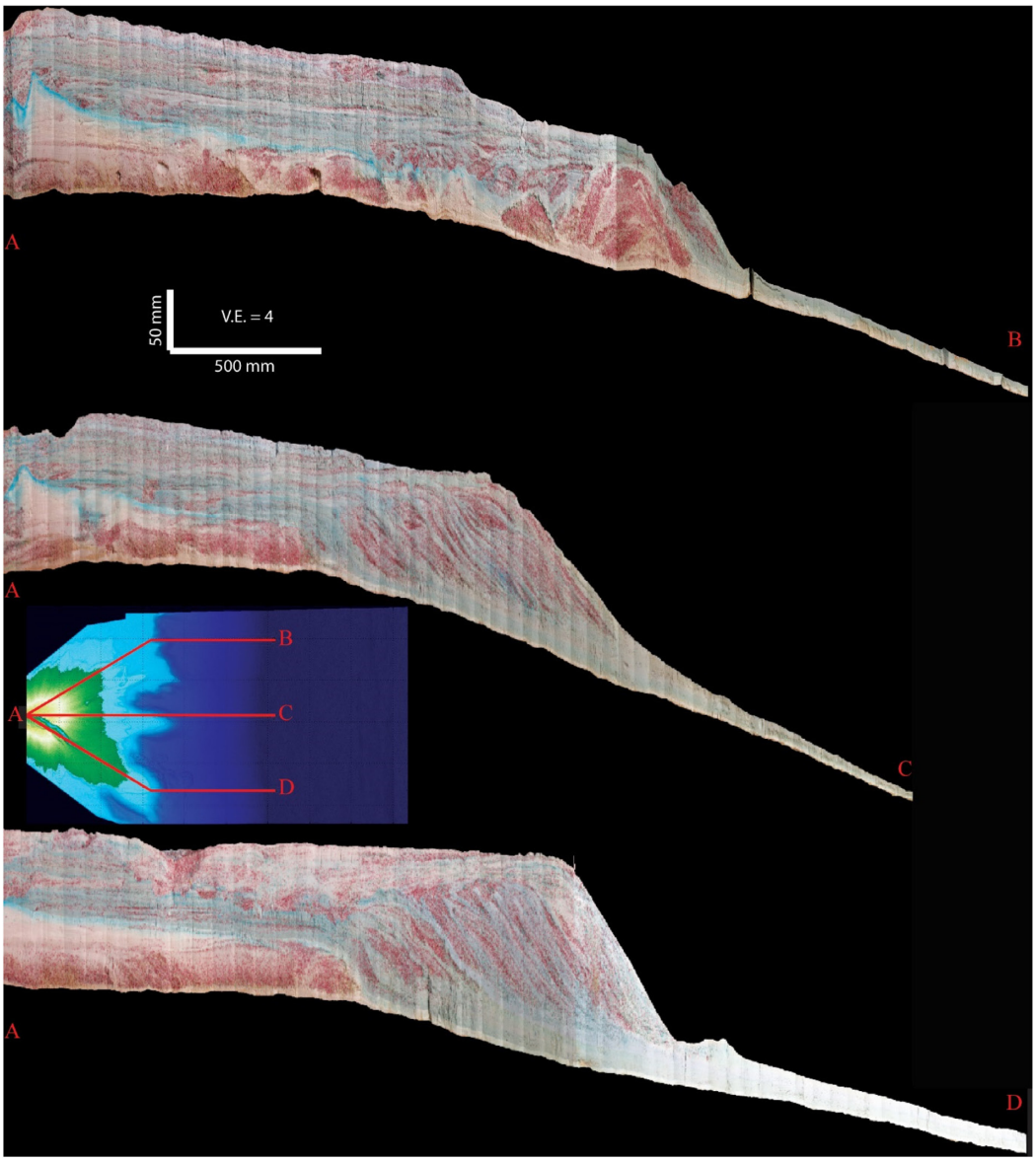

FIGURE 4 | Images of preserved physical stratigraphy of the three experimental stages. Primary transport direction is from left to right. Blue staining is from food coloring used to dye input flow and is primarily present on the fine grained strata. Insert panel gives location of sections, which are displayed with a 4X vertical exaggeration.

Stratigraphic Architecture

The surface dynamics discussed above resulted in a stratigraphic package with delta-top deposits that averaged roughly 0.07 m in thickness, shelf-edge delta foresets in excess of 0.15 m thick and slope deposits that tapered from roughly 0.03 m down to 0.005 m thick. Panels of the preserved strata were generated by vertically slicing the final deposit along three dominantly dip panels. I took advantage of the locations of the transport system during each stage of the experiment when selecting the location of the dip panels. These included: (1) a panel down the river left side of the basin that aligned with the longest lived autogenic channel path during stage 1, (2) a panel down the center of the basin that captured the strata deposited during several of the stage 2 cycles, and (3) a panel down the river right side of the basin that was aligned with the dominant flow path during stage 3 (**Figure 4**).

Delta-top strata along the center and river left transects were similar in nature and included interbedded layers of red sand and white fine grained strata with occasional oblique channel cuts of similar depth. The delta-top strata along the river right transect included the large erosional channel fill from stage 3. The coarsest deposits in each transect were found in the shelf-edge foresets with fine grained strata constructing the down dip slope strata.

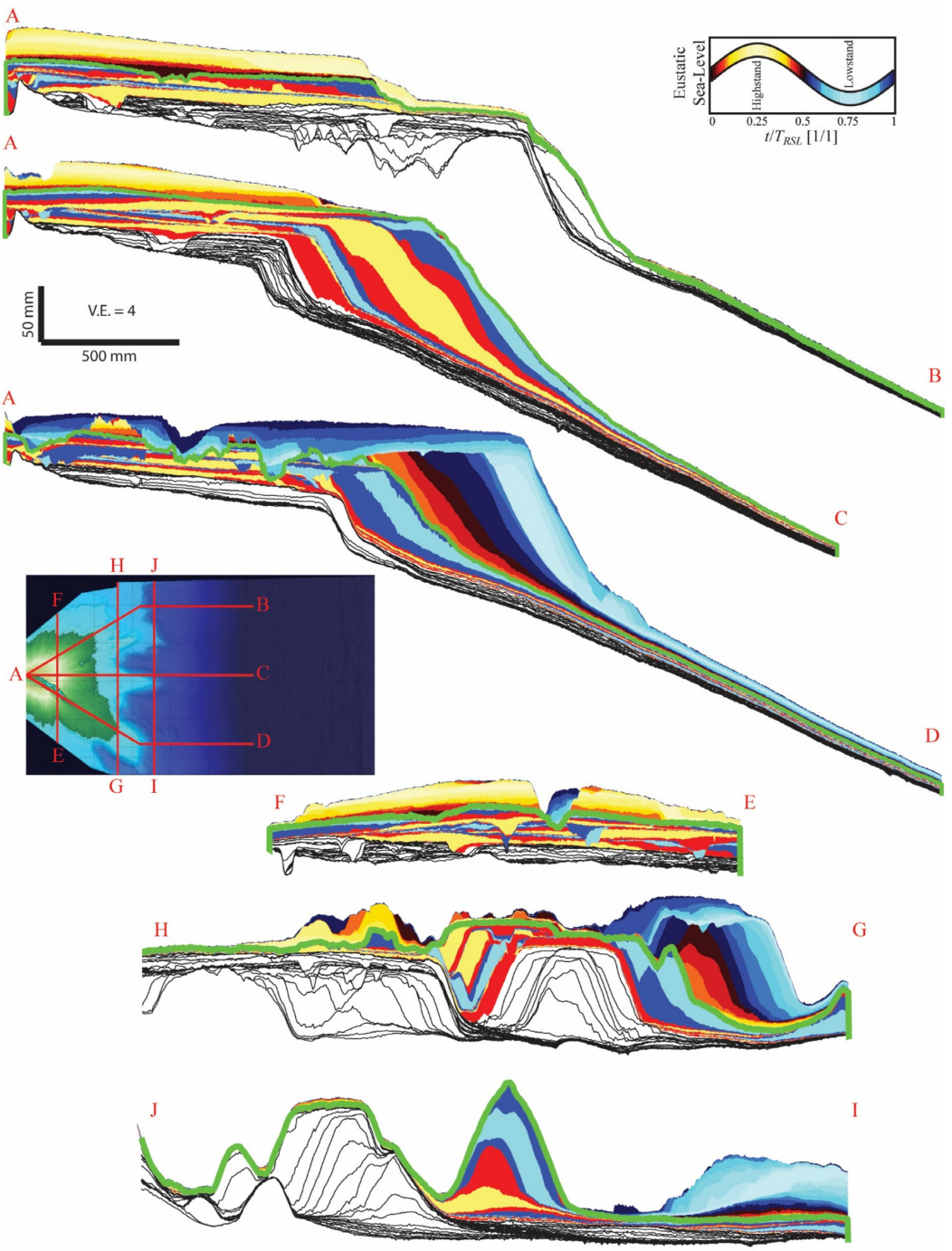

FIGURE 5 | Panels of synthetic stratigraphy with deposits painted as a function of time of deposition within a sea level cycle. Stage 1 strata is displayed without coloring, but with preserved time horizons as black solid lines. Thick green lines denote break between stage 2 and 3 strata. Insert map details location of each transect; color bar details how synthetic stratigraphic color corresponds to time of deposition.

To complement the facies information contained within images of the physical stratigraphy, I construct volumes of synthetic stratigraphy by stacking DEMs of topography that are clipped to account for erosion in the topographic time-series (**Figure 5**). As I know the run-time associated with each map and the corresponding sea level, I can paint panels of synthetic strata by position within an RSL cycle. The complete spatial coverage of the basin allows me to extract these cross-sections

along any path I wish. As sea level did not cycle in stage 1, I focus on a comparison of stage 2 and 3. I extract dip sections of synthetic stratigraphy along identical transects as our physical stratigraphy. The strata of the dip panel that ran down the middle of the basin shows that delta-top stratigraphy was constructed during both highstand and lowstand conditions of RSL during stage 2 and stage 3, but with a preference for deposition during highstand conditions. At least along this transect, a significant amount of the foreset strata was also deposited during highstand conditions, but with a cap on the foreset strata deposited during the subsequent lowstand.

Synthetic strata analyzed down the river right side of the basin, following the path of the dominant erosional channel of stage 3, reveals that foreset construction began during highstand, but its growth accelerated as sea level fell to its lowstand position. Preserved delta-top strata along this transect was deposited during lowstand conditions as earlier highstand delta-top deposits were largely eroded and transported down-dip.

I also extracted panels of strata oriented in the strike direction. Here I compare three panels: one oriented half-way down the delta-top, one near the initial shelf-slope break, and one near the toe of the dominant shelf-edge delta foresets. I see a general decrease in preserved strata deposited in highstand conditions and an increase in preserved lowstand strata as you progress from source to sink.

Quantifying the Relationship Between RSL and Mass Extraction

The central goal of this study is to quantify the conditions necessary for RSL cycles to influence the depositional patterns of linked shelf-edge delta and slope systems. It is common to assume that sea level cycles influence the location of deposition, with deposition moving basinward as sea level falls and vice versa with sea level rise (Van Wagoner et al., 1990; Catuneanu et al., 2009). I explore this in the experimental strata by constructing a set of modified Wheeler diagrams (Wheeler, 1964). First, I construct these for individual dip and strike sections. The dip section comes from the basin bisect line (**Figure 6A**), while the strike section is from the location of the shelf-edge at the beginning of the experiment (**Figure 6B**). I generate a matrix populated with the preserved deposition rates from sequential pairs of topographic maps. I note that these are preserved deposition rates and are thus constructed after topographic clipping has occurred to account for post depositional erosion. This is done for each downstream location on the dip section and each cross-stream location on the strike section, with the distance between measurement locations equal to the 5 mm topographic grid. To facilitate comparison of our experiment to field systems, I normalize deposition rates by the imposed long-term pseudo-subsidence rate:

$$D^* = \frac{D(x \, or \, y)}{\bar{r}} \tag{4}$$

Where $D(x \, or \, y)$ is the deposition rate at either a given downstream (x) or cross-stream (y) location.

On these two-dimensional sections, I observe extreme variability in deposition rates in space and time, with a large number of stratigraphic hiatuses. Measured D^* values peak at values in excess of 20 over delta foresets, but it is difficult to link depositional dynamics to the imposed sea level history in either dip or strike.

In an effort to decrease the "depositional noise" associated with looking at single dip or strike transects, I generated a second set of modified Wheeler diagrams. For this, an average dip-oriented Wheeler diagram was generated by averaging all dip oriented rows in the topographic dataset ($n = 531$) (**Figure 6C**). The same process was used to construct an average strike oriented diagram by averaging all strike oriented columns in the topographic dataset ($n = 923$) (**Figure 6D**).

I observe D^* values ranging from 0 to 3 in the basin averaged Wheeler diagrams with highest values over delta foresets (**Figure 6**). Looking at the dip section, in stage 1 peak D^* values initially move basinward, until making a rapid sourceward transition at the time of the first major avulsion. This is followed by smaller cycles of progradation then retrogradation of peak D^* values. I observe no clear imprint of the stage 2 small amplitude and short period cycles in the Wheeler diagram. In comparison to the short period sea level cycles, a much longer period autogenic progradation and then retrogradational cycle is observed. The high magnitude and long period sea level cycle of stage 3, though, drove a clear response in the location of peak deposition rates. The initial rise in sea level toward highstand conditions drove peak D^* values toward the sediment source, while falling sea level during this cycle drove a basinward shift in D^*. Stage 3 was also the only stage with a stratigraphic hiatus over the entire width of the proximal depositional system. This hiatus occurred during the falling portion of the stage 3 cycle as the terrestrial system entrenched through erosion and pushed sediment to the marine.

The basin averaged strike section again shows similar character in the first and second stages with zones of deposition shifting laterally to compensate for topographic lows. Stage 3, however, is characterized by deposition that remains on the river right side of the basin and a stratigraphic hiatus that spans most of the river left side of the basin during falling sea level. This stratigraphic hiatus is largely associated with inactivity rather than erosion, as the transport system was confined to the river right side of the basin at this time.

The modified Wheeler diagram presented above helps visualize movement of the peak depocenters in the experiment, but I am also interested in describing the cumulative extraction of mass to deposition as a function of distance from the sediment source and how this varies (1) between stages and (2) over the course of individual sea level cycles. This can be useful in identifying if sea level cycle characteristics promote the pumping of sediment to more distal locations and if the cumulative source to sink movement of the depocenter is in phase with imposed sea level cycles. To accomplish this I generate mass extraction curves as a function of downstream distance for each experimental stage. I use the Paola and Martin (2012)

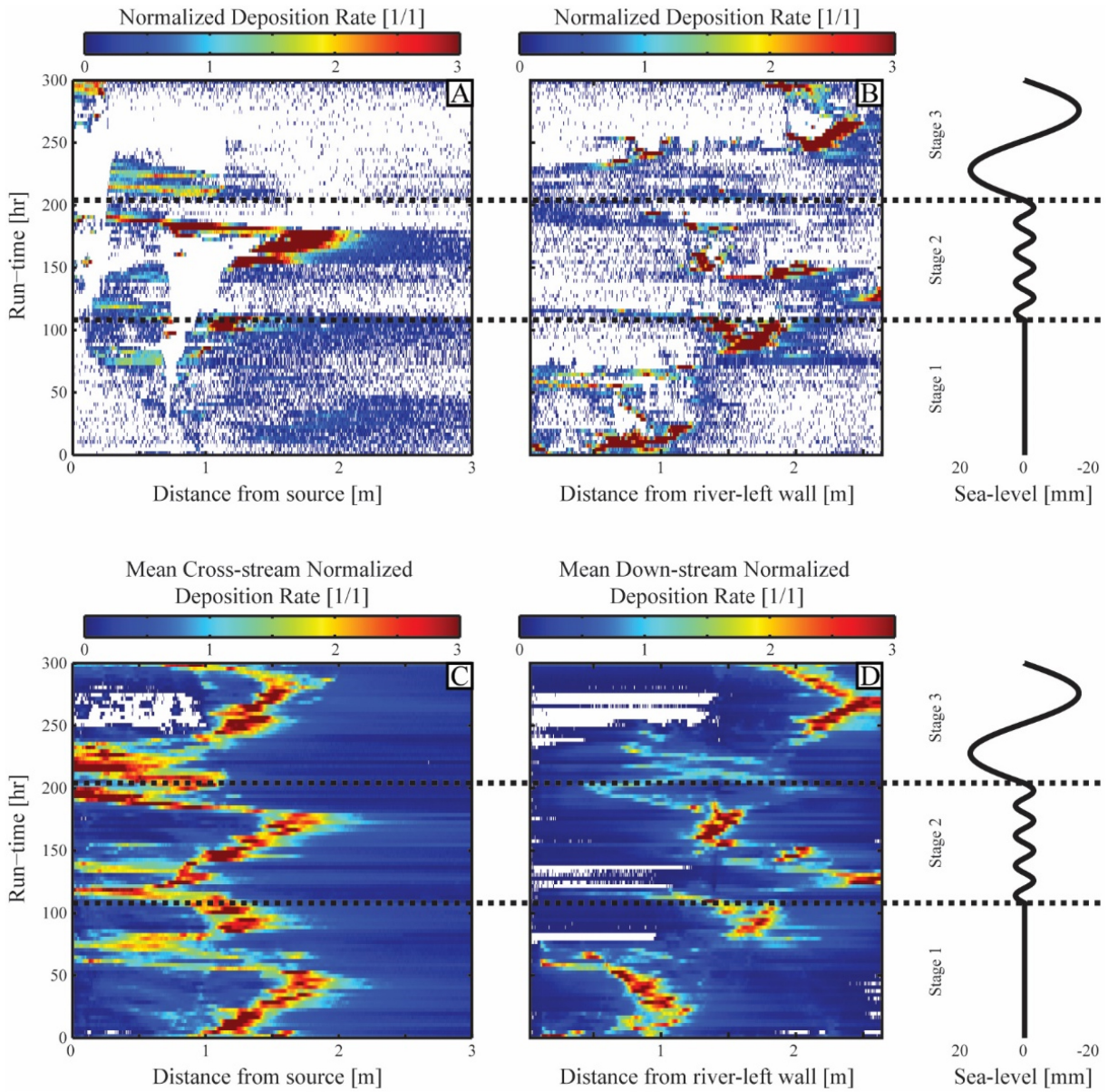

FIGURE 6 | Modified Wheeler diagrams detailing how mean deposition rate varies both with distance from source, lateral position in basin and run time. **(A)** Wheeler diagram generated from a single dip section down the basin centerline (transect A–C in **Figure 5**). **(B)** Wheeler diagram generated from a single strike transect located at the location of the shelf-edge at the beginning of the experiment (transect G–H in **Figure 5**). **(C)** Mean dip oriented Wheeler diagram generated from the average of all dip transects in the topographic maps. **(D)** Mean strike oriented Wheeler diagram generated from the average of all strike transects in the topographic maps. White locations on Wheeler diagrams represent stratigraphic hiatuses. Black dashed lines demarcate stage breaks and experimental sea level history is shown to aid analysis of time-space information.

definition of mass extraction as the total sediment flux lost to deposition up to a distance of interest, x, from the source normalized by the input sediment flux to the basin, Q_{S0}:

$$\chi(x) = \frac{1}{Q_{S0}} \int_0^x B(x)\overline{D}(x)dx \tag{5}$$

Where $B(x)$ is the width of the basin at location x. A tangible example of this transformation is $\chi(x) = 0.5$, where half of the sediment input to the basin is deposited upstream of location x and half of the sediment is still in flux. $\chi(x) = 0.5$ also represents the depositional midpoint of the basin (Paola and Martin, 2012).

I start the analysis of mass extraction by generating bulk $\chi(x)$ curves for each stage (**Figure 7A**). This is done with an isopach map generated by differencing topography at the end of each experimental stage from the topography at the start of the stage. The shape of the $\chi(x)$ curves is similar for the three

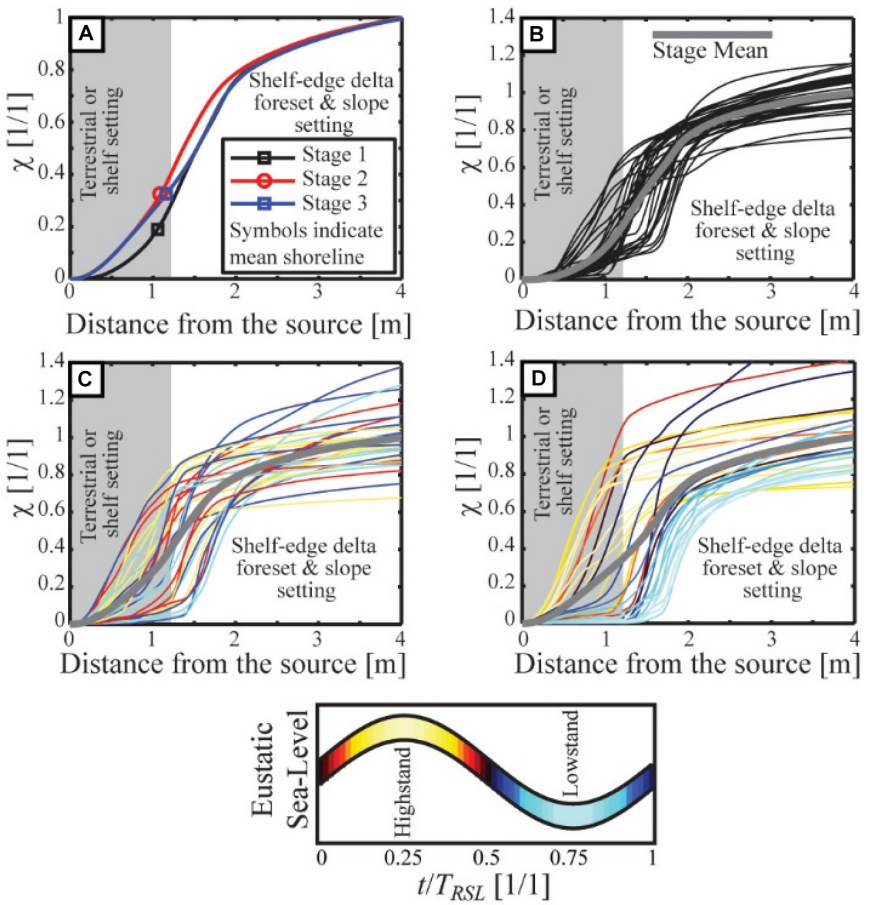

FIGURE 7 | Relationship between distance from source and mass extraction for experimental deposit. **(A)** $\chi(x)$ curve for bulk stage deposits with position of mean shoreline noted for each stage. **(B)** $\chi(x)$ curves for each 3 h window between topographic scans in stage 1, thick solid gray line is the mean stage trend. **(C,D)** $\chi(x)$ curves for 3 h windows between topographic scans in stage 2 and 3, respectively. Color of curve corresponds to time of sample window with respect to a sea level cycle and solid gray lines show the mean stage trends.

stages with an initial slow growth of $\chi(x)$ over distances from the sediment source that were typically delta-top environments. Then a rapid growth in $\chi(x)$ is observed between 1 and 2 m from the basin entrance, which was typically delta foreset and upper slope. Finally, $\chi(x)$ slowly grows over 2–4 m from the source, which was always a marine slope environment. Using the DEM database, I also calculate the average distance from the basin entrance to the shoreline for each stage and post this on the $\chi(x)$ curves (**Figure 7**). This allows me to measure the mass portioning between dominantly terrestrial and dominantly marine settings in each stage. I find that in stage 1, 19% of the input mass was deposited in the terrestrial, while both stages 2 and 3 had 32% of the input mass deposited in the terrestrial. The biggest difference in the $\chi(x)$ curves of the three stages is the slow initial growth of $\chi(x)$ in stage 1 relative to stage 2 and 3. The distance from the entrance to the mean shoreline is near identical for all stages, but the sediment extracted inbound of the shoreline is less in stage 1 relative to stages 2 and 3. This is likely linked to the long lived and relatively stable channel that was present through much of stage 1, which efficiently pumped sediment to the marine.

Next I calculate $\chi(x)$ curves for each sequential set of DEMs, following the clipping process for post-depositional erosion. This serves two purposes: (1) to characterize the amount of variability in the location of mass extraction due to both autogenic and allogenic reorganization of channel networks and (2) to identify if position in a sea level cycle results in predictable changes in the mass extraction trend. Regarding point 2, minus autogenic dynamics I might expect that sea level would be correlated with the proximal-distal trend of mass extraction: lower sea level might result in proximal bypass and more distal mass extraction, relative to the mean $\chi(x)$ curve of a sea level cycle.

A comparison of stage 1 and 2 suggest a similar amount of variability in $\chi(x)$ curves around the mean trend (**Figures 7B,C**). χ sometimes exceeds a value of 1 in these curves due to erosion and redeposition of previously deposited sediment, which can result in a greater volume of sediment deposited and preserved in a given 3 h period than input to the basin during that same time. A greater spread around the mean is observed for the $\chi(x)$ curves of stage 3 (**Figure 7D**), suggesting an imprint of the forcing that exceeds the stochastic variability.

The position within a sea level cycle does not produce predictable shifts in $\chi(x)$ curves for the low magnitude, short period cycles of stage 2. While some periods of low sea level correspond to a basinward shift in the mass extraction trend, relative to the mean stage trend, other periods of low sea level are associated with enhanced proximal mass extraction relative to the mean trend (**Figure 7C**). In contrast, a clear and predictable response of $\chi(x)$ is seen in stage 3 with low RSL associated with more distal mass extraction and vice versa (**Figure 7D**).

Earlier in the description of the synthetic stratigraphic panels I noted a general trend of a reduction in preserved strata deposited in highstand conditions and an increase in preserved lowstand strata with movement from source to sink. My goal here is to quantify this trend. This is done with a calculation of a parameter, α_D, first presented by Yu et al. (2017) which quantifies when, on average, during a sea level cycle deposition occurs, and how this changes as a function of mass extraction location. This metric is constructed as:

$$\alpha_D = \frac{1}{N}\sum_{i=1}^{N}\left(\frac{\overline{D_i}(\chi)}{\bar{r}}\frac{\eta_{SL,\,i}}{M_{RSL}/2}\right) \tag{6}$$

Where $\overline{D_i}(\chi)$ is the mean thickness of strata deposited during run hour i at a mass extraction location χ, $\eta_{SL,\,i}$ is the sea level during run hour i and N is the total number of run hours analyzed. For strata deposited during a given RSL cycle, α_D theoretically could take any value between -1 and 1. In descriptive terms, a value of -1 would represent a deposit at a mass extraction location of interest that was constructed only when sea level was at the trough of a cycle, while a value of 1 would represent deposits constructed only when sea level was at the peak of a cycle.

As no sea level cycles were present in stage 1, α_D remains a constant value of 0 for all χ locations. In stages 2 and 3 α_D is a positive value inbound of the mean stage shoreline suggesting a preference for highstand deposition (**Figure 8**). In both stages this preference increases with distance from the source until reaching peak values. However, the peak in α_D is significantly higher in stage 3 compared to stage 2 indicating rapid deposition in proximal locations during highstand conditions for large magnitude sea level cycles. At more distal mass extraction locations this trend is reversed. Between χ locations of 0.6 – 0.8, I observe negative α_D values in both stages, with the trend reaching lower values in stage 3 compared to stage 2. This indicates a preference for rapid marine deposition during lowstand conditions increases with the magnitude of a sea level cycle. Toward the end of the transport system, α_D starts to rise back toward 0, suggesting a loss in preference for deposition as a function of location in a sea level cycle. However, it should be denoted that at these extremely distal locations the deposit thickness drops dramatically, likely making identification of this signal in field scale systems difficult.

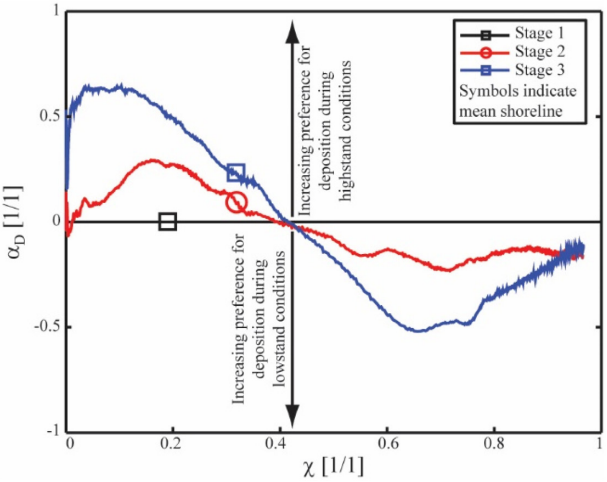

FIGURE 8 | Data defining average position within a sea level cycle in which sediment is deposited as a function of distance from basin entrance. Symbols indicate position of mean shoreline for each stage.

DISCUSSION

I start with a general summary of my experimental findings and a comparison to the observations from the numerical experiments of Harris et al. (2016, 2018). For this comparison I loosely upscale the experimental stages to field conditions using the emergent experimental autogenic scales. Here I provide a rough upscaling to a Mississippi River scale system by assuming similarity in morphodynamic response between experimental (denoted with e) and prototype (denoted with p) systems that share dimensionless ratios that compare autogenic and allogenic scales. I stress that, as with all stratigraphic experiments, this experiment is not a simulation of any one particular system as it is challenging to match many important dimensionless numbers that describe the flow and sediment transport fields when comparing lab to field systems. However some emergent geomorphic scales and the scale invariance of many processes allow some dynamics to be compared to field systems (Paola et al., 2009). As such, this comparison gives a rough feel for the time scales and responses that should be expected for field scale systems.

I start with upscaling the magnitude of the experimental sea level cycles:

$$\frac{M_{RSL,\,e}}{H_{C,\,e}} = H^* = \frac{M_{RSL,\,p}}{H_{C,\,p}} \tag{7}$$

Given that deep autogenic sections of the Mississippi River in its backwater reach are ∼50 m in depth (Nittrouer et al., 2012), the stage 2 and 3 sea level cycles scale to 25 and 100 m, respectively.

Next I upscale the duration or period of the experimental sea level cycles using the following relationship:

$$\frac{T_{RSL,\,e}}{T_{C,\,e}} = T^* = \frac{T_{RSL,\,p}}{T_{C,\,p}} \tag{8}$$

Using Equation 2 and a $\overline{r_D}$ value for the Mississippi River reported from biostratigraphic dates ($\overline{r_D}$ = 0.26 m/kyr) (Straub et al., 2009) the stage 2 and 3 sea level cycles scale to 96 and 384 kyrs, respectively.

The scaling above, however, only holds for the autogenic scales of the Mississippi River Delta. If we apply Equations 7, 8 to

compare our stages 2 and 3 to the Rhine River Delta, which has H_c and $\overline{r_D}$ values of 7 m and 1.2 mm/yr respectively (Zagwijn, 1989; Hijma et al., 2009), we get significantly different scaling. For the Rhine Delta, my stage 2 and 3 sea level cycles scale to 3.5 and 14 m with durations of 2.9 and 11.7 kyrs, respectively. The comparison of the Mississippi and Rhine River Delta systems suggest the following. First, not all river deltas respond to a given sea level cycle in the same way. Larger systems, with their larger autogenic scales, will be less sensitive to sea level cycles compared to their smaller neighboring systems. This point has been highlighted in a number of recent studies (Li et al., 2016; Yu et al., 2017; Trower et al., 2018). Second, these results suggest that care should be taken in universally applying one set of rules to icehouse condition deltas and another to greenhouse condition deltas. For example, the response of larger deltas with autogenic scales similar to icehouse sea level cycles might be similar to the response of smaller systems to high frequency and low magnitude greenhouse scale sea level cycle, like those proposed for the Late Cretaceous and earlier Paleogene (Tibert and Leckie, 2004; Miller, 2009). Third, while some large systems in icehouse conditions might behave like smaller systems in greenhouse conditions, on average the autogenic scales of deltas will be larger, relative to the scales of imposed sea level cycles, during greenhouse conditions and thus on average less sensitive to those cycles. This will facilitate more continuous connections between terrestrial and slope conditions during these times, similar to what has been proposed from numerical modeling studies (Sømme et al., 2009a).

Linking Mass Partitioning Along Source to Sink Profiles to Sea Level Cycles

In our experiments the relationship between mass extraction and physical distance from basin entrance was near identical in the three experimental stages (**Figure 7A**). The stage that pumped the most sediment to the marine was the one that lacked any sea level cycles, however this difference was only 13%. This increase in pumping of sediment to the marine in stage 1 can be linked to the long lived and relatively stable channel present for more than half of this stage. This channel produced a delta lobe that protruded far past the initial shelf-slope break. This is in line with a previous experiment that observed a stabilization of channels that are able to pump their sediment into deep waters (Kim et al., 2013). While avulsions still occur after this shelf-edge docking, their frequency is thought to be reduced, thus facilitating sediment flux to the marine.

The similarity in the $\chi(x)$ mean trend of stage 2 and 3 is striking and supports the notion that partitioning of sediment along a source to sink transect is largely driven by the long term basin accommodation production trend. By long-term, I mean time scales important for generation of basin subsidence, which exceed most Milinkovic sea level cycle fluctuations. While the bulk mass extraction trends for individual stages are similar (**Figure 7A**), my analysis of the average position within a sea level cycle during which preserved strata was constructed (**Figure 8**) suggest a preference for terrestrial strata constructed during highstands and marine strata constructed during lowstands. This preference is muted in the low magnitude and short period cycles of stage 2 in comparison to the high magnitude and long period cycle of stage 3, but still present.

It is important to note that the preference for terrestrial deposition during highstands and marine deposition during lowstands, apparent in our α_D analysis, is a time averaged result. Specifically, the signal present in the stage 2 deposit is the average result of the four cycles in this stage. Without excellent time control, this signal might be difficult to tease out from stratigraphic architecture constructed in marginal marine settings forced with small magnitude and short period sea level cycles. For example, the experimental transport system experiencing stage 2 scale sea level cycles did not always produce predictable products of the allogenic forcing. The variability in the short term mass extraction trends of stage 2 was similar to the variability in the mass extraction curves of the autogenic stage 1 (**Figures 7B,C**), which suggest that their stratigraphic architecture was also similar. In addition, lowstand conditions in stage 2 did not always force a basinward movement of the transport system. In contrast, the high magnitude and long period sea level cycle of stage 3 produced a predictable movement of the depocenter with position in a sea level cycles and the changes in the location of mass extraction during lowstand (or highstand) conditions exceeded the autogenic stochastic variability in depocenter location (**Figure 7D**).

I now return to the observations from numerical experiments detailed in the set of papers by Harris et al. (2016, 2018). An exact comparison of the numerical experiments of Harris et al. (2016, 2018) to our physical experiment is not possible due to experimental scaling parameters. In addition, the channel depths in the numerical experiments of Harris et al. are unknown, making estimation of H^* and T^* for their numerical experiments imprecise. However, many of their modeled sea level cycles are less than 30 m in magnitude and occur over less than 100 kyr in a domain with forcing conditions motivated by the passive margin of the northeast United States. This might suggest H^* and T^* values close to 1.

The physical experimental results support the finding of Harris et al. (2016, 2018) that only a small difference in sediment delivery exists between systems forced with constant vs. dynamic sea level histories. For systems experiencing sea level cycles that are small relative to their autogenic scales, the timing of sediment delivery to the marine does have a preference for lowstand conditions. Similar to the findings of Harris et al. (2016), I note that this response can be variable, and due to autogenic processes sometimes the opposite of those predicted by purely allogenic models. For example, the channel that formed between the second and third sea level cycles of stage 2 was able to keep sediment delivery to the marine high, even as sea level rose. This channel was similar to some of the autogenic stage 1 channels and its growth rate allowed it to continue to extend, even under long term shoreline transgression of the rest of the delta. However, the response to sea level cycles that are large in comparison to the system's autogenic scales seem to be predictable and in line with long standing theory (Van Wagoner et al., 1990). Large drops in sea level correlate with pronounced basinward

movement of the depocenter and increased sediment delivery to the marine. For a Mississippi scale system, this would mean sea level cycles with amplitudes in excess of 50 m and/or periods in excess of 200 kyrs. However, as previously mentioned, these scales will vary with the size of a system as autogenic time and space scales typically correlate with system size (Hajek and Straub, 2017). Thus smaller systems will more easily produce detectable responses in the delivery of sediment to the marine compared to a larger system exposed to the same sea level cycle (Li et al., 2016).

Pumping of Sediment Past Experimental Delta Foresets

A key point to highlight from the system described here is the difficulty in pumping sediment past delta foresets in physical experiments. The experimental design was crafted to promote pumping of sediment past shelf-edge delta fronts to continental slope settings. These conditions included frequent flood events and an input flow that had excess density relative to the receiving basin. Even with these design parameters ∼80% of the input sediment was stored in the delta top and foreset. In comparison, a detailed seismic analysis of a shelf-edge delta and linked submarine channels in the northeastern Gulf of Mexico found a 50:50 split between shelf and slope volumes (Sylvester et al., 2012). Clearly, more work is necessary to identify the experimental parameter space necessary to promote flux of high sediment volumes to the marine.

While the flux of sediment past delta foresets is not as high as some systems, I can still compare the resulting slope isopachs in the three stages. Stage 1 and 2 share similar slope deposits and volumes (**Figures 9A,B**) that were spread over the full width of the platform. In comparison, the high magnitude and long period sea level cycle of stage 3 produced a slope deposit that was more isolated in lateral extent, but with thicker deposits at distal locations compared with the other stages (**Figure 9C**).

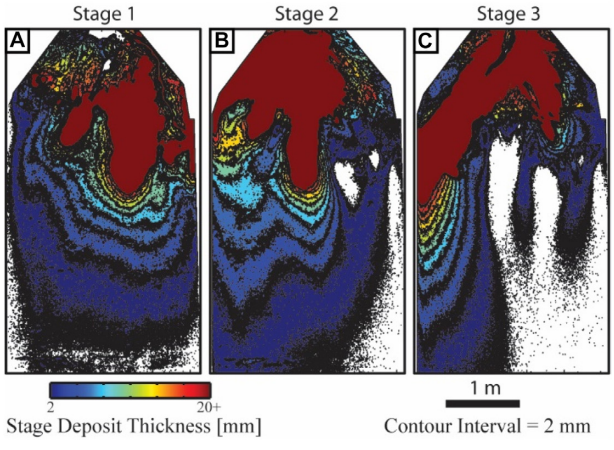

FIGURE 9 | Maps highlighting deposit thickness trends on experimental slope for three experimental stages. Colorbar limits set to highlight slope deposit patterns with a 2 mm contours overlain.

CONCLUSION

The key results, which directly relate to the development of process-based theory for source-to-sink sediment routing systems, are twofold:

(1) Results from a physical experiment on linked shelf-edge delta and slope systems suggest that the scale of sea level cycles does not strongly influence the pumping of sediment to the marine, if one averages sediment delivery over a full cycle. This delivery of sediment to the marine is similar to systems with no sea level cycles, which due to long autogenic scales when deltas dock at shelf-edge, can actually have sustained rates of deepwater sediment delivery for long periods.

(2) While the magnitude and period of sea level cycles does not influence the long term delivery of sediment to the marine (i.e., a rate averaged over an entire RSL cycle), these parameters do influence the timing of deep marine sediment delivery. Sea level cycles with scales in excess of autogenic dynamic scales produce predictable responses during a sea level cycle with maximum delivery during ultimate lowstands. In contrast, sea level cycles with scales less than autogenic scales produce varied responses. On average marine sedimentation is delivered during lowstands for small cycles, but this response can sometimes be flipped, with high marine delivery during highstands. The handoff between predictable to stochastic response can be on the order of 50 m and 200 kyrs for large river systems.

DATA AVAILABILITY

The datasets generated for this study are available on request to the corresponding author.

AUTHOR CONTRIBUTIONS

The author confirms being the sole contributor of this work and has approved it for publication.

FUNDING

This study was supported in part by the National Science Foundation (EAR-1424312).

ACKNOWLEDGMENTS

I thank the past and present members of the Tulane Sediment Dynamics and Stratigraphy Laboratory, particularly Anjali Fernandes and Tushar Bishnoi, for the help in setting up the experimental initial conditions and for the help in cutting the final deposit. Finally, I thank the editors DH and Julie Fosdick for handling the submission, and the reviewers JB and KM for the reviews that helped to increase the clarity of the manuscript.

REFERENCES

Allen, P. A. (2008). "Time scales of tectonic landscapes and their sediment routing systems", in *Landscape Evolution: Denudation, Climate and Tectonics Over Different Time and Space Scales Gallager*, K., Jones, and Wainwright, J. London: Geological Society Of London

Allen, P. A. (2017). *Sediment Routing Systems: The Fate of Sediment From Source to Sink*, Cambridge: Cambridge University Press.

Cantelli, A., Pirmez, C., Johnson, S., and Parker, G. (2011). Morphodynamic and stratigraphic evolution of self-channelized subaqueous fans emplaced by turbidity currents. *J. Sediment. Res.* 81, 233–247. doi: 10.2110/jsr.2011.20

Catuneanu, O., Abreu, V., Bhattacharya, J. P., Blum, M. D., Dalrymple, R. W., Eriksson, P. G., et al. (2009). Towards the standardization of sequence stratigraphy. *Earth Sci. Rev.* 92, 1–33.

Gilbert, G. K. (1890). *Lake Bonneville, U.S. Geologic Survey Monograph 1*. Washington, D.C, U.S. Government Printing Office

Granjeon, D. (1999). *Concepts and Applications of a 3-D Multiple Lithology, Diffusive Model in Stratigraphic Modeling*. France: Special Publications of SEPM

Hajek, E. A., and Straub, K. M. (2017). Autogenic sedimentation in clastic stratigraphy. *Ann. Rev. Earth Planet. Sci.* 45, 681–709. doi: 10.1146/annurev-earth-063016-015935

Hamilton, P., Gaillot, G., Strom, K., Fedele, J., and Hoyal, D., (2017). linking hydraulic properties in supercritical submarine distributary channels to depositional-lobe geometryP. hamilton et al. linking hydraulic properties in submarine channels to depositional-lobe geometry. *J. Sediment. Res.* 87, 935–950. doi: 10.2110/jsr.2017.53

Harris, A. D., Covault, J. A., Madof, A. S., Sun, T., Sylvester, Z., and Granjeon, D. (2016). Three-dimensional numerical modeling of eustatic control on continental-margin sand distributionA. d. harris et al. numerical modeling of eustatic control on continental-margin sand distribution. *J. Sediment. Res.* 86, 1434–1443. doi: 10.2110/jsr.2016.85

Harris, A. D., Baumgardner, S. E., Sun, T., and Granjeon, D. (2018). A poor relationship between sea level and deep-water sand delivery. *Sediment. Geol.* 370, 42–51. doi: 10.1016/j.sedgeo.2018.04.002

Hijma, M. P., Cohen, K., Hoffmann, G., Van der Spek, A. J., and Stouthamer, E. (2009). From river valley to estuary: the evolution of the Rhine mouth in the early to middle Holocene (western Netherlands, Rhine-Meuse delta). *Netherlands J. Geosci.* 88, 13–53. doi: 10.1017/s0016774600000986

Hoyal, D. C. J. D., and Sheets, B. A. (2009). Morphodynamic evolution of experimental cohesive deltas. *J. Geophys. Res. Earth Surf.* 114:F02009

Jerolmack, D. J., and Sadler, P. (2007). Transience and persistence in the depositional record of continental margins. *J. Geophys. Res. Earth Surf.* 112:F03S13.

Kim, W., Petter, A., Straub, K., and Mohrig, D. (2014). "Investigating the autogenic process response to allogenic forcing: Experimental geomorphology and stratigraphy": *From Depositional Systems to Sedimentary Successions on the Norwegian Continental Margin*, ed J. P. Wonham A. W. Martinius, Hoboken: John Wiley & Sons, Ltd, 127–138. doi: 10.1002/9781118920435.ch5

Kim, Y., Kim, W., Cheong, D., Muto, T., and Pyles, D. R. (2013). Piping coarse-grained sediment to a deep water fan through a shelf-edge delta bypass channel: tank experiments. *J. Geophys. Res. Earth Surf.* 118, 2279–2291. doi: 10.1002/2013jf002813

Li, Q., Yu, L., and Straub, K. M. (2016). Storage thresholds for relative sea-level signals in the stratigraphic record. *Geology* 44, 179–182. doi: 10.1130/g37484.1

Li, Q., Matthew Benson, W., Harlan, M., Robichaux, P., Sha, X., Xu, K., et al. (2017). Influence of sediment cohesion on deltaic morphodynamics and stratigraphy over basin-filling time scales. *J. Geophy. Res. Earth Surf.* 122, 1808–1826. doi: 10.1002/2017jf004216

Miller, K. G. (2009). Palaeoceanography: broken greenhouse windows. *Nat. Geosci.* 2:465. doi: 10.1038/ngeo563

Mohrig, D., Heller, P. L., Paola, C., and Lyons, W. J. (2000). Interpreting avulsion process from ancient alluvial sequences: Guadalope-Matarranya (northern Spain) and wasatch formation (western Colorado). *Geol. Soc. Am. Bull.* 112, 1787–1803.

Nittrouer, J. A., Shaw, J., Lamb, M. P., and Mohrig, D. (2012). Spatial and temporal trends for water-flow velocity and bed-material sediment transport in the lower mississippi river. *Geol. Soc. Am. Bull.* 124, 400–414. doi: 10.1130/b30497.1

Paola, C., Straub, K. M., Mohrig, D., and Reinhardt, L. (2009). The "unreasonable effectiveness" of stratigraphic and geomorphic experiments. *Earth Sci. Rev.* 97, 1–43. doi: 10.1016/j.earscirev.2009.05.003

Paola, C., and Martin, J. M. (2012). Mass-balance effects in depositional systems. *J. Sediment. Res.* 82, 435–450. doi: 10.1016/j.jenvrad.2016.07.028

Paola, C. (2016). A mind of their own: recent advances in autogenic dynamics in rivers and deltas. *SEPM Spec. Publ.* 106, 5–17. doi: 10.2110/sepmsp.106.04

Porębski, S. J., and Steel, R. J. (2003). Shelf-margin deltas: their stratigraphic significance and relation to deepwater sands. *Earth Sci. Rev.* 62, 283–326. doi: 10.1016/s0012-8252(02)00161-7

Sømme, T. O., Helland-Hansen, W., and Granjeon, D. (2009a). Impact of eustatic amplitude variations on shelf morphology, sediment dispersal, and sequence stratigraphic interpretation: Icehouse versus greenhouse systems. *Geology* 37, 587–590. doi: 10.1130/g25511a.1

Sømme, T. O., Helland-Hansen, W., Martinsen, O., and Thurmond, J. (2009b). Relationships between morphological and sedimentological parameters in source-to-sink systems: a basis for predicting semi-quantitative characteristics in subsurface systems. *Basin Res.* 21, 361–387. doi: 10.1111/j.1365-2117.2009.00397.x

Straub, K. M., Mohrig, D., McElroy, B., Buttles, J., and Pirmez, C. (2008). Interactions between turbidity currents and topography in aggrading sinuous submarine channels: a laboratory study. *Geol. Soc. Am. Bull.* 120, 368–385. doi: 10.1130/b25983.1

Straub, K. M., Paola, C., Mohrig, D., Wolinsky, M. A., and George, T. (2009). Compensational stacking of channelized sedimentary deposits. *J. Sediment. Res.* 79, 673–688. doi: 10.2110/jsr.2009.070

Straub, K. M., Mohrig, D., and Pirmez, C., (2012). Architecture of an aggradational tributary submarine-channel network on the continental slope offshore Brunei Darussalam, in *Application Of Seismic Geomorphology Principles To Continental Slope And Base-Of-Slope Systems: Case Studies From Seafloor And Sub-Seafloor Analogues* eds B. E., Prather M. E., Deptuck D., Mohrig, B., van Hoorn and R. B., Wynn Tulsa: Society for Sedimentary Geology

Straub, K. M., Li, Q., and Benson, W. M. (2015). influence of sediment cohesion on deltaic shoreline dynamics and bulk sediment retention: a laboratory study. *Geophys. Res. Lett.* 42, 9808–9815. doi: 10.1002/2015gl066131

Sweet, M. L., and Blum, M. D. (2016). Connections between fluvial to shallow marine environments and submarine canyons: implications for sediment transfer to deep water. *J. Sediment. Res.* 86, 1147–1162. doi: 10.2110/jsr.2016.64

Sylvester, Z., Deptuck, M., Prather, B., Pirmez, C., O'Byrne, C., Mohrig, D., et al. (2012). Seismic stratigraphy of a shelf-edge delta and linked submarine channels in the northeastern gulf of mexico: application of the principles of seismic geomorphology to continental-slope and base-of-slope systems: case studies from seafloor and near-seafloor analogues. *SEPM Spec. Publ.* 99, 31–59. doi: 10.2110/pec.12.99.0031

Tibert, N. E., and Leckie, R. M. (2004). High-resolution estuarine sea level cycles from the Late Cretaceous: Amplitude constraints using agglutinated foraminifera. *J Foram. Res.* 34, 130–143. doi: 10.2113/0340130

Trower, E. J., Ganti, V., Fischer, W. W., and Lamb, M. P. (2018). Erosional surfaces in the upper cretaceous castlegate sandstone (Utah, USA): sequence boundaries or autogenic scour from backwater hydrodynamics?. *Geology* 46, 707–710. doi: 10.1130/g40273.1

Vail, P. R., Mitchum, R. M., and Thompson, S., III. (1977). "Seismic stratigraphy and global changes of sea-level: Part 3. Relative changes of sea level from coastal onlap", in *Seismic Stratigraphy - Applications to Hydrocarbon Exploration* ed C. E., Payton Tulsa AAPG Memoir 63–82.

Van Wagoner, J. C., Mitchum, R. M., Campion, K. M., and Rahmanian, V. D. (1990). *Siliciclastic Sequence Stratigraphy in Well Logs, Cores, and Outcrops: Concepts for High-Resolution Correlation of Time and Facies*: Tulsa: American Association of Petroleum Geologists:

Vendettuoli, D., Clare, M., Clarke, J. H., Vellinga, A., Hizzet, J., Hage, S., et al. (2019). Daily bathymetric surveys document how stratigraphy is built and its extreme incompleteness in submarine channels. *Earth. Planet. Sci. Lett.* 515, 231–247. doi: 10.1016/j.epsl.2019.03.033

Wang, Y., Straub, K. M., and Hajek, E. A. (2011). Scale-dependent compensational stacking: An estimate of autogenic time scales in channelized sedimentary deposits: *Geology* 39, 811–814. doi: 10.1130/g32068.1

Wheeler, H. E. (1964). Baselevel, lithosphere surface, and time-stratigraphy. *Geol. Soc. Am. Bull.* 75, 599–610.

Xu, J. P., Nobel, M. A., and Rosenfeld, L. K., (2004). In-situ measurments of velocity structure within turbidity currents. *Geophys. Res. Lett.* 31:L09311

Yu, L., Li, Q., and Straub, K. M. (2017). Scaling the response of deltas to relative-sea-level cycles by autogenic space and time scales: a laboratory study. *J. Sediment. Res.* 87, 817–837. doi: 10.2110/jsr.2017.46

Zagwijn, W. H. (1989). The Netherlands during the tertiary and quaternary. a case history of coastal lowland evolution. *Geol. En Mijnbouw* 68, 107–120. doi: 10.1007/978-94-017-1064-0_6

Conflict of Interest Statement: The author declares that the research was conducted in the absence of any commercial or financial relationships that could be construed as a potential conflict of interest.

frontiers in Earth Science

PERSPECTIVE
published: 03 July 2019
doi: 10.3389/feart.2019.00164

Quantifying Biogenic Versus Detrital Carbonates on Marine Shelf: An Isotopic Approach

V. Pasquier[1,2], S. Revillon[2,3], E. Leroux[4], S. Molliex[2,5], L. Mocochain[6] and M. Rabineau[2]*

[1] Department of Earth and Planetary Sciences, Weizmann Institute of Science, Rehovot, Israël, [2] Laboratoire Geosciences Océan LGO, UMR 6538 (CNRS/Univ Brest/Univ Bretagne Sud), IUEM, Plouzané, France, [3] SEDISOR, IUEM, Plouzané, France, [4] IFREMER, Laboratoire Géodynamique et enregistrement Sédimentaire, Plouzané, France, [5] CRPG, UMR 7358, CNRS-Université de Lorraine, Vandœuvre-lès-Nancy, France, [6] Sorbonne Université, Institut des Sciences de la Terre de Paris (ISTeP), Paris, France

The terrigenous sedimentary budget of passive margins, records variations in past sedimentary fluxes, and thus can be used to infer past variations of Earth surface deformation processes or climate change. Accurate estimates of sediment fluxes over various times and spatial scales are therefore crucial. Traditionally, offshore sediment volume determination only considers siliciclastic accumulation, the carbonate fraction (i.e., $CaCO_3$) being considered only as *in situ* production. Here we propose a new geochemical methodology to decipher and quantify the number of detrital carbonates in comparison to *in situ* produced biogenic carbonates. This isotopic approach enables considering the export of detrital carbonates and investigating its effect on sediment budgets. This study, located in the Gulf of Lion, is based on a 300 m long sediment borehole located near the shelf break and covering the last 500 000 years (i.e., five glacial-interglacial periods). Strontium isotope ($^{87}Sr/^{86}Sr$) of carbonate fractions (0.70809 to 0.70858) are significantly less radiogenic than modern seawater (i.e., 0.7092) and show fluctuations in agreement with stratigraphic and climatic variations. These results suggest an unsuspected high export of detrital carbonates from the catchment area during both glacial (between 55 and 85% of the sedimentary carbonate fraction) and interglacial (between 30 and 50%) conditions. Thus, not only do detrital carbonate fluxes need to be factored into sediment flux calculations, but these results also suggest that detrital carbonate components could potentially have a strong influence on bulk carbonate $^{87}Sr/^{86}Sr$ ratios when not obtained from micro drilled biogenic carbonates, such as the entirety of the Precambrian Sr chemostratigraphic record.

Keywords: $^{87}Sr/^{86}Sr_{carbonate}$, detrital carbonate export, source-to-sink, glacial – interglacial, strontium isotope stratigraphy

OPEN ACCESS

Edited by:
Brian W. Romans,
Virginia Tech, United States

Reviewed by:
Lars Reuning,
University of Kiel, Germany
Mike Rogerson,
University of Hull, United Kingdom

****Correspondence:***
V. Pasquier
virgil.pasquier@weizmann.ac.il

Specialty section:
This article was submitted to Sedimentology, Stratigraphy and Diagenesis, a section of the journal Frontiers in Earth Science

Received: *06 March 2019*
Accepted: *07 June 2019*
Published: *03 July 2019*

Citation:
Pasquier V, Revillon S, Leroux E, Molliex S, Mocochain L and Rabineau M (2019) Quantifying Biogenic Versus Detrital Carbonates on Marine Shelf: An Isotopic Approach. Front. Earth Sci. 7:164. doi: 10.3389/feart.2019.00164

INTRODUCTION

An extensive dataset has been collected over the last decade on marine carbonates and fossils, to document past variations in the strontium isotopic composition record ($^{87}Sr/^{86}Sr$), as a tool to reconstruct changes in the seawater composition through Earth's history. These past variations are of interest for two reasons: first, $^{87}Sr/^{86}Sr$ ratios measured on marine carbonate offer a widely

used chronostratigraphic tool (SIS – Strontium Isotope Stratigraphy; for reviews of SIS the readers should referred to Elderfield, 1986; McArthur, 1994; Veizer et al., 1997, 1999; McArthur et al., 2012); second, secular changes in Sr isotope composition provide information about the geochemical cycling of strontium in the ocean, weathering processes, hydrothermal circulation, and carbonate dissolution at the sea-floor (Burke et al., 1982; De Paolo and Ingram, 1984; Veizer, 1989; Prokoph et al., 2008; Allègre et al., 2010 among others).

Since the rapid increase of calcifying organisms (i.e., Mesozoic), the SIS method relies on two assumptions: (i) strontium isotopes composition measurements from well preserved, non-altered, shell material (i.e., bivalves, rudist, belemnites, planktonic foraminifera) are assumed to reflect the seawater Sr isotope composition from which they precipitated (Veizer, 1989; McArthur et al., 2012); (ii) the world's ocean is homogenous with respect to $^{87}Sr/^{86}Sr$, and always has been. Such uniformity is expected because Sr residence time in the ocean (4 Myr; Broeker, 1963; Goldberg, 1963; Hodell et al., 1990) is far longer than their mixing time ($\sim 10^3$ years). Since the 1980s, the SIS tool relies on the extensive compilation of data, cross calibration between carbonate producers (ammonites, foraminifera, calcareous nannofossils) and/or other geochemical proxies ($\delta^{13}C$, $\delta^{18}O$). Extensive compilations of measured $^{87}Sr/^{86}Sr$ in marine material yield to the development of numerical age determination tools (McArthur et al., 2012 for a thorough review). The degree to which SIS numerical dating is correct mostly depends on the slope and the accuracy of the age model during the given time interval, as well as the quality and state of preservation of the studied material. Given the difficulty of dating sedimentary material, especially during the Paleozoic and Precambrian era, it could be tempting to use a "bulk" SIS approach by measuring the $^{87}Sr/^{86}Sr$ ratio of the entire carbonate fraction preserved in the sediment. However, such a carbonate component may not necessarily entirely be produced *in situ* and could include a significant detrital proportion. If so, not only would the SIS-derived ages be biased, but the inferred flux of detrital material to total sediment would also be underestimated. This is of great importance when calculating sedimentation rates in stratigraphic simulations studies (Allen, 1974; Castelltort and Van Den Driessche, 2003; Allen, 2008; Armitage et al., 2011, 2013; Simpson and Castelltort, 2012; Romans et al., 2016); but also when reconstructing temporal variations in the marine $^{87}Sr/^{86}Sr$ or to understand the relative Sr fluxes related to continental weathering versus hydrothermal inputs over time (e.g., Burke et al., 1982; Veizer, 1989; Veizer et al., 1999; Halverson et al., 2007; Prokoph et al., 2008).

In this study, we examined the Sr isotope compositions preserved in the sediment carbonate fractions from the Gulf of Lion which were deposited during one glacial advance and the following retreat between 160 to 120 ka, i.e., over the MIS 6 to MIS 5 transition. The goals of this exploratory project were first to test whether detrital carbonates could be preserved in shelf accumulation and developed an isotopic approach that could help in their quantification. We secondly explore their potential effect on sedimentary fluxes calculations.

GEOLOGICAL BACKGROUND AND ANALYTICAL RESULTS

The Gulf of Lion (GoL), located in the North-Western Mediterranean, is characterized by a wide continental shelf (70 km) that was sub-aerially exposed during glacial periods over the Late Quaternary period (Rabineau et al., 2005). The sedimentation is mainly dominated by the Rhône River inputs which currently provide about 80% of the total sediment flux (Aloisi et al., 1977; de Madron et al., 2000; Molliex et al., 2016). Rivers from the Pyrenees and Languedoc (Herault, Orb, Aude, Agly, Tech and Têt; **Figure 1**) supply the remaining fraction. The GoL catchment is composed of (i) crystalline rocks, located in mountainous areas (Inner Alps, Massif Central, Pyrenees), and (ii) a large part of carbonated rocks, mostly marl and limestone from the Mesozoic era (Jurassic and Cretaceous) located in Alpine foreland. Some Cenozoic carbonates (Eocene and Miocene), mostly bioclastic and continental sandy limestone, are also present in the downstream part of the catchment and in the foreland of the Alps and Pyrenees and (iii) Pliocene-Quaternary formations which consist of fluvial deposits (Molliex et al., 2016). This study is based on sediment samples collected from borehole PRGL1-4 (**Figure 1**), drilled in the framework of the EU PROMESS project[1], which sampled a 300 m long continuous record spanning the last five glacial-interglacial cycles. The sedimentary succession consists of five progradational units related to the 100-kyr glacio-eustatic cyclicity (Rabineau et al., 2005, 2006). In addition to the moving (regression-transgression) of the shoreline and associated sedimentary environments, the sea-level strongly controls the connection of the riverine inputs with the upper slope setting. As a consequence, the sediment column at PRGL1-4 is essentially composed of fine siliciclastic grains detrital sediment with several interbedded cm-thick sandy-size layers, made mostly of foraminifera shells accumulation, marking the periods of shelf maximum flooding during interglacial periods (**Figure 1**; Sierro et al., 2009; Frigola et al., 2012). The stacking of 100-kyr sequences is favored by a high subsidence rate in that area (Rabineau et al., 2014). Sediment provenance studies indicate a predominance of Rhône river sediment (Revillon et al., 2011). These studies however, only considered siliciclastic material and, no reliable information on carbonate export is available, although carbonated rocks constitute more than 50% of the Gulf of Lion catchment area, and 40% of the eroded volumes (Molliex et al., 2016).

A total of 12 sediment samples from PRGL1-4 were selected along the glacial retreat from MIS 6 (i.e., 160 ka) toward the MIS 5 climatic optimum (i.e., 120 ka), together with 10 samples from modern Rhône river tributaries riverbeds (see **Figure 1** for location). In the present study we analyzed the

[1]https://doi.pangaea.de/10.1594/PANGAEA.902768

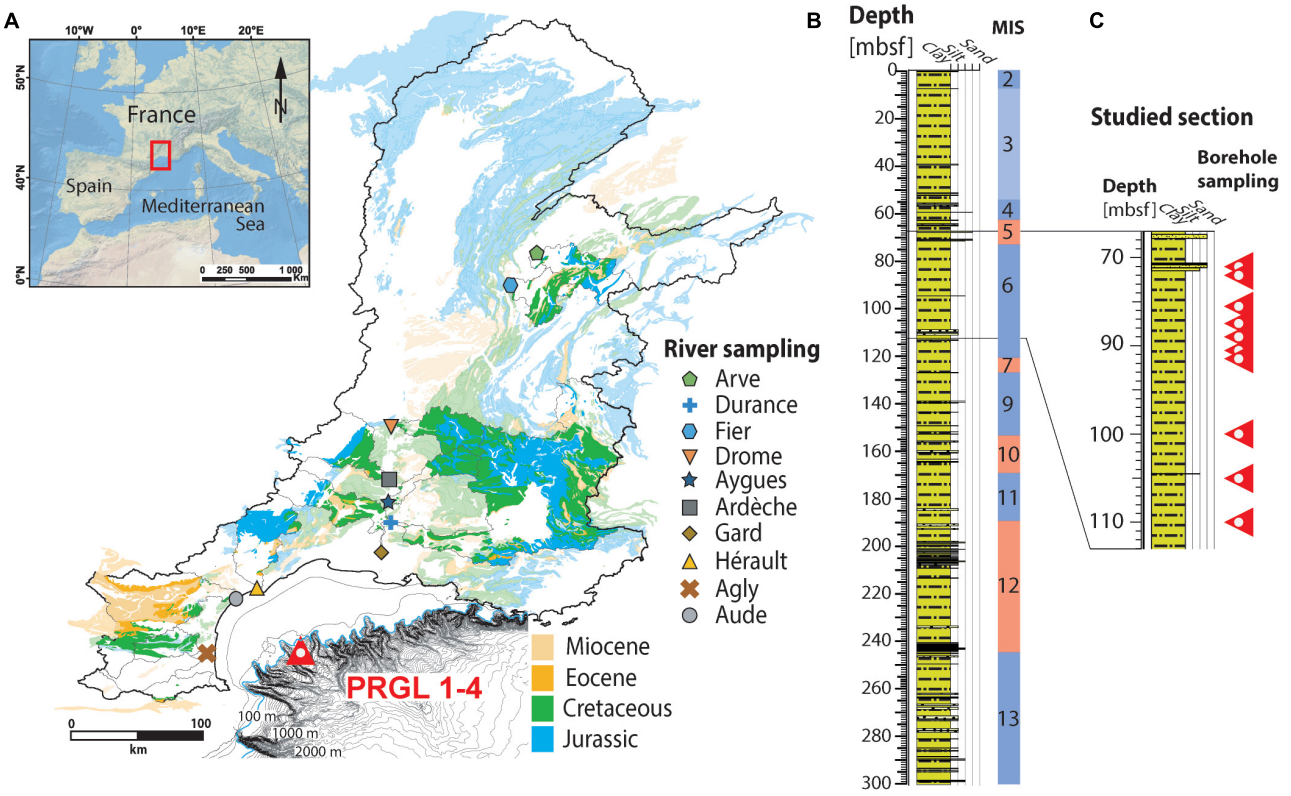

FIGURE 1 | (A) Map of the Gulf of Lion and its watershed with the location of the PRGL1-4 core (42.690N; 3.838E), and riverbed samples. Distribution of stratigraphic units containing carbonate rocks in the catchment are color-coded by age of deposition. **(B)** Composite lithological and sedimentological log of PRGL 1-4, and associated climatic context where pink and blue bands corresponds to interglacial and glacial periods (dark and light blue bands represent *sensu-stricto* and *sensu-lato*, respectively). MIS refers to Marine Isotopic Stage according to Railsback et al., 2015. **(C)** Close up view of the studied section with samples location.

Sr isotope compositions, trace elements, and $CaCO_3$ contents of bulk carbonate samples extracted (i.e., leached) from both marine (i.e., PRGL1-4) and river sediments (i.e., from very coarse sand to clay; **Supplementary Table S1**), using 5% acid acetic digestion. Strontium was isolated from the matrix by column chromatography using a Sr-Spec resin (Eichrom®) prior to analysis by TIMS (Thermo Fisher Scientific TRITON) at the Pôle Spectrometrie Océan (Brest, France). Purified Sr were loaded on single W and measured on static mode. All measured Sr ratios were normalized to ^{86}Sr / ^{88}Sr = 0.1194. During the course of analysis, Sr isotope compositions of standard solution NBS987 gave $^{87}Sr/^{86}Sr$ = 0.710259 ± 7 (2σ, n = 9, recommended value 0.710250). Total procedural blanks were <200 pg of Sr and therefore negligible in all cases (see **Supplementary Material** for a complete description of the methodology).

Throughout the studied interval, the Sr isotopic compositions of the carbonate fractions show significant variations from 0.70809 to 0.70858, whereas carbonate contents vary from 29.5 to 42.5 wt.%, (**Figure 2**). Within river samples, $^{87}Sr/^{86}Sr$ varies between 0.70741 and 0.70855 and the carbonate content ranges between 2.0 and 40.3 wt.% (**Supplementary Figure S1**). No clear trend was observed, neither in marine nor in river sediments, between $^{87}Sr/^{86}Sr$ ratio and $CaCO_3$ content (%$CaCO_3$), nor with [Sr], (**Supplementary Figure S2**). All data reported in this study are available within the **Supplementary Files**, and online at http://www.pangaea.de/Projects/PROMESS1/.

EVIDENCE FOR A DETRITAL CARBONATE INPUT

Seawater $^{87}Sr/^{86}Sr$ variations are often used to infer changes in the global strontium geochemical cycles, long-term variations of carbonate rocks erosion, or variations in the marine strontium reservoir through time. Most recently, $^{87}Sr/^{86}Sr$ variations in carbonates have been also used to establish continuous high-resolution seawater curves for the last 500 Myr (Howarth and McArthur, 1997; McArthur et al., 2001 among others). In this case-study, sediment was deposited offshore between 120 and 160 ka, a time-span shorter than the residence time of strontium in the ocean, i.e., 4 Myr (Broeker, 1963; Goldberg, 1963; Hodell et al., 1990) and during which the Mediterranean basin remained well connected to the open world ocean via the Strait of Gibraltar (Hernández-Molina et al., 2014; Rohling et al., 2014). Therefore, variations in the carbonate $^{87}Sr/^{86}Sr$ ratios analyzed here cannot reflect changes in seawater Sr isotope composition and the observed deviation between our $^{87}Sr/^{86}Sr$ results from

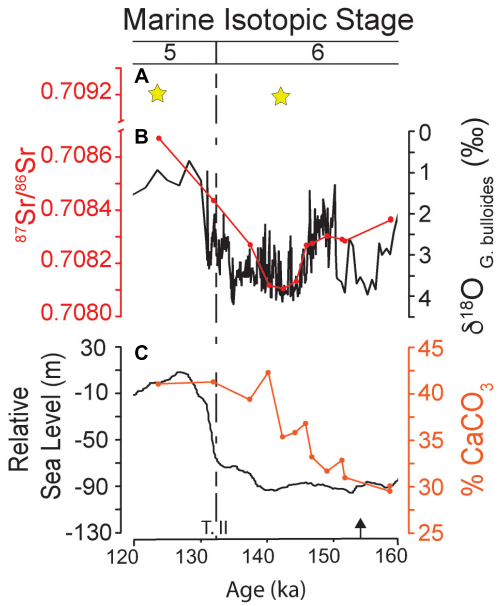

FIGURE 2 | (A) $^{87}Sr/^{86}Sr$ measured on pure biogenic foraminifera calcite (yellow stars, this study – PRGL 1-4), **(B)** $\delta^{18}O_{G.bulloides}$ (black line, Sierro et al., 2009) and $^{87}Sr/^{86}Sr$ measured on bulk carbonate (red line, this study – PRGL 1-4), **(C)** Red Sea sea level record (coreKL09, black curve, Grant et al., 2014) and $\%CaCO_3$ measured on bulk carbonate (orange line, this study – PRGL 1-4). The black arrow indicates evidence of extensive melting of the Alpine ice-cap and local glaciers (Toucanne et al., 2009; Bickel et al., 2015).

the present-day seawater Sr isotope composition has to be related to another process. In other words, if the carbonate components preserved in bulk marine samples were purely biogenic then their isotopic composition should be similar to the seawater: 0.709170 ($\pm 4.10^{-6}$, Mokedem et al., 2015; Meknassi et al., 2018 and references therein). In order to further confirm the invariance of the sea-water isotopic composition we performed laser-ablation – MC-ICPMS Sr isotope composition analyses on pure foraminifera and bivalves calcites on the most radiogenic samples (i.e., 120 ka, S.90-21/22) and the least radiogenic samples (i.e., 142 ka, S.110-59/60). Both samples are statistically indistinguishable from modern sea water composition with isotopic values of 0.70919 ± 0.0001 (2σ) and 0.70921 ± 0.0002 (2σ) respectively. This clearly demonstrates the continuous connectivity with the global ocean and the fact that short timescale variability recorded in our bulk $^{87}Sr/^{86}Sr$ cannot be explained by changes in the isotopic composition of the parent fluid (i.e., seawater). How then can such variability be explained?

In the Gulf of Lion context, the most likely mechanism to explain the observed data is through the export of detrital carbonates from the catchment area. Indeed, carbonates represent about 50% of the drainage area (relics of the Tethys Ocean, see **Figure 1**). Recent studies show that long-term denudation of carbonate rocks within the GoL catchment is significant and slope-dependent (Godard et al., 2016; Thomas et al., 2017), enhancing the transfer of carbonates trough rivers' suspended material (i.e., 30 to 60% of the coarse fraction; Pont et al., 2002). Our river samples contain between 2.0 and 40.3 wt.% of carbonates (**Supplementary Table S1** and **Supplementary Figure S1**) which strongly support these conclusions. Moreover, the riverine bedloads are characterized by Sr isotope compositions ranging between 0.70741 and 0.70855 (**Supplementary Table S1** and **Supplementary Figure S1**) which is close to the $^{87}Sr/^{86}Sr$ ratios of the different carbonates (i.e., Miocene, Eocene, Cretaceous, Jurassic) present in the catchment area (ranging from 0.70685 to 0.70895; **Figure 3** and **Supplementary Table S2**). Thus, our river ratios likely represent a mixture of the different carbonates end-members (of different age) exposed in the catchment areas (**Figure 3**). The observed inter-river isotope variability may result from different contributions of mechanical and chemical weathering processes in each watershed and/or reflect the relative proportion of each end-member carbonate unit. In this context, the export of detrital carbonates into marine sediment appears as the best mechanism to explain the observed dataset.

VARIATION THROUGH TIME: COMPOSITION OR PROPORTION?

A clear distinction in $^{87}Sr/^{86}Sr$ of leached carbonate fractions is observed between glacial and interglacial intervals (**Figure 2**) as deduced from the oxygen isotopic curve obtained in planktonic foraminifera (*Globigerina bulloides*) and associated age-model from the same core (Sierro et al., 2009; Pasquier et al., 2017). The two samples from interglacial MIS 5 are characterized by $^{87}Sr/^{86}Sr$ ratios of 0.70838 and 0.70858 (n = 2) in contrast with less radiogenic composition in glacial sediment (MIS 6) which range from 0.70809 to 0.70832 (n = 11, **Figure 2**). The lowest $^{87}Sr/^{86}Sr$ ratios (i.e., 0.70810 ± 0.00001, n = 3) correspond to maximal ice extension and sea-level lowstand.

Contrary to $^{87}Sr/^{86}Sr$ ratios, the $\%CaCO_3$ does not track climatic conditions, and is not modulated by depositional conditions across the termination II (T.II ∼130 ka). Instead, $\%CaCO_3$ shows a gradual rise from approx. 30 wt.% at the onset of MIS 6 (i.e., 160 ka) to 42 wt.% at the end of the penultimate glacial maxima (i.e., 140 ka); then it slightly decreases down to 39 wt.% during the beginning of T.II, before finally rising and reaching a constant value of ∼41 wt.% during the MIS 5 (**Figure 2**). During glacial times, we observe a greater $CaCO_3$ proportion of what is unexpected considering the low carbonate productivity observed in the western Mediterranean Sea (Hoogakker et al., 2004; Toucanne et al., 2015). Interestingly, this increase in carbonate content is concomitant with a higher detrital flux (Cortina et al., 2013, 2016; Pasquier et al., 2017, 2018); as the rise around 155 ka is synchronous with an extensive melting episode of Alpine ice-caps and local glaciers (Toucanne et al., 2009; Bickel et al., 2015 and reference therein), (**Figure 2**). This suggests a significant increase of detrital carbonates exported during glacial conditions. This increase might be due to enhanced mechanical glacial and peri-glacial processes such as frost cracking or ablation by glaciers.

The temporal variations in the $^{87}Sr/^{86}Sr$ ratios of the carbonate fraction can be explained either by changes in the relative

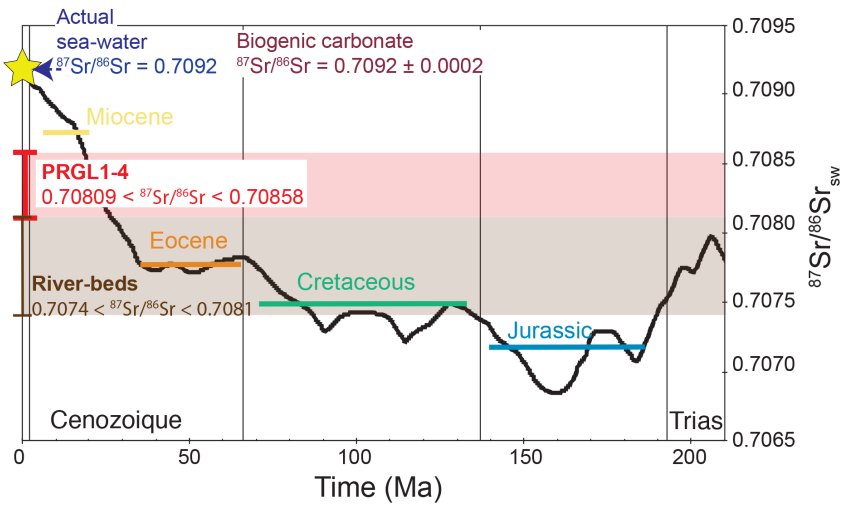

FIGURE 3 | $^{87}Sr/^{86}Sr$ evolution of sea-water over the last 210 Ma (black line; Howarth and McArthur, 1997; McArthur et al., 2001), pure biogenic calcite measured on foraminifera shells reflecting the actual sea-water composition. The range of PRGL1-4 leachate deposited over the last 500 kyr is illustrated by the red band and range of rivers sediment in the present-day GoL watershed by a brown band. The main carbonated stratigraphic units and their corresponding Sr isotope compositions in the GoL watershed are also highlighted with horizontal bars corresponding to their mean isotopic composition as defined in **Supplementary Table S2**.

proportions of biogenic versus detrital carbonates, changes in the isotope composition of detrital carbonates exported into GoL sediment or a combination of both processes.

In the former, the resulting isotope composition of biogenic plus the detrital carbonate mixing processes is typically related to their respective end-member proportion and compositions. Changes in the $^{87}Sr/^{86}Sr$ of the carbonate assemblage could be the natural result of an increase or decrease of biogenic carbonate production related to modification of *in situ* primary production through time. In shelf environments, the biogenic carbonate content is generally controlled by the surface water carbonate productivity, the total amount of carbonate being further controlled by terrigenous sediment dilution effects (Cremer et al., 1992; Hoogakker et al., 2004; Toucanne et al., 2015), with low biogenic $CaCO_3$ production during glacial periods and high biogenic $CaCO_3$ content during interglacial ones. These changes in carbonate production should affect the *in situ*-biogenic versus detrital carbonate proportions, leading to more (less) radiogenic $^{87}Sr/^{86}Sr$ during interglacial (glacial) times, as observed in our dataset. However, downcore fluctuations of $CaCO_3$ do not follow the $\delta^{18}O$ records. Instead, we observed the most important increase in $\%CaCO_3$ during the glacial *sensu stricto* period (**Figure 2**). This reveals that, at our site, the $\%CaCO_3$ is not strictly controlled by primary production. Thus, changes in the relative proportion of biogenic carbonates (within the carbonate mixing) cannot on their own explain the observed variation in $^{87}Sr/^{86}Sr$.

Interestingly, this increase in $\%CaCO_3$ happened during the period of lower sea level (i.e., glacial maxima), and the less radiogenic values are observed during the lowest sea level conditions (i.e., glacial *sensu stricto*). At that time, due to sea level fall, PRGL1-4 borehole site is closer to shore (~10 km) and is therefore more prone to receive and preserve detrital materials. During interglacial times, the sea-level rise and the biogenic carbonate production increase leading to a relative decrease in the proportion of detrital carbonates preserved in PRGL1-4 sediment. This is also observed at finer timescales during the entire penultimate glaciation where variability of $^{87}Sr/^{86}Sr$ closely mimics planktonic oxygen isotopes and sea-level reconstruction (**Figure 2** and **Supplementary Figure S3**). Therefore, $^{87}Sr/^{86}Sr$ fluctuations may be related to variation in the relative proportion of exported carbonates. Mixing calculations between biogenic and detrital carbonates are used to test this hypothesis.

$$(^{87}Sr/^{86}Sr)_m = [(^{87}Sr/^{86}Sr)_{sw}.X] - -[(^{87}Sr/^{86}Sr)_d.(1-X)]$$

Where $(^{87}Sr/^{86}Sr)_m$ represent the Sr isotopic composition measured in PRGL1-4 carbonate fractions; $(^{87}Sr/^{86}Sr)_{sw}$ corresponds to seawater composition and $(^{87}Sr/^{86}Sr)_d$ refers to the isotopic composition of the detrital carbonates. In this equation X represents the percentage of *in situ* biogenic carbonates, and (1-X) the required proportion of detrital carbonates in order to satisfy the isotopic mass balance.

Calculation results are shown in **Figure 4** where the shaded area illustrates the range of possible $^{87}Sr/^{86}Sr$ ratios for the detrital assemblage when considering mixing processes between biogenic carbonates (i.e., $^{87}Sr/^{86}Sr$ = 0.70917) and the minimum and maximum $^{87}Sr/^{86}Sr$ ratios recorded in the PRGL1-4 sediment carbonate fraction (bottom and top black line, respectively). In this space, the percentage of detrital carbonate can be predicted in order to satisfy the mass balance for a given detrital Sr isotope composition. We also investigated the impact of detrital assemblage isotope composition on the percentage of detrital carbonate required to fulfill the mixing mass balance equation (**Figure 4**). This detrital assemblage

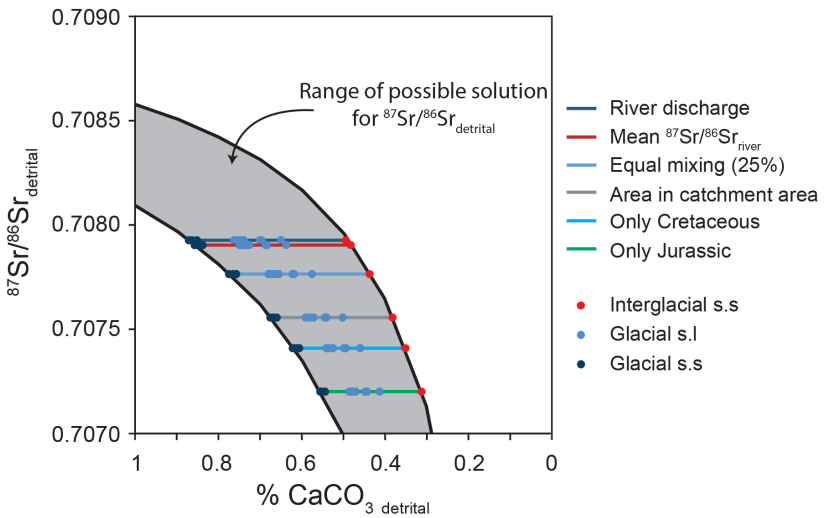

FIGURE 4 | Modeled mixing of a two components system with end-members representing marine biogenic carbonates ($^{87}Sr/^{86}Sr$ = 0.7092) and an unknown detrital source. The black lines are the predicted $^{87}Sr/^{86}Sr$ of the detrital end-member that satisfy the isotopic mass balanced, using the $^{87}Sr/^{86}Sr$ of the less (bottom boundary) and more (upper boundary) radiogenic PRGL1-4 samples. The gray shaded area shows the range of possible solutions according to the weight percentage of detrital carbonate in the sediment mixing. Colored horizontal bars represent possible detrital isotopic composition based on mean river discharges (dark blue line), mean $^{87}Sr/^{86}Sr$ riverbeds composition (dark red line), exposed surface area in the catchment area (gray line), $^{87}Sr/^{86}Sr$ of Cretaceous rocks (cyan line), $^{87}Sr/^{86}Sr$ of Jurassic (green line), and equal mixing ratio between carbonated rocks within the catchment area (light blue). Circles represent % of detrital carbonates in order to obtain the observed $^{87}Sr/^{86}Sr$ composition in PRGL1-4 sediment during glacial *sensu stricto* and *sensu lato* (i.e., dark and light blue circles, respectively), and interglacial *sensu stricto* (i.e., red circles).

isotope composition was calculated by averaging the mean river $^{87}Sr/^{86}Sr$ ratios (red line on **Figure 4**), using either a single carbonate value [as highlighted in **Figure 3** (i.e., using the average of the LOWESS numerical fitted curve of McArthur et al. (2012) giving Cretaceous $^{87}Sr/^{86}Sr$ = 0.707406, Jurassic $^{87}Sr/^{86}Sr$ = 0.707199, respectively cyan and green line on **Figure 4**)], or resulting from mixing in rivers. In the latter, we used several multi- component mixing, using individual river $^{87}Sr/^{86}Sr$ composition and assuming different relative proportions as a function of: (1) river discharges (i.e., $^{87}Sr/^{86}Sr$ = 0.70793; dark blue), (2) percentage of the exposed carbonated surface in the catchment area (i.e., $^{87}Sr/^{86}Sr$ = 0.70756; gray line), and (3) assuming an equal mixing between all carbonated rocks in the catchment (i.e., 25% of each carbonate unit exposed; $^{87}Sr/^{86}Sr$ = 0.7077; light blue), see **Figure 4** and **Supplementary Table S2**. Our results show variation of the relative contribution of detrital carbonates (i.e., %$CaCO_3$ detrital) over glacial-interglacial cycles (**Figure 4**). Using the different scenarios presented above, we also suggest that a higher proportion of detrital carbonates are preserved during glacial *sensu stricto* (55 and 87%) compared to interglacial (31 to 49%) samples, respectively dark blue and red points in **Figure 4**. We also note that this observation is independent of the isotopic composition of the detrital exported material because whatever the Sr isotope composition of the detrital carbonate fraction is, the required amount of detrital carbonate is always higher during glacial periods. Therefore, $^{87}Sr/^{86}Sr$ fluctuation may result from sea-level variability, with sea-level lowstand allowing a better deposition/preservation of detrital carbonates on the GoL's upper slope.

Alternatively, if we assume that detrital carbonates are exported at a constant rate, variation in their strontium isotopic composition could also explain our data. As we showed previously, the GoL catchment area is mainly composed of Mesozoic and Cenozoic marine limestone that are characterized by a large range of $^{87}Sr/^{86}Sr$ ratios, and where Miocene carbonate $^{87}Sr/^{86}Sr$ > Eocene carbonate $^{87}Sr/^{86}Sr$ > Cretaceous carbonate $^{87}Sr/^{86}Sr$ > Jurassic carbonate $^{87}Sr/^{86}Sr$ (**Figure 3**). Changes in the Sr isotope composition of the PRGL1-4 carbonate fraction can result from variations in the Sr isotope composition of the detrital end-member. Thus, our data could indicate sedimentary mixing of biogenic carbonate with less radiogenic detrital carbonates during glacial times, possibly enhanced by greater inputs of Jurassic or Cretaceous units. Indeed, at the time of minimum $^{87}Sr/^{86}Sr$ ratio (glacial) our mixing model predicts less radiogenic detrital carbonates, as indicated by the lower boundary of the shaded area (**Figure 4**). By contrast, more radiogenic detrital carbonates are required during interglacial stages, as indicated by the upper boundary (**Figure 4**). For instance, if we consider that 90% of the carbonates result from detrital export, then the isotopic composition of the detrital source should have evolved from 0.7080 during the glacial *sensu stricto* to 0.7850 during the interglacial *sensu stricto*. Such variability in the detrital $^{87}Sr/^{86}Sr$ ratio should be interpreted as the natural response to various mechanical and chemical weathering processes and/or spatial changes in sediment provenance in the catchment.

The directionality of the relation between sea-level change and $^{87}Sr/^{86}Sr_{carb}$ observed here, and the timing between the increase in %$CaCO_3$ and the Alpine ice cap collapse around 150

ka, argue for the export and preservation of detrital carbonates from the catchment to the GoL shelf. This provides a powerful way to reconstruct past detrital carbonate exports in Source-to-Sink systems.

IMPLICATION FOR FLUXES RECONSTRUCTIONS

Stratigraphic knowledge of the area relies on previous studies based on seismic and PROMESS drilling data in the Gulf of Lion (Rabineau, 2001; Rabineau et al., 2005, 2006; Bassetti et al., 2008; Leroux et al., 2016 among others; see detailed methodology in the Section "Materials and Methods").

We focused our sediment budget within the so-called Sequence 3, in which enough high-resolution seismic data allowed identification of two sedimentary units, U75 and U80, that, respectively correspond to an interglacial and glacial period (respectively Marine Isotopic Stages 9 and 8), (**Supplementary Figure S4**).

Previously reported sediment budgets obtained for these units were first corrected from porosity to calculate "deposited" terrigenous solid volumes. Considering that $\%CaCO_3$ reflects *in situ* biogenic primary production, "deposited" sediment volumes are corrected to get the "detrital" sediment budget.

In order to investigate the impact of the detrital/biogenic ratio on sediment flux calculation, we then applied the detrital carbonate estimations established for MIS 5 (i.e., 30–50%) and 6 (i.e., 55–85%), assuming it is suitable for MIS 8 and MIS 9, in order to calculate "true" detrital sediment budgets (**Supplementary Figure S5** and **Supplementary Table S3**). Considering the only uncertainties about detrital carbonate content, we observe that "true" detrital sediment estimates within a single unit yield a systematic increase whatever the climatic conditions. Additional detrital sediment represents an addition of 78 to 130 km^3.Myr and 128 to 199 km^3.Myr, respectively for MIS 9 and MIS 8, corresponding to +20 to +33% and +23 to +36% detrital fluxes, respectively. Our conclusions imply an overall under-estimate of (detrital) sediment supply in Source-to-Sink studies when carbonate content is not examined. This observation is valid for both glacial and interglacial periods, with variable magnitude but is high enough to be considered. Consequently, corrections from *in situ* carbonate production appears critical for future quantitative studies in Source-to-Sink routing systems.

As the terrigenous sediment budget of passive margin basins records variations in the continental relief, triggered by either deformation or climate, it becomes a major challenge to determine sediment accumulation histories in a large number of basins found in various geodynamic contexts (Guillocheau et al., 2012). Usually, Source-to-Sink studies try to relate significant changes in sediment flux to significant changes in terms of climate or deformation, through the geological history of the studied area. But the concept of "significance" is largely dependent on the uncertainties and the time-resolution of the study. And, as previous authors underlined, "the assessment of the associated uncertainties are as important as the accumulation values themselves." Indeed, if uncertainties are underestimated, some "apparent" changes in sediment fluxes may not be significant in terms of climate or tectonic changes and may lead to misinterpretations.

However, assessing these uncertainties still remains tricky. To do so, we need to consider and quantify to what extent each factor (i.e., autogenic and allogenic) impacts sediment budget measurement, in addition to the uncertainties strictly related to the method itself (e.g., such as the seismic resolution and borehole age uncertainties). Further work is therefore needed to refine our method, particularly in order to better define the characteristics of the detrital end-member and to therefore more accurately estimate its magnitude.

Moreover, Source-to-Sink sedimentary systems are important settings of carbon cycling, serving as sites of carbon transfer between terrestrial and marine reservoirs, and as the primary locations for organic carbon burial on Earth (Leithold et al., 2016). Whereas the order of magnitude for *in situ* carbonate correction that is measured in this study appears lower than many other uncertainties in some cases, it should be nevertheless interesting to analyze Sr isotopes in Source-to-Sink studies where *in situ* carbonate production (autogenic factor) can "introduce noise, lags and/or completely mask signals of external forcings" (Romans et al., 2016). It may be particularly true for basins with low sediment accumulation rates where small variations of detrital sediment fluxes, including detrital carbonate, can be significant in term of climate or tectonic change. As well as in Source-to-Sink systems (i) exhibiting small sediment supplies, (ii) including few carbonated rocks in the catchment area (i.e., detrital carbonate flux toward the sink), or (iii) bad preservation of detrital sediment (sediment by-pass). Conversely, Sr isotope analyses may also be relevant for areas where biogenic production (and carbonate preservation) is particularly high or where productivity (and associated export in the surrounding basin) is very unstable throughout time, such as a carbonated/mixed platform.

We can now wonder (i) how far this under-estimate can change from one basin to another, and (ii) how far this error could have led to potential previous misinterpretations in term of "true" changes on sediment history and processes at their origin, especially for studies exploring glacial and interglacial cycles.

Overall, as already postulated by Helland-Hansen et al. (2016), this study highlights the usefulness of developing isotopic tools and using combined approaches to better refine our understanding of Source-to-Sink systems and to unravel past source terrains.

IMPLICATIONS FOR DEEP-TIME SR ISOTOPE CHEMOSTRATIGRAPHY

Temporal variations in the marine $^{87}Sr/^{86}Sr$ record globally reflect variations in the relative age-weighted fluxes of continental weathering relative to hydrothermal inputs over time, although other sources such as oceanic islands have to be considered (Revillon et al., 2007). Such variations are linked to supercontinent breakup and assembly and sea-level changes

(e.g., Burke et al., 1982; De Paolo and Ingram, 1984; Haq et al., 1988; Veizer, 1989; Veizer et al., 1999; Prokoph et al., 2008) and are used extensively in the Precambrian era. Moreover, in the absence of robust biostratigraphic records and absolute chronological constraints, $^{87}Sr/^{86}Sr$ records are a critical tool for inter- and intra-basinal correlations in the Precambrian era. However, the absence of calcifying organisms means that all Precambrian (and many early Paleozoic) $^{87}Sr/^{86}Sr$ values come from microdrilled bulk carbonate samples (e.g., Halverson et al., 2007).

Most of the available geologic records of marine sedimentary rocks predominantly preserve sediment deposited on the continental paleo-shelf (Peters and Husson, 2017), where carbonate facies are abundant (Grotzinger, 1990; Grotzinger and Knoll, 1999; Higgins et al., 2009). Consequently, bulk samples can include detrital carbonates.

Still, if detrital carbonates had the ability to reach marine sediment since the emergence of the continent, we can wonder how much carbonated outcrops were likely to be weathered (and preserved over paleo-shelf). Currently, there is no reconstruction of such flux, but a simple geochemical argument can be made: CO_2 has been emitted into the ocean-atmosphere as long as volcanic activity existed, i.e., since the very beginning (Tailor and McLennan, 1985; Jacobsen, 1988; Ying et al., 2011). As CO_2 cannot indefinitely accumulate in the atmosphere, it sank as carbonate mineral and organic matter, at least since the last 3.8 billion years (Schidlowski, 2001). Carbon isotope compilation over the geological record (e.g., Schidlowski, 2001) suggests that approximatively 80% of the CO_2 source has been removed as carbonates over that entire time. This is a first-order approximation, and there is many details and caveats, but it reveals that carbonates have been formed over much of Earth's history. Today most carbonates form biologically, while in the Precambrian and early Proterozoic era they formed abiotically (Higgins et al., 2009). In addition, and in contrast with the Phanerozoic era, past ocean chemistry (i.e., high silica content) promoted silicification of most Precambrian and early Proterozoic depositional environments (Siever, 1992; Treguer et al., 1995; Hofmann and Wilson, 2007 among others). Meaning that deep-time carbonates were probably more competent upon uplift and exposure, and therefore were even more likely to be transported to the ocean and "contaminate" the bulk Sr samples.

The above considerations suggest that variations in the resulting $^{87}Sr/^{86}Sr$ values within and between basins could potentially also reflect differential detrital carbonate components, impacting both stratigraphic correlations as well as our understanding of tectonic evolution over time. Therefore, it seems critical to consider the potential impact that detrital carbonate may have on these records.

DATA AVAILABILITY

Publicly available datasets were analyzed in this study. This data can be found here: https://www.pangaea.de/?q=PROMESS1.

AUTHOR CONTRIBUTIONS

VP, SR, and MR conceived the work. VP, SR, LM, and SM organized the sampling. VP and SR carried out the geochemical analyses. VP, SR, EL, SM, and MR wrote the manuscript and the **Supplementary Information**. All authors discussed the interpretation of the results and contributed to the manuscript.

FUNDING

This work was supported by the "Laboratoires d'Excellence" LabexMER (ANR-10-LABX-19) that became ISblue (Interdisciplinary graduate School for the Blue Planet ANR-17-EURE-0015); and co-funded by a grant from the French government under the program "Investissements d'Avenir," and by a grant from the Regional Council of Brittany. It was further supported by the CNRS (INSU-Tellus-SYSTER for the Carboflux project), with additional support from the French Actions Marges program. The drilling operation was conducted within the European Commission Project PROMESS (contract EVR1-CT-2002-40024).

ACKNOWLEDGMENTS

The European Promess Scientific committee and colleagues at Ifremer are thanked for previous contributions of data acquisition, processing, interpretations, and permitting to resample the borehole. The authors warmly acknowledge C. Liorzou and P. Nonnotte who kindly helped during the analytical preparation of samples, and for assistance on the ICP-OES and TI-MS, respectively. D. Fike is thanked for fruitful discussion and his feedback along the entire study; Itay Halevy and Peter Crockford for providing comments and suggestions regarding the importance of such processes on deep time reconstructions.

SUPPLEMENTARY MATERIAL

The Supplementary Material for this article can be found online at: https://www.frontiersin.org/articles/10.3389/feart.2019.00164/full#supplementary-material

REFERENCES

Allègre, C. J., Louvat, P., Gaillardet, J., Meynadier, L., Rad, S., and Capmas, F. (2010). The fundamental role of island arc weathering in the oceanic Sr isotope budget. *Earth Planet. Sci. Lett.* 292, 51–56. doi: 10.1016/j.epsl.2010.01.019

Allen, J. R. (1974). Reaction, relaxation and lag in natural sedimentary systems: general principles, examples and lessons. *Earth Sci. Rev.* 10, 263–342. doi: 10.1016/0012-8252(74)90109-3

Allen, P. A. (2008). From landscapes into geological history. *Nature* 451, 274–276. doi: 10.1038/nature06586

Aloisi, C. J., Auffret, G. A., Auffret, J. P., Barusseau, J. P., Hommeril, P., Larsonneur, C., et al. (1977).. Essai de modélisation de la sédimentation actuelle sur les plateaux continentaux français. *Bull. Soc. Géol. France* 7, 183–195 doi: 10.2113/gssgfbull.s7-xix.2.183

Armitage, J. J., Duller, R. A., Whittaker, A. C., and Allen, P. A. (2011). Transformation of tectonic and climatic signals from source to sedimentary archive. *Nat. Geosci.* 4, 231–235. doi: 10.1038/ngeo1087

Armitage, J. J., Jones, T. D., Duller, R. A., Whittaker, A. C., and Allen, P. A. (2013). Temporal buffering of climate-driven sediment flux cycles by transient catchment response. *Earth Planet. Sci. Lett.* 36, 200–210. doi: 10.1016/j.epsl.2013.03.020

Bassetti, M. A., Berné, S., Jouet, G., Taviani, M., Dennielou, B., Flores, J. A., et al. (2008). The 100-ka and rapid sea level changes recorded by prograding shelf sand bodies in the gulf of lions (western Mediterranean Sea). *Geochem. Geophys. Geosyst.* 9:Q11R05. doi: 10.1029/2007GC001854

Bickel, L., Lüthgensa, C., Lomaxb, J., and Fiebig, M. (2015). The timing of the penultimate glaciation in the northern alpine foreland: new insights from luminescence dating. *Proc. Geol. Assoc.* 126, 536–550. doi: 10.1016/j.pgeola.2015.08.002

Broeker, W. (1963). "Radioisotopes and large-scale oceanic mixing," in *The Composition of Seawater: Comparative and Descriptive Oceanography. the Sea: Ideas and Observations on Progress in the Study of the Seas*, ed. M. N. Hill (New York, NY: Wiley Interscience).

Burke, W. H., Denison, R. E., Hetherington, E. A., Koepnick, R. B., Nelson, H. F., and Otto, J. B. (1982). Variation of seawater 87Sr/86Sr throughout phanerozoic time. *Geology* 10, 516–519.

Castelltort, S., and Van Den Driessche, J. (2003). How plausible are high-frequency sediment supply-driven cycles in the stratigraphic record? *Sediment. Geol.* 157, 3–13. doi: 10.1016/S0037-0738(03)00066-6

Cortina, A., Grimalt, J. O., Rigual-Hernández, A., Ballegeer, A.-M., Martrat, B., Sierro, F. J., et al. (2016). The impact of ice-sheet dynamics in western mediterranean environmental conditions during terminations: an approach based on terrestrial long chain n-alkanes deposited in the upper slope of the gulf of lions. *Chem. Geol.* 430, 21–33. doi: 10.1016/j.chemgeo.2016.03.015

Cortina, A., Sierro, F. J., Filippelli, G., Flores, J.-A., and Berné, S. (2013). Changes in planktic and benthic foraminifer assemblages in the gulf of lions, off south france: response to climate and sea level change from MIS 6 to MIS 11. *Geochem. Geophys. Geosyst.* 14, 1258–1276. doi: 10.1002/ggge.20096

Cremer, M., Grousset, F., Faugères, J. C., Duprat, J., and Gonthier, E. (1992). Sediment flux patterns in the northeastern atlantic: variability since the last interglacial. *Mar. Geol.* 104, 31–53. doi: 10.1016/0025-3227(92)90083-T

De Paolo, D. J., and Ingram, B. L. (1984). High-resolution stratigraphy with strontium isotopes. *Science* 227, 938–940.

de Madron, X. D., Abassi, A., Heussner, S., Monaco, A., Aloisi, J. C., Radakovitch, O., et al. (2000). Particulate matter and organic carbon budgets for the Gulf of Lions (NW Mediterranean). *Oceanologica Acta* 23, 717–730. doi: 10.1016/S0399-1784(00)00119-5

Elderfield, H. (1986). Strontium isotope stratigraphy. *Palaeogeogr. Palaeoclimatol. Palaeoecol.* 57, 71–90. doi: 10.1016/0031-0182(86)90007-6

Frigola, J., Canals, M., Cacho, I., Moreno, A., Sierro, F. J., Flores, J. A., et al. (2012). A 500 kyr record of global sea-level oscillations in the Gulf of Lion, mediterranean Sea: new insights into MIS 3 sea-level variability. *Clim. Past* 8, 1067–1077. doi: 10.5194/cp-8-1067-2012

Godard, V., Ollivier, V., Bellier, O., Miramont, C., Shabanian, E., Fleury, J., et al. (2016). Weathering-limited hillslope evolution in carbonate landscapes. *Earth Planet. Sci. Lett.* 446, 10–20. doi: 10.1016/j.epsl.2016.04.017

Goldberg, E. D. (1963). "The ocean as a chemical system"," in *The Sea*, ed. M. N. Hill (New York, NY: Intersciences).

Grant, K. M., Rohling, E. J., Ramsey, C. B., Cheng, H., Edwards, R. L., Florindo, F., et al. (2014). Sea-level variability over five glacial cycles. *Nat. Commun.* 5:5076. doi: 10.1038/ncomms6076

Grotzinger, J. P. (1990). Geochemical model for proterozoic stromatolite decline. *Am. J. Sci.* 290A, 80–103.

Grotzinger, J. P., and Knoll, A. H. (1999). Stromatolites in precambrian carbonates: evolutionary mileposts or environmental dipsticks. *Annu. Rev. Earth Planet. Sci.* 27, 313–358. doi: 10.1146/annurev.earth.27.1.313

Guillocheau, F., Rouby, D., Robin, C., Helm, C., and Rolland, N. (2012). Quantification and causes of the terrigeneous sediment budget at the scale of a continental margin: a new method applied to the Namibia-South Africa margin. *Basin Res.* 24, 3–30. doi: 10.1111/j.1365-2117.2011.00511.x

Halverson, G. P., Dudás, F. Ö, Maloof, A. C., and Bowring, S. A. (2007). Evolution of the 87Sr/86Sr composition of Neoproterozoic seawater. *Palaeoclimatol. Palaeoecol. Palaeogeogr.* 256, 103–129. doi: 10.1016/j.palaeo.2007.02.028

Haq, B. U., Hardenbol, J., and Vail, P. R. (1988). "Mesozoic, and cenozoic chronostratigraphy, and eustatic cycles. sea-level changes," in *Sea Level Changes: An Integrated Approach*, ed. C. K. Wilgus, et al. (Houston: SEPM Special Publication).

Helland-Hansen, W., Sømme, T. O., Martinsen, O. J., Lunt, I., and Thurmond, J. (2016). Deciphering earth's natural hourglasses: perspectives on source-to-sink analysis. *J. Sediment. Res.* 86, 1008–1033. doi: 10.2110/jsr.2016.56

Hernández-Molina, F. J., Stow, D. A. V., Alvarez-Zarikian, C. A., Acton, G., Bahr, A., Balestra, B., et al. (2014). Onset of mediterranean outflow into the North Atlantic. *Science* 344, 1244–1250. doi: 10.1126/science.1251306

Higgins, J. A., Fischer, W. W., and Schrag, D. P. (2009). Oxygenation of the ocean and sediments: consequences for the seafloor carbonate factory. *Earth Planet. Sci. Lett.* 284, 25–33. doi: 10.1016/j.epsl.2009.03.039

Hodell, D. A., Mead, G. A., and Mueller, P. A. (1990). Variation in the strontium isotopic composition of seawater (8 Ma to present) Implications for chemical weathering rates and dissolved fluxes to the oceans. *Isot. Geosci.* 80, 291–307. doi: 10.1016/0168-9622(90)90011-Z

Hofmann, A., and Wilson, A. H. (2007). "Silicified basalts, bedded cherts and other sea floor alteration phenomena of the 3.4 Ga Nondweni greenstone belt," in *Earth's Oldest Rocks*, eds J. Martin, R. Van Kranendonk, H. Smithies, C. Vickie, and J. Bennett. (Amsterdam: Elsevier)

Hoogakker, B. A. A., Rothwell, R. G., Rohling, E. J., Paterne, M., Stow, D. A. V., Herrle, J. O., et al. (2004). Variations in terrigenous dilution in western mediterranean sea pelagic sediments in response to climate change during the last glacial cycle. *Mar. Geol.* 211, 21–43. doi: 10.1016/j.margeo.2004.07.005

Howarth, R. J., and McArthur, J. M. (1997). Statistics for strontium isotope stratigraphy: a robust LOWESS fit to the marine Sr-isotope curve for 0 to 206 Ma, with look-up table for derivation of numeric age. *J. Geol.* 105, 441–456. doi: 10.1086/515938

Jacobsen, S. B. (1988). Isotopic constraints on crustal growth and recycling. *Earth Planet. Sci.* 90, 315–329. doi: 10.1016/0012-821X(88)90133-90131

Leithold, E. L., Blair, N. E., and Wegmann, K. W. (2016). Source-to-sink sedimentary systems and global carbon burial: a river runs through it. *Earth Sci. Rev.* 153, 30–42. doi: 10.1016/j.earscirev.2015.10.011

Leroux, E., Rabineau, M., Aslanian, D., Gorini, C., Molliex, S., Bache, F., et al. (2016). High-resolution evolution of terrigenous sediment yields in the provence basin during the last 6 Ma: relation with climate and tectonics. *Basin Res.* 29, 305–339. doi: 10.1111/bre.12178

McArthur, J. M. (1994). Recent trends in strontium isotope stratigraphy. *Terra Nova* 6, 331–358. doi: 10.1111/j.1365-3121.1994.tb00507.x

McArthur, J. M., Howarth, R. J., and Bailey, T. R. (2001). Strontium isotope stratigraphy: LOWESS Version 3: best Fit to the marine Sr-Isotope Curve for 0–509 Ma and accompanying look-up table for deriving numerical age. *J. Geol.* 109, 155–170. doi: 10.1086/319243

McArthur, J. M., Howarth, R. J., and Shields, G. A. (2012). "Strontium isotope stratigraphy," in *Gradstein*, eds J. G. Ogg, M. D. Schmitz, and G. M. Ogg (Amsterdam: Elsevier).

Meknassi, E. S., Dera, G., Cardone, T., De Rafélis, M., Brahmi, C., and Chavagnac, V. Sr. (2018). isotope ratios of modern carbonate shells: good and bad news for chemostratigraphy. *Geology* 46, 1003–1006. doi: 10.1130/G45380.1

Mokedem, F., Parkinson, I. J., Hathorne, E., Anand, P., Allen, J., Burton, K., et al. (2015). High-precision radiogenic strontium isotope measurements of the modern and glacial ocean: limits on glacial–interglacial variations in continental weathering. *Earth Planet. Sci. Lett.* 415, 111–120. doi: 10.1016/j.epsl.2015.01.036

Molliex, S., Rabineau, M., Leroux, E., Bourlès, D. L., Authemayou, C., Aslanian, D., et al. (2016). Multi-approach quantification of denudation rates in the Gulf of Lion source-to-sink system (SE France). *Earth Planet. Sci. Lett.* 444, 101–115. doi: 10.1016/j.epsl.2016.03.043

Pasquier, V., Sansjofre, P., Lebeau, O., Liorzou, C., and Rabineau, M. (2018). Acid digestion on river influenced shelf sediment organic matter: carbon and nitrogen contents and isotopic ratios. *Rapid Commun. Mass Spectrom.* 32, 86–92. doi: 10.1002/rcm.8014

Pasquier, V., Sansjofre, P., Rabineau, M., Revillon, S., Houghton, J., and Fike, D. A. (2017). Pyrite sulfur isotopes reveal glacial-interglacial environmental changes. *Proc. Natl. Acad. Sci. U.S.A.* 114, 5941–5945. doi: 10.1073/pnas.1618245114

Peters, S. E., and Husson, J. M. (2017). Sediment cycling on continental and oceanic crust. *Geology* 45, 323–326. doi: 10.1130/G38861.1

Pont, D., Simonnet, J. P., and Walter, A. V. (2002). Medium-term changes in suspended sediment delivery to the ocean: consequences of catchment heterogeneity and river management (Rhône River, France). *Estuar. Coast. Shelf Sci.* 54, 1–18. doi: 10.1006/ecss.2001.0829

Prokoph, A., Shields, G. A., and Veizer, J. (2008). Compilation and time-series analysis of a marine carbonate δ18O, δ13C, 87Sr/86Sr and δ34S database through earth history. *Earth Sci. Rev.* 87, 113–133. doi: 10.1016/j.earscirev.2007.12.003

Rabineau, M. (2001). *Un modèle géométrique et stratigraphique des séquences de dépôts quaternaires de la plate-forme du Golfe du Lion: enregistrement des cycles glacioeustatiques de 100 000 ans*. Ph.D thesis, Université de Rennes1, *1* Rennes.

Rabineau, M., Berné, S., Aslanian, D., Olivet, J.-L., Joseph, P., Guillocheau, F., et al. (2005). Sedimentary sequences in the Gulf of Lion: a record of 100,000 years climatic cycles. *Mar. Petrol. Geol.* 22, 775–804. doi: 10.1016/j.marpetgeo.2005.03.010

Rabineau, M., Berné, S., Olivet, J.-L., Aslanian, D., Guillocheau, F., and Joseph, P. (2006). Paleo sea levels reconsidered from direct observation of paleoshoreline position during glacial maxima (for the las 500,000 yr). *Earth Planet. Sci. Lett.* 252, 119–137. doi: 10.1016/j.epsl.2006.09.033

Rabineau, M., Leroux, E., Aslanian, D., Bache, F., Gorini, C., Moulin, M., et al. (2014). Quantifying subsidence and isostatic readjustment using sedimentary paleomarkers, example from the Gulf of Lion. *Earth Planet. Sci. Lett.* 388, 353–366. doi: 10.1016/j.epsl.2013.11.059

Railsback, L. B., Gibbard, P. L., Head, M. J., Voarintsoa, N. R. G., and Toucanne, S. (2015). An optimized scheme of lettered marine isotope substages for the last 1.0 million years, and the climatostratigraphic nature of isotope stages and substages. *Quat. Sci. Rev.* 111, 94–106. doi: 10.1016/j.quascirev.2015.01.012

Revillon, S., Jouet, G., Bayon, G., Rabineau, M., Dennielou, B., Hémond, C., et al. (2011). The provenance of sediments in the Gulf of Lions, western mediterranean Sea. *Geochem. Geophys. Geosyst.* 12, 1–20. doi: 10.1029/2011GC003523

Revillon, S., Teagle, D. A. H., Boulvais, P., Shafer, J., and Neal, C. R. (2007). Geochemical fluxes related to alteration of a subaerially-exposed seamount: nintoku seamount, ODP Leg 197, Site 1205. *Geochem. Geophys. Geosyst.* 8, 1–26.

Rohling, E. J., Foster, G. L., Grant, K. M., Marino, G., Roberts, A. P., Tamisiea, M. E., et al. (2014). Sea-level and deep-sea-temperature variability over the past 5.3 million years. *Nature* 508, 477–482. doi: 10.1038/nature13230

Romans, B. W., Castelltort, S., Covault, J. A., Fildani, A., and Walsh, J. P. (2016). Environmental signal propagation in sedimentary systems across timescales. *Earth Sci. Rev.* 153, 7–29. doi: 10.1016/j.earscirev.2015.07.012

Schidlowski, M. (2001). Carbon isotopes as biogeochemical recorders of life over 3.8 Ga of earth history: evolution of a concept. *Precambrian Res.* 106, 117–134. doi: 10.1016/S0301-9268(00)00128-125

Sierro, F. J., Andersen, N., Bassetti, M. A., Berné, S., Canals, M., Curtis, J. H., et al. (2009). Phase relationship between sea level and abrupt climate change. *Quat. Sci. Rev.* 28, 2867–2881. doi: 10.1016/j.quascirev.2009.07.019

Siever, R. (1992). The silica cycle in precambrian. *Geochim. Cosmochim. Acta* 56, 3365–3272.

Simpson, G., and Castelltort, S. (2012). Model shows that rivers transmit high-frequency climate cycles to the sedimentary record. *Geology* 40, 1131–1134. doi: 10.1130/G33451.1

Tailor, S. R., and McLennan, S. M. (1985). *The Continental Crust: its Composition and Evolution*. Hoboken, NY: Blackwell Scientific Publications.

Thomas, F., Godard, V., Bellier, O., Shabanian, E., Ollivier, V., Benedetti, L., et al. (2017). Morphological controls on the dynamics of carbonate landscapes under a mediterranean climate. *Terra Nova* 29, 173–182. doi: 10.1111/ter.12260

Toucanne, S., Minto'o, C. M. A., Fontanier, C., Bassetti, M.-A., Jorry, S. J., and Jouet, G. (2015). Tracking rainfall in the northern Mediterranean borderlands during sapropel deposition. *Quat. Sci. Rev.* 129, 178–195. doi: 10.1016/j.quascirev.2015.10.016

Toucanne, S., Zaragosi, S., Bourillet, J. F., Cremer, M., Eynaud, F., Van Vliet-Lanoë, B., et al. (2009). Timing of massive *Fleuve Manche* discharges over the last 350kyr: insights into the european ice-sheet oscillations and the european drainage network from MIS 10 to 2. *Quat. Sci. Rev.* 28, 1238–1256. doi: 10.1016/j.quascirev.2009.01.006

Treguer, P., Nelson, D. M., and Van Bennekom, A. J. (1995). The silica balance in the world ocean: a reestimate. *Science* 268, 375–379. doi: 10.1126/science.268.5209.375

Veizer, J. (1989). Strontium isotopes in seawater through time. *Annu. Rev. Earth Planet. Sci.* 17, 141–167. doi: 10.1146/annurev.earth.17.1.141

Veizer, J., Buhl, D., Diener, A., Ebneth, S., Podlaha, O. G., Bruckschen, P., et al. (1997). Strontium isotope stratigraphy: potential resolution and event correlation. *Palaeogeogr. Palaeoclimatol. Palaeoecol.* 132, 65–77. doi: 10.1016/S0031-0182(97)00054-0

Veizer, J. N., Ala, D., Azmy, K., Bruckschen, P., Buhl, D., Bruhn, F., et al. (1999). 87Sr/86Sr, d13C and d18O evolution of phanerozoic seawater. *Chem. Geol.* 161, 59–88. doi: 10.1016/S0009-2541(99)00081-9

Ying, J.-F., Zhou, X.-H., Su, B.-X., and Tang, Y.-J. (2011). Continental growth and secular evolution: constraints from U-Pb ages and Hf isotope of detrital zircons in *Proterozoic jixian* sedimentary section (1.8-0.8Ga), North China craton. *Precambrian Res.* 189, 229–238. doi: 10.1016/j.precamres.2011.07.007

Conflict of Interest Statement: The authors declare that the research was conducted in the absence of any commercial or financial relationships that could be construed as a potential conflict of interest.

frontiers in Earth Science

ORIGINAL RESEARCH
published: 30 August 2019
doi: 10.3389/feart.2019.00217

Partitioning Pervasive Detrital Geochronologic Age Distributions in the Southern Alaskan Forearc

*Emily S. Finzel**

Department of Earth and Environmental Sciences, University of Iowa, Iowa City, IA, United States

The extensive detrital zircon U-Pb geochronologic dataset presented here includes new and compiled data ($N = 38$; $n = 8{,}006$) from modern rivers that together comprehensively characterizes the geographic distribution of pervasive Mesozoic—Cenozoic igneous belts across mountainous regions in south-central Alaska, including the northern Chugach Mountains, Talkeetna Mountains, and western, central, and eastern Alaska Range. These data are compared to an extensive detrital zircon U-Pb dataset from Lower Cretaceous to Pliocene strata in the forearc basin ($N = 29$; $n = 8{,}678$) using a recently developed unmixing approach to investigate the variations in long-term provenance and sediment dispersal patterns in the basin in response to tectonic events. During the Early Cretaceous, the primary sediment source was an exhumed Jurassic arc located north of the basin, but new sediment derived from accretionary prism strata in the northern Chugach Mountains during the Late Cretaceous coincides with final suturing of the Insular terranes with North America and a change in plate kinematics. Eocene strata record major sediment derivation from the western Alaska Range after passage of a subducting spreading ridge. By the Oligocene, shallow subduction of the Yakutat microplate triggered a rejuvenation of exhumation in the northern Chugach Mountains that continued through the Early-Middle Miocene. And overall inboard shift of dominant source regions to the Talkeetna Mountains and central Alaska Range likely reflects the continued insertion of the shallow slab beneath south-central Alaska. The integrated approach of strategic modern river sampling and comprehensive basin strata characterization in conjunction with an inverse Monte Carlo approach of mixture modeling demonstrates a useful approach for partitioning of widespread and pervasive ages in sediment source terranes.

Keywords: detrital zircon, U-Pb geochronology, forearc basin, Alaska, mixture modeling

Edited by:
Miquel Poyatos Moré, University of Oslo, Norway

Reviewed by:
Daniel Stephen Coutts, University of Calgary, Canada
Andrea Stevens Goddard, Rowan University, United States
Jeffrey M. Amato, New Mexico State University, United States

***Correspondence:**
Emily S. Finzel
emily-finzel@uiowa.edu

Specialty section:
This article was submitted to Sedimentology, Stratigraphy and Diagenesis, a section of the journal Frontiers in Earth Science

Received: *26 April 2019*
Accepted: *09 August 2019*
Published: *30 August 2019*

Citation:
Finzel ES (2019) Partitioning Pervasive Detrital Geochronologic Age Distributions in the Southern Alaskan Forearc. Front. Earth Sci. 7:217. doi: 10.3389/feart.2019.00217

INTRODUCTION

Detrital zircon U-Pb geochronology of sandstone is routinely used for determining provenance and sediment dispersal patterns in basins, maximum depositional age of clastic strata, and magmatic and exhumational histories of sediment source regions (DeCelles et al., 1998; DeGraaff-Surpless et al., 2002; Fedo et al., 2003; Weislogel et al., 2006; Gehrels et al., 2008; Dickinson and Gehrels, 2009). For provenance, the usefulness of single-grain U-Pb dating of zircons in any specific area is contingent upon knowing the ages of zircons in all potential source regions, as well as having a

distribution of unique ages among the igneous sources. In many regions with prolonged magmatic histories, however, individual igneous belts can be geographically extensive and plutonic belts of different ages often overlap, making precise provenance determination difficult.

In south-central Alaska, widespread Middle to Late Jurassic magmatism was succeeded by profuse Late Cretaceous to early Eocene magmatism, followed by minor pulses of late Eocene-Oligocene magmatism. Detrital zircon grains with all these ages are abundant in the Late Mesozoic-Cenozoic forearc basin strata and compose ∼90% of the detrital age groups on average. Even so, these ages groups were previously difficult to interpret given the widespread nature of the source rocks and lack of extensive bedrock dating in the source regions. The new and compiled data presented here represents the first comprehensive geographic characterization of these igneous sources via U-Pb dating of detrital zircons from modern rivers (N = 38; n = 8,006) in the northern Chugach Mountains, Talkeetna Mountains, and western, central, and eastern Alaska Range. These data, in conjunction with an extensive detrital zircon U-Pb dataset from Lower Cretaceous to Pliocene strata in the forearc basin (N = 29; n = 8,678), are evaluated using a recently developed unmixing approach (Sundell and Saylor, 2017) to more fully resolve the long-term provenance and sediment dispersal patterns in the basin. Although not the goal of this paper, the resulting temporal variations in source areas and sediment dispersal patterns are interpreted to be related to several significant tectonic events in south-central Alaska, including Late Cretaceous accretion of the Insular terranes, Paleocene to Eocene migration of a subducting spreading ridge, and on-going shallow subduction of an oceanic plateau since Oligocene time. The main focus of this paper is to demonstrate that the combined approach of extensive and strategic modern river sampling to resolve age groups in potential sediment source areas and comprehensive characterization of detrital age groups in basin strata in conjunction with mixture modeling offers the ability to partition between widespread and pervasive ages in sediment source terranes.

EXISTING PROVENANCE AND TECTONIC MODELS

Convergence and subduction have been continuous along the outboard margin of south-central Alaska since at least Jurassic time, accompanied by several different subduction-related events, including terrane accretion, spreading-ridge subduction, and flat-slab subduction of an oceanic plateau. During Middle Jurassic to Late Cretaceous time, the Insular terranes, upon which the forearc basin and study areas are situated, collided with the outboard margin of western North America (Pavlis, 1982; McClelland et al., 1992; Trop et al., 2002, 2005; Manuszak et al., 2007); subduction along the outboard margin of the terranes continued during Late Cretaceous time (Plafker et al., 1994; Trop and Ridgway, 2007).

Mesozoic sedimentary and volcanic forearc basin strata are exposed along the southern margin of the Talkeetna Mountains in south-central Alaska (**Figure 1**). There, two lower Cretaceous sedimentary units have received very little attention and are simply mapped as the Ks unit (Cretaceous sandstone) and Kc unit (Cretaceous calcareous sandstone) in the Talkeetna Mountains (Grantz, 1960). Detrital zircon U-Pb geochronologic data and $\varepsilon Hf_{(t)}$ values from those units are interpreted to record increased erosional exhumation of the adjacent Jurassic arc and access to deeper and older parts of the batholith, as well as initial input of sediment from local Paleozoic basement sources (Reid et al., 2018).

Lying unconformably above the Lower Cretaceous strata is the Upper Cretaceous Matanuska Formation. Early work based on sandstone petrography, zircon U-Pb ages of granitic clasts, and sparse detrital zircon U-Pb ages inferred that the provenance of the upper Matanuska Formation was Jurassic–Cretaceous igneous rocks located north of the basin (Trop, 2008). More recently, Reid et al. (2018) presented new detrital zircon U-Pb data as well as $\varepsilon Hf_{(t)}$ values that also suggest sediment derivation from the proximal Jurassic and Late Cretaceous arc rocks as well as initial influx of sediment from older inboard terranes.

During Paleocene and Eocene time (ca. 62–50 Ma), either a spreading ridge that subducted from west to east across the entire southern margin, or a slab break-off event following final suturing of the Insular terranes, resulted in a hiatus in arc magmatism, emplacement of slab-window igneous rocks in the forearc and accretionary prism regions, and high-temperature/low-pressure metamorphism of accretionary prism strata (Bradley et al., 2003; Haeussler et al., 2003; Sisson et al., 2003; Cole et al., 2006; Terhune et al., 2019; Trop et al., 2019). In addition, previous detrital geochronologic and thermochronologic data from the Alaskan forearc basin demonstrate that after this event retro-arc sources become predominant over more proximal arc sources (Finzel et al., 2016).

Either subduction of oceanic crust with normal slab dip or a period of transform tectonics following slab break-off briefly occurred after spreading-ridge subduction until the late Eocene or early Oligocene (∼35 Ma) when subduction of the Yakutat microplate initiated shallow subduction along the outboard margin of south-central Alaska and continues to the present day (Finzel et al., 2011, 2015; Arkle et al., 2013; Terhune et al., 2019; Trop et al., 2019). The Yakutat microplate is an ∼11–30 km thick, wedge-shaped oceanic plateau that is subducting at a dip angle of 11–16°, decreasing from west to east, to near the modern coastline (Ferris et al., 2003; Eberhart-Phillips et al., 2006; Worthington et al., 2008, 2012; Christeson et al., 2010; Bauer et al., 2014). Yakutat shallow-subduction-related processes observed in the upper plate in Alaska include changes in (1) the style and location of volcanic arc magmatism, (2) sedimentary basin subsidence and inversion patterns, and (3) sediment sources as a result of accelerated surface uplift above the subducted flat slab (e.g., Enkelmann et al., 2008, 2019; Finzel et al., 2011, 2015, 2016; Trop et al., 2012; Arkle et al., 2013; Finzel and Enkelmann, 2017). Shallow subduction still characterizes the present-day margin of southern Alaska.

Cenozoic strata in the Cook Inlet forearc basin crop out in discontinuous belts along the margins of the basin and depositionally overlie or are in fault contact with rocks of the adjacent accretionary prism and volcanic arc

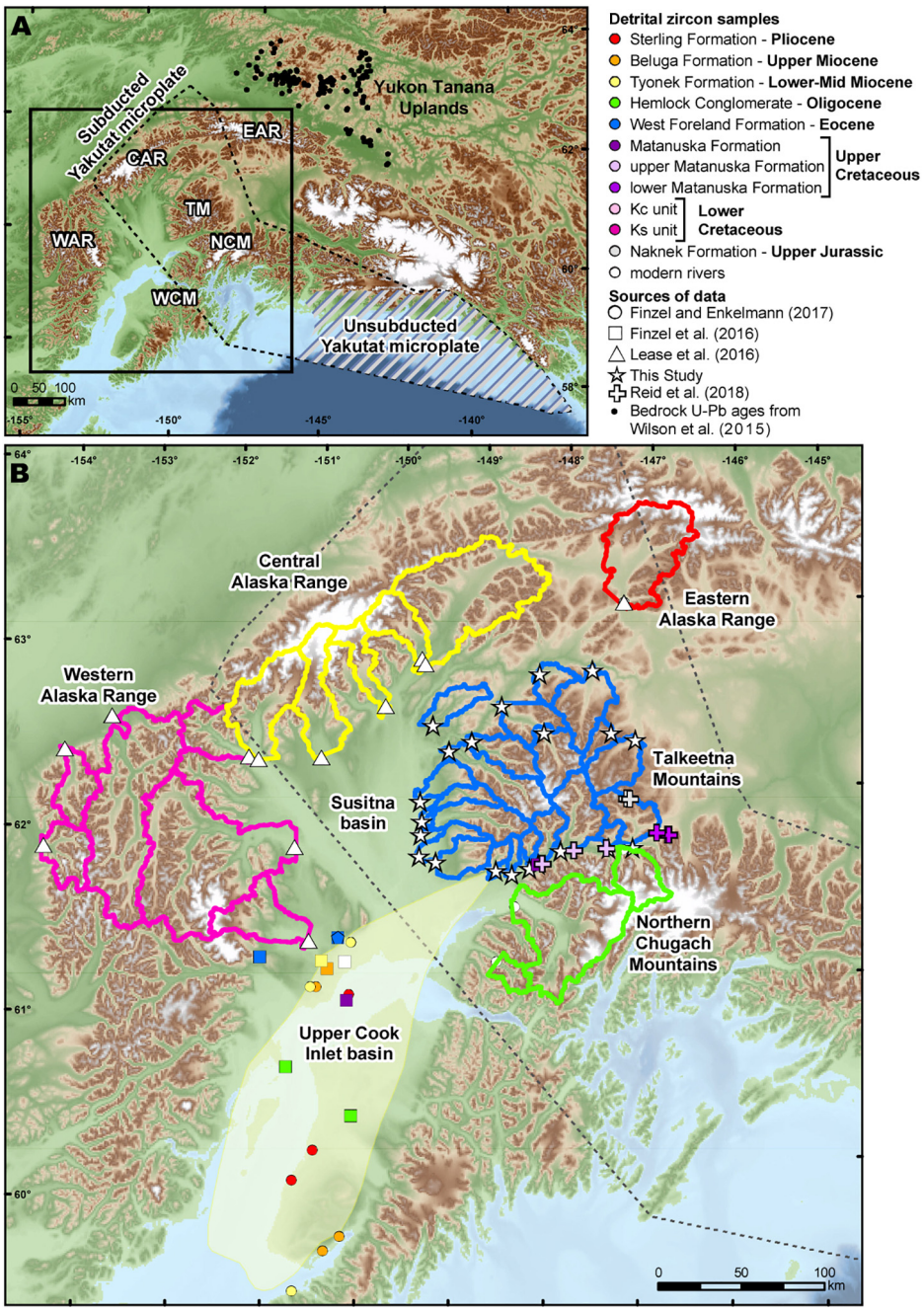

FIGURE 1 | (A) Location map of south-central Alaska showing extent of subducted and unsubducted Yakutat microplate, major mountain belts, the Yukon Tanana Uplands, and the study area (black box is area shown in **(B)**. WAR, western Alaska Range; CAR, central Alaska Range; EAR, eastern Alaska Range; TM, Talkeetna Mountains; NCM, northern Chugach Mountains; WCM, western Chugach Mountains. **(B)** Location map of the study area showing the watersheds for detrital zircon samples from modern rivers in the western Alaska Range (pink), central Alaska Range (yellow), eastern Alaska Range (red), Talkeetna Mountains (blue), and northern Chugach Mountains (green), locations of basin strata samples, and generalized outline of the modern-day Cook Inlet basin. Note that forearc strata are contained within the basin, whereas accretionary prism strata are found in the uplifted Chugach Mountains. The sample symbols denote both the source of the data (by shape) and the depositional age (by color).

(Magoon et al., 1976). In the center of the basin, the forearc strata unconformably overlie Mesozoic sedimentary and volcanic rocks (Jones and Silberling, 1979; Magoon and Egbert, 1986). The upper Paleocene to early Eocene West Foreland Formation reaches its maximum thickness along the western margin of the basin and thins toward the center of the basin (Calderwood and Fackler, 1972; Kirschner and Lyon, 1973; Houston, 1994; Swenson, 1997). The Oligocene Hemlock Conglomerate forms

a sheet that is ∼200–845 m thick across most of the basin (Magoon et al., 1976; Wolfe and Tanai, 1980; Flores et al., 2004). These units postdate spreading-ridge subduction and record the response to this event as an expansion of forearc depositional systems during middle Eocene to late Oligocene time (Finzel et al., 2015, 2016). Detrital zircon U-Pb and $\varepsilon Hf_{(t)}$ signatures reflect both a continuation of local arc-region-derived sediment and also a significant change to distal retro-arc region sediment sources, including the Yukon-Tanana Uplands (**Figure 1**).

Stratigraphic units that are dominantly Neogene in age were deposited in the basin as flat-slab subduction of the Yakutat slab was underway to the northeast (Finzel et al., 2011). The upper Oligocene to middle Miocene Tyonek Formation averages approximately 2,400 m thick across the entire basin (Wolfe and Tanai, 1980). The middle to upper Miocene Beluga Formation reaches its maximum thickness of ∼1,800 m near the western margin of the basin and thins to the east where it is truncated by the overlying Sterling Formation (Calderwood and Fackler, 1972; Kirschner and Lyon, 1973). The upper Miocene to Pliocene Sterling Formation is the only Cenozoic formation in the basin that is thickest near the eastern margin, where it is ∼3,300 m thick (Calderwood and Fackler, 1972; Kirschner and Lyon, 1973). Detrital zircon U-Pb and $\varepsilon Hf_{(t)}$ signatures in these strata record the shrinking of basin catchments and a shift toward more local sediment sources in the adjacent arc rocks in response to insertion of the shallow Yakutat slab (Finzel et al., 2016; Finzel and Enkelmann, 2017).

U-Pb GEOCHRONOLOGY DATA

This study focuses on the potential sources of Mesozoic and younger detrital zircon grains in the forearc strata, and therefore only ages younger than 250 Ma were used in the models. Source regions were characterized by detrital zircon U-Pb ages primarily from modern rivers, except for the Yukon Tanana Uplands that is characterized by bedrock data (**Figure 1**, **Table 1**, and **Supplementary Data Sheet S1**). Sampling of rivers provides a much more comprehensive view of all igneous ages present in a watershed when compared to bedrock sampling, which is often focused on individual igneous bodies or groups of bodies, or on solving a precise temporal problem. New samples from twenty rivers within the Talkeetna Mountains are presented here and fully characterize the bedrock of the entire mountain range with n_{total} = 5,820 and $n_{<250\ \text{Ma}}$ = 5,656 (**Figure 2**). Twenty sandstone samples were collected from rivers that drain the Talkeetna Mountains. Samples were processed using standard mineral separation techniques at the University of Iowa to extract a heavy mineral separate. The separate was sieved using disposable 350 μm screen and non-zircon was removed by magnetic and density separations. A random aliquot was handpicked under alcohol to remove all non-zircon, resulting in a final separate of approximately 500 grains for each sample. Mounts were made at the University of Iowa. Detrital zircons were analyzed for U-Pb isotopes by laser-ablation-multicollector-inductively coupled plasma-mass spectrometry (LA-MC-ICPMS) at the Arizona LaserChron Center following the methods of Gehrels et al. (2006) and Gehrels (2012). The majority of the analyses were conducted with a laser spot diameter of 20 μm. Approximately 315 detrital zircon grains from each sample were analyzed. The $^{206}Pb/^{238}U$ ages are presented for all grains. The U-Pb analytical data is reported in the **Supplementary Data Sheet S1**.

The detrital signature of the western Alaska Range is determined from seven previously published samples with n_{total} = 419 and $n_{<250\ \text{Ma}}$ = 397 (Finzel et al., 2016; Lease et al., 2016). Five samples from rivers draining the southern flank of the central Alaska Range have n_{total} = 487 and $n_{<250\ \text{Ma}}$ = 463 (Lease et al., 2016). The eastern Alaska Range is the least well-characterized with only two samples that produce with n_{total} = 186 and $n_{<250\ \text{Ma}}$ = 184 (Lease et al., 2016; Finzel and Enkelmann, 2017). To the south, the detrital signature of Permian-Cretaceous accretionary prism strata in the northern Chugach Mountains is represented by three samples with n_{total} = 969 and $n_{<250\ \text{Ma}}$ = 914 (Finzel and Enkelmann, 2017). No modern river data was available for the Yukon Tanana Uplands located northeast of the eastern Alaska Range (**Figure 1**), but that region was previously identified as an important sediment source area during the early Cenozoic based on Paleozoic and Precambrian ages present in the basin strata (Finzel et al., 2016). Therefore, 125 previously published monazite, sphene, titanite, and zircon U-Pb ages from bedrock were combined and are here treated as a detrital signature for the area.

Forearc basin strata were subdivided into individual or groups of formations that represent seven different time intervals (**Table 2**). Three samples from the Kc and Ks units from the Talkeetna Mountains (**Figure 1**) embody Early Cretaceous time with n_{total} = 1,081 and $n_{<250\ \text{Ma}}$ = 1,051. The Late Cretaceous is represented by eight samples from the Matanuska Formation that have n_{total} = 2,550 and $n_{<250\ \text{Ma}}$ = 2,314. Three samples from the West Foreland Formation characterize the Eocene

TABLE 1 | Data information for sediment source regions.

Geographic region	Sources of data	N =	n_{total} =	$N_{<250\ \text{Ma}}$ =	$\%_{<250\text{Ma}}$
Talkeetna Mountains	This study	21	5820	5656	97%
Western Alaska Range	Finzel et al., 2016; Lease et al., 2016	7	419	397	95%
Central Alaska Range	Lease et al., 2016	5	487	463	95%
Eastern Alaska Range	Lease et al., 2016; Finzel and Enkelmann, 2017	2	186	184	99%
Chugach Mountains	Finzel and Enkelmann, 2017	3	969	914	94%
Yukon Tanana Uplands*	Wilson et al., 2015	125	125	125	100%

Data from bedrock samples were filtered for <250 Ma.

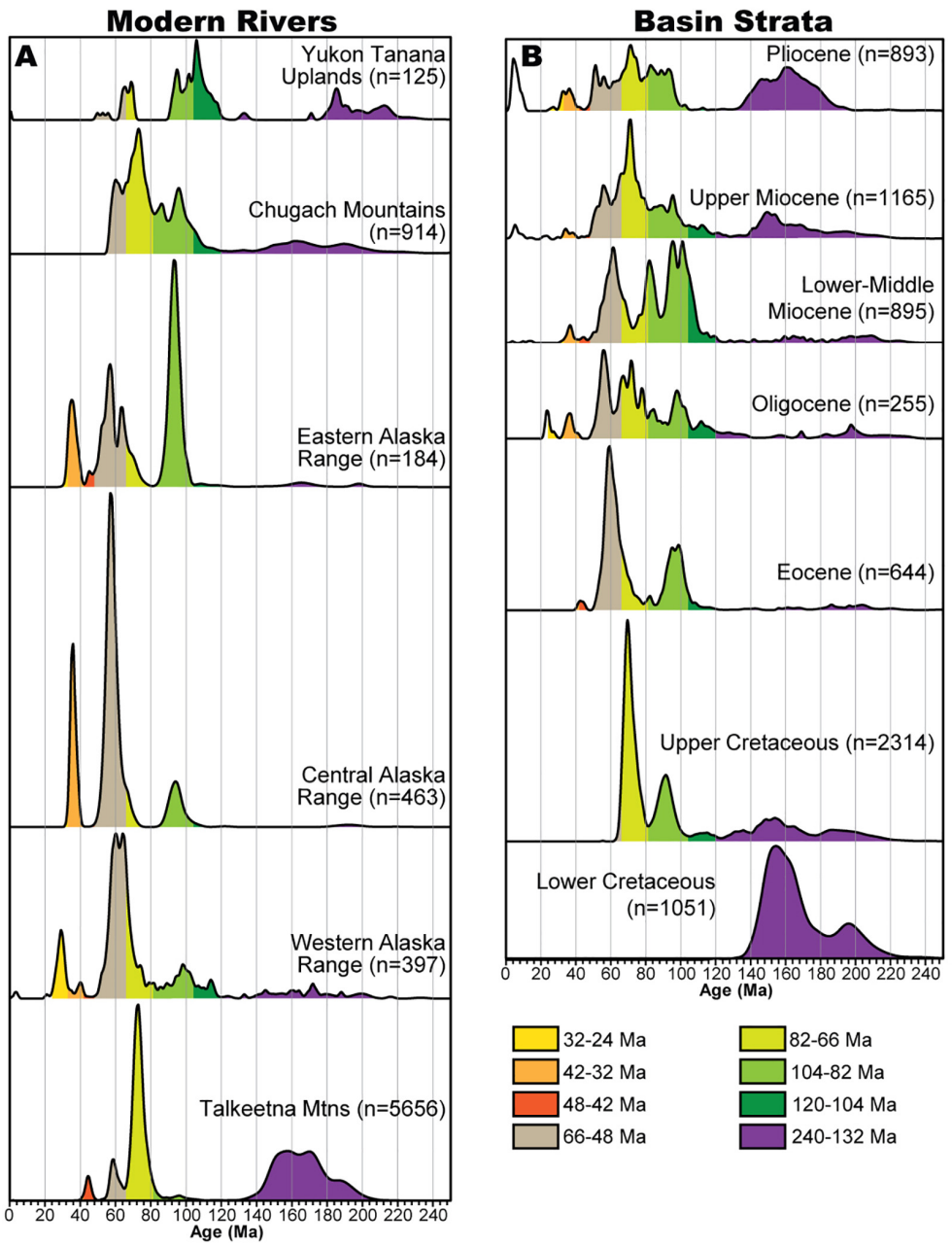

FIGURE 2 | Probability density plots of geochronological data from **(A)** potential source regions and **(B)** forearc basinal strata.

TABLE 2 | Data and model information for each stratigraphic interval.

Stratigraphic interval	Sources of data	*N* =	n_{total} =	n = $_{<250\ Ma}$	$\%_{<250\ Ma}$	Min. age	R^2
Pliocene	Finzel and Enkelmann, 2017	3	916	893	97%	20 Ma	0.697
Upper Miocene	Finzel et al., 2016; Finzel and Enkelmann, 2017	4	1248	1165	93%	20 Ma	0.931
Lower-Middle Miocene	Finzel et al., 2016; Finzel and Enkelmann, 2017	4	1023	895	87%	20 Ma	0.691
Oligocene	Finzel et al., 2016	2	342	255	75%	23 Ma	0.833
Eocene	Finzel et al., 2016; Enkelmann et al., 2019	3	900	644	72%	40 Ma	0.902
Upper Cretaceous	Finzel et al., 2016; Reid et al., 2018	8	2550	2314	91%	65 Ma	0.895
Lower Cretaceous	Reid et al., 2018	3	1081	1051	97%	84 Ma	0.856

with n_{total} = 900 and $n_{<250\ Ma}$ = 644. The Oligocene is epitomized by two samples from the Hemlock Formation that have n_{total} = 342 and $n_{<250\ Ma}$ = 255. Four samples from the Tyonek Formation represent the Early-Middle Miocene with n_{total} = 1,023 and $n_{<250\ Ma}$ = 895. The Late Miocene is represented by four samples from the Beluga Formation with n_{total} = 1,248 and $n_{<250\ Ma}$ = 1,165. Three samples from the Sterling Formation characterize Pliocene time and have n_{total} = 916 and $n_{<250\ Ma}$ = 893.

Some of the samples used in this study are n = 100, and recent work has suggested that small-n detrital zircon studies may not be reliable for comparisons of relative proportions of populations between samples (Gehrels, 2012; Pullen et al., 2014). Finzel et al. (2016) compared a small-n data set first published in Finzel et al. (2015) with an expanded large-n (n = 300) data set and illustrated that they do not show a significant difference in the presence of major populations, as well as most minor populations. The similarity between the two sets of analyses is likely due to the small number of age groups in each sample. For example, as in this study, most of the distributions have two or three main peaks, so a smaller number of analyses were sufficient to characterize the distribution both in terms of the presence and relative abundance of age groups. Therefore, in basins with sources that have fewer age populations from which to derive sediment, smaller-n datasets may suffice for drawing comparisons.

MODELING APPROACH

The mixing proportions of the various source regions for each of the defined stratigraphic intervals were modeled using an inverse Monte Carlo approach in combination with an optimized forward model (DZMix from Sundell and Saylor, 2017). Details about the modeling procedure can be found in Sundell and Saylor (2017). In general, the inverse model consisted of 10,000 iterations where each source region's entire probability density plot (PDP) and kernel density estimate (KDE) were scaled by randomly generated weights and then summed together to produce a single model source distribution. While the maximum age modeled for each stratigraphic interval was 250 Ma, the minimum modeled age was dependent upon the known depositional age of the formation(s) or was designated 20 Ma because previous work has demonstrated that igneous rocks younger than that are not found in any abundance in the modeled source regions (**Table 2**; Finzel et al., 2011, 2015). For each stratigraphic interval, the 1% best-fit Monte Carlo trials are shown in **Figures 3–9**, along with the mean cross-correlation coefficient (R^2). This statistical parameter has been suggested to be more discriminating than other tests (e.g., KS and Kuiper) as well as more sensitive to the overall number and proportions of ages in a distribution (Sundell and Saylor, 2017). The best-fits from the inverse model are then forward modeled to minimize 1-R^2. This is shown as the optimized best-fit model and its associated R^2 in **Figures 3–9**. In addition, CDFs from the source areas and composite stratigraphic interval, as well as the resultant relative contributions from each source region based on the optimized forward model, are displayed.

MODEL RESULTS

Model results for Lower Cretaceous strata suggest that the predominant sediment source region, with more than 90% of the zircon signature being derived, was in the Talkeetna Mountains (**Figure 3**). The R^2 for the optimized best-fit model is 0.856. The small misfit probably results from the model's inability to parse out and differentially weight individual age groups from the source signatures. That is, the weighting factor is applied

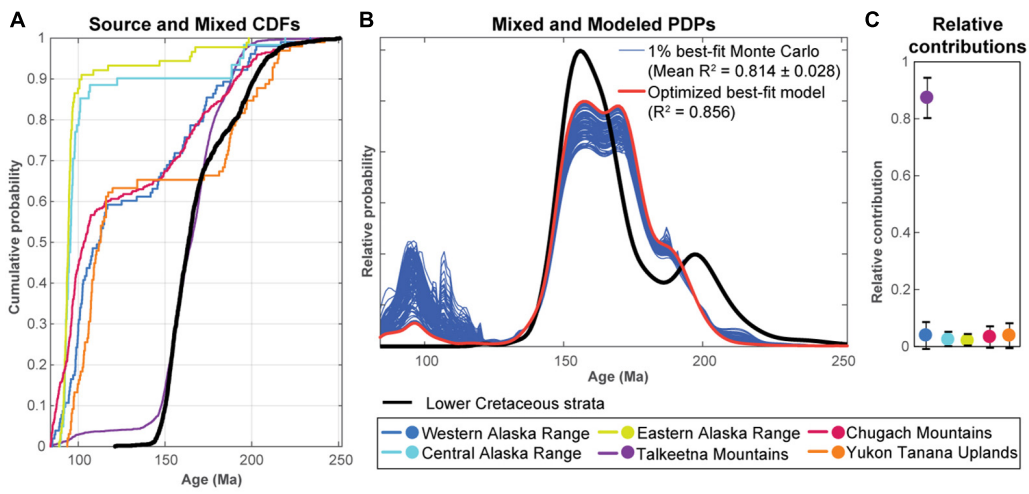

FIGURE 3 | Model results for Lower Cretaceous strata showing **(A)** cumulative density functions for the basin strata and potential source regions, **(B)** probability density plots of the basin strata (black), 1% best-fits from the Monte Carlo inverse model (blue), and optimized best-fit forward model (red), and **(C)** plot of relative contributions from each of the potential source regions produced from the optimized best-fit model.

to the entire age distribution, such that in this example, the model has to include some Cretaceous ages that are found in the Talkeetna Mountains today but do not appear in the zircon signature of the Lower Cretaceous strata. These results suggest a more localized source for the strata that is characterized solely by Jurassic zircon sources.

In contrast, sediment source regions for Upper Cretaceous strata include approximately equal contributions from the Talkeetna Mountains and the accretionary prism strata in the northern Chugach Mountains (**Figure 4**). The R^2 for the optimized best-fit model is 0.895. The small misfit here is due to the underfitting of the 74 Ma peak in the Upper Cretaceous signature. This could be remedied by scaling the individual age peaks within the source contributions, and therefore does not require another sediment source region to improve the fit.

By the Eocene, sediment sources for the basin had changed significantly with negligible contributions from the previously important Talkeetna Mountains and northern Chugach Mountains. In contrast, model results for Eocene strata suggest the primary source region was in the western Alaska Range (**Figure 5**). The R^2 for the optimized best-fit model is 0.902. Overall, all of the individual age peaks found in the Eocene strata are matched by a western Alaska Range source, so the very small misfit is attributable to the underfitting of age peaks as before, specifically ∼61 and 100 Ma.

A second shift in sediment sources for the forearc basin occurred by the Oligocene. Model results for Oligocene strata indicate the primary sediment source region as the northern Chugach Mountains (∼40%), with lesser contributions from the central Alaska Range (∼20%), and minor contributions from the remaining source regions (**Figure 6**). The R^2 for the optimized best-fit model is 0.833. The primary source of the small misfit can be attributed to a ∼26 Ma peak in the Oligocene strata that is not matched by the model results. The source for these zircons has previously been identified as intrusive rocks found in the eastern Alaska Range region, but lies outside of our modern river data coverage (Turner and Smith, 1974; Nokleberg et al., 1992).

Model results for Lower—Middle Miocene strata have the lowest R^2 of any stratigraphic interval at 0.691 for the optimized best-fit model. Regardless, the results suggest a variety of sediment source regions, including the northern Chugach Mountains and Yukon Tanana Uplands (∼30% each) and western and eastern Alaska Ranges (∼15% each; **Figure 7**). The moderate misfit is clearly due to the model underfitting peaks ∼83 and 102 Ma, and overfitting peaks ∼180–190 Ma. An ∼83 Ma peak is not present in the source data, although the northern Chugach Mountains signature contains a peak ∼85 Ma, suggesting that not all the potential sources for the basin have been included in the source dataset. Underfitting of the ∼102 Ma peak and overfitting of the Jurassic peaks is the result of not weighting individual age peaks in the source distributions differently. The Yukon Tanana Uplands signature provides both of these age groups, but in different relative proportions than in the Lower—Middle Miocene strata. The model's attempt to fit the relatively large ∼102 Ma peak in the basin strata results in an overestimation of the Jurassic ages.

The R^2 for the optimized best-fit model of Upper Miocene strata is the highest for any stratigraphic interval at 0.931. The primary sediment source regions lie above the present-day flat slab region (**Figure 1**) and include the northern Chugach Mountains (∼60%) and the Talkeetna Mountains (∼30%; **Figure 8**). The optimized best-fit model matches not only the age peaks present, but also the relative abundances for each age peak very closely.

Model results for Pliocene strata have the second lowest R^2 of any stratigraphic interval at 0.697 for the optimized best-fit model. The primary sediment source region is the Talkeetna Mountains (∼60%), with a smaller contribution from the eastern Alaska Range (∼20%) and northern Chugach Mountains (∼10%; **Figure 9**). The moderate misfit is again attributable to underfitting a peak ∼85 Ma, but also overfitting a peak ∼74 Ma and underfitting Jurassic peaks between ∼165-150 Ma. The latter misfits are related because in the model's attempt to fit the abundant Jurassic ages found in the Pliocene strata and sourced from the Talkeetna Mountains, it must also input a significant proportion of ∼74 Ma ages also found in that source region. These results suggest a more localized source for the Pliocene strata in the Talkeetna Mountains that is characterized by dominantly Jurassic zircon sources with relatively less Late Cretaceous ages.

SEDIMENT DISPERSAL AND TECTONICS

Early Cretaceous

During Late Jurassic and Early Cretaceous time, regional exhumation of the Jurassic oceanic island arc north of the forearc basin was related to either collision of the arc with the other Insular terranes outboard of the North American margin (Clift et al., 2005) or collision of the entire Insular belt terranes, including the Jurassic arc, with the North American margin itself (Nokleberg et al., 2001; Ridgway et al., 2002; Trop et al., 2002, 2005; Blodgett and Sralla, 2008; Bacon et al., 2012). Basins positioned along the inboard margin of the Insular terranes and the outboard margin of North America contain evidence for initial Late Jurassic collision and Aptian to Campanian final suturing (Nokleberg et al., 1992; Ridgway et al., 1997, 2002; Eastham and Ridgway, 2002; Trop et al., 2004; Davidson and McPhillips, 2007; Hampton et al., 2007; Kalbas et al., 2007; Manuszak et al., 2007).

Detrital zircon U-Pb geochronologic data and $\varepsilon Hf_{(t)}$ values from the Lower Cretaceous strata were previously interpreted to record exhumation of deeper and older parts of the adjacent Jurassic arc and input from local Paleozoic basement sources that are part of the Insular terranes (Reid et al., 2018). The bedrock in the Talkeetna Mountains is mostly composed of Peninsular terrane rocks, which was originally defined by Jones et al. (1977), Jones and Silberling (1979), and Plafker et al. (1989) to consist of late Paleozoic carbonate and volcanics, Late Triassic carbonate and basalt, Late Triassic–Late Jurassic ultramafic, andesitic, and granitic rocks, and Middle Jurassic–Cretaceous clastic basinal

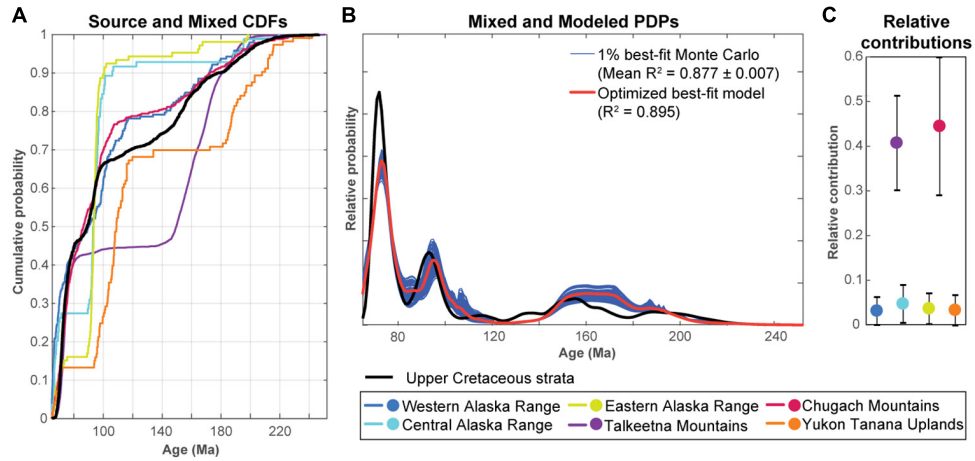

FIGURE 4 | Same as **Figure 3** except for the Upper Cretaceous strata.

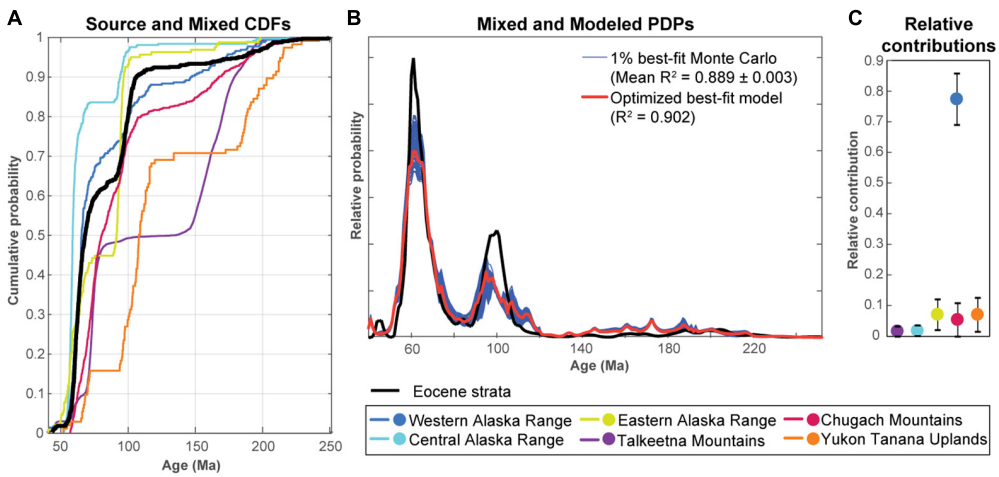

FIGURE 5 | Same as **Figure 3** except for the Eocene strata.

sequences. Recent work on the terrane has focused on the Early–Late Jurassic magmatic rocks of the Talkeetna oceanic island arc, and geochronologic bedrock data from the Talkeenta Mountains indicates magmatic activity between 202–181 Ma and 177–156 Ma, respectively (Rioux et al., 2007, 2010). The modeling results presented here support the previously inferred primary sediment source of the Talkeetna Mountains for grains younger than 250 Ma, and specifically a source characterized by Jurassic ages and less so by the older Insular basement rocks (**Figures 3**, **10**).

Late Cretaceous

By the Late Cretaceous, the Insular terranes were fully accreted to the North American margin, either at low paleolatitudes, near present-day Baja California, and then transported >3,000 km northward through strike-slip translation to its present-day position between Late Cretaceous and Paleocene time (Irving et al., 1985; Panuska, 1985; Umhoefer, 1987; Cowan et al., 1997; Stamatakos et al., 2001), or within ∼1,000 km of its present day position and subsequently transported northward over the same period (e.g., Irving et al., 1996; Butler et al., 1997; Keppie and Dostal, 2001). Detrital zircon U-Pb distributions and $\varepsilon Hf_{(t)}$ values in the Upper Cretaceous strata have pronounced Late Cretaceous peaks, diminished Jurassic grains, more abundant Paleozoic and Precambrian populations, and a wide range of negative $\varepsilon Hf_{(t)}$ values that signify an influx of sediment from the inboard Intermontane terranes to the forearc basin (Reid et al., 2018). That study also presented our preferred model where the forearc basin in south-central Alaska, the part of the Intermontane terranes that are today located in northern British Columbia, Yukon, and eastern Alaska, and the part of the Chugach-Prince William terrane found on Kodiak Island were all juxtaposed by Late Cretaceous (Turonian) time. Therefore, offset between the forearc basin and the potential sediment sources used in this study were not significant.

Modeling results for grains with ages <250 Ma in the Upper Cretaceous strata suggest an additional, previously undetected

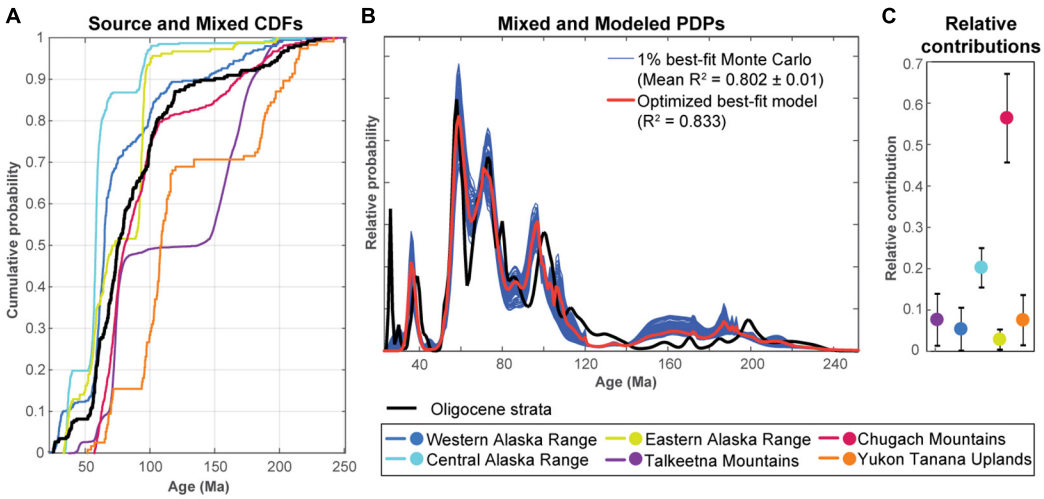

FIGURE 6 | Same as **Figure 3** except for the Oligocene strata.

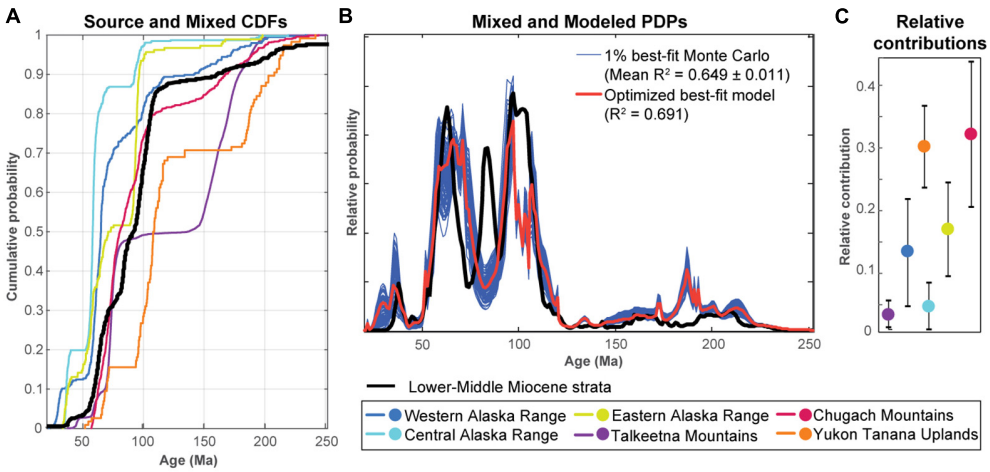

FIGURE 7 | Same as **Figure 3** except for the Lower-Middle Miocene strata.

source in the accretionary prism strata of the northern Chugach Mountains (**Figures 4, 10**). Coarse-grained sedimentation along the southern margin of the forearc basin contains diagnostic lithologies that imply local subaerial uplift and erosion of the accretionary prism by Early Cretaceous time (Trop and Ridgway, 2007). The results presented here indicate that Insular terrane rocks in the Talkeetna Mountains and accretionary prism strata in the northern Chugach Mountains contributed relatively equally to the zircon signature found in the Upper Cretaceous strata. This implies that the accretionary prism strata may have been extensively subaerially exhumed and eroding into the forearc basin during the Late Cretaceous.

Eocene

During Paleocene and Eocene time (~62–50 Ma), a spreading ridge was subducted while migrating from west to east across the entire southern Alaska margin. Deposition of middle Eocene (~44–41 Ma) strata postdates passage of the spreading ridge through the study area. Detrital zircon U-Pb and $\varepsilon Hf_{(t)}$ signatures from Eocene strata were previously interpreted to reflect a continuation of local arc region-derived sediment from the western and central Alaska Range and Talkeetna Mountains, based on Mesozoic and Cenozoic ages. In addition, a significant proportion of distal retro-arc region sources provided sediment based on Paleozoic and Precambrian ages (Finzel et al., 2015). Finzel et al. (2016) suggested that crustal thinning due to thermal erosion from upwelling asthenosphere (Cole and Stewart, 2009; Jacobson et al., 2011; Ling et al., 2013) and temporary arc cessation (Dickinson and Snyder, 1979; Thorkelson, 1996; Gorring and Kay, 2001) associated with passage of the subducting spreading-ridge permitted forearc fluvial systems to expand into the retroarc region.

Modeling results for grains with ages <250 Ma in the middle Eocene strata support arc-derived sediment flux, but point to a

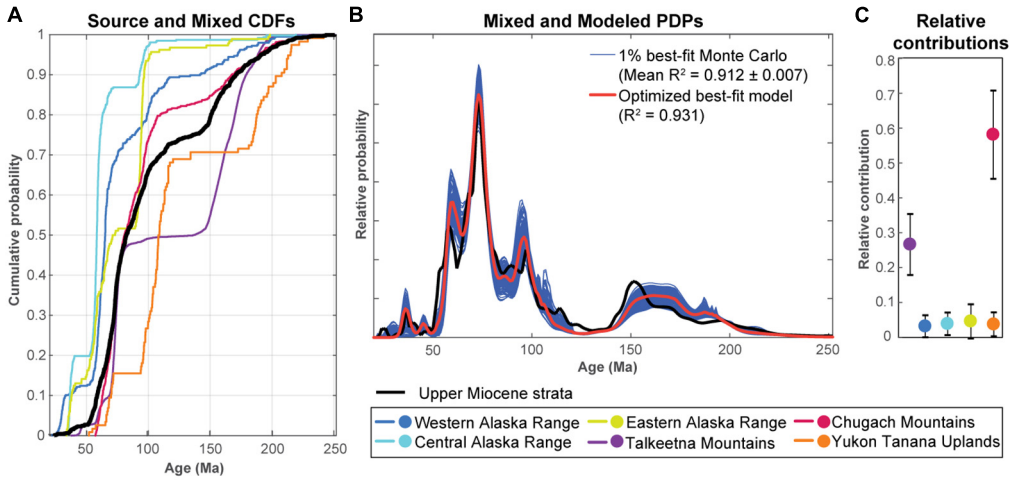

FIGURE 8 | Same as **Figure 3** except for the Upper Miocene strata.

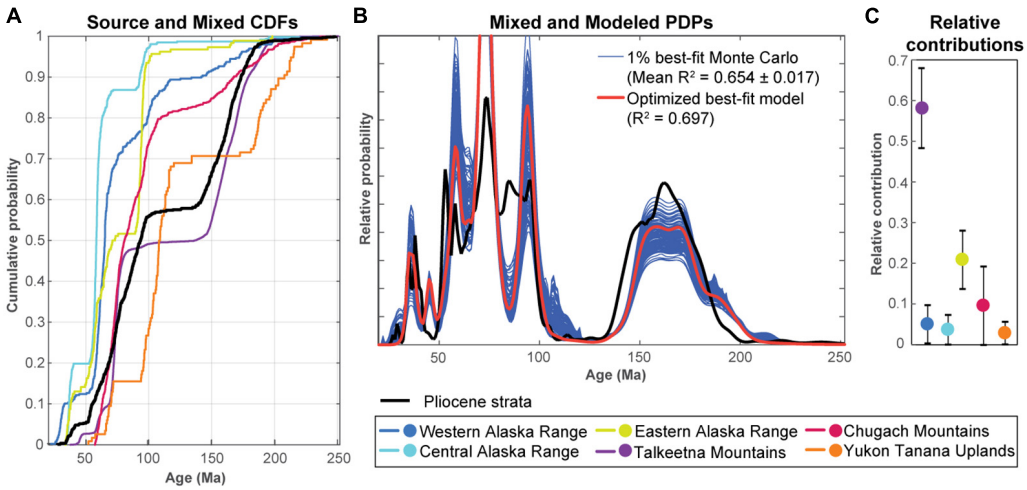

FIGURE 9 | Same as **Figure 3** except for the Pliocene strata.

more specific source from just the western Alaska Range. With an R^2 of 0.902 for the optimized best fit model, it appears as though ~80% of the <250 Ma zircons can be derived from the western Alaska Range (**Figures 5, 10**). In addition, the PDP of ages from the Eocene strata visually match very closely in age and relative abundance with that from the western Alaska Range, including a significant peak ~60 Ma, a lesser group of peaks ~100 Ma, and minor Jurassic populations (**Figure 2**). In comparison, the Eocene strata lack the presence of the large 74 Ma peak present in the Talkeetna Mountains, as well as the ~94 Ma peak found in the eastern Alaska Range.

Oligocene

Beginning in the late Eocene or early Oligocene (~35 Ma), the Yakutat microplate began subducting at a shallow angle along the outboard margin of south-central Alaska and continues to the present day (Finzel et al., 2011, 2015; Arkle et al., 2013). Detrital zircon distributions from upper Oligocene (~27–23 Ma) strata contain Devonian to Mississippian (~370–340 Ma) and Precambrian (2000–1800 Ma) U-Pb ages, as well as middle Cretaceous (120–90 Ma) zircons with evolved $\varepsilon Hf_{(t)}$ compositions and kyanite in the heavy mineral suite, that indicate continued derivation of sediment from the retroarc Yukon-Tanana Uplands northeast of the present-day Alaska Range.

Modeling results for grains with ages <250 Ma in the upper Oligocene strata again suggest an additional, previously undetected source in the accretionary prism strata of the northern Chugach Mountains, as well as minor contributions from the central Alaska Range (**Figures 6, 10**). Thermochronologic data from the northern Chugach Mountains indicate that exhumation began during late Eocene to early Oligocene time (ca. 35–30 Ma) and continued into early-middle Miocene time (ca. 16–11 Ma; Little and Naeser, 1989; Hoffman and Armstrong, 2006; Arkle et al., 2013; Enkelmann et al., 2019). Exhumation of this region

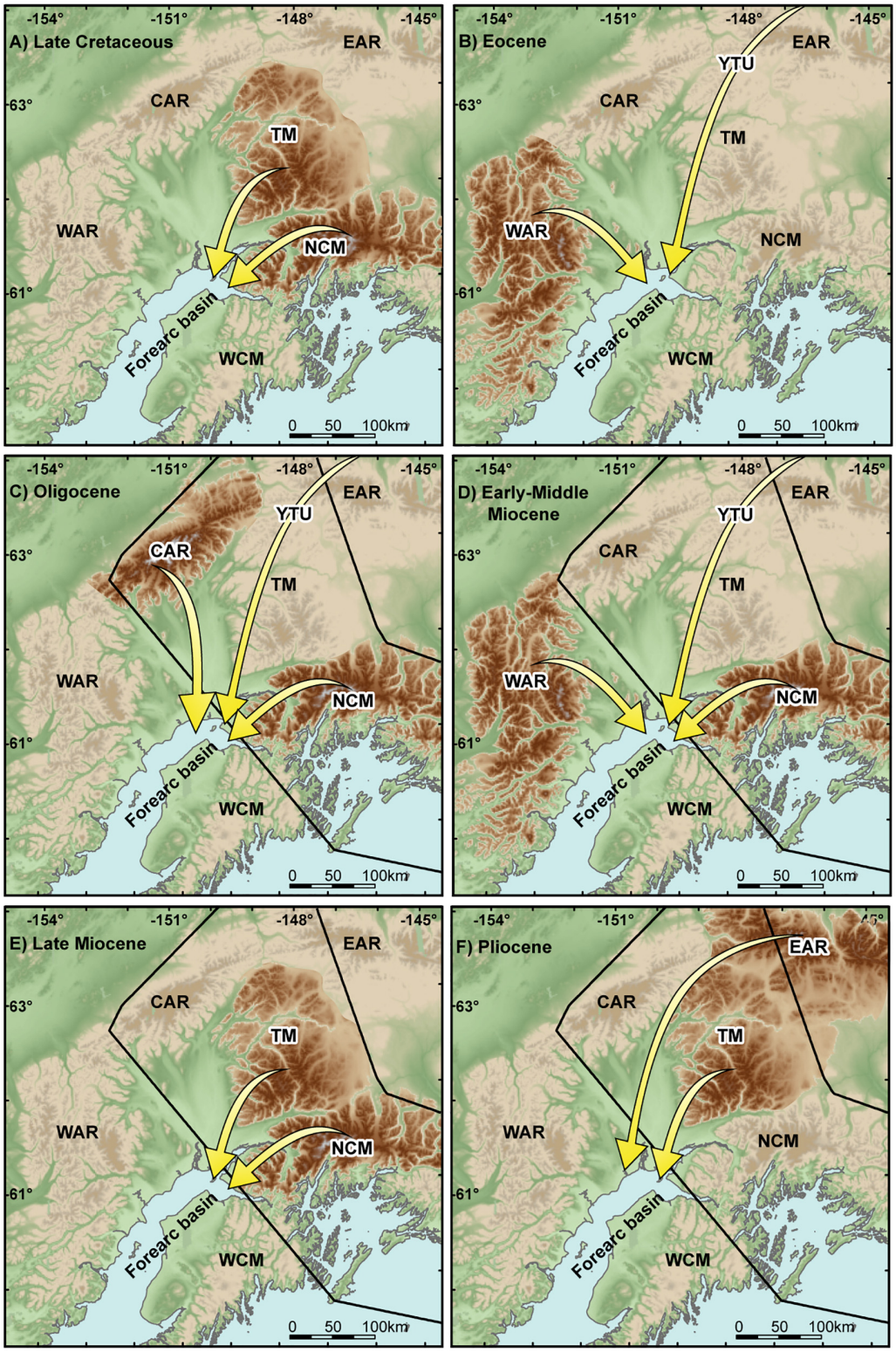

FIGURE 10 | Topographic map of the study area illustrating the predominant sedimentary source regions based on previous interpretations discussed in the text and the modeling results presented here for the **(A)** Late Cretaceous, **(B)** Eocene, **(C)** Oligocene, **(D)** Early-Middle Miocene, **(E)** Late Miocene, and **(F)** Pliocene. The black polygon in **(C—F)** is the present-day position of the Yakutat microplate. Note that forearc strata are contained within the basin, whereas accretionary prism strata are found in the uplifted Chugach Mountain Range. WAR, western Alaska Range; CAR, central Alaska Range; EAR, eastern Alaska Range; TM, Talkeetna Mountains; NCM, northern Chugach Mountains; WCM, western Chugach Mountains; YTU, Yukon Tanana Uplands.

is inferred to reflect initial insertion of the shallow Yakutat slab (Enkelmann et al., 2008, 2010; Finzel et al., 2011, 2015; Arkle et al., 2013). This nascent shallow subduction likely reinvigorated sediment flux from the Chugach accretionary prism into the forearc basin.

Miocene

Shallow subduction of the Yakutat microplate continued during the Miocene. Previous qualitative assessment of detrital zircon U-Pb distributions and $\varepsilon Hf_{(t)}$ values in Lower-Middle Miocene strata suggest that sediment was derived from all margins of the basin, including the central and eastern Alaska Range, western Talkeetna Mountains, and northern Chugach Mountains (Finzel and Enkelmann, 2017). Some of those regions, including the central Alaska Range, western Alaska Range, and eastern Alaska Range produce detrital zircon and apatite fission track ages that reflect late Oligocene to early Miocene (∼30–18 Ma) initial and widespread exhumation (Lease et al., 2016; Enkelmann et al., 2019). In addition, apatite thermochronologic ages <20 Ma in the western Chugach Mountains and Talkeetna Mountains indicate exhumation during the Miocene (Little and Naeser, 1989; Hoffman and Armstrong, 2006; Arkle et al., 2013; Valentino et al., 2016). Model results for Lower—Middle Miocene strata have the lowest R^2 of any stratigraphic interval, likely due to undifferentiated weighting of the source signatures, yet the results are consistent with a variety of sediment source regions, including the northern Chugach Mountains and Yukon Tanana Uplands (∼30% each) and western and eastern Alaska Ranges (∼15% each; **Figures 7, 10**). The widespread nature of the sediment source regions is likely related to coincident shallow subduction beneath south-central Alaska. Crustal thickening due to plateau subduction results in buoyancy and increased coupling between the upper plate and downgoing slab, which drives widespread surface uplift and concentrates stresses in the upper plate that result in strain concentration in rheologically weak zones and triggers significant vertical uplift creating topography and an increase in exhumation rates (Dickinson and Snyder, 1979; Jordan and Allmendinger, 1986; Gutscher et al., 2000; Hampel, 2002; Lallemand et al., 2005; Espurt et al., 2008).

Heavy mineral analyses and sandstone petrography of Upper Miocene strata suggest a provenance area in the Chugach Mountains, with a minor possible contribution from Mesozoic strata located around the flanks of the central Alaska Range (Kirschner and Lyon, 1973; Mongrain, 2012; Helmold et al., 2013; LePain et al., 2013). Detrital zircon U-Pb distributions and $\varepsilon Hf_{(t)}$ values in Upper Miocene strata indicate a dominantly eastern provenance from the northern Chugach and southern Talkeetna Mountains (Finzel and Enkelmann, 2017). The R^2 for the optimized best-fit model of Upper Miocene strata is the highest for any stratigraphic interval and also indicates primary sediment source regions in the northern Chugach Mountains (∼60%) and the Talkeetna Mountains (∼30%; **Figures 8, 10**). Both of these areas lie above the modern-day flat-slab region (**Figure 1**). The Yakutat microplate is interpreted as a wedge-shaped oceanic plateau that thickens from ∼11 km at its deepest observable extent in the mantle to ∼30 km thick at the modern coastline (Ferris et al., 2003; Eberhart-Phillips et al., 2006; Worthington et al., 2008, 2012; Christeson et al., 2010; Bauer et al., 2014). Therefore, as subduction of the microplate has progressed, increasingly thicker crust has been inserted beneath south-central Alaska, resulting in an overall inboard migration of exhumation and sediment bypass above the flat-slab region, and a relative increase in sediment flux toward areas adjacent to the flat-slab region (Finzel et al., 2011).

Pliocene

Previous assessment of detrital zircon U-Pb distributions and $\varepsilon Hf_{(t)}$ values in Pliocene strata indicate a continuation of a dominantly eastern provenance including the northern Chugach and southern Talkeetna Mountains, as well as a smaller sediment flux from the Alaska Range (Finzel and Enkelmann, 2017). Model results for Pliocene strata have the second lowest R^2 of any stratigraphic interval, probably again due to undifferentiated weighting of the source signatures, but still agree with previous interpretations. The relative contributions for the Pliocene strata are modeled as ∼60% from the Talkeetna Mountains, ∼20% from the eastern Alaska Range, and ∼10% from the northern Chugach Mountains (**Figures 9, 10**). This overall inboard shift in sediment source regions is consistent with progressively thicker portions of the Yakutat microplate being inserted beneath south-central Alaska and triggering exhumation in farther inboard source regions as a result.

DISCUSSION

Forearc Basin Response to External Tectonic Forcing

The southern margin of Alaska has experienced convergence and subduction since at least Jurassic time, resulting in prolonged magmatism that produced geographically extensive plutonic belts with different ages that often spatially overlap, making provenance determination as it relates to the complex tectonic history of the region difficult. The combined analysis of detrital zircon sampling of modern rivers and basin strata in conjunction with mixture modeling, however, presents a useful method for partitioning the widespread and pervasive zircon ages in the sediment source regions, permitting a more nuanced resolution of the tectonic forcing on the sedimentary systems. For example, evaluation of the model results reveals a predominance of sediment input from the Talkeetna Mountains during the Early Cretaceous (**Figure 11**). This time marks a period of ongoing accretion between the Insular terranes and the western margin of North America (Pavlis, 1982; McClelland et al., 1992; Trop et al., 2002, 2005; Manuszak et al., 2007). Early Cretaceous exhumation of the northern Talkeetna Mountains in response to accretion is recorded in spatially restricted non-marine Aptian—Cenomanian strata that unconformably overlie marine Jurassic-Cretaceous strata (Hampton et al., 2007). Therefore, contraction and exhumation of the Talkeetna Mountains due to collision of the Insular terranes resulted in that region being a primary sediment source for the forearc basin during Early Cretaceous time.

Terminal suturing of the terranes occurred during the Late Cretaceous (∼84–67 Ma) in south-central Alaska

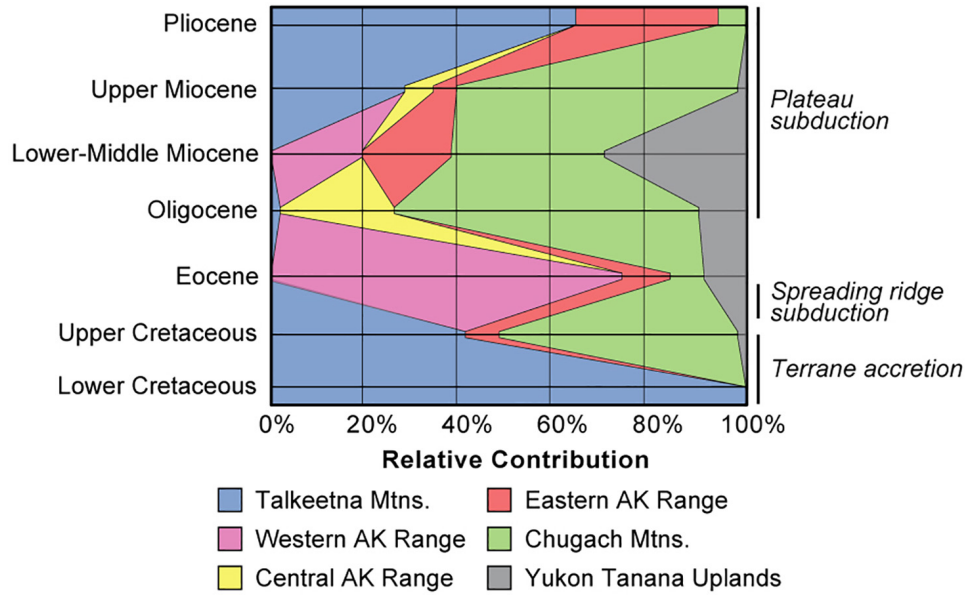

FIGURE 11 | Graph depicting temporal variations in relative contributions from the potential source regions in southern Alaska.

(Trop et al., 2019). Upper Cretaceous strata record the addition of a new source region in the Chugach Mountains, and to a much lesser extent, the eastern Alaska Range and Yukon-Tanana Uplands (**Figure 11**). A prominent 98 Ma zircon fission track peak from modern rivers draining the Talkeetna Mountains reveals ongoing exhumation in that region (Enkelmann et al., 2019). Late Cretaceous exhumation of the accretionary prism could be related to changes in plate kinematics induced by final suturing of the Insular terranes. Relative convergent plate motions between the terranes and the subducting plate that were previously partly accommodated by migration of the terranes toward North America must have been transferred elsewhere as the terranes were juxtaposed against the continental backstop. That convergence may have focused contractional deformation to the outboard margin of the terranes and contributed to the overall uplift of the accretionary prism strata.

By Eocene time, after the passage of a subducting spreading ridge or break-off of the subducting slab, the dominant sediment source region was the western Alaska Range with lesser contributions from the eastern Alaska Range, Chugach Mountains, and Yukon Tanana Uplands (**Figure 11**). Zircon and apatite fission track data from modern rivers sourced in the western Alaska Range record exhumation of that region during the Paleocene and Eocene, but the driving factors remain debated. By the Oligocene, however, the dominant sediment source area was again the Chugach Mountains with smaller contributions from the central Alaska Range and Yukon Tanana Uplands. Initiation of shallow subduction of the Yakutat microplate is inferred to have triggered uplift and exhumation in the Chugach Mountains (Arkle et al., 2013; Ferguson et al., 2015) and across the entire Alaska Range, which is also recorded in synorogenic Oligocene strata in the central Alaska Range (Benowitz et al., 2011, 2012, 2014; Fitzgerald et al., 2014; Riccio et al., 2014; Lease et al., 2016; Enkelmann et al., 2019; Terhune et al., 2019; Trop et al., 2019).

Shallow subduction strongly influenced sediment flux into the forearc basin, either turning off or completely swamping any sediment input from the formerly important inboard source regions in the Talkeetna Mountains and western Alaska Range with new renewed contributions from the Chugach Mountains. In fact, major contributions from the Chugach Mountains appear to be intricately linked to plate margin events. For example, during the final suturing of the Insular terranes in the Late Cretaceous, the Chugach Mountains were triggered as a primary sediment source region. Then again during insertion of the shallow slab in the Oligocene, sediment flux from that range was rejuvenated. As the shallow slab was progressively inserted beneath south-central Alaska during the Miocene-Pliocene, it continued to force changes in sediment source regions. Outboard sediment sources from the Chugach Mountains were progressively overwhelmed by more inboard sediment sources including the Talkeetna Mountains and eastern Alaska Range. It is clear that tectonic forcing on the forearc region has played a significant role in source region exhumation and sediment routing since Cretaceous time.

Benefits and Limitations of the Watershed Approach

Using sediment from modern drainage systems to constrain ancient sediment source regions has many advantages. Detrital zircon grains in modern rivers are derived from all available bedrock sources in a watershed. Dating of those grains provides

a quick and efficient way to characterize the distribution of ages present in potential source areas. This is especially important in regions that are underexplored or difficult to access. Modern river sampling also provides a unique opportunity to assess sediment recycling in a basin. A major difficulty associated with detrital zircons is that they are very robust and can remain intact for several sedimentary cycles. Consequently, recycling of detrital zircons from older strata is often a concern but cannot be adequately addressed due to poor characterization of older stratigraphic successions. Characterizing the detrital signature of multiple older successions would be costly and time-consuming, especially considering that the detrital zircon signature within an individual stratigraphic unit can vary greatly. In contrast, careful selection of watersheds and sampling sites allows rapid characterization of exhumed stratigraphic units. Combined with mixture modeling, this is a powerful tool to assess recycled versus primary sediment input into a basin.

The watershed approach also has limitations. For example, exposure of various bedrock units or the geometries of catchments may have varied over time. Therefore, it is important to constrain the landscape evolution of the potential source regions adjacent to a sedimentary basin in order to produce robust results. In south-central Alaska, significant changes to most of the landscape have not occurred during much of Cenozoic time. Combined U-Pb and fission track double-dating of detrital zircon from modern rivers in the Talkeetna and Chugach Mountains reveals a preponderance of unreset, magmatic zircon grains with Jurassic and Late Cretaceous ages, suggesting limited amounts of exhumation of those regions during Cenozoic time (Enkelmann et al., 2019). Furthermore, Terhune et al. (2019) suggest that significant paleotopography in the Talkeetna Mountains was created by Paleocene time based on $^{40}Ar/^{39}Ar$, apatite fission track, and apatite (U-Th)/He cooling ages, but the region has not experienced much exhumation since then. Minor and localized Miocene cooling ages there are geographically restricted to proximity with the active Castle Mountain fault. Probably the only regions that have experienced a noteworthy change in topography is the central and eastern Alaska Ranges, which have been uplifting since ∼30–25 Ma (Benowitz et al., 2011, 2012, 2014; Fitzgerald et al., 2014; Riccio et al., 2014; Lease et al., 2016).

CONCLUSION

The unified approach of extensive modern river sampling to characterize sediment source regions, comprehensive basin strata characterization, and mixture modeling demonstrates a valuable approach for not only apportioning of widespread and pervasive ages found in source terranes with long-lived magmatic histories, but also for resolving sedimentary recycling into a basin. In south-central Alaska, mixture modeling of the extensive detrital zircon U-Pb geochronologic dataset presented here provides an opportunity to more fully characterize the long-term variations of provenance within a forearc basin. Modeling of only the <250 Ma age component of the detrital zircon signatures reveals a previously undetected sediment source in recycling of the accretionary prism strata in the northern Chugach Mountains during the Late Cretaceous and Oligocene. Recognition of this important sediment source was previously hampered by overlap of detrital zircon U-Pb ages in the ancient strata with widespread igneous belts north of the basin. Rejuvenation of sediment flux from the Chugach Mountains can be linked to specific plate margin events, including Late Cretaceous suturing of the Insular terranes and Oligocene initiation of shallow subduction. The results of this analysis permit a better understanding of the tectonic forcing that influences sediment derivation and dispersal along active tectonic margins. This study also demonstrates that in basins where the topographic and exhumational evolution of provenance regions is well-constrained, strategically using sediment from modern rivers is a formidable technique to rapidly and efficiently characterize vast sediment source regions for resolving provenance of ancient strata.

DATA AVAILABILITY

The datasets generated for this study can be found in the **Supplementary Material**.

AUTHOR CONTRIBUTIONS

EF analyzed the data and wrote the manuscript.

FUNDING

This research was funded through NSF-EAR 1419683. Support for the University of Arizona LaserChron Center, where the geochronologic data was collected, is provided through NSF-EAR 1649254.

ACKNOWLEDGMENTS

The new data from the Talkeetna Mountains was collected in collaboration with Eva Enkelmann (University of Calgary) for an MS thesis written by Carsyn Ames at the University of Iowa. Enkelmann also provided valuable feedback on the manuscript.

SUPPLEMENTARY MATERIAL

The Supplementary Material for this article can be found online at: https://www.frontiersin.org/articles/10.3389/feart.2019.00217/full#supplementary-material

DATA SHEET S1 | The supplementary file associated with this manuscript contains reference and sample number information about the compiled data, age distributions used for each source area and stratigraphic interval used in the modeling, and raw isotopic data for the 20 new river samples from the Talkeetna Mountains.

REFERENCES

Arkle, J., Armstrong, P., Haeussler, P., Prior, M., Hartman, S., Sendziak, K., et al. (2013). Focused exhumation in the syntaxis of the western Chugach Mountains and Prince William Sound, Alaska. *Geol. Soc. Am. Bull.* 125, 776–793. doi: 10.1130/b30738.1

Bacon, C., Vazquez, J., and Wooden, J. (2012). Peninsular terrane basement ages recorded by paleozoic and paleoproterozoic zircon in gabbro xenoliths and andesite from Redoubt volcano, Alaska. *Geol. Soc. Am. Bull.* 124, 24–34. doi: 10.1130/b30439.1

Bauer, M., Pavlis, G., and Landes, M. (2014). Subduction geometry of the yakutat terrane, southeastern Alaska. *Geosphere* 10, 1161–1176. doi: 10.1130/ges00852.1

Benowitz, J. A., Haeussler, P. J., Layer, P. W., O'Sullivan, P. B., Wallace, W. K., and Gillis, R. J. (2012). Cenozoic tectono-thermal history of the Tordrillo Mountains, Alaska: paleocene-eocene ridge subduction, decreasing relief, and late Neogene faulting. *Geochem. Geophys. Geosyst.* 13:Q04009. doi: 10.1029/2011GC003951

Benowitz, J. A., Layer, P. W., Armstrong, P., Perry, S., Haeussler, P. J., Fitzgerald, P., et al. (2011). Spatial variations in focused exhumation along a continental-scale strike-slip fault: the Denali fault of the Eastern Alaska Range. *Geosphere* 7, 455–467. doi: 10.1130/GES00589.1

Benowitz, J. A., Layer, P. W., and Vanlaningham, S. (2014). "Persistent long-term (c. 24 Ma) exhumation in the Eastern Alaska Range constrained by stacked thermochronology," in *Advances in 40Ar/39Ar Dating: From Archeology to Planetary Sciences*, Vol. 378, eds F. Jourdan, D. F. Mark, and C. Verati, (London: Geological Society of London), 225–243. doi: 10.1144/sp378.12

Blodgett, R., and Sralla, B. (2008). "A major unconformity between Permian and Triassic strata at Cape Kekurnoi, Alaska Peninsula; old and new observations on stratigraphy and hydrocarbon potential," in *Studies by the U.S. Geological Survey in Alaska, 2006: U.S. Geological Survey Professional Paper 1739-E*, eds P. Haeussler, and J. Galloway, (Reston, VA: U.S. Geological Survey), 13.

Bradley, D., Kusky, T., Haeussler, P., Goldfarb, R., Miller, M., Dumoulin, J., et al. (2003). "Geologic signature of early tertiary ridge subduction in Alaska," in *Geology of a transpressional orogen developed during ridge-trench interaction along the north Pacific margin*, eds V. Sisson, S. Roekse, and T. Pavlis, (Boulder, CO: Geological Society of America), 19–49. doi: 10.1130/0-8137-2371-x.19

Butler, R., Gehrels, G., and Bazard, D. (1997). Paleomagnetism of paleozoic strata of the alexander terrane, southeastern Alaska. *Geol. Soc. Am. Bull.* 109, 1372–1388. doi: 10.1130/0016-76061997109<1372:Popsot<2.3.Co;2

Calderwood, K., and Fackler, W. (1972). Proposed stratigraphic nomenclature for Kenai Group, Cook Inlet basin, Alaska. *Am. Assoc. Petrol. Geol. Bull.* 56, 739–754.

Christeson, G., Gulick, S., van Avendonk, H., Worthington, L., Reece, R., and Pavlis, T. (2010). The yakutat terrane: dramatic change in crustal thickness across the Transition fault, Alaska. *Geology* 38, 895–898. doi: 10.1130/g31170.1

Clift, P., Draut, A., Kelemen, P., Blusztajn, J., and Greene, A. (2005). Stratigraphic and geochemical evolution of an oceanic arc upper crustal section: the jurassic talkeetna volcanic formation, south-central Alaska. *Geol. Soc. Am. Bull.* 117, 1368–1373.

Cole, R., Nelson, S., Layer, P., and Oswald, P. (2006). Eocene volcanism above a depleted mantle slab window in southern Alaska. *Geol. Soc. Am. Bull.* 118, 140–158. doi: 10.1130/b25658.1

Cole, R., and Stewart, B. (2009). Continental margin volcanism at sites of spreading ridge subduction: examples from southern Alaska and western California. *Tectonophysics* 464, 118–136. doi: 10.1016/j.tecto.2007.12.005

Cowan, D., Brandon, M., and Garver, J. (1997). Geologic tests of hypotheses for large coastwise displacements - A critique illustrated by the Baja British Columbia controversy. *Am. J. Sci.* 297, 117–173. doi: 10.2475/ajs.297.2.117

Davidson, C., and McPhillips, D. (2007). "Along strike variations in metamorphism and deformation of the strata of the Kahiltna basin, south-central Alaska," in *Tectonic Growth of a Collisional Continental Margin: Crustal Evolution of Southern Alaska*, eds K. Ridgway, J. Trop, J. Glen, and J. O'Neill, (Boulder, CO: Geological Society of America), 439–453. doi: 10.1130/2007.2431(17)

DeCelles, P., Gehrels, G., Quade, J., Ojha, T., Kapp, P., and Upreti, B. (1998). Neogene foreland basin deposits, erosional unroofing, and the kinematic history of the Himalayan fold-thrust belt, western Nepal. *Geol. Soc. Am. Bull.* 110, 2–21. doi: 10.1130/0016-76061998110<0002:Nfbdeu<2.3.Co;2

DeGraaff-Surpless, K., Graham, S., Wooden, J., and McWilliams, M. (2002). Detrital zircon provenance analysis of the Great Valley Group, California: evolution of an arc-forearc system. *Geol. Soc. Am. Bull.* 114, 1564–1580. doi: 10.1130/0016-76062002114<1564:Dzpaot<2.0.Co;2

Dickinson, W., and Gehrels, G. (2009). Use of U-Pb ages of detrital zircons to infer maximum depositional ages of strata: a test against a Colorado Plateau Mesozoic database. *Earth Planet. Sci. Lett.* 288, 115–125. doi: 10.1016/j.epsl.2009.09.013

Dickinson, W., and Snyder, W. (1979). Geometry of subducted slabs related to San-Andreas transform. *J. Geol.* 87, 609–627. doi: 10.1086/628456

Eastham, K., and Ridgway, K. (2002). "Stratigraphy and provenance data from the Upper Jurassic to Upper Cretaceous Kahiltna assemblage of south-central Alaska," in *Studies by the U.S. Geological Survey in Alaska, 2000: U.S. Geological Survey Professional Paper 1662*, eds F. Wilson, and J. Galloway, (Reston, VA: U.S. Geological Suvery), 45–53.

Eberhart-Phillips, D., Christensen, D., Brocher, T., Hansen, R., Ruppert, N., Haeussler, P., et al. (2006). Imaging the transition from Aleutian subduction to Yakutat collision in central Alaska, with local earthquakes and active source data. *J. Geophys. Res. Solid Earth* 111:B11303. doi: 10.1029/2005jb004240

Enkelmann, E., Garver, J., and Pavlis, T. (2008). Rapid exhumation of ice-covered rocks of the Chugach-St. *Elias orogen*, Southeast Alaska. *Geology* 36, 915–918. doi: 10.1130/g2252a.1

Enkelmann, E., Lohff, S. K. S., and Finzel, E. S. (2019). Detrital zircon double-dating of forearc basin strata reveals magmatic, exhumational, and thermal history of sediment source areas. *Geol. Soc. Am. Bull.* 131, 1364–1384. doi: 10.1130/B35043.1

Enkelmann, E., Zeitler, P., Garver, J., Pavlis, T., and Hooks, B. (2010). The thermochronological record of tectonic and surface process interaction at the Yakutat-North American collision zone in southeast Alaska. *Am. J. Sci.* 310, 231–260. doi: 10.2475/04.2010.01

Espurt, N., Funiciello, F., Martinod, J., Guillaume, B., Regard, V., Faccenna, C., et al. (2008). Flat subduction dynamics and deformation of the South American plate: insights from analog modeling. *Tectonics* 27:TC3011. doi: 10.1029/2007TC002175

Fedo, C., Sircombe, K., Rainbird, R., Hanchar, J., and Hoskin, P. (2003). Detrital zircon analysis of the sedimentary record. *Rev. Mineral. Geochem.* 53, 277–303. doi: 10.2113/0530277

Ferguson, K. M., Armstrong, P. A., Arkle, J. C., and Haeussler, P. J. (2015). Focused rock uplift above the subduction decollement at Montague and Hinchinbrook Islands, Prince William Sound, Alaska. *Geosphere* 11, 144–159. doi: 10.1130/GES01036.1

Ferris, A., Abers, G., Christensen, D., and Veenstra, E. (2003). High resolution image of the subducted Pacific (?) plate beneath central Alaska, 50-150 km depth. *Earth Planet. Sci. Lett.* 214, 575–588. doi: 10.1016/s0012-821x(03)00403-5

Finzel, E., and Enkelmann, E. (2017). Miocene-Recent sediment flux in the south-central Alaskan fore-arc basin governed by flat-slab subduction. *Geochem. Geophys. Geosyst.* 18, 1739–1760. doi: 10.1002/2016gc006783

Finzel, E., Enkelmann, E., Falkowski, S., and Hedeen, T. (2016). Long-term fore-arc basin evolution in response to changing subduction styles in southern Alaska. *Tectonics* 35, 1735–1759. doi: 10.1002/2016tc004171

Finzel, E., Ridgway, K., and Trop, J. (2015). Provenance signature of changing plate boundary conditions along a convergent margin: detrital record of spreading-ridge and flat-slab subduction processes, Cenozoic forearc basins, Alaska. *Geosphere* 11, 823–849. doi: 10.1130/ges01029.1

Finzel, E., Trop, J., Ridgway, K., and Enkelmann, E. (2011). Upper plate proxies for flat-slab subduction processes in southern Alaska. *Earth Planet. Sci. Lett.* 303, 348–360. doi: 10.1016/j.epsl.2011.01.014

Fitzgerald, P. G., Roeske, S. M., Benowitz, J. A., Riccio, S. J., Perry, S. E., and Armstrong, P. A. (2014). Alternating asymmetric topography of the Alaska range along the strike-slip Denali fault: strain partitioning and lithospheric control across a terrane suture zone. *Tectonics* 33, 1519–1533. doi: 10.1002/2013TC003432

Flores, R., Stricker, G., and Kinney, S. (2004). Alaska coal geology, resources, and coalbed methane potential. *U.S. Geol. Surv. Digit. Data Ser.* 77:68.

Gehrels, G. (2012). "Detrital zircon U-Pb geochronology: current methods and new opportunities," in *Tectonics of Sedimentary Basins: Recent Advances*, eds C. Busby, and A. Azor, (Hoboke, NJ: Blackwell Science Publication).

Gehrels, G., Valencia, V., and Pullen, A. (2006). Detrital zircon geochronology by laser ablation multicollector ICPMS at the arizona laserchron center. *Paleontol. Soc. Pap.* 12, 67–76. doi: 10.1017/s1089332600001352

Gehrels, G., Valencia, V., and Ruiz, J. (2008). Enhanced precision, accuracy, efficiency, and spatial resolution of U-Pb ages by laser ablation-multicollector-inductively coupled plasma-mass spectrometry. *Geochem. Geophys. Geosyst.* 9:Q03017. doi: 10.1029/2007gc001805

Gorring, M., and Kay, S. (2001). Mantle processes and sources of neogene slab window magmas from southern Patagonia, Argentina. *J. Petrol.* 42, 1067–1094. doi: 10.1093/petrology/42.6.1067

Grantz, A. (1960). *Geologic Map and Cross Section of Talkeetna Mountains (A-1) Quadrangle and the South Third of Talkeetna Mountains (B-1) Quadrangle, Alaska*. Reston, VA: U.S. Geological Survey.

Gutscher, M. A., Spakman, W., Bijwaard, H., and Engdahl, E. R. (2000). Geodynamics of flat subduction: seismicity and tomographic constraints from the Andean margin. *Tectonics* 19, 814–833. doi: 10.1029/1999TC001152

Haeussler, P., Bradley, D., Wells, R., and Miller, M. (2003). Life and death of the Resurrection plate: evidence for its existence and subduction in the northeastern Pacific in Paleocene-Eocene time. *Geol. Soc. Am. Bull.* 115, 867–880. doi: 10.1130/0016-76062003115<0867:Ladotr<2.0.Co;2

Hampel, A. (2002). The migration history of the Nazca Ridge along the Peruvian active margin: a re-evaluation. *Earth Planet. Sci. Lett.* 203, 665–679. doi: 10.1016/S0012-821X(02)00859-2

Hampton, B., Ridgway, K., O'Neill, J., Gehrels, G., Schmidt, J., and Blodgett, R. (2007). " Pre-, syn-, and postcollisional stratigraphic framework and provenance of upper triassic-upper cretaceous strata in the northwestern Talkeetna Mountains, Alaska," in *Tectonic Growth of a Collisional Continental Margin: Crustal Evolution of Southern Alaska*, eds K. Ridgway, J. Trop, J. Glen, and J. O'Neill, (Boulder, CO: Geological Society of America), 401–438. doi: 10.1130/2007.2431(16)

Helmold, K., LePain, D., Wilson, M., and Peterson, C. (2013). *Petrology and reservoir potential of Tertiary and Mesozoic sandstones, Cook Inlet, Alaska: A preliminary analysis of outcrop samples collected during 2007-2010 field seasons*. Alaska Division of Geological & Geophysical Surveys Preliminary Interpretive Report 2013-5. Fairbanks, AK: Alaska Division of Geological & Geophysical Surveys, 34.

Hoffman, M., and Armstrong, P. (2006). "Miocene exhumation of the southern Talkeetna Mountains, south central Alaska, based on apatite (U-Th)/He thermochronology," in *Proceeding of the GSA Abstracts with Programs*, (Boulder, CO: Geological Society of America).

Houston, W. (1994). *Lower Tertiary stratigraphy in Katmai National Park, Alaska-a lithologic and petrographic study*. M.S. Thesis, Colorado State University, Fort Collins, CO.

Irving, E., Woodsworth, G., Wynne, P., and Morrison, A. (1985). Paleomagnetic evidence for displacement from the south of the coast plutonic complex, British-Columbia. *Can. J. Earth Sci.* 22, 584–598. doi: 10.1139/e85-058

Irving, E., Wynne, P., Thorkelson, D., and Schiarizza, P. (1996). Large (1000 to 4000 km) northward movements of tectonic domains in the northern Cordillera, 83 to 45 Ma. *J. Geophys. Res. Solid Earth* 101, 17901–17916. doi: 10.1029/96jb01181

Jacobson, C., Grove, M., Pedrick, J., Barth, A., Marsaglia, K., Gehrels, G., et al. (2011). Late Cretaceous-early Cenozoic tectonic evolution of the southern California margin inferred from provenance of trench and forearc sediments. *Geol. Soc. Am. Bull.* 123, 485–506. doi: 10.1130/b30238.1

Jones, D., and Silberling, N. (1979). *Mesozoic stratigraphy; the key to tectonic analysis of southern and central Alaska*. U.S. Geological Survey Open-File Report79-1200.

Jones, D., Silberling, N., and Hillhouse, J. (1977). Wrangellia - displaced terrane in northwestern North-America. *Can. J. Earth Sci.* 14, 2565–2577. doi: 10.1139/e77-222

Jordan, T. E., and Allmendinger, R. W. (1986). The Sierras pampeanas of argentina - a modern analog of rocky-mountain foreland deformation. *Am. J. Sci.* 286, 737–764. doi: 10.2475/ajs.286.10.737

Kalbas, J., Ridgway, K., and Gehrels, G. (2007). "Stratigraphy, depositional systems, and provenance of the lower cretaceous kahiltna assemblage, western Alaska Range: basin development in response to oblique collision," in *Tectonic Growth of a Collisional Continental Margin: Crustal Evolution of Southern Alaska*, eds K. Ridgway, J. Trop, J. Glen, and J. O'Neill, (Boulder, CO: Geological Society of America), 307–343. doi: 10.1130/2007.2431(13)

Keppie, J., and Dostal, J. (2001). Evaluation of the Baja controversy using paleomagnetic and faunal data, plume magmatism, and piercing points. *Tectonophysics* 339, 427–442. doi: 10.1016/s0040-1951(01)00126-3

Kirschner, C., and Lyon, C. (1973). Stratigraphic and tectonic development of Cook Inlet petroleum province. *Am. Assoc. Petrol. Geol. Bull.* 19, 396–407.

Lallemand, S., Heuret, A., and Boutelier, D. (2005). On the relationships between slab dip, back-arc stress, upper plate absolute motion, and crustal nature in subduction zones. *Geochem. Geophys. Geosyst.* 6:Q09006. doi: 10.1029/2005GC000917

Lease, R., Haeussler, P., and O'Sullivan, P. (2016). Changing exhumation patterns during Cenozoic growth and glaciation of the Alaska Range: insights from detrital thermochronology and geochronology. *Tectonics* 35, 934–955. doi: 10.1002/2015tc004067

LePain, D., Stanley, R., Helmold, K., and Shellenbaum, D. (2013). "Geologic framework and petroleum systems of Cook Inlet Basin, south-central Alaska," in *Oil and Gas Fields fo the Cook Inlet Basin, Alaska*, eds D. Stone, and D. Hite, (Tulsa, OK: American Association of Petroleum Geologists), 37–116.

Ling, M., Li, Y., Ding, X., Teng, F., Yang, X., Fan, W., et al. (2013). Destruction of the North China craton induced by ridge subductions. *J. Geol.* 121, 197–213. doi: 10.1086/669248

Little, T., and Naeser, C. (1989). Tertiary tectonics of the border ranges fault system, Chugach Mountains, Alaska - deformation and uplift in a fore-arc setting. *J. Geophys. Res. Solid Earth Planets* 94, 4333–4359. doi: 10.1029/JB094iB04p04333

Magoon, L., Adkison, W., Chmelik, F., Dolton, G., Fisher, M., Hampton, M., et al. (1976). *Hydrocarbon Potential, Geologic Hazards, and Infrastructure for Exploration and Development of the Lower Cook Inlet, Alaska*. Open-File Report 97-26. Reston, VA: U.S. Geological Survey.

Magoon, L., and Egbert, R. (1986). "Framework geology and sandstone composition," in *Geologic studies of the lower Cook Inlet COST No. 1 well, Alaska Outer Continental Shelf*, ed. L. Magoon, (Reston, VA: U.S. Geological Survey), 17–22.

Manuszak, J., Ridgway, K., Trop, J., and Gehrels, G. (2007). "Sedimentary record of the tectonic growth of a collisional continental margin: upper jurassic-lower cretaceous nutzotin mountains sequence, eastern Alaska Range, Alaska," in *Tectonic Growth of a Collisional Continental Margin: Crustal Evolution of Southern Alaska*, eds K. Ridgway, J. Trop, J. Glen, and J. O'Neill, (Boulder, CO: Geological Society of America), 345–377. doi: 10.1130/2007.2431(14)

McClelland, W., Gehrels, G., and Saleeby, J. (1992). Upper jurassic-lower cretaceous basinal strata along the cordilleran margin - implications for the accretionary history of the alexander-wrangellia-peninsular terrane. *Tectonics* 11, 823–835. doi: 10.1029/92tc00241

Mongrain, J. (2012). *Depositional systems, paleoclimate, and provenance of the Late Miocene to Pliocene Beluga and Sterling Formations, Cook Inlet forearc basin, Alaska*. Ph.D. Thesis, University of Alaska, Anchorage, AK.

Nokleberg, W., Aleinikoff, J., Dutro, J., Lanphere, M., Silberling, N., Silva, S., et al. (1992). *Map, Tables, and Summary of Fossil and Isotopic Age Data, Mount Hayes Quadrangle, Eastern Alaska Range*. Reston, VA: U.S. Geological Survey.

Nokleberg, W., Parfenov, L., Monger, J., Norton, I., Khanchuk, A., Stone, D., et al. (2001). Phanerozoic tectonic evolution of the Circum-North Pacific. *U.S. Geol. Surv. Prof. Pap.* 1626:122.

Panuska, B. (1985). Paleomagnetic evidence for a post-Cretaceous accretion of Wrangellia. *Geology* 13, 880–883. doi: 10.1130/0091-7613198513<880:Pefapa<2.0.Co;2

Pavlis, T. (1982). Origin and age of the Border Ranges Fault of southern Alaska and its bearing on the late Mesozoic tectonic evolution of Alaska. *Tectonics* 1, 343–368. doi: 10.1029/TC001i004p00343

Plafker, G., Moore, J., and Winkler, G. (1994). "Geology of the southern Alaska margin," in *Geology of North America*, eds G. Plafker, and H. Berg, (Boulder, CO: Geological Society of America), 389–448.

Plafker, G., Nokleberg, W., and Lull, J. (1989). Bedrock geology and tectonic evolution of the wrangellia, peninsular, and chugach terranes along the trans-alaska crustal transect in the Chugach Mountains and southern Copper River Basin, Alaska. *J. Geophys. Res. Solid Earth Planets* 94, 4255–4295. doi: 10.1029/JB094iB04p04255

Pullen, A., Ibanez-Mejia, M., Gehrels, G., Ibanez-Mejia, J., and Pecha, M. (2014). What happens when n= 1000? Creating large-n geochronological datasets with

LA-ICP-MS for geologic investigations. *J. Analyt. Atom. Spectrom.* 29, 971–980. doi: 10.1039/c4ja00024b

Reid, M., Finzel, E., Enkelmann, E., and McClelland, W. (2018). "Detrital zircon provenance of upper jurassic–upper cretaceous forearc basin strata on the insular terranes, south-central Alaska," in *Tectonics, Sedimentary Basins, and Provenance: A Celebration of William R. Dickinson's Career*, eds R. Ingersoll, T. Lawton, and S. Graham, (Boulder, CO: Geological Society of America), 571–590.

Riccio, S. J., Fitzgerald, P. G., Benowitz, J. A., and Roeske, S. M. (2014). The role of thrust faulting inthe formation of the eastern Alaska Range: Thermochronological constraints from the Susitna Glacier Thrust Fault region of the intracontinental strike-slip Denali Fault sys-tem. *Tectonics* 33, 2195–2217. doi: 10.1002/2014TC003646

Ridgway, K., Trop, J., Nokleberg, W., Davidson, C., and Eastham, K. (2002). Mesozoic and Cenozoic tectonics of the eastern and central Alaska Range: progressive basin development and deformation in a suture zone. *Geol. Soc. Am. Bull.* 114, 1480–1504. doi: 10.1130/0016-76062002114<1480:Mactot<2.0.Co;2

Ridgway, K., Trop, J., and Sweet, A. (1997). Thrust-top basin formation along a suture zone, Cantwell basin, Alaska range: implications for development of the Denali fault system. *Geol. Soc. Am. Bull.* 109, 505–523. doi: 10.1130/0016-76061997109<0505:Ttbfaa<2.3.Co;2

Rioux, M., Hacker, B., Mattinson, J., Kelemen, P., Blusztajn, J., and Gehrels, G. (2007). Magmatic development of an intra-oceanic arc: high-precision U-Pb zircon and whole-rock isotopic analyses from the accreted Talkeetna arc, south-central Alaska. *Geol. Soc. Am. Bull.* 119, 1168–1184. doi: 10.1130/b25964.1

Rioux, M., Mattinson, J., Hacker, B., Kelemen, P., Blusztajn, J., Hanghoj, K., et al. (2010). Intermediate to felsic middle crust in the accreted Talkeetna arc, the Alaska Peninsula and Kodiak Island, Alaska: an analogue for low-velocity middle crust in modern arcs. *Tectonics* 29:TC3001. doi: 10.1029/2009tc002541

Sisson, V., Poole, A., Burner, H., Pavlis, T., Copeland, P., Donelick, R., et al. (2003). "Geochemical and geochronologic constraints for genesis of a tonalite-trondhjemite suite and associated mafic intrusive rocks in the eastern Chugach Mountains, Alaska: a record of ridge-transform subduction," in *Geology of a Transpressional Orogen Developed During Ridge-Trench Interaction Along the North Pacific Margin*, eds V. Sisson, S. Roekse, and T. Pavlis, (Boulder, CO: Geological Society of America), 293–326. doi: 10.1130/0-8137-2371-x.293

Stamatakos, J., Trop, J., and Ridgway, K. (2001). Late Cretaceous paleogeography of Wrangellia: paleomagnetism of the MacColl Ridge Formation, southern Alaska, revisited. *Geology* 29, 947–950. doi: 10.1130/0091-76132001029<0947:Lcpowp<2.0.Co;2

Sundell, K., and Saylor, J. (2017). Unmixing detrital geochronology age distributions. *Geochem. Geophys. Geosyst.* 18, 2872–2886. doi: 10.1002/2016gc006774

Swenson, R. (1997). "Introduction to Tertiary tectonics and sedimentation in the Cook Inlet Basin," in *1997 Guide to the Geology of the Kenai Peninsula, Alaska, Anchorage, Alaska*, eds S. Karl, T. Ryherd, and N. Vaughn, (Anchorage, AK: Alaska Geological Society).

Terhune, P. J., Benowitz, J. A., Trop, J. M., O'Sullivan, P. B., Gillis, R. J., and Freymueller, J. T. (2019). Cenozoic tectono-thermal history of the southern Talkeetna Mountains, Alaska: insights into a potentially alternating convergent and transform plate margin. *Geosphere* 15, 1–38. doi: 10.1130/GES02008.1

Thorkelson, D. (1996). Subduction of diverging plates and the principles of slab window formation. *Tectonophysics* 255, 47–63. doi: 10.1016/0040-1951(95)00106-9

Trop, J. (2008). Latest cretaceous forearc basin development along an accretionary convergent margin: South-central Alaska. *Geol. Soc. Am. Bull.* 120, 207–224. doi: 10.1130/b26215.1

Trop, J., Hart, W., Snyder, D., and Idleman, B. (2012). Miocene basin development and volcanism along a strike-slip to flat-slab subduction transition: stratigraphy, geochemistry, and geochronology of the central Wrangell volcanic belt, Yakutat-North America collision zone. *Geosphere* 8, 805–834. doi: 10.1130/ges00762.1

Trop, J., and Ridgway, K. (2007). "Mesozoic and Cenozoic tectonic growth of southern Alaska: A sedimentary basin perspective," in *Tectonic Growth of a Collisional Continental Margin: Crustal Evolution of Southern Alaska*, eds K. Ridgway, J. Trop, J. Glen, and J. O'Neill, (Boulder, CO: Geological Society of America), 55–94. doi: 10.1130/2007.2431(04)

Trop, J., Ridgway, K., Manuszak, J., and Layer, P. (2002). Mesozoic sedimentary-basin development on the allochthonous wrangellia composite terrane, Wrangell Mountains basin, Alaska: a long-term record of terrane migration and arc construction. *Geol. Soc. Am. Bull.* 114, 693–717. doi: 10.1130/0016-76062002114<0693:Msbdot<2.0.Co;2

Trop, J. M., Ridgway, K. D., and Sweet, A. R. (2004). Stratigraphy, palynology, and provenance of the Colorado Creek basin, Alaska, USA: oligocene transpressional tectonics along the central Denali fault system. *Can. J. Earth Sci.* 41, 457–480. doi: 10.1139/e04-003

Trop, J., Szuch, D., Rioux, M., and Blodgett, R. (2005). Sedimentology and provenance of the upper Jurassic Naknek formation, Talkeetna Mountains, Alaska: bearings on the accretionary tectonic history of the Wrangellia composite terrane. *Geol. Soc. Am. Bull.* 117, 570–588. doi: 10.1130/b25575.1

Trop, J. M., Benowitz, J., Cole, R. B., and O'Sullivan, P. (2019). Cretaceous to Miocene magmatism, sedimentation, and exhumation within the Alaska Range suture zone: a polyphase reactivated terrane boundary. *Geosphere* 15, 1–36. doi: 10.1130/GES02014.1

Turner, D., and Smith, T. (1974). *Geochronology and generalized geology of the central Alaska Range, Clearwater Mountains, and northern Talkeetna Mountains*. Alaska Division of Geological and Geophysical Surveys Open-File Report 72.

Umhoefer, P. (1987). Northward translation of Baja British-Columbia along the late Cretaceous to Paleocene margin of western North-America. *Tectonics* 6, 377–394. doi: 10.1029/TC006i004p00377

Valentino, J., Spotila, J., Owen, L., and Buscher, J. (2016). Rock uplift at the transition from flat-slab to normal subduction: the Kenai Mountains, Southeast Alaska. *Tectonophysics* 671, 63–75. doi: 10.1016/j.tecto.2016.01.022

Weislogel, A., Graham, S., Chang, E., Wooden, J., Gehrels, G., and Yang, H. (2006). Detrital zircon provenance of the late triassic songpan-ganzi complex: sedimentary record of collision of the North and South China blocks. *Geology* 34, 97–100.

Wilson, F. H., Hults, C. P., Mull, C. G., and Karl, S. M. (2015). Geologic map of Alaska. *U.S. Geol. Surv. Sci. Invest. Map* 3340:196. doi: 10.3133/sim3340

Wolfe, J., and Tanai, T. (1980). The Miocene Seldovia Point flora from the Kenai Group, Alaska. *U.S. Geol. Surv. Prof. Pap.* 1105:52.

Worthington, L., Gulick, S., and Pavlis, G. (2008). "Identifying active structures in the kayak island and pamplona zones: implications for offshore tectonics of the Yakutat Microplate, Gulf of Alaska," in *Active Tectonics and Seismic Potential of Alaska*, eds J. Freymueller, P. Haeussler, R. Wesson, and G. Ekstrom, (Washington DC: American Geophysical Union), 257–268. doi: 10.1029/179gm14

Worthington, L., Van Avendonk, H., Gulick, S., Christeson, G., and Pavlis, T. (2012). Crustal structure of the yakutat terrane and the evolution of subduction and collision in southern Alaska. *J. Geophys. Res. Solid Earth* 117:B01102. doi: 10.1029/2011jb008493

Conflict of Interest Statement: The author declares that the research was conducted in the absence of any commercial or financial relationships that could be construed as a potential conflict of interest.

frontiers in Earth Science

ORIGINAL RESEARCH
published: 31 October 2019
doi: 10.3389/feart.2019.00279

Interaction of Sea-Level Pulses With Periodically Retreating Barrier Islands

Daniel J. Ciarletta[1], Jorge Lorenzo-Trueba[1] and Andrew D. Ashton[2]*

[1] Department of Earth and Environmental Studies, Montclair State University, Montclair, NJ, United States, [2] Geology & Geophysics Department, Woods Hole Oceanographic Institution, Woods Hole, MA, United States

Submerged barrier deposits preserved on continental shelf seabeds provide a record of paleocoastal environmental change from the last glacial maximum through the Holocene. The formation of these offshore deposits is often attributed to intermittent periods of rapidly rising sea levels, especially glacial meltwater pulses, which are expected to lead to partial or complete drowning – overstepping – of migrating barrier islands. However, recent cross-shore modeling and field evidence suggests that even for constant sea-level rise and shelf slope, the internal dynamics of migrating barriers could plausibly drive periodic retreat accompanied by autogenic partial overstepping and deposition of barrier sediment. We hypothesize that the interaction of periodic retreat with changes in external (allogenic) forcing from sea-level rise may create novel retreat responses and corresponding relict barrier deposits. Specifically, we posit that autogenic deposits can be amplified by an increased rate of relative sea-level rise, while in other cases internal dynamics can disrupt or mask the production of allogenic deposits. Here, we model barriers through a range of autogenic–allogenic interactions, exploring how barriers with different inherent autogenic periods respond to discrete, centennial-scale sea-level-rise pulses of variable magnitude and timing within the autogenic transgressive barrier cycle. Our results demonstrate a diversity of depositional signals, where production of relict sands is amplified or suppressed depending on both the barrier's internal dynamic state and the pulse magnitude. We also show that millennial-scale autogenic periodicity renders barriers vulnerable to complete drowning for relatively low pulse rates of rise (<15 mm/year).

Keywords: barrier island, autogenic, modeling, sea level, Holocene, meltwater pulse, overstepping

OPEN ACCESS

Edited by:
Brian W. Romans, Virginia Polytechnic Institute and State University, United States

Reviewed by:
Alexander Ray Simms, University of California, Santa Barbara, United States
Mehrdad Sardar Abadi, The University of Oklahoma, United States
Cari Johnson, The University of Utah, United States

****Correspondence:***
Daniel J. Ciarletta
ciarlettad1@montclair.edu

Specialty section:
This article was submitted to Sedimentology, Stratigraphy and Diagenesis, a section of the journal Frontiers in Earth Science

Received: *15 July 2019*
Accepted: *17 October 2019*
Published: *31 October 2019*

Citation:
Ciarletta DJ, Lorenzo-Trueba J and Ashton AD (2019) Interaction of Sea-Level Pulses With Periodically Retreating Barrier Islands. Front. Earth Sci. 7:279. doi: 10.3389/feart.2019.00279

INTRODUCTION

Submerged and remnant transgressive barrier island deposits can be a major component of shelf bathymetry and stratigraphy, commonly found on continental shelves across the world (Rampino and Sanders, 1980; Mellett et al., 2012a; De Falco et al., 2015). Formation of these barrier deposits is typically attributed to changes in allogenic forcing, such as changes in the rate of sea-level rise, alteration of sediment supply, or variation in antecedent topography (Cattaneo and Steel, 2003; Storms et al., 2008; Mellett et al., 2012a). Because these drowned or "overstepped" barrier features are associated with variations in external environmental (allogenic) forcing, recent studies have

investigated them to gain insights into how modern barriers might respond to future environmental changes, for example, an increase in rate of relative sea-level rise (Donoghue, 2011; Cooper et al., 2016; Emery et al., 2019; Mulhern et al., 2019). Understanding how barrier systems previously responded to periods of increased sea-level rise can also help inform future socioeconomic risks. This is particularly pertinent because centennial-scale processes driving transgressive barrier evolution are not well understood or commonly considered in modern coastal management (Cooper et al., 2018; Cowell and Kinsela, 2018; McNamara and Lazarus, 2018).

Recently, morphodynamic modeling of barriers by Lorenzo-Trueba and Ashton (2014) and modeling with field comparison by Ciarletta et al. (2019) have implicated internally driven (autogenic) periodic retreat as a plausible agent of remnant barrier deposition. This periodic mode of retreat, common for many barrier configurations, is defined by alternating episodes of migration and aggradation, driven by a temporal lag in shoreface response to overwash. During the transition from aggradation to migration, a portion of the lower shoreface is stranded on the continental shelf, producing a deposit of relict barrier sand (Ciarletta et al., 2019).

While not invoking the same mechanism, the deposition of barrier sands during landward migration was initially conceptualized in a series of studies and replies by Rampino and Sanders (1980, 1981, 1982, 1983), who described a drowned barrier system off of the coast of Long Island, NY, United States. Specifically, their work suggested that a rapid increase in the rate of relative sea-level rise could induce complete drowning and overstepping of a barrier, or potentially trigger a mode of combined partial overstepping and retreat (Rampino and Sanders, 1982). The latter concept is intriguing, with Rampino and Sanders (1982) detailing a scenario in which a barrier aggrades during rapid sea-level rise before later undergoing migration (as aggradation increasingly fails to maintain pace with rise). In the context of the Long Island system, the authors referred to this process as a means to describe how both lower shoreface and back-barrier lagoon sediments could be preserved on the modern shelf seabed (Rampino and Sanders, 1983). Earlier, it had been assumed that barriers retreat primarily as steady-state phenomena (Swift, 1975), precluding partial overstepping behaviors. More recently, the acknowledgment that barriers experience variable phases of retreat, potentially resulting in complex future changes in response to increasing sea-level rise, has led to renewed interest in the evolution of barriers at centennial scales (Cooper et al., 2018). This interest is further motivated by the increasing number of globally distributed drowned barrier deposits observed in different geologic settings (Mellett and Plater, 2018).

Whereas Rampino and Sanders (1982) suggested externally driven sediment supply as a mechanism to provide for aggradation even under rapid sea-level rise, we theorize that autogenically driven periodic barrier retreat provides another means for barrier aggradation to coincide with a rapid increase in sea-level rise. To evaluate this hypothesis, we model periodically retreating barriers subjected to high magnitude, century-scale "pulses" in the rate of sea-level rise. Such pulses occurred commonly during the late Pleistocene and early Holocene due to episodes of enhanced glacial melt and possible glacial outburst floods (Liu and Milliman, 2004). We later compare modeled deposits with barrier remnants observed in nature, as well as briefly consider the impact of enhanced sea-level rise on modern barriers.

MATERIALS AND METHODS

Interplay of Autogenic and Allogenic Forcing

We are partly inspired to model a periodically retreating barrier subjected to a rapid increase in relative sea-level rise based on a recently compiled set of chronologically controlled drowned barriers (Mellett and Plater, 2018) that correlate in time with a sea-level-rise pulse (or pulses) associated with the 8.2 kyr event – an abrupt cooling of global climate linked to glacial lake outburst floods and enhanced meltwater runoff during the collapse of the Laurentide Ice Sheet (LIS) (Hijma and Cohen, 2010; Mellett and Plater, 2018). The timing, duration, and magnitude of the pulse(s) associated with the 8.2 kyr event remains an active area of research [and to varying degrees depends on the location within the global ocean due to the effects of glacial isostatic adjustment (Kendall et al., 2008; Whitehouse, 2018)], but Hijma and Cohen (2010), using sea-level index points derived from radiocarbon dating of basal peats in Rotterdam (NL), suggest a pulse beginning 8450 $\pm$ 44 years BP with a magnitude of 2.11 $\pm$ 0.89 m over 200 years – an average rate of rise of 10.6 mm/year. Lawrence et al. (2016) additionally identified this pulse using microfossils at the Cree Estuary in Scotland, potentially finding a succession of up to three pulses between 8760 and 8218 years BP. This series includes a relatively prominent jump in sea level beginning at 8595 years BP with a mean magnitude of 0.7 m over 130 years – a corresponding average rate of rise of 5 mm/year. For reference, Hijma and Cohen suggest the background rate of rise at Rotterdam was ~9.75 mm/year, while Lawrence et al. (2016) [using the sea level reconstruction of Bradley et al. (2011)] suggest a background rate of rise at the Cree Estuary between 2 and 3.5 mm/year – in both cases the centennial-scale rate of sea-level rise more than doubled.

How the pulse(s) associated with the 8.2 kyr event potentially interacted with barrier islands during the early-mid Holocene [potentially including the drowned system off Long Island (Rampino and Sanders, 1981)] to create relict deposits remains an open question. If barriers were periodically retreating, the production of remnant deposits – influenced by a combination of autogenic and allogenic forcing – could follow rules of interaction similar to those observed and modeled in alluvial-deltaic systems. In these environments, interpreting environmental signals from the sedimentary record – assigning the driver, timescale, and magnitude of past allogenic forcing – is complicated by internal, non-linear processes affecting deposition and erosion (Foreman and Straub, 2017).

Examining the timescales of autogenic–allogenic interaction in alluvial-deltaic systems using a numerical model, Jerolmack and Paola (2010) demonstrated that environmental (allogenic)

signals tend to be preserved in the sedimentary record when they have temporal periods that are longer than the period of autogenic fluctuations. Conversely, allogenically driven variations in deposition are likely to be destroyed if they fall within the timescales of autogenic processes. However, Jerolmack and Paola (2010) also suggest that allogenic signals with periods shorter than the timescales of autogenic processes can be preserved if their magnitudes are large enough to override any autogenic influence. Li et al. (2016), partly exploring this latter case, showed that for deltas this magnitude directly relates to a storage threshold, based on the delta's spatial extent. Climate signals are attenuated or masked by autogenic processes as the size of the delta system increases in proportion to the depositional potential of allogenic forcing (Li et al., 2016). Modeling of barrier islands by Ciarletta et al. (2019) suggests that periodic deposits with amplitudes (seabed anomalies) greater than half a meter could be expected to occur over centennial to millennial scales, which in the context of alluvial-deltaic studies implies that centennial-scale pulses may have to be relatively high-magnitude to be recorded on the seabed. We explore this thought in the results presented here, modeling a century-scale pulse, but specifically varying the autogenic period of the barrier island and adjusting the pulse timing and magnitude (rate of sea-level rise).

Morphodynamic Model

The goal of our work is to explore the diversity of barrier retreat behavior and seabed responses that result from differences in the timing and magnitude of a sea-level pulse interacting with variable internally driven periodicity. We accomplish this by expanding upon Ciarletta et al. (2019), using the cross-shore morphodynamic model of barrier migration by Lorenzo-Trueba and Ashton (2014) – the "LTA" model. Within the LTA model, barrier retreat is governed by the interplay of sea-level rise, shoreface dynamics, and overwash, with cross-shore barrier geometry defined by three moving boundaries: the shoreface toe, ocean shoreline, and backbarrier shoreline (**Figure 1**). As sea level rises, the barrier height is reduced. In response, barrier shorelines are moved landward by storm-driven overwash, while shoreface dynamics – encapsulated by a shoreface response rate K – adjust the configuration of the shoreface toe and ocean shoreline toward a steady-state geometry. The shoreface toe is additionally constrained by a "depth of closure," or a depth at which sediment exchange between the seabed and the shoreface is negligible (Hallermeier, 1981).

Functionally, the shoreface described by the LTA model spans the portion of the barrier between the shoreface toe and the ocean shoreline, while the "barrier island" comprises the entire structure between the shoreface toe and backbarrier shoreline. As employed in the current study, the model does not consider other processes, such as mass loss or gain driven by alongshore transport gradients [although this process can be accommodated in the model framework (Ashton and Lorenzo-Trueba, 2018)]. This setup reduces the number of environmental variables to isolate the fundamental morphological changes that can be caused by sea-level pulses.

The LTA model can simulate a range of migration and drowning behaviors, including dynamic rollover (constant migration) and periodic retreat. It also captures width drowning, a condition where onshore-directed shoreface fluxes fail to compensate for rapid changes in the geometry of the upper shoreface driven by overwash. Height drowning additionally arises when the rate of sea-level rise outpaces the ability of overwash to maintain the subaerial portion of the barrier.

Physically, periodic retreat is defined by a cycle of aggradation and migration (**Figure 1**), with the barrier oscillating around an equilibrium profile. During this cycle, as the barrier migrates landward into shallower water, decreasing back-barrier accommodation space and increasing shoreface flux results in widening of the barrier until overwash fluxes no longer reach the back-barrier shoreline. Under rising sea level, such a condition results in aggradation and steepening of the shoreface, with the direction of shoreface fluxes beginning to reverse ("Aggraded Barrier," **Figure 1**). The modeling framework would consider this seaward-directed transport to represent net fluxes driven by various wave conditions, with normal storm waves playing the most significant role (Ortiz and Ashton, 2016). Over time, offshore-moving sediment erodes the shoreline while the barrier aggrades in place, causing the barrier to narrow until overwash can again reach the back-barrier shoreline, reinitiating migration ("Migrating Barrier," **Figure 1**) and gradually increasing the rate of landward-directed shoreface fluxes, creating a self-reinforced and repeating response.

Modeling Periodic Retreat

In the LTA model, a shoreface response rate is supplied as a constant for the entire shoreface, and subsequently describes the rate at which the lower shoreface will respond to changes in slope in the form of sediment fluxes. This approach is consistent with the study of Ortiz and Ashton (2016), who suggest that changes in the geometry of the upper shoreface by overwash are not immediately translated to changes in the lower shoreface. Specifically, a primary assumption of the LTA model is the existence of an equilibrium shoreface slope, where offshore directed flux (driven by gravity) is balanced by onshore directed flux (driven by wave-driven transport). As the upper shoreface (ocean shoreline) is driven landward by storm-driven overwash it flattens the overall shoreface, and onshore directed transport responds to this out-of-equilibrium geometry as a function of the response rate – estimatable based on wave height/period, grain size/settling velocity, and depth of closure (Lorenzo-Trueba and Ashton, 2014, supplementary materials). A low response rate effectively causes changes in the upper shoreface to be dominated by overwash until the shoreface flattens enough that onshore-directed fluxes can counterbalance landward shoreline advance.

Subsequently, if the shoreface response rate is small relative to the rate of overwash, this increases the temporal lag within the model framework, whereby the barrier experiences increasingly pronounced and sustained deviations from its equilibrium geometry. If the barrier does not drown, these deviations are expressed as cyclical alternations between phases of landward migration and aggradation, creating a regular pattern of ravinement and deposition on the shelf seabed as the barrier geometry oscillates through out-of-equilibrium shoreface configurations (**Figure 1**). This periodic form of

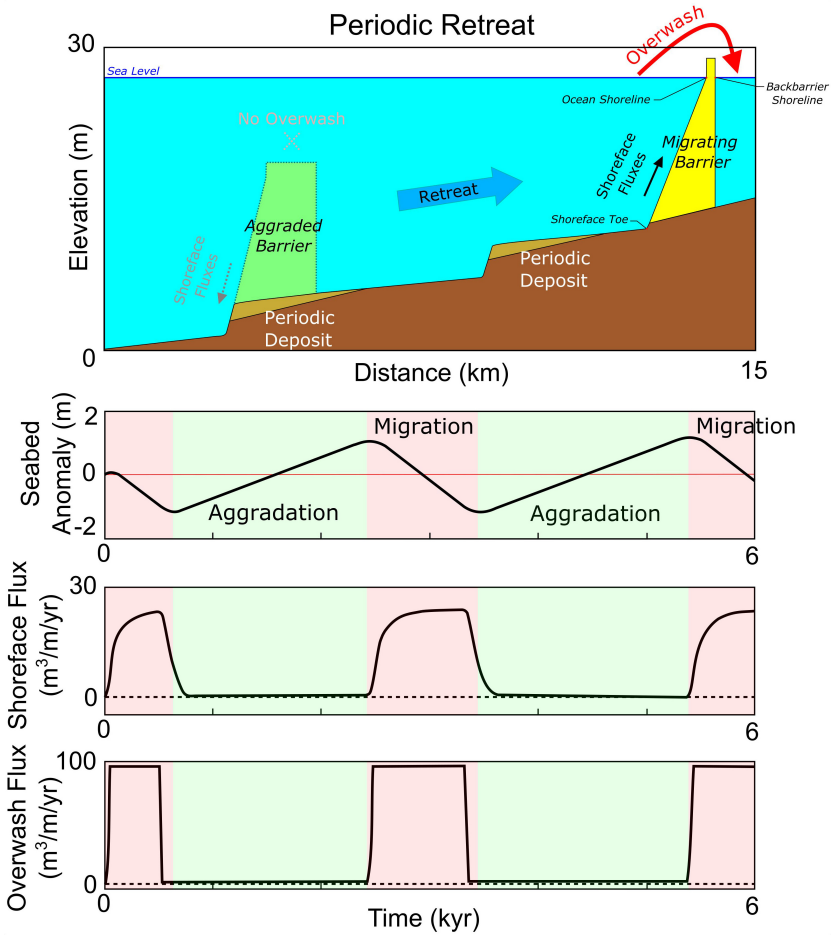

FIGURE 1 | Periodic barrier retreat, defined by an autogenic cycle of alternating episodes of migration (red) and aggradation (green), modeled under constant sea-level rise forcing and shelf slope.

retreat, arising from the morphodynamic nature of the LTA model (Ashton and Lorenzo-Trueba, 2018), is not captured by previous explorations using morphokinematic models, which focus on mass conservation and preservation of (or relaxation to) an idealized barrier geometry as sea level rises (Cowell et al., 1995; Stolper et al., 2005; Moore et al., 2010). Fundamentally, morphokinematic approaches assume that overwash instantaneously drives a landward sediment flux, whereas, in the LTA, a delayed shoreface response is necessary to drive autogenic periodicity.

Modeling Sea-Level Pulses

Within the LTA model, we simulate a pulse inspired by sea-level rise associated with 8.2 kyr event over a 200-year interval (**Figure 2**), exploring a range of pulse magnitudes from 0 to 30 mm/year with a background rate of sea-level rise of 2 mm/year. This background rate is comparable to that of modern Holocene eustatic rise, as well as the background rate at the Cree Estuary during the 8.2 kyr event (Lawrence et al., 2016). We choose 0–30 mm/year for our pulse magnitudes in light of insights from Liu and Milliman (2004) who suggest that earlier glacial meltwater pulses had mean rates of rise of an order of magnitude higher than observed modern sea-level rise. We also consider that tests with the LTA model suggest rates of rise in excess of 30 mm/year generally result in complete drowning of the barrier system over a 200-year interval. Functionally, the pulse injected into the model has a highly simplified square wave or "top-hat pulse" profile, in which the pulse rate of rise is constant for the pulse duration, simulating the mean pulse described by Hijma and Cohen (2010) (**Figure 2**).

We explore pulse interaction with periodicity in four steps, modeling a transgressive barrier with an equilibrium geometry described by Ciarletta et al. (2019) on a shelf slope of 1 m/km (**Table 1**). In our initial results, we create a baseline reference (no periodicity) by subjecting a barrier in dynamic rollover to a pulse. Next, we begin to explore pulse interaction with a periodically retreating barrier, altering the timing of pulse initiation with respect to the start of the model run, such that the pulse occurs during different phases of the aggradation and migration cycle (**Figure 2**, lower panel). Later, we explore how this interaction affects barrier drowning, adjusting the timing and magnitude of the pulse for different rates of shoreface response

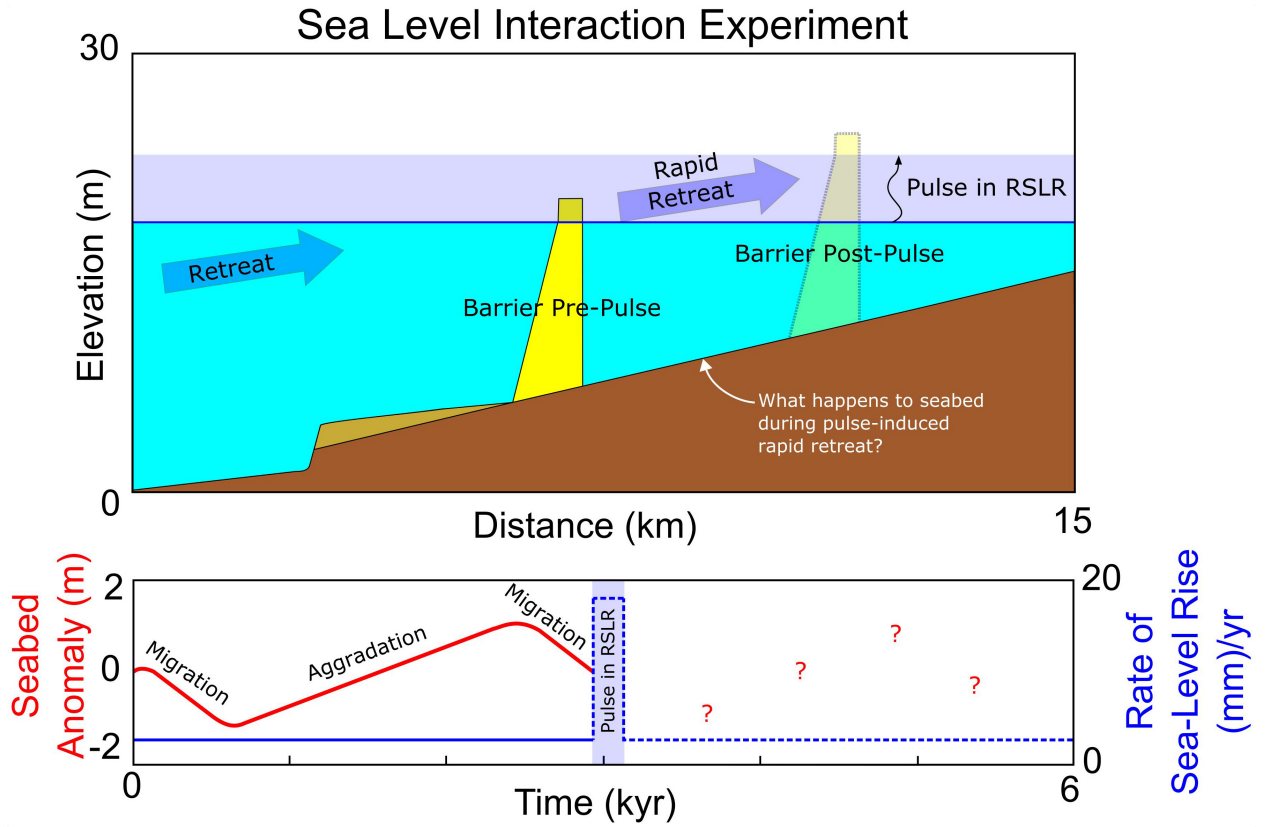

FIGURE 2 | Setup of sea-level interaction experiment. A periodically retreating barrier encounters a pulse in the rate of sea-level rise (in this case, 18 mm/year) for 200 years (comparable to the estimated duration of the 8.2 kyr rise event). To explore autogenic–allogenic interactions, the timing of the pulse is shifted to different times within the periodic cycle (migration and aggradation).

TABLE 1 | Model input parameters.

Parameter	(units)	Symbol	Inputs (Figures 1, 2, 4, 5, 6, 7)
Slope	(m/km)	β	1
Shoreface toe depth	(m)	D_t	15
Equilibrium width	(m)	W_e	800
Equilibrium height	(m)	H_e	2
Equilibrium shoreface slope	(m/m)	α_e	0.02
Maximum overwash flux	(m^3/m/year)	$Q_{OW,max}$	100*
Maximum deficit volume	(m^3/m/year)	$V_{d,max}$	$0.5.H_e.W_e$
Shoreface response	(m^3/m/year)	K	2000 (low), 3000 (med), 6000 (high), 9000 (v. high)
Background sea level rise rate	(mm/year)	$\dot{Z}$	2
Pulse (excess) rate of rise	(mm/year)	$\dot{Z}_p$	0–30
Pulse duration	(years)	t_p	200

**Figure 8* additionally evaluates maximum overwash fluxes of 50, 75, and 125 m^3/m/year.*

(increasing/decreasing periodicity). Finally, we characterize the barrier's behavior as recorded by the seabed and consider the combined effect of different shoreface response rates and maximum overwash fluxes.

RESULTS

Effect of a Pulse on a Rollover Barrier

As a reference case, we initially model the barrier with a "very high" shoreface response rate – for this rate, the barrier is in dynamic rollover, as there is almost no lag between the shoreface response and overwash. This dynamic rollover behavior is similar to the response that could be assumed under a morphokinematic approach, with the barrier assuming a constant steady-state geometry as it retreats (expect for minor fluctuations immediately after initialization) (**Figure 3A**). Subjecting this smoothly transgressing barrier to a 20 mm/year magnitude pulse (**Figure 3B**) temporarily disturbs the barrier from its steady state, creating purely allogenically driven deposition with a seabed anomaly "amplitude" over 2 m, followed by corresponding ravinement. In this case, the 200-year sea-level-rise pulse results in barrier response that persists for >1000 years.

Effect of a Pulse on a Periodically Retreating Barrier

Next, we model a barrier with a "low" shoreface response rate, which, in combination with our other input parameters (**Table 1**), induces an autogenic periodic cycle lasting ~2900 years

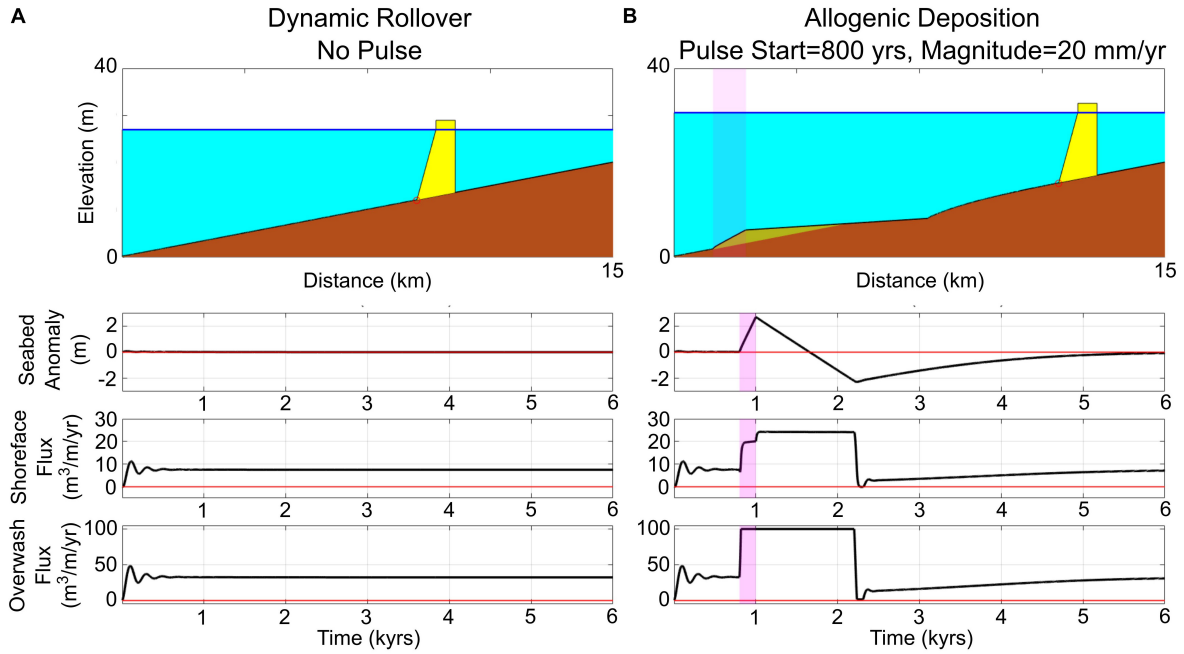

FIGURE 3 | Barrier undergoing dynamic rollover at a very high shoreface response rate K = 9000 m^3/m/year. **(A)** Example with constant forcing and balance between shoreface fluxes and overwash fluxes. **(B)** The constant rollover barrier is subjected to a 200-year pulse (duration and distance affected highlighted in magenta), beginning 800 years into the model run, with a magnitude of 20 mm/year.

(**Figure 4A**). By altering the timing of pulse initiation with respect to the start of the model run, the pulse interacts with the barrier's periodic cycle at different intervals. Our aim is to illustrate the effect of pulse timing on the barrier's retreat behavior and depositional response.

Varying the timing of applied sea-level-rise pulses for a periodically retreating barrier yields diverse behaviors and different types of deposit production during and after pulse interaction (**Figure 4**). For example, where the barrier is in the aggradational phase of the periodic cycle (**Figure 4A**), interaction with a pulse (**Figure 4B**) initially causes the barrier to accelerate its vertical growth due to the sudden increase in height accommodation. At the same time, the barrier begins eroding at the shoreward edge, until its width becomes narrow enough that it eventually migrates landward. This sequence of events can be seen in the double-step that occurs in the overwash flux, with shoreface fluxes beginning to increase in tandem with the second step (when pulse-induced migration begins). Such an interaction can amplify the height of already-forming autogenic deposits (**Figure 4B**).

Conversely, if the barrier is in the migrational phase of the periodic cycle when the pulse occurs, interaction with the pulse can lead to two different outcomes (**Figures 4C,D**). First, if the pulse occurs late enough in the migrational phase, then the pulse will not induce deposition (**Figure 4C**) – the shoreface is already responding to migration due to overwash, and the pulse simply prolongs this overwash cycle. However, if the pulse occurs earlier in the migrational phase, when the shoreface is only beginning to respond, then the pulse can induce deposition when none would be expected based on the autogenic cycle – a deposit is allogenically forced by the sea-level pulse (**Figure 4D**).

Effect of Pulse Timing and Shoreface Response Rates on Barrier Drowning

To further explore the influence of autogenic periodicity on behavioral response, we model sea-level pulses of variable timing and magnitude interacting with periodically retreating barriers across a range of shoreface response rates. In particular, we seek to determine under what conditions a sea-level pulse can lead to drowning of a barrier that would otherwise be expected to maintain itself during transgression. Model results suggest that the likelihood of drowning is affected by both the pulse characteristics (timing and magnitude) and the shoreface response rate (**Figure 5**).

Barrier drowning is more likely for lower shoreface response rates, with pulse timing also strongly affecting whether or not a barrier drowns (**Figure 5C**). At higher shoreface response rates (**Figure 5A**), the periodic cycle exerts relatively little influence on whether the barrier drowns; much of the barrier behavior at high shoreface response is also taken up by dynamic rollover at low pulse rates of rise. In all cases (high to low shoreface response rate), complete drowning of the periodically retreating barrier occurs most readily during the transition between aggradation to migration, when landward-directed shoreface fluxes are initially slow to catch up to overwash fluxes and

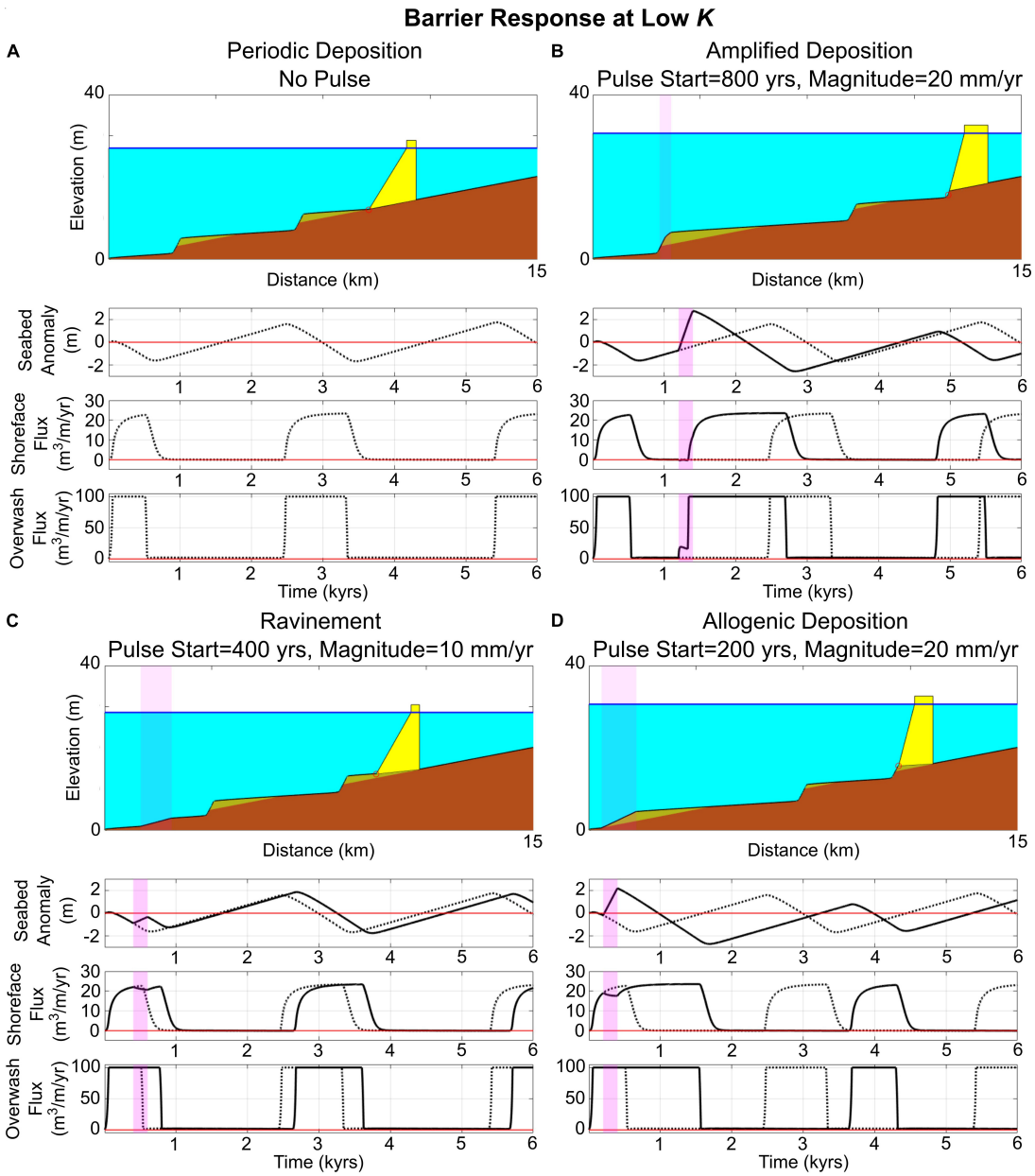

FIGURE 4 | Range of behavioral/depositional responses of a periodically retreating barrier with a low shoreface response rate (K = 2000 m^3/m/year) subjected to a pulse in the rate of sea-level rise. Magenta highlights correspond to duration and distance affected by pulse. **(A)** Periodic deposition (autogenic), with no pulse; dashed lines in subsequent subplots **(B–D)** refer to subplots shown here. **(B)** 20 mm/year pulse coinciding with the aggradational phase of periodic retreat; amplified deposit produced. **(C)** 10 mm/year pulse coinciding with migrational phase of periodic retreat; no deposition/ravinement. **(D)** 20 mm/year pulse coinciding with migrational phase of periodic retreat; deposition occurs where periodic retreat suggests none should occur.

backbarrier accommodation is maximized. Conversely, complete drowning of the barrier can be mitigated if the pulse occurs during the transition between migration to aggradation, where landward-directed shoreface fluxes are peaking and backbarrier accommodation is reduced.

Seabed Response to Pulses

For our final model explorations, we more closely examine the influence of pulse and barrier characteristics (both shoreface response and overwash rates) on the seabed response by constructing a detailed classification of corresponding seabed deposition for different pulse magnitudes and timing. We begin by exploring a barrier with a low shoreface response rate for a full periodic cycle of migration-aggradation (**Figure 5C**; cycle). For barriers that do not drown, we then determine the maximum amplitude of the seabed deposits. If the deposit amplitudes are larger than those that occur during periodic retreat, or deposition occurs when the periodic cycle indicates there should

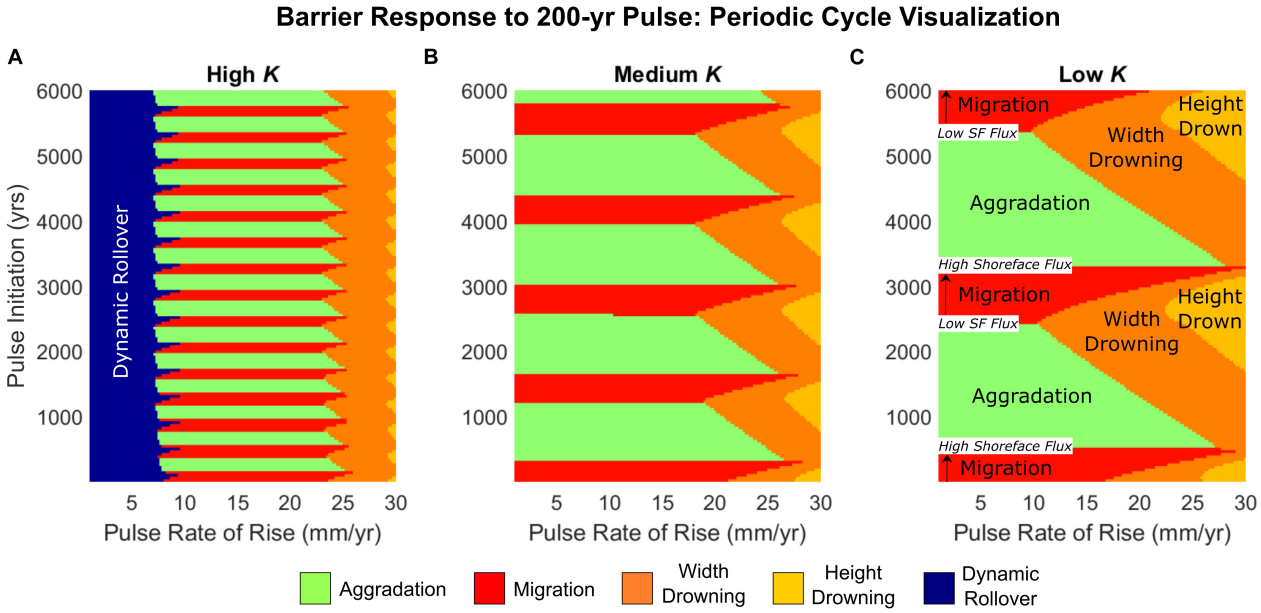

FIGURE 5 | Regime plots depicting the barrier behavioral response to a 200-year sea-level pulse, for different timing of the pulse initiation (relative to the start of the model run) and rate of rise of the pulse. Responses shown for barriers with **(A)** high *K*, **(B)** medium *K*, and **(C)** low *K* (see **Table 1**). Labels on panel **(C)** highlight the autogenic cycle of migration-aggradation, which increases in duration at low *K* (compare panels **A–C**).

be ravinement, we classify the deposit as "allogenic" in origin – created partly or solely in response to forcing from sea-level rise (**Figure 6**). When allogenic deposition coincides with the aggradational phase of periodic retreat, the results are classified as "amplified deposits" (e.g., **Figure 4B**), or more accurately, periodic deposits with enhanced amplitudes. Conversely, when allogenic deposits are produced during the migrational phase, the results are classified as "emergent" to "large" allogenic deposits (**Figure 4D**). We define emergent allogenic deposits as having amplitudes smaller than periodic deposits, while large allogenic deposits equal or exceed periodic deposit amplitudes.

Next, we explore how differences in shoreface response rate affect seabed deposition. A comparison of seabed response at high to low shoreface response rates (**Figure 7**) shows that a barrier with a high shoreface response rate exhibits a relatively simple response regime (compare High *K* with Low *K*), characterized mainly by large allogenic deposits resulting from sea-level pulses with magnitudes of 7–25 mm/year. The highly responsive barrier is also unaffected by lower magnitude pulses (below 7–10 mm/year), remaining in a mode of dynamic rollover. Periodic deposition is almost non-existent at high *K* and cannot be reliably detected, which explains the lack of amplified deposits.

As suggested by **Figure 6**, the presence of the periodic cycle, in combination with decreasing shoreface response rate, increasingly limits the production of allogenic deposits. With lower shoreface response rate there is also no dynamic rollover for any pulse magnitude, with periodic deposition/ravinement and drowning the most likely responses. We note more generally that, for all shoreface response rates, the greatest deposit amplitudes occur when barriers are close to the width drowning regime (**Figure 7**, bottom panel).

To broaden our investigation, we also test the sensitivity of seabed response to different values of the maximum overwash rate (**Figure 8**). In terms of mediating allogenic versus autogenic deposition, the rate of overwash operates inversely to the shoreface response rate, in that increased overwash induces more temporal lag across the barrier shoreface – this enhances the periodic response at higher rates of overwash. Our sensitivity analysis shows that maximum overwash rates from 50 to 125 m^3/m/year can induce seabed responses during pulse interaction that are comparable to our results with variable shoreface response rate. Moreover, where a high overwash rate compounds with low shoreface response rate, the modeled barrier is especially vulnerable to width drowning for even low pulse magnitudes (**Figure 8**, lower right). Conversely, the co-occurrence of high shoreface response rate and low overwash rate results in a uniform response to increasing pulse magnitude, the barrier rendered insensitive to pulse timing and all deposition driven solely by change in the rate of sea-level rise (**Figure 8**, upper left).

DISCUSSION

Our model results suggest barrier island response to a sea-level pulse is governed by the pulse magnitude, the timing of the pulse, and the interaction of barrier shoreface response rate with overwash (**Figure 9** and **Table 2**). By adjusting each parameter independently, we explore the relative contribution of both internal (autogenic) and external (allogenic) controls on the long-term retreat behavior of the barrier, as well as the types of deposits produced on the seabed. We believe the results of

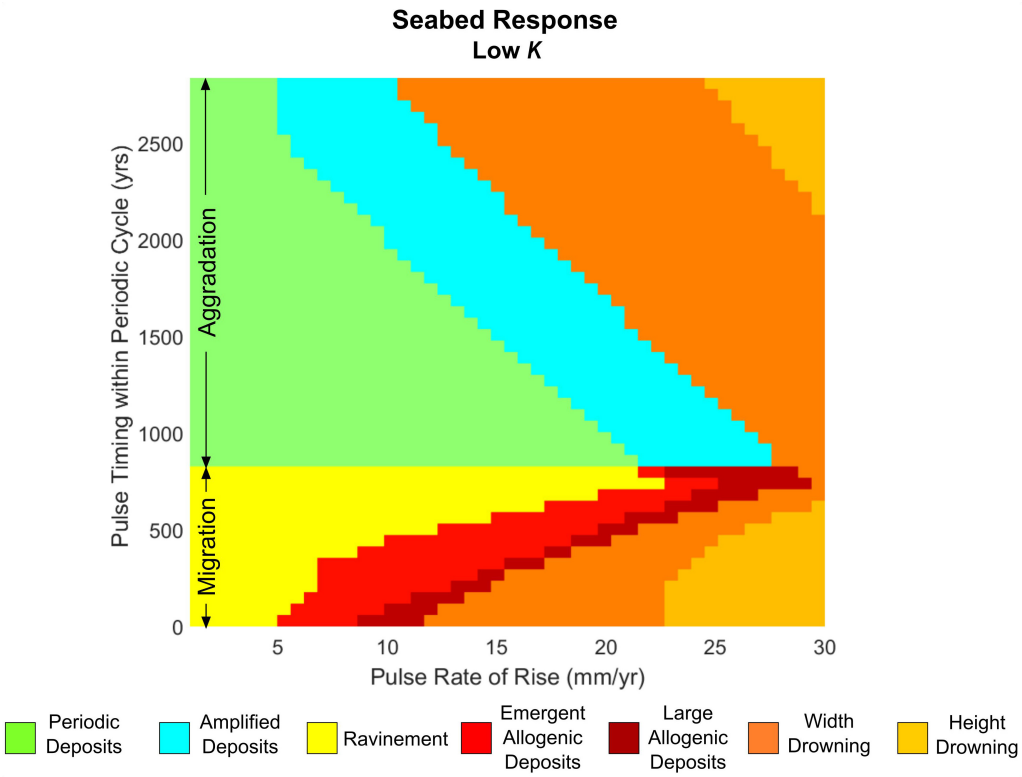

FIGURE 6 | Seabed response classification of a full periodic cycle (migration-aggradation) based on the amplitudes of resulting deposits.

our model explorations are compatible with the observationally inspired concept put forward by Rampino and Sanders (1982) that barrier island retreat involves a suite of states between rollover and complete drowning that are capable of producing remnant deposits on the seabed. Moreover, our work shows that the internal dynamics of a barrier can create an autogenic filter that, despite being regularly oscillating with phases of aggradation and migration, produces a complicated response on the seabed – particularly when considering pulse magnitude and timing.

The rules governing this complicated response within the modeled barrier system share similarities with concepts applied to alluvial-deltaic systems by Jerolmack and Paola (2010) and Li et al. (2016), among others. While we do not test pulses of variable duration, our results show that decreasing periodicity, with aggradational/migrational phases scaling toward the duration of our modeled 200-year pulse, results in an increasingly allogenic depositional response. Conversely, with increasing periodicity, the internal dynamics of the barrier act as an autogenic filter, and only relatively high magnitude pulses can produce an allogenic depositional response – however, the range of pulse magnitudes that can produce allogenic deposition is also variable based on the timing of the pulse within the periodic cycle.

While we can model barrier response under autogenic–allogenic interaction, identifying such a signal in real-world seabed deposits is likely to be difficult based on the similar range of deposit amplitudes produced across the input regime space explored in this study (**Figure 7**). In particular, this suggests that the internal dynamics of barrier islands are superficially similar to deltas in the way they shred the signals of allogenic forcing operating on sub-autogenic timescales (Foreman and Straub, 2017). One possibility to interpret the response of the barrier from relict deposits is to utilize, where available, a more continuous record of deposition, with multiple deposits [e.g., offshore eastern Texas (Rodriguez et al., 2004)]. Although, presently, most known field sites contain either very short sequences of deposits or just one primary deposit (Mellett and Plater, 2018; Ciarletta et al., 2019). Especially for amplified deposition (**Figures 4B,D**), pulse interaction can produce a noticeable disruption in amplitude during subsequent deposition, suggesting autogenic–allogenic interaction could be inferred in cases where periodicity is already suspected – this could be supplemented, where available, by age control to correlate timing with known pulses, as has already been accomplished for some field sites (e.g., Mellett and Plater, 2018, describing a barrier system that likely drowned during interaction with the 8.2 kyr event rise per Mellett et al., 2012a,b).

It may also be possible to constrain the potential for past auto/allogenic interaction based on determining the shoreface response rate and maximum overwash rate of the barrier system if a modern analog is available (or a paleobarrier can be reconstructed from relict morphology or other data). For example, recent work by Aagaard and Hughes (2017) quantified shoreface response, or more specifically the balance of onshore-offshore transport as it relates to equilibrium slope,

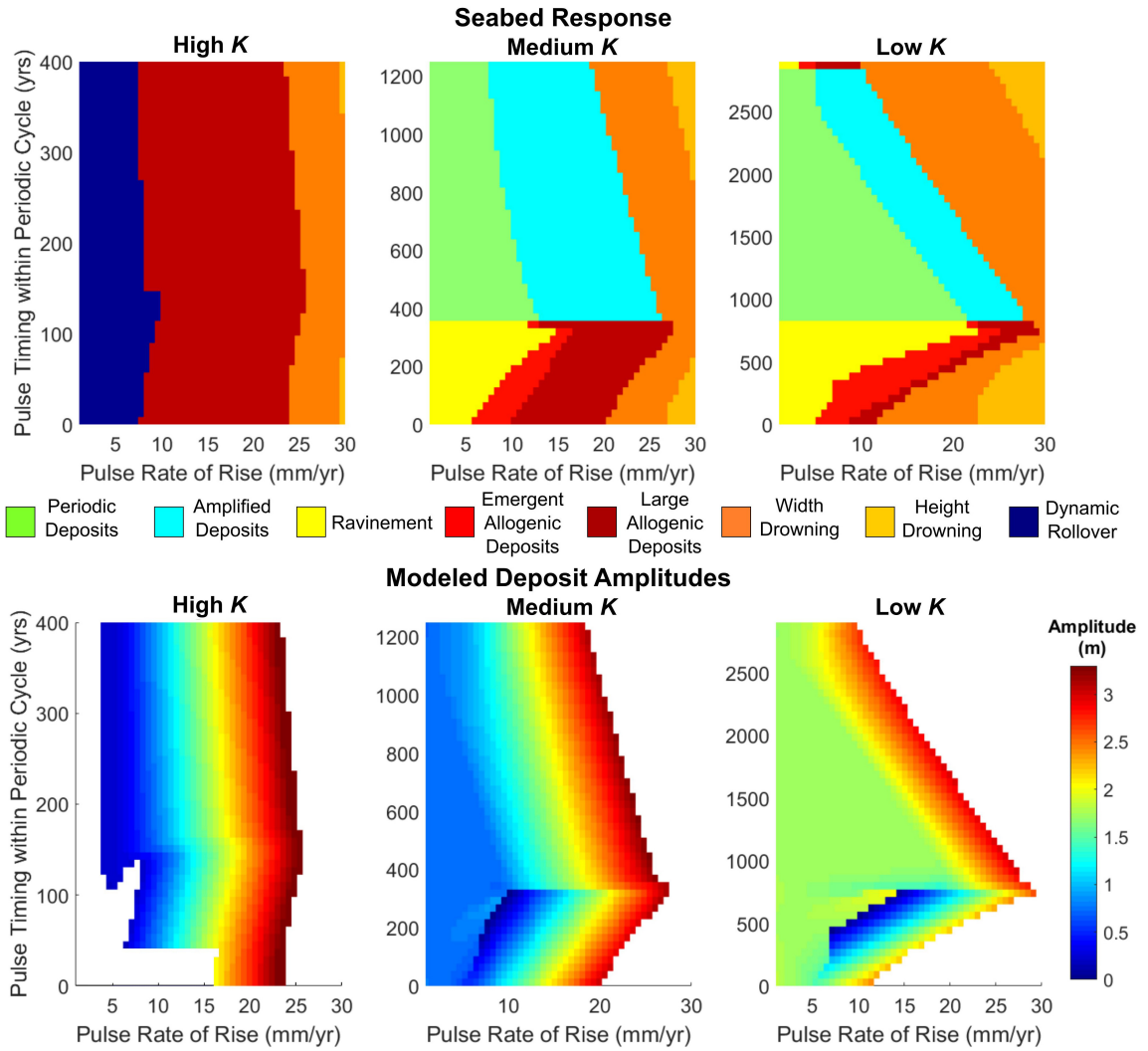

FIGURE 7 | Top: classification of a full periodic cycle with increasing autogenic influence. **Bottom:** corresponding plots of deposit amplitude. White regions in amplitude plots indicate no detection of a deposit or complete drowning of the barrier.

from a combination of field measurements and modeling for coastal Denmark. As for paleobarriers, we note that the shoreface response scales partly as a function of time due to increasing depth of closure over longer timescales (Ortiz and Ashton, 2016), which suggests that estimating the lifetime of such systems [e.g., as accomplished by Mellett et al. (2012b) and Storms et al. (2008), among others] could aid in parameterizing this value. Age dating of paleobarriers, in combination with modeling, could also be applicable to modern barriers to gain insight into future evolution, and could help describe the vulnerability or resilience of specific systems to anthropogenic sea-level rise. Periodic barriers with low shoreface response rates (**Figures 5**–**7**) are generally more susceptible to drowning during rapid sea-level rise, although in some cases our results demonstrate that they could withstand up to 30 mm/year of rise (although shoreline retreat and overwash rates would be rapid).

We note that, in addition to shoreface response rate, one of the most important components driving the periodic response produced by the LTA model is storm-driven overwash flux – increasing this flux enhances the lag in the shoreface response to overwash, lengthening the periodic cycle and increasing the potential for diverse seabed responses (**Figure 8**). We use a maximum overwash rate ranging from 50 to 125 m^3/m/year in our results (**Table 1**), which we estimate compares favorably to real-world barriers. For example, calculation of overwash at barrier sites in New Jersey yields long-term rates in the range 0–100 m^3/m/year using a storm return interval of 50 years (Miselis and Lorenzo-Trueba, 2017), which is typical for the region (Scileppi and Donnelly, 2007). Of concern, modern climate change, driving the current anthropogenic "pulse" in the rate of sea-level rise, may reduce this return interval and increase the intensity of storms (Emanuel, 2013), potentially driving overwash rates beyond what we model here.

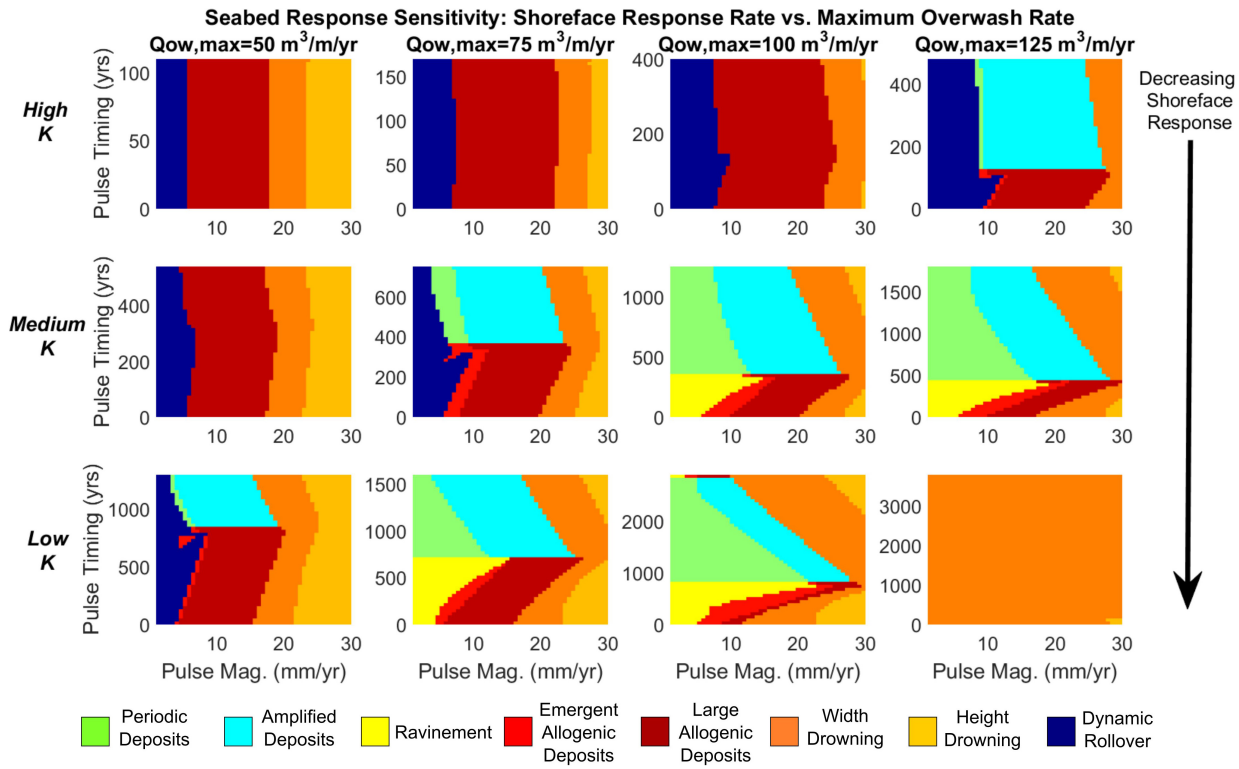

FIGURE 8 | Classification of seabed response based on variable shoreface response rate, maximum overwash rate, sea-level pulse magnitude, and sea-level pulse timing (within a periodic cycle). Shoreface response rate decreases top to bottom (rows), while maximum overwash rate ($Q_{ow,max}$) decreases right to left (columns).

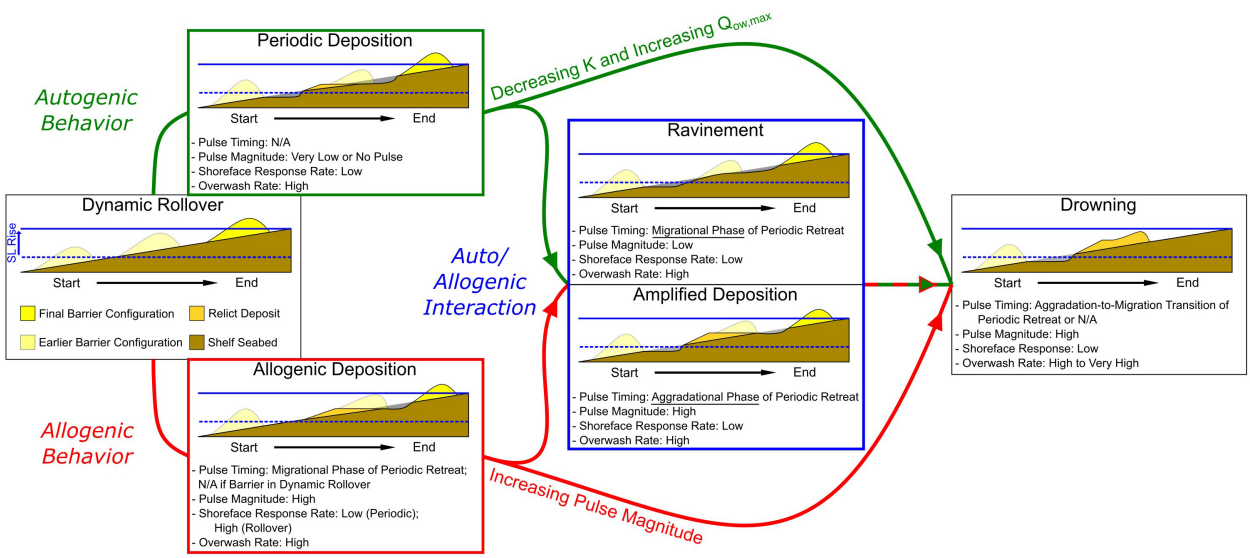

FIGURE 9 | Depiction of barrier response as a function of increasing sea-level pulse magnitude (allogenic behavior – red) and decreasing shoreface response rate *K*/increasing rate of overwash $Q_{ow,max}$ (autogenic behavior – green). Auto/allogenic interaction, where pulses occur in conjunction with periodic deposition, can result in amplified deposits or ravinement, depending on the phase (migrational or aggradational) of periodic retreat and the magnitude of the sea-level pulse. Increasing pulse magnitude, as well as decreasing shoreface response/increasing rate of overwash, ultimately result in barrier drowning. Note that thresholds in internal and external forcing that result in drowning during auto/allogenic interaction are highly variable and depend on the timing of the interaction (see **Figure 8**). Red and green arrows only represent the relative pathways between barrier responses – they do not imply similar forcing magnitudes between interaction and non-interaction response scenarios.

TABLE 2 | Summary of model explorations.

Tested parameter	Barrier depositional/behavioral response
Pulse timing (**Figures 4**, **5**, **6**)	If pulse occurs during aggradational phase of periodic cycle: amplification of deposit volume is possible If pulse occurs during migrational phase of periodic cycle: allogenic deposition (early in migration) or no deposition (later in migration) is possible
Pulse magnitude (**Figures 4**, **5**, **6**)	Larger pulse magnitude results in larger deposits (allogenic and amplified autogenic, depending on phase of periodic cycle), with larger pulses also increasing the likelihood of drowning
Shoreface response rate K (**Figures 5**, **7**, **8**)	Lower shoreface response rates result in larger depositional magnitude and period of autogenic pulses. Thus, barriers with lower shoreface response rates are more likely to drown during a sea-level pulse. Higher response rates suppress autogenic deposition, increasing the possibility of dynamic rollover and favoring purely allogenic deposition or amplified deposition
Rate of overwash $Q_{ow,max}$ (**Figure 8**)	Behavior opposite of shoreface response rate. Lower overwash fluxes reduce system sensitivity to changes in pulse timing. Higher overwash fluxes result in variable response to pulses, with enhanced autogenic periodicity and drowning

Not accounting for external sediment supply contributions (anthropogenic or natural), we suggest interaction of modern sea-level rise with periodically retreating barriers could lead to more variability in behavioral response than our explorations indicate, as well as increased vulnerability to drowning for systems already experiencing high rates of overwash. Additionally, our model does not account for changes in sediment grain size and availability across the shelf environment, assuming a uniform and sandy substrate during transgression. In comparing with modern barrier systems, we suggest our model is therefore conservative, and reduction in sand availability could further increase drowning potential or lead to enhanced periodicity.

Furthermore, the potential for auto/allogenic interactions to be expressed in globally distributed field sites (both ancient and modern) will be affected by two important considerations – the shelf slope and barrier volume. Antecedent shelf slopes for observed barrier systems cover an order of magnitude range, from less than a meter per kilometer (West Florida; Locker et al., 2003) to around 2 m per kilometer (Long Island; Rampino and Sanders, 1980), and in excess of 5 m per kilometer (South Africa – Salzmann et al., 2013; Pretorius et al., 2016; Sardinia – De Falco et al., 2015). Additionally, the spacing and size of remnant deposits seen in nature (potentially a proxy for barrier volume) is highly variable, for example, with small ($<$3000 m^3/m) deposits found at sub-kilometer spacing (KwaZulu-Natal shelf, South Africa; Pretorius et al., 2016) and large ($>$12,000 m^3/m) deposits spaced across multiple kilometers (New Jersey; Nordfjord et al., 2009). The previous investigation by Ciarletta et al. (2019) showed that, for the barrier dimensions modeled here, antecedent slopes in excess of 3 m per kilometer can result in an abrupt reduction in autogenic periodicity, with a corresponding decrease in deposit size and spacing. However, tests with the model also suggest that smaller barriers with very low shoreface response rates could allow for autogenic partial overstepping on steeper slopes. Such a relationship is intriguing, as recently Green et al. (2018), studying the role of antecedent topography on overstepped deposits in South Africa, suggest that barrier volume is inversely related to shelf slope.

Of relevance to this study, late Pleistocene/early Holocene sea-level pulses are believed to be coincident with the deposition of relatively small remnant barriers found at steeply sloping sites in South Africa and Sardinia (De Falco et al., 2015; Pretorius et al., 2016). Future modeling explorations may therefore provide insight on whether autogenic partial overstepping interacting with sea-level pulses could play a role in driving deposit size/spacing on high-gradient coastlines. Specifically, we plan to examine Green et al.'s (2018) suggestion that a steep shelf may result in enhanced reworking of remnant barrier deposits due to focused transgressive ravinement – a process that could potentially complicate the ability of steeply sloping coasts to retain a reliable record of pulse interaction, even with sequences of deposits.

CONCLUSION

Using a morphodynamic model, we demonstrate that autogenic periodicity during barrier island migration could act to filter the response of transgressive systems to rapid changes in rate of sea-level rise (pulses). Our results support the suggestion of Rampino and Sanders (1980, 1981, 1982, 1983) that barrier island retreat and drowning comprises of spectrum of responses that can be recorded on the shelf seabed. In some cases, we show that increasing autogenic periodicity can suppress the depositional response from a sea-level-rise pulse. Conversely, adjustments in the timing and magnitude of a pulse during interaction with a periodically retreating barrier can lead to amplification of autogenic deposition, fully allogenic deposition, or complete drowning of the barrier.

We consider that identifying such autogenic–allogenic interaction in the field presents significant challenges, as the amplitudes of individual relict deposits are not sufficient on their own to characterize the contributions of internal dynamics versus external controls. This exploration suggests, however, that a series of relict deposits could more readily record such an interaction, as sea-level-rise pulses affect the amplitudes of successive periodic deposits. As periodicity strongly affects barrier drowning, we also consider that insights from this exploration could be extended to modern transgressive barriers, providing guidance on their relative vulnerability to differing magnitudes of enhanced sea-level rise.

DATA AVAILABILITY STATEMENT

The datasets generated for this study are available on request to the corresponding author. A copy of the model script (MATLAB and Python) used in this study, as well as scripts to produce animations and figures, are available at our model development page https://github.com/ciarletd/LTAModel-Extension.

AUTHOR CONTRIBUTIONS

DC conceived the model experiments, planned the explorations with JL-T, carried out the simulations, and took the lead in writing the manuscript, with critical feedback from JL-T and AA.

FUNDING

This material is based upon work supported by the National Science Foundation under Grant No. 1518503, and the American Chemical Society Petroleum Research Fund under Grant No. 58817-DNI8 awarded to JL-T; the views presented herein are solely those of the authors and not of the NSF or the ACS PRF.

ACKNOWLEDGMENTS

This manuscript benefited significantly from constructive evaluations by the reviewers. We would also like to acknowledge our colleagues in the MSU Coastal Research Group for their continued support and feedback; Jesse Kolodin, Arye Janoff, Christopher Tenebruso, William Anderson, and Isamar Cortés.

REFERENCES

Aagaard, T., and Hughes, M. G. (2017). Equilibrium shoreface profiles: a sediment transport approach. *Mar. Geol.* 390, 321–330. doi: 10.1016/j.margeo.2016.12.013

Ashton, A. D., and Lorenzo-Trueba, J. (2018). "Morphodynamics of barrier response to sea-level rise," in *Barrier Dynamics and Response to Changing Climate*, eds L. J. Moore, and A. B. Murray, (Cham: Springer), 277–304. doi: 10.1007/978-3-319-68086-6_9

Bradley, S. L., Milne, G. A., Shennan, I., and Edwards, R. (2011). An improved glacial isostatic adjustment model for the British Isles. *J. Q. Sci.* 26, 541–552. doi: 10.1002/jqs.1481

Cattaneo, A., and Steel, R. J. (2003). Transgressive deposits: a review of their variability. *Earth Sci. Rev.* 62, 187–228. doi: 10.1016/s0012-8252(02)00134-4

Ciarletta, D. J., Lorenzo-Trueba, J., and Ashton, A. D. (2019). Mechanism for retreating barriers to autogenically form periodic deposits on continental shelves. *Geology* 47, 239–242. doi: 10.1130/g45519.1

Cooper, J. A. G., Green, A. N., and Loureiro, C. (2018). Geological constraints on mesoscale coastal barrier behaviour. *Glob. Planet. Change* 168, 15–34. doi: 10.1016/j.gloplacha.2018.06.006

Cooper, J. A. G., Green, A. N., Meireles, R. P., Klein, A. H., Souza, J., and Toldo, E. E. (2016). Sandy barrier overstepping and preservation linked to rapid sea level rise and geological setting. *Mar. Geol.* 382, 80–91. doi: 10.1016/j.margeo.2016.10.003

Cowell, P. J., and Kinsela, M. A. (2018). "Shoreface controls on barrier evolution and shoreline change," in *Barrier Dynamics and Response to Changing Climate*, eds L. J. Moore, and A. B. Murray (Cham: Springer), 243–275. doi: 10.1007/978-3-319-68086-6_8

Cowell, P. J., Roy, P. S., and Jones, R. A. (1995). Simulation of large-scale coastal change using a morphological behaviour model. *Mar. Geol.* 126, 45–61. doi: 10.1016/0025-3227(95)00065-7

De Falco, G., Antonioli, F., Fontolan, G., Presti, V. L., Simeone, S., and Tonielli, R. (2015). Early cementation and accommodation space dictate the evolution of an overstepping barrier system during the Holocene. *Mar. Geol.* 369, 52–66. doi: 10.1016/j.margeo.2015.08.002

Donoghue, J. F. (2011). Sea level history of the northern Gulf of Mexico coast and sea level rise scenarios for the near future. *Clim. Change* 107:17. doi: 10.1007/s10584-011-0077-x

Emanuel, K. A. (2013). Downscaling CMIP5 climate models shows increased tropical cyclone activity over the 21st century. *Proc. Natl. Acad. Sci. U.S.A* 110, 12219–12224. doi: 10.1073/pnas.1301293110

Emery, A. R., Hodgson, D. M., Barlow, N. L., Carrivick, J. L., Cotterill, C. J., Mellett, C. L., et al. (2019). Topographic and hydrodynamic controls on barrier retreat and preservation: an example from Dogger Bank, North Sea. *Mar. Geol.* 416:105981. doi: 10.1016/j.margeo.2019.105981

Foreman, B. Z., and Straub, K. M. (2017). Autogenic geomorphic processes determine the resolution and fidelity of terrestrial paleoclimate records. *Sci. Adv.* 3:e1700683. doi: 10.1126/sciadv.1700683

Green, A. N., Cooper, J. A. G., and Salzmann, L. (2018). The role of shelf morphology and antecedent setting in the preservation of palaeo-shoreline (beachrock and aeolianite) sequences: the SE African shelf. *Geo Mar. Lett.* 38, 5–18. doi: 10.1007/s00367-017-0512-8

Hallermeier, R. J. (1981). *Seaward Limit of Significant Sand Transport by Waves: An Annual Zonation for Seasonal Profiles (No. CERC-CETA-81-2)*. Fort Belvoir, VA: Coastal Engineering Research Center.

Hijma, M. P., and Cohen, K. M. (2010). Timing and magnitude of the sea-level jump preluding the 8200 yr event. *Geology* 38, 275–278. doi: 10.1130/g30439.1

Jerolmack, D. J., and Paola, C. (2010). Shredding of environmental signals by sediment transport. *Geophys. Res. Lett.* 37:L19401.

Kendall, R. A., Mitrovica, J. X., Milne, G. A., Törnqvist, T. E., and Li, Y. (2008). The sea-level fingerprint of the 8.2 ka climate event. *Geology* 36, 423–426.

Lawrence, T., Long, A. J., Gehrels, W. R., Jackson, L. P., and Smith, D. E. (2016). Relative sea-level data from southwest Scotland constrain meltwater-driven sea-level jumps prior to the 8.2 *kyr BP event*. *Quat. Sci. Rev.* 151, 292–308. doi: 10.1016/j.quascirev.2016.06.013

Li, Q., Yu, L., and Straub, K. M. (2016). Storage thresholds for relative sea-level signals in the stratigraphic record. *Geology* 44, 179–182. doi: 10.1130/g37484.1

Liu, J. P., and Milliman, J. D. (2004). Reconsidering melt-water pulses 1A and 1B: global impacts of rapid sea-level rise. *J. Ocean Univ. China* 3, 183–190. doi: 10.1007/s11802-004-0033-8

Locker, S. D., Hine, A. C., and Brooks, G. R. (2003). Regional stratigraphic framework linking continental shelf and coastal sedimentary deposits of west-central Florida. *Mar. Geol.* 200, 351–378. doi: 10.1016/s0025-3227(03)00191-9

Lorenzo-Trueba, J., and Ashton, A. D. (2014). Rollover, drowning, and discontinuous retreat: distinct modes of barrier response to sea-level rise arising from a simple morphodynamic model. *J. Geophys. Res.* 119, 779–801. doi: 10.1002/2013jf002941

McNamara, D. E., and Lazarus, E. D. (2018). "Barrier islands as coupled human–landscape systems," in *Barrier Dynamics and Response to Changing Climate*, eds L. J. Moore, and A. B. Murray (Cham: Springer), 363–383. doi: 10.1007/978-3-319-68086-6_12

Mellett, C. L., Hodgson, D. M., Lang, A., Mauz, B., Selby, I., and Plater, A. J. (2012a). Preservation of a drowned gravel barrier complex: a landscape evolution study from the north-eastern English Channel. *Mar. Geol.* 315, 115–131. doi: 10.1016/j.margeo.2012.04.008

Mellett, C. L., Mauz, B., Plater, A. J., Hodgson, D. M., and Lang, A. (2012b). Optical dating of drowned landscapes: a case study from the English Channel. *Quat. Geochronol.* 10, 201–208. doi: 10.1016/j.quageo.2012.03.012

Mellett, C. L., and Plater, A. J. (2018). "Drowned barriers as archives of coastal-response to sea-level rise," in *Barrier Dynamics and Response to Changing Climate*, eds L. J. Moore, and A. B. Murray (Cham: Springer), 57–89. doi: 10.1007/978-3-319-68086-6_2

Miselis, J. L., and Lorenzo-Trueba, J. (2017). Natural and human-induced variability in barrier-island response to sea level rise. *Geophys. Res. Lett.* 44, 11922–11931.

Moore, L. J., List, J. H., Williams, S. J., and Stolper, D. (2010). Complexities in barrier island response to sea level rise: insights from numerical model experiments, North Carolina Outer Banks. *J. Geophys. Res.* 115:F03004.

Mulhern, J. S., Johnson, C. L., and Martin, J. M. (2019). Modern to ancient barrier island dimensional comparisons: implications for analog selection

and paleomorphodynamics. *Front. Earth Sci.* 7:109. doi: 10.3389/feart.2019.00109

Nordfjord, S., Goff, J. A., Austin, J. A. Jr., and Duncan, L. S. (2009). Shallow stratigraphy and complex transgressive ravinement on the New Jersey middle and outer continental shelf. *Mar. Geol.* 266, 232–243. doi: 10.1016/j.margeo.2009.08.010

Ortiz, A. C., and Ashton, A. D. (2016). Exploring shoreface dynamics and a mechanistic explanation for a morphodynamic depth of closure. *J. Geophys. Res.* 121, 442–464. doi: 10.1002/2015jf003699

Pretorius, L., Green, A., and Cooper, A. (2016). Submerged shoreline preservation and ravinement during rapid postglacial sea-level rise and subsequent "slowstand". *Bulletin* 128, 1059–1069. doi: 10.1130/b31381.1

Rampino, M. R., and Sanders, J. E. (1980). Holocene transgression in south-central Long Island, New York. *J. Sediment. Res.* 50, 1063–1079.

Rampino, M. R., and Sanders, J. E. (1981). Evolution of the barrier islands of southern Long Island, New York. *Sedimentology* 28, 37–47. doi: 10.1111/j.1365-3091.1981.tb01661.x

Rampino, M. R., and Sanders, J. E. (1982). Holocene transgression in south-central Long Island, New York: reply. *J. Sediment. Res.* 52, 1020–1025.

Rampino, M. R., and Sanders, J. E. (1983). Barrier island evolution in response to sea-level rise: reply. *J. Sediment. Res.* 53, 1031–1033.

Rodriguez, A. B., Anderson, J. B., Siringan, F. P., and Taviani, M. (2004). Holocene evolution of the east Texas coast and inner continental shelf: along-strike variability in coastal retreat rates. *J. Sediment. Res.* 74, 405–421. doi: 10.1306/092403740405

Salzmann, L., Green, A., and Cooper, J. A. G. (2013). Submerged barrier shoreline sequences on a high energy, steep and narrow shelf. *Mar. Geol.* 346, 366–374. doi: 10.1016/j.margeo.2013.10.003

Scileppi, E., and Donnelly, J. P. (2007). Sedimentary evidence of hurricane strikes in western Long Island, New York. *Geochem. Geophys. Geosyst.* 8:Q06011.

Stolper, D., List, J. H., and Thieler, E. R. (2005). Simulating the evolution of coastal morphology and stratigraphy with a new morphological-behaviour model (GEOMBEST). *Mar. Geol.* 218, 17–36. doi: 10.1016/j.margeo.2005.02.019

Storms, J. E., Weltje, G. J., Terra, G. J., Cattaneo, A., and Trincardi, F. (2008). Coastal dynamics under conditions of rapid sea-level rise: late pleistocene to early holocene evolution of barrier–lagoon systems on the northern Adriatic shelf (Italy). *Quat. Sci. Rev.* 27, 1107–1123. doi: 10.1016/j.quascirev.2008.02.009

Swift, D. J. (1975). Barrier-island genesis: evidence from the central Atlantic shelf, eastern USA. *Sediment. Geol.* 14, 1–43. doi: 10.1016/0037-0738(75)90015-9

Whitehouse, P. L. (2018). Glacial isostatic adjustment modelling: historical perspectives, recent advances, and future directions. *Earth Surface Dyn.* 6, 401–429. doi: 10.5194/esurf-6-401-2018

Conflict of Interest: The authors declare that the research was conducted in the absence of any commercial or financial relationships that could be construed as a potential conflict of interest.

frontiers in Earth Science

ORIGINAL RESEARCH
published: 15 November 2019
doi: 10.3389/feart.2019.00298

Fluvial and Eolian Sediment Mixing During Changing Climate Conditions Recorded in Holocene Andean Foreland Deposits From Argentina (31–33°S)

Tomas N. Capaldi[1], Sarah W. M. George[1], Jaime A. Hirtz[1], Brian K. Horton[1,2] and Daniel F. Stockli[1]*

[1] Department of Geological Sciences, Jackson School of Geosciences, The University of Texas at Austin, Austin, TX, United States, [2] Institute for Geophysics, Jackson School of Geosciences, The University of Texas at Austin, Austin, TX, United States

OPEN ACCESS

Edited by:
Julie Fosdick, University of Connecticut, United States

Reviewed by:
Kurt Eric Sundell, The University of Arizona, United States
Pedro Val, Universidade Federal de Ouro Preto, Brazil

***Correspondence:**
Tomas N. Capaldi
tcapaldi@utexas.edu

Specialty section:
This article was submitted to Sedimentology, Stratigraphy and Diagenesis, a section of the journal Frontiers in Earth Science

Received: *16 August 2019*
Accepted: *29 October 2019*
Published: *15 November 2019*

Citation:
Capaldi TN, George SWM, Hirtz JA, Horton BK and Stockli DF (2019) Fluvial and Eolian Sediment Mixing During Changing Climate Conditions Recorded in Holocene Andean Foreland Deposits From Argentina (31–33°S). Front. Earth Sci. 7:298. doi: 10.3389/feart.2019.00298

Continental drainage systems archive complex records of rock uplift, source area relief, precipitation, glaciation, and carbon cyclicity driven largely by tectonics and climate. Significant progress has been made in linking such external environmental forcings to the geomorphic expression of landscapes and the stratigraphic record of depositional basins in coastal and offshore areas. However, there are large uncertainties in the degree to which sediment dispersal processes can modify signals between the erosional sources and the depositional sinks. We investigate a Holocene sediment transfer zone with contrasting fluvial and eolian sediment transport mechanisms to understand how river and wind processes impact the propagation of environmental signals in continental-scale drainage systems. To quantify these processes, we employ sediment fingerprinting methods for unconsolidated sand samples (detrital zircon U-Pb geochronology), incorporate sediment mixing models, and correlate the findings with the regional geologic and geomorphic framework. Three contrasting source regions deliver sediment to the Andean foreland: volcanic rocks of the Frontal Cordillera, sedimentary rocks of the Precordillera, and metamorphic basement of the Sierras Pampeanas. Although all samples of Holocene eolian dunes accurately record sediment input from three fluvial source regions, spatial variations in U-Pb results are consistent with north-directed paleowinds, whereby river sediments from Frontal Cordillera sources are transported northward and progressively mixed with river sediments from Precordillera and Sierras Pampeanas sources. In contrast, samples of modern rivers show progressive southward (downstream) mixing along a large axial fluvial system. Sediment mixing induced by eolian transport and reworking of various sources is likely a critical, climate-modulated process in the propagation of environmental signals, potentially involving the aliasing of tectonic signals, local storage and recycling of synorogenic river sediment, and cyclical patterns of sediment starvation and delivery to distal zones of accumulation.

Keywords: detrital zircon, Quaternary, eolian transport, fluvial megafan, modern river sediments, source to sink, Andes, Argentina

INTRODUCTION

Sediment routing systems link erosional landscapes to depositional basins and are fundamental in the transmission of surface processes, lithospheric dynamics, regional tectonics, and climate cycles to the stratigraphic record. These systems are characterized by three domains with associated sedimentary processes: (1) sediment source regions marked by relatively high-relief areas of enhanced erosion, (2) sediment transfer zones that show lower relief and generally exhibit limited erosion or accumulation, and (3) sedimentary sinks that record net sediment accumulation (**Figure 1**). Sediment routing systems respond to variations in rock uplift and source area relief (driven largely by *tectonics*), precipitation and glaciation (driven largely by *climate*), the areal extent of river drainage networks, sediment source lithology, and subsidence. Such changes in *environmental signals* are manifest as perturbations in sediment production, dispersal, and/or deposition (Romans et al., 2016). Significant progress has been made in linking environmental signals to the geomorphic expression of landscapes (Jackson et al., 2019; Sharman et al., 2019), and the stratigraphic response within the ultimate basin sink (Blum et al., 2018). However, uncertainties remain regarding the degree to which eolian transfer zones redistribute sediment and modify signals from the erosional source region to a sedimentary basin. Transfer zones are capable of altering or completely removing environmental signals through temporary non-marine sediment storage and weathering (Johnsson et al., 1988, 1991; DeCelles and Hertel, 1989), transport and mechanical breakdown (Ingersoll et al., 1993; Garzanti et al., 2015), climatic fluctuations (Castelltort and Van Den Driessche, 2003; Lawton and Buck, 2006; Mason et al., 2017, 2019; Fildani et al., 2018), autogenic processes (Jerolmack and Paola, 2010), and along-shore drift sediment mixing (Sickmann et al., 2016).

Arid to semiarid regions susceptible to the interplay of fluvial and eolian forces account for ∼17.5% of global land area (Williams and Balling, 1996; Bullard and McTainsh, 2003; Belnap et al., 2011), with sand dunes between 30°N and 30°S currently comprising 10% of the land area, which decreased from 50% during the late Pleistocene (Mehl et al., 2018). Quaternary eolian environments are primarily found in distal foreland basins of Cordilleran (e.g., Andes and North America) and collisional systems (e.g., Zagros and Himalaya), cratonic settings (e.g., Australia and Africa) (Al-Masrahy and Mountney, 2015), and comparable Martian environments (Kocurek and Ewing, 2012). Cratonic eolian systems are long-term recorders of aridification where wind reworks sediment in internally and externally drained catchments (Pell et al., 1997; Lancaster et al., 2002; Maroulis et al., 2007; Vermeesch et al., 2010). Many studies have investigated sediment routing dynamics in continental-scale transport systems associated with collisional orogens (Clift et al., 2008; East et al., 2015; Rittner et al., 2016; Garzanti et al., 2017; Wang et al., 2018). However, an understanding of how climatically influenced eolian systems affect sediment routing across orogenic systems remains an outstanding problem in sediment systems research (Muhs and Zárate, 2001; Latrubesse et al., 2012; Tripaldi and Zárate, 2016; Mason et al., 2019).

Forecasting and characterizing sediment supply in continental drainage systems reflects the interplay of multiple interdependent variables as sediment is transported from erosional source to the accumulating sink (**Figure 1**). Detrital zircon (DZ) U-Pb geochronology provenance signatures have been integrated into sediment routing studies to track source-to-sink system response to tectonic, climatic, and anthropogenic forcings (Dickinson and Gehrels, 2008; Mackey et al., 2012; Blum and Pecha, 2014; Fildani et al., 2016; Sharman et al., 2017; Blum et al., 2018; Horton, 2018; Sickmann et al., 2019). While numerous studies have explored signal propagation in modern fluvial environments (e.g., Amidon et al., 2005; Saylor et al., 2013; Horton et al., 2015; Capaldi et al., 2017; Jackson et al., 2019; Mason et al., 2019), few have explored how subsequent eolian transport, the primary transport mechanism in arid regions, either integrates, removes, or propagates tectonic signals. Additionally, the eolian record is likely to be especially fragmentary because both accumulation and preservation are characterized by a complex balance between sediment supply,

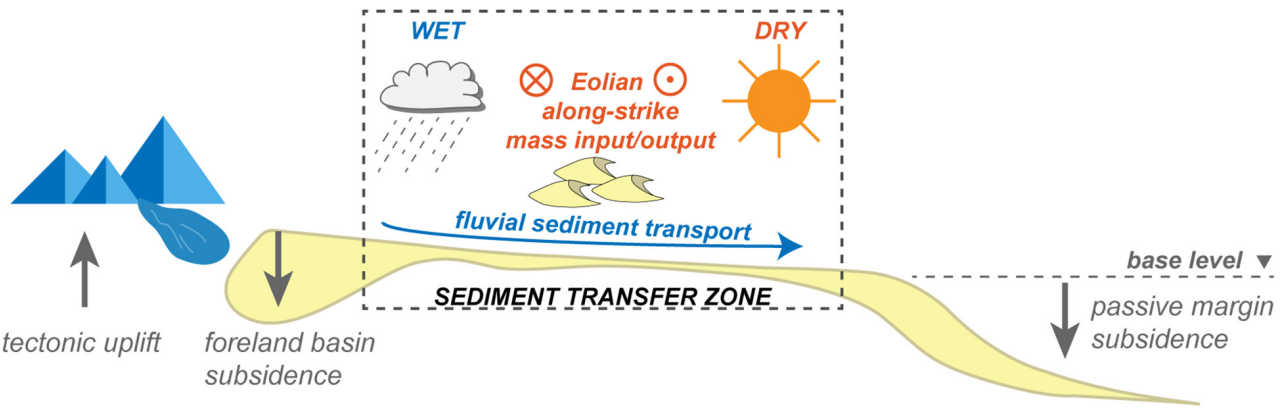

FIGURE 1 | Schematic 2-D profile of the Andean-to-Atlantic margin sediment-routing system of central Argentina emphasizing erosion, transfer, and accumulation zones and important controls of tectonics, climate, base level, and along strike along-strike eolian processes (modified after Romans et al., 2016).

sediment availability and the transport capacity of the wind (Kocurek and Lancaster, 1999; Rodríguez-López et al., 2014). Nevertheless, DZ geochronology is employed on ancient eolian strata to interpret paleoclimatic signals and tectonic events (e.g., Soreghan et al., 2008; Levina et al., 2014; Lawton et al., 2015; Peri et al., 2016; George et al., 2019; Lawton, 2019). This study assesses how modern to Quaternary eolian systems in central Argentina drive either remobilization or storage of Andean river sediment, ultimately feeding or starving down track changes in slope basin systems along the distal Atlantic margin. To quantify the influence of eolian transport in continental drainage systems we: (1) use sediment fingerprinting methods for sand-sized fractions (DZ U-Pb geochronology), (2) incorporate sediment mixing models, and (3) correlate the findings to the regional geomorphology. The Pleistocene to present day Andean Piedmont sand dune fields west central Argentina (Iriondo, 1990; **Figure 2**) offers an ideal location to evaluate the role of eolian influenced transfer zones on sediment routing due in part to well preserved sand dune geomorphology (Tripaldi et al., 2010) and clearly defined Andean tectonic provinces with DZ U-Pb age signatures (Capaldi et al., 2017). Using our results, we assess the relative contributions from fluvial point sources that are reworked and transported within orogen-parallel dune fields, and constrain how tectonic signals are transmitted or modified in eolian conditions induced by climatic shifts. Examining how provenance signatures are propagated through modern source-to-sink systems and preserved in the stratigraphic record will shed light on comparable ancient systems.

GEOLOGIC AND GEOMORPHIC SETTING

Fluvial Megafans of the Argentina Andes

Active sedimentation in the proximal Andean foreland basin of west-central Argentina (31–33°S; **Figure 2A**) is dominated by fluvial megafans fed by large catchments (>10,000 km^2) with localized entry points into the basin, which include the Río Mendoza, Río San Juan, and Río Bermejo fluvial systems (**Figure 2B**). These rivers feed the Río Desaguadero, an axial fluvial system with broad floodplains and ephemeral lagoonal environments that flows southward into the Río Colorado, which ultimately routes Andean orogenic sediment eastward to the distal Atlantic passive margin (**Figure 2A**).

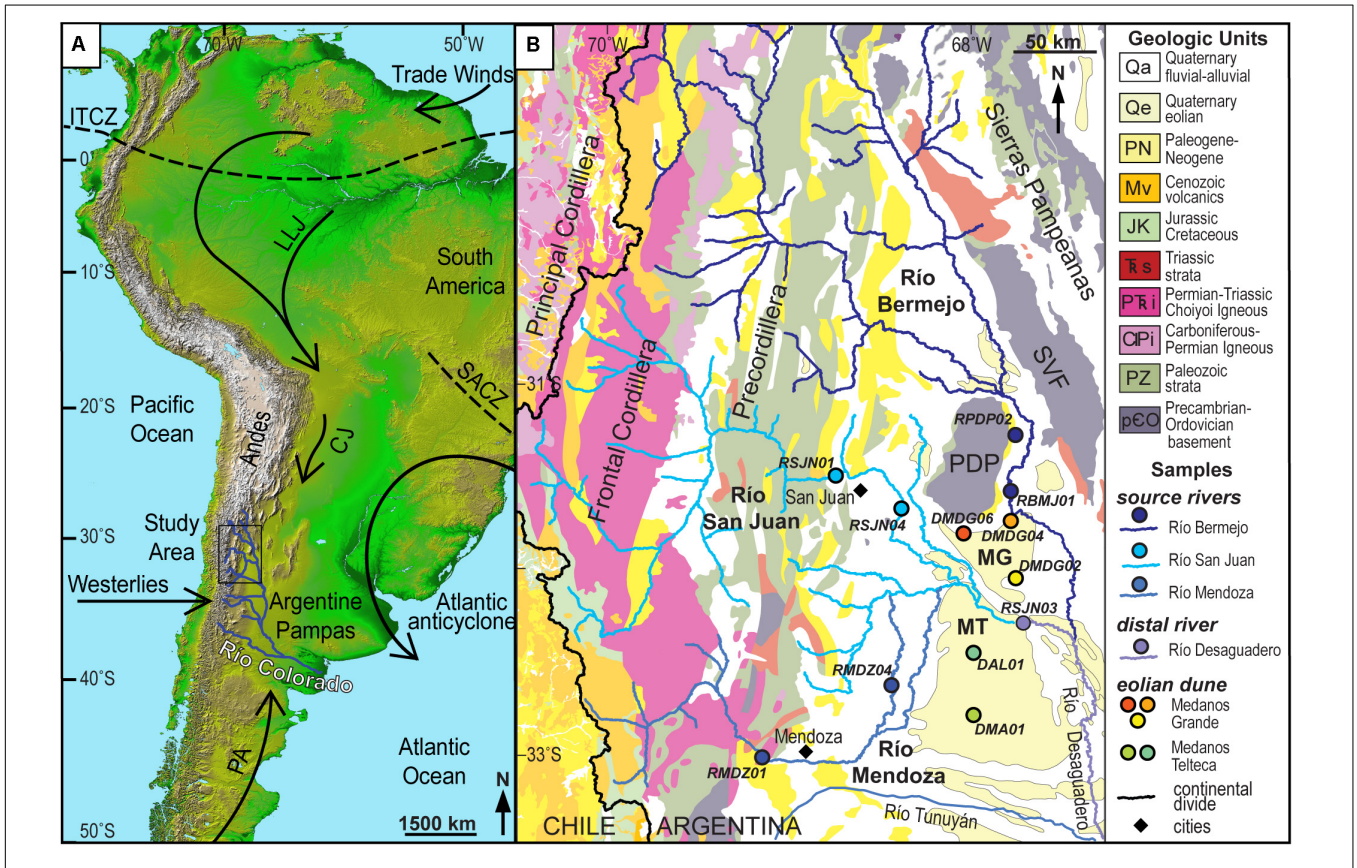

FIGURE 2 | (A) Topographic relief map of South America highlighting Río Colorado sediment routing network and regional wind currents (black lines), Intertropical Convergence Zone (ITCV), Low Level Jet (LLJ), South American Convergent Zone (SACZ), Chaco Jet (CJ), Polar Advections (PA) (modified from Tripaldi and Forman, 2016). **(B)** Geologic map of west-central Argentina indicating the tectonic provinces, fluvial networks (blue lines), and modern river and eolian sample locations (colored circles). Medanos Telteca (MT), Medanos Grande (MG), Sierra Pie de Palo (PDP), Sierra Valle Fértil (SVF).

The Río Mendoza drains high-elevation watersheds dominated by Frontal Cordillera hinterland sources. The Andean hinterland is predominantly composed of reverse-fault blocks that exhume late Paleozoic–Triassic granodiorite intrusions and associated andesitic and rhyolitic lavas, ignimbrites, and pyroclastic rocks of the Choiyoi Igneous complex (unit PTri **Figure 2B**; Heredia et al., 2002). In the west, the Principal Cordillera along the Chile-Argentina border consists of Neogene volcanic and volcaniclastic materials derived from the Andean arc (unit Mv) and deformed Mesozoic rift-related strata (unit JK) (**Figure 2B**; Cristallini and Ramos, 2000; Mackaman-Lofland et al., 2019).

The Río San Juan is fed by an integrative trellis drainage network spanning the Precordillera fold-thrust belt involving a Paleozoic marine clastic and carbonate succession (units PZ) (Ramos, 1988; von Gosen, 1992). Neogene foreland basin deposits (unit PN) are preserved in footwall blocks of major thrust faults with preferential erosion forming intermontane valleys between thrust-generated ranges (Jordan et al., 2001; Levina et al., 2014; Capaldi et al., 2017).

Distal eastern portions of the basin are structurally partitioned by roughly NNW-trending basement-cored uplifts (Sierras Pampeanas) and intervening subsiding zones within a broken foreland basin province. The flanking Río Bermejo flows southward along the western ranges of the Sierras Pampeanas, sourcing broadly folded Triassic-Jurassic fluvial red beds and underlying exhumed Precambrian-lower Paleozoic basement (units Trs and unit PcO) along the Sierra Valle Fertile (SVF; **Figure 2B**) and Sierra Pie de Palo uplifts (PDP; **Figure 2B**), as well as Neogene basin fill (unit PN), and modern alluvial fans along basin-bounding structures (Damanti, 1993).

Holocene Andean Foreland Eolian Dune Fields

The central foreland basin is dominated by a >10,000 km^2 north-trending zone of eolian landforms, including the southern Medanos Telteca and northern Medanos Grande eolian dune fields (**Figure 2B**). Both Medanos Telteca and Grande systems have been estimated to be last active during the Holocene, exhibiting high-relief (50 m) parallel ridges of dominantly longitudinal (seif) dunes and asymmetric transverse dunes, and litharenite to feldspathic litharenite sand composition (Iriondo, 1999; Zárate, 2003; Zárate and Tripaldi, 2012; Tripaldi et al., 2013; Tripaldi and Forman, 2016; Tripaldi and Zárate, 2016). Detailed optically stimulated luminescence (OSL) geochronology has been established across the major eolian provinces of central Argentina, providing a framework to analyze sediment transport across the sediment routing system during the Holocene (Tripaldi and Forman, 2007, 2016; Latrubesse and Ramonell, 2010).

The study region is characterized by low precipitation and winds from the west and southeast. Precipitation in western Argentina is associated with monsoon-type circulation that is generated by humid air masses from the Atlantic anticyclone, and is concentrated (>70%) during October to March. Precipitation decreases from east to west; from 90 to 100 cm/year in the northeastern Pampas to <25–30 cm/year in the Andean piedmont study area (Compagnucci et al., 2002; Tripaldi and Forman, 2016). Regionally, wind conditions are controlled by the subtropical high-pressure cells (Pacific and Atlantic anticyclones), which modulates the Westerlies and Polar advection wind activity. In general, Westerly (Zonda) winds are generated off the Andes and are dominant along the downslope Andean piedmont, and southeasterly Polar Advection (Pampero) winds prevail throughout the year across the eastern Argentine Pampas (**Figure 2A**).

METHODOLOGIES

Detrital Zircon U-Pb Geochronology

We collected and analyzed five Holocene eolian sands sampled at dune crests in the Medanos Telteca (DMA01, DAL01) and Medanos Grande (DMDG02, DMDG06, DMDG04) dune fields, and two modern river sands sampled along active channel bedforms from a tributary of the Río Bermejo (RPDP02) and main trunk of the Río San Juan (RSJN04). U-Pb DZ geochronological data are integrated with previously published U-Pb age results from modern foreland river deposits of Río Mendoza (RMDZ01 and RMDZ04), Río San Juan (RSJN01 and RSJN03), and Río Bermejo (RBMJ01) (Capaldi et al., 2017; **Figure 2**). Standard mineral separation techniques included water table, heavy-liquid density, and magnetic susceptibility separations for all samples. Non-magnetic heavy mineral separates were poured onto double sided tape on 1" epoxy resin mounts and zircon grains were chosen randomly for analysis by laser ablation–inductively coupled plasma–mass spectrometry (LA-ICP-MS) to obtain zircon U-Pb ages. Sample mounts were loaded into a large-volume HelEx sample cell and analyzed with a single-collector, magnetic sector Element 2 ICP-MS with a Photon Machine Analyte G2 excimer laser (Horton et al., 2016; Odlum et al., 2019). Corrections for depth-dependent, elemental and isotopic fractionation were performed using zircon standards GJ1 (600.4 ± 0.1 Ma; Jackson et al., 2004), and secondary standards Plešovice (PL-1; 337.2 ± 0.4 Ma; Sláma et al., 2008; Whitehouse, 2008), and 91500 (1065 Ma; Wiedenbeck et al., 1995). Zircon U-Pb ages and 2σ uncertainty (**Supplementary Table S1**) are reported for analyses with less than 10% $^{206}Pb/^{238}U$ uncertainties, less than 30% discordance, and less than 5% reverse discordance. Reported dates and percent discordance for grains younger than 850 Ma are $^{206}Pb/^{238}U$ ages and discordance $^{206}Pb/^{238}U$ vs. $^{207}Pb/^{235}U$, and for grains older than 850 Ma ages are $^{207}Pb/^{206}Pb$ dates with $^{206}Pb/^{238}U$ vs. $^{207}Pb/^{206}Pb$ discordance.

Results are organized based on spatial relationship among eolian samples from south to north with U-Pb ages for individual samples displayed as probability density functions (PDF), kernel density estimates (KDE) with set bandwidth of 15 Myr, and histogram age bins of 25 Myr. Zircon U-Pb age distributions are described in terms of broad age components of modes for samples that reflect particular Andean provenance signatures. The relative percentage for each of the six age groups are calculated for each fluvial and eolian sample

(**Supplementary Table S2**). Diagnostic age components are as follows, from oldest to youngest.

(1) Proterozoic 1450–950 Ma basement ages have a minor component of 1450–1350 Ma ages recycled from the Laurentian-derived Cuyania terrane. Dominate 1200–950 Ma Sunsás (Grenville) age component are sourced from numerous metamorphic basement units across the western Sierras Pampeanas and are ubiquitous in most Ordovician to Permian sedimentary sequences from the Precordillera (Ramos, 2004, 2009; Bahlburg et al., 2009; Rapela et al., 2016);
(2) The Eastern Sierras Pampeanas (725–520 Ma) age group are recycled from Carboniferous to Permian sedimentary sequences found in the Precordillera fold-thrust belt (Fosdick et al., 2015; Capaldi et al., 2017). The Eastern Sierras Pampeanas (725–520 Ma) age group is composed of a minor 725–540 Ma age component initially recycled from sourced from metasedimentary rocks (Puncoviscana Formation) and a dominant 538–515 Ma age peak from Cambrian rocks of the Pampean magmatic arc (Rapela et al., 2007; Schwartz et al., 2008);
(3) The Western Sierras Pampeanas (510–380 Ma) age group is derived from sources throughout the western Sierras Pampeanas involving 495–440 Ma Famatinian continental arc rocks and subsequent 460–385 Ma metamorphic assemblages (Mulcahy et al., 2014; Otamendi et al., 2017). Recycled Western Sierras Pampeanas 510–380 Ma DZ age components are derived from Carboniferous-Permian sedimentary units in the Precordillera fold-thrust belt and Triassic sedimentary sequences overlying western Sierras Pampeanas uplifts (Capaldi et al., 2017);
(4) Late Paleozoic 375–280 Ma zircon ages are from minor 360–335 Ma igneous suite spanning the study area and dominate 340–280 Ma Carboniferous arc rocks of the Principal and Frontal Cordilleras (Mpodozis and Kay, 1992; Dahlquist et al., 2013) and minor recycled sources from Triassic sedimentary deposits in the Sierras Pampeanas and Neogene deposits throughout the Frontal Cordillera, and Precordillera (Fosdick et al., 2015, 2017);
(5) Permian Triassic 280–205 Ma age group includes dominant Choiyoi Igneous Complex and subsequent Triassic plutons exposed in the Frontal Cordillera (**Figure 2B**; Mpodozis and Kay, 1992; del Rey et al., 2016). Additional sources of Permian Triassic 280–205 Ma age components include recycled Jurassic to Cretaceous sedimentary deposits in the High Andes and Neogene deposits across the Precordillera (Capaldi et al., 2017; Mackaman-Lofland et al., 2019);
(6) Andean Arc 120–0 Ma Cretaceous to Neogene Andean arc volcanic and volcaniclastic rocks of the Principal Cordillera, Frontal Cordillera, Precordillera, and Sierras Pampeanas, and recycled from Neogene basin fill (Kay and Mpodozis, 2002; Jones et al., 2015).

Comparison among fluvial and eolian sand samples DZ U-Pb age distributions was accomplished by visual inspection of the relative abundance of age groups (**Supplementary Table S2**), and using commonly applied metrics of similarity using PDFs, KDEs, and cumulative distribution functions (CDFs) (**Supplementary Table S3**). Comparison among DZ PDF and KDE employed cross-plot (R^2 cross-correlation coefficient), Similarity, and Likeness. Whereas statistical test on CDF age distributions included Kolmogorov-Smirnov (K-S) test (D value), and Kuiper's test (V value). We apply these comparative methods using the program DZ Stats (Saylor and Sundell, 2016). The relative measure of similarity among age distributions provide quantitative comparison metrics to determine whether samples were drawn from the same parent population and degree of similarity between sample age distributions. For this study we utilize R^2 cross-correlation coefficient on KDEs, which is sensitive to the number and relative proportions of detrital age modes and more discriminating than other test (Saylor and Sundell, 2016). Additional DZ U-Pb age distributions comparison was established through metric multidimensional scaling (MDS) plots to identify greater similarity for samples that cluster together and less similar for those that plot farther apart. Metric MDS is applied by constructing a pairwise dissimilarity matrix of detrital age distributions among the fluvial and eolian samples using R^2 cross-correlation coefficient. Metric MDS plot and results was created using the program DZmds (Saylor et al., 2018).

Sediment DZ "unmixing" modeling approaches allow for discrimination of the potential proportions of different contribution sources mixed in eolian and fluvial transport using the DZmix program (Sundell and Saylor, 2017). Mixture modeling of DZ U-Pb data was used to determine the contributions of sediment sources from the three fluvial systems (i.e., Río Mendoza, Río San Juan, and Río Bermejo) by randomly mixing potential fluvial source age distribution KDEs and comparing model output to target downstream eolian and river sand samples DZ age distribution. The mixing model determines a range of best mixtures of potential sources using an inverse Monte Carlo approach of randomly scaling each source age distribution by a random set of percent contributions that sum to 100%, summing the scaled distributions to give a single model distribution and quantitatively comparing that model distribution to a eolian or river sample distribution through R^2 cross correlation. This process is repeated 100,000 times for each basin sample KDE, and the best 1000 model fits (1%) are used to calculate the mean and standard deviation (1σ) contribution from each potential source (**Supplementary Table S4**).

RESULTS

Detrital Zircon Age Distributions

Fluvial Megafan Sediment Input

Detrital zircon U-Pb age distributions from modern river sands in the southern Central Andean foreland demonstrate distinctive age signatures from several competing sediment inputs, including the Río Mendoza and Río San Juan fluvial megafans, which have been shown to accurately reflect the distribution of source units within retroarc hinterland and

thrust belt catchment areas. DZ ages from the broken foreland drainage network along the Río Bermejo axial trunk river represent local contributions from foreland basement-cored uplifts of the Sierras Pampeanas (**Figure 2B**; Capaldi et al., 2017). This well-characterized modern river age distributions provides a valuable opportunity to apply DZ provenance results to track sediment mixing and redistribution by fluvial and eolian processes within a sediment transfer zone between source and sink.

The southern Río Mendoza fluvial megafan consists of modern river drainage networks that source Neogene Andean volcanic rocks and the Choiyoi Permian-Triassic volcanic complex. The composite DZ U-Pb age spectra (samples RMDZ04 and RMDZ01) is dominated by a bimodal Permian-Triassic (280–205 Ma) and late Paleozoic (375–280 Ma) age populations with all other diagnostic ages being nearly absent (**Figure 3**). The strong bimodal DZ age signature from the Río Mendoza is indicative of hinterland volcanic material derived from the Frontal Cordillera, which is inferred to be representative of the age signature for the more southern Río Tunuyán (**Figure 2B**).

The western Río San Juan fluvial megafan is fed by the Precordillera fold-thrust belt, which reflects erosion and recycling of Paleozoic and Neogene basin fill, and upstream hinterland volcanic sources in the Frontal Cordillera. Detrital zircon U-Pb results from Río San Juan (samples RSJN01 and RSJN04) show multimodal age distribution that include Andean arc (<120 Ma) and Permian-Triassic arc (280–205 Ma) age components indicating recycling from exhumed Neogene strata between Precordillera thrust sheets. Additionally, significant Eastern Sierras Pampeanas (725–520 Ma) and Proterozoic (1450–925 Ma) age zircon grains are derived from the recycling of Paleozoic sedimentary sequences from the core of the thrust sheets (**Figure 3**).

The northern Río Bermejo megafan drains the western Sierras Pampeanas basement-involved uplifts in the distal reach of an expansive drainage network encompassing Precordillera and Frontal Cordillera source. The DZ age distributions from modern river sands (samples RPDP02 and RBMJ01) that includes western Sierras Pampeanas (510–380 Ma), Eastern Sierras Pampeanas (725–520 Ma), and Proterozoic (1450–925 Ma) age groups. Age distributions dominated by older> 350

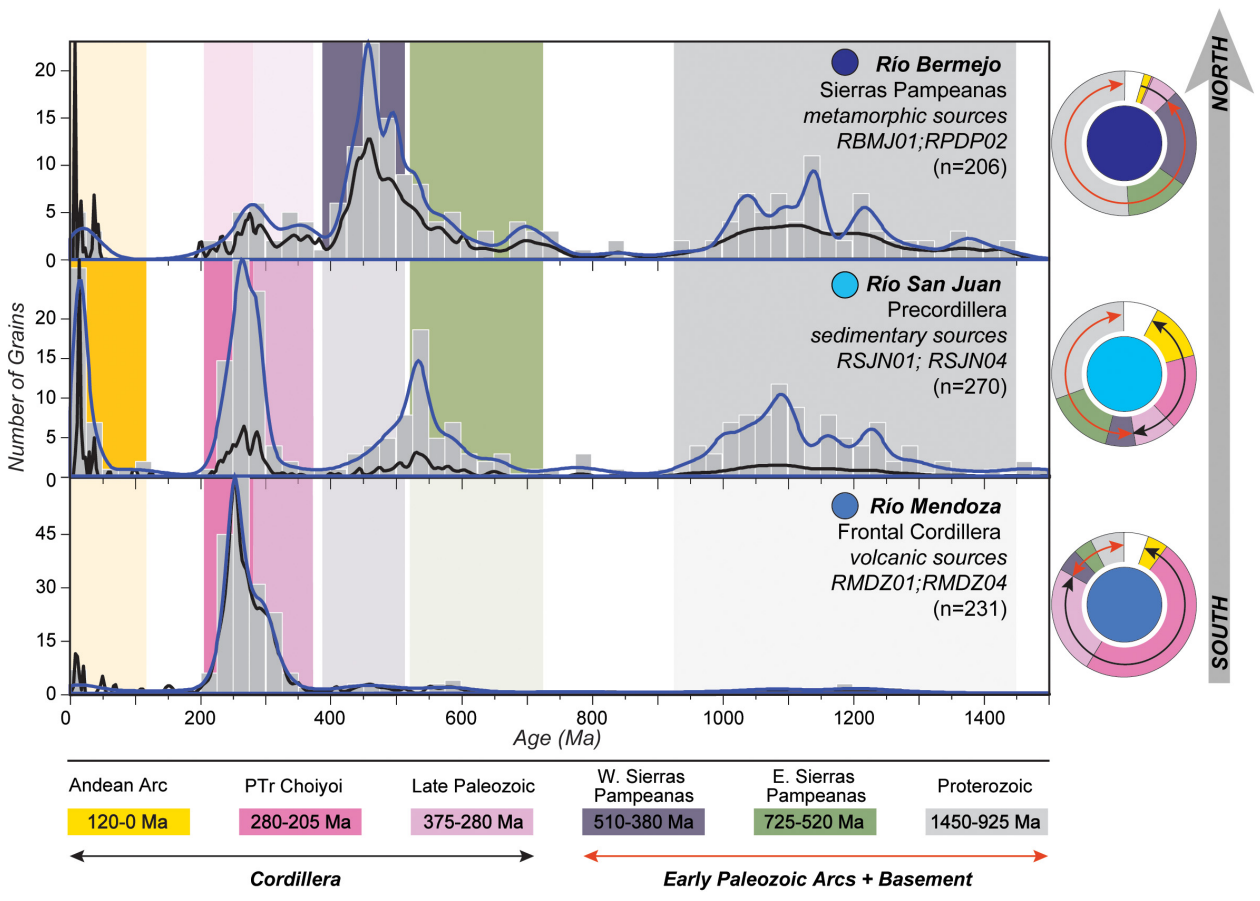

FIGURE 3 | Comparative plot of detrital zircon (DZ) U-Pb age distributions for modern river sands, depicted as age histograms (gray rectangles), kernel density estimates (blue line), and relative probability density plots (black line), with emphasis on key age populations (dark color shading) and minor to no age populations (transparent color shading). Donut diagrams represent percent abundance of key age populations in each sample, with Cordillera (black arrows) and Early Paleozoic Arcs and Basement (red arrow) age groups emphasized, and inner colored circle corresponds to sample locations in **Figure 2B**.

Ma age populations are indicative of sediment recycling of both the overlaying Mesozoic strata and exhumed Ordovician-Precambrian crystalline basement cores of the active western Sierras Pampeanas uplifts rather than hinterland age signatures (**Figures 2B**, **3**; Capaldi et al., 2017).

Fluvial-Eolian Transfer Zone Deposits

The fluvial sediment sources southern Río Mendoza, western Río San Juan, and northern Río Bermejo deliver sediment to the Andean foreland proximal to the Holocene eolian system (**Figures 2**, **5B**). New DZ age distributions from eolian sand samples are compared to proximal fluvial sand samples to distinguish spatial variations in Andean signals in relationship to contradictory south-flowing rivers and north-directed wind patterns (**Figure 4**). Results demonstrate the ability to track sedimentary signals from Andean rivers across the Holocene eolian Andean foreland, and compare observed Holocene spatial patterns to modern fluvial signatures (RSJN03).

The southern Medanos Telteca eolian field is proximal to the Río Mendoza and Río Tunuyán fluvial megafan system draining the Frontal Cordillera volcanic units. Both southern and northern Medanos Telteca samples DMA01 and DAL01 exhibit similar DZ U-Pb age distributions that are characterized by dominant (26–27%) Permian-Triassic (280–205 Ma) age peak, subordinate (18–21%) Proterozoic ages, and minor (8–17%) late Paleozoic (375–280 Ma) Western and Eastern Sierras Pampeanas (510–380 Ma and 725–520 Ma) populations (**Figure 4**). Comparison with fluvial megafan inputs yield cross correlation R^2 coefficient results that indicate higher similarity (0.71–0.75 R^2 values) with Río Mendoza age distributions, and moderate similarity (0.54–0.57 R^2 values) with Río San Juan (**Table 1**).

The northern Medanos Grande eolian field is located between the Río San Juan and Río Bermejo fluvial systems, these rivers erode predominantly Neogene age sedimentary sequences and Paleozoic metasedimentary units in the Precordillera and crystalline basement rocks along the Sierras Pampeanas (**Figure 2B**). In general, Medanos Grande eolian deposits (DMDG02, DMDG04, and DMDG06) exhibit greater abundances of older zircon ages (>380 Ma) than samples from the southern Medanos Telteca (**Figure 4**). The DZ age distributions from Medanos Grande samples are dominated by (25–31%) Proterozoic ages and (20–29%) Western Sierras Pampeanas (510–380 Ma) age populations, with subordinate amounts (8–17%) of late Paleozoic (375–280 Ma) and Eastern Sierras Pampeanas (725–520 Ma), and minor components (7–10%) of Andean arc (<120 Ma) and Permian-Triassic (280–205 Ma) age populations (**Figure 4**). Medanos Grande samples are compared with each fluvial megafan sample age distributions, which yield moderately-low similarity (0.21–0.34 R^2 values) with Río Bermejo composite age signature (**Table 1**). However, the southern Medanos Grande sample DMDG02 exhibits moderate similarity (>0.35 R^2 values) with Río Mendoza fluvial source, than samples DMDG04 and DMDG06 from northern and western Medanos Grande that show low similarity with Río Mendoza (<0.2 R^2 values). Medanos Grande samples (DMDG02, DMDG04, DMDG06) are moderately similar (0.29 to 0.50 R^2 values) to Río San Juan age distribution.

Modern river sample RSJN03 reflects the geomorphic transition from Río Mendoza and Río San Juan fluvial megafan, to distal Río Desaguadero axial river headwaters (**Figure 2B**). The DZ age distribution contains strong (24%) late Paleozoic (375–280 Ma) and (23%) Proterozoic age populations, with subordinate (12–16%) Permian-Triassic (280–205 Ma), Western and Eastern Sierras Pampeanas (510–380 Ma and 725–520 Ma), and minor (8%) Andean arc ages (**Figure 4**). The distal fluvial sample DZ spectrum is similar to Río Mendoza (0.61 R^2 value) and Río San Juan (0.57 R^2 value), and dissimilar to Río Bermejo age distribution (0.02 R^2 value) (**Table 1**).

Fluvial-Eolian DZ Sample Comparison

Comparisons among the three diagnostic fluvial megafan DZ age distributions and Holocene eolian DZ age distributions show complementary south-to-north mixing trends (**Table 1** and **Supplementary Table S3**). Specifically, R^2 cross-correlation coefficient values from eolian sample comparison with fluvial source display a south-to-north decrease in similarity with Mendoza fluvial megafan samples, where southern Medanos Telteca samples DMA01 and DAL01 has high R^2 values of 0.71–0.75 and northern Medanos Grande samples DMDG have low R^2 values of 0.1–0.35 (**Table 1**). Comparison of eolian samples with Bermejo fluvial megafan samples yield an inverse trend of south to north increase in R^2 cross-correlation coefficient values, from low R^2 values 0.02–0.04 for southern Medanos Telteca samples to relatively higher R^2 values 0.2 to 0.34 in northern Medanos Grande. However, sample comparison among eolian and Río San Juan fluvial samples only exhibit a slight south to north decrease R^2 values from 0.57 to 0.3 (**Table 1**).

A clear trend appears from the CDF plot, where the eolian samples DZ age distributions uniquely plot between the Río Mendoza, Río San Juan, and Río Bermejo fluvial megafan sediment input samples (**Figure 5A**). Comparing trends among eolian samples reveals a progressive variation from southern Medanos Telteca samples (DMZ01 and DAL01) and northern Medanos Grande (DMDG). Cenozoic to Mesozoic age segments of the eolian CDFs plot between Río San Juan and Río Mendoza for the southern Medanos Telteca samples and the northern Medanos Grande samples plot between Río San Juan and Río Mendoza CDFs (**Figure 5A**). Paleozoic age segments of all the eolian CDFs plot between Río Bermejo and Río Mendoza where southern Medanos Telteca samples are most similar to Río Mendoza and the northern Medanos Grande samples plot closer to Río Bermejo CDF. Precambrian age segments of the southern Medanos Telteca samples are most similar to Río Mendoza and the northern Medanos Grande samples plot closer to Río San Juan CDF (**Figure 5A**). These CDF age distribution trends indicate fluvial inputs are end members in terms of DZ age distributions, which further suggests the eolian deposits contain mixed age distributions from the fluvial sources.

Detrital zircon samples from the Andean foreland transfer zone were compared to each other and to the fluvial megafan composite age distributions using two-dimensional (2D) MDS plot (**Figure 5B**). The misfit from conversion of sample dissimilarity to disparity in Cartesian space via linear transformation gives a good correlation as indicated by a low

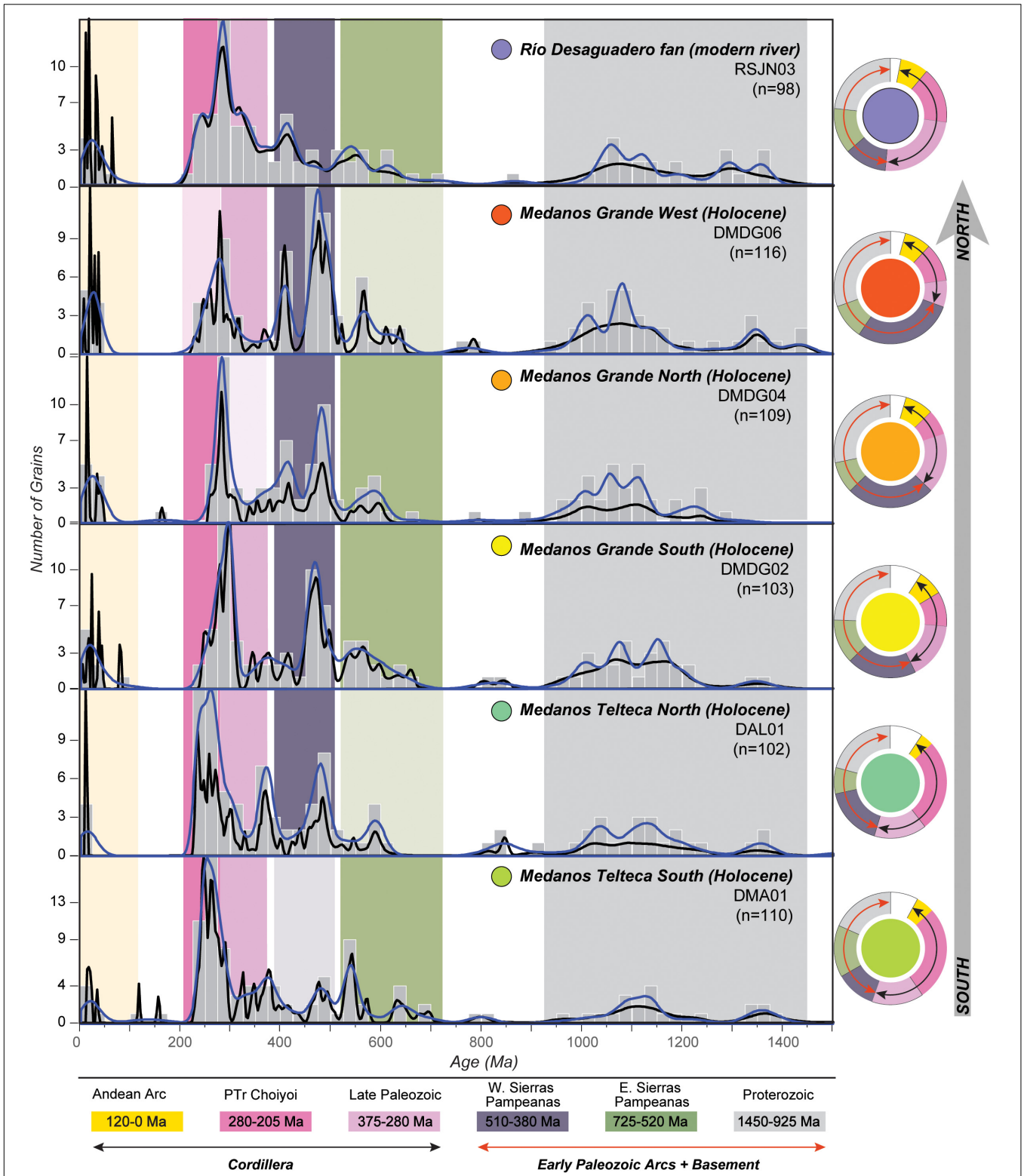

FIGURE 4 | Comparative plot of DZ U-Pb age distributions for Holocene eolian samples and modern river sand, depicted as age histograms (gray rectangles), kernel density estimates (blue line) and relative probability density plots (black line), with emphasis on key age populations (dark color shading) and minor to no age populations (transparent color shading). Donut diagrams represent percent abundance of key age populations in each sample, with Cordillera (black arrows) and Early Paleozoic Arcs and Basement (red arrow) age groups emphasized, and inner colored circle corresponds to sample locations in **Figure 2B**.

TABLE 1 | Inter sample KDE cross correlation R^2 coefficient results.

	Mendoza	San Juan	Bermejo	DMA01	DAL01	RSJN03	DMDG02	DMDG04	DMDG06
Mendoza	1	0.52	0.01	0.71	0.75	0.61	0.35	0.1	0.19
San Juan	0.52	1	0.09	0.54	0.57	0.57	0.5	0.3	0.43
Bermejo	0.01	0.09	1	0.02	0.04	0.02	0.21	0.34	0.34
DMA01	0.71	0.54	0.02	1	0.81	0.57	0.45	0.23	0.35
DAL01	0.75	0.57	0.04	0.81	1	0.64	0.62	0.39	0.5
RSJN03	0.61	0.57	0.02	0.57	0.64	1	0.57	0.38	0.35
DMDG02	0.35	0.5	0.21	0.45	0.62	0.57	1	0.75	0.69
DMDG04	0.1	0.3	0.34	0.23	0.39	0.38	0.75	1	0.77
DMDG06	0.19	0.43	0.34	0.35	0.5	0.35	0.69	0.77	1

Darker red shading indicates greater R^2 value.

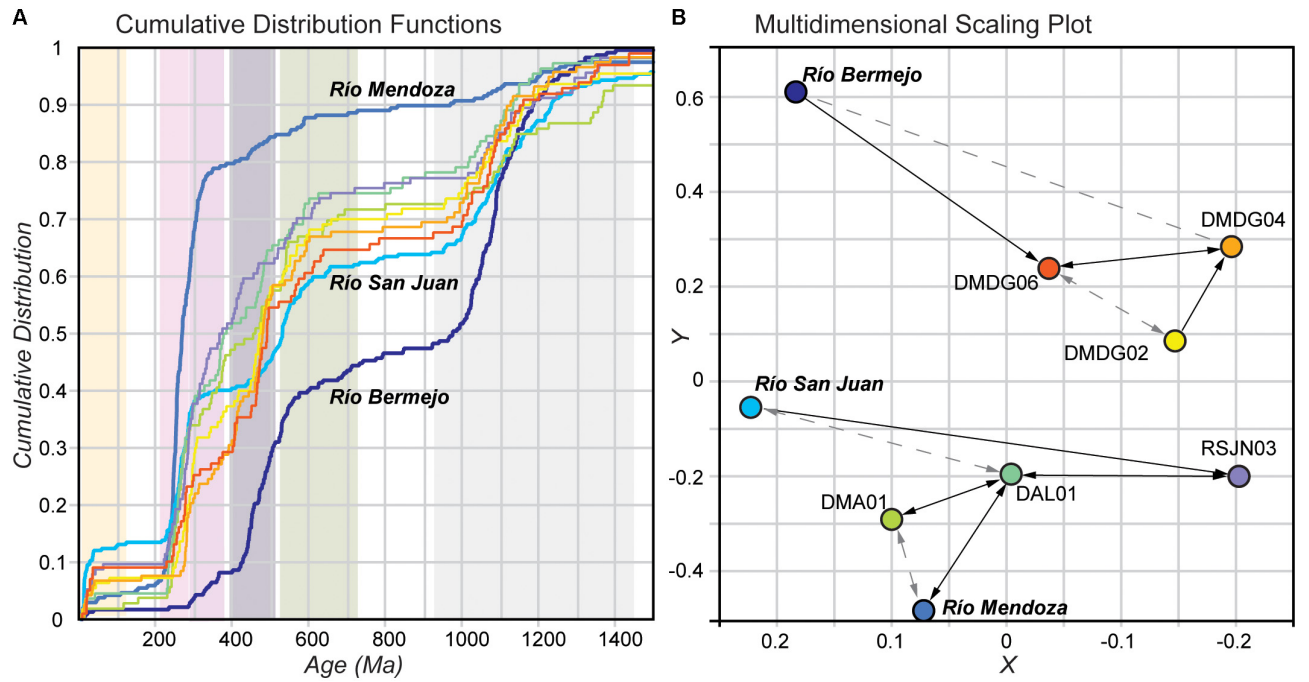

FIGURE 5 | Comparison plots of fluvial sources (blue and labeled) and eolian mixed samples (color coded and labeled). **(A)** Detrital zircon U-Pb age distribution cumulative density functions (CDF), where line color corresponds to colored circles in **B** and sample locations in **Figure 2B**, with emphasis on key age populations (color shading). Notice all samples plot in between fluvial sources Río Mendoza and Río Bermejo in CDF space. **(B)** Two-dimensional multidimensional scaling (MDS) plot of detrital zircon U-Pb age distributions generated for river sources and mixed eolian samples using R2 cross-correlation coefficient on KDEs. Lines represent nearest neighbor (black lines), second nearest neighbor (gray dashed line), and axis are unitless.

stress minimal (0.09). Results show that Medanos Telteca samples are most similar to each other and to Río Mendoza source (**Figure 5B**). Medanos Grande samples DMDG02, DMDG04, and DMDG06 are the most similar to Río Bermejo. The distal foreland fluvial fan sample RSJN03 uniquely plots in MDS space away from Holocene eolian samples, with closet neighbor being upstream composite samples of Río San Juan and closest eolian sample DAL01.

DZ Mixing Model Results

The mixing model results for the Holocene eolian and modern river sand using KDE Cross Correlation R^2 similarity metric show a similar progressive mixing of south to north fluvial sources (**Figure 6** and **Supplementary Table S4**). Modeled age distributions indicate that the southern parent source Río Mendoza decreased from 56 to 14% south to north. In contrast, northern Río Bermejo sediment input is shown to increased northward from 18 to 64%. An apparent outlier to this trend is sample DAL04 that shows a stark decrease in Río San Juan contribution to 4%, relative to nearest eolian samples that show 31% in DMA01 and 30% in DMDG02 Río San Juan contribution. Whereas modeled age distribution for the modern distal foreland sample (RSJN03) shows comparable contribution among Río Mendoza (44%), Río San Juan (31%), Río Bermejo (25%) (**Figure 6**). The CDF based mixing model results (i.e., Kuiper's test V value and K-S test D value) also show similar

trends to that of KDE and PDP based models, with higher Río Mendoza proportion in southern Medanos Grande samples (∼50%), in contrast Río Bermejo signature dominated the northern Medanos Telteca samples (56 to 63%) (**Supplementary Table S4**). However, the Río San Juan component in the CDF based mixing model results are low and invariant, where the Río San Juan component in the Kuiper's test ranges from 2 to 10% and the K-S test ranges from 8 to 13%, compared to the 20–37% range from the KDE based mixing models. Due to the observed CDF based mixing model insensitivity with multimodal Río San Juan source age distribution, the discussion focuses on the KDE Cross-Correlation mixing model results and trends. In summary, the results from each modeling approach indicate a Holocene south-north progressive mixing of fluvial sources, and modern mixed fluvial sample displays more proportional contribution from each fluvial megafan source.

DISCUSSION

Holocene Eolian Sediment Mixing Along Orogen Parallel Paleocurrents

Fluvial point sources at the orogenic front carry primary tectonic signals, reflecting the bedrock material of their respective Andean catchments (**Figure 3**; Capaldi et al., 2017). These fluvial megafans deliver sediment downstream to the Argentina foreland sediment transfer zone that is controlled by fluvial-alluvial and eolian processes during the Holocene. As tectonic signals enter the transfer zone, eolian processes become more dominant and modify the primary fluvial signals, thereby diluting tectonic signals across climate-driven paleoflow directions (**Figure 7**).

Each eolian sample DZ age distribution contains contributions from all fluvial point sources indicating substantial mixing and homogenization by eolian transport and reworking. These results are also supported by the sediment mixing model which suggests that signals from the Río Mendoza, Bermejo, and San Juan are represented in all eolian samples (**Figure 4**). Despite the persistence of similar age modes between eolian samples (e.g., **Figure 5A**), defined spatial and temporal mixing trends persist. Generally, eolian samples taken from the southernmost portion of the dune fields in the Medanos Telteca, proximal to the Río Mendoza, reflect the highest proportions of sediment derived from the Río Mendoza, while samples taken from the northern portions of the Medanos Grande dune field reflect the highest proportions of sediment from the proximal Río Bermejo (**Figure 6**).

Holocene dune crest orientations are useful for understanding the south-north trend in the DZ age distributions. Both the Medanos Telteca and Medanos Grande dune fields display prominent longitudinal (sheif) sand dune morphologies (**Figure 7**). Longitudinal dunes parallel the resultant vector of two paleocurrents that typically have 40° between the two converging vectors (Tsoar, 1983; Bristow et al., 2000). Longitudinal dunes form in wide unimodal or bi-directional wind regimes so the resultant vector transport direction is approximately parallel to the dune trend, and tend to flow parallel with river direction (Liu and Coulthard, 2015). The southern Medanos Telteca longitudinal dunes trend ∼320° in the south-southwestern region and ∼280° in the distal western edge. The northern Medanos Grande longitudinal dunes trend ∼290° in the southern tip and progressively trends to ∼315° in the northwest region and ∼355° in the northern tip (**Figure 7**). From the longitudinal dune trends two paleocurrent directions can be interpreted to involve winds that flowed from the Andes to the east (i.e., Westerlies/Zonda) and winds that flowed along Pampas plain to the north-northwest (i.e., Polar Advection/Pampero; **Figure 2A**). Modern wind data collected show a strong south to southwesterly component with a resultant drift potential of winds capable of transporting sands is due north at 352° (**Figure 7B**; Tripaldi and Forman, 2007).

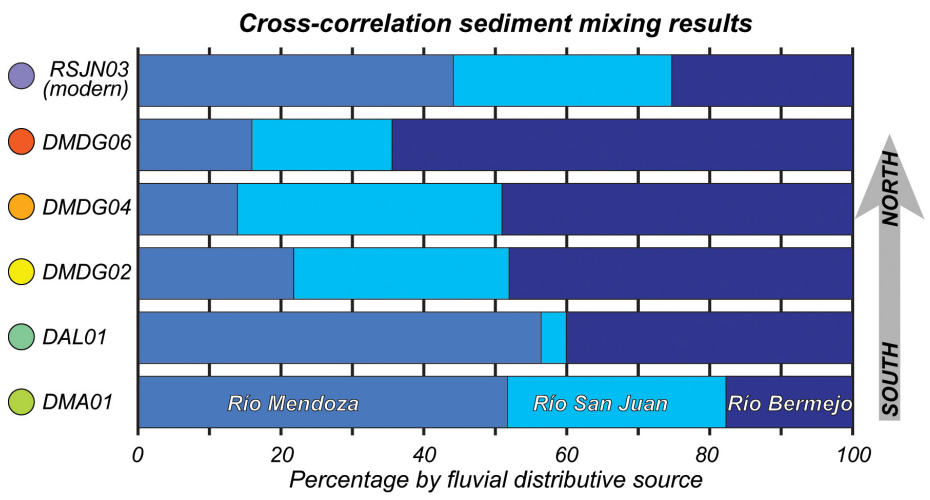

FIGURE 6 | DZ age distribution mixing model results for Holocene eolian and modern distal fluvial samples comparing the relative contribution (in%) from Río Bermejo, Río San Juan, and Río Mendoza age distributions using KDE R^2 cross-correlation coefficient test. Note south to north trend in Holocene eolian samples and equal proportioned modern distal fluvial sample (RSJN03).

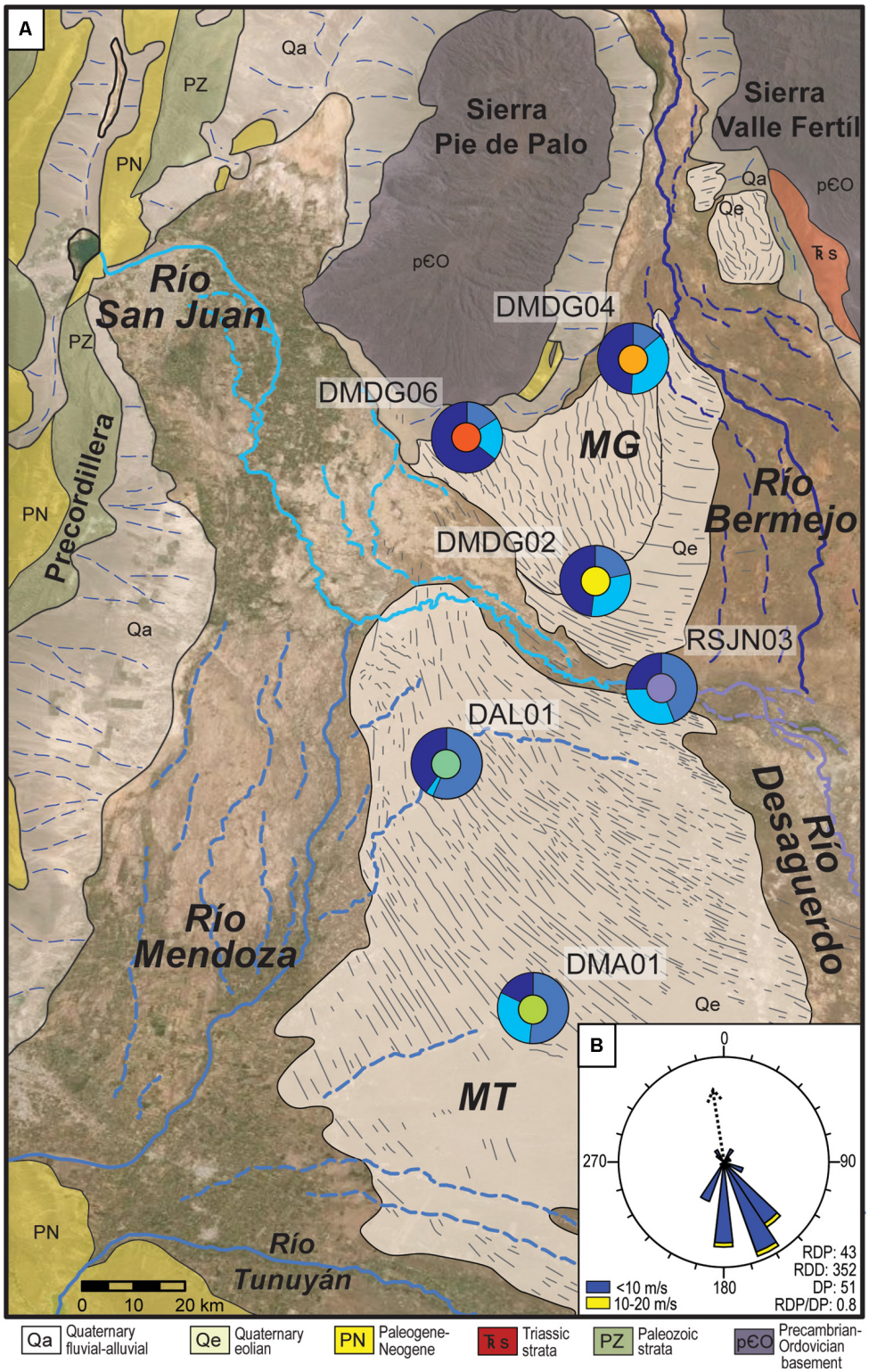

FIGURE 7 | Geomorphic map of eolian and fluvial megafan systems in Andean foreland sediment transfer zone. **(A)** Holocene eolian and modern distal fluvial samples detrital zircon mixing model results are plotted as donut diagrams (see **Figure 6**), where Medanos Telteca (MT) and Medanos Grande (MG) sands have distinct mixed proportions of fluvial megafan sediment inputs. **(B)** Rose diagram of modern wind vectors collected from San Juan that are capable of transporting sand-sized sediments (<10 and 10–20 m/s) (modified from Tripaldi and Forman, 2007).

Integrating Holocene paleocurrent vectors with DZ age distribution mixing models provide a mechanism for the mixing of fluvial megafan signatures observed in the eolian deposits (**Figure 7**). The Andean southerly winds explain the reworking and transport of southern Río Mendoza fluvial megafan deposits northward across the Medanos Telteca and into the northern Medanos Grande. Similarly, the Polar Advection/Pampero southeasterly winds helps account for the presence of Río Bermejo and Río San Juan fluvial age signatures in the southern Medanos Telteca dune field that increase in the northern Medanos Grande dune field. The presence of northern Río Bermejo and northwestern Río San Juan signatures in the southern Medanos Telteca eolian samples is likely from reworked deposits along the axial-fluvial Río Desaguadero eastern floodplain (**Figure 7A**). Overall these results show that sediment fluxes in the Argentine foreland are controlled by a combination of fluvial and eolian processes, whose relative importance can be assessed with DZ U-Pb geochronology. Importantly, eolian transport has the potential to overprint primary tectonic signals, but in this case, leaves a resolvable mixing trend along the Holocene paleo-wind vector.

Aridification Drives Orogen Parallel Eolian Activity

The driver of eolian activity can be linked to Quaternary climate variability and increased aridity in the Andean foreland and Argentine Pampas plain during the Holocene (Iriondo, 1999). Quaternary glacial/interglacial cycles drove regional wind systems to change strength and latitudinal positions, affecting their capacity for erosion and transport of sand and mineral dust from the sources to depositional areas (**Figure 8**; Gili et al., 2017). Eolian deposition spans most of the Holocene to ca. 400 years ago, associated with an inferred mean annual precipitation of 100–450 mm and drier conditions compared to the late 20th century (Tripaldi and Forman, 2016). Holocene eolian events along the Andean foreland are well constrained with OSL geochronology and have occurred over 4.3–4, 2.1, and 0.6–0.4 ka (**Figure 8A**; Tripaldi and Forman, 2007). Eolian activity is synchronous with local Andean glacial advances during 4.3–4.7, 2.5–2.2, and 0.4–0.3 ka intervals (**Figure 8B**; Espizua, 2005; Espizua and Pitte, 2009). The shared temporal histories of both Holocene Andean glaciation and eolian deposition suggest that the Argentina sediment transfer zone is sensitive to changes in regional climate regimes.

Changes to global circulation cells driven by sea surface temperature change is a potential mechanism for the variable wet and arid Quaternary climates recorded by the transfer zone deposits. In the Andean foreland dune fields, winds capable of transporting sand-sized sediments are controlled by the South Atlantic Anticyclone and the low-level meridional Chaco Jet (**Figure 2A**; Forman et al., 2014). Wet conditions in western Argentina are associated with cooler sea surface temperatures in the equatorial South Atlantic Ocean and strengthened South Atlantic Convergent Zone and Chaco Low Level jets, increasing the landward flux of Atlantic-derived moisture (Doyle and Barros, 2002). Dry conditions appear to be associated with higher sea surface temperatures that lead to a weakened South Atlantic Convergent Zone and more zonal transport of moisture by the Chaco Low Level Jet toward southeastern Brazil (Liebmann et al., 2004). Migration of the Chaco jet eastward reduces South American monsoonal moisture entering the Andean Piedmont of Argentina, increasing aridification, and decreasing fluvial transport capacity.

Understanding eolian system processes from historical ($<10^3$ year) to intermediate Pleistocene-Holocene (10^3–10^6) year time periods provides invaluable characterization that can be applied to ancient ($>10^7$ year) systems in the stratigraphic record (Allen, 2008). For example, Miocene aridity (from ca. 6.1 to 5.2 Ma) is recorded by numerous stable isotope proxies from stratigraphic and fossil records (Ruskin and Jordan, 2007; Hynek et al., 2012; Pingel et al., 2016). Miocene aridity is

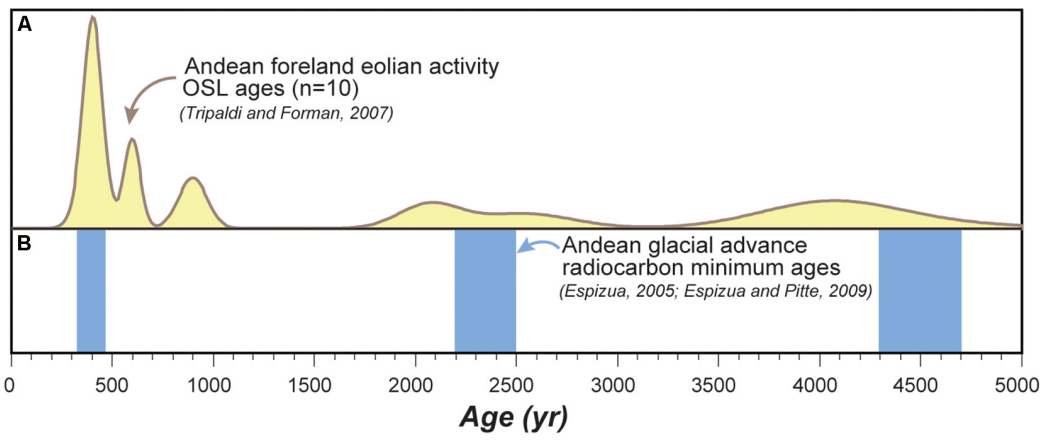

FIGURE 8 | Holocene chronology of eolian and glacial activity in NW Argentina. **(A)** Optically Stimulated luminescence (OSL) ages from Andean Piedmont eolian fields Medanos Grande and Medanos Negros located east of Sierra Valle Fertile (**Figure 7** for location; Tripaldi and Forman, 2007). **(B)** Radiocarbon minimum ages from terminal moraine glacial deposits in the Andes of Mendoza province (Espizua, 2005; Espizua and Pitte, 2009). Note the overlap between glacial advance and subsequent eolian activity.

expressed as a decrease in fluvial sedimentation and erosion rates, without preservation of eolian strata (Amidon et al., 2017; Stevens Goddard and Carrapa, 2018). Preserved Oligocene-Miocene eolian strata along the southern Central Andes (Tripaldi and Limarino, 2005; Levina et al., 2014; Fosdick et al., 2017) suggest a protracted history of fluctuating arid conditions in this region throughout the Cenozoic. Moreover, a thorough understanding of processes operating in eolian systems is important for predicting how these regions will continue to evolve as anthropogenic warming and increased agricultural development continues to shape the Earth's landscape, resource management, and human land use (Munson et al., 2011; Sickmann et al., 2019).

Tectonic and Climate Signal Propagation in Fluvial-Eolian Transfer Zones

The Andean foreland basin and associated fluvial-eolian sediment transfer zone serves as an intermediate terrestrial sink that modulates sedimentary delivery to the Atlantic passive margin. During wet periods with high precipitation rates, the regionally integrated fluvial drainage systems serve as the primary mechanism for transporting sediment through the transfer zone to offshore sinks. Sediment mixing in these fluvial systems generally reflects equal contributions from fluvial point sources flowing southward (**Figure 9A**). During times of high precipitation, fluvial sediment should accurately reflect the bedrock lithologies being eroded, thereby preserving the tectonic signals in the transfer zone fluvial sediments (DeCelles and Hertel, 1989; Capaldi et al., 2017). Climatic shifts toward more arid conditions may activate eolian transport and cause integrated drainages to dry up, leaving only fluvial megafans and ephemeral streams (**Figure 9B**). During intensely arid climatic conditions, eolian transport would be the primary transport mechanism in transfer zones and would mix sediment along prevailing wind vectors, producing a climatic signal in the sedimentary record (**Figure 9B**). Northward orogen-parallel sediment mixing initiated by eolian transport during arid climate periods likely disrupted an otherwise simple pattern of southward fluvial transport within the foreland basin. By inhibiting fluvial sediment transfer downstream to the Río Desaguadero axial system and Río Colorado en route to the Atlantic margin, eolian redistribution and mixing of sediment likely modified the original Andean orogenic signals recognized in rivers of the proximal foreland basin.

Sediment signal propagation depends on the timescales of tectonic and climatic perturbations influencing sediment discharge and the capacity of a system to response to those changes (Romans et al., 2016). Numerical models predict that the erosional dynamics of mountain catchments significantly dampen the transfer of sediment discharge variations driven by high frequency (~105 year) climate oscillations (Armitage et al., 2013). This suggests that sediment routing systems operate over the long term (millions of years) as consistent conveyors of sediment to distal zones of accumulation and are less sensitive climate signals (Castelltort and Van Den Driessche, 2003; Allen, 2008). Others have shown that large low-gradient foreland settings increase sediment signal buffering

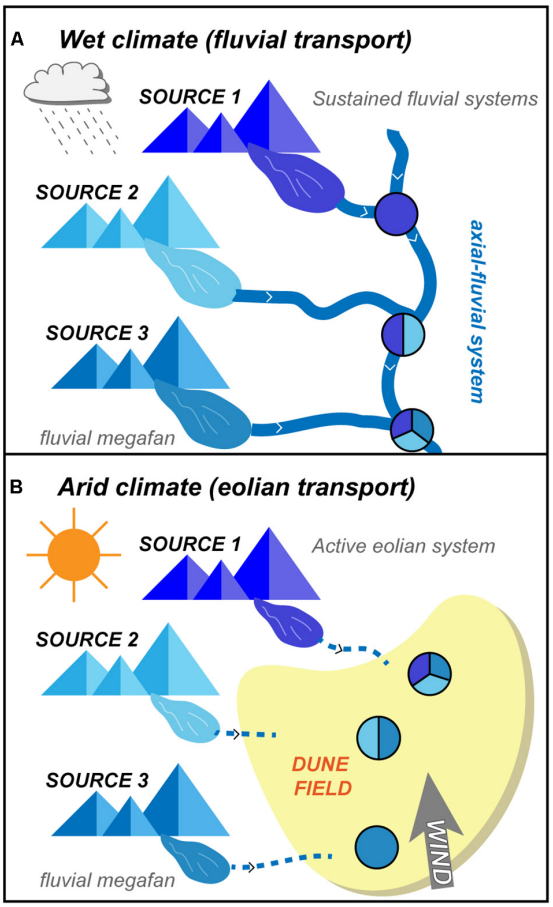

FIGURE 9 | Schematic depiction of three distinct environmental signals propagated from their source regions and transported by fluvial sediment-routing networks to distal eolian systems in an arid foreland basin. Hypothetical fluvial signatures are indicated by pie diagrams according to the respective sample location. **(A)** Fluvial-dominated end-member sediments contain signals dominated by the provenance of the river sources that mix southward along confluences. **(B)** Simplified eolian-dominated end-member where fluvial megafan deposits are reworked northward along orogen parallel wind currents.

(Jerolmack and Paola, 2010) and decrease the potential to transfer a source sediment signal to the ultimate sink (Covault et al., 2013; Nyberg et al., 2018). However, climate shifts may drive significant longer-term changes in transport mechanisms within long-lived continental systems that are sensitive to climate variations on intermediate timescales (<106 year) (Goodbred, 2003; Simpson and Castelltort, 2012). Our results show that climatically modulated eolian activity in the foreland basin prevents a simple downslope propagation of tectonic signals through the Andean transfer zone. Similar findings from other fluvial and eolian transport systems indicate that sediment storage in the eolian system can inhibit or delay environmental signal propagation from the orogenic sources to the ultimate sink (East et al., 2015). Future work collecting provenance and geochronology constraints along downstream Río Desaguadero and Río Colorado fluvial and eolian systems would provide

additional insights into how environmental signatures propagate throughout the Quaternary sediment transfer zone.

Understanding environmental signal propagation through fluvial-eolian sedimentary transfer zones over 10^2 to 10^5 years timescales sheds light on how strengthened wind transport and/or weakening of the hydrological cycle impacted sediment routing and potentially inhibited transmission of unambiguous tectonic signals from source to sink. During drier conditions, the sediment transport direction is reversed and sediment is redistributed northward by orogen-parallel paleowinds, which rework and disrupt the original tectonic signals exiting the erosional domain of the Andean orogen (**Figure 9B**). Importantly, these results suggest that eolian environments generally induce sediment mixing over 10^2 to 10^4 years timescales, and preserve regional, rather than local, records of erosion in adjacent source regions. Wetter interglacial periods display provenance signatures indicative of fluvial transport from southward, preserving Andean tectonic signatures (**Figure 9A**). Our data show promise of recording climatic conditions in foreland settings and provide a basis for understanding how fluvial-eolian transport processes interact and impact signal propagation through a continental-scale drainage network linking a major orogenic belt to a distal passive margin.

CONCLUSION

We investigated a Holocene sediment transfer zone with contrasting fluvial and eolian sediment transport mechanisms to understand how river and wind processes impact the propagation of environmental signals in continental-scale drainage systems. Detrital zircon U-Pb age distributions from Holocene eolian dunes record the progressive sediment mixing of the three fluvial point sources along a norward trend. In contrast, modern river sands show progressive southward (downstream) mixing along a large axial fluvial system. Reversal in sediment transport directions indicates that sediment routing networks in the Andean transfer zone are sensitive to changes in regional climate regimes. South flowing fluvial systems are characteristic of wet inter-glacial periods, whereas northward eolian transport, preserved by dune crest morphology, is prevalent during Holocene glaciation in the central Andes. Sediment mixing induced by eolian transport and reworking of various synorogenic river sediment is likely a critical, climate-modulated process that inhibits downstream transmission of primary Andean tectonic signals to distal zones of accumulation.

DATA AVAILABILITY STATEMENT

All datasets generated for this study are included in the article/**Supplementary Material**.

AUTHOR CONTRIBUTIONS

TC designed the project and carried out the field work. JH, TC, and SG processed the samples, and carried out the analysis and data interpretation. DS facilitated the geochronology analysis. TC, SG, and JH wrote the manuscript. BH and DS provided critical discussions and contributions to the manuscript.

FUNDING

This research was funded by the Geological Society of America, American Association of Petroleum Geologists, Society for Sedimentary Geology, and Jackson School of Geosciences at The University of Texas at Austin (Grants awarded to TC).

ACKNOWLEDGMENTS

We thank Margo Odlum, Mark Helper, Sharon Mosher, Patricia Alvarado, and Gustavo Ortiz for discussions and logistical assistance in Argentina. This manuscript benefited from discussions with Brian Romans, Edgardo Latrubesse, David Mohrig, Ryan Anderson, and Lisa Stockli. We are grateful for the constructive reviews and comments from reviewers PV and KS, and the editor JF, which improved the manuscript.

SUPPLEMENTARY MATERIAL

The Supplementary Material for this article can be found online at: https://www.frontiersin.org/articles/10.3389/feart.2019.00298/full#supplementary-material

TABLE S1 | Detrital zircon U-Pb results.

TABLE S2 | Percentage age group.

TABLE S3 | Statistical coefficient results.

TABLE S4 | Mixing model results.

REFERENCES

Allen, P. A. (2008). Time scales of tectonic landscapes and their sediment routing systems. *Geol. Soc. Lon. Spe. Publ.* 296, 7–28. doi: 10.1144/sp296.2

Al-Masrahy, M. A., and Mountney, N. P. (2015). A classification scheme for fluvial–aeolian system interaction in desert-margin settings. *Aeolian Res.* 17, 67–88. doi: 10.1016/j.aeolia.2015.01.010

Amidon, W. H., Burbank, D. W., and Gehrels, G. E. (2005). U-Pb zircon ages as a sediment mixing tracer in the Nepal Himalaya. *Earth Planet. Sci. Lett.* 235, 244–260. doi: 10.1016/j.epsl.2005.03.019

Amidon, W. H., Fisher, G. B., Burbank, D. W., Ciccioli, P. L., Alonso, R. N., Gorin, A. L., et al. (2017). Mio-pliocene aridity in the south-central Andes associated with Southern Hemisphere cold periods. *Proc. Natl. Acad. Sci. U.S.A.* 114, 6474–6479. doi: 10.1073/pnas.1700327114

Armitage, J. J., Jones, T. D., Duller, R. A., Whittaker, A. C., and Allen, P. A. (2013). Temporal buffering of climate-driven sediment flux cycles by transient catchment response. *Earth Planet. Sci. Lett.* 369, 200–210. doi: 10.1016/j.epsl.2013.03.020

Bahlburg, H., Vervoort, J. D., Du Frane, S. A., Bock, B., Augustsson, C., and Reimann, C. (2009). Timing of crust formation and recycling in accretionary

orogens: insights learned from the western margin of South America. *Earth Sci. Rev.* 97, 215–241. doi: 10.1016/j.earscirev.2009.10.006

Belnap, J., Munson, S. M., and Field, J. P. (2011). Aeolian and fluvial processes in dryland regions: the need for integrated studies. *Ecoydrology* 4, 615–622. doi: 10.1002/eco.258

Blum, M., and Pecha, M. (2014). Mid-cretaceous to paleocene North American drainage reorganization from detrital zircons. *Geology* 42, 607–610. doi: 10.1130/g35513.1

Blum, M., Rogers, K., Gleason, J., Najman, Y., Cruz, J., and Fox, L. (2018). Allogenic and autogenic signals in the stratigraphic record of the deep-sea bengal fan. *Sci. Rep.* 8:7973. doi: 10.1038/s41598-018-25819-5

Bristow, C. S., Bailey, S. D., and Lancaster, N. (2000). The sedimentary structure of linear sand dunes. *Nature* 406, 56–59. doi: 10.1038/35017536

Bullard, J. E., and McTainsh, G. H. (2003). Aeolian-fluvial interactions in dryland environments: examples, concepts and Australia case study. *Progress Phys. Geogr.* 27, 471–501. doi: 10.1191/0309133303pp386ra

Capaldi, T. N., Horton, B. K., McKenzie, N. R., Stockli, D. F., and Odlum, M. L. (2017). Sediment provenance in contractional orogens: the detrital zircon record from modern rivers in the Andean fold-thrust belt and foreland basin of western Argentina. *Earth Planet. Sci. Lett.* 479, 83–97. doi: 10.1016/j.epsl.2017.09.001

Castelltort, S., and Van Den Driessche, J. (2003). How plausible are high-frequency sediment supply-driven cycles in the stratigraphic record? *Sediment. Geol.* 157, 3–13. doi: 10.1016/s0037-0738(03)00066-6

Clift, P. D., Hodges, K. V., Heslop, D., Hannigan, R., Van Long, H., and Calves, G. (2008). Correlation of Himalayan exhumation rates and Asian monsoon intensity. *Nat. Geosci.* 1, 875–880. doi: 10.1038/ngeo351

Compagnucci, R. H., Agosta, E. A., and Vargas, W. M. (2002). Climatic change and quasi-oscillations in central-west Argentina summer precipitation: main features and coherent behaviour with southern African region. *Clim. Dyn.* 18, 421–435. doi: 10.1007/s003820100183

Covault, J. A., Craddock, W. H., Romans, B. W., Fildani, A., and Gosai, M. (2013). Spatial and temporal variations in landscape evolution: historic and longer-term sediment flux through global catchments. *J. Geol.* 121, 35–56. doi: 10.1086/668680

Cristallini, E. O., and Ramos, V. A. (2000). Thick-skinned and thin-skinned thrusting in the La Ramada fold and thrust belt: crustal evolution of the High Andes of San Juan, Argentina (32°SL). *Tectonophysics* 317, 205–235. doi: 10.1016/s0040-1951(99)00276-0

Dahlquist, J. A., Pankhurst, R. J., Gaschnig, R. M., Rapela, C. W., Casquet, C., Alasino, P. H., et al. (2013). Hf and Nd isotopes in Early Ordovician to Early Carboniferous granites as monitors of crustal growth in the proto-Andean margin of Gondwana. *Gondwana Res.* 23, 1617–1630. doi: 10.1016/j.gr.2012.08.013

Damanti, J. F. (1993). Geomorphic and structural controls on facies patterns and sediment composition in a modern foreland basin. *Spec. Publ. Int. Ass. Sediment.* 17, 221–233.

DeCelles, P. G., and Hertel, F. (1989). Petrology of fluvial sands from the Amazonian foreland basin. Peru and Bolivia. *GSA Bull.* 101, 1552–1562. doi: 10.1130/0016-7606(1989)101<1552:pofsft>2.3.co;2

del Rey, A., Deckart, K., Arriagada, C., and Martínez, F. (2016). Resolving the paradigm of the late Paleozoic–Triassic Chilean magmatism: isotopic approach. *Gondwana Res.* 37, 172–181. doi: 10.1016/j.gr.2016.06.008

Dickinson, W. R., and Gehrels, G. E. (2008). Sediment delivery to the Cordilleran foreland basin: insights from U-Pb ages of detrital zircons in upper jurassic and cretaceous strata of the Colorado Plateau. *Am. J. Sci.* 308, 1041–1082.

Doyle, M. E., and Barros, V. R. (2002). Midsummer low-level circulation and precipitation in subtropical South America and related sea surface temperature anomalies in the South Atlantic. *J. Clim.* 15, 3394–3410. doi: 10.1175/1520-0442(2002)015<3394:MLLCAP>2.0.CO;2

East, A. E., Clift, P. D., Carter, A., Alizai, A., and VanLaningham, S. (2015). Fluvial-eolian interactions in sediment routing and sedimentary signal buffering: an example from the Indus basin and Thar desert. *J. Sediment. Res.* 85, 715–728. doi: 10.2110/jsr.2015.42

Espizua, L. E. (2005). Holocene glacier chronology of valenzuela valley, Mendoza Andes, Argentina. *Holocene* 15, 1079–1085. doi: 10.1191/0959683605hl866rr

Espizua, L. E., and Pitte, P. (2009). The little ice age glacier advance in the central Andes (35°S), Argentina. *Palaeogeogr. Palaeoclimatol. Palaeoecol.* 281, 345–350. doi: 10.1016/j.palaeo.2008.10.032

Fildani, A., Hessler, A. M., Mason, C. C., McKay, M. P., and Stockli, D. F. (2018). Late pleistocene glacial transitions in North America altered major river drainages, as revealed by deep-sea sediment. *Sci. Rep.* 8:13839. doi: 10.1038/s41598-018-32268-7

Fildani, A., McKay, M. P., Stockli, D., Clark, J., Dykstra, M. L., Stockli, L., et al. (2016). The ancestral mississippi drainage archived in the late wisconsin mississippi deep-sea fan. *Geology* 44, 479–482. doi: 10.1130/g37657.1

Forman, S. L., Tripaldi, A., and Ciccioli, P. L. (2014). Eolian sand sheet deposition in the San Luis paleodune field, western Argentina as an indicator of a semi-arid environment through the Holocene. *Palaeogeogr. Palaeoclimatol. Palaeoecol.* 411, 122–135. doi: 10.1016/j.palaeo.2014.05.038

Fosdick, J. C., Carrapa, B., and Ortíz, G. (2015). Faulting and erosion in the Argentine Precordillera during changes in subduction regime: reconciling bedrock cooling and detrital records. *Earth Planet. Sci. Lett.* 431, 73–83. doi: 10.1016/j.epsl.2015.09.041

Fosdick, J. C., Reat, E. J., Carrapa, B., Ortiz, G., and Alvarado, P. M. (2017). Retroarc basin reorganization and aridification during Paleogene uplift of the southern central Andes. *Tectonics* 36, 493–514. doi: 10.1002/2016TC004400

Garzanti, E., Resentini, A., Andò, S., Vezzoli, G., Pererira, A., and Vermeesch, P. (2015). Physical controls on sand composition and relative durability of detrital minerals during ultra-long distance littoral and aeolian transport (Namibia and southern Angola). *Sedimentology* 62, 971–996. doi: 10.1111/sed.12169

Garzanti, E., Vermeesch, P., Al-Ramadan, K. A., AndÒ, S., Limonta, M., Rittner, M., et al. (2017). Tracing transcontinental sand transport: from Anatolia–zagros To the Rub'Al Khali Sand Sea. *J. Sediment. Res.* 87, 1196–1213. doi: 10.2110/jsr.2017.65

George, S. W., Horton, B. K., Jackson, L. J., Moreno, F., Carlotto, V., and Garzione, C. N. (2019). "Sediment provenance variations during contrasting mesozoic-early cenozoic tectonic regimes of the northern Peruvian Andes and Santiago-Marañón foreland basin," in *Andean Tectonics*, eds B. K. Horton, and A. Folguera, (Cambridge, MA: Elsevier), 269–296. doi: 10.1016/b978-0-12-816009-1.00012-5

Gili, S., Gaiero, D. M., Goldstein, S. L., Chemale, F. Jr., Jweda, J., Kaplan, M. R., et al. (2017). Glacial/interglacial changes of Southern Hemisphere wind circulation from the geochemistry of South American dust. *Earth Planet. Sci. Lett.* 469, 98–109. doi: 10.1016/j.epsl.2017.04.007

Goodbred, S. L. Jr. (2003). Response of the ganges dispersal system to climate change: a source-to-sink view since the last interstade. *Sediment. Geol.* 162, 83–104. doi: 10.1016/s0037-0738(03)00217-3

Heredia, N., Rodriguez-Fernandez, L. R., Gallastegui, G., Busquets, P., and Colombo, F. (2002). Geological setting of the argentine frontal cordillera in the flat-slab segment (30°00'–31°30'S latitude. *J. South Am. Earth Sci.* 15, 79–99. doi: 10.1016/s0895-9811(02)00007-x

Horton, B. K. (2018). Sedimentary record of Andean mountain building. *Earth Sci. Rev.* 178, 279–309. doi: 10.1016/j.earscirev.2017.11.025

Horton, B. K., Anderson, V. J., Caballero, V., Saylor, J. E., Parra, M., and Mora, A. (2015). Application of detrital zircon U-Pb geochronology to surface and subsurface correlations of provenance, paleodrainage, and tectonics of the middle magdalena valley Basin of Colombia. *Geosphere* 11, 1790–1811. doi: 10.1130/ges01251.1

Horton, B. K., Fuentes, F., Boll, A., Starck, D., Ramirez, S. G., and Stockli, D. F. (2016). Andean stratigraphic record of the transition from backarc extension to orogenic shortening: a case study from the northern Neuquén Basin, Argentina. *J. South Am. Earth Sci.* 71, 17–40. doi: 10.1016/j.jsames.2016.06.003

Hynek, S. A., Passey, B. H., Prado, J. L., Brown, F. H., Cerling, T. E., and Quade, J. (2012). Small mammal carbon isotope ecology across the Miocene–Pliocene boundary, northwestern Argentina. *Earth Planet. Sci. Lett.* 321, 177–188. doi: 10.1016/j.epsl.2011.12.038

Ingersoll, R. V., Kretchmer, A. G., and Valles, P. K. (1993). The effect of sampling scale on actualistic sandstone petrofacies. *Sedimentology* 40, 937–953. doi: 10.1111/j.1365-3091.1993.tb01370.x

Iriondo, M. (1990). The map of the South American plains. Its present state. *Quat. South Am. Anct. Pen* 6, 297–306.

Iriondo, M. (1999). Climatic changes in the South American plains: records of a continent-scale oscillation. *Quat. Int.* 57, 93–112. doi: 10.1016/s1040-6182(98)00053-6

Jackson, L. J., Horton, B. K., and Vallejo, C. (2019). Detrital zircon U-Pb geochronology of modern Andean rivers in Ecuador: fingerprinting tectonic provinces and assessing downstream propagation of provenance signals. *Geosphere* 15. doi: 10.1130/GES02126.1

Jackson, S. E., Pearson, N. J., Griffin, W. L., and Belousova, E. A. (2004). The application of laser ablation-inductively coupled plasma-mass spectrometry to in situ U-Pb zircon geochronology. *Chem. Geol.* 211, 47–69. doi: 10.1016/j.chemgeo.2004.06.017

Jerolmack, D. J., and Paola, C. (2010). Shredding of environmental signals by sediment transport. *Geophys. Res. Lett.* 37, 1–5.

Johnsson, M. J., Stallard, R. F., and Lundberg, N. (1991). Controls on the composition of fluvial sands from a tropical weathering environment: sands of the Orinoco river drainage basin, Venezuela and Colombia. *GSA Bull.* 103, 1622–1647. doi: 10.1130/0016-7606(1991)103<1622:cotcof>2.3.co;2

Johnsson, M. J., Stallard, R. F., and Meade, R. H. (1988). First-cycle quartz arenites in the Orinoco River basin. Venezuela and Colombia. *J. Geol.* 96, 263–277. doi: 10.1086/629219

Jones, R. E., Kirstein, L. A., Kasemann, S. A., Dhuime, B., Elliott, T., Litvak, V. D., et al. (2015). Geodynamic controls on the contamination of Cenozoic arc magmas in the southern Central Andes: insights from the O and Hf isotopic composition of zircon. *Geochim. Cosmoch. Acta* 164, 386–402. doi: 10.1016/j.gca.2015.05.007

Jordan, T. E., Schlunegger, F., and Cardozo, N. (2001). Unsteady and spatially variable evolution of the Neogene Andean Bermejo foreland basin. Argentina. *J. South Am. Earth Sci.* 14, 775–798. doi: 10.1016/s0895-9811(01)00072-4

Kay, S. M., and Mpodozis, C. (2002). Magmatism as a probe to the Neogene shallowing of the Nazca plate beneath the modern Chilean flat-slab. *J. South Am. Earth Sci.* 15, 39–57. doi: 10.1016/s0895-9811(02)00005-6

Kocurek, G., and Ewing, R. C. (2012). "Source-to-sink: an earth/mars comparison of boundary conditions for eolian dune systems," in *Sedimentary Geology of Mars*, eds J. P. Grotzinger, and R. E. Milliken, (Tulsa, OK: Society for Sedimentary Geology), 151–168. doi: 10.2110/pec.12.102.0151

Kocurek, G. A., and Lancaster, N. (1999). Aeolian system sediment state: theory and mojave desert dune field example. *Sedimentology* 46, 505–515. doi: 10.1046/j.1365-3091.1999.00227.x

Lancaster, N., Kocurek, G., Singhvi, A., Pandey, V., Deynoux, M., Ghienne, J. F., et al. (2002). Late pleistocene and holocene dune activity and wind regimes in the western Sahara Desert of Mauritania. *Geology* 30, 991–994.

Latrubesse, E. M., and Ramonell, C. G. (2010). Landforms and chronology in the Pampean Sand Sea, Argentina. *Int. Sediment. Congress* 18:529.

Latrubesse, E. M., Stevaux, J. C., Cremon, E. H., May, J. H., Tatumi, S. H., Hurtado, M. A., et al. (2012). Late quaternary megafans, fans and fluvio-aeolian interactions in the Bolivian Chaco, Tropical South America. *Palaeogeogr. Palaeoclimatol., Palaeoecol.* 356, 75–88. doi: 10.1016/j.palaeo.2012.04.003

Lawton, T. F. (2019). "Transient influences upon late Paleozoic sediment provenance and dispersal in Laurentian Pangea," in *GSA Annual Meeting in Phoenix*, (Arizona).

Lawton, T. F., and Buck, B. J. (2006). Implications of diapir-derived detritus and gypsic paleosols in lower triassic strata near the castle valley salt wall. Paradox Basin, Utah. *Geology* 34, 885–888.

Lawton, T. F., Buller, C. D., and Parr, T. R. (2015). Provenance of a permian erg on the western margin of Pangea: depositional system of the Kungurian (late Leonardian) castle valley and white rim sandstones and subjacent cutler group, paradox basin, Utah, USA. *Geosphere* 11, 1475–1506. doi: 10.1130/ges01174.1

Levina, M., Horton, B. K., Fuentes, F., and Stockli, D. F. (2014). Cenozoic sedimentation and exhumation of the foreland basin system preserved in the Percordillera thrust belt (31-32°S), south central Andes, Argentina. *Tectonics* 33, 1659–1680. doi: 10.1002/2013TC003424

Liebmann, B., Vera, C. S., Carvalho, L. M. V., Camilloni, I. A., Hoerling, M. P., Allured, D., et al. (2004). An observed trend in central South American precipitation. *J. Clim.* 17, 4357–4367. doi: 10.1175/3205.1

Liu, B., and Coulthard, T. J. (2015). Mapping the interactions between rivers and sand dunes: implications for fluvial and aeolian geomorphology. *Geomorphology* 231, 246–257. doi: 10.1016/j.geomorph.2014.12.011

Mackaman-Lofland, C., Horton, B. K., Fuentes, F., Constenius, K. N., and Stockli, D. F. (2019). Mesozoic to cenozoic retroarc basin evolution during changes in tectonic regime, southern Central Andes (31–33°S): Insights from zircon U-Pb geochronology. *J. South Am. Earth Sci.* 89, 299–318. doi: 10.1016/j.jsames.2018.10.004

Mackey, G. N., Horton, B. K., and Milliken, K. L. (2012). Provenance of the paleocene-eocene wilcox group, western gulf of mexico basin: evidence for integrated drainage of the southern laramide rocky mountains and cordilleran arc. *GSA Bull.* 124, 1007–1024. doi: 10.1130/b30458.1

Maroulis, J. C., Nanson, G. C., Price, D. M., and Pietsch, T. (2007). Aeolian-fluvial interaction and climate change: source-bordering dune development over the past 100 ka on cooper creek, central Australia. *Quat. Sci. Rev.* 26, 386–404. doi: 10.1016/j.quascirev.2006.08.010

Mason, C. C., Fildani, A., Gerber, T., Blum, M. D., Clark, J. D., and Dykstra, M. (2017). Climatic and anthropogenic influences on sediment mixing in the Mississippi source-to-sink system using detrital zircons: late Pleistocene to recent. *Earth Planet. Scie. Lett.* 466, 70–79. doi: 10.1016/j.epsl.2017.03.001

Mason, C. C., Romans, B. W., Stockli, D. F., Mapes, R., and Fildani, A. (2019). Detrital zircons reveal sea-level and hydroclimate controls on Amazon River to deep-sea fan sediment transfer. *Geology* 47, 563–567. doi: 10.1130/g45852.1

Mehl, A., Tripaldi, A., and Zárate, M. (2018). Late quaternary aeolian and fluvial-aeolian deposits from southwestern Pampas of Argentina, southern South America. *Palaeogeogr. Palaeoclimatol. Palaeoecol.* 511, 280–297. doi: 10.1016/j.palaeo.2018.08.014

Mpodozis, C., and Kay, S. M. (1992). Late paleozoic to triassic evolution of the gondwana margin: evidence from chilean frontal cordilleran batholiths (28 S to 31 S). *Geol. Soc. Am. Bull.* 104, 999–1014. doi: 10.1130/0016-7606(1992)104<0999:lptteo>2.3.co;2

Muhs, D. R., and Zárate, M. (2001). "Late quaternary eolian records of the Americas and their paleoclimatic significance," in *Interhemispheric Climate Linkages*, ed. V. Markgraf, (Amsterdam: Elsevier), 183–216. doi: 10.1016/b978-012472670-3/50015-x

Mulcahy, S. R., Roeske, S. M., McClelland, W. C., Ellis, J. R., Jourdan, F., Renne, P. R., et al. (2014). Multiple migmatite events and cooling from granulite facies metamorphism within the Famatina arc margin of northwest Argentina. *Tectonics* 33, 1–25. doi: 10.1002/2013tc003398

Munson, S. M., Belnap, J., Okin, G. S., and Schlesinger, W. H. (2011). Responses of wind erosion to climate-induced vegetation changes on the Colorado Plateau. *Proc. Natl. Acad. Sci. U.S.A.* 108, 3854–3859. doi: 10.1073/pnas.1014947108

Nyberg, B., Gawthorpe, R. L., and Helland-Hansen, W. (2018). The distribution of rivers to terrestrial sinks: implications for sediment routing systems. *Geomorphology* 316, 1–23. doi: 10.1016/j.geomorph.2018.05.007

Odlum, M. L., Stockli, D. F., Capaldi, T. N., Thomson, K. D., Clark, J., Puigdefàbregas, C., et al. (2019). Tectonic and sediment provenance evolution of the South Eastern Pyrenean foreland basins during rift margin inversion and orogenic uplift. *Tectonophysics* 765, 226–248. doi: 10.1016/j.tecto.2019.05.008

Otamendi, J. E., Ducea, M. N., Cristofolini, E. A., Tibaldi, A. M., Camilletti, G. C., and Bergantz, G. W. (2017). U-Pb ages and Hf isotope compositions of zircons in plutonic rocks from the central Famatinian arc. Argentina. *J. South Am. Earth Sci.* 76, 412–426. doi: 10.1016/j.jsames.2017.04.005

Pell, S. D., Williams, I. S., and Chivas, A. R. (1997). The use of protolith zircon-age fingerprints in determining the protosource areas for some Australian dune sands. *Sediment. Geol.* 109, 233–260. doi: 10.1016/s0037-0738(96)00061-9

Peri, V. G., Naipauer, M., Pimentel, M., and Barcelona, H. (2016). Eolian deposits of the southwestern margin of the Botucatú paleoerg: reconstruction of the gondwana landscape in central northern Argentina. *Sediment. Geol.* 339, 234–257. doi: 10.1016/j.sedgeo.2016.03.019

Pingel, H., Mulch, A., Alonso, R. N., Cottle, J., Hynek, S. A., Poletti, J., et al. (2016). Surface uplift and convective rainfall along the southern Central Andes (Angastaco Basin, NW Argentina). *Earth Planet. Sci. Lett.* 440, 33–42. doi: 10.1016/j.epsl.2016.02.009

Ramos, V. A. (1988). Tectonics of the Late Proterozoic—Early Paleozoic: a collisional history of southern South America. *Episodes* 11, 168–174. doi: 10.18814/epiiugs/1988/v11i3/003

Ramos, V. A. (2004). Cuyania, an exotic block to Gondwana: review of a historical success and the present problems. *Gondwana Res.* 7, 1009–1026. doi: 10.1016/s1342-937x(05)71081-9

Ramos, V. A. (2009). "Anatomy and global context of the Andes: main geologic features and the Andean orogenic cycle," in *Backbone of the Americas: Shallow Subduction, Plateau Uplift, and Ridge and Terrane Collision*, eds S. M. Kay, V. A. Ramos, and W. R. Dickinson, (Boulder, CO: GSA Memoir), 31–65.

Rapela, C. W., Pankhurst, R. J., Casquet, C., Fanning, C. M., Baldo, E. G., González-Casado, J. M., et al. (2007). The Río de la Plata craton and the assembly of SW Gondwana. *Earth Sci. Rev.* 83, 49–82. doi: 10.1016/j.earscirev.2007.03.004

Rapela, C. W., Verdecchia, S. O., Casquet, C., Pankhurst, R. J., Baldo, E. G., Galindo, C., et al. (2016). Identifying laurentian and SW gondwana sources in the Neoproterozoic to early paleozoic metasedimentary rocks of the sierras pampeanas: paleogeographic and tectonic implications. *Gondwana Res.* 32, 193–201.

Rittner, M., Vermeesch, P., Carter, A., Bird, A., Stevens, T., Garzanti, E., et al. (2016). The provenance of Taklamakan desert sand. *Earth Planet. Sci. Lett.* 437, 127–137. doi: 10.1016/j.epsl.2015.12.036

Rodríguez-López, J. P., Clemmensen, L. B., Lancaster, N., Mountney, N. P., and Veiga, G. D. (2014). Archean to recent aeolian sand systems and their sedimentary record: current understanding and future prospects. *Sedimentology* 61, 1487–1534. doi: 10.1111/sed.12123

Romans, B. W., Castelltort, S., Covault, J. A., Fildani, A., and Walsh, J. P. (2016). Environmental signal propagation in sedimentary systems across timescales. *Earth Sci. Rev.* 153, 7–29. doi: 10.1016/j.earscirev.2015.07.012

Ruskin, B. G., and Jordan, T. E. (2007). Climate change across continental sequence boundaries: paleopedology and lithofacies of iglesia basin, Northwestern Argentina. *J. Sediment. Res.* 77, 661–679. doi: 10.2110/jsr.2007.069

Saylor, J. E., Jordan, J. C., Sundell, K. E., Wang, X., Wang, S., and Deng, T. (2018). Topographic growth of the Jishi Shan and its impact on basin and hydrology evolution, NE Tibetan Plateau. *Basin Res.* 30, 544–563. doi: 10.1111/bre.12264

Saylor, J. E., Knowles, J. N., Horton, B. K., Nie, J., and Mora, A. (2013). Mixing of source populations recorded in detrital zircon U-Pb age spectra of modern river sands. *J. Geol.* 121, 17–33. doi: 10.1086/668683

Saylor, J. E., and Sundell, K. E. (2016). Quantifying comparison of large detrital geochronology data sets. *Geosphere* 12, 203–220. doi: 10.1130/ges01237.1

Schwartz, J. J., Gromet, L. P., and Miro, R. (2008). Timing and duration of the calc-alkaline arc of the pampean orogeny: implications for the late neoproterozoic to Cambrian evolution of Western Gondwana. *J. Geol.* 116, 39–61. doi: 10.1086/524122

Sharman, G. R., Covault, J. A., Stockli, D. F., Wroblewski, A. F. J., and Bush, M. A. (2017). Early Cenozoic drainage reorganization of the United States Western Interior–Gulf of Mexico sediment routing system. *Geology* 45, 187–190. doi: 10.1130/g38765.1

Sharman, G. R., Sylvester, Z., and Covault, J. A. (2019). Conversion of tectonic and climatic forcings into records of sediment supply and provenance. *Sci. Rep.* 9, 1–7. doi: 10.1038/s41598-019-39754-6

Sickmann, Z. T., Chheda, T. D., Capaldi, T. N., Thomson, K. D., Paull, C. K., and Graham, S. A. (2019). Using provenance analysis in an Anthropocene natural laboratory. *Quat. Sci. Rev.* 221:105890. doi: 10.1016/j.quascirev.2019.105890

Sickmann, Z. T., Paul, C. K., and Graham, S. A. (2016). Detrital-zircon mixing and partitioning in fluvial to deep marine systems, central California, USA. *J. Sediment. Res.* 86, 1298–1307. doi: 10.2110/jsr.2016.78

Simpson, G., and Castelltort, S. (2012). Model shows that rivers transmit high-frequency climate cycles to the sedimentary record. *Geology* 40, 1131–1134. doi: 10.1130/g33451.1

Sláma, J., Košler, J., Condon, D. J., Crowley, J. L., Gerdes, A., Hanchar, J. M., et al. (2008). Plešovice zircon—a new natural reference material for U–Pb and Hf isotopic microanalysis. *Chem. Geol.* 249, 1–35. doi: 10.1016/j.chemgeo.2007.11.005

Soreghan, M. J., Soreghan, G. S., and Hamilton, M. A. (2008). Glacial-interglacial shifts in atmospheric circulation of western tropical Pangaea. *Palaeogeogr. Palaeoclimatol. Palaeoecol.* 268, 260–272. doi: 10.1016/j.palaeo.2008.03.051

Stevens Goddard, A., and Carrapa, B. (2018). Effects of miocene–pliocene global climate changes on continental sedimentation: a case study from the southern Central Andes. *Geology* 46, 647–650. doi: 10.1130/g40280.1

Sundell, K. E., and Saylor, J. E. (2017). Unmixing detrital geochronology age distributions. *Geochem., Geophys., Geosyst.* 18, 2872–2886. doi: 10.1002/2016GC006774

Tripaldi, A., Ciccioli, P. L., Alonso, M. S., and Forman, S. L. (2010). Petrography and geochemistry of late quaternary dune fields of western Argentina: provenance of aeolian materials in southern South America. *Aeol. Res* 2, 33–48. doi: 10.1016/j.aeolia.2010.01.001

Tripaldi, A., and Forman, S. L. (2007). Geomorphology and chronology of Late Quaternary dune fields of western Argentina. Palaeogeography, Palaeoclimatology. *Palaeoecology* 251, 300–320. doi: 10.1016/j.palaeo.2007.04.007

Tripaldi, A., and Forman, S. L. (2016). Eolian depositional phases during the past 50 ka and inferred climate variability for the Pampean Sand Sea, western Pampas. Argentina. *Quat. Sci. Rev.* 139, 77–93. doi: 10.1016/j.quascirev.2016.03.007

Tripaldi, A., and Limarino, C. O. (2005). Vallecito Formation (Miocene): the evolution of an eolian system in an Andean foreland basin (northwestern Argentina). *J. South Am. Earth Sci.* 19, 343–357. doi: 10.1016/j.quascirev.2016.03.007

Tripaldi, A., and Zárate, M. A. (2016). A review of late quaternary inland dune systems of South America east of the Andes. *Quat. Int.* 410, 96–110.

Tripaldi, A., Zárate, M. A., Forman, S. L., Badger, T., Doyle, M. E., and Ciccioli, P. (2013). Geologic evidence for a drought episode in the western Pampas (Argentina, South America) during the early-mid 20th century. *Holocene* 23, 1731–1746. doi: 10.1177/0959683613505338

Tsoar, H. (1983). Dynamic processes acting on a longitudinal (seif) sand dune. *Sedimentology* 30, 567–578. doi: 10.1111/j.1365-3091.1983.tb00694.x

Vermeesch, P., Fenton, C. R., Kober, F., Wiggs, G. F. S., Bristow, C. S., and Xu, S. (2010). Sand residence times of one million years in the Namib Sand Sea from cosmogenic nuclides. *Nat. Geosci.* 3, 862–865. doi: 10.1038/ngeo985

von Gosen, W. (1992). Structural evolution of the argentine Precordillera: The San Juan section. *J. Struct. Geol.* 14, 643–667. doi: 10.1016/0191-8141(92)90124-f

Wang, X., Ma, J., Yi, S., Vandenberghe, J., Dai, Y., and Lu, H. (2018). Interaction of fluvial and eolian sedimentation processes, and response to climate change since the last glacial in a semiarid environment along the Yellow River. *Quat. Res.* 570–583. doi: 10.1017/qua.2018.22

Whitehouse, M. J. (2008). Plešovise zircon – a new natural reference material for U-Pb and Hf isotopic microanalysis. *Chem. Geol.* 249, 1–35. doi: 10.1016/j.chemgeo.2007.11.005

Wiedenbeck, M., Alle, P., Corfu, F., Griffin, W. L., Meier, M., Oberli, F. V., et al. (1995). Three natural zircon standards for U—Th—Pb, Lu—Hf, trace element and REE analyses. *Geostand. Newslett.* 19, 1–23. doi: 10.1111/j.1751-908x.1995.tb00147.x

Williams, M. A., and Balling, R. C. Jr. (1996). *Interactions of Desertification and Climate*. London: Hodder Headline, PLC.

Zárate, M. A. (2003). Loess of southern South America. *Quat. Sci. Rev.* 22, 1987–2006. doi: 10.1016/s0277-3791(03)00165-3

Zárate, M. A., and Tripaldi, A. (2012). The aeolian system of central Argentina. *J. Aeol. Res.* 3, 401–417. doi: 10.1016/j.aeolia.2011.08.002

Conflict of Interest: The authors declare that the research was conducted in the absence of any commercial or financial relationships that could be construed as a potential conflict of interest.

frontiers in Earth Science

ORIGINAL RESEARCH
published: 20 November 2019
doi: 10.3389/feart.2019.00303

Manifestation of Tectonic and Climatic Perturbations in Deep-Time Stratigraphy – An Example From the Paleocene Succession Offshore Western Norway

Tor Oftedal Sømme[1], Jakob Skogseid[1], Patricia Embry[2] and Helge Løseth[3]*

[1] Equinor, Oslo, Norway, [2] Equinor, Houston, TX, United States, [3] Equinor, Trondheim, Norway

Sediment routing systems may be exposed to different external controls that can modulate long and short-term sediment delivery to nearby basins. Here we investigate a Paleocene depositional system offshore western Norway that was subjected to long-term (∼10 Myr) tectonic perturbation and significant hinterland erosion. Superimposed on this long-term uplift, the system was also subjected to a short-lived climatic perturbation, which lasted ∼200 kyr. Regional 3D seismic reflection data is integrated with high resolution borehole and biostratigraphic data to map the stratigraphic responses to these different scales of perturbations on the Paleocene system. The initiation of the tectonic perturbation is marked by an angular unconformity in seismic data at the base of the Paleocene. An increase in sediment supply followed, causing progradation of a confined shelf-slope wedge during the Middle and Late Paleocene. The end of the tectonic perturbation is marked by onlap in the lowermost Eocene and a shift from a confined to a more lateral extensive depositional system. Calculations indicate that the tectonic uplift caused an order of magnitude increase in sediment supply to the basin. This period coincided with the Paleocene-Eocene Thermal Maximum (PETM), which is documented by biostratigraphic data as a discrete event within the overall regressive system. Although the PETM has been associated with increased continental runoff in the North Atlantic, no peak in sediment supply can be resolved in the available dataset. This study shows that the system response to tectonic perturbations may vary along strike, depending on the size of the routing systems and the antecedent topography prior to hinterland uplift. A low supply system may produce a tectonically linked shelf-slope wedge that is of similar thickness as a climatically linked wedge in a high supply system. This study documents how the same routing system responded to perturbations operating at different spatial and temporal scales and may help recognize similar process-response relationships in other areas.

Keywords: tectonic perturbation, climatic perturbation, deep-time, sediment routing, sediment supply, shelf-slope wedge, uplift, dynamic topography

OPEN ACCESS

Edited by:
Brian W. Romans,
Virginia Tech, United States

Reviewed by:
Pedro Val,
Universidade Federal de Ouro Preto, Brazil
David De Vleeschouwer,
University of Bremen, Germany

****Correspondence:***
Tor Oftedal Sømme
tooso@equinor.com

Specialty section:
This article was submitted to Sedimentology, Stratigraphy and Diagenesis, a section of the journal Frontiers in Earth Science

Received: *16 July 2019*
Accepted: *31 October 2019*
Published: *20 November 2019*

Citation:
Sømme TO, Skogseid J, Embry P and Løseth H (2019) Manifestation of Tectonic and Climatic Perturbations in Deep-Time Stratigraphy – An Example From the Paleocene Succession Offshore Western Norway. Front. Earth Sci. 7:303. doi: 10.3389/feart.2019.00303

INTRODUCTION

Landscapes and their sediment routing systems are exposed to different tectonic and climatic perturbations affecting sediment production, transport and delivery to nearby sedimentary basins. Tectonic forcing operates on many temporal and spatial scales, from long-lived collision of continental plates, to changes in lithospheric stress, mantle dynamics and short-lived, intra-catchment fault movements. Whereas local fault activity can result in rapid changes in sediment supply (Whittaker et al., 2010), perturbations related to mantle dynamics and plate tectonic processes can cause re-arrangement of entire continent-scale fluvial networks and often result in distinct changes in basin physiography and accommodation trends that can readily be recognized in the deep-time ($>10^{\wedge 6}$ yr) depositional record (e.g., Campanile et al., 2008; Baby et al., 2018). The impact of such tectonic perturbations have be inferred qualitatively by linking pulses of coarse-grained material to phases of magmatic activity (e.g., White and Lovell, 1997), and quantitatively by analyzing sediment mass budgets linked to inferred changes in onshore denudation rates (Jones et al., 2002; Tinker et al., 2008; Braun et al., 2014). Similarly, sediment production and transport related to climatic perturbations also operate at different scales, from long-lived migration of global climate belts to high-frequency perturbations within the Milankovitch band (Séranne, 1999; Peizhen et al., 2001; Watkins et al., 2018). Although high-frequency changes in climate forcing often are difficult to recognize in seismic reflection data; detailed outcrop studies have documented how these perturbations have influenced the internal dynamics of sediment routing systems (e.g., Schmitz and Pujalte, 2003; Foreman et al., 2012; Duller et al., 2019).

It is questionable to what extent and in which form a tectonic or climatic signal is transmitted to the offshore stratigraphic record (e.g., Castelltort and Van den Driessche, 2003; Forzoni et al., 2014; Romans et al., 2016; Wu et al., 2019). It is generally thought that small systems are more reactive and tend to transmit signals more effectively than larger systems that are more buffered (Allen, 2008), and recent work also suggest that the duration of the signal relative to the frequency of autogenic processes is key for preservation (Toby et al., 2019). In addition, sediment supply signals may have a significant lag-time relative to the perturbation, such that the observed stratigraphic response is out of phase with the forcing factor (Willenbring et al., 2013; Li et al., 2018).

Many studies focusing on signal characteristics from climatic and tectonic forcings are based on numerical or physical models where input parameters are known and can be tested individually with high temporal resolution. Deep-time stratigraphy is, however, often more difficult to decipher because we often lack key information about the state of the landscape that supplied sediment to the offshore basins. In addition, it is evident that both tectonic and climatic perturbations operate in concert at similar or overlapping spatial and temporal scales (Overeem et al., 2001; Mancin et al., 2009; Samanta et al., 2016), making it challenging to isolate the effect of the individual controls. This is also supported by modeling studies suggesting non-unique stratigraphic response to different forcing factors that are difficult to separate in the stratigraphic record (Burgess and Prince, 2015). A key challenge is therefore to understand how these various tectonic and climatic perturbations interact to form signals that can be recognized in the stratigraphic record. This is especially difficult in deep-time, seismic reflection data where the temporal stratigraphic resolution struggles to resolve high-frequency events.

The North Atlantic is a suitable area to investigate the interaction between tectonic and climatic perturbations on sediment routing systems. It has long been recognized that the margins along western Norway, the British Isles and eastern Greenland experienced significant tectonic uplift during the Paleocene, followed by regional subsidence during the Early Eocene (e.g., Torske, 1975; Jones and Milton, 1994; Jordt et al., 1995; Nadin and Kusznir, 1995; Riis, 1996; Stuevold and Eldholm, 1996; Dam et al., 1998; Faleide et al., 2002; Mackay et al., 2005; Praeg et al., 2005; Anell et al., 2009).

The Paleocene-Eocene transition also marks a period of major climate change known as the Paleocene-Eocene Thermal Maximum (PETM) (e.g., Svensen et al., 2004; Sluijs et al., 2007). This short-lived climatic perturbation lasted for a few hundred thousand years and has been recognized regionally in the North Atlantic, both in borehole data and in outcrops (Svensen et al., 2004; Dypvik et al., 2011; Kender et al., 2012; Kjoberg et al., 2017). Despite operating at different temporal scales, the interaction of these two perturbations is manifested in the Paleocene-Early Eocene stratigraphy offshore SW Norway.

In this study we investigate the Upper Maastrichtian-Eocene succession along the SW Norwegian margin with the goal of identifying the stratigraphic response to climatic and tectonic perturbations within the same sediment routing systems. The area of investigation covers the northern Stord Basin, the Horda Platform and the Måløy Slope (**Figure 1**). During the Paleocene, this area received sediment from a drainage system covering parts of southern Norway. Because the areal extent of the paleo-drainage system is believed to have been relatively fixed during the Paleocene-Eocene (Sømme et al., 2013b), this area is ideal to investigate how a single sediment routing system responds to tectonic and climatic forcing operating at different spatial and temporals scales in deep-time.

The main aims of this study are to: (1) identify stratigraphic characteristics of a shelf-slope wedge linked to long-term tectonic perturbation using seismic reflection and borehole data; (2) use thickness maps and biostratigraphic data to estimate sediment supply from the onshore catchment area before, during and after tectonic perturbation to investigate the response to a phase of hinterland uplift; (3) use seismic reflection data and borehole information to identify stratigraphic characteristics of a shelf-slope wedge linked to short-lived climatic perturbation during the PETM, and (4) discuss how different perturbations can be recognized in the deep-time stratigraphic record.

GEOLOGICAL SETTING

After peak Caledonian deformation in the Devonian, the Norwegian continental margin experienced extensional collapse

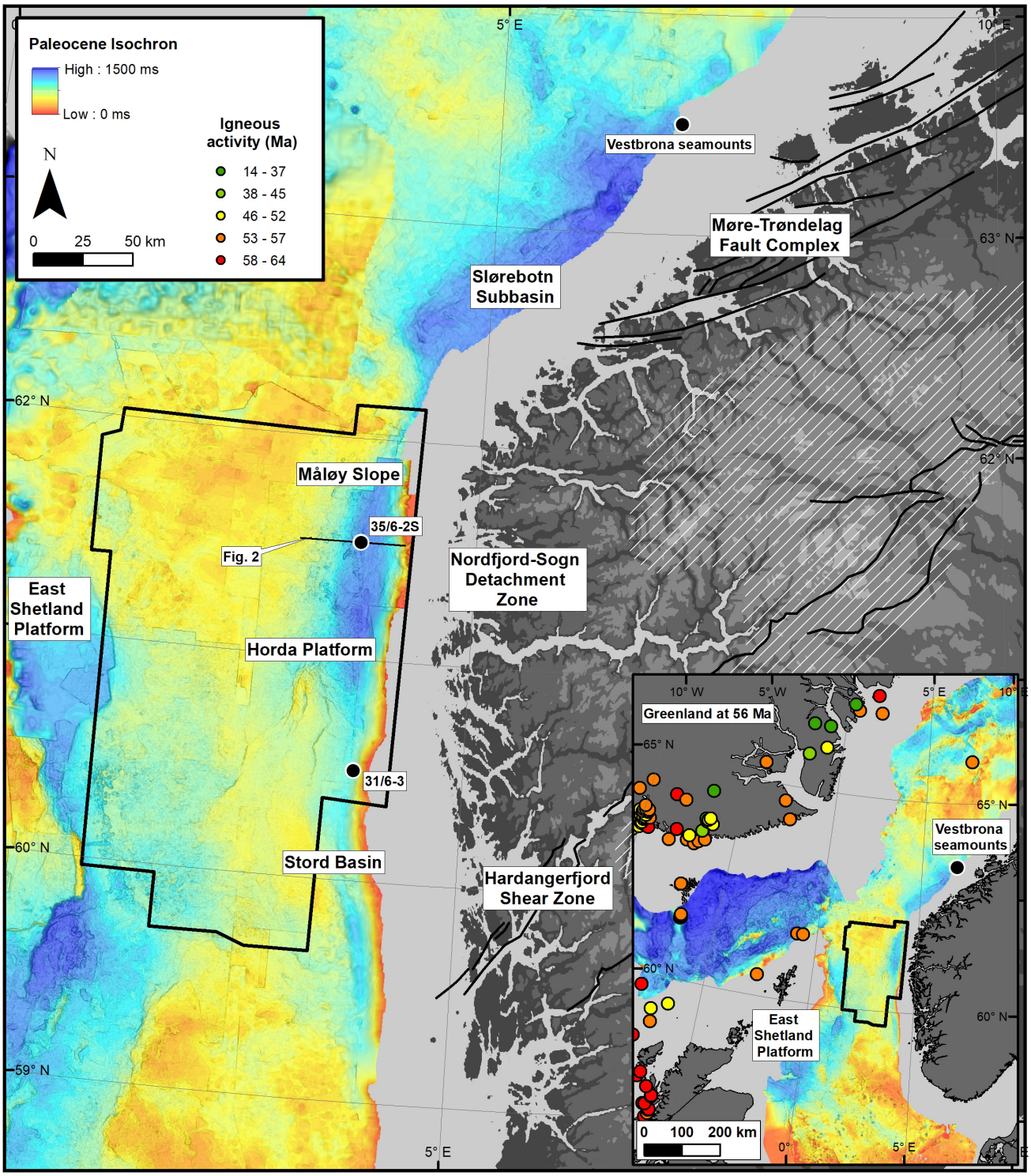

FIGURE 1 | Overview of the study area and regional isochron map of Paleocene sediments. The black outline shows the extent of seismic survey CGG18M01 which has been used to map Paleocene and Eocene stratigraphic units. Black lines represent main faults. The NE-SW trending Hardangerfjord Shear Zone is believed to represent the most landward possible extent of the Paleocene catchment. The white hatched polygon represents the area of inferred high Paleocene topography as suggested by Sømme et al. (2013b). Inset map shows reconstructed North Atlantic plate setting at 56 Ma with the distribution of igneous ages for the North Atlantic Igneous Province (from Steinberger et al., 2019).

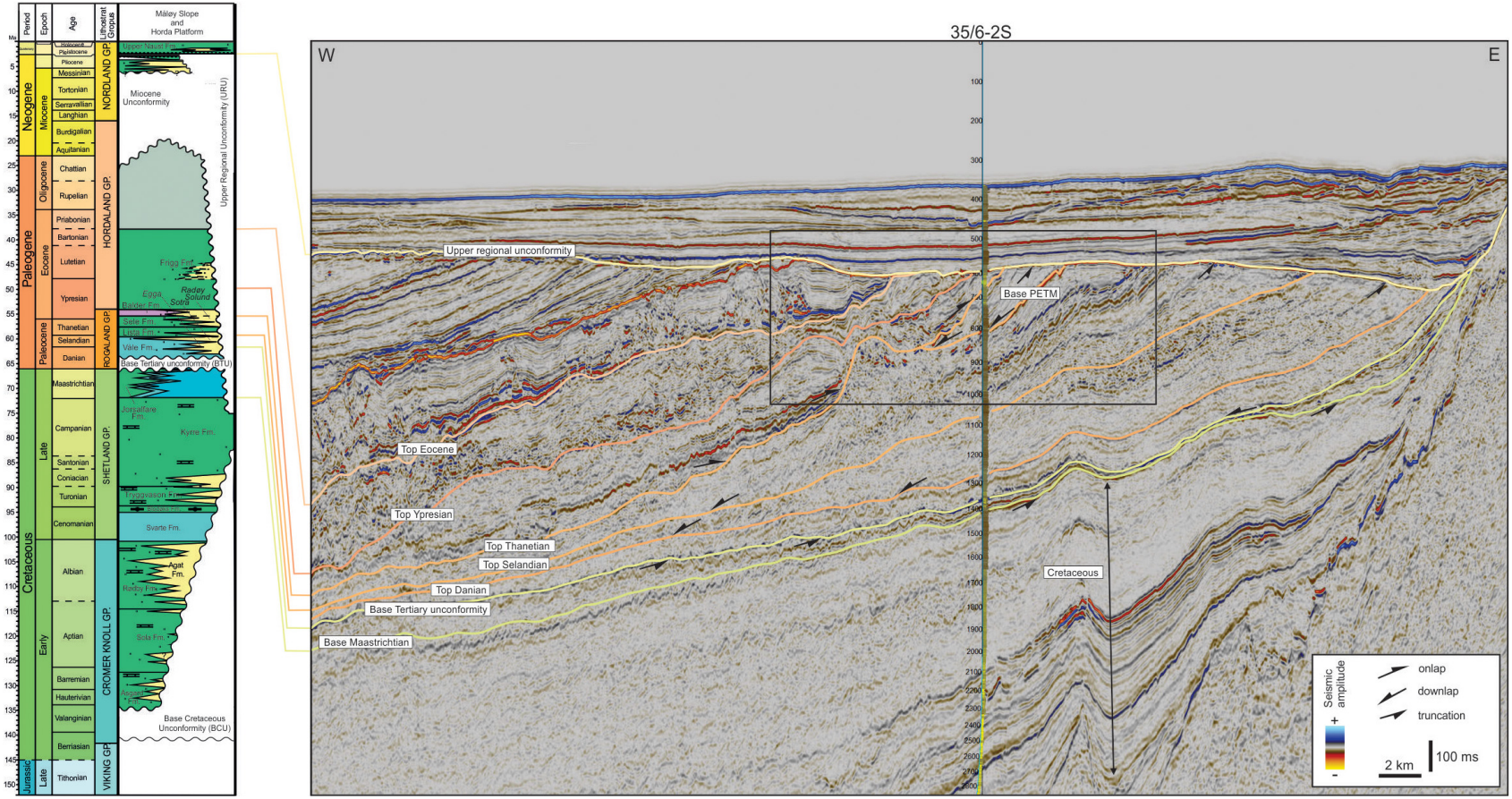

FIGURE 2 | Seismic dip-line and lithostratigraphic overview of key surfaces and units discussed in the text. Note the transition from basinward thickening wedge in the Cretaceous to basinward thinning wedge in the Paleocene. The line intersects borehole 35/6-2S which documents the Paleocene-Eocene Thermal Maximum (PETM). Black box shows the extent of **Figure 5**.

along a number of deep-crustal fault zones (Andersen, 1998; Fossen and Dunlap, 1998; Fossen et al., 2017), which defined the structural template for later Mesozoic basin formation and onshore topography (Gabrielsen et al., 2010; Sømme et al., 2013b). Renewed Triassic extension was characterized by fault block topography and deposition of marine, lacustrine and alluvial sediments (Steel, 1993). Regional marine incursion took place in the Early Jurassic and in the Middle Jurassic the North Sea was dominated by shallow, post-rift basins (Steel and Ryseth, 1990). Sediment was mainly delivered from the south, although the Norwegian mainland also represented an important sediment source (Morton, 1992). Renewed rifting in the North Sea started in the late Mid Jurassic and peaked in the Late Jurassic – earliest Cretaceous, when the rift axis shifted westward to the Faroe-Shetland and Møre basins. Deep-water basins formed in the central part of the rift zones, receiving sediments from local fault blocks and the nearby hinterland (Bugge et al., 2001; Martinsen et al., 2005). In the study area (**Figure 1**), the Upper Cretaceous succession is dominated by mudstones interbedded with relatively thin sandstone units deposited in a deep-water environment (Martinsen et al., 2005; Jackson et al., 2008). The last pulse of clastic input took place in the Turonian-Coniacian and is recognized by small channel complexes and terminal lobes in an underfilled, deep-water slope to basin floor setting on the Måløy Slope and Slørebotn Subbasin, in close proximity to the Møre-Trøndelag Fault complex (MTFC) (Sømme et al., 2013a). To the south, the Horda Platform area was probably only 200–300 m deep in the Late Cretaceous (Wien and Kjennerud, 2005), but only biogenic chalk deposits are recognized in this area. The structural trend marking the northern part of the Horda Platform and the offshore continuation of the Nordfjord-Sogn Detachment Zone (NSDZ) thus marks a long-lived change in basin physiography and sediment input along strike. Similarly, the MTFC, NSDZ, and Hardangerfjord Shear Zone (HFSZ) have likely also dictated the distribution of onshore topography, which is believed to have been highest along these long-lived fault zones (Redfield et al., 2005; Gabrielsen et al., 2010; Sømme et al., 2013b).

The Cretaceous-Paleocene boundary is marked by a change in basin physiography in the study area and elsewhere in the North Sea (Jarsve et al., 2014), marking the transition from fine-grained siliciclastic and carbonate dominated deposition in an underfilled basin setting, to regional input of coarse siliciclastic sediments in an overfilled setting (Dmitrieva et al., 2018). For the first time since the Late Jurassic, sediment supply from mainland Norway was higher than the available offshore accommodation, causing the shelf-slope margin to prograde westward (**Figure 2**). Large input of clastic sediment also took place further north in the Slørebotn Basin (Gjelberg et al., 2001) and in the Faroe-Shetland Basin (Mudge, 2015), and to a lesser extent from southwestern Norway (Hamberg et al., 2005). Elsewhere in the North Sea, most of the Danian was dominated by pelagic ooze and fined-grained deposition. The Selandian and Thanetian was characterized by increased sediment supply from both the Norwegian mainland and the British Iles (Liu and Galloway, 1997; Faleide et al., 2002), where deep-marine deposits eventually covered large parts of the North Sea (Mudge, 2015). This marked increase in sediment input from the Norwegian mainland has been taken as evidence for regional uplift (Jordt et al., 1995, 2000; Martinsen et al., 1999; Skogseid et al., 2000; Anell et al., 2010), although the mechanisms are debated (Anell et al., 2009).

In addition to changing basin configuration, the latest Cretaceous and Paleocene period was also characterized by a renewed phase of crustal extension, which culminated in final break-up and sea-floor spreading between Norway and Greenland around 55 Ma (Eldholm et al., 1989). Pre break-up Selandian and Thanetian volcanism has been documented in the Faroe-Shetland Basin and on Greenland (Ritchie et al., 1999), but the main phase of extrusive volcanic activity in the North Atlantic Igneous Province was associated with break-up (**Figure 1**) and the formation of thick wedges of volcanic flows (seaward dipping reflectors) and lava deltas along the outer margin (Eldholm et al., 1989; Planke and Alvestad, 1999; Abdelmalak et al., 2016). Contemporaneous igneous sill intrusions in the Mesozoic sedimentary successions caused large volumes of methane and carbon dioxide to be released into the atmosphere (Svensen et al., 2004; Kjoberg et al., 2017) that is interpreted to have resulted in global warming and the PETM (Kennett and Stott, 1991; Sluijs et al., 2007). In the North Sea, the PETM has been recognized as a period of increased continental run-off and higher eustatic sea levels (Kender et al., 2012). Large input of siliciclastic material to the margins of the North Sea continued also after the PETM, in the Early Eocene, however, sediment supply generally decreased during the Mid and Late Eocene (Martinsen et al., 1999; Faleide et al., 2002; Anell et al., 2010). Toward the end of the Cenozoic, the margin was tilted during one or several phases of uplift resulting in differential erosion of the underlaying stratigraphic units below the Quaternary upper regional unconformity (URU; **Figure 2**; Ottesen et al., 2014; Baig et al., 2019).

RATIONALE AND METHODOLOGY

The SW Norwegian margin makes a suitable area for identifying deep-time stratigraphic response to external forcing in subsurface data. The region is covered by numerous regional 3D seismic reflection data sets and hundreds of boreholes, which allows stratigraphic packages to be mapped and dated with sub-stage temporal resolution.

In this study, stratigraphic packages at Stage level have been mapped on seismic reflection data and tied to boreholes with biostratigraphic information. The outline of depositional systems (e.g., channel and lobe complexes) have been mapped using seismic attribute data (**Figures 3**, **4**). Mass-balance calculations were performed on all packages at Stage level to reveal changes in sediment supply through time in response to hinterland denudation.

Step one in this process was to depth-convert the top and base surface of every package at Stage level using a regional seismic velocity model. The maps were then cut to the area of active deposition as suggested by attribute maps, thickness and borehole data (**Figure 3**) to constrain the volume of the active depositional system. Present day rock volumes (km^3) were calculated for each unit and this value was converted to mass (MT) using the average density from all boreholes penetrating the

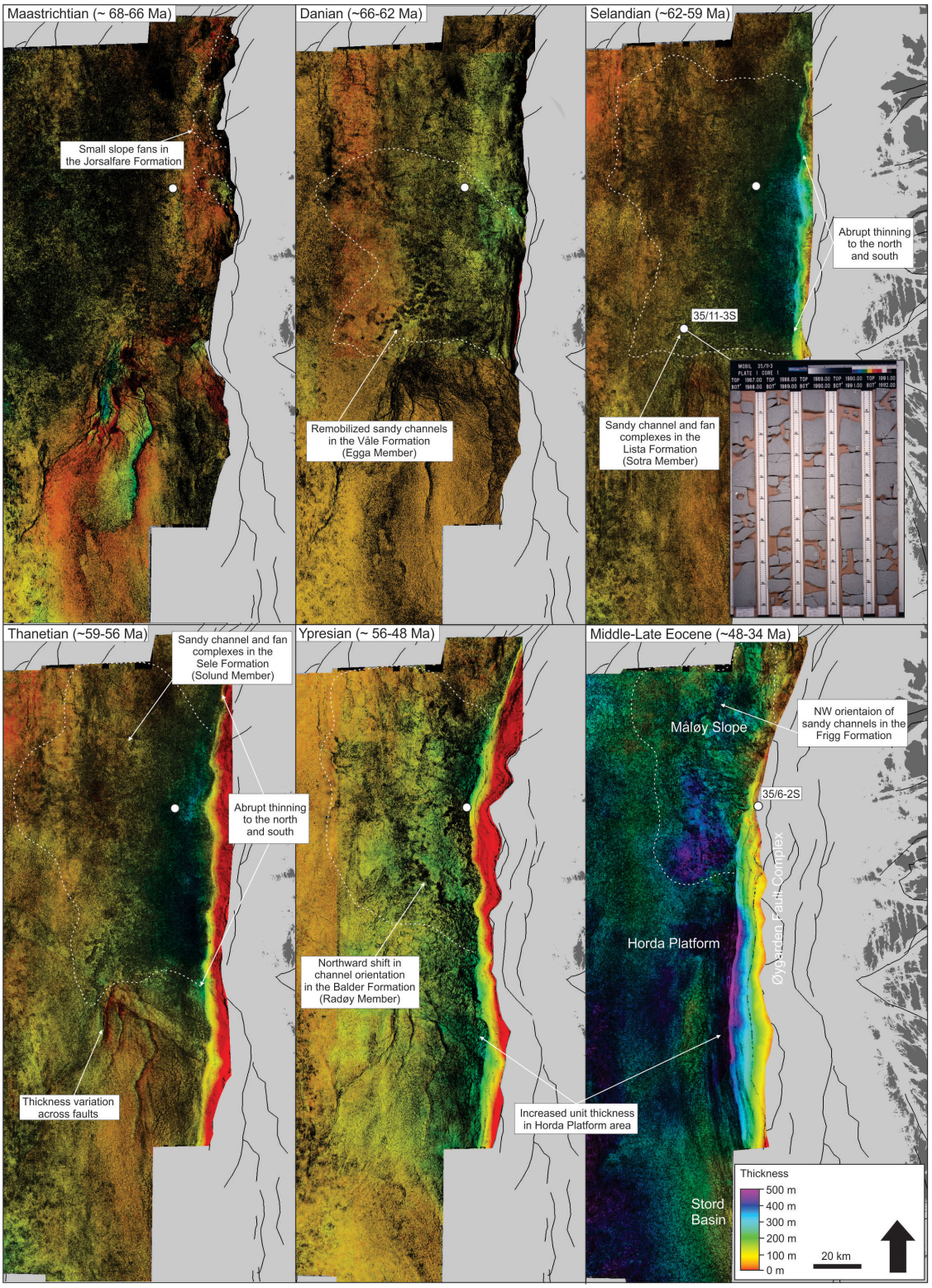

FIGURE 3 | Co-blended variance and isopach maps of the Maastrichtian to Eocene stratigraphic units. The approximate extent of the slope to deep-water fan systems is shown by a white hatched line. Maastrichtian fans are not drilled, but indicated from small channel-lobe geometries in attribute maps. High input of coarse-grained material in the Våle, Sotra and Lista Formations is well documented. Inset shows cored example of a sandy, deep-water channel in the Lista Formation (Sotra Member). Image from www.npd.no. Sandy channels are recognized by linear features in the variance blend (black shading). Note the shift from a localized, point-sourced depocenter in the Paleocene to a more lateral extensive depocenter in the Ypresian coinciding with onlap and redistribution of sediment along strike after the PETM.

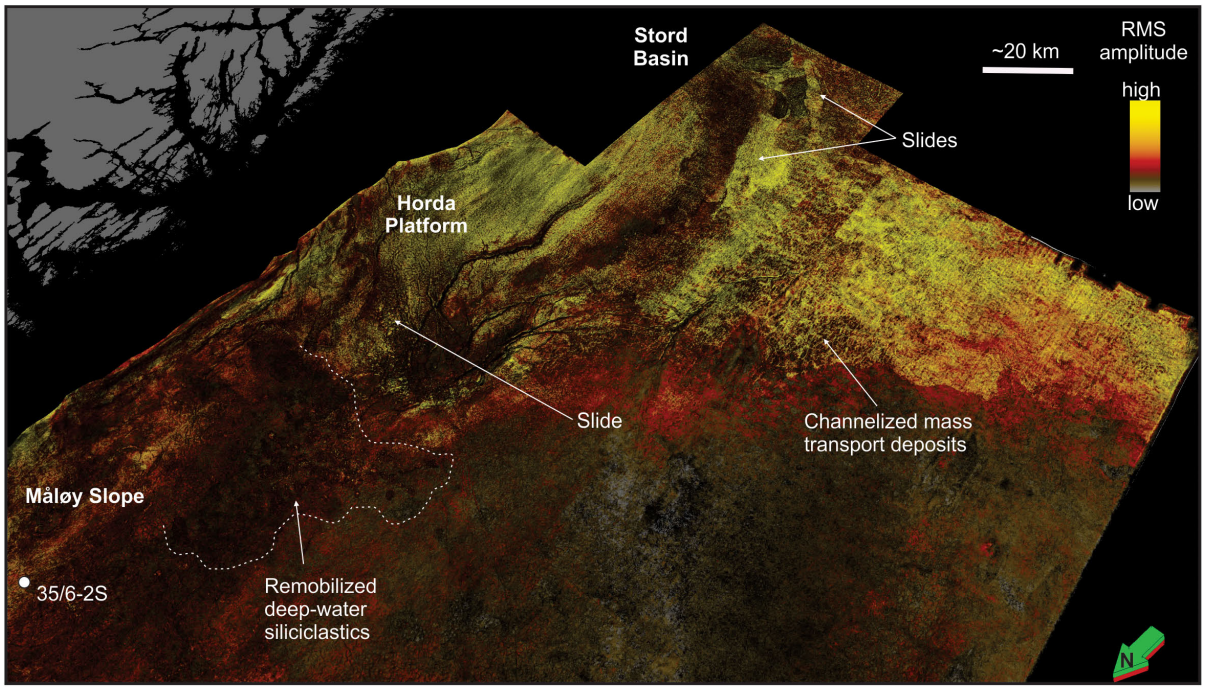

FIGURE 4 | Oblique view of co-blended root mean square (RMS) and variance attributes 20 ms above the Base Tertiary unconformity. The map shows the transition from siliciclastic dominated and remobilized deep-water channel and lobe complexes on the Måløy Slope, to large slides and mass-transport deposits on the Horda Platform and in the Stord Basin. The approximate basinward extent of Danian deep-water deposits is indicated by the white hatched line. The mass-transport deposits mostly comprise chalk and argillaceous shales. The present-day Norwegian coastline is show in gray.

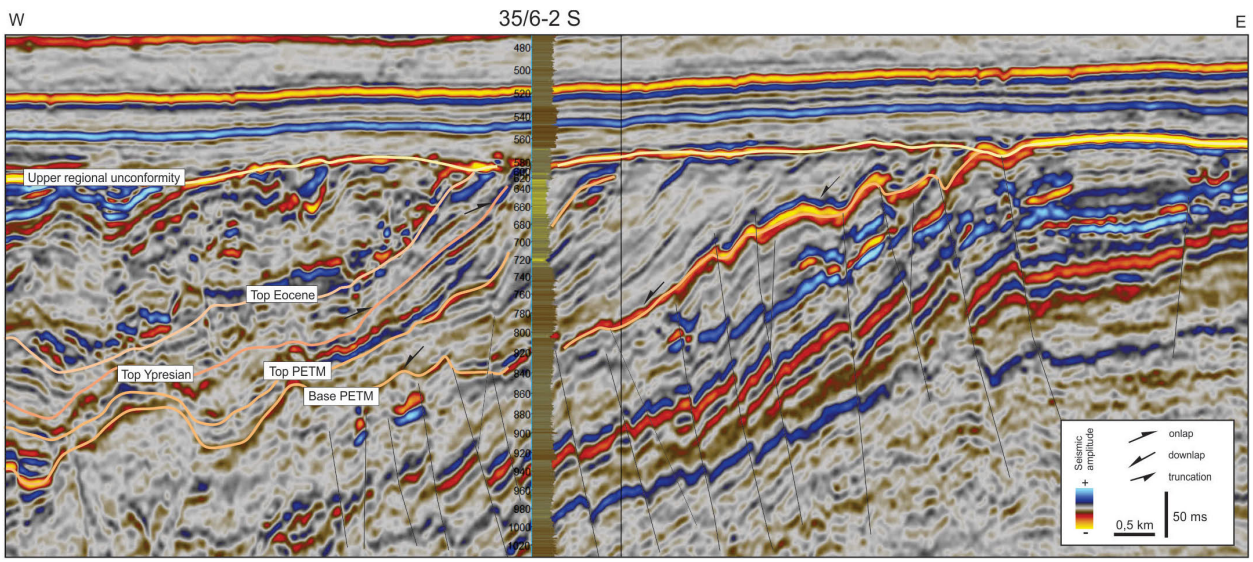

FIGURE 5 | Dip-line of the PETM succession through borehole 35/6-2S. The onset of the PETM is marked by a distinct downlap surface indicating a minor relative sea-level rise and reorganization of the feeder system. The underlying Thanetian succession was remobilized and locally faulted just prior to PETM progradation, controlling the thickness and distribution of PETM strata. The end of the PETM interval is not marked by distinct stratal relationships and progradation continued during deposition of the early Ypresian Balder Fm above 680 m. See **Figure 2** for location on regional dip-line.

relevant units (**Supplementary Table S1**). Changes in sediment supply (MT/yr) through time was finally calculated using stage ages from Gradstein et al. (2012).

High-resolution biostratigraphic data from borehole 35/6-2S (**Figures 5**, **6**) was used to constrain the mapping of the PETM deposits. This is the most proximal borehole penetrating the

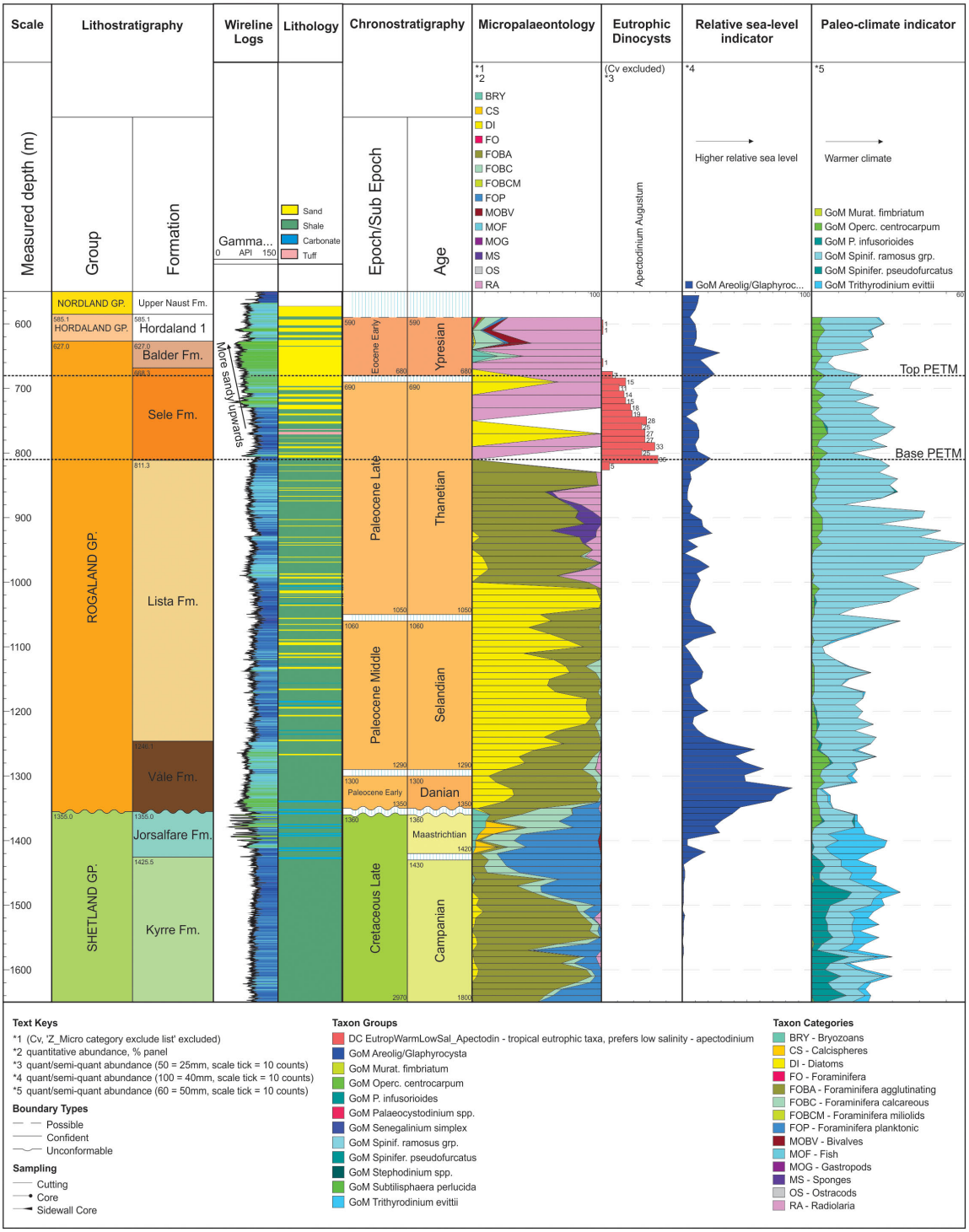

FIGURE 6 | Biostratigraphic information for borehole 35/6-2S. The PETM is defined in micropaleontological data by the extinction of benthic fauna and in dinoflagellates by the presence of *A. Augustum* between ~680 and ~810 m. Peaks in *Areoligera/Glaphyrocysta* and *Spiniferites ramosus grp.* are considered indicators of relative sea-level and climate variability, respectively. The data indicate relative sea-level rise at the base of the Paleocene succession and within the Balder Fm. Increasing relative sea-level toward the top of the Balder Fm is also indicated by more shale-dominated lithologies and an increase in gamma ray in the wireline log. High gamma ray and blue colors are indicative of shale-dominated lithologies whereas low gamma and green colors are indicative of sand and carbonate dominated lithologies.

PETM event in this area and provides information on paleo-environmental changes prior to and during the PETM.

Uncertainties in the volumetric calculation varies between the different units. The Maastrichtian succession shows a basinward thickening geometry (**Figure 2**) and it is possible that fine-grained material has been transported basinward of the small slope-fans inferred from attribute maps, thus underestimating the overall sediment supply. However, no boreholes indicate the presence of an active Maastrichtian supply system. The Danian, Selandian and Thanetian successions are all well-defined on thickness maps as the depocenters clearly thins both in strike and dip-direction (**Figure 3**). Although biostratigraphic data from several boreholes indicate minor stratigraphic breaks internally, the 3D volumetric control is adequate. The main uncertainty is related to the amount of erosion by the upper regional unconformity (URU) (**Figure 2**). Although shelf-breaks are observed locally, especially in the uppermost part of the Paleocene succession, most of the topsets have been removed by later erosion. The amount of missing strata is difficult to estimate, but this and other studies (Martinsen et al., 1999) suggest that the Paleocene progradation occurred by forced regression, and it is believed that little material was retained in the topsets.

In order to quantify the onshore topography associated with the Paleocene tectonic event, inverse application of the BQART model (Syvitski and Milliman, 2007) was conducted. The aim is to use a large modern data set to investigate the best-fit topography associated with the observed sediment supply through time. The best-fit topography is calculated using a Monte Carlo approach where all key uncertainties are included in the estimations. The method and discussion of uncertainty parameters are outlined in Sømme et al. (2013b) and in the **Appendix**.

CHARACTERISTICS OF THE PALEOCENE SHELF-SLOPE WEDGES LINKED TO TECTONIC PERTURBATION

In the study area, the Maastrichtian succession is extensively eroded by the angular base Tertiary unconformity (BTU), and the amount of erosion generally increases eastward and above the crests of older fault blocks (**Figures 2**, **3**). A seismic attribute map of the Danian succession just above the unconformity reveals that the transition between the Maastrichtian and the Paleocene was dominated by significant mass-wasting (**Figure 4**). On the Horda Platform and in the northern part of the Stord Basin, several large slides are observed together with channelized mass-transport deposits. Boreholes penetrating these deposits show that they mostly comprise fine-grained argillaceous shale and chalk material eroded from underlying lowermost Danian and uppermost Cretaceous strata. Further north on the Horda Platform, the Danian is characterized by an up to 200 m thick succession of slope to basin floor channel and fan complexes that are downlapping the BTU (Egga Member of the Våle Formation, **Figures 2**, **3**; Dmitrieva et al., 2018). Biostratigraphic data form 35/6-2S suggest that this period was characterized by relative sea-level rise (**Figure 6**).

Progradation continued during the Selandian and Thanetian with only a minor stratigraphic breaks in borehole 35/6-2S. Seismic attribute data (**Figure 3**) show continued progradation of sandy slope channel complexes (Sotra and Solund members of the Lista and Sele Formations) (**Figures 2**, **3**). Biostratigraphic data from boreholes penetrating these units show reworking of Cretaceous fauna, suggesting that underlying stratigraphy was eroded somewhere along the routing system to the east. The isochore maps of the Selandian and Thanetian successions show thicknesses of up to 350 m in the main depocenter, abruptly thinning toward the north and south (**Figure 3**). The uppermost part of the Thanetian succession comprises the succession associated with the PETM (**Figures 5**, **6**), which will be discussed separately below.

Paleocene strata are overlain by a relatively thin unit of early Ypresian age [Balder Fm (**Figures 2**, **3**)]. In 35/6-2S and locally in the northern part of the study area, the Balder Fm is sand-dominated (Radøy Member; **Figure 3**; Martinsen et al., 1999), and the unit shows a progradational to aggradational stacking pattern (**Figure 5**). To the south and away from the main sediment entry point, the unit shows an aggradational to backstepping pattern. The thickness of the Ypresian succession is up to 270 m, showing only minor variation along strike (**Figure 3**), indicating a transition from a well-defined point source to a more laterally extensive depocenter. Despite overall aggradation and onlap onto the upper slope of the underlying Thanetian succession, borehole and seismic attribute data suggest that the northernmost part of the Ypresian system on the Måløy Slope represents sand-dominated slope to deep-water channel and lobe complexes (Frigg Formation) (**Figures 2**, **3**); whereas on the northern Horda Platform, the succession is fine-grained without evidence of coarse-grained input.

A similar situation is evident from the Middle to Upper Eocene succession, which is up to 530 m thick on the southernmost part of the Måløy Slope (**Figure 3**). Also here, borehole and seismic attribute data suggest that the coarse-grained material was delivered to the Måløy Slope area (Frigg Fm, **Figure 1**), whereas the northern Horda Platform was dominated by fine-grained sediments (Martinsen et al., 1999).

Further south, in the Stord Basin, another Paleocene wedge has been mapped on 2D and 3D seismic reflection data (**Figures 7**, **8**). This wedge represents the distal part of a different routing system that was associated with significantly lower sediment supply compared to the northern system during the Paleocene (the total thickness of the Paleocene wedge is only ∼400 m compared to ∼900 m in the north). The southern system has preserved the topsets of the ∼200 m thick Thanetian prograding wedge (**Figure 7**), allowing more detailed analysis of changes in accommodation to be made. The lower part of the wedge shows downlap-toplap geometries, indicating forced regression. This is overlain by an aggradational unit, which again is onlapped by lower Ypresian strata as in the north. This wedge has been tied to borehole 31/6-3 (**Figure 8**), where biostratigraphic data shows that a major unconformity is present within the Thanetian. The PETM is not recognized as a mappable seismic unit in the southern depocenter. Since the entire

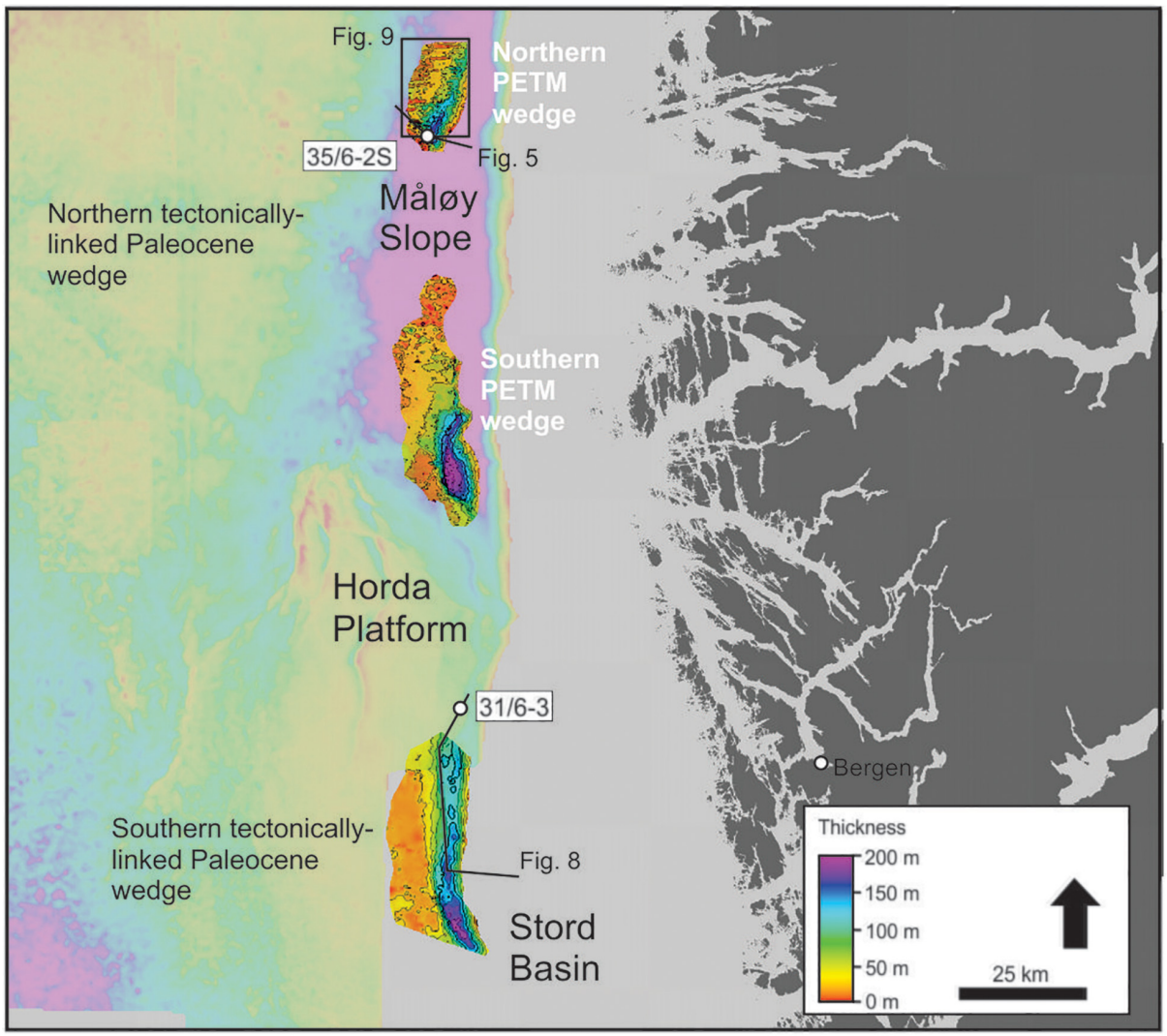

FIGURE 7 | Map showing the two (northern and southern) PETM depocenters on the Horda Platform and the Måløy Slope together with the northern and southern tectonically-linked depocenters on the Måløy Slope and in the Stord Basin (the former is made transparent for visualization purposes). Note the similarity in thickness between the PETM wedges and the southern tectonically-linked wedge. The PETM climatic wedges represent ∼150–200 kyr of deposition, whereas the tectonically linked wedges are believed to represents up to ∼3 Myr of deposition.

landward part of the wedge has been eroded by the URU, no attempts have been made to calculate sediment supply for this unit.

CHARACTERISTICS OF THE UPPERMOST THANETIAN SHELF-SLOPE WEDGES LINKED TO CLIMATE PERTURBATION

Although the PETM only lasted about 150–200 kyr (Röhl et al., 2007; Sluijs et al., 2007), the corresponding stratigraphic record can still be recognized and mapped on seismic reflection data in areas where the sediment supply was high. In the North Atlantic, the PETM has been recognized by the presence of *Apectodinium Augustum* dinocysts and an abrupt extinction of benthic foraminifera (Gradstein et al., 1994; Sluijs et al., 2007; Nagy et al., 2013; Eldrett et al., 2014). Biostratigraphic data from borehole 35/6-2S shows the extinction of benthic foraminifera and the presence of *A. Augustum* at ∼810–680 m, indicating that the PETM is represented by ∼130 m of stratigraphy in the Sele Fm (**Figure 6**). The base of the PETM succession can be tied to a distinct, but local downlap surface on seismic data, which marks the transition from low-angle to more steeply dipping clinoform geometries (**Figure 5**). In 35/6-2S, the surface is characterized by shale-dominated lithologies and a minor increase in gamma ray (GR) (**Figure 6**). In map view, the surface is characterized by a polygonal fault pattern and little variation in the RMS amplitudes indicating relatively homogenous lithologies (**Figure 9**). The fine-grained lithologies and the downlapping geometry of the lower

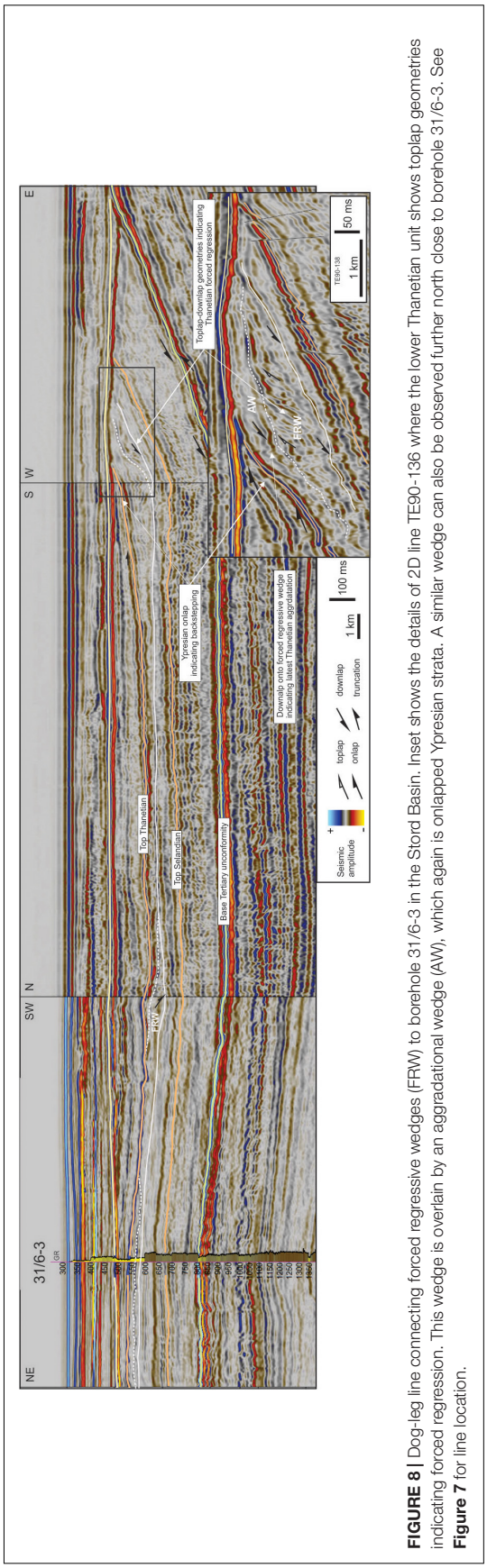

FIGURE 8 | Dog-leg line connecting forced regressive wedges (FRW) to borehole 31/6-3 in the Stord Basin. Inset shows the details of 2D line TE90-136 where the lower Thanetian unit shows toplap geometries indicating forced regression. This wedge is overlain by an aggradational wedge (AW), which again is onlapped Ypresian strata. A similar wedge can also be observed further north close to borehole 31/6-3. See **Figure 7** for line location.

surface indicates that the onset of the PETM was characterized by re-arrangement of the main dispersal system to the north of the main Paleocene wedge (**Figure 7**). Clinoform geometries appear to steepen upward in the succession, indicating progradation into deeper water.

In the area around borehole 35/6-2S, the PETM succession prograded across a rugged seafloor created by remobilization of underlying sediments (**Figures 5**, **9**). This might suggest that PETM progradation was relatively rapid, causing increased pore-pressure and remobilization of older, underlying sediments prior and during PETM progradation. Borehole logs and cutting descriptions from 35/6-2S also show that the base of the PETM succession is dominated by shales, whereas increasing amount of sand is present in the uppermost part of the unit (**Figure 6**). Increasing sediment input toward the end of the PETM is also corroborated by the presence of channel and lobe complexes observed in the attribute data in **Figure 9**.

Apectodinium Augustum is also an indicator of increased nutrient supply and runoff from the continent, which has been documented in several locations in the North Atlantic (Carmichael et al., 2017). However, the only difference described from the cutting data is a marked change in sorting within the PETM sands, from well sorted below and above, to very poor sorting within the PETM interval. The last occurrence of *A. Augustum* in borehole 35/6-2S is at ∼680 m, which is below the top of the sandy progradational unit and at least 50 m below the regional Ypresian onlap surface described above. Consequently, the end of the PETM does not appear to be characterized by any specific stratal relationship in seismic data and the system continued to prograde also after the PETM. Continued sediment delivery is also evident in seismic attribute data, however, post-PETM channels appear straighter and are more widely spaced along strike (**Figure 9**).

The basal surfaces of the PETM wedge and the lower Ypresian onlap surface penetrated by 35/6-2S can also be tied further south where another wedge is present (**Figure 7**). The thickest part of this southern wedge has not been penetrated by boreholes and the suggested PETM age is thus based on correlation along strike from borehole 35/6-2S and from other boreholes penetrating the distal slope setting. This is interpreted as another local PETM depocenter situated to the south of the main Paleocene wedge.

ESTIMATING SEDIMENT SUPPLY AND PALEOTOPOGRAPHY

In order to investigate stratigraphic response to climatic and tectonic forcing, the mapped depositional units were converted to sediment supply rates as described in section "Rationale and Methodology". These values were then used as input to the reverse BQART model, which estimates the topography needed to explain observed sediment loads along the margin.

Sediment Supply

Calculations show that the system delivering sediment to the SW Norwegian margin supplied less than 0.06 MT/yr during

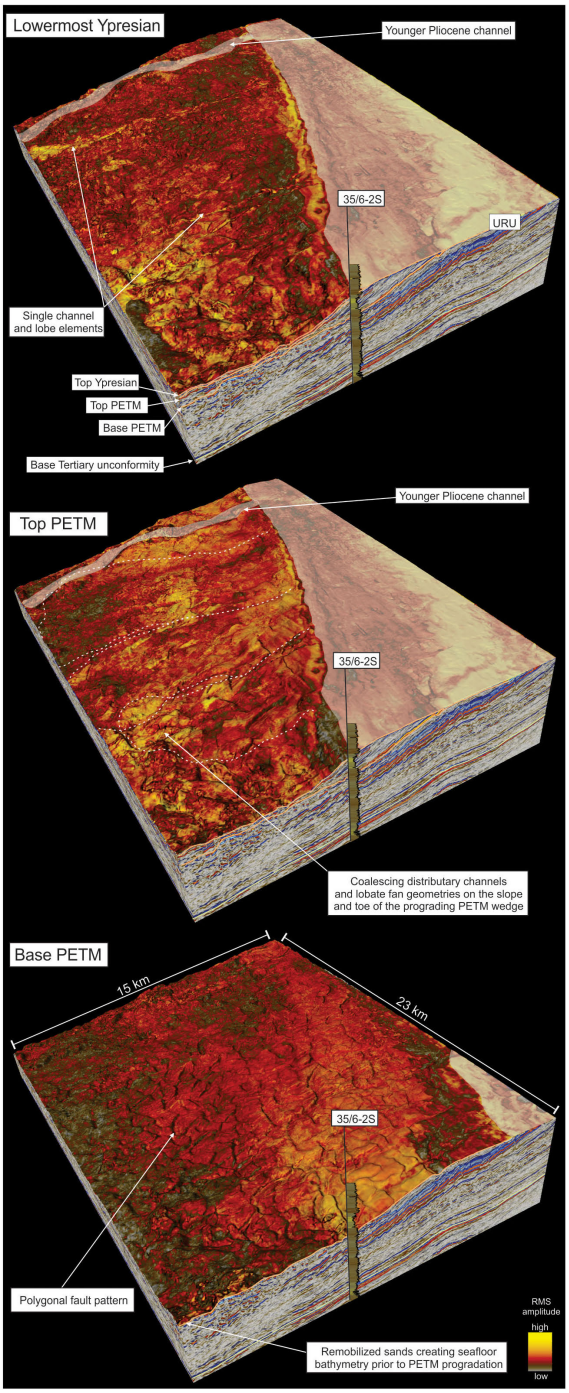

FIGURE 9 | Oblique view of co-blended root mean square (RMS) and variance attribute maps showing the evolution of the PETM wedge around and north of borehole 35/6-2S. The basal surface downlapped by the PETM wedge show polygonal fault pattern and little variation in amplitude, indicating fine-grained lithologies as shown in the borehole (**Figure 6**). Near the top of the PETM wedge, high-amplitude channel and lobe geometries can be observed along strike of the prograding shelf-slope wedge, indicating sandy and more mixed lithologies. In 35/6-2S, this is recognized by a sand-dominated interval. Sand appears to have been shed into the area also after the PETM, but the amplitude maps show different geometries with more straight channels and smaller terminal lobes. See **Figure 7** for location.

the Maastrichtian, prior to earliest Paleocene uplift (**Figure 10**). The sediment load increased to ∼0.32 MT/yr in the Danian, ∼ 0.82 in the Selandian and ∼0.79 MT/yr in the Thanetian, respectively (**Supplementary Table S1**). The sediment load then decreased to 0.38 MT/yr during the earliest Ypresian (Balder Fm), followed by ∼0.44 MT/yr in the Ypresian and finally ∼0.35 MT/yr for the remainder of the Eocene. Since parts of the sediments were eroded during the late Quaternary, the estimated loads are absolute minimum values. Nevertheless, the estimates suggest that hinterland uplift resulted in at least one order of magnitude increase in sediment supply during the Paleocene.

Paleocene-Eocene Thermal Maximum sediment loads have also been estimated based on the preserved volumes in the two depocenters on the Horda Platform (**Figure 7**). If it is assumed that all sediments were deposited in about 170 kyr (Röhl et al., 2007), the total PETM supply is ∼0.53 MT/yr. This number is lower than the more long-term Thanetian load, but higher than the earliest Ypresian load. The PETM load is likely underestimated since the unit is relatively thin (<10 m) and below seismic resolution away from large sediment entry points (Kender et al., 2012).

Paleotopography and Denudation

Assuming the extent of the catchment feeding sediment to the SW Norwegian margin did not change significantly in size during the Paleocene-Eocene, the observed changes in sediment supply are believed to reflect long-term increase in onshore topography. When the uncertainty of input parameters to the BQART model have been accounted for in the Monte Carlo simulation (see **Appendix**), the model shows that the best-fit scenario for the observed sediment supply is ∼0.1 km of relief during deposition of the small Maastrichtian slope fans (**Figure 3**), increasing to ∼0.4 km in the Danian as more sediment is supplied to the basin (**Figure 10**). A relief of 0.8–0.9 km is estimated for the Selandian and Thanetian during the main phase of progradation, falling to ∼0.4 km in the Eocene when the depocenter is less confined. These estimates suggest that significant topography on the scale of 0.6-1.1 km must be inferred to explain the at least one order of magnitude increase in sediment supply during the Paleocene. However, it should be stressed that these estimates do not necessarily reflect total vertical motion or amount of denudation, as the area inboard the Møre-Trøndelag Fault Complex (**Figure 1**) already had pre-existing topography of around 0.5 km in the Late Cretaceous prior to dynamic uplift (Sømme et al., 2013b).

In order to speculate on the amount of catchment denudation this offshore volume amounts to, we convert the present-day Paleocene volumes to solid rock volumes by removing the porosity using average values from the offshore boreholes (45%). If we average the Paleocene solid rock volumes across the inferred range of catchment sizes (∼850–3500 km^2, see **Appendix**), we obtain rates of ∼25–100 m/Myr in the Danian and ∼60–250 m/Myr in the Selandian and Thanetian during peak uplift. However, since erosion rates heavily depend on slope gradients, it is inferred that high-elevation areas would have seen higher rates than what is suggested here.

DISCUSSION

We start the discussion by looking into the driver for regional uplift in the Paleocene. We then go on to discuss how that uplift together with climate perturbation is expressed along strike depending on pre-uplift, antecedent topography. We suggest that the combination of antecedent topography and dynamic topography governed sediment supply and geomorphic character of the tectonically and climatically linked shelf-slope wedges.

Mechanism for Regional Uplift

Rapid increase in sediment supply to the flanks of the North Sea basin in the Paleocene has long been attributed to hinterland uplift (e.g., Jordt et al., 1995, 2000; Martinsen et al., 1999; Skogseid et al., 2000; Anell et al., 2009, 2010). Several mechanisms have been proposed to explain this uplift, including intraplate compressional stresses linked to plate reorganization and far-field compression, lithospheric flexure driven by differential loading, and rift-related mantle dynamic processes such as emplacement of the Iceland Plume below the lithosphere (e.g., Stuevold and Eldholm, 1996; Skogseid et al., 2000; Redfield et al., 2005; Guarnieri, 2015; Stoker et al., 2018).

An angular unconformity at the BTU overlain by slides and channelized mass-transport deposits (**Figure 4**) together with relative ocean deepening as indicated by biostratigraphic data in borehole 35/6-2S (**Figure 6**), suggests regional tilting and changing slope gradients along the flanks of the basin (Gradstein and Backstrøm, 1996; Praeg et al., 2005). A similar lower Paleocene slide have also been documented on the East Shetland Platform and has been linked to mantle plume activity (Soutter et al., 2018). Isochore maps also show Paleocene thickness variations across large normal faults on the Horda Platform (**Figure 3**), indicating syn-tectonic deposition of at least part of the Paleocene shelf-slope wedge. Faulting and extensional stress is also indicated by Paleocene reactivation of old Caledonian fault zones onshore (Fossen et al., 2017; Kziensyk pers. comm.), suggesting that at least part of the deformation was taken up along major faults (Redfield et al., 2005).

Long-term increase in sediment supply further indicates that the mechanism driving onshore uplift was not instantaneous, but gradually increased over almost 10 Myr, from the earliest Danian to the latest Thanetian. This trend stopped with a phase of early Ypresian onlap and relative sea-level rise within and above the Balder Fm (**Figures 5**, **6**) and just after sea-floor spreading at ∼55 Ma.

Increasing sediment supply during the Paleocene coincides with increasing dynamic topography for SW Norway as predicted by Barnett-Moore et al. (2017) (**Figure 10**). This period also coincides with high volcanic intensity in the North Atlantic Igneous Province, which peaked at the end of the Paleocene ∼56–54.5 Ma (Steinberger et al., 2019). This is also supported by the micropaleontology data which shows high diatom productivity in borehole 35/6-2S, pointing to higher nutrient supply to the basin in response increasing volcanic activity (Mitlehner, 1996). High magmatic activity has been attributed to the development of the Iceland Plume, and although most of the earliest (i.e., 62–63 Ma) magmatic activity is constrained to the British Isles and the breakup related magmatism (∼54–55 Ma) is found along the entire western margin of Eurasia (**Figure 1**), the near-coastal Vestbrona seamounts outboard the MTFC has been interpreted to represent a regional sill complex emplaced around 57–58 Ma (Hafeez et al., 2017). This documents that melt was present at lithospheric levels and in proximity to deep crustal fault complexes that are believed to have been active during the latest Cretaceous-Paleocene (Redfield et al., 2005).

In a more regional perspective, the observed changes in sediment supply and the stratigraphic relationships observed along the Norwegian mainland mirrors what has been observed along the margin of the British Isles. Recent work by Gale and Lovell (2018) suggest that incipient uplift of the British Isles started in the Late Cretaceous to Early Paleocene, similar to the onset of mass wasting along the Norwegian margin. In terms of sediment supply, Liu and Galloway (1997) observed a similar peak in sediment load around the Selandian-Thanetian transition, and White and Lovell (1997) suggested that pulses of increased sand delivery could be related to dynamic uplift of the British Isles.

Work by Smallwood and Gill (2002), Shaw Champion et al. (2008), Hartley et al. (2011) and Stucky de Quay et al. (2017) along the north-western and eastern margins of the British Isles further suggest that late Paleocene uplift and forced regression (Jones and Milton, 1994; Underhill, 2001) culminated with a phase of uplift of at least 300–500 m around the Thanetian-Ypresian transition. Subsequently, the margin was onlapped and transgressed in the Early Eocene (e.g., Underhill, 2001; Smallwood and Gill, 2002; Mudge, 2015), a process that has been linked to decreasing rates of dynamic uplift (Mackay et al., 2005; Shaw Champion et al., 2008). Similarity in timing of maximum forced regression and subsequent Ypresian transgression suggest that both the British Isles and western Norway experienced and responded to the same forcing mechanism.

Figure 10 compares the predicted dynamic uplift, igneous intensity, peak sediment supply and the timing of maximum forced regression during the PETM. The order of magnitude increase in sediment supply required significant relief of 0.6-1.1 km. If we take into account antecedent topography of around 0.5 km in the inboard areas prior to uplift (Sømme et al., 2013b), minimum values for net dynamic uplift was in the order of 0.1–0.6 km (this is discussed more in section "Along-Strike Variability and the Role of Pre-existing Topography"). These values are comparable to the predicted amplitude of dynamic uplift of ∼0.5 km at 60 ± 5 Ma from Barnett-Moore et al. (2017). If we further assume that the estimated basin-averaged denudation rates of 60–250 m/Myr reflect uplift rate, these are also similar, but on the low side of the uplift rates estimated for the northern British Isles (e.g., Shaw Champion et al., 2008; Stucky de Quay et al., 2017).

Our favored model is that regional uplift was driven by the arrival of the Iceland mantle plume as modeled by Barnett-Moore et al. (2017). But in contrast to previous studies from the British Isles (Shaw Champion et al., 2008; Hartley et al., 2011; Stucky de Quay et al., 2017), which focus on the last ∼3 Myr

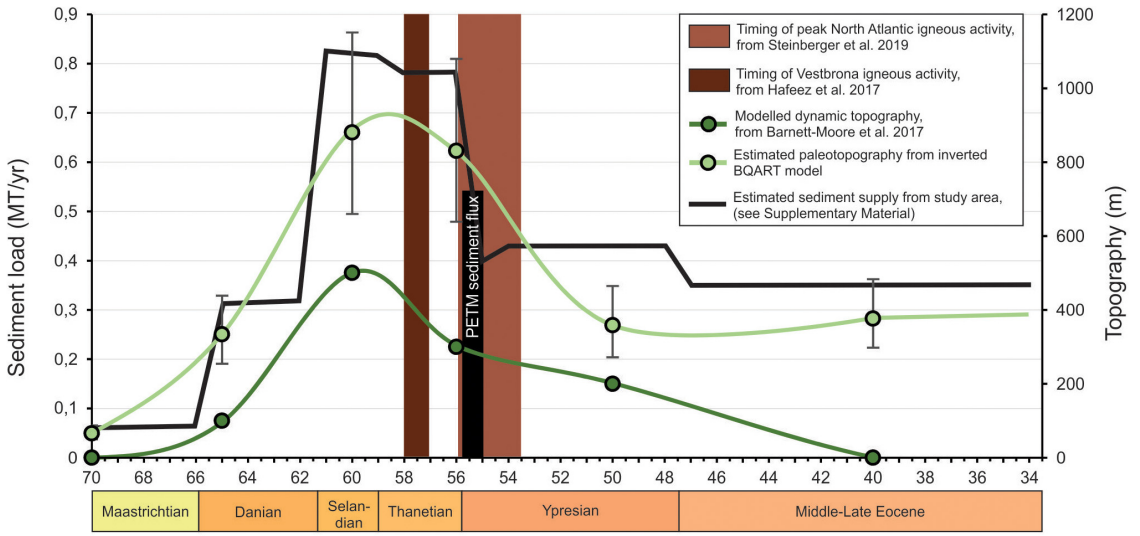

FIGURE 10 | Plot showing calculated sediment supply and estimated paleotopography from this study together with predicted dynamic topography (uncertainty range ± 5 Myr) and magmatic intensity in the North Atlantic Igneous Province. Also shown is the estimated PETM sediment supply from this study. Maximum forced regression occurred around the PETM and coincides with the timing of peak volcanic activity in the North Atlantic and just after the Vestbrona volcanics (**Figure 1**).

before break-up, we suggest that the initial phase of dynamic topography started already in the Danian. Despite favoring a mantle driver for the required uplift, we cannot rule out that also other factors played a role.

Along-Strike Variability and the Role of Pre-existing Topography

Caledonian structural inheritance is believed to have played an important role controlling the distribution of topography and drainage systems in southern Norway during the Mesozoic and Cenozoic (Gabrielsen et al., 2010). Apatite fission track data and absolute dating of faults suggest that some of these Caledonian structures have been reactivated numerous times during the during the Mesozoic and Cenozoic (Redfield et al., 2005; Medvedev and Hartz, 2015; Ksienzyk et al., 2016). It has been suggested that Late Cretaceous topography was asymmetric with the highest areas along the MTFC and lower topographies inboard the HFSZ (Gabrielsen et al., 2010), and Sømme et al. (2013b) estimated relief of around 0.5 km inboard the MTFC in the Late Cretaceous based on the presence of coarse clastic fan systems along the margin. Similarly, Sømme et al. (2013b) estimated that the Late Cretaceous topography was <0.5 km further south, inboard the Stord Basin, based on the absence of coarse clastic material in Late Cretaceous fine-grained sediments. This antecedent topography probably dominated the landscape prior to uplift and the modeled distribution of the Iceland plume (Skogseid et al., 2000; Barnett-Moore et al., 2017) suggest that this pattern was amplified during the Paleocene.

A strong north-south topographic gradient is also inferred from the stratigraphic units mapped in this study (**Figure 11**). On the northern Horda Platform and on the Måløy Slope where also the onshore-offshore gradient was relatively steep (**Figure 2**) and where the rejuvenated topography is estimated to have been 0.6-1.1 km, the Paleocene unit covers an area of ∼12000 km^2 and is up to ∼900 m thick. In the Stord Basin where the onshore-offshore gradients were more gentle, lower dynamic uplift of an already lower antecedent landscape (<0.5 km) produced a significantly smaller (∼600 km^2) and thinner Paleocene unit, which only reached ∼400 m in the Stord Basin.

Another difference between the northern and southern depocenters is the timing of onlap and backstepping. In the area around 35/6-2S, onlap and backstepping occurred in the Ypresian, after the PETM (**Figure 5**). In the Stord Basin, the transition from forced regression to aggradation occurred earlier, within the Thanetian unit, and the main phase of onlap occurred at the top Thanetian horizon (**Figure 8**). This indicates that the transition from low A/S (accommodation space vs. sediment supply) to high A/S conditions took place earlier in southern depocenter. This could be related to regional differences in dynamic topography during the waning phase. Or it could be related to lag-times between timing of uplift and transfer of the erosional signal to the offshore depocenter (Willenbring et al., 2013; Li et al., 2018). Despite a phase of Early Eocene onlap in the north, the area continued to supply coarse clastics throughout the Eocene, indicating significant onshore topography long after break-up (**Figure 3**). In the south, on the other hand, no more coarse clastics were supplied to the basin in the Eocene, suggesting regional backstepping of the depocenter.

Recognizing Tectonic and Climatic Perturbations in Subsurface Data

The initial response to long-term (∼10 Myr) dynamic uplift of SW Norway was the formation of the angular BTU. The BTU is overlain by large slides and channelized mass-transport deposits in the southern part, and sand-dominated slope channels and fan complexes in the northern part of the

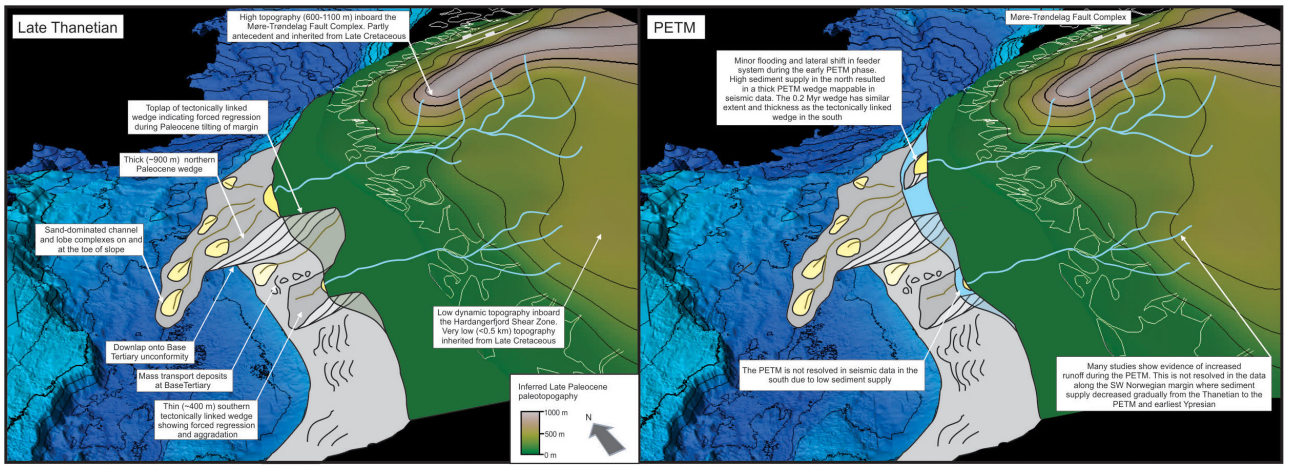

FIGURE 11 | Cartoon showing the inferred topographic and depositional situation in the Late Paleocene and during the PETM. The lower blue surface is the Base Tertiary unconformity. Two tectonically linked wedges prograde into the basin, but the areal extent, internal seismic stratigraphic geometries and thickness depend on along-strike variability in inherited Cretaceous topography and Paleocene dynamic topography. During the 0.2 Myr PETM event, only the northern system had sufficient sediment supply to form a mappable wedge in seismic data. The PETM in the southern area is below seismic resolution. White line shows the present-day coastline. Light blue lines indicate the approximate location of the Paleocene river systems. Cartoon is not to scale.

study area (**Figure 4**). This phase also marks the transition from underfilled (basinward thickening wedge) to overfilled basin configuration (landward thickening wedge), associated with shelf-slope progradation (**Figure 2**). This pattern of angular truncation, mass-wasting, followed by downlap of the shelf-slope wedge is thus considered to be the manifestation of the initial phase of tectonic perturbation along the margin.

Timing of peak dynamic uplift was associated with sediment supply about one order of magnitude higher than before uplift started. The peak uplift phase was also dominated by forced regression where relatively coarse-grained sediments were delivered to local depocenters showing little evidence of lateral shifting of sediment entry points (Selandian and Thanetian in **Figures 3**, **11**). In terms of sediment partitioning, it is expected that most sediments were bypassed to and beyond the shelf break and that little was retained in topset during this phase, similar to what has been described on the East Shetland Platform (e.g., Underhill, 2001).

Decreasing sediment supply in the latest Thanetian (Stord Basin) to early Ypresian (Måløy Slope) coincides with the aggradation, onlap and backstepping of depocenters, as discussed above. Forced regressive wedges overlain by aggradational to backstepping deposits documenting a significant shift toward high A/S conditions and a widening of the depocenters are thus considered to be a manifestation of the relaxing phase of the tectonic perturbation.

High-frequency climate change during the PETM occurred toward the end of the phase of maximum tectonic perturbation. Although the entire margin is believed to have experienced forced regression with high sediment input during the end of the Thanetian, the base of the PETM interval is characterized by a distinct downlap surface, suggesting that a rapid rise in base-level (perhaps in the order of 20–30 m, Sluijs et al., 2008) was sufficient to flood parts of the shelf (**Figures 5**, **9**). Also, the location of the two PETM depocenters on the flanks of the underlying Thanetian wedge indicates compensational stacking and reorganization of the sediment entry points (**Figure 7**). Despite initial reorganization, the PETM interval is overall regressive indicating high sediment supply. But although several PETM sites describe increased continental run-off and sediment supply (Schmitz and Pujalte, 2003; Foreman et al., 2012; Kender et al., 2012; Stassen et al., 2012; Carmichael et al., 2017), the data resolution in this study is not able to resolve a deviation from the longer-term trend (**Figure 10**), and the PETM supply is lower than the preceding Thanetian supply and higher than the following early Ypresian (Balder Fm) supply (**Supplementary Table S1**). The seismic data does not reveal the top of the PETM interval as a key surface and borehole 35/6-2S (**Figure 6**) suggest that the system continued to supply sandy sediment also after the PETM (**Figure 9**). Similar observations have also been described from outcrops, pointing to a potential lag-time between the perturbation of the climate system and the stratigraphic response (Foreman et al., 2012).

Climatic perturbations linked to global warming and relative sea-level rise can thus be recognized by a local downlap surface and reorganization of feeder systems. This is well expressed where the climate perturbation is superimposed on a period of forced regression, but might have been more difficult to identify if the perturbation was superimposed on a longer-term phase of increasing accommodation or strong autogenic behavior (Toby et al., 2019). The climatic events can also readily be recognized in biostratigraphic data, but this study shows that they may not cause a change in sediment supply that is detectable in seismic data. In addition, these PETM depocenters are local (~80–120 km^2) compared to the overall Thanetian wedge (~12000 km^2), indicating that they could have been missed if only 2D seismic reflection data was available, or wrongly interpreted without borehole and biostratigraphic data.

Since the thickness and lateral extent of the climatic wedges in the north are similar to the tectonic wedge in the south (**Figure 7**), it is clear that the morphometrics of the individual routing system and the resulting sediment supply is instrumental for how tectonic and climatic perturbations can be recognized and separated in subsurface data. In a relatively low-supply system like the one in the Stord Basin, a short-lived event like the PETM will be below seismic resolution and can only be recognized in borehole data with high-resolution biostratigraphic sampling (**Figure 11**; e.g., Kender et al., 2012). Only a multi-million-year tectonic perturbation leaves a mappable shelf-slope wedge in this area (**Figure 8**). If the sediment supply from a catchment is sufficiently high (>∼0.9 MT/yr) like in the northern area, and if the sediments are deposited in areas with relatively high accommodation, we infer that short-lived climatic perturbations can produce stratigraphic units that are mappable on seismic data. This study shows that thickness, sediment supply and areal extent of the resulting shelf-slope wedges may not be sufficient to recognize the same perturbations in different systems and that internal stratigraphic architecture is the best recognition criteria across all scales.

CONCLUSION

- This study documents a tectonically linked, shelf-slope wedge (up to 900 m thick) that resulted from ∼10 million years of gradual uplift and hinterland denudation of the Norwegian landmass in the Paleocene. The thickness of the wedge varies significantly along strike depending on antecedent topography and later dynamic uplift.
- The wedge is recognized by an angular unconformity at the base, which formed in response to slope steepening and mass-wasting of underlying sediments. The unconformity is downlapped by progradational shelf-slope wedges that can be tied to specific sediment entry points. In the Stord Basin, internal toplap geometries indicates forced regression. The top of the wedges is marked by a regional onlap surface of earliest Eocene age.
- Superimposed on the tectonically linked Paleocene wedge, two localized, climatically linked depocenters have been mapped. The areal extent of these wedges is an order of magnitude smaller than the underlying tectonic wedge. The northern wedge, which is well-constrained by biostratigraphic data, is up to 130 m thick and represents 150–200 kyr of deposition during the PETM.
- The climatically linked wedges are marked by a minor flooding surface at the base, which is recognized in both seismic and borehole data, documenting early PETM reorganization of the sediment dispersal system to the flanks of the underlying Thanetian system. The top of the wedge is not characterized by changes in lithology or specific stratal terminations in seismic data.
- Recognition of high-frequency climatic perturbations in seismic data depends on sediment supply and available accommodation space at the time of deposition. In relatively high accommodation settings where sediment supply is least 0.9 MT/yr, climate perturbations operating at 10^4 year time-scales have the potential to leave stratigraphic units that can be mapped in seismic data. In areas with significantly lower supply, the resulting stratigraphic response might be below seismic resolution, like in the southern Stord Basin.
- Key differences between tectonically and climatically linked wedges within the same routing system are the areal extent and the internal stratal geometries of the depositional units.
- When comparing different systems along strike, thickness, areal extent and sediment supply estimates alone is not diagnostic of specific perturbations. Internal stacking patterns and stratal termination styles are the best tools to separate climatic vs. tectonic perturbations in the study area.

DATA AVAILABILITY STATEMENT

The main dataset used in this study (seismic survey CGG18M01) is not publicly available and is the property of CGG MCNV. 2D seismic reflection lines from TE90 and original borehole data are publicly available by request through the Diskos databank (https://portal.diskos.cgg.com/whereoil-data/).

AUTHOR CONTRIBUTIONS

TS designed the study, conducted the main analysis, and wrote the main body of the manuscript. JS, PE, and HL were involved in data interpretation, discussion, and manuscript writing.

FUNDING

This study was funded by Equinor ASA.

ACKNOWLEDGMENTS

We thank Equinor for permission to publish this study and CGG MCNV for allowing us to publish seismic data. Torbjørn Dahlgren, Torbjørn Fristad, and Arthur Guillien have provided input and valuable discussions. Trond Torsvik kindly provided age data for the North Atlantic Igneous Province. The editor and reviewers contributed valuable comments and suggestions, which helped to improve the manuscript.

SUPPLEMENTARY MATERIAL

The Supplementary Material for this article can be found online at: https://www.frontiersin.org/articles/10.3389/feart.2019.00303/full#supplementary-material

TABLE S1 | Morphometrics and calculated sediment supplies for the different stratigraphic units.

REFERENCES

Abdelmalak, M., Planke, S., Faleide, J., Jerram, D., Zastrozhnov, D., Eide, S., et al. (2016). The development of volcanic sequences at rifted margins: new insights from the structure and morphology of the Vøring Escarpment, mid – Norwegian Margin. *J. Geophys. Res.* 121, 5212–5236. doi: 10.1002/2015jb012788

Andersen, T. B. (1998). Extensional tectonics in the caledonides of southern Norway, an overview. *Tectonophysics* 285, 333–351. doi: 10.1016/s0040-1951(97)00277-271

Allen, P.A. (2008). "Time scales of tectonic landscapes and their sediment routing systems," in *Landscape Evolution : Denudation, Climate and Tectonics Over Different Time and Space Scales*, eds K. Gallagher, S.J. Jones, & J. Wainwright. (London: Geological Society Of London), 7–28. doi: 10.1144/sp296.2

Anell, I., Thybo, H., and Artemieva, I. M. (2009). Cenozoic uplift and subsidence in the North Atlantic region: geological evidence revisited. *Tectonophysics* 474, 78–105. doi: 10.1016/j.tecto.2009.04.006

Anell, I., Thybo, H., and Stratford, W. (2010). Relating Cenozoic North Sea sediments to topography in southern Norway: the interplay between tectonics and climate. *Earth Planet. Sci. Lett.* 300, 19–32. doi: 10.1016/j.epsl.2010.09.009

Baby, G., Guillocheau, F., Morin, J., Ressouche, J., Robin, C., Broucke, O., et al. (2018). Post-rift stratigraphic evolution of the Atlantic margin of Namibia and South Africa: implications for the vertical movements of the margin and the uplift history of the South African Plateau. *Mar. Pet. Geol.* 97, 169–191. doi: 10.1016/j.marpetgeo.2018.06.030

Baig, I., Faleide, J. I., Mondol, N. H., and Jahren, J. (2019). Burial and exhumation history controls on shale compaction and thermal maturity along the Norwegian North Sea basin margin areas. *Mar. Pet. Geol.* 104, 61–85. doi: 10.1016/j.marpetgeo.2019.03.010

Barnett-Moore, N., Hassan, R., Flament, N., and Muller, R. D. (2017). The deep Earth origin of the Iceland plume and its effects on regional surface uplift and subsidence. *Solid Earth* 8, 235–254. doi: 10.5194/se-8-235-2017

Braun, J., Guillocheau, F., Robin, C., Baby, G., and Jelsma, H. (2014). Rapid erosion of the Southern African Plateau as it climbs over a mantle superswell. *J. Geophys. Res.* 119, 6093–6112. doi: 10.1002/2014jb010998

Bugge, T., Tveiten, B., and Bäckström, S. (2001). "The depositional history of the Cretaceous in the northeastern north sea," in *Sedimentary Environments Offshore Norway - Palaeozoic to Recent*, eds O. J. Martinsen, and T. Dreyer, (Berlin: Elsevier), 279–291. doi: 10.1016/s0928-8937(01)80018-7

Burgess, P. M., and Prince, G. D. (2015). Non-unique stratal geometries: implications for sequence stratigraphic interpretations. *Basin Res.* 27, 351–365. doi: 10.1111/bre.12082

Campanile, D., Nambiar, C. G., Bishop, P., Widdowson, M., and Brown, R. (2008). Sedimentation record in the Konkan-Kerala Basin: implications for the evolution of the Western Ghats and the Western Indian passive margin. *Basin Res.* 20, 3–22. doi: 10.1111/j.1365-2117.2007.00341.x

Carmichael, M. J., Inglis, G. N., Badger, M. P., Naafs, B. D. A., Behrooz, L., Remmelzwaal, S., et al. (2017). Hydrological and associated biogeochemical consequences of rapid global warming during the Paleocene-Eocene Thermal Maximum. *Glob. Planet. Change* 157, 114–138. doi: 10.1016/j.gloplacha.2017.07.014

Castelltort, S., and Van den Driessche, J. (2003). How plausible are high-frequency sediment supply-driven cycles in the stratigraphic record? *Sedimentary Geol.* 157, 3–13. doi: 10.1016/s0037-0738(03)00066-6

Dam, G., Larsen, M., and Sønderholm, M. (1998). Sedimentary response to mantle plumes: implications from Paleocene onshore successions, West and East Greenland. *Geology* 26, 207–210.

Dmitrieva, E., Jackson, C. A.-L., Huuse, M., and Kane, I. A. (2018). "Regional distribution and controls on the development of post-rift turbidite systems: insights from the Paleocene of the eastern North Viking Graben, offshore Norway," in *Proceedings of the Geological Society, London, Petroleum Geology Conference series*, London.

Duller, R. A., Armitage, J. J., Manners, H. R., Grimes, S., and Jones, T. D. (2019). Delayed sedimentary response to abrupt climate change at the Paleocene-Eocene boundary, northern Spain. *Geology* 47, 159–162. doi: 10.1130/g45631.1

Dypvik, H., Riber, L., Burca, F., Rüther, D., Jargvoll, D., Nagy, J., et al. (2011). The Paleocene–Eocene thermal maximum (PETM) in Svalbard—clay mineral and geochemical signals. *Palaeogeogr. Palaeoclimatol. Palaeoecol.* 302, 156–169. doi: 10.1016/j.palaeo.2010.12.025

Eide, C. H., Müller, R., and Helland-Hansen, W. (2018). Using climate to relate water discharge and area in modern and ancient catchments. *Sedimentology* 65, 1378–1389. doi: 10.1111/sed.12426

Eldholm, O., Thiede, J., and Taylor, E. eds (1989). "Evolution of the Vøring volcanic margin," in *Proceedings of the Ocean Drilling Program. Scientific Results*, (Ocean Drilling Program: College Station. TX), 1033-1065.

Eldrett, J., Greenwood, D., Polling, M., Brinkhuis, H., and Sluijs, A. (2014). A seasonality trigger for carbon injection at the Paleocene–Eocene Thermal Maximum. *Clim. Past* 10, 759–769. doi: 10.5194/cp-10-759-2014

Faleide, J. I., Kyrkjebø, R., Kjennerud, T., Gabrielsen, R. H., and Jordt, H. (2002). "Tectonic impact on sedimentary processes during Cenozoic evolution of the northern North Sea and surrounding areas," in *Exhumation of the North Atlantic Margin: Timing, Mechanisms, and Implications for Petroleum Exploration: Geological Society (London) Special Publication*, eds A. G. Doré, J. A. Cartwright, M. S. Stoker, J. P. Turner, and N. White, (London: Geological Society Of London), 235–269. doi: 10.1144/gsl.sp.2002.196.01.14

Foreman, B. Z., Heller, P. L., and Clementz, M. T. (2012). Fluvial response to abrupt global warming at the Palaeocene/Eocene boundary. *Nature* 491:92. doi: 10.1038/nature11513

Forzoni, A., Storms, J. E., Whittaker, A. C., and de Jager, G. (2014). Delayed delivery from the sediment factory: modeling the impact of catchment response time to tectonics on sediment supply and fluvio-deltaic stratigraphy. *Earth Surf. Process. Landforms* 39, 689–704. doi: 10.1002/esp.3538

Fossen, H., and Dunlap, W. J. (1998). Timing and kinematics of Caledonian thrusting and extensional collapse, southern Norway: evidence from Ar-40/Ar-39 thermochronology. *J. Struct. Geol.* 20, 765–781. doi: 10.1016/s0191-8141(98)00007-8

Fossen, H., Khani, H. F., Faleide, J. I., Ksienzyk, A. K., and Dunlap, W. J. (2017). Post-Caledonian extension in the West Norway–northern North Sea region: the role of structural inheritance. *Geol. Soc. Lond. Special Publ.* 439, 465–486. doi: 10.1144/sp439.6

Gabrielsen, R. H., Faleide, J. I., Pascal, C., Braathen, A., Nystuen, J. P., Etzelmuller, B., et al. (2010). Latest Caledonian to Present tectonomorphological development of southern Norway. *Mar. Pet. Geol.* 27, 709–723. doi: 10.1016/j.marpetgeo.2009.06.004

Gale, A. S., and Lovell, B. (2018). The Cretaceous–Paleogene unconformity in England: uplift and erosion related to the iceland mantle plume. *Proceedings of the Geologists'. Association* 129, 421–435. doi: 10.1016/j.pgeola.2017.04.002

Gjelberg, J. G., Enoksen, T., Kjaernes, P., Mangerud, G., Martinsen, O. J., Roe, E., et al. (2001). "The Maastrichtian and Danian depositional setting, along the eastern margin of the Møre Basin (mid-Norwegian Shelf): implications for reservoir development of the Ormen Lange Field," in *Sedimentary Environments Offshore Norway - Paleozoic to Recent*, eds O. J. Martinsen, and T. Dreyer, (Berlin: Elsevier), 421–440. doi: 10.1016/s0928-8937(01)80025-4

Gradstein, F., and Backstrøm, S. (1996). Cainozoic biostratigraphy and palaeobathymetry, northern North Sea and Haltenbanken. *Norsk Geol. Tidsskrift* 76, 3–32.

Gradstein, F. M., Kaminski, M. A., Berggren, W. A., Kristiansen, I. L., and D'Iorio, M. A. (1994). Cenozoic Biostratigraphy of the North Sea and Labrador Shelf. *Micropaleontology* 40, 3–32. doi: 10.2307/1485906

Gradstein, F. M., Ogg, J. G., Schmitz, M., and Ogg, G. (2012). *The Geologic Time Scale 2012*. Berlin: Elsevier.

Guarnieri, P. (2015). Pre-break-up palaeostress state along the East Greenland margin. *J. Geol. Soc.* 172, 727–739. doi: 10.1144/jgs2015-053

Hafeez, A., Planke, S., Jerram, D. A., Millett, J. M., Maharjan, D., and Prestvik, T. (2017). Upper Paleocene ultramafic igneous rocks offshore mid-Norway: reinterpretation of the Vestbrona Formation as a sill complex. *Interpretation* 5, SK103–SK120.

Hall, A. M., Gilg, H. A., Fallick, A. E., and Merritt, J. W. (2015). Kaolins in gravels and saprolites in north-east Scotland: evidence from stable H and O isotopes for Palaeocene–Miocene deep weathering. *Palaeogeogr. Palaeoclimatol. Palaeoecol.* 424, 6–16. doi: 10.1016/j.palaeo.2015.02.019

Hamberg, L., Dam, G., Wilhelmson, C., and Ottesen, T. G. (2005). "Paleocene deep-marine sandstone plays in the Siri Canyon, offshore Denmark-southern Norway," in *Petroleum Geology; North-West Europe and Global Perspectives; Proceedings of the 6th Petroleum Geology Conference*, eds A. G. Doré, and B. A. Vining, (London: Geological Society London), 1185–1198. doi: 10.1144/0061185

Hartley, R. A., Roberts, G. G., White, N., and Richardson, C. (2011). Transient convective uplift of an ancient buried landscape. *Nat. Geosci.* 4:562. doi: 10.1038/ngeo1191

Jackson, C. A. L., Barber, G. P., and Martinsen, O. J. (2008). Submarine slope morphology as a control on the development of sand-rich turbidite depositional systems: 3D seismic analysis of the Kyrre Fm (Upper Cretaceous), Maloy Slope, offshore Norway. *Mar. Pet. Geol.* 25, 663–680. doi: 10.1016/j.marpetgeo.2007.12.007

Jarsve, E. M., Faleide, J., Gabrielsen, R., Nystuen, J. P., Martinius, A., Ravnås, R., et al. (2014). "Mesozoic and Cenozoic basin configurations in the North Sea," in *From Depositional Systems to Sedimentary Successions on the Norwegian Continental Margin*, eds A. W. Martinius, R. Ravnås, J. Howell, T. Olsen, R. J. Steel, and J. Wonham, 417–452. doi: 10.1002/9781118920435.ch15

Jones, R. W., and Milton, N. J. (1994). Sequence development during uplift: palaeogene stratigraphy and relative sea-level history of the outer Moray Firth. UK North Sea. *Mar. Pet. Geol.* 11, 157–165. doi: 10.1016/0264-8172(94)90092-2

Jones, S. M., White, N., Clarke, B. J., Rowley, E., and Gallagher, K. (2002). "Present and past influence of the Iceland Plume on sedimentation," in *Geological Society, London, Special Publications*, eds A. G. Doré, J. A. Cartwright, M. S. Stoker, J. P. Turner, and N. J. White, (London: Geological Society London), 13–25. doi: 10.1144/gsl.sp.2002.196.01.02

Jordt, H., Faleide, J. I., Bjorlykke, K., and Ibrahim, M. T. (1995). Cenozoic Sequence Stratigraphy of the Central and Northern North-Sea Basin – Tectonic Development, Sediment Distribution and Provenance Areas. *Mar. Pet. Geol.* 12, 845–879. doi: 10.1016/0264-8172(95)98852-v

Jordt, H., Thyberg, B. I., and Nottvedt, A. (2000). "Cenozoic evolution of the central and northern North Sea with focus on differential vertical movements of the basin floor and surrounding clastic source areas," in *Dynamics of the Norwegian margin: Geological Society (London) Special Publication*, eds A. Nøttvedt, and B. T. Larsen, (London: Geological Society London), 219–243. doi: 10.1144/gsl.sp.2000.167.01.09

Kender, S., Stephenson, M. H., Riding, J. B., Leng, M. J., Knox, R. W. B., Peck, V. L., et al. (2012). Marine and terrestrial environmental changes in NW Europe preceding carbon release at the Paleocene–Eocene transition. *Earth Planet. Sci. Lett.* 353, 108–120. doi: 10.1016/j.epsl.2012.08.011

Kennett, J. P., and Stott, L. (1991). Abrupt deep-sea warming, palaeoceanographic changes and benthic extinctions at the end of the Palaeocene. *Nature* 353:225. doi: 10.1038/353225a0

Kjoberg, S., Schmiedel, T., Planke, S., Svensen, H. H., Millett, J. M., Jerram, D. A., et al. (2017). 3D structure and formation of hydrothermal vent complexes at the Paleocene-Eocene transition, the Møre Basin, mid-Norwegian margin. *Interpretation* 5, SK65–SK81.

Ksienzyk, A. K., Wemmer, K., Jacobs, J., Fossen, H., Schomberg, A. C., Süssenberger, A., et al. (2016). Post-Caledonian brittle deformation in the Bergen area, West Norway: results from K–Ar illite fault gouge dating. *Nor. J. Geol.* 96, 275–299.

Li, Q., Gasparini, N. M., and Straub, K. M. (2018). Some signals are not the same as they appear: how do erosional landscapes transform tectonic history into sediment supply records? *Geology* 46, 407–410. doi: 10.1130/g40026.1

Liu, X., and Galloway, W. E. (1997). Quantitative determination of tertiary sediment supply to the North Sea Basin. *AAPG Bull.* 81, 1482–1509.

Mackay, L., Turner, J., Jones, S., and White, N. (2005). Cenozoic vertical motions in the Moray Firth Basin associated with initiation of the Iceland Plume. *Tectonics* 24:23. doi: 10.1029/2004TC001683

Mancin, N., Di Giulio, A., and Cobianchi, M. (2009). Tectonic vs. climate forcing in the Cenozoic sedimentary evolution of a forelandbasin (Eastern Southalpine system. Italy). *Basin Res.* 21, 799–823. doi: 10.1111/j.1365-2117.2009.00402.x

Martinsen, O. J., Boen, F., Charnock, M. A., Mangerud, G., and Nottvedt, A. (1999). "Cenozoic development of the Norwegian margin 60-64 degrees N; sequences and sedimentary response to variable basin physiography and tectonic setting," in *Petroleum Geology of Northwest Europe: Proceedings of the 5th Conference: Geological Society (London)*, eds A. J. Fleet, S. A. R. Boldy, and S. D. Burley, (London: Geological Society London), 293–304. doi: 10.1144/0050293

Martinsen, O. J., Lien, T., and Jackson, C. (2005). "Cretaceous and Palaeogene turbidite systems in the North Sea and Norwegian Sea Basins: source, staging area and basin physiography controls on reservoir development," in *Petroleum Geology: North-West Europe and Global Perspectives - Proceedings of the 6th Petroleum Geology Conference: Geological Society (London)*, ed. A. Vining, (London: Geological Society London), 1147–1164. doi: 10.1144/0061147

Medvedev, S., and Hartz, E. H. (2015). Evolution of topography of post-Devonian Scandinavia: effects and rates of erosion. *Geomorphology* 231, 229–245. doi: 10.1016/j.geomorph.2014.12.010

Mitlehner, A. G. (1996). Palaeoenvironments in the North Sea Basin around the Paleocene-Eocene boundary: evidence from diatoms and other siliceous microfossils. *Geol. Soc. Lond. Special Publ.* 101, 255–273. doi: 10.1144/gsl.sp.1996.101.01.15

Morton, A. C. (1992). "Provenance of Brent Group sandstones: heavy mineral constraints," in *Geology of the Brent Group*, eds A. C. Morton, R. S. Hasszeldine, M. R. Giles, and S. Brown, (London: Geological Society London), 227–244. doi: 10.1144/gsl.sp.1992.061.01.13

Mudge, D. C. (2015). "Regional controls on Lower Tertiary sandstone distribution in the North Sea and NE Atlantic margin basins," in *Geological Society, London, Special Publications*, eds T. McKie, P. T. S. Rose, A. J. Hartley, D. W. Jones, and T. L. Armstrong, (London: Geological Society London), 17–42. doi: 10.1144/sp403.5

Nadin, P., and Kusznir, N. (1995). Palaeocene uplift and Eocene subsidence in the northern North Sea Basin from 2D forward and reverse stratigraphic modelling. *J. Geol. Soc.* 152, 833–848. doi: 10.1144/gsjgs.152.5.0833

Nagy, J., Jargvoll, D., Dypvik, H., Jochmann, M., and Riber, L. (2013). Environmental changes during the Paleocene–Eocene Thermal Maximum in Spitsbergen as reflected by benthic foraminifera. *Pol. Res.* 32:19737. doi: 10.3402/polar.v32i0.19737

Nielsen, O. B., Rasmussen, E. S., and Thyberg, B. I. (2015). Distribution of clay minerals in the Northern North Sea basin during the Paleogene and Neogene: a result of source-area geology and sorting processes. *J. Sedimentary Res.* 85, 562–581. doi: 10.2110/jsr.2015.40

Ottesen, D., Dowdeswell, J. A., and Bugge, T. (2014). Morphology, sedimentary infill and depositional environments of the Early Quaternary North Sea Basin (56–62 N). *Mar. Pet. Geol.* 56, 123–146. doi: 10.1016/j.marpetgeo.2014.04.007

Overeem, I., Weltje, G. J., Bishop-Kay, C., and Kroonenberg, S. (2001). The Late Cenozoic Eridanos delta system in the Southern North Sea Basin: a climate signal in sediment supply? *Basin Res.* 13, 293–312. doi: 10.1046/j.1365-2117.2001.00151.x

Peizhen, Z., Molnar, P., and Downs, W. R. (2001). Increased sedimentation rates and grain sizes 2–4 Myr ago due to the influence of climate change on erosion rates. *Nature* 410:891. doi: 10.1038/35073504

Planke, S., and Alvestad, E. (1999). Seismic volcanostratigraphy of the extrusive breakup complexes in the northeast Atlantic: implications from ODP/DSDP drilling. *Proc. Ocean Drill. Prog.* 163, 3–16.

Praeg, D., Stoker, M. S., Shannon, P. M., Ceramicola, S., Hjelstuen, B., Laberg, J. S., et al. (2005). Episodic Cenozoic tectonism and the development of the NW European 'passive' continental margin. *Mar. Pet. Geol.* 22, 1007–1030. doi: 10.1016/j.marpetgeo.2005.03.014

Redfield, T. F., Osmundsen, P. T., and Hendriks, B. W. H. (2005). The role of fault reactivation and growth in the uplift of western Fennoscandia. *J. Geol. Soc.* 162, 1013–1030. doi: 10.1144/0016-764904-149

Riis, F. (1996). Quantification of Cenozoic vertical movements of Scandinavia by correlation of morphological surfaces with offshore data. *Glob. Planet. Change* 12, 331–357. doi: 10.1016/0921-8181(95)00027-5

Ritchie, J., Gatliff, R., and Richards, P. (1999). "Early Tertiary magmatism in the offshore NW UK margin and surrounds," in *Proceedings of the Geological Society, London, Petroleum Geology Conference series*, London.

Röhl, U., Westerhold, T., Bralower, T. J., and Zachos, J. C. (2007). On the duration of the Paleocene – Eocene thermal maximum (PETM). *Geochem. Geophys. Geosyst.* 8.

Romans, B. W., Castelltort, S., Covault, J. A., Fildani, A., and Walsh, J. (2016). Environmental signal propagation in sedimentary systems across timescales. *Earth Sci. Rev.* 153, 7–29. doi: 10.1016/j.earscirev.2015.07.012

Samanta, A., Bera, M. K., and Sarkar, A. (2016). Climate-modulated sequence development in a tropical rift basin during the Late Palaeocene to Early Eocene super greenhouse Earth. *Sedimentology* 63, 917–939. doi: 10.1111/sed.12243

Schmitz, B., and Pujalte, V. (2003). Sea-level, humidity, and land-erosion records across the initial Eocene thermal maximum from a continental-marine transect in northern Spain. *Geology* 31, 689–692.

Séranne, M. (1999). Early Oligocene stratigraphic turnover on the west Africa continental margin: a signature of the Tertiary greenhouse-to-icehouse transition? *Terra Nova Oxford* 11, 135–140. doi: 10.1046/j.1365-3121.1999.00246.x

Shaw Champion, M., White, N., Jones, S., and Lovell, J. (2008). Quantifying transient mantle convective uplift: an example from the Faroe – Shetland basin. *Tectonics* 27:TC1002.

Skogseid, J., Planke, S., Faleide, J. I., Pedersen, T., Eldholm, O., and Neverdal, F. (2000). NE Atlantic continental rifting and volcanic margin formation. *Geol. Soc. Lond. Special Publ.* 167, 295–326. doi: 10.1144/gsl.sp.2000.167.01.12

Sluijs, A., Bowen, G., Brinkhuis, H., Lourens, L., and Thomas, E. (2007). The Palaeocene-Eocene Thermal Maximum super greenhouse: biotic and geochemical signatures, age models and mechanisms of global change. *Deep Time Pers. Clim. Change* 2, 323–349. doi: 10.1144/tms002.15

Sluijs, A., Brinkhuis, H., Crouch, E. M., John, C. M., Handley, L., Munsterman, D., et al. (2008). Eustatic variations during the Paleocene – Eocene greenhouse world. *Paleoceanography* 23, A4216.

Smallwood, J. R., and Gill, C. E. (2002). The rise and fall of the Faroe–Shetland Basin: evidence from seismic mapping of the balder Formation. *J. Geol. Soc.* 159, 627–630. doi: 10.1144/0016-764902-064

Sømme, T. O., Jackson, C. A. L., and Vaksdal, M. (2013a). Source-to-sink analysis of ancient sedimentary systems using a subsurface case study from the Møre-Trøndelag area of southern Norway: Part 1 – depositional setting and fan evolution. *Basin Res.* 25, 489–511. doi: 10.1111/bre.12013

Sømme, T. O., Martinsen, O. J., and Lunt, I. (2013b). Linking offshore stratigraphy to onshore paleotopography: the Late Jurassic–Paleocene evolution of the south Norwegian margin. *Geol. Soc. Am. Bull.* 125, 1164–1186. doi: 10.1130/b30747.1

Soutter, E. L., Kane, I. A., and Huuse, M. (2018). Giant submarine landslide triggered by Paleocene mantle plume activity in the North Atlantic. *Geology* 46, 511–514. doi: 10.1130/g40308.1

Stassen, P., Dupuis, C., Steurbaut, E., Yans, J., and Speijer, R. P. (2012). Perturbation of a Tethyan coastal environment during the Paleocene–Eocene thermal maximum in Tunisia (Sidi Nasseur and Wadi Mezaz). *Palaeogeogr. Palaeoclimatol. Palaeoecol.* 317, 66–92. doi: 10.1016/j.palaeo.2011.12.011

Steel, R., and Ryseth, A. (1990). "The Triassic—Early Jurassic succession in the northern North Sea: megasequence stratigraphy and intra-Triassic tectonics," in *Geological Society, London, Special Publications*, eds R. F. P. Hardman, and J. Brooks, (London: Geological Society London), 139–168. doi: 10.1144/gsl.sp.1990.055.01.07

Steel, R. J. (1993). "Triassic-Jurassic megasequence stratigraphy in the Northern North Sea: rift to post-rift evolution," in *Petroleum Geology of Northwest Europe: Proceedings of the 4th Conference: Geological Society London*, eds J. R. Parker, and I. D. Bartholomew, (London: Geological Society London), 299–315. doi: 10.1144/0040299

Steinberger, B., Bredow, E., Lebedev, S., Schaeffer, A., and Torsvik, T. H. (2019). Widespread volcanism in the Greenland–North Atlantic region explained by the Iceland plume. *Nat. Geosci.* 12:61. doi: 10.1038/s41561-018-0251-0

Stoker, M. S., Holford, S. P., and Hillis, R. R. (2018). A rift-to-drift record of vertical crustal motions in the Faroe–Shetland Basin, NW European margin: establishing constraints on NE Atlantic evolution. *J. Geol. Soc.* 175, 263–274. doi: 10.1144/jgs2017-076

Stucky de Quay, G., Roberts, G., Watson, J., and Jackson, C. L. (2017). Incipient mantle plume evolution: constraints from ancient landscapes buried beneath the North Sea. *Geochem. Geophys. Geosyst.* 18, 973–993. doi: 10.1002/2016gc006769

Stuevold, L. M., and Eldholm, O. (1996). Cenozoic uplift of Fennoscandia inferred from a study of the mid-Norwegian margin. *Glob. Planet. Change* 12, 359–386. doi: 10.1016/0921-8181(95)00028-3

Svensen, H., Planke, S., Malthe-Sørenssen, A., Jamtveit, B., Myklebust, R., Eidem, T. R., et al. (2004). Release of methane from a volcanic basin as a mechanism for initial Eocene global warming. *Nature* 429:542. doi: 10.1038/nature02566

Syvitski, J. P. M., and Milliman, J. D. (2007). Geology, geography, and humans battle for dominance over the delivery of fluvial sediment to the coastal ocean. *J. Geol.* 115, 1–19. doi: 10.1086/509246

Tinker, J., de Wit, M., and Brown, R. (2008). Linking source and sink: evaluating the balance between onshore erosion and offshore sediment accumulation since Gondwana break-up, South Africa. *Tectonophysics* 455, 94–103. doi: 10.1016/j.tecto.2007.11.040

Toby, S. C., Duller, R. A., De Angelis, S., and Straub, K. M. (2019). A stratigraphic framework for the preservation and shredding of environmental signals. *Geophys. Res. Lett.* 46, 5837–5845.

Torske, T. (1975). Possible Mesozoic mantle plume activity beneath the continental margin of Norway. *Norges Geologiske Undersøkelse* 322, 73–90.

Torsvik, T. H., Amundsen, H. E., Trønnes, R. G., Doubrovine, P. V., Gaina, C., Kusznir, N. J., et al. (2015). Continental crust beneath southeast Iceland. *Proc. Natl. Acad. Sci. U.S.A.* 112, E1818–E1827. doi: 10.1073/pnas.1423099112

Underhill, J. R. (2001). Controls on the genesis and prospectivity of Paleogene palaeogeomorphic traps, East Shetland Platform, UK North Sea. *Mar. Pet. Geol.* 18, 259–281. doi: 10.1016/s0264-8172(00)00067-2

Watkins, S. E., Whittaker, A. C., Bell, R. E., McNeill, L. C., Gawthorpe, R. L., Brooke, S. A., et al. (2018). Are landscapes buffered to high-frequency climate change? A comparison of sediment supplyes and depositional volumes in the Corinth Rift, central Greece, over the past 130 ky. *Bulletin* 131, 372–388. doi: 10.1130/b31953.1

White, N., and Lovell, B. (1997). Measuring the pulse of a plume with the sedimentary record. *Nature* 387, 888–891. doi: 10.1038/43151

Whittaker, A. C., Attal, M., and Allenn, P. A. (2010). Characterising the origin, nature and fate of sediment exported from catchments perturbed by active tectonics. *Basin Res.* 22, 809–828. doi: 10.1111/j.1365-2117.2009.00447.x

Wien, S. T., and Kjennerud, T. (2005). "3D cretaceous to Cenozoic palaeobathymetry of the northern North Sea," in *Onshore-Offshore Relationships on the North Atlantic Margin: Norwegian Petroleum Society Special Publication*, eds B. Wandås, T. G. E. Eide, A. F. Gradstein, and J. Nystuen, (Berlin: Elsevier), 241–253. doi: 10.1016/s0928-8937(05)80051-7

Willenbring, J. K., Gasparini, N. M., Crosby, B. T., and Brocard, G. (2013). What does a mean mean? The temporal evolution of detrital cosmogenic denudation rates in a transient landscape. *Geology* 41, 1215–1218. doi: 10.1130/g34746.1

Wu, H., Ji, Y., Wu, C., Duclaux, G., Gao, C., Li, L., et al. (2019). Stratigraphic response to spatiotemporally varying tectonic forcing in rifted continental basin: insight from a coupled tectonic-stratigraphic numerical model. *Basin Res.* 31, 311–336. doi: 10.1111/bre.12322

Zhang, L., Hay, W. W., Wang, C., and Gu, X. (2019). The evolution of latitudinal temperature gradients from the latest Cretaceous through the Present. *Earth Sci. Rev.* 189, 147–158. doi: 10.1016/j.earscirev.2019.01.025

Conflict of Interest: All authors were employed by company Equinor ASA.

APPENDIX

Here we describe the procedure and uncertainties associated with the inverse BQART modeling used to estimate changes in topography during the Maastrichtian-Eocene. A more detailed description can be found in Sømme et al. (2013b). Syvitski and Milliman (2007) showed that the sediment supply (Qs) from modern catchments best can be explained by the combination of an anthropogenic and lithology factor (B), water discharge (Q), catchment area (A), relief (R) and temperature (T), so that $Qs = wBQ^{0.31}A^{0.5}RT$. Here we assume that all parameters going into the equation can be estimated for the Maastrichtian, Paleocene and Eocene, so that the equation can be solved with respect to R to estimate topography for the respective time intervals. The uncertainty range associated with each parameter is used in a Monte Carlo simulation to make a statistical weighted prediction of the paleotopography.

Sediment supply (Qs) is based on seismically defined isochores. The volume is converted to mass using density data from all boreholes penetrating the relevant succession. The calculated mass per stage is considered to be absolute minimum supply, since parts of the Paleocene-Eocene wedge is truncated by the BTU. In order to accommodate for this, we add 25% to the mass as a maximum case (see Sømme et al., 2013b for discussion). Since the Paleocene-Eocene wedge prograded by forced regression, the amount of sediment initially trapped in topsets is considered to have been very low. Local preservation of what appears to be shelf breaks also indicate that the amount of erosion was limited.

Water discharge (Q) is difficult to constrain for the Paleocene. Paleo water discharge is therefore estimated using the inferred size of the catchment together with the overall climatic setting (Syvitski and Milliman, 2007). Here we use a revised version of the discharge prediction as suggested by Eide et al. (2018) for wet climates, so that $Q = 0.0873A^{0.9164}$.

Maximum catchment area (A) is taken to extend around 100 km inland and is constrained by the inner boundary faults of the Hardangerfjord Shear Zone. This, together with the Møre-Trøndelag Fault Complex is believed to have been active in the Paleocene (Redfield et al., 2005; Fossen et al., 2017, Kziensyk pers comm), setting up a regional drainage divide (**Figure 11**). A minimum extent of around 50 km inland is assumed based on dating of active faults between the inner boundary fault and the basin margin (Kziensyk pers comm).

Paleocene-Eocene temperatures (T) in the North Sea are generally believed to have been warm and humid to tropical (Nielsen et al., 2015). The presence of temperate to tropical *Spiniferites ramosus grp* in 35/6-2S suggest paleoclimatic changes throughout the succession, with the warmest period in the Thanetian (**Figure 6**). Recent review by Zhang et al. (2019) suggest terrestrial Paleocene-Eocene temperatures in the range of 20–25°C, which is similar to 23 ± 5°C as suggested by Hall et al. (2015) based in deep weathering in Scotland. Here we use the latter range of 23 ± 5°C as input to the model.

frontiers in Earth Science

ORIGINAL RESEARCH
published: 28 November 2019
doi: 10.3389/feart.2019.00302

Selective Recording of Tectonic Forcings in an Oligocene/Miocene Submarine Channel System: Insights From New Age Constraints and Sediment Volumes From the Austrian Northern Alpine Foreland Basin

Julian Hülscher[1], Gero Fischer[1], Patrick Grunert[2], Gerald Auer[3] and Anne Bernhardt[1]**

[1] Institute of Geological Sciences, Tectonics and Sedimentary Systems, Freie Universität Berlin, Berlin, Germany, [2] Institute of Geology and Mineralogy, University of Cologne, Cologne, Germany, [3] Research Institute for Marine Resources Utilization (Biogeochemistry Program), Japan Agency for Marine-Earth Science and Technology, Yokosuka, Japan

OPEN ACCESS

Edited by:
Julie Fosdick,
University of Connecticut,
United States

Reviewed by:
Reinhard F. Sachsenhofer,
University of Leoben, Austria
Jorge Lorenzo-Trueba,
Montclair State University,
United States

***Correspondence:**
Julian Hülscher
julian.huelscher@fu-berlin.de
Anne Bernhardt
anne.bernhardt@fu-berlin.de

Specialty section:
This article was submitted to Sedimentology, Stratigraphy and Diagenesis, a section of the journal Frontiers in Earth Science

Received: 04 July 2019
Accepted: 31 October 2019
Published: 28 November 2019

Citation:
Hülscher J, Fischer G, Grunert P, Auer G and Bernhardt A (2019) Selective Recording of Tectonic Forcings in an Oligocene/Miocene Submarine Channel System: Insights From New Age Constraints and Sediment Volumes From the Austrian Northern Alpine Foreland Basin. Front. Earth Sci. 7:302. doi: 10.3389/feart.2019.00302

Detailed characterization of variations in sediment architecture, flux, and transport processes in peri-orogenic basins offers insights into external climatic or tectonic forcings. We tested how four well-known tectonic/erosional events in the Oligocene/Miocene Alpine source area are recorded in the sediment-accumulation rates (SARs) of the deep marine sink in the Northern Alpine Foreland Basin (NAFB): exhumation of the Lepontine Dome (starting at 30 Ma) and the Tauern Window (23-21 Ma), erosion of the Augenstein Formation (~21 Ma), and the visco-elastic relaxation of the European Plate. The Upper Austrian NAFB offers a unique opportunity to investigate external forcings on sedimentary infill due to the large amount of data on the Alpine hinterland and foreland. Deep-marine sedimentation, forming the Puchkirchen Group and the basal Hall Formation, was controlled by a basin-axial submarine channel (3–5 km wide, >100 km length). Two basin-wide unconformities were recognized in seismic-reflection data: the Northern Slope Unconformity (NSU) and the Base Hall Unconformity (BHU). We combine biostratigraphic and chemostratigraphic analyses of 316 drill-cutting samples from three wells with a large 3D-seismic-reflection data set (3300 km^2, >5 km depth) to determine age and duration of the unconformities and to calculate spatially averaged SARs for the submarine channel and its overbanks, separately. Deepening of the basin, recorded by the NSU, occurred between 28.1 and 26.9 Ma. The Puchkirchen Group (26.9–19.6 Ma) is characterized by constant SARs (within standard deviation) in the channel [432–623 (t/m^2/Ma)] and on the overbanks [240–340 (t/m^2/Ma)]. The visco-elastic relaxation of the European Plate results in low SARs on the overbanks [186 (t/m^2/Ma)], a decrease in sediment grain size in channel deposits and a decrease in sea level at the BHU (19.6–19.0 Ma). In the upper Hall Formation (19.0–18.1 Ma), clinoforms prograding from the south filled up the basin

[1497 (t/m^2/Ma)] within 1 Myrs. We conclude that only two of the tectonic signals are recorded in this part of the deep-marine sink, erosion of Augenstein Formation and visco-elastic relaxation of the European Plate; the exhumation of the Tauern Window and Lepontine Dome remain unrecorded.

Keywords: foraminiferal analysis, calcareous nannoplankton analysis, chemostratigraphy, submarine channel, Molasse Basin, environmental signal propagation, turbidity currents, time-scale invariant sediment accumulation rates

INTRODUCTION

Sediment production, paleotopography, sediment-routing and transport processes control the temporal and spatial infill of peri-orogenic basins. The identification of the dominating control processes offers insights into the underlying external environmental forcing mechanisms such as climatic transitions or deep-seated tectonic processes (Clift, 2006; Guillocheau et al., 2012; Gulick et al., 2015). Calculation of spatially averaged sediment-accumulation rates (SARs) allow to investigate these external environmental forcings and intrinsic controls within the sediment-routing system (Romans et al., 2016). Nevertheless, the correct interpretation of external environmental forcings from the sedimentary record remains challenging as its signal might be buffered (Clift and Giosan, 2014), shredded (Jerolmack and Paola, 2010), delayed (Schlunegger and Castelltort, 2016), or masked by autogenic processes (Murray et al., 2009). The attempt of correlating changes in the stratigraphic record to changes in external forcing necessarily involves an evaluation of preceding and contemporaneous tectonic events, sea-level changes, and changes in sediment-routing pathways, as all these internal factors shape the production and storage of sediments in all compartments of the source-to-sink system (Carvajal and Steel, 2012). Moreover, the precise evaluation of all depositional environments of the sedimentary system, both in space and in time, is crucial, as environmental signals may be recorded differently in different depositional environments within a single sedimentary system (e.g., Romans et al., 2016).

The Upper Austrian Northern Alpine Foreland Basin (NAFB, **Figure 1**) offers an excellent opportunity to investigate such signals. The sediment-source area, the European Alps, form one of the most extensively studied orogens in the world with well-constrained phases of uplift and denudation, and relatively well understood tectonic drivers (e.g., Handy et al., 2015). Similarly, the Upper Austrian NAFB is one of the most thoroughly studied foreland-basin systems (Gross et al., 2018). During the deposition of the Oligocene to Miocene Zupfing Formation, Puchkirchen Group – consisting of the Lower (LPF) and Upper Puchkirchen (UPF) Formations – and the lower Hall Formation, sediment routing in the basin was largely controlled by a submarine channel system along the basin axis (**Figures 2**, **3**) (De Ruig and Hubbard, 2006; Hubbard et al., 2009). This channel system received detritus (**Figure 4**) from the Central and Eastern Alps (Sharman et al., 2018) and separated the basin into a wide, gently sloping northern (De Ruig and Hubbard, 2006) and a steep tectonically active southern margin (Covault et al., 2009). The deep marine conditions of the Upper Austrian NAFB are in contrast to the fluvial, continental depositional environment in Oligocene/Miocene (Lower Freshwater Molasse, **Figure 3**) times in the central and western part of the NAFB (Kuhlemann and Kempf, 2002). Due to its economic importance as a hydrocarbon province (Boote et al., 2018), the basin is densely covered by exploration and production wells and by a large, 3D seismic-reflection dataset covering 3300 km^2 and >5 km in depth (**Figure 1**). The post-stack, 3D time-migrated seismic-reflection data cube and the well data are provided by the RAG Austria AG (Vienna).

To relate changes in sediment fill to external or internal forcings, well-constrained stratigraphic control is essential. A long history of stratigraphic work in the Upper Austrian NAFB indicate Chattian to earliest Aquitanian age for the Lower and Upper Puchkirchen formations and a Burdigalian age for the Hall Formation (Küpper and Steininger, 1975; Papp, 1975; Rögl et al., 1979). However, recent publications suggest a younger, late Chattian to Burdigalian age (24.5 to 19.5 – 18.9 Ma) for the Puchkirchen Group on the northern basin slope (Grunert et al., 2013, 2015) in agreement with previous interpretations from surface outcrops of coeval lithostratigraphic units in Bavaria (Martini, 1981; Reiser, 1987; Wenger, 1987).

In this study, we re-evaluate and extend the stratigraphic concept introduced by Grunert et al. (2013, 2015) for the late Oligocene/early Miocene Upper Austrian NAFB by using benthic foraminifera and geochemistry (TOC, S, $CaCO_3$) for the identification of lithostratigraphic boundaries, calcareous nannoplankton and stable carbon isotopy ($\delta^{13}C$) of bulk sediment for chronostratigraphic information. Drill cuttings from three wells were analyzed, one from the northern and two from the southern basin margin (**Figure 1**, Well H, W, Z). The new age constraints are then used to calculate spatially averaged SARs (t/m^2/Ma) for discrete time intervals by using the 3D seismic-reflection cube and well data. We calculated sediment volumes as this reduces the dependence on timescales $< 10^1$ a (Sadler and Jerolmack, 2015) below the maximal resolution estimated to c. 100 ka based on the available bio- and chemostratigraphic constraints.

We hypothesize to detect the externally induced signals of four tectonic events in the Alps (for a detailed discussion of expected environmental signal see section 2.1): (1) the exhumation of the Lepontine Dome led to a doubling in SAR from 25 Ma onward; (2) the exhumation of the Tauern Window increased the SAR in early Miocene; (3) a reduction of SAR due to uplift in the foreland and decreasing elevation in the hinterland at the BHU; (4) the unroofing and erosion of the Augenstein Formation increase the SAR from 21 Ma onward. Our results shed new light on the

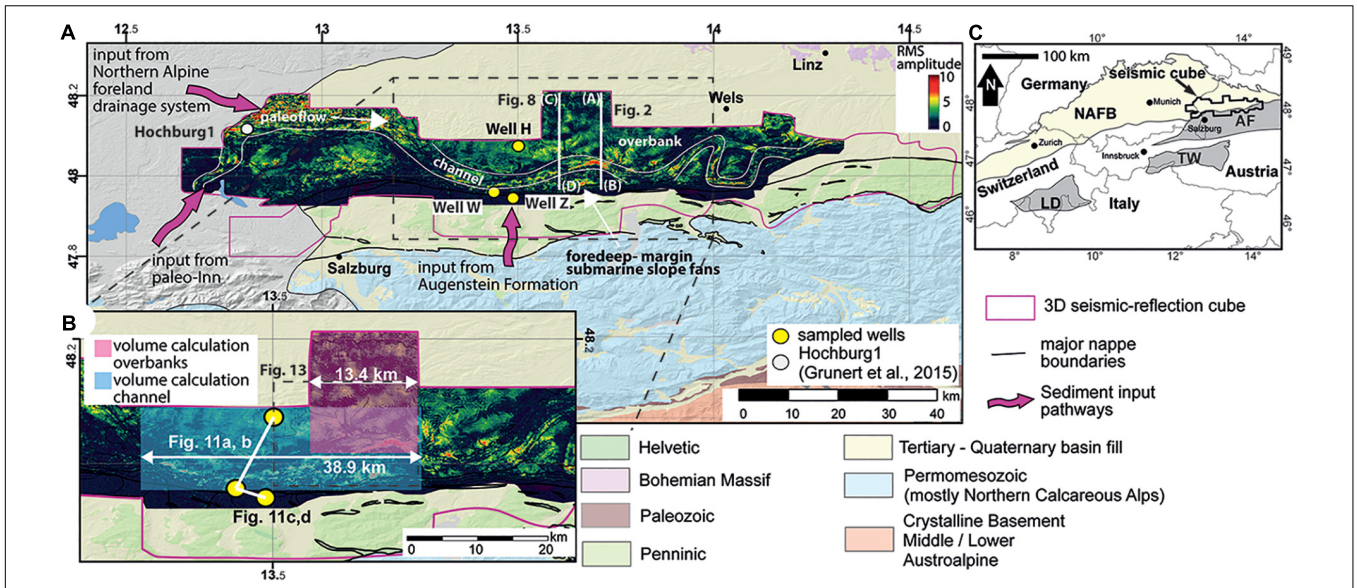

FIGURE 1 | (A) Simplified geological map of the Upper Austrian NAFB and position of the three analyzed wells and reference well Hochburg1 (Grunert et al., 2015). The pink outline shows the extent of the 3D-seismic cube provided by RAG. The inset shows a root mean square (RMS) amplitude map of the seismic-reflection surface of the Base Hall Unconformity outlining the axial channel, the extensive overbank deposits on the northern basin margin and the slope fans on the southern tectonically active margin. **(B)** Detail of **(A)** with location and extent of the volume calculation, the position of the three wells and the seismic cross sections between them. **(C)** Present location of the NAFB, the Lepontine Dome (LD), Tauern Window (TW), and 3D-seismic cube in central Europe. Additionally, the approximated position of the nowadays mostly eroded Augenstein Formation (AF) is marked.

development of the Upper Austrian NAFB during the Oligocene and Miocene and the forcings that controlled the sediment fill and the formation of two basin-wide unconformities.

GEOLOGICAL OVERVIEW AND STRATIGRAPHY

The NAFB is located on the northern border of the Alpine orogen in central Europe (**Figure 1**) and extends from Switzerland through Germany and into Austria for c. 1000 km in a west-east direction and up to 120 km in a north-south direction (Kuhlemann and Kempf, 2002). The development of the NAFB commenced in the upper Eocene due to flexure of the southern European continent. From 32–30 Ma to ∼6 Ma, proximal, conglomeratic sediments (the Molasse) were deposited in the basin (Sissingh, 1998). The sediments in the German and Swiss part of the basin are characterized by two shallowing-upward megacycles, which are further subdivided into the Lower Marine Molasse (32–28 Ma), the Lower Freshwater Molasse (28–20 Ma), the Upper Marine Molasse (20–16 Ma), and the Upper Freshwater Molasse (16–6 Ma) (Kuhlemann and Kempf, 2002).

The eastern part of the NAFB is located in Upper Austria (**Figure 1**) and hosted a deep-marine environment (1000 – 1500 m water depth, Rögl et al., 1979) in the Oligocene and early Miocene (Wagner, 1998). After a period of neritic environmental conditions in the Eggerding Formation [nannoplankton zone (NP) 23, **Figure 3**] the basin rapidly deepened (Sachsenhofer et al., 2010; Soliman, 2012) and deep-marine (water depth ∼1000 m) conditions are recorded in the overlying Zupfing Formation (ZFM) (Wagner, 1998). The ZFM contains the Rupelian/Chattian boundary (**Figure 3**) and is located in NP 24 (Wagner, 1998; Soliman, 2012). The benthic index foraminifera of the ZFM are *Cancris bavaricus* and *Uvigerina moravia* (Cicha et al., 1998).

During deposition of the ZFM and the overlying LPF, UPF, and basal Hall Formation (BHF), the basin was characterized by a gently sloping northern margin and a steep, tectonically active southern margin (**Figures 1–3**). Depositional processes in the basin were largely controlled by a 3–6 km wide, deep-marine, gravity-flow dominated channel system flowing parallel to the Alpine front from west to east for >100 km (De Ruig and Hubbard, 2006). The submarine channel system is characterized by intercalated sandstones (structured and structureless), conglomerates (clast-supported and matrix-supported) and silty marls which are interpreted as the deposits of turbidity currents (high to low density), debris flows, and hemipelagic suspension settling (De Ruig and Hubbard, 2006; Hubbard et al., 2009; Bernhardt et al., 2012). To the north, the channel is flanked by wide overbank deposits (≤15 km, **Figure 2**), which are formed by hemipelagic silty marls and subordinate turbiditic sandstones resulting from northward-directed overspill of sediment by gravity flows in the channel (De Ruig and Hubbard, 2006; Hubbard et al., 2009; Bernhardt et al., 2012; Masalimova et al., 2015). From the southern basin margin, submarine turbidite fans prograded northward into the basin (Covault et al., 2009) and large (≤30 km^3) mass-wasting events were shed into the channel (Kremer et al., 2018).

The lower boundary of the LPF is defined by the occurrence of the agglutinated foraminifera *Psammosiphonella cylindrica*

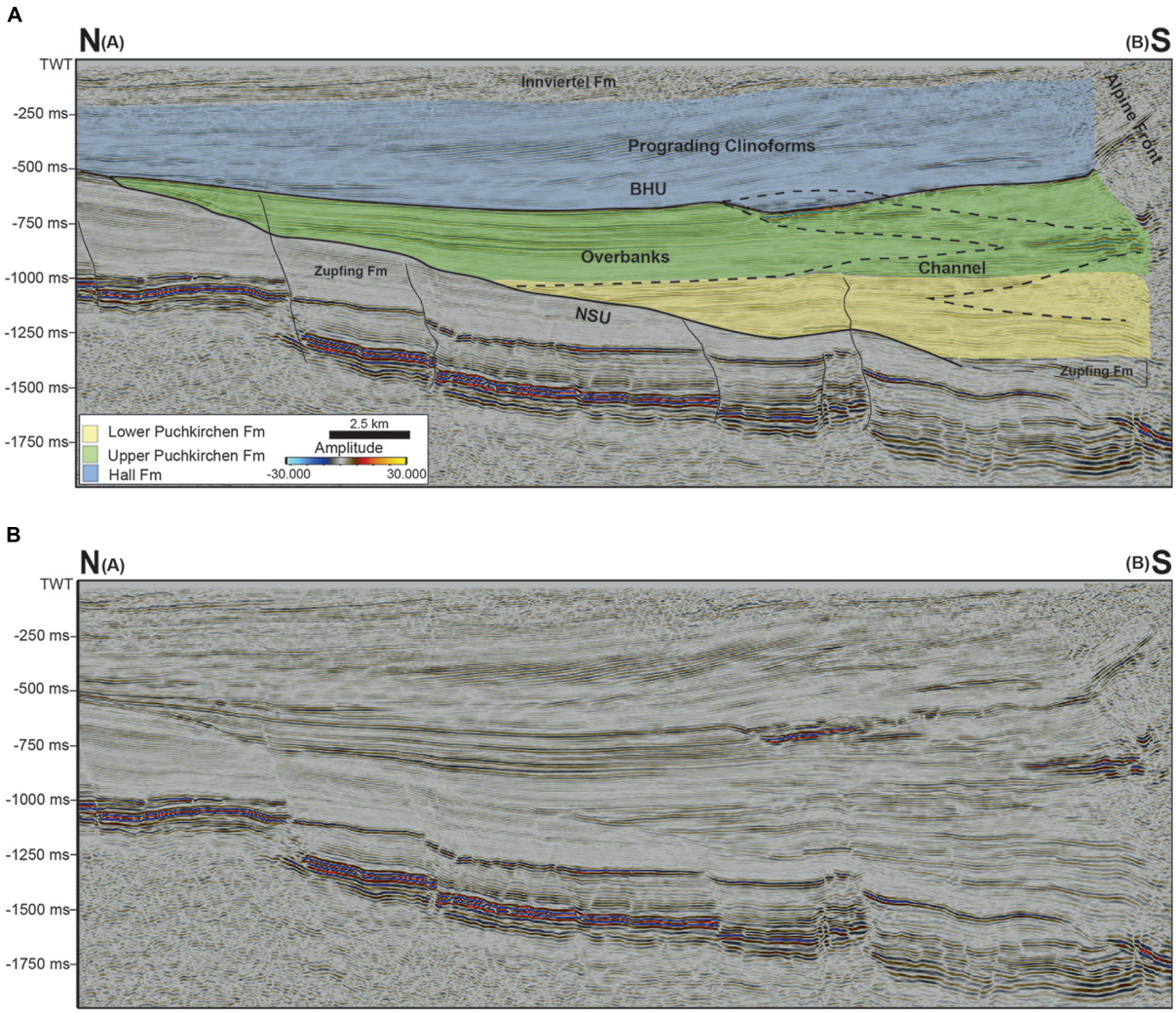

FIGURE 2 | Cross section (N – S) through the Upper Austrian Molasse Basin (for position see **Figure 1**) showing the lateral migration of the main channel belt in the Puchkirchen and Hall formations (black, dotted lines). On the northern slope the NSU (thick black line) is visible with the Zupfing Formation below it. The wide (≤15 km) overbanks of the UPF and BHF north of the channel are illustrated. The BHU is characterized by truncated reflectors in the channel and two strong reflectors on the overbanks. Above the BHU a small segment with transparent reflectors is visible before clinoforms start to prograde from the southern margin into the basin. **(A)** Interpreted seismic cross section; **(B)** uninterpreted seismic cross section.

(formerly "*Rhabdammina linearis*"). The agglutinated species *Reticulophragmium acutidorsatum, R. rotundidorsatum,* and *R.* aff. *amplectens* are typical. Of the calcareous foraminiferal species, *Uvigerina steyri* is common (Cicha et al., 1998). The lower boundary of the UPF is defined by the first occurrence (FO) of *Gaudryinopsis austriacus* (sometimes referred to as *"Bigenerina* sp. 7") and the disappearance of *Psammosiphonella cylindrica* (Cicha et al., 1998). The lower boundary of the HFM is defined by the FO of *Uvigerina posthantkeni* (Cicha et al., 1998).

Channel sedimentation terminated contemporaneously with a rise in sea level during the deposition of the BHF (**Figure 3**), a deep-marine environment dominated by hemipelagic sediments (**Figure 2**) was established in the Hall Formation (HFM) (Zweigel, 1998; Grunert et al., 2013). Clinoforms started to prograde from the southern margin during the middle HFM and filled the basin. The overlying mid-Burdigalian Innviertel Group was deposited in a tide-influenced shelf sea (<200 m water depth) (Grunert et al., 2012, 2013). The base of the Innviertel Group (**Figure 3**) is marked by the FO of *Amphicoryna ottnangensis* (Cicha et al., 1998).

Two large unconformities have been described in the basin, the Northern Slope Unconformity (NSU) and the Base Hall Unconformity (BHU, from bottom to top, **Figure 2**) (De Ruig and Hubbard, 2006; Masalimova et al., 2015). The NSU is located on the northern basin slope and is present for at least 20 km in N-S direction and 100 km in W-E direction throughout the entire 3D seismic-reflection cube. Puchkirchen Group strata lap onto the unconformity. Masalimova et al. (2015) interpreted the unconformity as an over-steepened slope, characterized by sediment bypass.

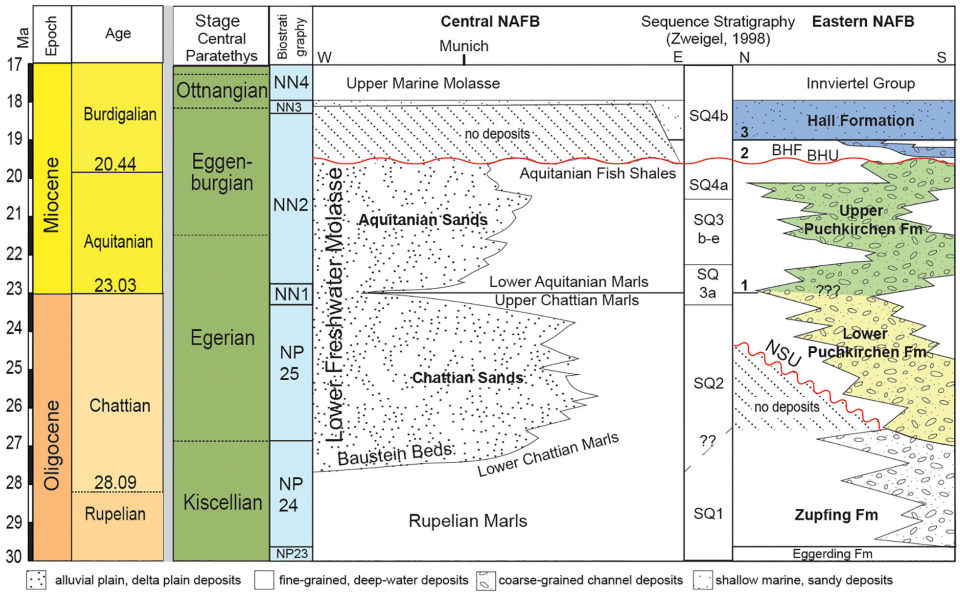

FIGURE 3 | Schematic correlation of the global stages (Gradstein et al., 2012), the stages of the Central Paratethys (Piller et al., 2007), the calcareous nannoplankton after Backman et al. (2012) and Agnini et al. (2014), the stratigraphic and facies evolution (from W to E) in the central NAFB (Kuhlemann and Kempf, 2002), the sequence stratigraphy for the eastern NAFB (Zweigel, 1998), and the stratigraphy and facies evolution (N-S cross section) in the deep-marine Puchkirchen Trough. Depositional ages of the Eggerding and Zupfing Fm from Sachsenhofer et al. (2010) and Soliman (2012). Please note: Correlation between the eastern and the central NAFB is highly speculative. Only the Oligocene/Miocene (1) boundary (SQ 3a), the BHU (2), and the maximum flooding surface (mfs) in the HFM (3) can be used as reliable temporal markers.

The age and duration of the NSU and the process that led to the oversteepening of the slope are currently unknown (Masalimova et al., 2015).

The BHU (**Figure 2**) separates the UPF from the HFM and forms a basin-wide, deep-marine unconformity which was also described on the Bavarian Shelf to the east (Zweigel, 1998; De Ruig and Hubbard, 2006). In the 3D seismic-reflection data, the unconformity is characterized within the submarine channel system by truncated reflectors and on both margins by two high-impedance reflectors (**Figure 2**). Wenger (1987), Jin et al. (1995), and Zweigel (1998) pointed to a sea-level fall at the UPF/HFM boundary (**Figure 4**). Grunert et al. (2015) suggest an age of 19.5 – 18.9 Ma for the formation of the BHU. Additionally, Zweigel (1998) and Kuhlemann (2000) proposed a decrease in the subsidence and sedimentation rates at that time.

The so-called Puchkirchen Trough was fed by three different sources (Kuhlemann and Kempf, 2002). (1) A large, eastward prograding delta close to the present position of Munich received sediment from the Central Alps (Kuhlemann and Kempf, 2002; Sharman et al., 2018) (**Figure 4**). (2) The paleo-Inn Fan fed by intra-Alpine material served as a second source for detritus to the Puchkirchen Trough (Kuhlemann and Kempf, 2002). (3) A series of rivers were running from the central Eastern Alps through the Augenstein deposits into the NAFB (Frisch et al., 2001; Covault et al., 2009). With the change of the paleo-drainage system at the beginning of the UMM, the NAFB was flooded (**Figure 4**), the Puchkirchen Trough was cut off from the Central Alpine sediment supply (Kuhlemann and Kempf, 2002; Grunert et al., 2013).

Expected Tectonic Forcings

We hypothesize to detect the externally induced signals of four tectonic events in the results of the SARs calculation:

(1) The exhumation of the Lepontine Dome in the Central Alps (**Figure 1C**) – starting ∼32 Ma, accelerating at 25.5 Ma (Schlunegger and Castelltort, 2016) – has led to a twofold increase of SARs on the proximal megafans in the Swiss NAFB (250–450 m/Ma to 400–600 m/Ma, compacted rates) at 25.5 Ma (Schlunegger and Norton, 2015). Zweigel (1998) also reported an increase of SAR on the Bavarian Shelf (**Figure 4**) from 25 Ma onward. We expect to see a similar twofold increase in the SARs of the Upper Austrian NAFB.

(2) Between 23 and 21 Ma, the rapid exhumation of the Tauern Window (**Figure 1C**) began in the Eastern Alps (Scharf et al., 2013; Favaro et al., 2015). In the proximal Chiemgau Fan (**Figure 4**), the Chattian deposits reach a (compacted) thickness of 1200–1500 m, whereas the Aquitanian contains 1250 m thick deposits (Ganss, 1977). SARs increase from 237–296 m/Ma in Chattian times to 483 m/Ma in Aquitanian times. Due to the short lag time (2–4 Ma) of apatite fission track ages in the Aquitanian deposits (deposition age: 21 Ma) (Kuhlemann et al., 2006), the increase in SARs is interpreted to be related to the exhumation of the Tauern Window. Therefore, we expect to find a similar ∼65 – 100% increase in our SAR in Aquitanian times.

(3) Zweigel (1998) explains her findings in the German NAFB (low SARs, angular unconformity, uplift in the

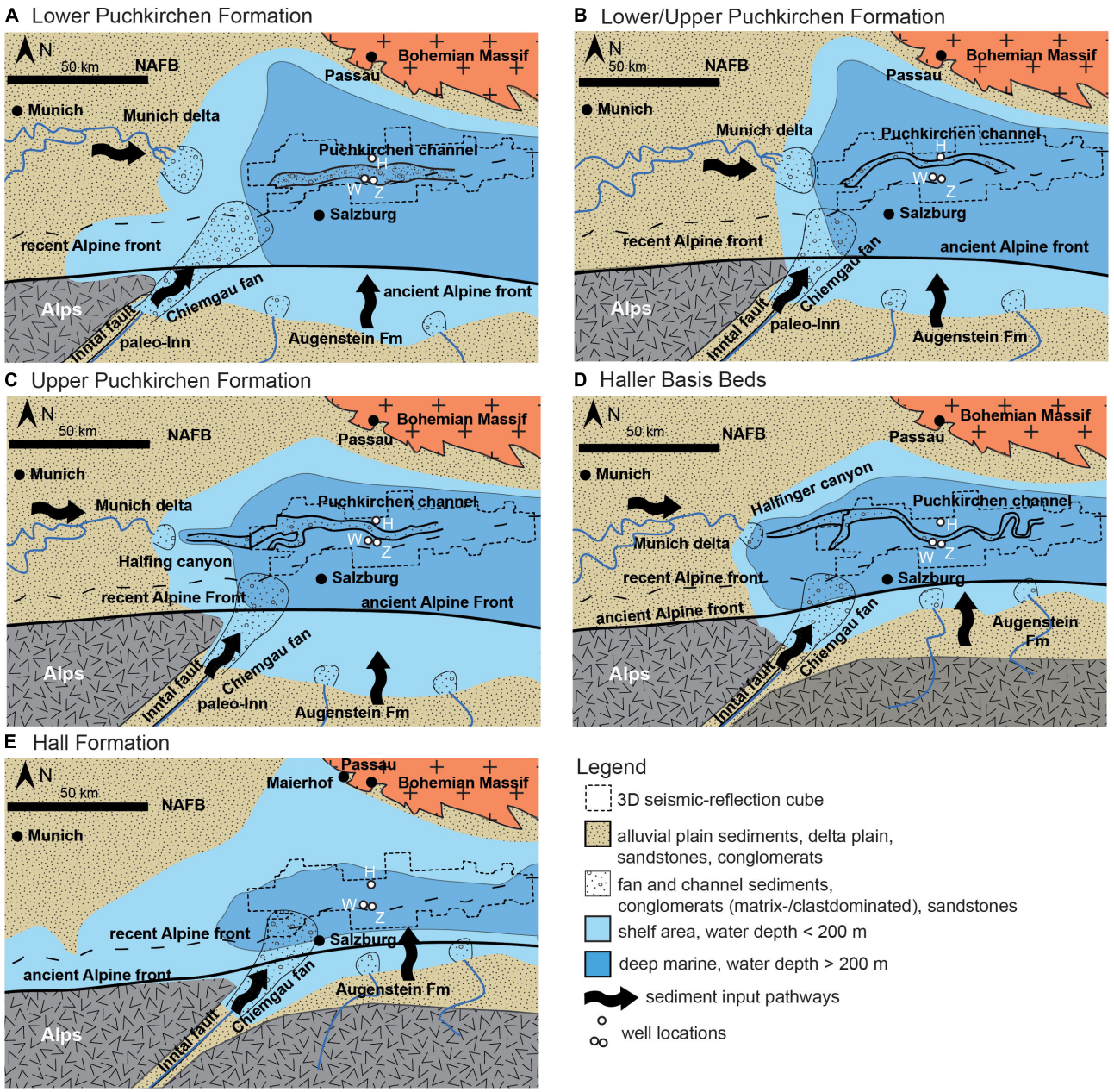

FIGURE 4 | Paleogeographic reconstructions of the Upper Austrian and SE German NAFB during the late Oligocene through Early Miocene **(A–E)** and their main sediment input pathways. Channel geometries were mapped in the 3D seismic cube. Information compiled from Reiser (1987); Wenger (1987), Lemcke (1988); Zweigel (1998), Kuhlemann and Kempf (2002), and Grunert et al. (2013). During the deposition of the LPF **(A)** the channel shows a low sinuosity and is located at the southern basin margin. The Puchkirchen Trough was fed from the paleo-Inn, the Augenstein deposits, and the Munich delta from which clinoforms prograded into the basin, the shoreline moved to the east. At the L/UPF boundary **(B)** the shoreline reached its easternmost position, the channel started to meander and reached its northernmost position. In the UPF **(C)** the depositional system on the Bavarian Shelf changed, the Halfing canyon developed and was connected to the Puchkirchen channel. The shoreline was located further to the west compared to **(B)**. During the formation of the BHU **(D)** a major sea-level fall occurred and the channel acquired its highest sinuosity; the Halfinger canyon was still active. In the HFM **(E)** the sedimentation system in the Molasse Basin changed completely due to reestablishment of marine conditions in the western NAFB (Upper Marine Molasse), channel sedimentation ended and clinoforms started to prograde into the basin from the south.

northern part of the basin, sea-level decrease, reduction in deposited grain size) during the establishment of the BHU with the model of a visco-elastic relaxation of the European Plate. A visco-elastic behaving lithosphere loses strength with time depending on temperature, rheology, and initial stress of the lithospheric plate. Even without an additional load, the elevation in the hinterland can be reduced and the forebulge can migrate to the orogenic

front (Beaumont, 1981), leading to a reduction in grain size and sediment flux from the hinterland, whereas the foreland is uplifted causing the angular unconformity and the decrease in sea level (Zweigel, 1998). An alternative explanation for Zweigel's (1998) findings might be the proposed slab-tearing event underneath the Eastern Alps at 20–25 Ma that may have led to a retreat and steepening of the European slab (Handy et al., 2015), causing a decrease in elevation in the orogen. The proposed slab-polarity switch underneath the Eastern Alps (Lippitsch et al., 2003) is still controversially discussed. However, the published literature does not conclude which of those models is more realistic. We hypothesize to find a reduction in SARs and redeposition of shelf strata.

(4) The unroofing and redeposition of the Augenstein Formation (**Figure 4**) into the Puchkirchen Trough, caused by the beginning uplift of the underlying but sealed Northern Calcareous Alps, started ∼21 Ma (Frisch et al., 2001). These fluvial sands and gravels with an estimated thickness of 1.8–2.2 km are today only persevered as relicts, hampering a precise evaluation of the expected material that might have been relocated (Frisch et al., 2001). However, we expect to detect an increase in the SAR with the beginning of the unroofing and the redeposition of the Augenstein Formation into the Puchkirchen Trough.

MATERIALS AND METHODS

Samples for bio- and chemostratigraphy were collected from three drill sites (sampling interval 10–40 m), one from the northern margin (Well H; **Figures 1**, **5**) and two from the southern margin of the basin (Well W and Well Z, **Figures 6**, **7**). In Well W, a ∼800 m thick mass-wasting deposit shed from the south was excluded from sampling (**Figure 6**). All named depth (m) are measured depth and not corrected for deflection of the wells.

Biostratigraphy

For the analysis of foraminiferal assemblages, the drill-cuttings (each representing about 2 m of sediment thickness) were wet-sieved (20 – 100 g per sample) under addition of diluted hydrogen peroxide (30%) through mesh-sizes of 250, 125, and 63 μm. The fraction > 250 μm was barren of foraminifera, all analyses were therefore conducted on the 125 to 250 μm size fraction. Taxonomic identification relied on the Atlas of Oligocene – Miocene foraminifera of the Central Paratethys (Cicha et al., 1998). For Well Z, already existing biostratigraphic constraints from a RAG internal report were used (Ćorić and Spezzaferri, 2009).

The preparation of smear slides followed the methodology of Bown (1998). Sediment was suspended in NH_3-buffered ultrapure milli-Q water and fully disaggregated by ultrasonic treatment. One drop of the suspension was placed on coverslips (24 × 30 mm) and slowly dried at a temperature of ∼ 50°C. The slides were mounted using Norland No. 61® optical adhesive and investigated using an Olympus BX53 light microscope under parallel and crossed nicols at a 1000X magnification. Coccoliths were identified to species level if possible, following the taxonomic concepts of Bown (1998) and Galović and Young (2012), supplemented by the Nannotax 3 website (Young et al., 2014) and the handbook of calcareous nannofossils (Aubry, 1984, 1988, 1989, 1999, 2013). Calcareous nannoplankton zonation used in this study is based on the standard zonation of Martini (1971, recalibrated in Gradstein et al., 2012) as well as the revised zonal scheme of Backman et al. (2012) and Agnini et al. (2014).

Chemostratigraphy

From Well H, W, and Z, 151, 103, and 71 samples, respectively, were chosen for analyses of stable carbon isotopes ($\delta^{13}C_{carb}$), total organic carbon content (TOC), sulfur content (S), and carbonate content. $\delta^{13}C_{carb}$ measurements were performed at the GeoZentrum Nordbayern, University of Nürnberg-Erlangen, using a Gasbench II connected to a ThermoFisher Delta V Plus mass spectrometer. Samples were dried, homogenized with a mortar and the carbonate powders reacted with 100% phosphoric acid at 70°C. Values are reported in the conventional $\delta^{13}C_{carb}$ notation in ‰ relative to Vienna Pee Dee Belemnite standard (VPDB). Reproducibility and accuracy were monitored by replicate analysis of laboratory standards calibrated by assigning $\delta^{13}C$ values of +1.95‰ to NBS19 and −47.3‰ to IAEA-CO9. Reproducibility for $\delta^{13}C_{carb}$ was ±0.05‰.

The measurements for TOC, S and carbonate content were performed at the Institute for Earth Science, University of Graz, using a Leco CS-300 device. The dried, homogenized and mortared samples were analyzed for their total carbon (TC) and TOC content, total inorganic carbon (TIC) was calculated by subtracting TOC from TC. Carbonate content was calculated from TIC as calcite equivalent percentages ($CaCO_3$ = 8.34*TIC; Grunert et al., 2015).

Seismic Interpretation and Sediment-Accumulation Rates

Sediment-mass calculations were performed by using Petrel E&P software platform [(*) = Mark of Schlumberger], a cell-based modeling software, by integrating the 3D reflection-seismic data and density well logs. Two models were built (**Figure 1B**), one including the channel-belt strata (in the following referred to as "channel model") and one including the overbank deposits ("overbanks model"). The term geobody is used here to describe the separation of the models into different 3-dimensional segments for which masses were calculated (**Figure 8**). The SARs are spatially averaged over large areas (variations between 31 and 255 km^2, **Table 1**) and long-time intervals (0.4 to 3.9 Ma) and, hence, should be time-scale invariant according to Sadler and Jerolmack (2015). The local erosional processes which may influence small scale SAR calculations are averaged out with increasing temporal and spatially scale (Sadler and Jerolmack, 2015).

The seismic-reflection data have a dominant frequency of ∼28 Hz and the average velocity in the area of interest is c. 3700 m/s, which results in a theoretical vertical resolution of ∼33 m (De Ruig and Hubbard, 2006; Masalimova et al., 2015).

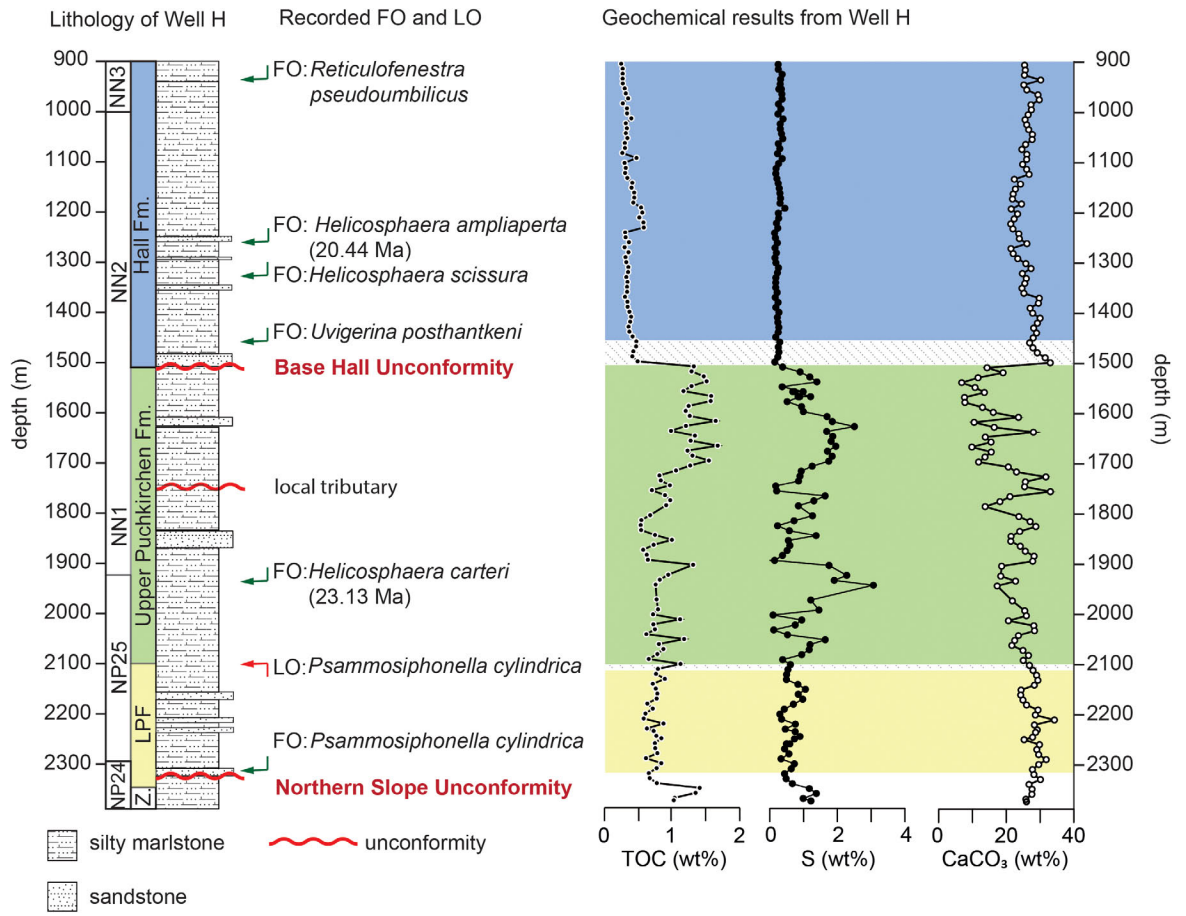

FIGURE 5 | Simplified lithological section of Well H (see **Figure 1** for location) with FO and last occurrence (LO) of index taxa (nannofossils and benthic foraminifera). Total organic carbon (TOC) and sulfur (S) increase from moderate levels with low variance in the LPF (from 2100 m) to very high levels in the upper half of the UPF showing great variance, indicating highly unstable ecologic conditions. Above the BHU, TOC, and S values drop to very low and stable levels, while $CaCO_3$ dramatically increases. Uncertainties are due to sampling resolution and preservation. See text for discussion.

The extent of the channel-belt strata and overbank deposits was mapped out based on 3-dimensional, time-migrated seismic reflectors. The models were built by using the 'Structural Modeling' toolbox in Petrel (*). The toolbox generates a grid, based on input data (geometry, upper, and lower boundary, cell size) with a certain number of cells. Cell size was established as 10 m*10 m*5.5 milliseconds. Mapped seismic-reflection horizons were merged into geobodies and were loaded via the Geometrical Modeling tool into the model (**Figure 8**). This tool allows the user to generate properties for cells in the model. The model was converted into elevation depth (m) by using an in-house velocity model provided by RAG, which changed the individual *z*-axis of each cell (variation between 7 and 15 m).

Density ($\rho(\frac{kg}{m^3})$) and lithology well data of 52 and 16 wells for the channel and overbank model, respectively, were downsampled into the depth-converted models. The downsampling for the lithological logs was accomplished by using the "most of" average method. Each model cell is assigned to a single lithology that is given by the most abundant lithology in the well section within the model cell, e.g., a 40% claystone and 60% sandstone cell will be assigned as a sandstone cell. Based on these modeled cells along the well paths, Petrel's (*) 'Facies Modeling' process assigns lithologies to the cells in between the individual wells using the horizontal and vertical trends in the data to guide the interpolation process.

The downsampling of the density data was performed by using the arithmetic mean of the well data for each individual cell intersected by a well. Data was then interpolated between the individual wells of the model by using Petrel's (*) 'Petrophysical Modeling' tool. The interpolation of the density data between the wells is based on the results of the facies modeling, so that the modeled density data reflects the modeled trends from the lithological interpolation.

Masses are calculated by using m (kg)=V (m^3)* ρ ($\frac{kg}{m^3}$) for each individual cell and then summed up for an entire geobody. Calculations were run for three geobodies in the channel model and six geobodies within the overbank model (**Table 1** and **Figure 8**). Geobody boundaries were selected based on good temporal control on base and top. For each geobody, a calculation with a minimum (−5%), average and maximum (+5%) ρ was

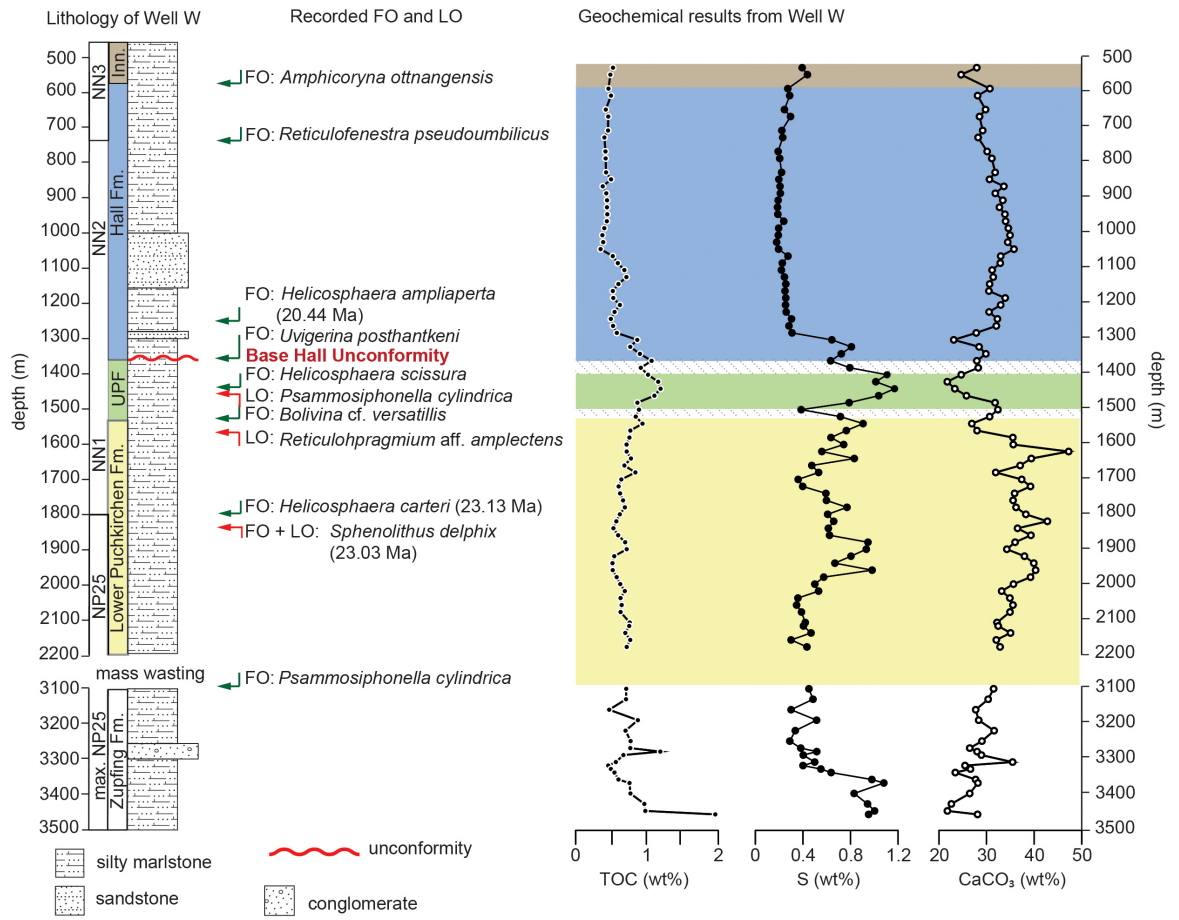

FIGURE 6 | Simplified lithological section of Well W (for position see **Figure 1**) with FO and LO of index taxa (nannofossils and benthic foraminifera), above 3200 m TOC- and S-values decrease compared to the underlying section and TOC-values show low variance, while S-values fluctuate heavily, until 1600m, the $CaCO_3$-content steadily rises. The UPF shows higher S and slightly higher TOC and greatly decreased $CaCO_3$-values. In the HFM, after 1300 m, TOC- and S-values drop to very low and stable levels, while $CaCO_3$ increases. Uncertainties are due to sampling resolution and preservation. See text for discussion.

run (**Table 1**). The mass of each geobody was calculated twice, first within the mapped boundaries and a second time by adding a 35 m segment on every boundary to account for erroneous seismic-reflection interpretation and the resolution of the seismic-reflection data. The calculated masses were divided by the base area [A (m^2)] of the geobody (**Table 1**) resulting in the areal density N($\frac{kg}{m^2}$).

Calculated SARs (Q_S) are based on the presented bio- and chemostratigraphic results (t_n, t_m,. . .). For the geobodies in the channel model, the temporal information from the overbank geobodies was assumed (**Table 1**), except for the beginning of the LPF (see section Revisiting the **S**tratigraphic **C**oncept for the Upper Austrian Molasse). The calculated areal densities were divided by the time interval following Q_S (kg/(m^2 *Ma))= $\frac{N}{t_n - t_m}$. The results represent the arithmetical mean rates and standard deviation (1σ; SD) from the six calculated rates of every geobody. Every geobody was calculated also in age brackets t ± 0.1 Ma based on the highest temporal resolution of our bio- and chemostratigraphic results. We note that this is an optimist boundary condition for temporal uncertainty quantification, however, the influence of spatial uncertainties on uncertainty dimensions exceeds the temporal ones (**Table 1**). To further constrain the sediment transport direction in the upper HFM clinoforms were mapped in the 3D seismic data (see **Supplementary Figure S1**).

RESULTS

Foraminifera and Calcareous Nannoplankton

The abundance of benthic foraminifera is generally <50 specimen per sample and several barren intervals are present (see **Supplementary Table S1** for a complete list of species and **Supplementary Figure S2** for representative specimens). Especially the index species are very rare and often poorly preserved. Calcareous nannoplankton abundance in the samples ranges from common to very rare, with index species often being very rare (see **Supplementary Table S2** and **Supplementary Figure S3** for complete list and representative specimens).

TABLE 1 | Results from the channel and overbank model of the volume and SAR calculation.

Data Volume calculation	Area Size (km^2)		Volume (km^3)		Mass sediments ($\times 10^8$ t)		Time markers from the bio-/chemostratigraphy		Depositional ages (Ma)		SAR (1σ SD) ($t/m^2/Ma$)
	Minimum	Maximum	Minimum	Maximum	Minimum	Maximum	Beginning	End	Beginning	End	
Channel geobodies											
Lower Puckirchen Formation Geobody	169.8	478.3	145.9	181.7	3603.3	4960.9	Beginning NP25	Boundary L/UPF[2]	26.9	23.5	390 (±103)
Upper Puchkirchen Formation Geobody	102.4	293.5	160.0	226.8	3896.2	5888.9	Boundary L/UPF	BHU[5]	23.5	19.6	518 (±39)
Haller Basis Beds	177.8	181.4	19.3	35.6	456.6	876.7	BHU	MFS above BHU[6]	19.6	19	622 (±189)
Overbank geobodies											
Geobody 1	31.7	32.5	2.2	3.8	54.8	103.5	Peak 1[1]	Boundary L/UPF[2]	24.5	23.5	243 (±65)
Geobody 2	140.0	140.8	13.0	20.2	320.6	547.3	Boundary L/UPF	FO *H. carteri*[3]	23.5	23.1	869 (±277)
Geobody 3	255.3	256.1	49.1	61.6	1190.7	1650.5	FO *H. carteri*	Peak 11[4]	23.1	21.5	339 (±44)
Geobody 4	238.0	238.8	38.5	48.8	909.4	1273.6	Peak 11	BHU[5]	21.5	19.6	240 (±31)
Geobody 5	245.8	246.6	5.6	16.1	132.0	419.2	BHU	MFS above BHU[6]	19.6	19	185 (±94)
Geobody 6	202.4	203.2	103.2	113.0	2477.7	2952.6	MFS above BHU	Hall/Innviertel FM boundary[7]	19	18.1	1497 (±159)

Note that the maximal and minimal area size of the channel model vary greatly due to the different width of the channel through time (Hubbard et al., 2009). Depositional ages are gained from 1 = onset of sedimentation on the northern slope; 2 = $\delta^{13}C_{carb}$-peak 4 (Well H); 3 = FO Helicosphaera carteri (Well H); 4 = $\delta^{13}C_{carb}$-peak 11 (Well H); 5 = $\delta^{13}C_{carb}$-peak 14 (Well H); 6 = mfs and Sr-Isotopy from Maierhof; 7 = Hall Fm./Innviertel Group boundary (Grunert et al., 2013).

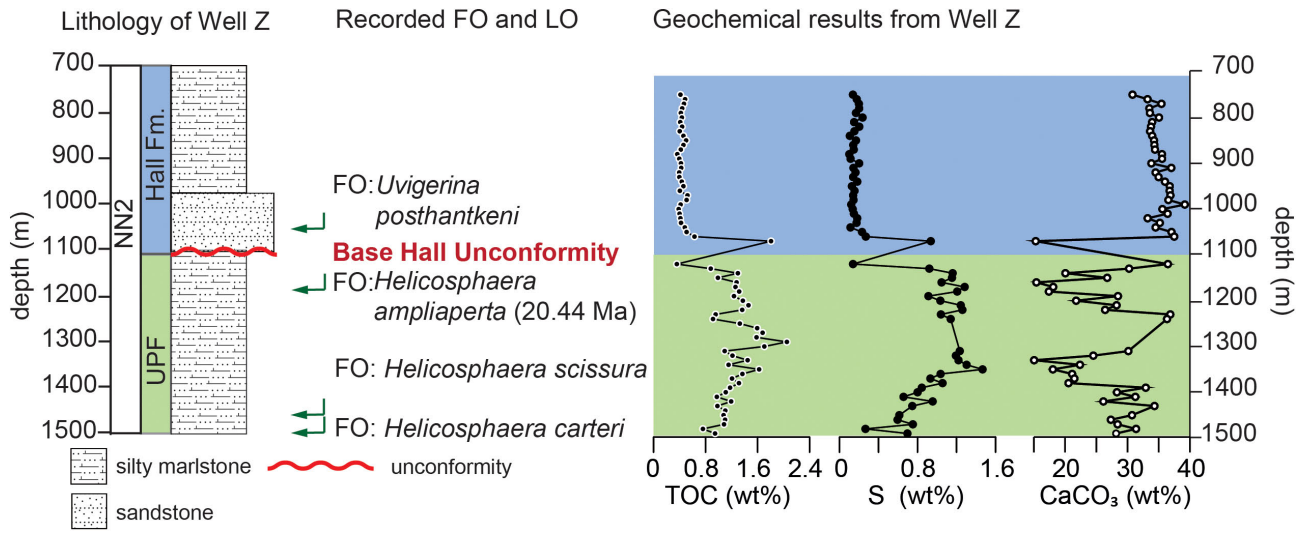

FIGURE 7 | Simplified lithological section of Well Z (for position see **Figure 1**) with FO and LO of index taxa [nannofossils and benthic foraminifera (Ćorić and Spezzaferri, 2009)], TOC- and S-values are high in the UPF and $CaCO_3$-content is highly variable (A1-horizon after Gross et al., 2018). At 1125 m TOC- and S-contents show a decrease, increase again and finally decrease to low and stable levels until the end of the section. See text for discussion.

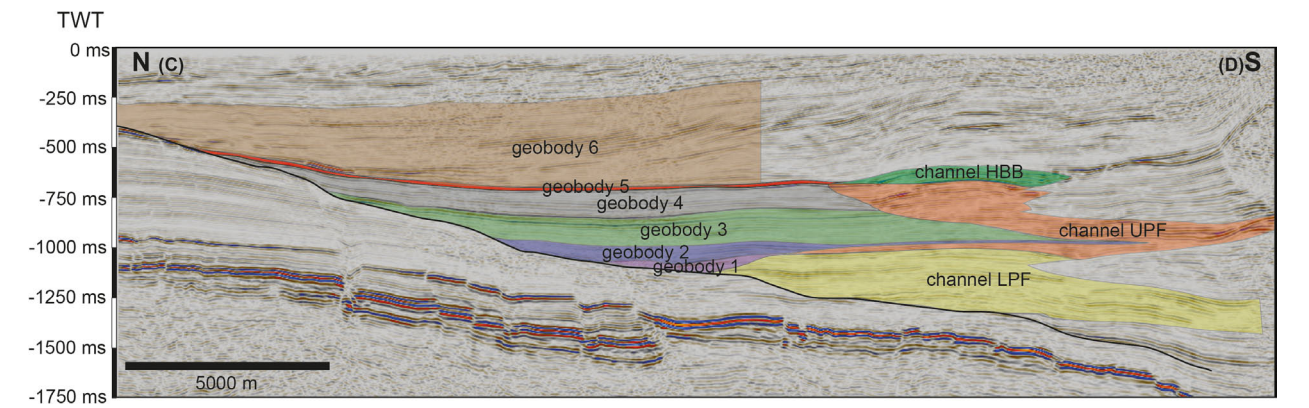

FIGURE 8 | Cross section (N – S) through the Upper Austrian Molasse Basin (for position see **Figure 1**) showing the extent of the geobodies in the channel and overbank model. Note the varying base area of the geobodies.

Their preservation ranges from good to poor. The scarcity and preservation state impose a challenge for taxonomic identification and biostratigraphic interpretation. We had to resort to secondary marker species, co-occurrences and the interpretation of the assemblage as a whole.

Well H

The FO and LO of *Psammosiphonella cylindrica* indicates the Lower Puchkirchen Formation between 2325 and 2100 m (**Figure 5**). The fauna in the lower part of the LPF (2325–2190 m) consists of *Lenticulina* sp., *Praeglobobulimina* sp., *Virgulinella* sp., *Psammosiphonella cylindrica, Heterolepa* sp., *Bathysiphon* sp., *Bulimina* sp., *Cibicides* sp., and *Asterigerinata* sp. following a widespread absence of foraminifera for several tens of meters, *Praeglobobulimina* sp. re-appears as first species at 2150 m and soon dominates the assemblages, outnumbering the few *Bathysiphon* sp. and *Bolivina* sp. This is followed above by a second interval of widespread absence of foraminifera for 30 m. In the UPF (from 2100 m), some *Bathysiphon* specimens were found while above 1960 m *Bulimina* sp. and *Lenticulina* sp. occur.

Above 1960 up to 1450 m benthic foraminifera are generally scarce (**Supplementary Table S1**). Only between 1540 to 1510 m depth, very few specimens of *Bulimina* sp., *Lenticulina* sp. and *Cibicidoides* sp. occur. *Uvigerina posthantkeni* and some *Lenticulina* specimens were found just above this interval at 1455 m marking the base of the Hall Formation. All samples above 1455 m are barren of benthic foraminifera.

The FO of *Helicosphaera carteri* was found at 1920 m (**Figure 5**). The FO of *Helicosphaera ampliaperta* at 1260 m, shows specimen already at full size (>10 μm; **Supplementary Figure S3**). The FO of *R. pseudoumbilicus* > 7 μm is recorded at 910 m. Samples barren of nannofossils are recorded for 2165 m,

intervals from 2110 to 2085 m, 1900 to 1800 m, and sample 1540 m (**Supplementary Table S2**).

Well W

The samples from 3470 to 3100 m are barren, with only a few, single specimens of no stratigraphic relevance (**Figure 6**). The FO of *Psammosiphonella cylindrica* at 3100 m marks the beginning of the LPF. The LO of *Reticulophragmium* aff. *amplectens* (1560 m) and the FO of *Bolivina versatilis* (1520 m) indicate the boundary of the Upper and Lower Puchkirchen Formation between 1560 and 1520 m. The FOs of *Uvigerina posthantkeni* and *Fontbotia wuellerstorfi* (1360 m) mark the onset of the Hall Formation. The base of the Innviertel Group is marked by the FO of *Amphicoryna ottnangensis* at 580 m (**Figure 6**).

From 3230 to 3100 m, *Bulimina* sp., *Heterolepa* sp., few *Praeglobobulimina* sp., and *Valvulineria* sp. were found. *Valvulineria* sp. becomes increasingly rare above 2200 m and is replaced by *Praeglobobulimina* sp., becoming very common especially from 2200 to 2152 m. In the same interval *Cibicides* sp. becomes a relevant constituent of the assemblage. From 1800 m upward, the samples are functionally barren up to 1600 m. With the onset of the Upper Puchkirchen Formation at 1520 m, a new faunal assemblage is established consisting of *Bolivina* sp., *Lenticulina* sp., *Heterolepa* sp., *Bulimina* sp., and *Asterigerinata* sp. All samples from the 900 to 760 m interval and from 520 to 420 m are barren (**Supplementary Table S1**).

The FOs of the calcareous nannofossil taxa *Helicosphaera carteri* and *Sphenolithus delphix* occur at 1800 m (**Figure 6**). The crossover in the dominance of *Helicosphaera euphratis* and *Helicosphaera carteri* was identified at 1400 m, shortly above the FO of *Helicosphaera scissura* at 1424 m. At 1260 m also the FO of already comparatively large (>10 μm) *Helicosphaera ampliaperta* was recorded. *Reticulofenestra pseudoumbilicus* first occurs at 760 m. The interval of 1440 to 1520 m, 1220 to 1240 m, 820 to 1140 m and the sample from 400 m are devoid of nannofossils (**Supplementary Table S2**).

TOC, S, and Carbonate Content

Well H

In Well H (**Supplementary Table S3**), the lowermost samples (2385 – 2360 m) show high TOC [Average (A) = 1.2 wt%, standard deviation (σ) = 0.2 wt%] and S [A = 1.2 wt%, σ = 0.1 wt%] values that rapidly decrease at 2350 m (A = 0.8 wt% TOC and 0.6 wt% S; **Figure 5**). These TOC contents are stable with small variations until 2100 m (S σ = 0.2 wt%; TOC σ = 0.1 wt%). The $CaCO_3$ content remains stable from 2385 until 2100 m with an average of 28 wt% (σ = 2 wt%). From 2100 m until 1510 m, $CaCO_3$ content shows higher variations (σ = 7 wt%, A = 20 wt%) and TOC (A = 1.0 wt%, σ = 0.3 wt%) and S (A = 1.1 wt%, σ = 0.6 wt%) contents are high compared to the underlying interval. Especially, from 1700 m until 1510 m, the S content and TOC (**Figure 5**) are high (>1 wt%, σ < 0.5 wt%) and the $CaCO_3$ content decreases (<20 wt%, σ = 6 wt%). At 1500 m, the TOC and S content both decrease and remain stable until the top of the section with small variations (TOC A = 0.4 wt%, σ = 0.1 wt%; S A = 0.3 wt%, σ = 0.1 wt%), whereas the $CaCO_3$ content increases to values around 25 wt% (σ = 3 wt%).

Well W

The variations of the LECO data in Well W (**Supplementary Table S3**) are similar to the variations in Well H. The deepest samples (3460 – 3370 m) show high TOC (A = 1.1 wt%, σ = 0.4 wt%) and S contents (A = 1.0 wt%, σ = 0.8 wt%) but low carbonate contents (A = 25 wt%, σ = 3 wt%) (**Figure 6**). From 3360 m upward until 1560 m, the TOC shows only minor variations (σ = 0.1 wt%) around an average content of 0.7 wt%. The S content (*A* = 0.6 wt%) is more variable (σ = 0.2 wt%) in this section and the $CaCO_3$ content is high compared to the underlying section (*A* = 35 wt%, σ = 4 wt%). From 1540 to 1380 m, the TOC (*A* = 1.0 wt%, σ = 0.1) and S (*A* = 0.9 wt%, σ = 0.3 wt%) values are increased, whereas the carbonate content is decreased (*A* = 27 wt%, σ = 4 wt%). At 1380 m, a decrease in the S content (from 1.1 to 0.3 wt%) and TOC (from 1.0 to 0.6 wt%) starts that lasts until 1280 m, in the same interval the $CaCO_3$ content increases (from 25 to 32 wt%; **Figure 6**). After this decrease, TOC (*A* = 0.5 wt%, σ = 0.2 wt%), S (*A* = 0.3 wt%, σ = 0.2 wt%), and carbonate content (*A* = 31 wt%, σ = 3 wt%) show little variation until the top of the sampled section.

Well Z

In Well Z (**Supplementary Table S3**) from 1495 m upward high TOC (*A* = 1.2 wt%, σ = 0.2 wt%) and S content (*A* = 1.0 wt%, σ = 0.3 wt%) with high standard deviations (**Figure 7**) were found, accompanied by $CaCO_3$ contents of 26 wt% (σ = 6 wt%), At 1125 m the TOC and *S* values decrease and rapidly increase to >1wt% at 1075 m again, where the $CaCO_3$ is low again (15 wt%). From 1065 m until the top of the sampled interval (755 m), the TOC (*A* = 0.4 wt%, σ = 0.1 wt%) and S (*A* = 0.2 wt%, σ = 0.1 wt%) are low and show low standard deviations. In contrast, the carbonate content is high (*A* = 35 wt%, σ = 2 wt%) in this uppermost section.

$\delta^{13}C_{carb}$

Results for $\delta^{13}C_{carb}$ are shown in detail in **Figure 9** (Well H, Z) and the **Supplementary Data** (Well W, **Supplementary Figure S4** and **Supplementary Table S3**). $\delta^{13}C_{carb}$ from Well H varies between −2.03 and +1.34‰ with the lowest values at the lowest part of the sampled section (2385 – 2350 m). At 2290 m, the $\delta^{13}C_{carb}$ values show a first maximum (0.82‰). They then decrease to values around 0.23‰ from 2250 to 2020 m with distinct negative and positive peaks at 2120 and 2070 m, respectively. From 2020 to 1840 m, the $\delta^{13}C_{carb}$ data show an increase to values around 1.00‰ (**Figure 9**). This plateau is present until 1740 m. At this depth, $\delta^{13}C_{carb}$ values show a decreasing trend until a minimum value of −1.27‰ at 1480 m. An interruption of this decreasing trend appears between 1610 and 1560 m with values up to 0.94‰. From 1480 to 1360 m, the $\delta^{13}C_{carb}$ values again increase to around 0.04‰ which then vary (σ = 0.19‰) around this value until the top of the section at 700 m. An outlier is present at 1090 m with a $\delta^{13}C_{carb}$ of −0.88‰.

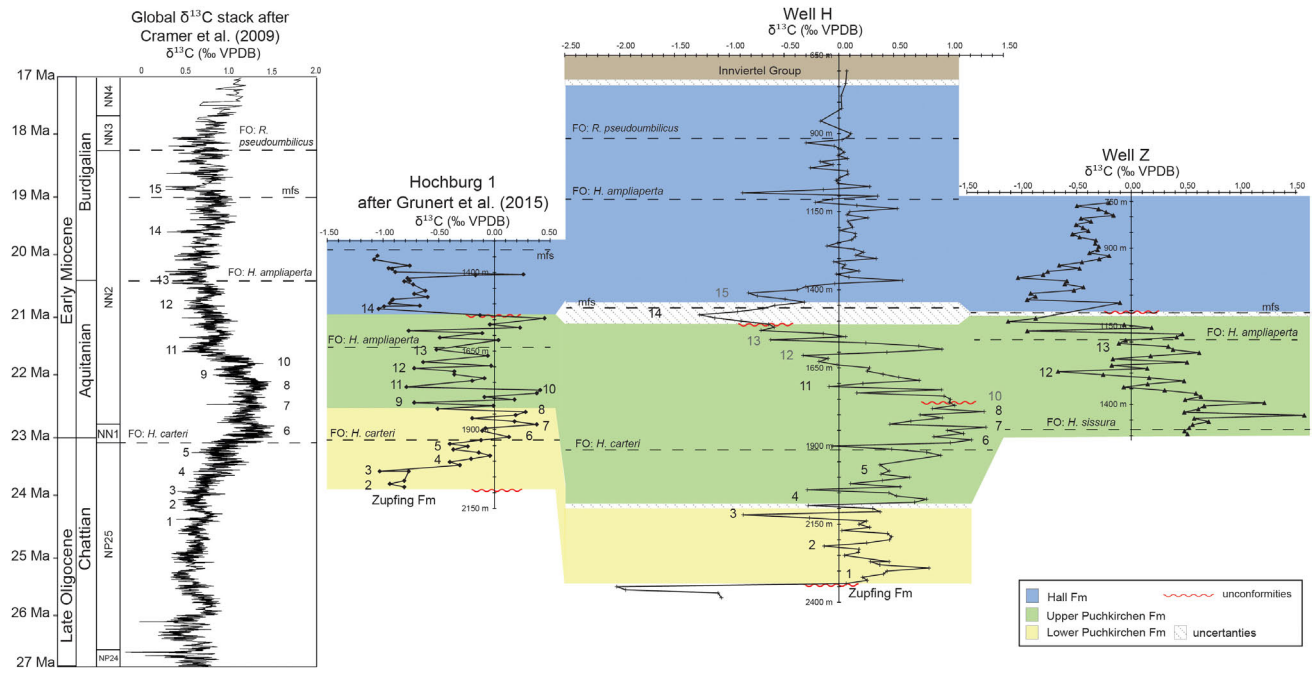

FIGURE 9 | Correlation of $\delta^{13}C_{carb}$ data from the Upper Austrian NAFB (Hochburg1, Well H and Z) and the global stack of Cramer et al. (2009). Numbers indicate minima and maxima in the global stack that are used for correlation. FO of *Helicosphaera ampliaperta, Helicosphaera carteri,* and *Reticulofenestra pseudoumbilicus* are shown. Maximum flooding surface (mfs) is taken from Grunert et al. (2013) in Hochburg1 and correlated by seismic interpretation to Well H and Z.

Data from Well W $\delta^{13}C_{carb}$ show a large variability between −4.85 and 2.86‰. The section from 3640 to 3100 m is characterized by values around 0.50 to 1.00‰, except for the deepest sample, which shows a value of −4.85‰. From 2200 to 1360 m, the values vary between 0.40 and 0.70‰. Exceptions are the intervals from 2020 to 1960 m (−0.10 to 0.22‰), from 1660 to 1620 m (1.06–2.68‰) and at 1500 m with a value of −0.51‰. Isotopic values from 1360 to 1260 m show a pronounced decrease from 0.77 to −0.56‰. Above 1260 m depth, the values show an increasing trend to 0.37‰ at 820 m. From 820 m to 400 m, $\delta^{13}C_{carb}$ data show only small variation (σ = 0.08‰) around 0.20‰ except for an outlier at 420 m depth with a value of −1.45‰.

Well Z shows $\delta^{13}C_{carb}$ values from −1.12 to 1.58‰ (**Figure 9**). The lowest part of the sampled section shows a plateau with mean $\delta^{13}C_{carb}$ values around 0.69‰ and σ = 0.09‰, with two outliers at 1435 and 1395 m (**Figure 9**). Isotopic values then decrease until 1295 m to −0.67‰ and vary until 1175 m around 0.14‰ (σ = 0.11‰). From 1175 m upward, the values decrease until they reach −1.12‰ at 1135 m. The values then increase slightly to −0.20‰ until 925 m, an outlier is located at 1075 m (−0.10‰). From 925 m until the top of the section at 755 m, the $\delta^{13}C_{carb}$ values show only small variations (σ = 0.01 ‰) around −0.36‰.

Sediment-Accumulation Rates and Transport Direction

In the channel model, SARs vary between 390 and 622 (t/m^2/Ma) (**Figure 10**). In the LPF, the geobody (**Figure 10**) shows a SAR of 390 (±103) (t/m^2/Ma). The UPF has a slightly increased SAR of 518 (±39) (t/m^2/Ma) and in the BHF the rates reach a maximum of 622 (±189) (t/m^2/Ma) (**Table 1** and **Figure 10**). The SARs of all three geobodies in the channel model overlap within their 1σ SD.

SARs of the overbank model vary widely between 186 and 1497 (t/m^2/Ma) (**Figure 10**). Geobody 1 (**Figure 8**) shows a SAR of 243 (±65) (t/m^2/Ma). In geobody 2, the SAR increases to 869 (±277) (t/m^2/Ma), and geobody 3 shows a SAR of 340 (±44) (t/m^2/Ma). In geobody 4, the SAR decreases to values of 240 (±31) (t/m^2/Ma). This decrease in SAR is continued in geobody 5 with a rate of 186 (±94) (t/m^2/Ma). Geobody 6 shows the highest SARs of both models of 1497 (±159) (t/m^2/Ma) (**Table 1** and **Figures 8**, **10**).

The rates of overbank geobodies 1, 3, and 4 illustrate the "background" SAR [243 ± 65 (t/m^2/Ma) from 24.5 to 23.5 Ma; 340 ± 44 (t/m^2/Ma) from 23.1 to 21.5 Ma; 240 ± 31 (t/m^2/Ma) from 21.5 to 19.6 Ma]. The differences (increase of ∼40% from geobody 1 to 3, decrease of ∼30% from geobody 3 to 4) overlap in their 1σ standard deviation.

Due to insufficient age-control points, the channel model consists of a single geobody in the UPF. To enable direct comparison of the SARs between the channel and the overbanks in the UPF, we combined geobody 2, 3, 4 of the overbank model (**Figure 9**). SAR in the overbank model in the UPF is 355 (±46) (t/m^2/Ma), ∼ 2/3 of the SAR in the channel model during UPF [518 (±39) (t/m^2/Ma); **Figure 9**].

The results of the clinoform dip-azimuth calculation show small variations between the eastern part (NNW dip) of

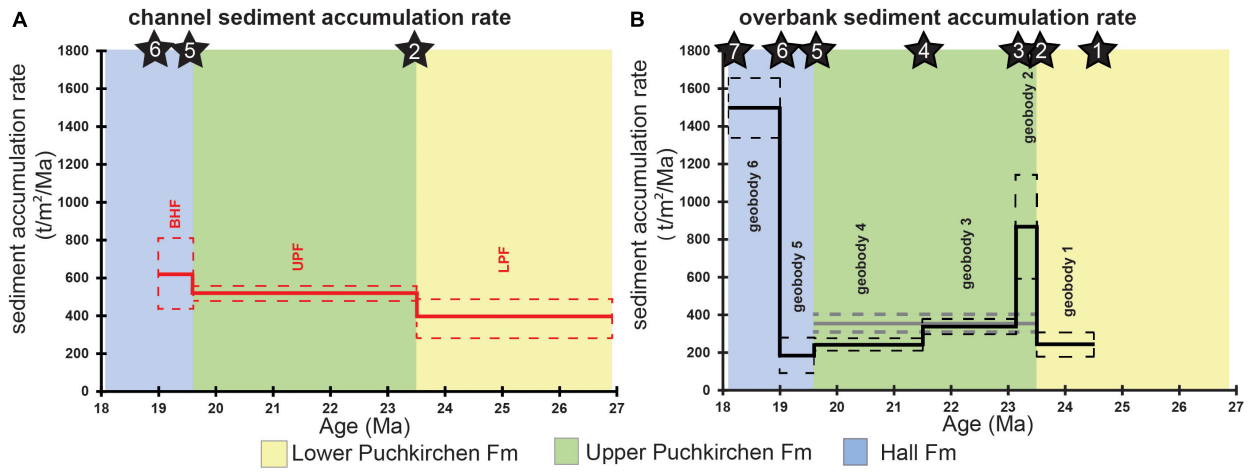

FIGURE 10 | Calculated sediment accumulation rates [SARs, (t/m^2/Ma)] of the channel **(A)** and the northern overbanks **(B)**, stars indicate the bio- and/or chemostratigraphic constrains of Well H (see **Table 1**); 1 = Peak 1 in $\delta^{13}C_{carb}$; 2 = U/LPF boundary (Peak 4 in $\delta^{13}C_{carb}$); 3 = FO *Helicosphaera carteri*; 4 = Peak 11 (carbon isotopy Well H); 5 = Peak 14 (carbon isotopy Well H); 6 = mfs and Sr-Isotopy from Maierhof; 7 = Hall/Innviertel boundary (Grunert et al., 2013). The gray bar in **(B)** indicates the combined, average SAR during the UPF onto the northern overbanks. SARs in the channel show variation within their 1σ standard deviation (SD). Note that during geobody 6 (star 6–7) channel sedimentation had ended; therefore, geobody 6 does not represent an overbank setting.

the basin and the western part (NNE dip). However, a dominating northern dip direction was found in the whole basin (**Supplementary Figure S1**).

DISCUSSION

Formation Boundaries

In Well H (**Figure 5**), the ZFM occurs from 2375 to 2325 m. Due to the absence of foraminiferal index species, this interpretation relies on the geochemical data (high TOC and S values, highly negative $\delta^{13}C_{carb}$ values). As nannofossil markers indicative of NP25 or younger are absent, we suggest an age of NP24 which is in agreement with Sachsenhofer et al. (2010) and Soliman (2012). The base of the LPF is defined in Well H by the FO of *Psammosiphonella cylindrica* (2325 m), what is supported by an increase in abundances diversity of the fauna (**Figure 5**). A distinctive decrease from very high S and TOC values (**Figure 5**) implies dysoxic to anoxic conditions compared to the more oxygenated conditions of the LPF.

The base of the UPF is located at 2100 m based on the LO of *Psammosiphonella cylindrica* (**Figure 5**) which is in agreement with the more variable TOC (σ = 0.3 wt%), S (σ = 0.6 wt%), and $CaCO_3$ (σ = 7 wt%) content compared to the LPF (TOC σ = 0.1 wt%; S σ = 0.2 wt%; $CaCO_3$ σ = 2 wt%) (Grunert et al., 2015). The FO of *Helicosphaera carteri* at 1920 m indicates nannoplankton zone NN1 (Aubry, 1989). Below 1920 m, we interpret NP25 based on the general assemblage including common and continuous occurrences of *Sphenolithus ciperoensis* and *Reticulofenestra bisecta*.

The HFM is defined by the FO of *Uvigerina posthantkeni* at 1455 m in Well H. However, based on a pronounced decrease in both, TOC and S, the base of the HFM is placed about 50 m deeper in the section at 1500 m (**Figure 5**). This significant change in the geochemical signature is typical for the base of the HFM (Sachsenhofer et al., 2017). Hence, we regard this change as a more reliable marker for the HFM than *U. posthantkeni*, which occurs in a single sample between foraminifera-barren intervals (**Supplementary Table S1**). In the HFM the FO of *H. ampliaperta* together with *Helicosphaera scissura* at 1120 m indicates NN2 and the FO of *R. pseudoumbilicus* > 7 μm indicates nannofossil zones NN3–NN4 at 910 m (**Figure 5**). Both findings support the stratigraphic concept of Grunert et al. (2013).

In Well W, the ZFM (3470 – 3200 m) appears similar to the ZFM in Well H, without indicators for neither NP24 nor NP25, high TOC and S values and no index foraminifera indicating the ZFM (**Figure 6**) nor the Puchkirchen Group. The $CaCO_3$ content is low (A = 25 wt%) and matches values reported in Sachsenhofer et al. (2010) for the ZFM.

From 3320 m upward, the geochemical data show low variability, which is indicative for the LPF (Grunert et al., 2015). Nevertheless, due to the FO *Psammosiphonella cylindrica* (3100 m), we interpret the base of the LPF to be located at 3100 m. The FO of *H. carteri* and presence of *S. delphix* (23.21 – 22.97 Ma; Backman et al., 2012) indicate the Oligocene/Miocene boundary and the lower boundary of NN1 at 1800 m. The base of the UPF is located between 1560 and 1520 m (**Figure 6**). The FO of *H. scissura* is recorded at 1424 m, a clear indicator for NN2 (**Figure 6**; Backman et al., 2012).

The HFM was defined by the FO of *U. posthantkeni* at 1360 m. This is supported by the decrease of TOC and S values that initiates at 1360 m but terminates at 1300 m (**Figure 6**). The FO of *H. ampliaperta* at 1260 m indicates mid-NN2. The FO of *R. pseudoumbilicus* > 7 μm indicates NN3 at 760 m. The FO of *Amphicoryna ottnangensis* (580 m) points to the Innviertel Group.

In Well Z, the geochemical data at 1500 m depth indicates that the section is part of the UPF. TOC and S content are above 1 wt% in the section until 1150 m where both contents decrease (**Figure 7**). At 1125 m, both curves indicate a minimum, which we interpret as the BHU (**Figure 7**), whereas the FO of *U. posthantkeni* is recorded shortly above that at 1110 m. The FO of *H. ampliaperta* at 1190 m indicates mid-NN2 (Ćorić and Spezzaferri, 2009).

When our new data are compared to the stratigraphic concept of Grunert et al. (2015), the positions of FOs of the calcareous nannoplankton with regard to the formation boundaries from foraminiferal analysis vary between the analyzed drill sites and the published data. The findings of Well H indicate the FO of *H. carteri* in the UPF (**Figures 5**, **11**) whereas Grunert et al. (2015) report it from the LPF. The FO of *H. ampliaperta* in Well H is located in the HFM, which Grunert et al. (2015) found in the UPF. An earlier occurrence is possibly not recorded as the 400 m below the FO are barren of nannofossils. In Well W, the FOs of *H. carteri* and *S. delphix* (1800 m) mark the Oligocene/Miocene boundary within the LPF (**Figures 6**, **11**) and support the results of Grunert et al. (2015). However, the FO of *H. ampliaperta* is recorded within the HFM at this site. *H. ampliaperta* specimens were large in size (∼10 μm), indicating that the recorded FO does not correspond to the actual base of the taxon range, as specimens are generally smaller (∼4 – 6 μm) at its stratigraphic base occurrence (Holcová, 2009; Grunert et al., 2015). The FO of *H. scissura* is already recorded below the BHU. This FO normally occurs before *H. ampliaperta* (Grunert et al., 2015). Therefore, we interpret the FO of *H. ampliaperta* in Well W as delayed, due to the erosive activity of the channel at the BHU (**Figure 11**). In Well Z, the FO *H. ampliaperta* is also reported below the BHU

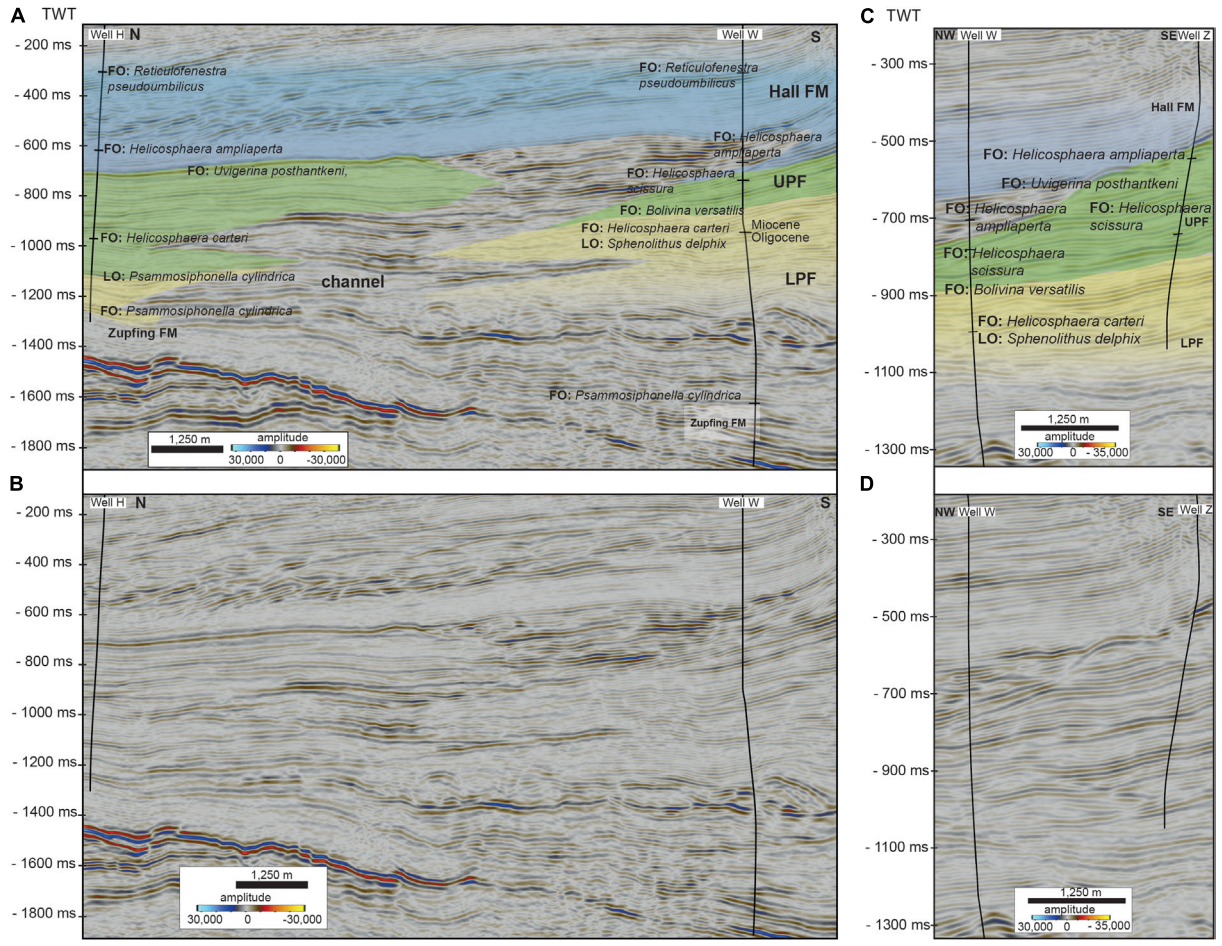

FIGURE 11 | (A,B) Seismic cross section from Well H to W (for location see **Figure 1**), **(A)** interpreted section, **(B)** un-interpreted section, with first and last occurrences of index taxa, note the difference in strata thickness on the northern and southern side of the channel. In Well W, the boundary of ZFM/LPF was drilled ∼600 m deeper, than in Well H. The boundary LPF/UPF differs significantly on the northern and southern side of the channel, probably due to differences in biofacies, while the facies independent nannofossil *Helicosphaera carteri* has its FO approximately at the same depth. **(C,D)** Seismic cross section from Well Z to W (for location see **Figure 1**), **(C)** interpreted section, **(D)** un-interpreted section, with first and last occurrences of index taxa, note the great lateral variability of sediment thickness on the southern slope and the filled up, paleo-relief created by slope failure. The erosive character of the channel is well visible in Well W and is responsible for the delayed FO of *Helicosphaera ampliaperta.* Note that the UPF/LPF boundary in Well Z is correlated from Well W. In **(A,C)** the channel was excluded from the interpretation.

(Ćorić and Spezzaferri, 2009) which agrees with the concept of Grunert et al. (2015).

Sample contamination of the investigated drill cuttings by sediment movement during the drilling process and upward transport of cuttings potentially pose significant obstacles for biostratigraphic interpretation. We consider contamination unlikely in the present study, because the order of FO of the index nannofossils in each sampled well is agreement with their order of appearance in the open ocean (Martini, 1971). The results of the $\delta^{13}C_{carb}$ analysis and its good match to the global record (Cramer et al., 2009) further suggest comparable depositional ages. This illustrates that the temporal lag of migration of the nannoplankton between the open ocean and the Oligocene/Miocene western part of the Paratethys – a highly restricted marginal sea (Rögl, 1998) – is small and mainly controlled by our sampling rate and/or the preservation.

The variations in the position of the Oligocene/Miocene boundary (LPF in Well W and Hochburg1; Grunert et al., 2015; UPF in Well H, **Figures 5**, **6**, **11**) is attributed to the facies-dependency of benthic foraminifera that are used to define the formations (Küpper and Steininger, 1975). Benthic foraminifera are highly responsive to ecological changes at the sea floor (Murray, 2006). The proximity of the channel creates a highly dynamic paleoenvironment with significant lateral biofacies variability ultimately impacting the correlation across the channel-belt by benthic foraminifera analysis (**Figure 11**) (Grunert et al., 2013, 2015). This influences the formation boundaries which are based on benthic foraminifera as these changes are very likely to be local rather than basin-wide. This also heavily impacts the correlation across the channel-belt (**Figure 11**). These problems are manifest in problems with the identification of the LPF/UPF boundary. The boundary is hard to identify (**Figures 5**, **6**), facies-dependent (**Figure 11**), and an artificial one.

The FOs of the nannofossils are facies independent and therefore a more reliable way to correlate strata across the channel-belt and to global chronostratigraphy (**Figure 11**) (Backman et al., 2012). However, the low abundance, generally poor preservation of nannofossils, and sampling resolution complicate biostratigraphic correlation, resulting in the observed diachroneity of nannofossil datums between wells (**Figure 11**). On the southern basin slope, the proximity of our sampled locations to their sediment sources created a sedimentological environment that is laterally highly variable (**Figure 11C**) and further complicated by occasional mass-wasting events (Hinsch, 2008; Covault et al., 2009; Kremer et al., 2018).

Stratigraphic Correlation Based on $\delta^{13}C_{carb}$, Biostratigraphy and Temporal Duration of Unconformities

The newly acquired results from the $\delta^{13}C_{carb}$ analysis are supported by our biostratigraphic results. When compared to the global curve after Cramer et al. (2009), the $\delta^{13}C_{carb}$ data from Well H show similar trends (**Figure 9**). A prominent feature of the global carbon isotope curve is a plateau of positive values at the beginning of the Aquitanian (NN1 to lower part of NN2, ∼23.13 to 21.7 Ma) with four positive peaks. This plateau occurs in the global $\delta^{13}C_{carb}$ stack after a steady increase during the upper part of NP25 interrupted by four local minima, at 23.3, 23.5, 23.9, and 24.2 Ma. Data from Well H suggest a similar trend of increasing $\delta^{13}C_{carb}$ values from 2250 m with distinct minima at 2010 – 1960 m, 2090 m, 2120 m and 2200 m (upper NP25). At 24.5 Ma the global $\delta^{13}C_{carb}$ curve indicates a maximum, a similar feature is shown at 2290 m in the data from Well H. These findings imply a duration of ∼24.5 to 23.5 – 23.2 Ma for the deposition of the LPF (**Figure 9**).

The plateau (23.0 to 21.8 Ma, **Figure 9**) in the $\delta^{13}C_{carb}$ curve (Cramer et al., 2009) is mirrored in the data from Well H between 1890 and 1740 m. This interpretation is in good agreement with the FO *Helicosphaera carteri* at 1920 m, indicating an age of 23.13 Ma.

The global $\delta^{13}C_{carb}$ data decrease quickly from the previous plateau to lower values at ∼21.5 Ma and stay at low values during the remaining NN2. Significant negative excursions are noticeable at 20.8, 20.4, 20.2, 20, 19.6, and 18.8 Ma (**Figure 9**). The decrease in isotopic values of the global stack is recorded by the data of Well H at 1710 m, indicating an age of 21.5 Ma and for the minima in $\delta^{13}C_{carb}$ data at 1610 m an age of 20.8 Ma. We correlate the maxima at 1590 m and two minima at 1560 and 1480 m in the $\delta^{13}C_{carb}$ record from Well H to minima in the global curve at 20.2, 20, or 19.6 Ma. In contrast to well Hochburg1 (Grunert et al., 2015), erosion at Well H was minor or absent at the BHU (**Figure 11**). Grunert et al. (2015) assigned an age of 19.5 – 18.9 Ma for the BHU by extrapolating sedimentation rates. We suggest that the negative $\delta^{13}C_{carb}$ values in our samples at the BHU (1510 m) can be correlated to the negative excursion at 19.6 Ma on the global $\delta^{13}C$ curve. This implies a time span of 23.5 – 23.2 Ma to 19.6 Ma for the UPF at Well H (**Figure 9**).

This interpretation is supported by $^{87}Sr/^{86}Sr$ data from Janz and Vennemann (2005). These authors presented the isotopic composition (O, C, Sr, and Nd) of brackish ostracods from an outcrop at Maierhof at the northern boundary of the NAFB (**Figure 4E**). The outcrop is interpreted to record a middle Eggenburgian maximum flooding surface (mfs) accompanied by the FO *Elphidium ortenburgense* (Wenger, 1987). Janz and Vennemann (2005) inferred open marine conditions at Maierhof in the middle Eggenburgian from their results. When tuned to the global $^{87}Sr/^{86}Sr$ curve (McArthur et al., 2012), the isotopic values from Maierhof indicate a depositional age of 19.1 to 18.9 Ma. Grunert et al. (2013) postulated that the termination of submarine channel sedimentation in the BHF was associated with a maximum flooding surface at well Hochburg1 and the FO of *Elphidium ortenburgense*. The interpretation that the negative $\delta^{13}C_{carb}$ excursion at 1480 m is related to the negative excursion at 19.6 Ma on the global carbon isotopic stack is supported by these ages, as there is no other large negative excursion at that time in the global record (**Figure 9**). Increasing $\delta^{13}C_{carb}$ values above the BHF can be correlated to the global stack of Cramer et al. (2009) at 19 Ma. These results imply a time span of 19.6 to 19.1 – 18.9 Ma for the BHF and the timing of the BHU on the overbanks. From 1370 m until the top of the section, the $\delta^{13}C_{carb}$ data from Well H do not reflect global trends.

Diagenetic alteration of the original $\delta^{13}C_{carb}$ signal due to the release of ^{12}C from sedimentary organic matter or clay minerals (Marshall, 1992) is unlikely to explain the trend in $\delta^{13}C_{carb}$ in Well H. In most samples from Well H, the $CaCO_3$ content is > 20 wt% and statistical analysis shows no correlation between carbonate content and the carbon isotope record (R^2 = 0.03). Only in samples from 1740 – 1510 m, $CaCO_3$ contents are low (≥7 wt%), nevertheless, the $CaCO_3$ and $\delta^{13}C_{carb}$ values show no correlation (R^2 = 0.07) in this part. The $\delta^{13}C_{carb}$ and the $\delta^{18}O_{carb}$ data from Well H do not correlate (R^2 = 0.1). Therefore, we argue against an influence of diagenetic alteration to this data set.

The $\delta^{13}C_{carb}$ values from Well W (**Supplementary Figure S4**) do not resemble the trends of the global stack or the wells H and Hochburg1 (Cramer et al., 2009). The $\delta^{13}C_{carb}$ values from Well W show a moderate correlation (R^2 = 0.58) to the $\delta^{18}O_{carb}$ values of the section, we thus refrained from using the data due to a diagenetic overprint.

In Well Z, the $\delta^{13}C_{carb}$ data of the lowermost section show a plateau with three distinct peaks (1435, 1395, 1325 m, **Figure 9**). Based on the FO of *Helicosphaera scissura* at 1490 m (**Figure 7**), we suggest a lower NN2 age for the base of the well. The rapid decrease to negative values (−0.67‰) at 1295 m may represent the abrupt decrease of the global $\delta^{13}C_{carb}$ curve at 20.8 Ma. The FO of *Helicosphaera ampliaperta* at 1190 m in Well Z supports the interpretation that the second negative excursion represents the global decrease at 20.44 Ma in the global $\delta^{13}C_{carb}$ curve. From 1190 m upward, the $\delta^{13}C_{carb}$ data of Well Z are highly variable making unambiguous correlation to the global stack difficult (**Figure 9**). These findings indicate a timespan from 20.92 Ma to <20.44 Ma for the investigated section of the UPF, with the BHU having an age of <20.44 Ma.

In context of possible alteration of the isotopic signal due to ^{12}C from organic matter or clays (Marshall, 1992), the data from Well Z indicate only sporadic samples with $CaCO_3$ values of <20 wt%. The isotopic data from the UPF section shows no correlation with the $CaCO_3$ content (R^2 = 0.03), but the data from above the BHU indicate a weak correlation (R^2 = 0.39). Therefore, diagenetic alteration is considered unlikely for the samples within the UPF, whereas in the HFM such a bias may be present.

Revisiting the Stratigraphic Concept for the Upper Austrian Molasse

Grunert et al. (2015) have introduced a new stratigraphic concept for the Puchkirchen Group and the overlying Hall Formation. The results presented here support, improve and expand this concept (**Figure 12**). The samples from the ZFM

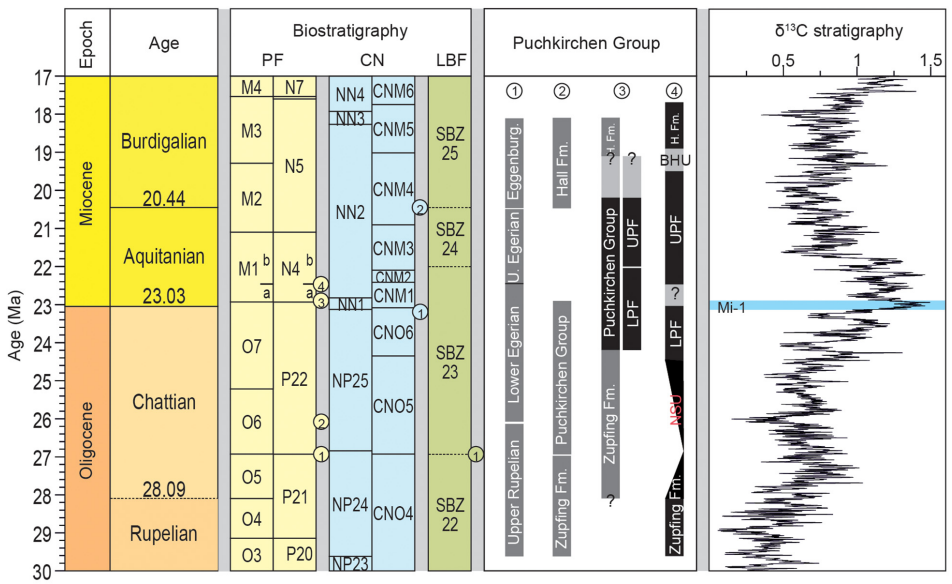

FIGURE 12 | Summary of the proposed stratigraphic concepts (number 1, 2, 3) of the Puchkirchen Group and the concept presented here (4). Planktonic foraminifera (PF) zonation follows Wade et al. (2011) and Gradstein et al. (2012); calcareous nannoplankton (CN) zonation follows Backman et al. (2012); Gradstein et al. (2012), and Agnini et al. (2014); larger benthic foraminifera zonation follows Cahuzac and Poignant (1997) and Gradstein et al. (2012). Global $\delta^{13}C$ stack from Cramer et al. (2009). Gray bars indicate uncertainties, BHF summarized as BHU. See text for details. Redrawn after Grunert et al. (2015).

in Well H and Well W suggest an intra-NP24 age. This intra-NP24 age is in agreement with the results of Sachsenhofer et al. (2010) and Soliman (2012) from dinoflagellate cysts and calcareous nannoplankton, respectively. Furthermore, Soliman (2012) stated that the ZFM contains the Rupelian/Chattian boundary (28.09 Ma), indicated by a peak in *Rhombodinium draco* in the lower part of the ZFM. Therefore, a depositional age of 29.6 to 28.1 – 26.9 Ma for the ZFM is likely.

The base of the Puchkirchen Group on the northern slope is now well dated to ∼ 24.5 Ma based on the data from this study and Grunert et al. (2015). Sedimentation on the northern basin slope started after a period of non-deposition from <28.1 Ma (Soliman, 2012) to ∼ 24.5 Ma (**Figure 12**), which is expressed in the NSU (Masalimova et al., 2015). Nevertheless, it is unclear whether a similar hiatus is present along the axis of the basin or if deposition of the Puchkirchen Group began earlier here than on the northern slope. In the 3D seismic-reflection data, no indication for a large-scale hiatus was found. Our efforts to date the ZFM/LPF boundary in Well W were unsuccessful due to diagenetic alteration of $\delta^{13}C_{carb}$ and further investigations are necessary to solve this question. Today, a difference in depth of ∼600 m is separating the ZFM/LPF boundary in Well H and W (**Figure 11**). The diachronic deposition of sediments on a passive margin and the axial part is a well-documented feature of underfilled, wedge-shaped foreland basin (DeCelles and Giles, 1996) and has also been described in the western part of the NAFB (Sinclair, 1997). Therefore, we argue against a significant hiatus in the central part of the basin and propose an age of 26.9 Ma (base NP25) to 24.5 Ma for the base of the LPF (**Figure 12**).

The age of the boundary between the Lower and Upper Puchkirchen Formation can be constrained by carbon isotope data to ∼23.5 Ma in Well H (**Figure 9**), from calcareous nannoplankton in Well W to 23.1 – 20.4 Ma (**Figure 6**) and to >20.4 Ma from chemo- and biostratigraphy in Well Z (**Figure 7**). Grunert et al. (2015) postulated an age of 22.2 – 22 Ma (**Figure 12**). The differences can be explained by the facies dependency of the foraminiferal index taxa (see section Formation Boundaries).

The top of the UPF in Well W and Well Z has been eroded precluding unambiguous correlation with global chronostratigraphy. Nannofossils from Well W and Z indicate an age of <23.1 Ma and <20.4 Ma, respectively. At Well H, seismic reflections show no erosion at the BHU (**Figure 11**). Carbon isotopic correlation indicates an age of ∼19.6 Ma (**Figure 12**), which is in good agreement with estimates of Grunert et al. (2015) and $^{87}Sr/^{86}Sr$ data by Janz and Vennemann (2005). The termination of channel sedimentation and the BHF at 19.1 – 18.9 Ma result from a sea-level increase resulting in a mfs at Hochburg1 (Grunert et al., 2013) and Maierhof (Wenger, 1987; Janz and Vennemann, 2005). This correlates well with the middle Eggenburgian mfs which was correlated to global 3rd order sequence Bur2 (Piller et al., 2007) and the mfs in the Swiss NAFB (Garefalakis and Schlunegger, 2019). Nannofossil biostratigraphy from Well H suggests an age of 18.1 Ma for the base of the Ottnangian Innviertel Group above the Hall Formation, which is in good accordance with previous results (Grunert et al., 2010, 2013).

This stratigraphic framework with the Puchkirchen Group on the northern basin margin ranging from 24.5 to 19.6 Ma – in the axial part of the basin, sedimentation of the Puchkirchen Group is likely to have started before 24.5 Ma – and the Hall Formation spanning from 19.6 to 18.1 Ma agrees with the data from Grunert et al. (2013, 2015) but differs significantly (**Figure 12**) from previous concepts (Küpper and Steininger, 1975; Rögl et al., 1979). Reasons for these differences were discussed by Grunert et al. (2015). These authors also discussed the complications of the stratigraphic correlation in the Paratethys which arise from the assignment of lithostratigraphic units to regional stages. The regional stages are often defined by locally restricted ecostratigraphy what hampers the correlation (Grunert et al., 2015).

External Forcings Detected in SARs

Comparing the SARs between the channel and overbank models is not straightforward as sediment is eroded in the channel (Hubbard et al., 2009). Furthermore, the channel continues toward the east where it is affected by thrust tectonics. Hence, the channel in the study area is also subject to sediment bypass and does not form the ultimate sediment sink of the sedimentary system. In fact, the position of the final sink, the submarine fan that is associated with this submarine channel is currently unknown (Hubbard et al., 2009). The Puchkirchen channel system represents a sediment-transfer zone for the Alpine detritus. Therefore, decreased channel SARs may be interpreted as decreased sediment supply or as periods of increased sediment bypass. Sediment on the northern overbanks might remain in the basin over longer time scales as it is remobilized only by channel-meander bend migration and associated erosion into the underlying overbank deposits, channel avulsion (undocumented in the study area), and/or levee breaches (Hubbard et al., 2009). Therefore, the overbanks may represent a local, terminal sink.

Overbank geobody 2 shows a 3.5-fold increase compare to Overbank geobody 1 in SAR from 23.5 to 23.1 Ma (**Figure 10**). On the shelf, Zweigel (1998) showed prograding and aggrading clinoforms with a high SAR which might be linked to increased sediment flux from the exhumation of the Lepontine Dome. This is followed by a sea-level highstand at the Oligocene/Miocene boundary as indicated by the deposition of marly claystones (Zweigel, 1998). The increase in the overbank SAR around 23.5 Ma might be related to the high SARs on the shelf before the Chattian/Aquitanian boundary, which in turn may be related to the exhumation on the Lepontine Dome.

However, we favor an alternative explanation related to an autogenic process within the channel system, because of the drastic SAR increase and the short duration (∼0.4 Ma) of the increase: During the deposition of overbank geobody 1, the channel showed a slightly sinuous course and a northward-directed, subtle meander bend located on the northern edge of the seismic cube (**Figure 13A**). During the deposition of overbank geobody 2, the channel meander adjacent to the overbank volume abruptly changed its course to the south (**Figure 13B**) forming a pronounced meander bend and a broad northern overbank plain (**Figures 2**, **8**, **13**). The channel

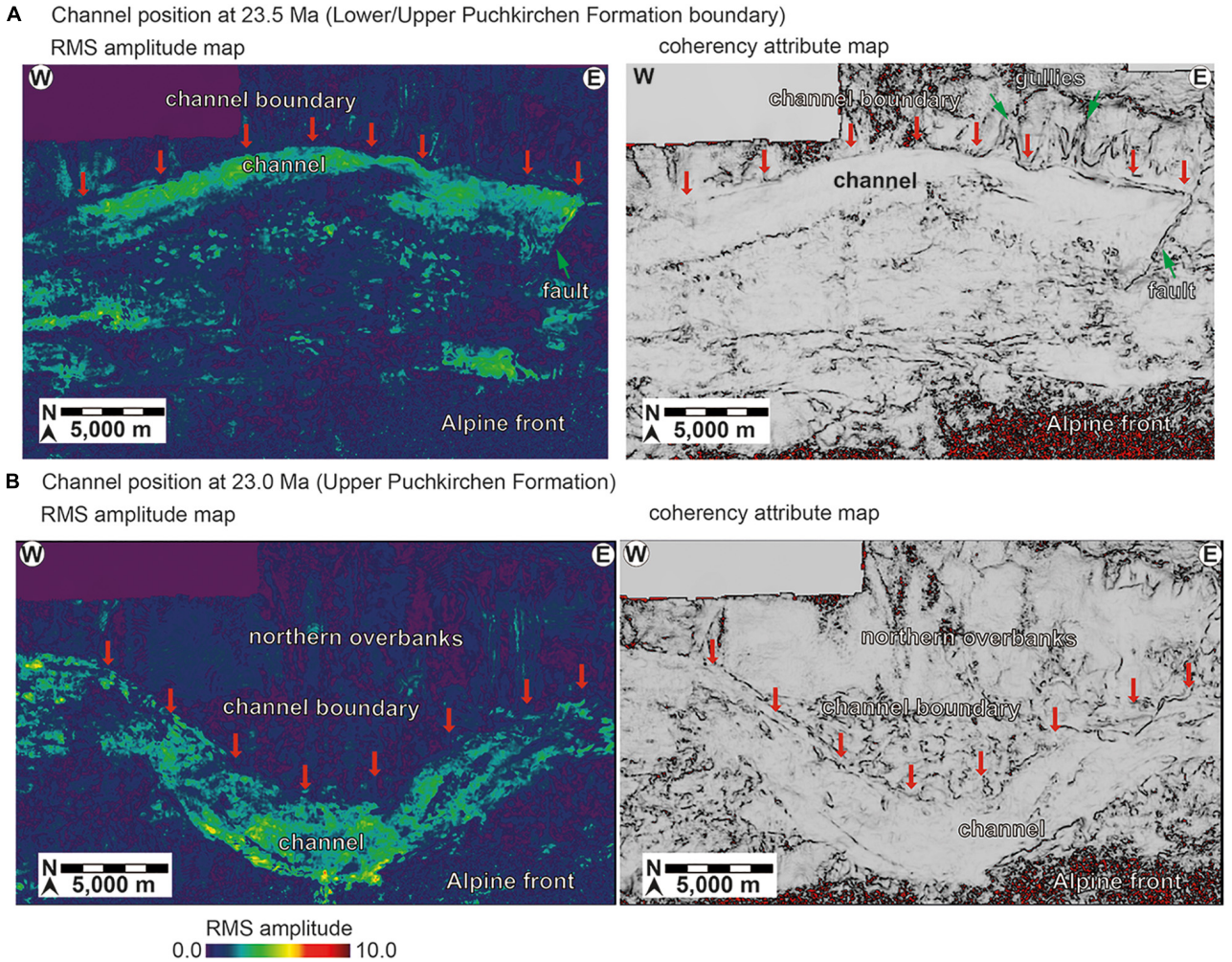

FIGURE 13 | RMS amplitude and coherency maps of the channel and overbank area (for position see **Figure 1B**) at 23.5 Ma **(A)** and 23.0 Ma **(B)**. At 23.5 Ma **(A)** the channel is close to the northern border of the seismic cube, the overbanks are narrow. Until 23.0 Ma **(B)** the channel changes its position close to the Alpine thrust front and creates wide, northern overbanks. Red arrows mark the channel boundary, green arrows the gullies on the NSU and a fault.

was forced to change its geometry due to plugging by debris-flow deposits sourced from the west (Masalimova et al., 2015). The increase in sinuosity probably led to an increase of flow stripping of the upper part of channel-traversing turbidity currents onto the northern overbanks. The upper surface of the NSU is characterized by southward (channel)- directed gullies, that transported material into the main channel belt (**Figure 13A**, Masalimova et al., 2015). Such gullies are absent after the change in channel-meander geometry (**Figure 13B**). Increased flow stripping and the absence of gullies have led to a uniform and widespread deposition of sandstones on the overbanks (Masalimova et al., 2015). Therefore, the dramatic increase in SAR between 23.5 and 23.1 Ma (**Figure 10B**) is interpreted to be the result of an autogenic change in channel geometry.

Results from laboratory and numerical models suggest, that overbanks of high sinuous channels show increased SARs due to overspill than those overbanks of low sinuous channels (Amos et al., 2010; Huang et al., 2012). The observed increase in sinuosity of the channel from ∼1.05 at 23.5 Ma to ∼1.14 at 23.0 Ma (**Figure 13**) is in line with these results and further supports our interpretation of an autogenic SAR increase. Furthermore, on the Monterey Fan and channel system, Fildani et al. (2006) observed a similar fourfold increase in sedimentation rates in areas of increased flow stripping when compared with background overbank sedimentation.

Geobody 5 records stable and low SAR on the overbanks (compare to geobody 4 overlap within their standard deviation; **Figure 10** and **Table 1**). As reported by De Ruig and Hubbard (2006), the uppermost UPF and BHF show a decrease in grain size and an increase in mud content, which suggests a reduction of turbidity-current height, density and/or competence. The turbidity currents in the channel became less efficient in spilling their diluted tops onto the overbanks. This process also explains the two characteristics of the BHU in the seismic-reflection data

(**Figure 2**): Whereas on the northern overbanks the section above and below the BHU is characterized by continuous, high-amplitude reflectors, the channel around the BHU is highly erosive – evidenced by truncated reflectors and the biostratigraphic results from Well W (**Figures 2**, **6**, **11**, late appearance of *H. ampliaperta*, see section Formation Boundaries for discussion).

The SARs from the channel and overbank model in the time interval from 19.6–19.0 Ma are directly linked to the process which has caused the formation of the BHU. Zweigel (1998) pointed out that on the Bavarian Shelf the SAR became negative (erosion) in her Sequence 4a (interval below BHU, **Figure 3**). Sequence stratigraphy (Jin et al., 1995; Zweigel, 1998) as well as foraminifera analysis (Wenger, 1987) indicate a major sea-level decrease in the eastern NAFB. Erosion on the shelf (Zweigel, 1998) points to a redeposition of shelf sediments into the deeper basin in the period from 19.6 – 19.0 Ma also evident by the foraminiferal fauna in the channel sediments in Hochburg1 (**Figure 1**) (Grunert et al., 2013). If from 19.6 – 19.0 Ma the channel was mainly fed by redeposited material from the Bavarian Shelf, sediment-supply rate from the hinterland must have dropped accordingly within this period to maintain the relatively constant and low SARs. Consistently, Kuhlemann (2000) described on the Egerian/Eggenburgian boundary a ∼45% decrease in sediment-supply rates from the Eastern Alps and a decrease of ∼35% in rates from the Central Alps.

Zweigel (1998) explained her findings on the shelf (sediment starvation, an angular unconformity, uplift in the northern part of the NAFB, decrease in sea level, deepening of the basin at the axis) with the visco-elastic relaxation of the European Plate that has caused an uplift of the forebulge, propagation of the bulge toward the orogenic front and a decrease in elevation in the hinterland. This would explain the decrease in sea level, the erosion and redeposition of older foreland sediments into the deeper basin through uplift and subareal exposure of parts of the shelf, and the decrease in sediment-supply rates and grain size related to a decrease in elevation in the Alpine hinterland. Zweigel's (1998) model is further in line with the ceasing of northward progradation of the Eastern Alpine front during the UPF (Hinsch, 2013). The uplift and progradation of the forebulge does not require a northward progradation of the thrust front as the stress relaxation of the lithospheric plate is dependent on temperature, rheology, and initial stress (Beaumont, 1981). The doubling in lag times in apatite fission track ages from the proximal archives of the paleo-Inn from 2–4 Ma in Aquitanian to 6–8 Ma in Burdigalian sediments (Kuhlemann et al., 2006) further support the idea of a relief reduction in the hinterland. We therefore interpret the BHU as the result of a period of non-sedimentation on the overbanks and, likely, in the channel, followed by a period when the channel was fed by remobilized shelf sediments. Grunert et al. (2013) pointed out that the channel in Hochburg1 (**Figure 1**) cuts into the UPF, deposited middle Eggenburgian strata but lower Eggenburgian strata is missing. Therefore, we suggest that the period of non-sedimentation extends over the entire early Eggenburgian.

After the mfs at 19 Ma, the SAR indicates a 8-fold increase compared to the geobody 5 (**Figure 10**, 4.5-fold increase compared to geobody 3). During this period – the beginning of the Upper Marine Molasse – channel sedimentation terminated and hemipelagic sedimentation (**Figures 2–4**) was established (middle Eggenburgian), which was replaced by clinoform progradation from the southern margin into the basin in the late Eggenburgian. These clinoforms indicate a sediment transport direction roughly from S to N (**Figures 2**, **7** and **Supplementary Figure S1**) (Grunert et al., 2013). It is likely that the clinoform progradation caused the tremendous increase in the SAR from 19 to 18.1 Ma (**Figure 10**).

During the period from 19.0 to 18.1 Ma, the basin shallowed from 1,000 – 1,500 m water-depth (Grunert et al., 2013) to water-depths <200 m (Grunert et al., 2012). The basin was transformed from an underfilled foreland basin (characterized by wedge-shaped deposits) to a filled one (sedimentary deposits tabular) (**Figure 2**), an evolution that occurred ∼11 Ma earlier in the Swiss part of the NAFB (Sinclair, 1997). The shallowing trend cannot be explained by eustatic sea-level fall (Haq et al., 1987) or a drastic change in subsidence patters in the basin (Genser et al., 2007). Instead, the basin was filled-up by sediments deposited by prograding clinoforms (**Figures 2**, **10**). The migration direction of the clinoforms (from S to N, **Figure 2** and **Supplementary Figure S1**) indicate a southern source. Detrital zircon U-Pb ages further suggest a change in provenance, when compared to the underlying UPF (Sharman et al., 2018). The provenance change and the predominantly northward directed sediment supply is consistent with redeposition of the Augenstein Formation on top of today's Northern Calcareous Alps (Frisch et al., 2001).

Two of the four expected external forcings are mirrored in the SARs of the Oligocene/Miocene Upper Austrian NAFB; the visco-elastic relaxation of the European Plate at 19.6 – 19 Ma and the unroofing and redeposition of the Augenstein Formation from 19.0 Ma onward. However, our data do not record the initially hypothesized doubling in SAR in connection with the external signals of the exhumation of the Lepontine Dome and the Tauern Window. Both signals were described within the proximal sedimentary archives in the Swiss NAFB (Schlunegger and Norton, 2015) and the south-east German NAFB (**Figure 4**; Ganss, 1977). In case of the external forcing of the Lepontine Dome, signal shredding may have occurred within the fluvial sediment-transfer zone. Sediments traveled a distance of ∼500–600 km from the proximal archives into the deep-marine sink. The intermittent basins, the Swiss and German NAFB, created transient accommodation space along the sediment-routing system in which the excessive sediment load was stored (Kuhlemann and Kempf, 2002) and, hence, the tectonic signal is not manifested in the SARs of the marine transfer zone of the study area.

The increase in SAR of ∼65–100% (Ganss, 1977) described from the deep-marine section (Wenger, 1987) of the Chiemgau Fan (**Figure 4**) and related to the exhumation of the Tauern Window in the Eastern Alps is also not recorded in our SAR results. At present, the Chiemgau Fan is located

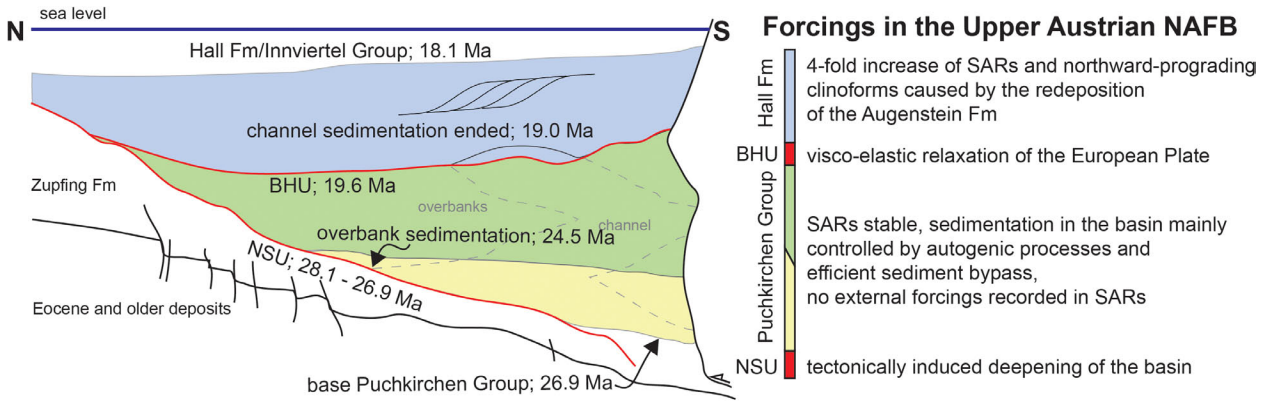

FIGURE 14 | Schematic cross section through the Upper Austrian NAFB, with the Puchkirchen Group (yellow and green) and the Hall Fm (blue) and the dominating processes in the basin. Important steps in basin evolution were newly dated with the NSU (lower red line) being established at 28.1 – 26.9 Ma. Puchkirchen Group sedimentation started at 26.9 Ma in the axial part of the basin and at 24.5 Ma on the overbanks. The BHU (upper red line) is now dated to 19.6 – 19.0 Ma and the termination of channel sedimentation to 19.0 Ma. The Hall Fm (19.6 – 18.1 Ma) recorded the filling of the basin. See text for discussion.

merely ∼70 km south-west of our research area (**Figure 4**). This implies that the Puchkirchen channel system has been very efficient in bypassing sediment. The channel system is characterized by low sinuosity (1.05 – 1.5; De Ruig and Hubbard, 2006) and the absence of avulsions (Hubbard et al., 2009) throughout the >7.4 Myrs of channel activity, possibly due to the lack of available space in the narrow (<20 km) foreland (Hubbard et al., 2009). These channel characteristics may increase bypass efficiency through the reduction of areas of sediment deposition, such as channel-avulsion strata and lateral accretion at inner meander bends. The bypass efficiency of the system may be an additional reason for the non-recording of the signal from Lepontine-Dome exhumation.

After the reorganization of the NAFB at 19 Ma, resulting in the termination of channel sedimentation and the decrease of bypass efficiency of the sediment-routing system, the basin in the study area evolved from the marine transfer zone to the marine, terminal sediment sink. Hence, the sedimentary archive in the Upper Austrian NAFB was able to record the redeposition of the Augenstein Formation.

Geodynamic Implications

With the new stratigraphic results, we are able to further constrain the evolution of the basin. The NSU formed between 28.1 (Soliman, 2012) and 26.9 Ma (**Figure 14**). Masalimova et al. (2015) suggested a tectonically induced oversteepening of the northern basin slope due to a deepening of the basin axis. A temporal correlation exists with a northward advance of the Alpine thrust front (Kuhlemann and Kempf, 2002) as well as the final nappe stacking and crustal thickening in the Eastern Alps (Frisch et al., 2000). Both processes lead to an extra load onto the European Plate and could account for the basin deepening.

During the deposition of the Puchkirchen Group, sedimentation rates in the basin were mainly controlled by autogenic processes (**Figure 14**). However, minor tectonic activity is evident in the basin on the southern slope where Penninic and Helvetic thrust sheets overthrusted and partly incorporated Puchkirchen strata (Covault et al., 2009; Hinsch, 2013). The northward progradation of the Alpine front ceased in the UPF and the deformation stepped back into the orogenic wedge (Hinsch, 2013).

The northern NAFB was uplifted (Zweigel, 1998) at 19.6–19.0 Ma, reflected in the change in sediment-transport direction (**Figures 2**, **4**, **14**). The Puchkirchen channel consistently funneled sediments to the east (De Ruig and Hubbard, 2006) indicating an eastward-directed slope in the basin. The northward migration of the clinoforms in the HFM (**Figure 2** and **Supplementary Figure S1**) indicate that either the deep eastern basin part was cut off from the Puchkirchen Trough or the eastern part was uplifted. In the upper HFM (19.0–18.1 Ma), the Upper Austrian NAFB turned from an underfilled basin to a filled one further indicating an absence of subsidence (**Figure 14**). In contrast, the Southern Alpine Foreland Basin (Venetian and Friuli Basin) of the Eastern Alps from late Burdigalian (∼17 Ma) onward experienced higher subsidence rates and South-Alpine thrusts emerged (Mellere et al., 2000). These findings might indicate that the former pro-wedge foreland basin, the NAFB, was turned into a retro-wedge position, and the former retro-wedge basin, the Southern Alpine Foreland Basin, into a pro-wedge one. Taking this interpretation further, our and Zweigel's (1998) findings could be interpreted as the surface expression of the postulated northward retreat and tearing event of European lithospheric mantle underneath the Eastern Alps at 25–20 Ma (Handy et al., 2015) as part of an early Miocene switch in subduction polarity to present northward subduction of the Adriatic Plate (Lippitsch et al., 2003). However, the subduction polarity switch and the exact timing and geometry of slab tearing are subject of extensive ongoing research (Handy et al., 2015, ongoing research of the Priority Program "SPP - Mountain building processes in 4D" of the German Research Foundation). At the current stage, the model of a slab polarity switch fails

to explain the uplift of the forebulge in the German NAFB (Zweigel, 1998) and the redeposition of shelf strata into the deeper basin. Therefore, at present we prefer the model of visco-elastic relaxation of the lithosphere (Zweigel, 1998) to explain our results.

CONCLUSION

The results from the analysis of foraminifera, calcareous nannoplankton, geochemistry (TOC, S, $CaCO_3$, $\delta^{13}C_{carb}$) and spatially averaged SARs provide new constraints for the evolution of the Upper Austrian NAFB. Deep-marine sedimentation in the basin started with the Zupfing Formation (NP24), the Puchkirchen Group formed during NP25 to NN2 (26.9 – 19.6 Ma), and the Hall Formation accumulated during NN2 – NN3 (19.6 – 18.1 Ma). Deposits of the Puchkirchen Group are diachronic between the central basin axis and the northern overbanks. The differentiation between Upper and Lower Puchkirchen Formation first postulated by Papp and Steininger (1975) and perpetuated in most following studies proved to be difficult to identify and facies dependent.

Both large-scale unconformities in the basin were dated. The NSU was established between 28.1 – 26.9 Ma, possibly due to a tectonically induced oversteepening of the basin caused by an extra load onto the European Plate either related to a thrust front progradation or the final nappe stacking period in the Eastern Alps. The BHU (19.6 – 19.0 Ma) resulted from a period of non-sedimentation in the basin, followed by a period of redeposition of sediments from the shelf in Bavaria (Grunert et al., 2013).

The results of our SAR calculation show changes in SARs which are possibly related to two of the four expected tectonic forcings in the Oligocene/Miocene Upper Austrian NAFB. We did not detect the hypothesized doubling of SAR caused by the exhumation of the Lepontine Dome (Central Alps) and the Tauern Window (Eastern Alps), which is present in proximal (Bavarian and Swiss) sediment archives. These signals were either 'shredded' in the foreland during long (500–600 km) eastward sediment transport or not recorded in the deep-marine setting due to efficient sediment bypass within the submarine channel system.

A change in the foraminiferal assemblages suggests sediment reworking on the shelf and stable SARs despite a sea-level fall from 19.6-19.0 Ma. This period of sediment remobilization is interpreted as the result of the visco-elastic relaxation of the European Plate. This relaxation induced uplift in the shelf area of the basin and a decrease in relief in the hinterland, leading to stable SARs by the enhanced input of reworked shelf sediment.

The maximum SARs from 19.0 Ma onward are interpreted to result from unroofing and redeposition of the Augenstein Formation. This interpretation is furthermore supported by a shift in sediment-transport direction from east to north via northward prograding clinoforms and a major shift in sediment provenance (Sharman et al., 2018). During this time, the study area was transformed from a deep-marine transfer zone to a final sediment sink, efficiently preserving the tectonic signal in the SARs.

In the Hall Formation (19.6 – 18.1 Ma), the Upper Austrian NAFB experienced major changes in basin geometry (from underfilled to filled), subsidence, drainage network, and the ceasing of deformation along the Alpine thrust front (Hinsch, 2013). These changes may point to a large-scale orogen-wide reorganization triggered by a change in slab polarity (Lippitsch et al., 2003; Handy et al., 2015) which turned the former pro-wedge (>19.0 Ma) Upper Austrian NAFB into a retro-wedge setting.

DATA AVAILABILITY STATEMENT

All datasets generated for this study are included in the article/**Supplementary Material**.

AUTHOR CONTRIBUTIONS

JH and GF wrote the manuscript with major contributions from PG, GA, and AB. JH and GF drew the figures. GF carried out the foraminiferal analyses under the supervision of PG. GA carried out the calcareous nannoplankton analyses. JH undertook the interpretation of the seismic-reflection data and sediment-volume calculation. AB developed the project idea and provided funding.

FUNDING

RAG Austria AG provided funding for this study.

ACKNOWLEDGMENTS

We would like to thank the RAG Austria AG for providing the 3D seismic-reflection data set and access to the samples. Claudia Puschenjak (University of Graz) is thanked for Leco analysis. Prof. Joachimski (GeoZentrum Nordbayern, University of Nürnberg-Erlangen) coordinated the isotopic analysis. Schlumberger is acknowledged for the donation of the Petrel (*) license. JH would like to thank Schlumberger's Support for their help and the Deutsche Bahn for unexpected extension of working time. We thank Mark Handy for comments on an earlier version of the manuscript. We also thank R. Sachsenhofer and J. Lorenzo-Trueba, for their constructive criticism and Associate Editor JF for carefully handling the manuscript.

SUPPLEMENTARY MATERIAL

The Supplementary Material for this article can be found online at: https://www.frontiersin.org/articles/10.3389/feart.2019.00302/full#supplementary-material

REFERENCES

Agnini, C., Fornaciari, E., Raffi, I., Catanzariti, R., Pälike, H., Backman, J., et al. (2014). Biozonation and biochronology of Paleogene calcareous nannofossils from low and middle latitudes. *Newslett. Stratigr.* 47, 131–181. doi: 10.1127/0078-0421/2014/0042

Amos, K. J., Peakall, J., Bradbury, P. W., Roberts, M., Keevil, G., and Gupta, S. (2010). The influence of bend amplitude and planform morphology on flow and sedimentation in submarine channels. *Mar. Pet. Geol.* 27, 1431–1447. doi: 10.1016/j.marpetgeo.2010.05.004

Aubry, M. (1988). *Handbook of Cenozoic Calcareous Nannoplankton, book 2, Ortholithae (Holococcoliths, Ceratoliths, Ortholiths and Other). American Museum of Natural History*. New York, NY: Micropaleontol Press.

Aubry, M.-P. (1984). *Handbook of Cenozoic Calcareous Nannoplankton, American Museum of Natural History*. Newyork, NY: Micropaleontology Press.

Aubry, M.-P. (1989). *Handbook of Cenozoic Calcareous Nannoplankton: Ortholithae (Pentaliths, and Others); Heliolithae (Fasciculiths, Sphenoliths and Others)*. New York, NY: Micropaleontology Press.

Aubry, M.-P. (1999). *Handbook of Cenozoic Calcareous Nannoplankton: Book 5: Heliolithae (Zygoliths and Rhabdoliths), American Museum of Natural History*. New York, NY: Micropaleontology Press.

Aubry, M.-P. (2013). *Cenozoic Coccolithophores: Braarudosphaerales*. New York, NY: Micropaleontology Press.

Backman, J., Raffi, I., Rio, D., Fornaciari, E., and Pälike, H. (2012). Biozonation and biochronology of miocene through pleistocene calcareous nannofossils from low and middle latitudes. *Newslett. Stratigr.* 45, 221–244. doi: 10.1127/0078-0421/2012/0022

Beaumont, C. (1981). Foreland basins. *Geophys. J. Intern.* 65, 291–329.

Bernhardt, A., Stright, L., and Lowe, D. R. (2012). Channelized debris-flow deposits and their impact on turbidity currents: the puchkirchen axial channel belt in the Austrian Molasse Basin. *Sedimentology* 59, 2042–2070. doi: 10.1111/j.1365-3091.2012.01334.x

Boote, D., Sachsenhofer, R., Tari, G., and Arbouille, D. (2018). Petroleum provinces of the paratethyan region. *J. Pet. Geol.* 41, 247–297. doi: 10.1111/jpg.12703

Bown, P. (1998). *Calcareous Nannofossil Biostratigraphy*. London: Chapman and Hall.

Cahuzac, B., and Poignant, A. (1997). Essai de biozonation de l'oligo-miocène dans les bassins européens à l'aide des grands foraminifères néritiques. *Bull. Soc. Géologique France* 168, 155–169.

Carvajal, C., and Steel, R. (2012). "Source-to-sink sediment volumes within a tectono-stratigraphic model for a laramide shelf-to-deep-water basin: methods and results", in *Tectonics of Sedimentary Basins*, eds C. Busby, and A. Azor (Blackwell Publishing Ltd.), 131–151. doi: 10.1002/9781444347166.ch7

Cicha, I., Rogl, F., and Rupp, C. (1998). *Oligocene-Miocene Foraminifera of the Central Paratethys*. Philadelphia, PA: W Kramer Associates Inc.

Clift, P., and Giosan, L. (2014). Sediment fluxes and buffering in the post-glacial Indus Basin. *Basin Res.* 26, 369–386. doi: 10.1111/bre.12038

Clift, P. D. (2006). Controls on the erosion of Cenozoic Asia and the flux of clastic sediment to the ocean. *Earth Planet. Sci. Lett.* 241, 571–580. doi: 10.1016/j.epsl.2005.11.028

Ćorić, S., and Spezzaferri, S. (2009). ZIEG - 1: Mikropaläontologische und Biostratigraphische Auswertung (750m – 1500m).

Covault, J. A., Hubbard, S. M., Graham, S. A., Hinsch, R., and Linzer, H.-G. (2009). Turbidite-reservoir architecture in complex foredeep-margin and wedge-top depocenters, Tertiary Molasse foreland basin system, Austria. *Mar. Pet. Geol.* 26, 379–396. doi: 10.1016/j.marpetgeo.2008.03.002

Cramer, B., Toggweiler, J., Wright, J., Katz, M., and Miller, K. (2009). Ocean overturning since the Late Cretaceous: inferences from a new benthic foraminiferal isotope compilation. *Paleoceanography* 24:PA4216,

De Ruig, M. J., and Hubbard, S. M. (2006). Seismic facies and reservoir characteristics of a deep-marine channel belt in the Molasse foreland basin. Puchkirchen Formation, Austria. *AAPG Bull.* 90, 735–752. doi: 10.1306/10210505018

DeCelles, P. G., and Giles, K. A. (1996). Foreland basin systems. *Basin Res.* 8, 105–123. doi: 10.1046/j.1365-2117.1996.01491.x

Favaro, S., Schuster, R., Handy, M. R., Scharf, A., and Pestal, G. (2015). Transition from orogen-perpendicular to orogen-parallel exhumation and cooling during crustal indentation—key constraints from 147Sm/144Nd and 87Rb/87Sr geochronology (Tauern Window. Alps). *Tectonophysics* 665, 1–16. doi: 10.1016/j.tecto.2015.08.037

Fildani, A., Normark, W. R., Kostic, S., and Parker, G. (2006). Channel formation by flow stripping: large-scale scour features along the monterey east channel and their relation to sediment waves. *Sedimentology* 53, 1265–1287. doi: 10.1111/j.1365-3091.2006.00812.x

Frisch, W., Dunkl, I., and Kuhlemann, J. (2000). Post-collisional orogen-parallel large-scale extension in the Eastern Alps. *Tectonophysics* 327, 239–265. doi: 10.1016/s0040-1951(00)00204-3

Frisch, W., Kuhlemann, J., Dunkl, I., and Székely, B. (2001). The dachstein paleosurface and the augenstein formation in the northern calcareous Alps–a mosaic stone in the geomorphological evolution of the Eastern Alps. *Intern. J. Earth Sci.* 90, 500–518. doi: 10.1007/s005310000189

Galović, I., and Young, J. (2012). Revised taxonomy and stratigraphy of middle miocene calcareous nannofossils of the Paratethys. *Micropaleontology* 58, 305–334.

Ganss, O. (1977). *Geologische Karte von Bayern 1: 25 000, Erläuterungen zum Blatt Nr. 8140 Prien a. Chiemsee und Blatt Nr. 8141 Traunstein*. Germany: Bayerisches Geologisches Landesamt.

Garefalakis, P., and Schlunegger, F. (2019). Tectonic processes, variations in sediment flux, and eustatic sea level recorded by the 20 Myr old Burdigalian transgression in the Swiss Molasse basin. *Solid Earth* 10, 2045–2072.

Genser, J., Cloetingh, S. A., and Neubauer, F. (2007). Late orogenic rebound and oblique Alpine convergence: new constraints from subsidence analysis of the Austrian Molasse basin. *Glob. Planet. Change* 58, 214–223. doi: 10.1016/j.gloplacha.2007.03.010

Gradstein, F., Ogg, J., Schmitz, M., and Ogg, G. (2012). *The Geologic Time Scale 2012*. Amsrerdam: Elsevier.

Gross, D., Sachsenhofer, R., Bechtel, A., Gratzer, R., Grundtner, M. L., Linzer, H. G., et al. (2018). Petroleum systems in the Austrian sector of the North Alpine Foreland Basin: an overview. *J. Pet. Geol.* 41, 299–317. doi: 10.1111/jpg.12704

Grunert, P., Auer, G., Harzhauser, M., and Piller, W. E. (2015). Stratigraphic constraints for the upper Oligocene to lower miocene puchkirchen group (north alpine foreland basin. central paratethys). *Newslett. Stratigr.* 48, 111–133. doi: 10.1127/nos/2014/0056

Grunert, P., Hinsch, R., Sachsenhofer, R. F., Bechtel, A., Ćorić, S., Harzhauser, M., et al. (2013). Early Burdigalian infill of the puchkirchen trough (north alpine foreland basin, central paratethys): facies development and sequence stratigraphy. *Mar. Pet. Geol.* 39, 164–186. doi: 10.1016/j.marpetgeo.2012.08.009

Grunert, P., Soliman, A., Ćorić, S., Roetzel, R., Harzhauser, M., and Piller, W. E. (2012). Facies development along the tide-influenced shelf of the burdigalian seaway: an example from the ottnangian stratotype (early miocene, middle burdigalian). *Mar. Micropaleontol.* 84, 14–36. doi: 10.1016/j.marmicro.2011.11.004

Grunert, P., Soliman, A., Ćorić, S., Scholger, R., Harzhauser, M., and Piller, W. E. (2010). Stratigraphic re-evaluation of the stratotype for the regional ottnangian stage (central paratethys, middle burdigalian). *Newslett. Stratigr.* 44, 1–16. doi: 10.1127/0078-0421/2010/0001

Guillocheau, F., Rouby, D., Robin, C., Helm, C., and Rolland, N. (2012). Quantification and causes of the terrigeneous sediment budget at the scale of a continental margin: a new method applied to the Namibia-South Africa margin. *Basin Res.* 24, 3–30. doi: 10.1111/j.1365-2117.2011.00511.x

Gulick, S. P., Jaeger, J. M., Mix, A. C., Asahi, H., Bahlburg, H., Belanger, C. L., et al. (2015). Mid-Pleistocene climate transition drives net mass loss from rapidly uplifting st. elias mountains, alaska. *Proc. Natl. Acad. Sci. U.S.A.* 112, 15042–15047. doi: 10.1073/pnas.1512549112

Handy, M. R., Ustaszewski, K., and Kissling, E. (2015). Reconstructing the Alps–Carpathians–Dinarides as a key to understanding switches in subduction polarity, slab gaps and surface motion. *Intern. J. Earth Sci.* 104, 1–26. doi: 10.1007/s00531-014-1060-3

Haq, B. U., Hardenbol, J., and Vail, P. R. (1987). Chronology of fluctuating sea levels since the Triassic. *Science* 235, 1156–1167. doi: 10.1126/science.235.4793.1156

Hinsch, R. (2008). New insights into the Oligocene to Miocene geological evolution of the Molasse Basin of Austria. *Oil Gas Eur. Magazine* 34, 138–143.

Hinsch, R. (2013). Laterally varying structure and kinematics of the molasse fold and thrust belt of the central eastern alps: implications for exploration. *AAPG Bull.* 97, 1805–1831. doi: 10.1306/04081312129

Holcová, K. (2009). Morphometrical variability of Helicosphaera ampliaperta (calcareous nannoplankton) in the Central Paratethys: biostratigraphic and paleogeographic applications. *Neues Jahrbuch Geol. Paläontologie Abhandlungen* 253, 341–356. doi: 10.1127/0077-7749/2009/0253-0341

Huang, H., Imran, J., and Pirmez, C. (2012). The depositional characteristics of turbidity currents in submarine sinuous channels. *Mar. Geol.* 329, 93–102. doi: 10.1016/j.margeo.2012.08.003

Hubbard, S. M., de Ruig, M. J., and Graham, S. A. (2009). Confined channel-levee complex development in an elongate depo-center: deep-water Tertiary strata of the Austrian Molasse basin. *Mar. Pet. Geol.* 26, 85–112. doi: 10.1016/j.marpetgeo.2007.11.006

Janz, H., and Vennemann, T. W. (2005). Isotopic composition (O, C, Sr, and Nd) and trace element ratios (Sr/Ca, Mg/Ca) of Miocene marine and brackish ostracods from North Alpine Foreland deposits (Germany and Austria) as indicators for palaeoclimate. *Palaeogeogr. Palaeoclimatol. Palaeoecol.* 225, 216–247. doi: 10.1016/j.palaeo.2005.06.012

Jerolmack, D. J., and Paola, C. (2010). Shredding of environmental signals by sediment transport. *Geophys. Res. Lett.* 37, L19401.

Jin, J., Aigner, T., Luterbacher, H., Bachmann, G. H., and Müller, M. (1995). Sequence stratigraphy and depositional history in the south-eastern German Molasse Basin. *Mar. Pet. Geol.* 12, 929–940. doi: 10.1016/0264-8172(95)98856-z

Kremer, C. H., McHargue, T., Scheucher, L., and Graham, S. A. (2018). Transversely-sourced mass-transport deposits and stratigraphic evolution of a foreland submarine channel system: deep-water tertiary strata of the Austrian Molasse Basin. *Mar. Pet. Geol.* 92, 1–19. doi: 10.1016/j.marpetgeo.2018.01.035

Kuhlemann, J. (2000). Post-collisional sediment budget of circum-Alpine basins (Central Europe). *Mem. Sci. Geol. Padova* 52, 1–91.

Kuhlemann, J., Dunkl, I., Brügel, A., Spiegel, C., and Frisch, W. (2006). From source terrains of the eastern alps to the molasse basin: detrital record of non-steady-state exhumation. *Tectonophysics* 413, 301–316. doi: 10.1016/j.tecto.2005.11.007

Kuhlemann, J., and Kempf, O. (2002). Post-Eocene evolution of the north alpine foreland basin and its response to alpine tectonics. *Sedimentary Geol.* 152, 45–78. doi: 10.1016/s0037-0738(01)00285-8

Küpper, I., and Steininger, F. (1975). Faziostratotypen der puchkirchener schichtengruppe. *Chronostratigr. Neostratotypen* 5, 205–229.

Lemcke, K. (1988). *Das bayerische Alpenvorland vor der Eiszeit. Geologie von Bayern I*. Stuttgart: Schweizerbart.

Lippitsch, R., Kissling, E., and Ansorge, J. (2003). Upper mantle structure beneath the Alpine orogen from high-resolution teleseismic tomography. *J. Geophys. Res.: Solid Earth* 108, 2376.

Marshall, J. D. (1992). Climatic and oceanographic isotopic signals from the carbonate rock record and their preservation. *Geol. Magazine* 129, 143–160. doi: 10.1017/s0016756800008244

Martini, E. (1971). "Standard tertiary and quaternary calcareous nannoplankton zonation," in *Proceedings of the Second Planktonic Conference Roma, 1970* (Roma: Edizioni Tecnoscienza), 739–785.

Martini, E. (1981). Nannoplankton in der Ober-Kreide, im Alttertiär und im tieferen Jungtertiär von Süddeutschland und dem angrenzenden Österreich. *Geol. Bavarica* 82, 345–356.

Masalimova, L. U., Lowe, D. R., Mchargue, T., and Derksen, R. (2015). Interplay between an axial channel belt, slope gullies and overbank deposition in the puchkirchen formation in the molasse basin. *Aust. Sedimentol.* 62, 1717–1748. doi: 10.1111/sed.12201

McArthur, J., Howarth, R., and Shields, G. (2012). "Strontium isotope stratigraphy," in *The Geologic Time Scale*, ed. F. M. Gradstein, (Elsevier: Berlin), 127-144.

Mellere, D., Stefani, C., and Angevine, C. (2000). Polyphase tectonics through subsidence analysis: the oligo-miocene venetian and friuli basin, north-east italy. *Basin Res.* 12, 159–182. doi: 10.1046/j.1365-2117.2000.00120.x

Murray, J. (2006). *Ecology and Applications of Benthic Foraminifera*. Cambridge: Cambridge University Press. doi: 10.1017/CBO9780511535529

Murray, A. B., Lazarus, E., Ashton, A., Baas, A., Coco, G., Coulthard, T., et al. (2009). Geomorphology, complexity, and the emerging science of the Earth's surface. *Geomorphology* 103, 496–505. doi: 10.1016/j.geomorph.2008.08.013

Papp, A. (1975). "Die Grossforaminiferen des egerien," in *Chronostratigraphie und Neostratotypen Miozän der Zentralen Paratethys*, eds T. Báldi, and J. Seneš, (Bratislava: VEDA), 289–307.

Papp, A., and Steininger, F. (1975). "Die Entwicklung der Puch kirchener Schichtengruppe, der Melker und der Michelstettener Schichten in Österreich," in *Chronostratigraphie und Neostratotypen, Miozän der Zentralen Paratethys 5: OM"- Egerian. Die Egerer, Pouzdřaner, Puchkirchener Schichtengruppe und die Bretkaer Formation*, ed. E. Brestenská (Bratislava: Verlag der Slowakischen Akademie der Wissenschaften), 71–75.

Piller, W. E., Harzhauser, M., and Mandic, O. (2007). Miocene central paratethys stratigraphy–current status and future directions. *Stratigraphy* 4, 151–168.

Reiser, H. (1987). Die Foraminiferen der bayerischen oligozän-molasse systematik, stratigraphie und paläobathymetrie. *Zitteliana* 16:340.

Rögl, F. (1998). Palaeogeographic considerations for Mediterranean and Paratethys seaways (Oligocene to Miocene). *Annalen Naturhistorischen Museums Wien. Serie Mineralogie Petrographie Geol. Paläontol. Anthropologie Prähistorie* 99, 279–310.

Rögl, F., Hochuli, P., and Muller, C. (1979). Oligocene–early miocene stratigraphic correlations in the molasse basin of austria. *Ann. Geol. Pays Helleniques. Tome Hors Series* 30, 1045–1050.

Romans, B. W., Castelltort, S., Covault, J. A., Fildani, A., and Walsh, J. (2016). Environmental signal propagation in sedimentary systems across timescales. *Earth Sci. Rev.* 153, 7–29.

Sachsenhofer, R., Popov, S., Bechtel, A., Coric, S., Francu, J., Gratzer, R., et al. (2017). Oligocene and lower miocene source rocks in the paratethys: palaeogeographical and stratigraphic controls. *Geol. Soc. Lond. Spec. Public.* 464:S464.

Sachsenhofer, R. F., Leitner, B., Linzer, H.-G., Bechtler, A., Æoric, S., Gratzer, R., et al. (2010). Deposition, erosion and hydrocarbon source potential of the oligocene eggerding formation (Molasse Basin, Austria). *Aust. J. Earth Sci.* 103, 1–76.

Sadler, P. M., and Jerolmack, D. J. (2015). Scaling laws for aggradation, denudation and progradation rates: the case for time-scale invariance at sediment sources and sinks. *Geol. Soc. Lond. Special Publ.* 404, 69–88.

Scharf, A., Handy, M. R., Favaro, S., Schmid, S. M., and Bertrand, A. (2013). Modes of orogen-parallel stretching and extensional exhumation in response to microplate indentation and roll-back subduction (Tauern Window. Eastern Alps). *Intern. J. Earth Sci.* 102, 1627–1654. doi: 10.1007/s00531-013-0894-894

Schlunegger, F., and Castelltort, S. (2016). Immediate and delayed signal of slab breakoff in oligo/miocene molasse deposits from the european alps. *Sci. Rep.* 6:31010. doi: 10.1038/srep31010

Schlunegger, F., and Norton, K. P. (2015). Climate vs. tectonics: the competing roles of Late Oligocene warming and Alpine orogenesis in constructing alluvial megafan sequences in the North Alpine foreland basin. *Basin Res.* 27, 230–245. doi: 10.1111/bre.12070

Sharman, G. R., Hubbard, S. M., Covault, J. A., Hinsch, R., Linzer, H.-G., and Graham, S. A. (2018). Sediment routing evolution in the northern alpine foreland basin, austria: interplay of transverse and longitudinal sediment dispersal. *Basin Res.* 30, 426–447.

Sinclair, H. (1997). Tectonostratigraphic model for underfilled peripheral foreland basins: An Alpine perspective. *Geol. Soc. Am. Bull.* 109, 324–346.

Sissingh, W. (1998). Comparative tertiary stratigraphy of the rhine graben, bresse graben and molasse basin: correlation of alpine foreland events. *Tectonophysics* 300, 249–284.

Soliman, A. (2012). Oligocene dinoflagellate cysts from the north alpine foreland basin: new data from the eggerding formation (Austria). *Geol. Carpathica* 63, 49–70.

Wade, B. S., Pearson, P. N., Berggren, W. A., and Pälike, H. (2011). Review and revision of Cenozoic tropical planktonic foraminiferal biostratigraphy and calibration to the geomagnetic polarity and astronomical time scale. *Earth Sci. Rev.* 104, 111–142.

Wagner, L. R. (1998). Tectono-stratigraphy and hydrocarbons in the molasse foredeep of salzburg, upper and lower Austria. *Geol. Soc. Lond. Special Publ.* 134, 339–369.

Wenger, W. F. (1987). Die Foraminiferen des Miozän ans der bayerischen Molasse und ihre stratigraphische sowie paläogeographische Auswertung. *Zitteliana* 16:132.

Young, J., Bown, P., and Lees, J. (2014). *Nannotax3 website. International Nannoplankton Association*. Available at: http://www.mikrotax.org/Nannotax3 (accessed April 21, 2017)

Zweigel, J. (1998). Eustatic versus tectonic control on foreland basin fill. *Contrib. Sedimentary Geol.* 20:140.

Conflict of Interest: The authors declare that the research was conducted in the absence of any commercial or financial relationships that could be construed as a potential conflict of interest.

The reviewer RS declared a past co-authorship with one of the authors PG to the handling Editor.

frontiers in Earth Science

ORIGINAL RESEARCH
published: 13 December 2019
doi: 10.3389/feart.2019.00334

Grain-Size and Discharge Controls on Submarine-Fan Depositional Patterns From Forward Stratigraphic Models

Nicolas Hawie[1]*, *Jacob A. Covault*[2] *and Zoltán Sylvester*[2]

[1] Beicip Franlab, Rueil-Malmaison, France, [2] Bureau of Economic Geology, Jackson School of Geosciences, The University of Texas at Austin, Austin, TX, United States

Submarine fans are important components of continental margins; they contain a stratigraphic record of environmental changes and host large accumulations of oil and gas. The grain size and volume of sediment supply to fans is thought to control the heterogeneity of deep-water deposits; predicting spatial variability of sandy and muddy deposits is an important applied challenge in the characterization of fans. Here, we use DionisosFlow stratigraphic-forward models to evaluate the sensitivity of submarine-fan deposition to a range of grain sizes, with corresponding diffusion coefficients ranging from 10 to 100 km^2/kyr for coarse sand to silt/clay, and discharges. In general, finer grains are transported farther in our models because they have larger diffusion coefficients. Coarser grains typical of a sand-rich fan tend to pile up and compensationally stack at the mouth of a proximal feeder channel. Increasing sediment-gravity-flow discharge resulted in a thicker depositional system; however, relatively coarse sediment piled up at the mouth of the feeder channel, which created a slope that promoted basinward sediment transport. Our modeling results can be applied to predict the overall geometry, stacking, and grain-size distribution of submarine fans. Improved understanding of grain-size and discharge controls also informs interpretation of the stratigraphic record of submarine fans. For example, outcrop observations of heterogeneity and compensational stacking of depocenters can be related to changing boundary conditions, namely changes in the caliber and overall supply of sediment delivery to deep-water basin margins.

Keywords: sediment supply, grain size, compensational stacking, forward stratigraphic modeling, deep-water depositional settings, submarine fan, diffusion coefficient, sediment transport

OPEN ACCESS

Edited by:
William Helland-Hansen, University of Bergen, Norway

Reviewed by:
Michal Janocko, Equinor ASA, Norway
Cornel Olariu, Jackson School of Geosciences, The University of Texas at Austin, United States
Ian Antony Kane, University of Manchester, United Kingdom

***Correspondence:**
Nicolas Hawie
nicolas.hawie@beicip.com

Specialty section:
This article was submitted to Sedimentology, Stratigraphy and Diagenesis, a section of the journal Frontiers in Earth Science

Received: *15 August 2019*
Accepted: *29 November 2019*
Published: *13 December 2019*

Citation:
Hawie N, Covault JA and Sylvester Z (2019) Grain-Size and Discharge Controls on Submarine-Fan Depositional Patterns From Forward Stratigraphic Models. Front. Earth Sci. 7:334. doi: 10.3389/feart.2019.00334

INTRODUCTION

Submarine fans are deep-water depositional systems that received terrigenous sediment from canyons and channels that extend across continental margins (Piper and Normark, 2001). The deposits of fans host a relatively complete and readily dated record of environmental changes, including tectonic deformation and climate, in their upstream sedimentary systems compared to onshore records (Clift et al., 2000; Clift and Gaedicke, 2002; Romans et al., 2016). The deposits of fans are also globally important oil and gas reservoirs (Weimer and Pettingill, 2007). The reservoir properties of sandy architectural elements of submarine fans and their lateral continuity and

vertical connectivity are important issues for petroleum geology (Piper and Normark, 2001). Piper and Normark (2001) suggested that the distribution of sandy architectural elements is primarily controlled by grain size and sediment supply, and the overall geometry of submarine fans is influenced by basin setting.

Forward stratigraphic modeling can be applied to predict the location and heterogeneity of depositional systems and petroleum reservoirs (Miller et al., 2008), as well as the depositional response to controlling factors (Piper and Normark, 2001). For example, in an exploration scenario with low-resolution seismic-reflection data (generally two-dimensional, 2-D, profiles with frequencies of 5–20 Hz; Normark et al., 1993; Prather et al., 2012) and no lithologic control from well penetrations, seismic-stratigraphic interpretation and structural restoration can be applied to create a paleotopographic surface for modeling the location, size, shape, and sub-seismic heterogeneity and stacking of deposits (Groenenberg et al., 2010; Aas et al., 2014; Deville et al., 2015; Hawie et al., 2017; Barabasch et al., 2019). Commonly used geostatistical methods in reservoir modeling use semivariograms, geometric parameters, and/or training images to reproduce spatial statistics from available seismic-reflection and well data (Pyrcz and Deutsch, 2014; Pyrcz et al., 2015). Recently, stratigraphic-forward modeling has been used to incorporate quantitative, process-based geologic information to constrain reservoir modeling. For example, Sacchi et al. (2016) used a depth-averaged flow in the 2-D horizontal plane, basin-scale stratigraphic-forward model called SimClast (Dalman and Weltje, 2008, 2012) to simulate fluvio-deltaic stratigraphic evolution and create a 3-D probability distribution of facies proportions. This probability cube was used as additional input for a geostatistical reservoir model. Similarly, Falivene et al. (2014) improved DionisosFlow basin-scale stratigraphic-forward model predictions of stratigraphic trap and reservoir presence by calibrating the models to independent constraints, such as thicknesses from seismic-reflection or well data.

Hawie et al. (2018) used DionisosFlow at finer temporal and spatial resolution (i.e., 10^3-10^4 yr time steps within an area of 17 × 17 km with cell sizes of 200 × 200 m) to simulate the stratigraphic evolution and sub-seismic heterogeneity of a Pleistocene submarine fan on the continental slope of tectonically active eastern Trinidad (**Figure 1**). A regional seismic-stratigraphic horizon was used as an initial paleotopographic surface input to the forward stratigraphic model. Over a range of time steps, compensational-stacking patterns governed the lateral continuity and vertical connectivity of sandy and muddy architectural elements of the submarine fan (Hawie et al., 2018); similar compensational stacking patterns in fans are common in other settings (e.g., Deptuck et al., 2008; Prelat et al., 2010; Jobe et al., 2017; Sweet et al., 2019). However, in all models of Hawie et al. (2018), thicknesses in the proximal areas of the models exceeded thicknesses observed in the field (**Figure 2**).

Here, we revise the reference-case forward stratigraphic model of Hawie et al. (2018) to achieve a better thickness match with the field example offshore Trinidad. Then, we evaluate the sensitivity of this model to input variables, namely: diffusion coefficients related to a range of grain sizes and sediment-gravity-flow discharges. We use an automated multi-simulation workflow using a Latin Hypercube Experimental Design (McKay et al., 1979) with thickness calibration to quantify the variance of thickness and sand distribution, which can be applied to de-risk petroleum-reservoir presence. Our forward stratigraphic models show the influence of key controlling factors, namely grain size, with corresponding diffusion coefficients ranging from 10 to 100 km^2/kyr for coarse sand to silt/clay, and sediment supply (Piper and Normark, 2001), on fan deposition. Understanding controls can be applied to the interpretation of fan stratigraphy in outcrops and subsurface datasets (e.g., Burgess et al., 2019).

PREVIOUS WORK

Hawie et al. (2018) used seismic-reflection horizons from the tectonically active continental slope east of the Columbus basin and along the southern margin of the Barbados accretionary wedge (Brami et al., 2000; Wood and Mize-Spansky, 2009; the "NW" depocenter between the Darien and Haydn ridges in block 25A offshore of Trinidad) to define the top and base of a submarine fan. They simulated the evolution of this fan (124.5–24.5 ka) with a series of DionisosFlow forward stratigraphic models within a domain of 17 × 17 km (200 × 200 m cell sizes), and assessed the impact of duration of time step (20, 10, 5, and 1 kyr) on sub-seismic stacking and heterogeneity of leveed-channel and lobe architectural elements (**Figure 1**). They used the regional seismic-reflection horizon at the base of the fan, which overlies mass-transport deposits mapped by Moscardelli et al. (2006), as the initial topography of the model. A single 300–600 m-wide feeder channel was located in the south of the model domain; it delivered grain sizes ranging from silt/clay to coarse sand. No differential subsidence was used in the model. Hawie et al. (2018) simulated the transport of relatively coarse grains: 20% coarse sand, 30% medium sand, 40% fine sand, and 10% silt/clay. The transport parameters used for the reference-case model ranged from 10 to 100 km^2/kyr for water-driven diffusion (or, in the case of submarine fans, sediment-gravity-flow-driven diffusion; K_w) and 0.001–0.1 km^2/kyr for slope-driven transport (K_s).

In all of the models of Hawie et al. (2018), varying the simulated time step (20, 10, 5, and 1 kyr) resulted in a similar thickness trend and compensational stacking of depocenters. All models showed three to four major phases of sediment diversion during the migration of a relatively coarse depocenter. Moreover, the overall proximal-to-distal trend from relatively coarse leveed-channel to finer lobe deposits was similar in all models. However, the proximal and distal areas of all the models exhibited thickness differences, locally greater than two-fold, compared to the field (**Figure 2**). In light of this previous work, we are motivated to explore two questions: (1) How can we achieve a better thickness match between model and field cases? (2) Furthermore, how do variable diffusion coefficients related to a range of grain sizes and discharges influence submarine-fan depositional patterns (Piper and Normark, 2001)?

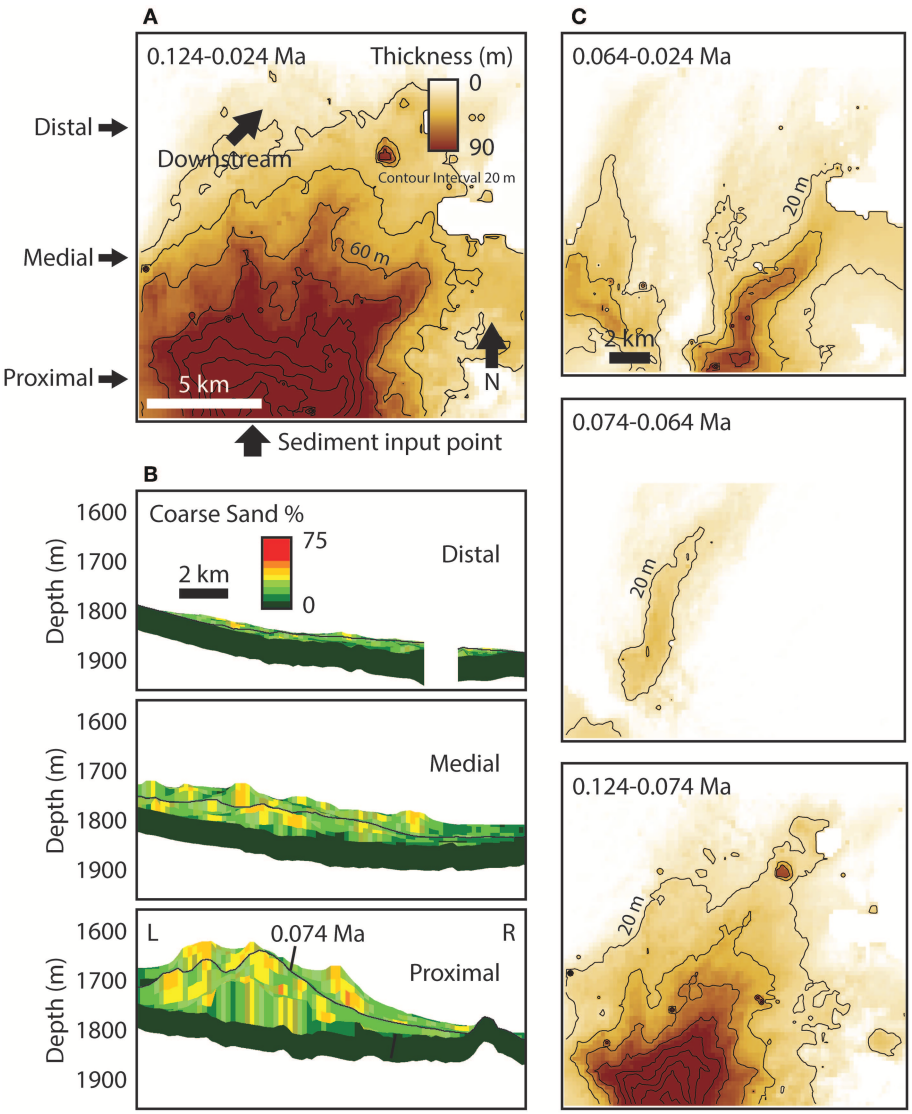

FIGURE 1 | Reference-case model (10 kyr time step) modified from Hawie et al. (2018). **(A)** Isochore map of the entire model. **(B)** Cross sections of the model. Left (L) and right (R) orientations in cross sections are left and right in map in part **(A)**. Cross-section locations are indicated in part **(A)**. **(C)** Isochore maps of depositional sequences within the model showing major phases of sediment diversion.

METHODS

Forward Stratigraphic Modeling

DionisosFlow software is a 4-D process-based deterministic multi-lithology forward stratigraphic model that simulates basin filling (Granjeon, 1997, 2014; Granjeon and Joseph, 1999). A range of sedimentary processes are modeled including diffusive sediment transport, delta autoretreat, incision, large-scale avulsion, and slope failure in response to tectonic, climate, and sea-level fluctuations during millennia and longer time scales (e.g., Pinheiro-Moreira, 2000; Rabineau et al., 2005; Alzaga-Ruiz et al., 2009; Gvirtzman et al., 2014; Harris et al., 2016; Hawie et al., 2017). Detailed fluid dynamics are not considered in this model; the goal is to simulate the large-scale (10^2-10^3 m cell size) and long-term (10^3-10^5 yr time steps) evolution of basin fill.

Sediment transport equations are used to simulate the transport of various classes of grain size (e.g., clay to sand) across a basin. This stratigraphic model combines (1) linear slope-driven diffusion (transport proportional to slope), referred to as hillslope creep, and (2) non-linear water- and slope-driven diffusion, referred to as water-discharge-driven transport (Willgoose et al., 1991; Tucker and Slingerland, 1994; Granjeon, 1997; Granjeon and Joseph, 1999; Deville et al., 2015):

$$Q_s = -\left(K_s/\vec{\nabla}h + K_w Q_w^m S^n\right) \quad (1)$$

where Q_s is sediment discharge (km^3/Myr), K_s and K_w are the slope- and water-driven diffusion coefficients, respectively (km^2/kyr), Q_w is water discharge (m^3/s), n and m are exponents

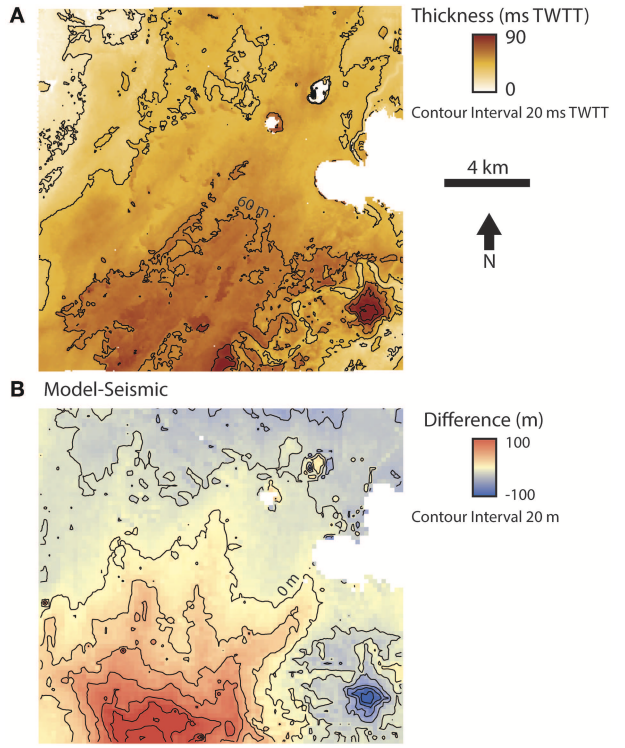

FIGURE 2 | (A) Isochron map of the slope fan from Moscardelli et al. (2006) and Moscardelli and Wood (2008). **(B)** Difference in thickness between the model and the slope fan in block 25A, offshore Trinidad (modified from Hawie et al., 2018).

that affect sediment transport capacity with values between 1 and 2 (Tucker and Slingerland, 1994), S is the dimensionless local gradient of the basin, and h (m) is topographic elevation (Granjeon, 2014). Sedimentation and erosion rates are quantified by a mass balance equation in 3-D for each class of grain size (Euzen et al., 2004). In general, if slope is not sufficiently large to promote sediment transport downstream, deposition occurs. Large K_w and Q_w values can promote sediment transport across lower slopes, as indicated in Equation (1). Sediment-gravity flows, commonly turbidity currents, are the primary agents of sediment transport, erosion, and deposition in submarine fans (Bouma et al., 1985). We liken the water-driven diffusion coefficient and the water discharge to a sediment-gravity-flow-driven diffusion coefficient and gravity-flow discharge, respectively, which govern the rate of sediment transport though the system. That said, the diffusion equation (Equation 1) does not account for stratification of flow; both the velocity and concentration maxima of turbidity currents occur near the base of the flow (Sequeiros et al., 2010; Eggenhuisen and McCaffrey, 2012). Choosing K_w values for different grain sizes is a challenge because published values span orders of magnitude and they depend on many factors in addition to grain size, such as lithology, roundness, and discharge (Rivenaes, 1992; Falivene et al., 2014; Gvirtzman et al., 2014; Harris et al., 2016). Following Hawie et al. (2018), we used a range of K_w from 10 to 100 km^2/kyr for coarse sand to silt/clay. In a recent publication using DionisosFlow to simulate sedimentation across a larger region offshore Trinidad, Deville et al. (2015) used a range of K_w from 100 to 1,000 km^2/kyr. They used much larger K_w values in order to transport sediment across a much larger area (1,200 × 1,200 km); their individual cell sizes are nearly the size of our entire model domain (Deville et al., 2015). Ideally, we would tune diffusion coefficients to produce geometries and grain-size distribution similar to deposits of a field case (Harris et al., 2016). We created a reference-case model during an initial phase of model calibration. In lieu of grain-size information confirmed by well penetrations, we tuned the variables of the diffusion equation, K_w and Q_w, to achieve a thickness trend that is similar to that published in Hawie et al. (2018) (**Figure 1**).

In addition to the assumptions presented above, there are limitations to the use of diffusion-based models to simulate sediment transport and deposition. For example, diffusion does not model particle-particle nor particle-fluid interactions (Equation 1). Moreover, cell size within the model domain is hundreds of meters by hundreds of meters and time steps are thousands of years; therefore, diffusion only provides an approximation of particle transport and depocenter location across the model domain during a time step. Stratigraphic forward model results should be compared to stratigraphic interpretations based on real geological and geophysical data; we compare the thickness of our model to that published in Hawie et al. (2018).

Experimental Designs

In order to achieve a better thickness match between model and the Trinidad field case of Hawie et al. (2018), we manually generated simulations of various grain sizes (i.e., sand- vs. silt/clay-rich) during 10 kyr time steps. We slightly modified some of the other input variables of Hawie et al. (2018), such as the discharges and diffusion coefficients (**Table 1**). Similar to Hawie et al. (2018), we used the regional seismic-reflection horizon at the base of the fan, which overlies mass-transport deposits mapped by Moscardelli et al. (2006), as the initial topography of the model. A single 300–600 m-wide feeder channel was located in the south of the model domain; it delivered grain sizes ranging from silt/clay to coarse sand. We extended the model domain 5 km to the south (17 km wide × 22 km long) to better match the feeder-channel location observed in the seismic-reflection data (**Figure 3**). Sediment enters the model domain from the south (**Figure 3A**). Once we improved the thickness match with the field case of Hawie et al. (2018), we tested two experimental designs: (1) 80–20% silt/clay proportion (22 simulations) and (2) ±20% gravity-flow discharge (22 simulations). We performed multiple automated simulations using a Latin Hypercube Experimental Design to quantify the standard deviations of thickness and sand-depositional patterns. Latin Hypercube Experimental Design samples variables from uniform distributions and ensures that the ensemble of samples is representative of the natural variability of the system, contrary to simple random sampling in Monte Carlo studies (McKay et al., 1979). In statistical sampling, a square grid containing sample positions is a Latin square if there is only one sample in each

TABLE 1 | Reference-case model inputs.

Model size	**17 × 22 km**
Cell size	200 × 200 m
Duration	124.5–24.5 ka
Time step	10 kyr
Sediment discharge	215 km^3/Myr
Grain size classes	5% coarse sand (0.5 mm)
	10% medium sand (0.3 mm)
	30% fine sand (0.125 mm)
	55% silt/clay (0.004 mm)
Water discharge	65 m^3/s
K_w	10 km^2/kyr coarse sand
	15 km^2/kyr medium sand
	30 km^2/kyr fine sand
	100 km^2/kyr silt/clay
K_s	0.018 km^2/kyr coarse sand
	0.014 km^2/kyr medium sand
	0.012 km^2/kyr fine sand
	0.001 km^2/kyr silt/clay

row and each column. A Latin Hypercube is the generalization of this concept to an arbitrary number of variables, whereby each sample is the only one in each axis-aligned hyperplane containing it. When sampling a function of N variables, the range of each variable is divided into M equally probable intervals. M sample points are then placed to satisfy the Latin Hypercube requirements; this forces the number of intervals, M, to be equal for each variable. The maximum number of combinations for a Latin Hypercube of N variables and M intervals can be computed with the following equation (Audze and Eglais, 1977; McKay et al., 1979; Iman et al., 1980, 1981):

$$\left(\prod_{n=0}^{M-1}(M-n)\right)^{N-1} = (M!)^{N-1} \quad (2)$$

The following are features of Latin Hypercube Experimental Design: (1) it treats every variable as equally important and ensures uniformly distributed sampling; (2) it samples the full range of a variable; (3) it allows for multiple, multidimensional variables (e.g., 1-D sediment load and/or 3-D topographic variables); and (4) we, the designers, determine the number of simulations, which include output grids of properties for comparison to a reference case (Hawie et al., 2017).

Some caveats to our experimental designs include: (1) we restricted our model domain to the submarine fan, excluding the upstream canyon-channel system; and (2) we opened the northern boundary of the model and closed the eastern and western boundaries. Focusing only on the submarine fan required us to strongly vary diffusion coefficients in order to achieve a fan shape (e.g., Hawie et al., 2018). For example, more diffusion is required to produce the relatively flat, sheet-like geometries of the distal fan.

RESULTS

We improved the thickness match between our manually calibrated stratigraphic-forward model and the field case of Hawie et al. (2018) by modifying the grain-size inputs to be 5% coarse sand (10 km^2/kyr), 10% medium sand (15 km^2/kyr), 30% fine sand (30 km^2/kyr), and 55% silt/clay (100 km^2/kyr) (**Figure 3B**). This grain-size distribution is more similar to mud-rich continental margins (e.g., Reading and Richards, 1994), such as offshore Trinidad, compared to the relatively sand-rich models of Hawie et al. (2018). Approximately 1/3 of the total sediment load was transported beyond the northern boundary of the model, and ∼80% of this sediment load was silt/clay. Although we improved the thickness match, especially in the proximal and central parts of the model domain, with model-thickness values >75% of the field case, there is still a mismatch in the western and thinner, peripheral parts of the model (∼30–60% of the field case). The overall architecture of the model is similar to the models of Hawie et al. (2018): compensationally stacked proximal leveed-channel depositional elements transition downstream to lobes (**Figures 3C**, **4**; **Supplementary Animations 1, 2**). The model output shows at least four phases of depocenter migration (**Figures 3C**, **4**; **Supplementary Animations 1, 2**). Initially, the depocenter was oriented southwest-to-northeast (0.124–0.104 Ma), then it shifted to the west and was oriented more south-to-north (0.104–0.094 Ma), followed by a more gradual shift to the east (0.094–0.064 Ma), where it split into three channels covering the model domain, and it was predominantly oriented southwest-to-northeast at the end of the simulation (0.054–0.024 Ma) (**Figure 3C**; **Supplementary Animations 1, 2**).

Following this initial phase of manual calibration, we implemented the two experimental designs. In the first experimental design, we varied silt/clay load, hereafter simply called mud load, 80–20%. **Figures 5**, **6** show the thicknesses and the distributions of coarse and medium sand in the maximum and minimum mud-load simulations (**Supplementary Animations 3–6**). Lower mud load results in relatively thick accumulations in the northeast distal part of the model domain, immediately downstream from the feeder channel; higher mud load results in a relatively thick band across the northern, central, and eastern regions of the model (**Figure 7A**). Both high- and low-mud-load cases resulted in similar patterns of shifting depocenters (**Figures 5**, **6**; **Supplementary Animations 3–6**). The map of thickness standard deviation of the 22 simulations shows larger variance in thickness (± nearly 20 m) near the proximal feeder channel (**Figure 7C**). The thickness standard deviation is also greater along channel forms extending to the northeast away from the feeder channel (**Figure 7C**). At first glance, the coarse and medium sand proportion maps look similar in both the high and low mud-load simulations (**Figures 5**, **6**). However, the map of sand proportion standard deviation shows large variance (± >10%) along the boundaries of the model domain, especially the western and southeastern boundaries (**Figure 7E**).

In the second experimental design, we varied the sediment-gravity-flow discharge ±20% relative to the manually calibrated model. **Figures 8**, **9** show the thicknesses and the

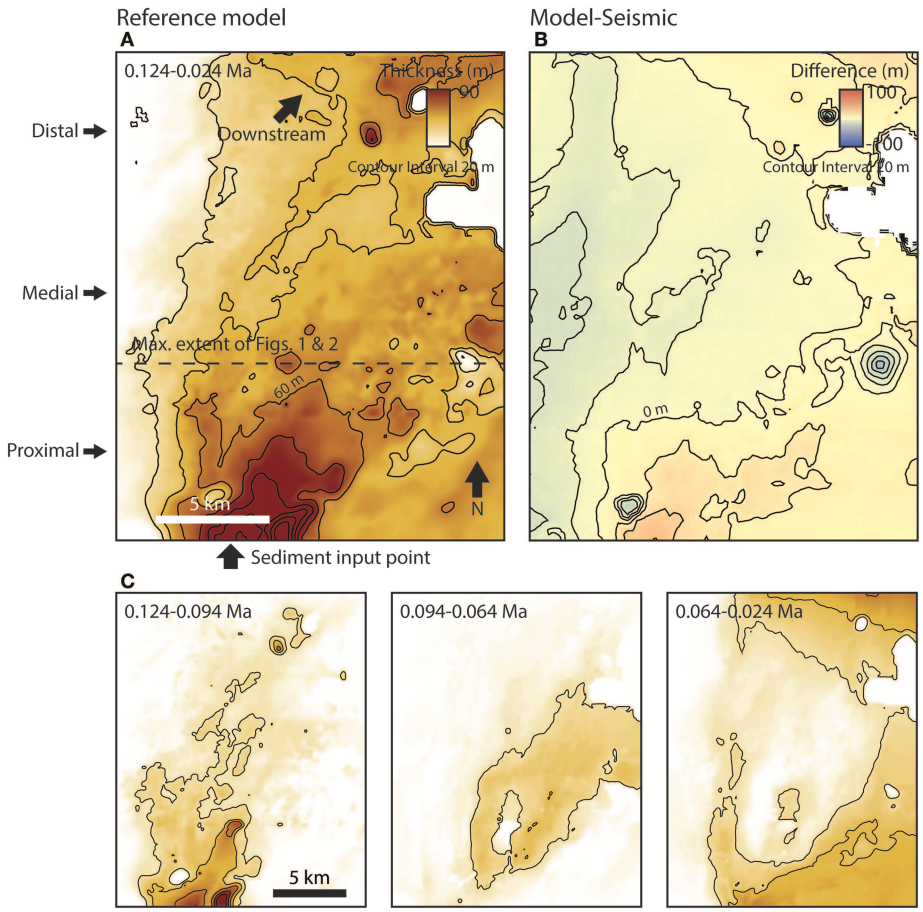

FIGURE 3 | New extended reference-case model. **(A)** Isochore map of the new model. **(B)** Difference in thickness of the model and the slope fan in block 25A, offshore Trinidad (Hawie et al., 2018). **(C)** Isochore maps of depositional sequences within the model showing major phases of sediment diversion.

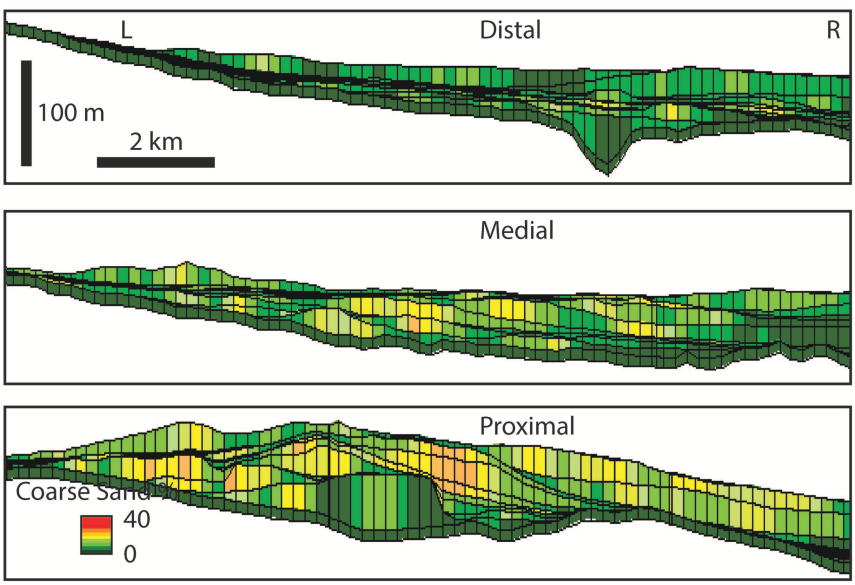

FIGURE 4 | Cross sections of the new extended reference-case model. Left (L) and right (R) orientations in cross sections are left and right in map in **Figure 3A**.

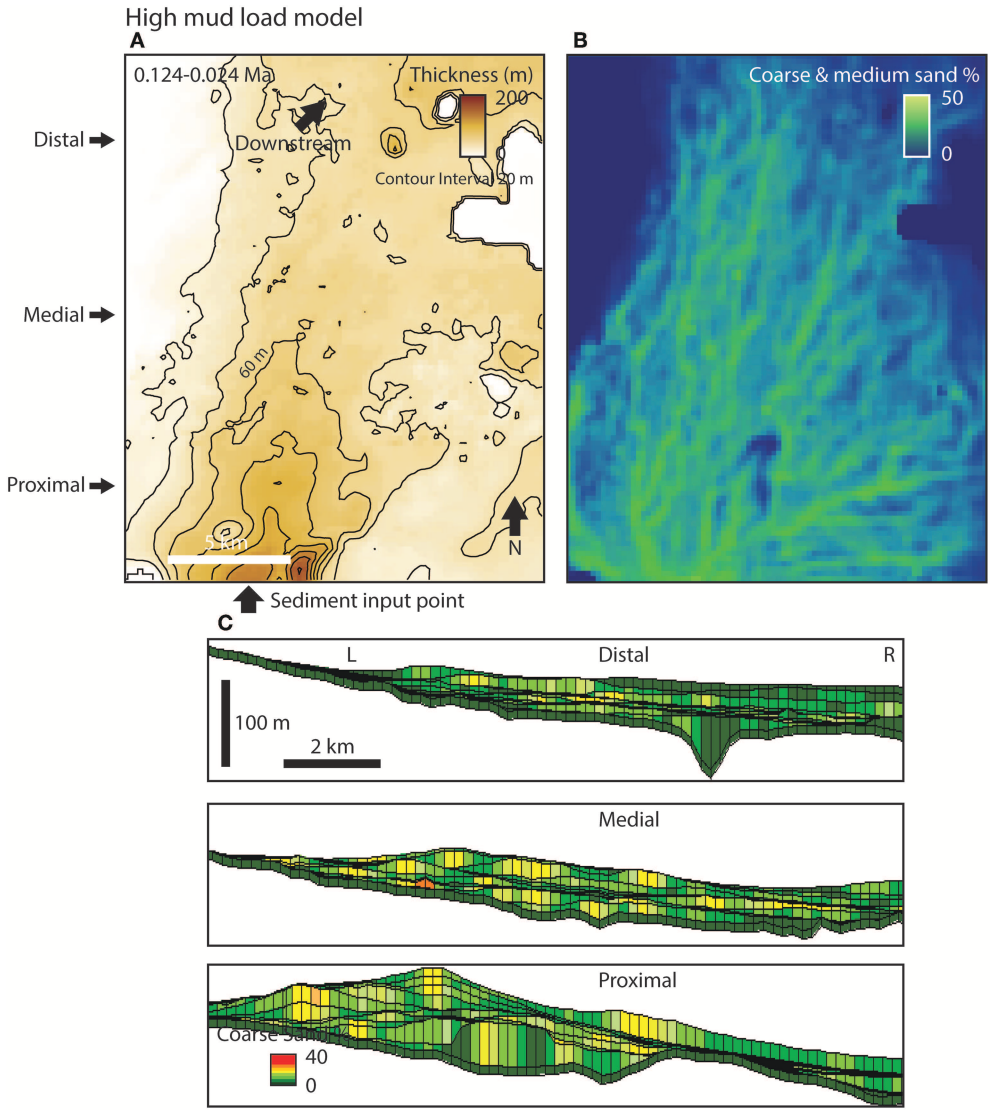

FIGURE 5 | (A) Isochore map of the high mud load model. **(B)** Coarse and medium sand percentage within the model. **(C)** Proximal, medial, and distal cross sections showing the coarse sand content in the model. Left (L) and right (R) orientations in cross sections are left and right in maps. Cross-section locations are indicated in part **(A)**.

distributions of coarse and medium sand in the maximum (+20%) and minimum (−20%) discharge simulations (**Supplementary Animations 7–10**). Discharge appears to play an important role in thickness difference, with nearly uniformly greater thickness corresponding with higher discharge (**Figure 10A**). In detail, higher discharge results in fewer major depocenters (at least two to three dominant depocenter- and channel-orientation directions) compared to lower discharge (similar to the manually calibrated model, at least four or five major depocenters) (**Figures 8**, **9**; **Supplementary Animations 7–10**). Moreover, the largest difference in thickness, with excess thickness in the case of higher discharge, is observed in the most proximal and distal parts of the model (**Figure 10A**). The map of thickness standard deviation of the 22 simulations shows larger variance (± nearly 20 m) in the central region of the model domain, extending from the proximal feeder channel basinward to the northern distal part (**Figure 10C**). As in the first experimental design, the coarse and medium sand proportion maps look similar in both the maximum and minimum discharge simulations (**Figures 8**, **9**). The map of sand proportion standard deviation of the 22 simulations shows larger variance (± nearly 10%) along the northwestern region of the model domain (**Figure 10E**).

Interpretations

Improved Model-Field Match

We improved the thickness match between our manually calibrated stratigraphic-forward model and the field case of Hawie et al. (2018) by modifying the grain-size inputs to be finer (**Figure 3**). In our modeling, sediment discharge is a function

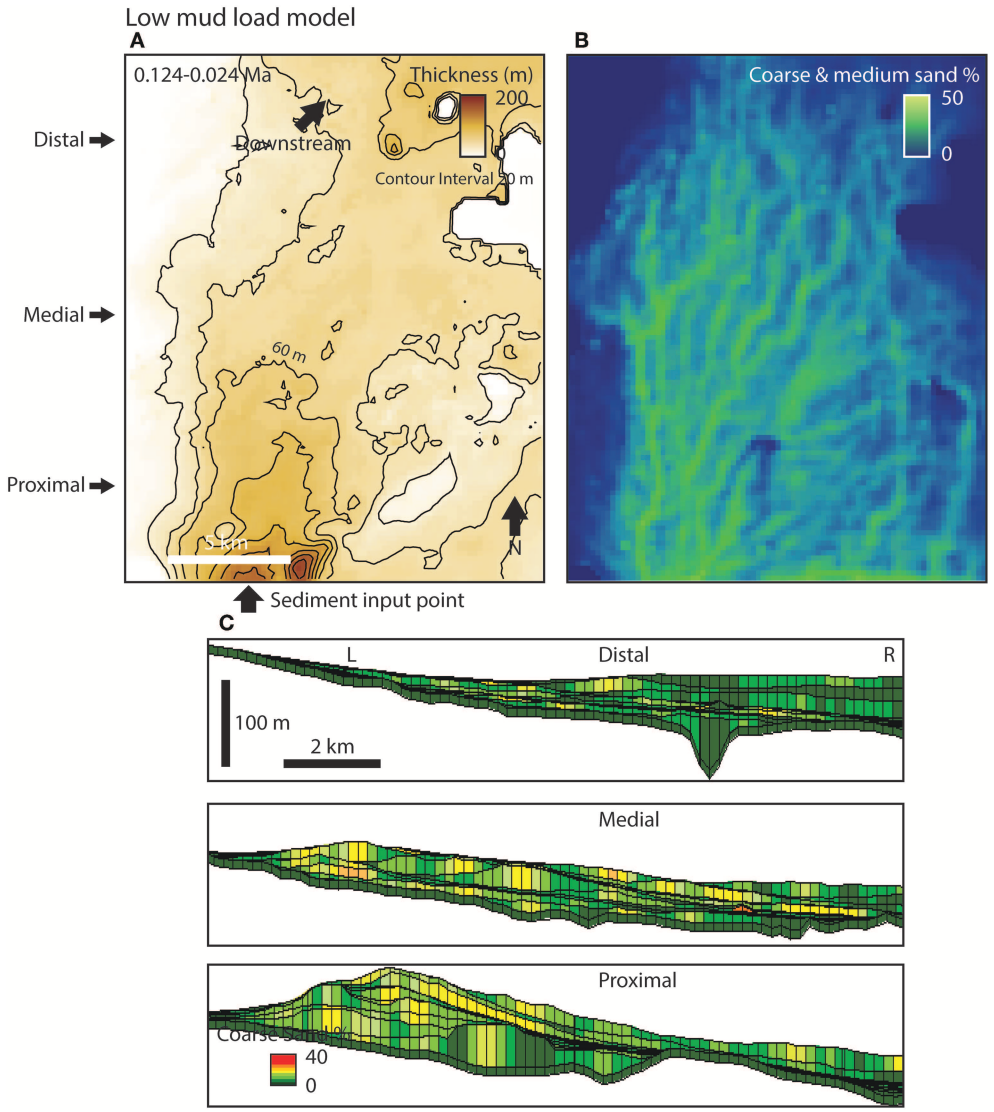

FIGURE 6 | (A) Isochore map of the low mud load model. **(B)** Coarse and medium sand percentage within the model. **(C)** Proximal, medial, and distal cross sections showing the coarse sand content in the model. Left (L) and right (R) orientations in cross sections are left and right in maps. Cross-section locations are indicated in part **(A)**.

of the diffusion coefficient K_w (Equation 1), which is larger for smaller grain sizes (**Table 1**). So, larger grain sizes assigned smaller K_w values will tend to pile up at the mouth of the feeder channel, like in the models of Hawie et al. (2018). By modifying the grain sizes in our new manually calibrated model to be finer, with correspondingly larger K_w values, the sediment-transport equations of the model diffused sediment farther across the model domain and achieved a better match with the field. Similar to Hawie et al. (2018), the model shows repeated cycles of channel avulsion, compensational stacking, and unconfined deposition at the mouths of channels (e.g., Sun et al., 2010). In particular, compensational stacking is a key characteristic of submarine-fan deposits (e.g., Deptuck et al., 2008), and our results show that relatively simple diffusion-based models can produce realistic compensation patterns. In our model, topographic build up by deposition promotes compensation and depocenter migration around the model domain. However, the thickness of compensationally stacked depocenters in the proximal region of the model, near the feeder channel, is less pronounced than in the models of Hawie et al. (2018). This is because our new model comprises relatively fine grains with larger diffusion coefficients, which are more easily transported over topography and generate an overall smoother, more elongate fan geometry.

Experimental Design 1: Grain Size

The first experimental design highlights the influence of changes in diffusion coefficients related to a range of grain sizes on

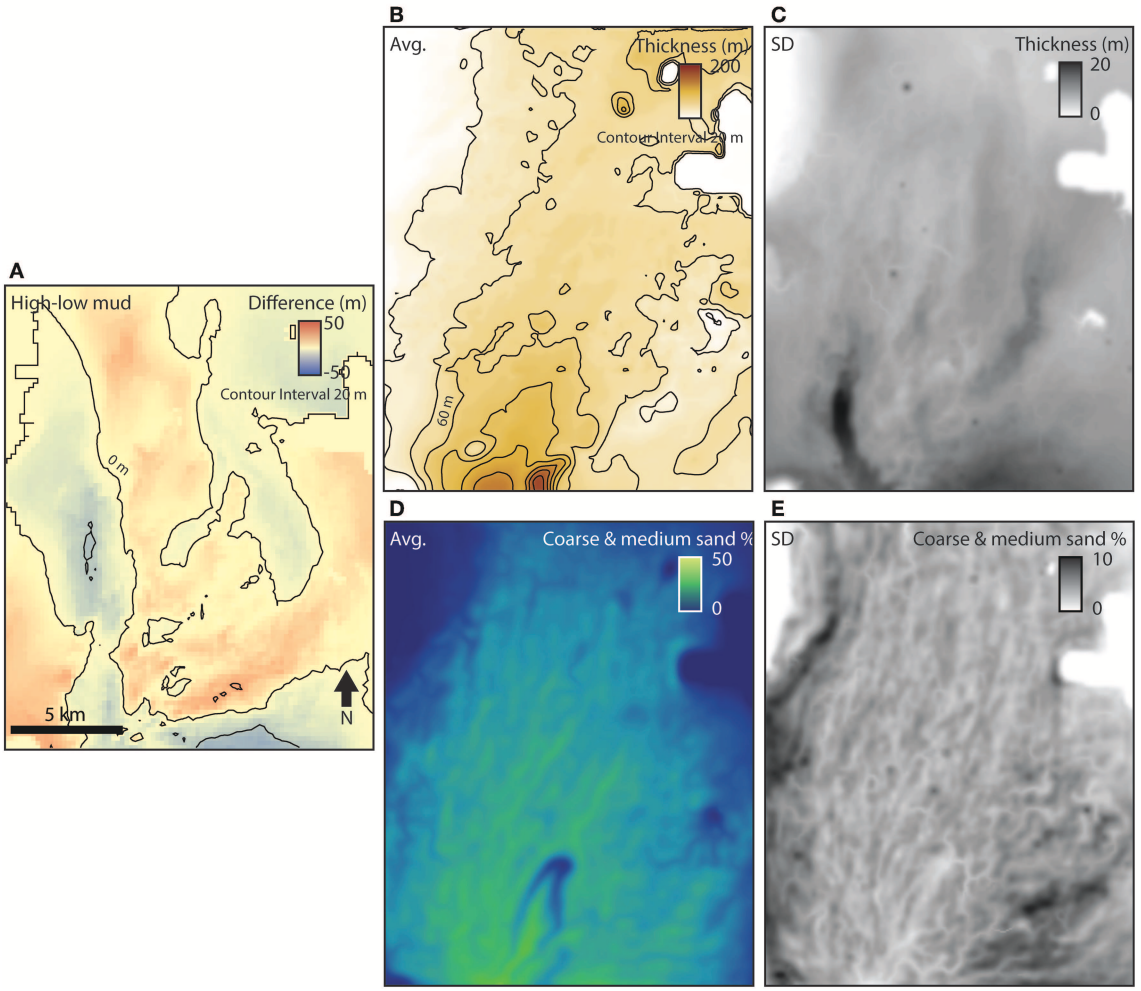

FIGURE 7 | (A) Difference in thickness between the high and low mud load models. **(B–E)** Simulation results. **(B)** Average of thicknesses. **(C)** Standard deviation of thicknesses. **(D)** Average of coarse and medium sand percentages. **(E)** Standard deviation of coarse and medium sand percentages.

fan deposition (**Figures 5**–**7**; **Supplementary Animations 3**–**6**). In the higher-mud-load case, a relatively thick band of deposits is spread across the northern, central, and eastern regions of the model as a result of the larger diffusion coefficient K_w (Equation 1) of finer sediment compared to the lower-mud-load case (**Figure 7A**). The larger diffusion coefficient promotes the basinward transport of finer sediment across the model. In the lower-mud-load case, coarser sediment piles up at the mouth of the feeder channel, which creates a steeper proximal slope that bypasses sediment to the distal northeast part of the model (**Figure 8A**). Moreover, the lower-mud-load case is relatively thick near the western and southeastern boundaries of the model domain, reflecting more compensational stacking (**Figure 6**). As diffusion is predominantly driven by slope and the diffusion coefficient, higher slopes and lower diffusion coefficients will promote more topographically directed, compensationally stacked deposits. The difference in depocenters in the high- vs. low-mud-load cases is also reflected in the maps of thickness and sand proportion standard deviations; the largest variance in thicknesses of the 22 simulations is at the mouth of the feeder channel in the proximal, central region of the model domain, and the largest variance in sand is at the western and southeastern boundaries of the model domain, where thicker, coarser deposits accumulated in the lower-mud-load case (**Figure 7**).

Experimental Design 2: Discharge

The second experimental design highlights the influence of sediment-gravity-flow discharge on fan deposition (**Figures 8**–**10**; **Supplementary Animations 7**–**10**). Intuitively, higher discharge (+20%) results in a thicker depositional system (**Figure 10A**). However, higher discharge results in fewer major depocenters because, initially, voluminous relatively coarse sediment accumulates in front of the proximal feeder channel and builds up a slope that dominates the direction of sediment transport during the simulation. The buildup of a slope in the proximal region of the model promotes bypass of finer sediment to the distal region, thereby causing some of the largest thickness differences between the high and low discharge cases along a

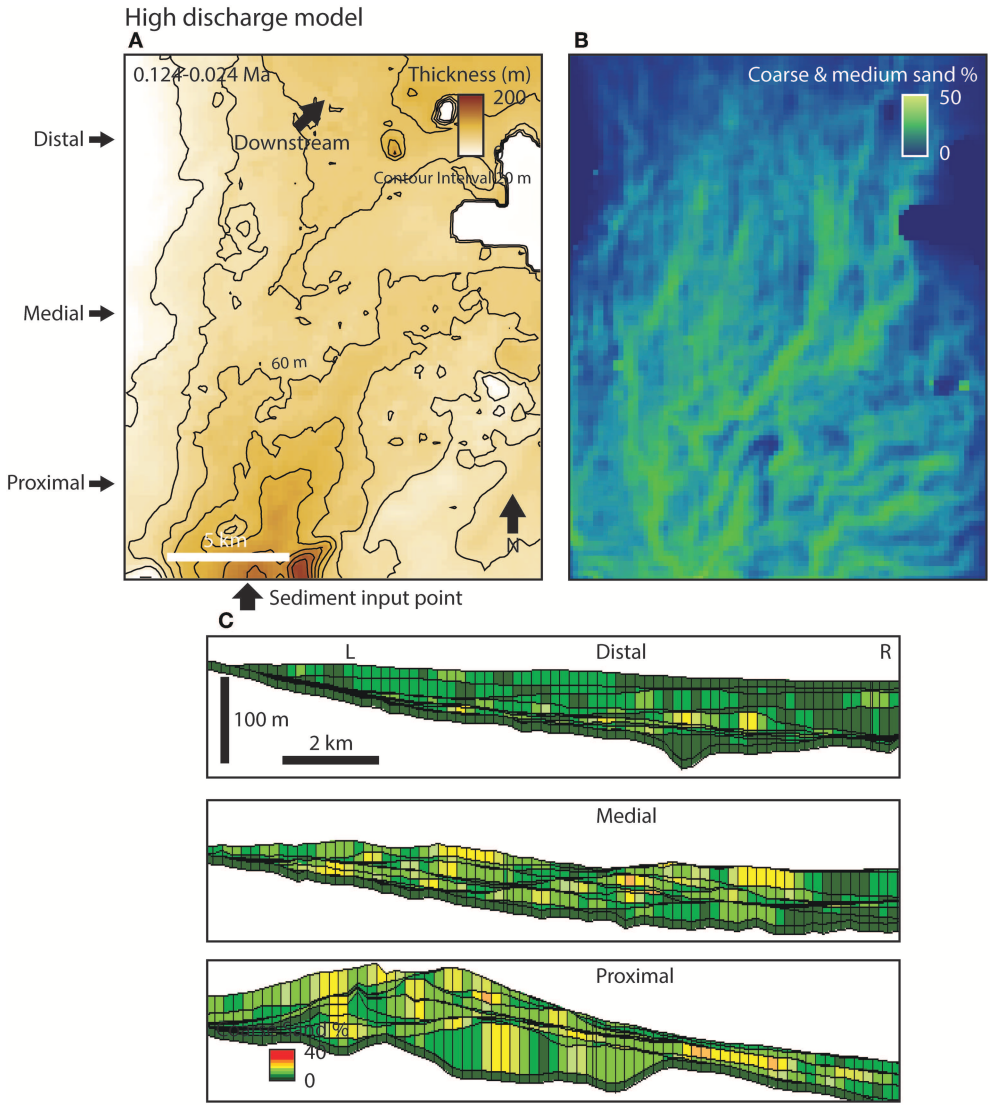

FIGURE 8 | (A) Isochore map of the high discharge model. **(B)** Coarse and medium sand percentage within the model. **(C)** Proximal, medial, and distal cross sections showing the coarse sand content in the model. Left (L) and right (R) orientations in cross sections are left and right in maps. Cross-section locations are indicated in part **(A)**.

region extending from the proximal feeder channel basinward to the northern distal part of the model (**Figure 10A**). Moreover, the largest variance in thicknesses of the 22 simulations is along this north-to-south region, where thickness probably depends on whether high enough discharge promotes the development of a single major north-to-south depocenter, as in the higher discharge case (**Figure 10C**). The large variance in sand proportions of the 22 simulations is located in the northwest because sandy depocenters did not visit that region of the model domain in every simulation (**Figure 10E**). In contrast, the central region is immediately down slope of the proximal feeder channel and consistently received the bulk of the relatively coarse sediment load. Mud transport is less sensitive to topography and, as a result, can more easily spread uniformly across the model.

DISCUSSION

The primary goals of our experiments were to understand the submarine-fan depositional response to changes in diffusion coefficients related to a range of grain sizes and discharges. In the models of Hawie et al. (2018), thicknesses in proximal areas exceeded thicknesses observed in the field. We increased the proportion of mud (i.e., silt/clay), with correspondingly larger K_w values, to the model by a factor of 5.5 in order to improve the thickness match between our reference-case model and the field case of Hawie et al. (2018). Rather than sand piling up in the proximal region of the model, at the mouth of the feeder channel, a mixed sediment load was more uniformly distributed across the model. Indeed, this is consistent with general models of submarine-fan run-out based on their mud- vs. sand-rich

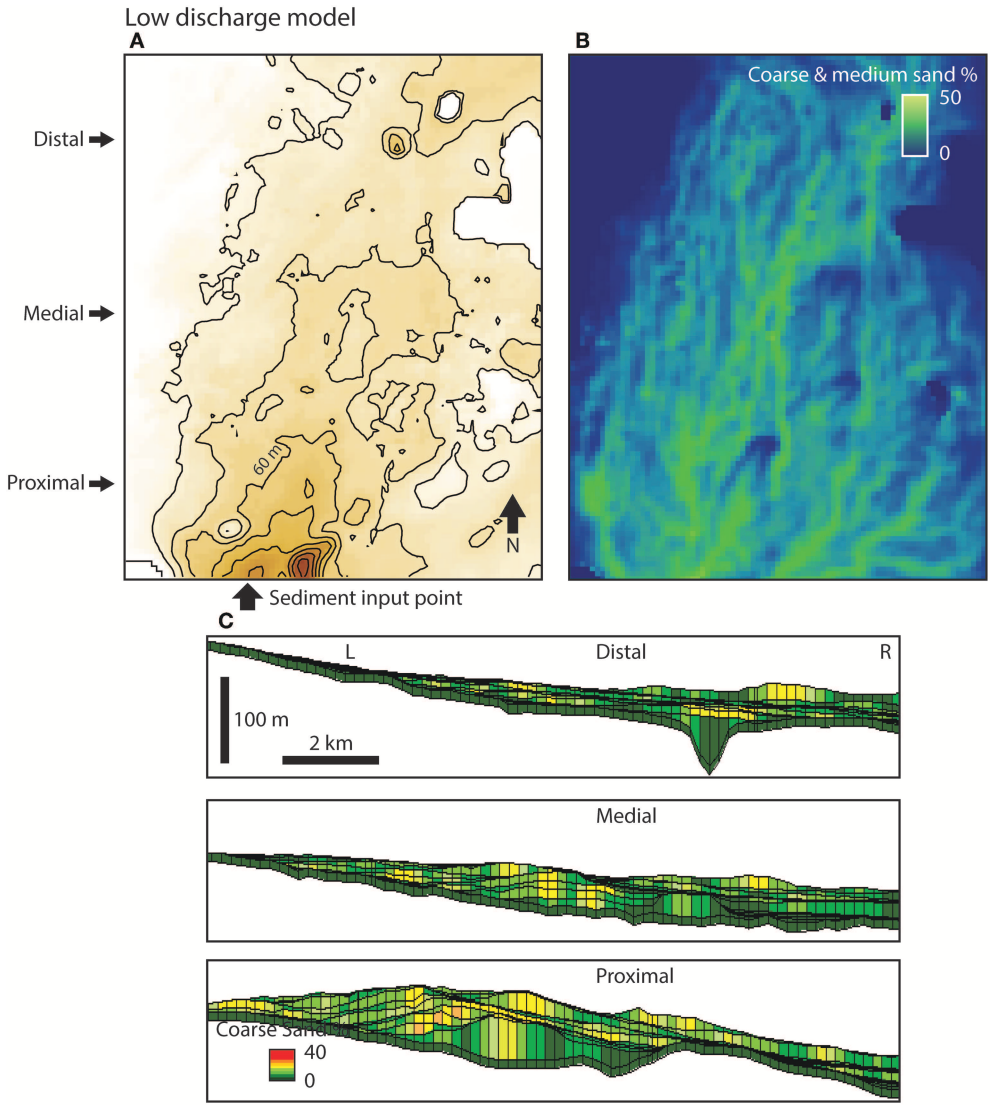

FIGURE 9 | (A) Isochore map of the low discharge model. **(B)** Coarse and medium sand percentage within the model. **(C)** Proximal, medial, and distal cross sections showing the coarse sand content in the model. Left (L) and right (R) orientations in cross sections are left and right in maps. Cross-section locations are indicated in part **(A)**.

sediment supply (e.g., Reading and Richards, 1994; Richards et al., 1998). Some of the largest, longest run-out submarine fans in the world are characterized as mud rich with highly "efficient" sediment transport (Richards et al., 1998; and references therein). Finer grain sizes are transported farther in our model; this has also been demonstrated for deposition on natural submarine-fan systems, such as the Amazon fan (Pirmez and Imran, 2003), and in physical experiments (Baas et al., 2004). Simple models of sediment transport and deposition using an advection-settling scheme also predict this behavior (Straub et al., 2008; and references therein). For example:

$$x = U\frac{z_i}{w_s} \quad (3)$$

where the distance the particle travels (x) is equal to the velocity of the particle (U) multiplied by the of the initial height of the particle above the bed (z_i) divided by the particle settling velocity (w_s). Although this advection-settling scheme is different than how Equation (1) diffuses sediment across our model domain, it supports our experimental results that show, in general, keeping all other variables constant, a finer, slower settling grain will be transported a longer distance compared to a coarser, faster settling grain.

We also explored an experimental design of variable mud load (80–20%). Decreasing mud load (i.e., increasing sand load) resulted in more widely distributed, coarser depocenters across the model, from the western to southeastern boundary of the model domain (**Figure 7A**). This is consistent with conceptual models of sandy submarine fans based on outcrops

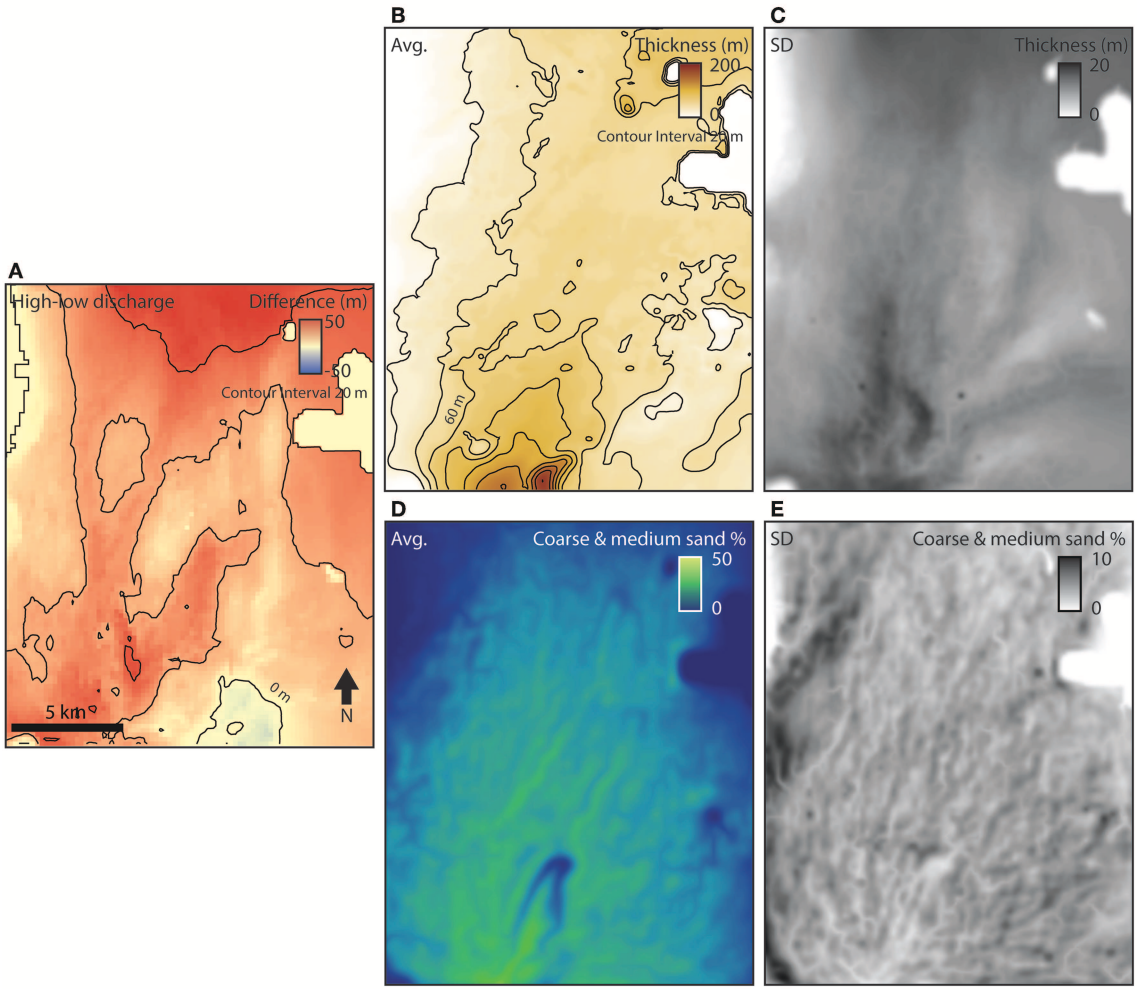

FIGURE 10 | (A) Difference in thickness between the high and low discharge models. **(B–E)** Simulation results. **(B)** Average of thicknesses. **(C)** Standard deviation of thicknesses. **(D)** Average of coarse and medium sand percentages. **(E)** Standard deviation of coarse and medium sand percentages.

and high-resolution, shallow-subsurface data in tectonically active settings; they tend to have limited channel extension and more frequent avulsions associated with steep basin-margin slopes (Hoyal et al., 2014). These concepts have been further developed in physical experiments (e.g., Spinewine et al., 2009; Hamilton et al., 2015; Postma et al., 2016) and reduced-complexity modeling of submarine-fan evolution over an evolving topography (e.g., Burgess et al., 2019). Although our models do not capture the high-resolution detail of morphodynamic interaction between flow and topography as in some physical experiments, including a potentially important hydraulic jump flow transformation and resultant depositional architecture (Mutti and Normark, 1987), our models show sandier sediment supply associated with the general trend of more frequent avulsions resulting in a larger number of depocenters.

Increasing sediment-gravity-flow discharge had the intuitive result of overall thicker deposits. However, this also resulted in fewer depocenters because relatively coarse sediment piled up at the mouth of the feeder channel, which created a slope that promoted basinward sediment transport along a dominant south-to-north fairway. Piper and Normark (2001), in their analysis of the distribution of sandy and muddy architectural elements of submarine fans, interpreted that steepening of proximal channels promotes basinward sand bypass and the development of a pattern of sand distribution similar to detached lobes of Mutti (1979), with lobe deposition displaced from the limit of sandy channel deposition. Although this interpretation was related to depositional patterns of channels and lobes in response to avulsions on the Amazon fan (Pirmez and Flood, 1995), steeper channels appear to promote basinward sediment bypass in our models as well (**Figures 8–10**).

Our modeling results can be applied to predict the overall geometry, stacking, and grain-size distribution of submarine-fan oil and gas reservoirs. In tectonically active, stepped-slope profiles, like offshore eastern Trinidad, increasing sand delivery to deep water (e.g., Moscardelli et al., 2012), can result in more compensational stacking of relatively sand-rich, proximal

depocenters (Piper and Normark, 2001). Increasing sediment supply, but maintaining grain-size distribution, can result in basinward sediment transport along a dominant fairway, thereby potentially producing isolated, "detached lobe" depositional architectures downstream of primary feeder channels. Our modeling also informs the interpretation of the depositional record of submarine fans. Observing some of the aforementioned depositional patterns, such as more/less frequent avulsions and compensational stacking of depocenters (e.g., Straub and Pyles, 2012), can be interpreted in the context of changing boundary conditions, namely changes in the caliber and overall supply of sediment to deep water. In order to better understand the results of our modeling experiments, we maintain our input variables (e.g., silt/clay proportion and discharge) as constant for the entire simulation time of 100 kyr. Of course, in nature, boundary conditions change during periods as long as 100 kyr, and future work will follow some of the more recent forward modeling work of Sylvester et al. (2015) and Burgess et al. (2019), which vary inputs, including substrate mobility and discharge. We also aim to pursue more numerous simulations, of the order of thousands, in order to achieve better calibration with the subsurface; new developments in high-performance parallelized computing processes can accelerate computations of high-resolution DionisosFlow models by as many as five times (Granjeon et al., 2018).

CONCLUSION

We used DionisosFlow forward stratigraphic models to understand the submarine-fan depositional response to changes in diffusion coefficients related to a range of grain sizes and discharges. Finer-grained loads were transported farther across the model domain; coarser loads resulted in the active migration of the depocenter across the model domain. This is consistent with general models of submarine-fan run-out and compensational stacking based on their mud- vs. sand-rich sediment supply. Higher discharge resulted in a thicker depositional system, but fewer channel avulsions because an initial relatively coarse-grained sediment buildup at the mouth of the proximal feeder channel promoted bypass of finer sediment to the distal region of the model domain. Our modeling results can be applied to predict the depositional architecture of submarine fans; changes in diffusion coefficients related to a range of grain sizes and discharges have an effect on the overall geometry, stacking, and heterogeneity of our models. Our results can also be applied to the interpretation of fan stratigraphy in outcrops and subsurface datasets. For example, observations of compensational stacking in outcrops can be related to changes in sediment supply to the depositional system. Our future work will evaluate the depositional response to temporally varying the inputs of more numerous simulations. We envision thousands of simulations to generate facies probability maps to be integrated in reservoir models.

DATA AVAILABILITY STATEMENT

All datasets generated for this study are included in the article/**Supplementary Material**.

AUTHOR CONTRIBUTIONS

NH, JC, and ZS designed the experiments and wrote the manuscript. NH performed the experiments. NH and JC created figures.

ACKNOWLEDGMENTS

We thank the sponsors of the Quantitative Clastics Laboratory (http://www.beg.utexas.edu/qcl) and Beicip-Franlab for access to DionisosFlow and CougarFlow forward stratigraphic modeling and multi-simulation software. We are grateful for thought-provoking comments from Tim Demko and Mauricio Perillo, as well as recommendations from reviewers Michal Janocko, Cornel Olariu, and Ian Kane and editors David Hodgson and William Helland-Hansen.

SUPPLEMENTARY MATERIAL

The Supplementary Material for this article can be found online at: https://www.frontiersin.org/articles/10.3389/feart.2019.00334/full#supplementary-material

Supplementary Animation 1 | Reference case model of the coarse sand distribution (overhead view).

Supplementary Animation 2 | Reference case model of the coarse sand distribution (perspective view).

Supplementary Animation 3 | High mud load model of the coarse sand distribution (overhead view).

Supplementary Animation 4 | High mud load model of the coarse sand distribution (perspective view).

Supplementary Animation 5 | Low mud load model of the coarse sand distribution (overhead view).

Supplementary Animation 6 | Low mud load model of the coarse sand distribution (perspective view).

Supplementary Animation 7 | High discharge model of the coarse sand distribution (overhead view).

Supplementary Animation 8 | High discharge model of the coarse sand distribution (perspective view).

Supplementary Animation 9 | Low discharge model of the coarse sand distribution (overhead view).

Supplementary Animation 10 | Low discharge model of the coarse sand distribution (perspective view).

REFERENCES

Aas, T. E., Basani, R., Howell, J., and Hansen, E. (2014). Forward modelling as a method for predicting the distribution of deep-marine sands: an example from the Peïra Cava Sub-basin. *Geol. Soc. Lond. Spec. Publ.* 387, 247–269. doi: 10.1144/SP387.9

Alzaga-Ruiz, H., Granjeon, D., Lopez, M., Seranne, M., and Roure, F. (2009). Gravitational collapse and Neogene sediment transfer across the western

margin of the Gulf of Mexico: insights from numerical models. *Tectonophysics* 470, 21–41. doi: 10.1016/j.tecto.2008.06.017

Audze, P., and Eglais, V. (1977). New approach to design of experiments. *Probl. Dyn. Strength* 35, 104–107.

Baas, J. H., Van Kesteren, W., and Postma, G. (2004). Deposits of depletive high-density turbidity currents: a flume analogue of bed geometry, structure and texture. *Sedimentology* 51, 1053–1088. doi: 10.1111/j.1365-3091.2004.00660.x

Barabasch, J., Ducros, M., Hawie, N., Daher, S. B., Nader, F. H., and Littke, R. (2019). Integrated 3D forward stratigraphic and petroleum system modeling of the Levant Basin, Eastern Mediterranean. *Basin Res.* 31, 228–252. doi: 10.1111/bre.12318

Bouma, A. H., Normark, W. R., and Barnes, N. E. (1985). *Submarine Fans and Related Turbidite Systems*. Berlin; New York, NY: SpringerVerlag Inc. doi: 10.1007/978-1-4612-5114-9

Brami, T. R., Pirmez, C., Archie, C., Heeralal, S., and Holman, K. L. (2000). "Late Pleistocene deep-water stratigraphy and depositional processes, offshore Trinidad and Tobago," in *Deep-Water Reservoirs of the World: Gulf Coast Section Sepm 20th Annual Research Conference* (Houston, TX), 104–115. doi: 10.5724/gcs.00.15.0104

Burgess, P. M., Masiero, I., Toby, S. C., and Duller, R. A. (2019). A big fan of signals? Exploring autogenic and allogenic process and product in a numerical stratigraphic forward model of submarine-fan development. *J. Sediment. Res.* 89, 1–12. doi: 10.2110/jsr.2019.3

Clift, P. D., Degnan, P., Hannigan, R., and Blusztajn, J. (2000). Sedimentary and geo-chemical evolution of the Dras forearc basin, Indus suture, Ladakh Himalaya, India. *Geol. Soc. Am. Bull.* 112, 450–466. doi: 10.1130/0016-7606(2000)112<450:SAGEOT>2.0.CO;2

Clift, P. D., and Gaedicke, C. (2002). Accelerated mass flux to the Arabian Sea during the middle to late Miocene. *Geology* 30, 207–210. doi: 10.1130/0091-7613(2002)030<0207:AMFTTA>2.0.CO;2

Dalman, R. A., and Weltje, G. J. (2008). Sub-grid parameterisation of fluvio-deltaic processes and architecture in a basin-scale stratigraphic model. *Comput. Geosci.* 34, 1370–1380. doi: 10.1016/j.cageo.2008.02.005

Dalman, R. A., and Weltje, G. J. (2012). SimClast: an aggregated forward stratigraphic model of continental shelves. *Comput. Geosci.* 38, 115–126. doi: 10.1016/j.cageo.2011.05.014

Deptuck, M. E., Piper, D. J., Savoye, B., and Gervais, A. (2008). Dimensions and architecture of late Pleistocene submarine lobes off the northern margin of East Corsica. *Sedimentology* 55, 869–898. doi: 10.1111/j.1365-3091.2007.00926.x

Deville, E., Mascle, A., Callec, Y., Huyghe, P., Lallemant, S., Lerat, O., et al. (2015). Tectonics and sedimentation interactions in the east Caribbean subduction zone: an overview from the Orinoco delta and the Barbados accretionary prism. *Mar. Petroleum Geol.* 64, 76–103. doi: 10.1016/j.marpetgeo.2014.12.015

Eggenhuisen, J. T., and McCaffrey, W. D. (2012). The vertical turbulence structure of experimental turbidity currents encountering basal obstructions; implications for vertical suspended sediment distribution in non-equilibrium currents. *Sedimentology* 59, 1101–1120. doi: 10.1111/j.1365-3091.2011.01297.x

Euzen, T., Joseph, P., Du Fornel, E., Lesur, S., Granjeon, D., and Guillocheau, F. (2004). Three-dimensional stratigraphic modelling of the Grès d'Annot system, Eocene-Oligocene, SE France. *Geol. Soc. London Spec. Publ.* 221, 161–180. doi: 10.1144/GSL.SP.2004.221.01.09

Falivene, O., Frascati, A., Gesbert, S., Pickens, J., Hsu, Y., and Rovira, A. (2014). Automatic calibration of stratigraphic forward models for predicting reservoir presence in exploration. *AAPG Bull.* 98, 1811–1835. doi: 10.1306/02271413028

Granjeon, D. (1997). *Modélisation stratigraphique déterministe: conception et applications d'un modéle diffusif 3 D multilithologique* (Ph.D. dissertation). Université de Rennes, Rennes.

Granjeon, D. (2014). "3D forward modelling of the impact of sediment transport and base level cycles on continental margins and incised valleys," in *Depositional Systems to Sedimentary Successions on the Norwegian Continental Margin: International Association of Sedimentologists*, Vol. 46, eds A. W. Martinius, R. Ravnås, J. A. Howell, R. J. Steel, and J. P. Wonham (Chichester: John Wiley & Sons), 453–472. doi: 10.1002/9781118920435.ch16

Granjeon, D., Have, P., Coatleven, J., Pegaz-Fiornet, S., and Chauveau, B. (2018). "High performance stratigraphic modeling of shelf to deep-water plays," in *AAPG 2018 Annual Convention and Exhibition* (Salt Lake City, UT).

Granjeon, D., and Joseph, P. (1999). "Concepts and applications of a 3-D multiple lithology, diffusive model in stratigraphic modeling," in *Numerical Experiments in Stratigraphy: Recent Advances in Stratigraphic and Sedimentologic Computer Simulations,* Vol. 62, eds J. W. Harbaugh, W. L. Watney, E. C. Rankey, R. Slingerland, R. H. Goldstein, and E. K. Franseen (Tulsa, OK: SEPM Society for Sedimentary Geology), 197–210. doi: 10.2110/pec.99.62.0197

Groenenberg, R. M., Hodgson, D. M., Prelat, A., Luthi, S. M., and Flint, S. S. (2010). Flow–deposit interaction in submarine lobes: insights from outcrop observations and realizations of a process-based numerical model. *J. Sediment. Res.* 80, 252–267. doi: 10.2110/jsr.2010.028

Gvirtzman, Z., Csato, I., and Granjeon, D. (2014). Constraining sediment transport to deep marine basins through submarine channels: the Levant margin in the Late Cenozoic. *Mar. Geol.* 347, 12–26. doi: 10.1016/j.margeo.2013.10.010

Hamilton, P. B., Strom, K. B., and Hoyal, D. C. (2015). Hydraulic and sediment transport properties of autogenic avulsion cycles on submarine fans with supercritical distributaries. *J. Geophys. Res. Earth Surface* 120, 1369–1389. doi: 10.1002/2014JF003414

Harris, A. D., Covault, J. A., Madof, A. S., Sun, T., Sylvester, Z., and Granjeon, D. (2016). Three-dimensional numerical modeling of Eustatic control on continental-margin sand distribution. *J. Sediment. Res.* 86, 1434–1443. doi: 10.2110/jsr.2016.85

Hawie, N., Covault, J. A., Dunlap, D., and Sylvester, Z. (2018). Slope-fan depositional architecture from high-resolution forward stratigraphic models. *Mar. Petrol. Geol.* 91, 576–585. doi: 10.1016/j.marpetgeo.2017.12.033

Hawie, N., Deschamps, R., Granjeon, D., Nader, F. H., Gorini, C., Muller, C., et al. (2017). Multi-scale constraints of sediment source to sink systems in frontier basins: A forward stratigraphic modeling case study of the Levant region. *Basin Res.* 29, 418–445. doi: 10.1111/bre.12156

Hoyal, D. C. H., Demko, T., Postma, G., Wellner, R. W., Pederson, K., Abreu, V., et al. (2014). "Evolution, architecture and stratigraphy of Froude supercritical submarine fans," in *American Association of Petroleum Geologists Annual Convention and Exhibition* (Houston, TX).

Iman, R. L., Davenport, J. M., and Zeigler, D. K. (1980). *Latin Hypercube Sampling (Program User's Guide)*. Albuquerque, NM: Department of Energy, Sandia Laboratories.

Iman, R. L., Helton, J. C., and Campbell, J. E. (1981). An approach to sensitivity analysis of computer models: Part I—Introduction, input variable selection and preliminary variable assessment. *J. Qual. Technol.* 13, 174–183. doi: 10.1080/00224065.1981.11978748

Jobe, Z. R., Sylvester, Z., Howes, N., Pirmez, C., Parker, A., Cantelli, A., et al. (2017). High-resolution, millennial-scale patterns of bed compensation on a sand-rich intraslope submarine fan, western Niger Delta slope. *GSA Bull.* 129, 23–37. doi: 10.1130/B31440.1

McKay, M. D., Beckman, R. J., and Conover, W. J. (1979). Comparison of three methods for selecting values of input variables in the analysis of output from a computer code. *Technometrics* 21, 239–245. doi: 10.1080/00401706.1979.10489755

Miller, J. K., Sun, T., Li, H., Stewart, J., Genty, C., Li, D., et al. (2008). "Direct modeling of reservoirs through forward process-based models: can we get there?" in *International Petroleum Technology Conference* (Kuala Lumpur). doi: 10.2523/12729-MS

Moscardelli, L., and Wood, L. (2008). New classification system for mass transport complexes in offshore Trinidad. *Basin Res.* 20, 73–98. doi: 10.1111/j.1365-2117.2007.00340.x

Moscardelli, L., Wood, L., and Mann, P. (2006). Mass-transport complexes and associated processes in the offshore area of Trinidad and Venezuela. *AAPG Bull.* 90, 1059–1088. doi: 10.1306/02210605052

Moscardelli, L., Wood, L. J., and Dunlap, D. B. (2012). Shelf-edge deltas along structurally complex margins: a case study from eastern offshore Trinidad. *AAPG Bull.* 96, 1483–1522. doi: 10.1306/01241211046

Mutti, E. (1979). Turbidites et cones sous-marins profonds. *Sédimentation détritique* 1, 353–419.

Mutti, E., and Normark, W. R. (1987). "Comparing examples of modern and ancient turbidite systems: problems and concepts," in *Marine Clastic Sedimentology*, eds J. K. Leggett and G. G. Zuffa (Dordrecht: Springer), 1–38.

Normark, W. R., Posamentier, H., and Mutti, E. (1993). Turbidite systems: state of the art and future directions. *Rev. Geophys.* 31, 91–116. doi: 10.1029/93RG02832

Pinheiro-Moreira, J. L. (2000). *Stratigraphie sismique et modélisation stratigraphique des dépôts de l'Éocène du Bassin de Santos (marge brésilienne)* (Ph.D. dissertation). Université de Rennes, Rennes.

Piper, D. J., and Normark, W. R. (2001). Sandy fans–from Amazon to Hueneme and beyond. *AAPG Bull.* 85, 1407–1438. doi: 10.1306/8626CACD-173B-11D7-8645000102C1865D

Pirmez, C., and Flood, R. D. (1995). "Morphology and structure of Amazon Channel," in *Proceedings of the Ocean Drilling Program. Initial Reports* (College Station, TX: Ocean Drilling Program), 23–45. doi: 10.2973/odp.proc.ir.155.103.1995

Pirmez, C., and Imran, J. (2003). Reconstruction of turbidity currents in Amazon Channel. *Mar. Petrol. Geol.* 20, 823–849. doi: 10.1016/j.marpetgeo.2003.03.005

Postma, G., Hoyal, D. C., Abreu, V., Cartigny, M. J., Demko, T., Fedele, J. J., et al. (2016). "Morphodynamics of supercritical turbidity currents in the channel-lobe transition zone," in *Submarine Mass Movements and Their Consequences*, Vol 41, eds G. Lamarche, J. Mountjoy, S. Bull, T. Hubble, S. Krastel, E. Lane, A. Micallef, L. Moscardelli, C. Mueller, I. Pecher, and S. Woelz (Cham: Springer International Publishing), 469–478. doi: 10.1007/978-3-319-20979-1_47

Prather, B. E., Pirmez, C., and Winker, C. D. (2012). "Stratigraphy of linked intraslope basins: Brazos-Trinity system western Gulf of Mexico," in *Application of the Principles of Seismic Geomorphology to Continental-Slope and Base-of-Slope Systems: Case Studies from Seafloor and Near-Seafloor Analogues,* Vol. 99, B. E. Prather, M. E. Deptuck, D. Mohrig, B. V. Hoorn, and R. B. Wynn (Tulsa, OK: SEPM Society for Sedimentary Geology), 83–110. doi: 10.2110/pec.12.99.0083

Prelat, A., Covault, J. A., Hodgson, D. M., Fildani, A., and Flint, S. S. (2010). Intrinsic controls on the range of volumes, morphologies, and dimensions of submarine lobes. *Sediment. Geol.* 232, 66–76. doi: 10.1016/j.sedgeo.2010.09.010

Pyrcz, M. J., and Deutsch, C. V. (2014). *Geostatistical Reservoir Modeling*. Oxford: Oxford University Press.

Pyrcz, M. J., Sech, R. P., Covault, J. A., Willis, B. J., Sylvester, Z., and Sun, T. (2015). Stratigraphic rule-based reservoir modeling. *Bull. Can. Petrol. Geol.* 63, 287–303. doi: 10.2113/gscpgbull.63.4.287

Rabineau, M., Berné, S., Aslanian, D., Olivet, J. L., Joseph, P., Guillocheau, F., et al. (2005). Sedimentary sequences in the Gulf of Lion: a record of 100,000 years climatic cycles. *Mar. Petrol. Geol.* 22, 775–804. doi: 10.1016/j.marpetgeo.2005.03.010

Reading, H. G., and Richards, M. (1994). Turbidite systems in deep-water basin margins classified by grain size and feeder system. *AAPG Bull.* 78, 792–822. doi: 10.1306/A25FE3BF-171B-11D7-8645000102C1865D

Richards, M., Bowman, M., and Reading, H. (1998). Submarine-fan systems I: characterization and stratigraphic prediction. *Mar. Petrol. Geol.* 15, 689–717. doi: 10.1016/S0264-8172(98)00036-1

Rivenaes, J. C. (1992). Application of a dual-lithology, depth-dependent diffusion equation in stratigraphic simulation. *Basin Res.* 4, 133–146. doi: 10.1111/j.1365-2117.1992.tb00136.x

Romans, B. W., Castelltort, S., Covault, J. A., Fildani, A., and Walsh, J. P. (2016). Environmental signal propagation in sedimentary systems across timescales. *Earth Sci. Rev.* 153, 7–29. doi: 10.1016/j.earscirev.2015.07.012

Sacchi, Q., Borello, E. S., Weltje, G. J., and Dalman, R. (2016). Increasing the predictive power of geostatistical reservoir models by integration of geological constraints from stratigraphic forward modeling. *Mar. Petrol. Geol.* 69, 112–126. doi: 10.1016/j.marpetgeo.2015.10.018

Sequeiros, O. E., Spinewine, B., Beaubouef, R. T., Sun, T., García, M. H., and Parker, G. (2010). Characteristics of velocity and excess density profiles of saline underflows and turbidity currents flowing over a mobile bed. *J. Hydraulic Eng.* 136, 412–433. doi: 10.1061/(ASCE)HY.1943-7900.0000200

Spinewine, B., Sequeiros, O. E., Garcia, M. H., Beaubouef, R. T., Sun, T., Savoye, B., et al. (2009). Experiments on wedge-shaped deep sea sedimentary deposits in minibasins and/or on channel levees emplaced by turbidity currents. Part II. Morphodynamic evolution of the wedge and of the associated bedforms. *J. Sediment. Res.* 79, 608–628. doi: 10.2110/jsr.2009.065

Straub, K. M., Mohrig, D., McElroy, B., Buttles, J., and Pirmez, C. (2008). Interactions between turbidity currents and topography in aggrading sinuous submarine channels: a laboratory study. *GSA Bull.* 120, 368–385. doi: 10.1130/B25983.1

Straub, K. M., and Pyles, D. R. (2012). Quantifying the hierarchical organization of compensation in submarine fans using surface statistics. *J. Sediment. Res.* 82, 889–898. doi: 10.2110/jsr.2012.73

Sun, T., Ghayour, K., Hall, B., and Miller, J. (2010). "Process-based modeling of deep water depositional systems," in *Seismic Imaging of Depositional and Geomorphic Systems: Gulf Coast Section SEPM Foundation 30th Annual Bob F. Perkins Research Conference* (Houston, TX: SEPM Society for Sedimentary Geology), 88–112. doi: 10.5724/gcs.10.30.0088

Sweet, M. L., Gaillot, G. T., Jouet, G., Rittenour, T. M., Toucanne, S., Marsset, T., et al. (2019). Sediment routing from shelf to basin floor in the Quaternary Golo System of Eastern Corsica, France, western Mediterranean Sea. *Geol. Soc. Am. Bull.* doi: 10.1130/B35181.1. [E-pub ahead of print].

Sylvester, Z., Cantelli, A., and Pirmez, C. (2015). Stratigraphic evolution of intraslope minibasins: Insights from surface-based model. *AAPG Bull.* 99, 1099–1129. doi: 10.1306/01081514082

Tucker, G. E., and Slingerland, R. L. (1994). Erosional dynamics, flexural isostasy, and long-lived escarpments: a numerical modeling study. *J. Geophys. Res. Solid Earth* 99, 12229–12243. doi: 10.1029/94JB00320

Weimer, P., and Pettingill, H. S. (2007). "Deep-water exploration and production: a global overview," in *Atlas of Deep-Water Outcrops: AAPG Studies in Geology 56*, eds T. H. Nilsen, R. D. Shew, G. S. Steffens, and J. Studlick (Tulsa, OK: AAPG).

Willgoose, G., Bras, R. L., and Rodriguez-Iturbe, I. (1991). A coupled channel network growth and hillslope evolution model: 1. *Theory Water Resour. Res.* 27, 1671–1684. doi: 10.1029/91WR00935

Wood, L. J., and Mize-Spansky, K. L. (2009). Quantitative seismic geomorphology of a Quaternary leveed-channel system, offshore eastern Trinidad and Tobago, northeastern South America. *AAPG Bull.* 93, 101–125. doi: 10.1306/08140807094

Conflict of Interest: The authors declare that the research was conducted in the absence of any commercial or financial relationships that could be construed as a potential conflict of interest.

The reviewer CO declared a shared affiliation, with no collaboration, with one of the authors, JC and ZS, to the handling editor at time of review.

frontiers in Earth Science

ORIGINAL RESEARCH
published: 22 January 2020
doi: 10.3389/feart.2019.00361

Paleohydrology and Machine-Assisted Estimation of Paleogeomorphology of Fluvial Channels of the Lower Middle Pennsylvanian Allegheny Formation, Birch River, WV

Oluwasegun Abatan and Amy Weislogel**

Department of Geology and Geography, West Virginia University, Morgantown, WV, United States

OPEN ACCESS

Edited by:
Brian W. Romans, Virginia Tech, United States

Reviewed by:
Adrian John Hartley, University of Aberdeen, United Kingdom
Tara Nicole Jonell, The University of Queensland, Australia

***Correspondence:**
Oluwasegun Abatan
olabatan@mix.wvu.edu
Amy Weislogel
amy.weislogel@mail.wvu.edu

Specialty section:
This article was submitted to Sedimentology, Stratigraphy and Diagenesis, a section of the journal Frontiers in Earth Science

Received: *15 August 2019*
Accepted: *30 December 2019*
Published: *22 January 2020*

Citation:
Abatan O and Weislogel A (2020) Paleohydrology and Machine-Assisted Estimation of Paleogeomorphology of Fluvial Channels of the Lower Middle Pennsylvanian Allegheny Formation, Birch River, WV. Front. Earth Sci. 7:361. doi: 10.3389/feart.2019.00361

Rivers transport sediments in a source to sink system while responding to allogenic controls of the depositional system. Stacked fluvial sandstones of the Middle Pennsylvanian (Desmoinesian Stage, ~310–306 Ma) Allegheny Formation (MPAF) exposed at Birch River, West Virginia exhibit change in sedimentary structure and depositional style, reflecting changes in allogenic behavior. Paleohydrologic and numerical analysis were used to quantify geomorphological and paleohydrologic variations reflected by MPAF fluvial deposits with the goal of understanding the controls on resulting fluvial sandstone architecture in these different systems. Channel body geometry, sedimentary structures, and sandstone grain size distribution were used to reconstruct the paleoslope and flow velocity of the MPAF fluvial systems. In order to enhance paleohydrological estimates, machine learning methods including multiple regression and support vector regression (SVR) algorithms were used to improve the dune height, and channel depth estimated from cross-set thickness. Results show that the channel depths of the lower MPAF beneath the Lower Kittanning coal beds tend to decrease upsection; this decrease is interpreted to reflect a transition from fluvial systems formed in a humid ever-wet climate to fluvial systems formed in less humid, seasonally wet, semi-arid climate. Paleohydrologic estimations enabled the evaluation of hydraulic changes in the fluvial depositional systems of the Appalachian Basin during the Desmoinesian stage. Paleoslope estimates indicated that the slope was low, which indicated that the fluvial gradient response was not driven by the effect of tectonic subsidence or uplift and sea-level change.

Keywords: fluvial, paleohydrology, sedimentology, allegheny, source-to-sink, machine-learning

INTRODUCTION

Fluvial systems are the main terrestrial conduits for transporting the sediment load of a source to sink system. The source to sink system involves source rock erosion in the initial catchment area and sediment transportation through fluvial environments and to ultimate deposition in a basinal sink (e.g., Bhattacharya et al., 2016; Lin and Bhattacharya, 2017). The fluvial system

responds to external factors, such as climate, tectonics, and eustasy and is driven to maintain equilibrium while efficiently routing sediments. Changes in fluvial hydrology lead to changes in sediment transport and deposition, which alter channel aggradation, channel incision, and channel morphology (Leeder, 1993, 2009; Holbrook and Wanas, 2014). For example, fluvial channels in seasonal semi-arid climates have different geomorphology and hydrologic processes from fluvial channels of ever-wet humid climates (Fielding et al., 2009; Allen et al., 2014; Plink-Björklund, 2015). Modern fluvial depositional system analogs indicate that fluvial systems in seasonal semi-arid climatic regions typically have a greater channel width to depth ratio than fluvial channels of ever-wet humid climatic region (Fielding et al., 2009; Gibling et al., 2014).

Channel depth and width data combined with sedimentologic data from outcrop can be used to estimate paleohydrology for ancient fluvial systems (Rubin and McCulloch, 1980; Bhattacharya et al., 2016), which can then be tied to climate controls. Improved knowledge of the relationship between paleohydrology and depositional products of fluvial systems can also be used to improve reservoir characterization and reservoir quality prediction. In particular, the continuity and quality of fluvial sandstone reservoirs are dependent on the channel style of the fluvial depositional system (Miall, 1996; Bridge, 2009). Fluvial systems with high net-to-gross sandstone ratios form reservoirs with higher quality compared to fluvial systems with abundant overbank fine-grained sediments. Braided fluvial systems produce laterally continuous sandstone bodies with sheet geometries, while sinuous fluvial systems (meandering or anastomosing) produce laterally restricted sandstone bodies with ribbon and lens geometry (Miall, 1996). Braided channels have higher flow velocities because they are formed in areas with high slope, whereas sinuous fluvial system has relatively lower velocities because they are formed in areas with relatively lower slope (Schumm, 1981; Miall, 1996).

This paper proposes an enhanced methodology with which to estimate the paleohydrology and paleo-geomorphology of fluvial channels, using the fluvial sandstone deposits of the lower part of the Middle Pennsylvanian Allegheny Formation (MPAF) of Central West Virginia as a case example (**Figures 1**, **2**). The MPAF is characterized by repetitive cycles of clastic and chemical sediments known as cyclothems (Cecil, 1990). The MPAF at the Birch River area central West Virginia lacks marine zones where it is well exposed along a continuous road cut ˜110 m high and 500 m long along US 19 as it crosses Powell Mountain near Birch River in central West Virginia (**Figure 1**). The lower part of the MPAF (from here on referred to as MPAF) includes sandstones overlying the Lower Kittanning coal (LKC) beds, the Upper No. 5 Bock coal beds, and the No. 5 Block coal beds (**Figures 2**, **3**). Facies analysis determined channel style and geometry of the lower MPAF sandstones and revealed a range of channel forms, including high sinuosity, low sinuosity, and braided. This interval was selected for paleohydrological analysis because previous coal paleobotany studies indicate fluctuation between a humid and a seasonally wet-dry climate during MPAF deposition (Cecil, 1990; Eble, 2002; Cecil et al., 2003; Falcon-Lang, 2004; Greb et al., 2008; Falcon-Lang and Dimichele, 2010), and, thus, provides important independent constraints on paleoclimate variability with to investigate fluvial system response to paleohydrological controls.

Fluvial paleohydrology can be modeled from numerical equations based on grain size along with channel depth and width measurements and augmented by flow depth estimates from estimated dune bedform height (Ethridge and Schumm, 1977; Bridge and Tye, 2000; Leclair and Bridge, 2001; Leclair, 2002; Bhattacharya et al., 2016). These empirical equations relate sandstone grain size and channel geometry to estimates of paleohydrology. To build upon previous attempts at reconstructing paleohydrology of ancient fluvial systems, machine-assisted algorithms were developed to improve the accuracy of the estimated dune height from cross-set thickness using data of cross-set thickness and dune height from flume experiments reported by Leclair (2002) and Leclair and Bridge (2001). Multi-variate regression analysis was performed on the original data set to highlight the statistical significance (p-value) of the relationship between the variables in the data set. Support vector regression algorithm (herein and after referred to as SVR) was selected to better assess the relationship between variables with acceptable statistical significance (i.e., p-value < 0.05) because it can be used where bivariate relationships are established between geological properties with multivariate relationships (Ethridge and Schumm, 1977; Davis and Sampson, 1986; Bridge, 2009). Through this approach, the paleohydrological controls on MPAF fluvial architecture can be assessed to provide insights into the evolution of fluvial style and fluvial basin-fill record of the Alleghany foreland basin.

GEOLOGICAL SETTING

Geologic History

The MPAF (Desmoinesian Stage, ∼310–306 Ma) is part of an Upper Paleozoic cratonward prograding clastic wedge shed from the adjacent orogenic highlands of the Allegheny orogeny during the late Middle Pennsylvanian (Arkle et al., 1979; Donaldson and Shumaker, 1981; Ettensohn, 2008). The collision of Laurasia and Gondwanaland (∼325 Ma) initiated the Alleghenian orogeny, which was characterized by collision and compressional deformation structures that formed the Allegheny fold-thrust belt (Donaldson and Shumaker, 1981; Ettensohn, 2005, 2008; Sak et al., 2012). The Alleghenian orogeny resulted in the formation of a broad shallower foreland basin than the Acadian and Taconic orogeny (Ettensohn, 2005, 2008). Paleoclimate models developed using coal beds, paleosol, soil carbonate-based, and fossil leaf-based proxies indicate that paleoclimate shifted from ever-wet humid to seasonally arid conditions during the Middle Pennsylvanian (Cecil et al., 2003, 2004; Tabor and Poulsen, 2008; DiMichele et al., 2010; Falcon-Lang and Dimichele, 2010; Montañez et al., 2016). In particular, palynomorph studies of the MPAF showed tree ferns, which are common in less humid environments, increased and became more common in No. 5 Block and Upper No. 5 Block coal beds sections of the MPAF, whereas lycopsids, which are common in very humid environments, dominated the LKC bed (Kosanke and Cecil, 1996; Eble, 2002; Falcon-Lang and Dimichele, 2010).

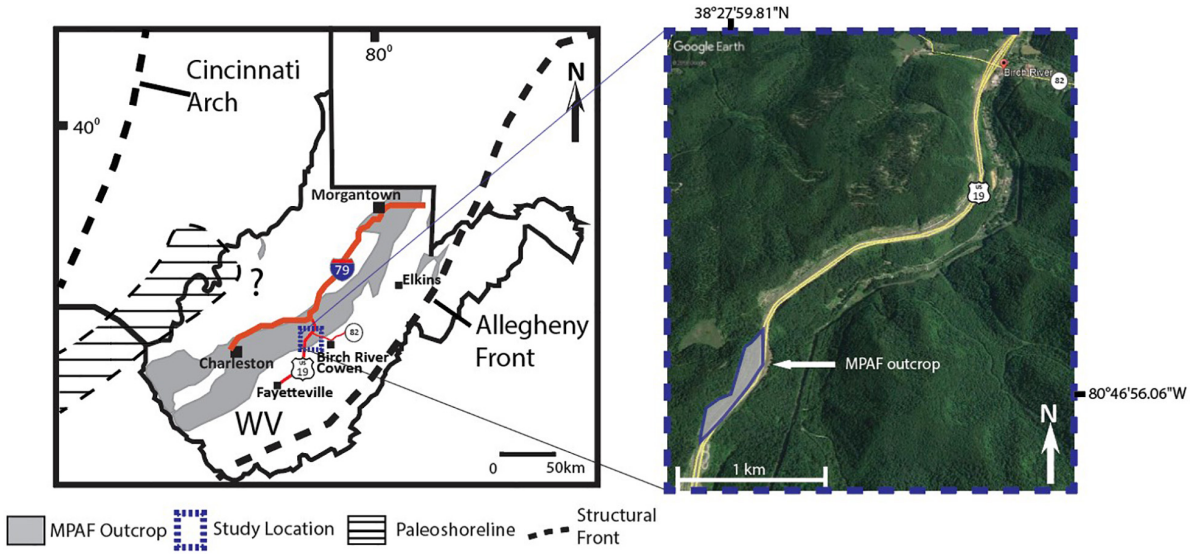

FIGURE 1 | Study location, Birch River, West Virginia. The gray fill is the MPAF outcrop belt, WV. Dashed square is the outcrop location.

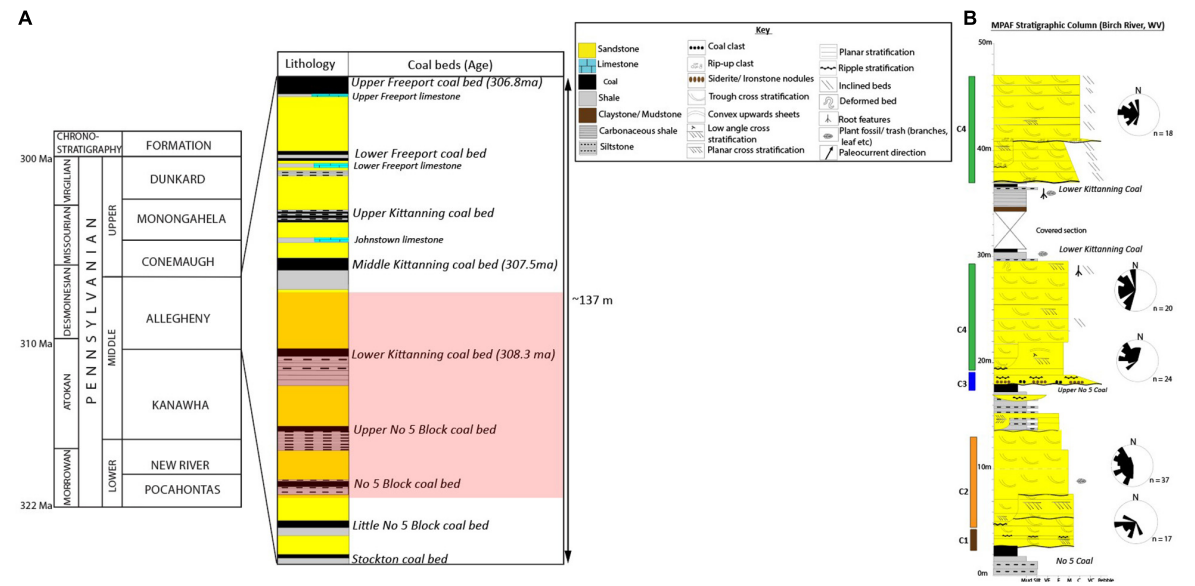

FIGURE 2 | Chronostratigraphic column and lithostratigraphic column of the Middle Pennsylvanian Allegheny Formation (MPAF). **(A)** Chronostratigraphy of the lower MPAF study interval includes No. 5 Block, Upper No. 5 Block, and Lower Kittanning coal beds and associated clastic deposits (shaded square). Coal ages are reported in Montañez et al. (2016). **(B)** Lithostratigraphic column of the MPAF, Birch River, West Virginia. Modified from Blake et al. (2002) and Cecil et al. (2004). C is the channel belt and *n* is the number of paleocurrent measurements.

The major driver of the paleoclimate change was attributed to the low paleo-latitudinal position of the Appalachian Basin during Middle Pennsylvanian; and the effect of glacial volumes at the poles on Hadley Cell circulation patterns along the Intertropical Convergence Zone (ITCZ) (Cecil and Dulong, 2003; Cecil et al., 2004). Changes to the Haley Cell circulation patterns along the ITCZ resulted in the seasonality of rainfall in low latitudes during glacial minimum and high rainfall during glacial maximum. The development of a rain shadow on the Alleghenian foreland basin, which is located on the downwind side of the orogenic highlands, may have also contributed to the drier climate (Tabor and Montanez, 2002; Tabor and Poulsen, 2008). Paleobotanical and sedimentologic studies indicate that earlier MPAF depositional systems formed in a humid climate, while the MPAF above the LKC beds were deposited in a semi-arid climate (Cecil, 1990; Cecil et al., 2003; Greb et al., 2008; DiMichele et al., 2010; DiMichele, 2013; Montañez et al., 2016). Paleogeographic reconstructions of the North American

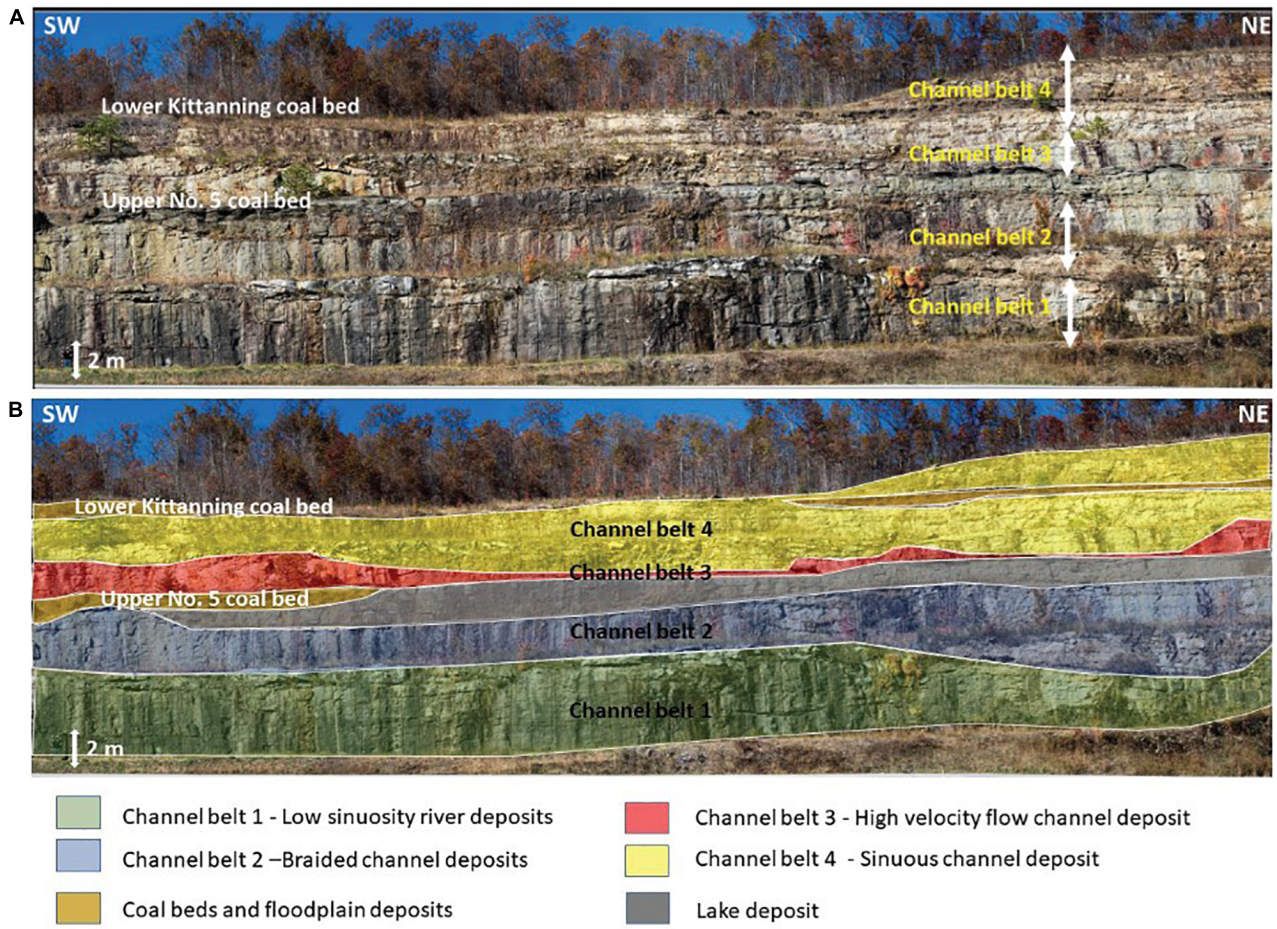

FIGURE 3 | The Middle Pennsylvanian Allegheny Formation outcrop, Birch River, West Virginia. **(A)** Outcrop with scale (white bar), position of coal beds, and channel belt locations. **(B)** Birch River outcrop with interpreted channel belt boundaries.

craton suggest that the Appalachian basin was near the paleo-equator with Appalachian highlands to the northeast and coastal lowlands located to the west (Archer and Greb, 1995; Cecil et al., 2004). The resulting paleo-gradient resulted in south and western drainage directions (Donaldson and Shumaker, 1981; Cecil et al., 2003, 2004). Paleodrainage models based on sedimentary analysis indicate the MPAF clastic wedge is composed of swamp, lacustrine, fluvial, and deltaic deposits (Donaldson and Shumaker, 1981; Cecil, 1990). Marine fossils observed in MPAF sandstones suggest the downdip extent of the fluvial segments of the MPAF prograding clastic wedge is located in southeast Ohio (Stubbs, 2018).

MPAF Channel Belts, Birch River, WV

The MPAF clastic units are subdivided based on coal beds, which stratigraphically oldest to youngest include: No. 5 Block, Upper No. 5 Block, Lower Kittanning (No. 6 Block Coal), and Middle Kittanning coal beds (Arkle et al., 1979; Blake et al., 2002; Eble, 2002). Palynomorph studies found that more lysosomes (fungi) spores, which are common in humid ever-wet environment are more abundant in early Middle Pennsylvanian deposits below the MPAF, whereas herbaceous fern plants, which are common in less humid environments, were more abundant in late Middle to early Upper Pennsylvanian deposits (Cecil et al., 1985; Kosanke and Cecil, 1996; Peppers, 1996; Eble, 2002). Sedimentologic models used lithologic climate indicators such as presence of caliche, calcareous pedogenic concretions, and siderite to assess climatic fluctuations during the Pennsylvanian, including parts of the upper MPAF which includes the Middle Kittanning, Upper Kittanning, Lower Freeport, and Upper Freeport coal beds and their associated clastic deposits (Donaldson and Shumaker, 1981; Cecil et al., 1985; Cecil, 1990; Cecil and Dulong, 2003).

MATERIALS AND METHODS

Facies Architecture of the MPAF Channel Belts

Facies associations and architecture were used to interpret the fluvial styles (Miall, 1996; Bridge, 2009). Facies and facies association were identified from a 45-m thick and 495-m wide outcrop (Miall, 1996; Bridge, 2009). Data were measured using

a Wentworth calibrated grain-size card, measuring staff and ruler. Paleocurrent data were acquired from the left and right limbs of trough cross-strata using the best-fit circle method to determine paleocurrent direction on a stereographic plot (DeCelles et al., 1983).

Paleochannel Geometry Measurements and Estimation

Sedimentological data for the study was acquired from road cut (outcrop) along Route 19, Central West Virginia (**Figures 1**, **3**). Units of MPAF present at Birch River outcrop include the No. 5 Block coal bed, the LKC bed, shale and sandstone units above and below No. 5 Block, the Upper No. 5 Block, and LKC coal beds (Blake et al., 2002; Eble, 2002; Cecil et al., 2004; **Figures 1**, **2**). Sedimentologic data acquired from the outcrop include grain size, cross-bedding height, and barform height. These data were used to determine channel geometry (width and depth) by the methods outlined below.

Channel Depth

Channels were measured from preserved paleochannel boundaries corrected for compression during burial. Channel depths that were estimated from bar height involved the measurement of fully preserved channel bars in outcrop (Allen, 1970; Lin and Bhattacharya, 2017). The thickness of lateral or downstream accretion bars from outcrop, adjusted for 10% compaction factor, is representative of the bankfull channel depth (Ethridge and Schumm, 1977; Davidson and Hartley, 2010). The thickness of lateral or downstream accretion bars was determined using the fining upward sequence concept, where the lower and mid-section of the bar is characterized by planar, trough cross, planar cross, and inclined bedded sandstone that is relatively coarser than the upper section of the bar, which is characterized by massive and ripple bedded sandstone with plant debris and/or rooting structure (Bridge and Tye, 2000). The paleochannel flow depth was estimated from the thickness of lateral or downstream accretion macroforms using the equation by Ethridge and Schumm (1977):

$$d = D^{*}/0.9 \tag{1}$$

where D^* is the maximum channel depth, which is represented by the thickness of the sandstone macroform, 0.9 compensates for the compaction factor. Errors associated with this method can be up to 100% if it is used for muddy sections (Holbrook and Wanas, 2014).

Channel depths were also estimated from dune-scale cross-set thickness, using empirical equations and machine-assisted algorithms. Previous work developed empirical equations which have been applied in the estimation of paleochannel dimension and morphology for ancient fluvial channel deposits. These equations determined relationships between the mean value of the exponential tail of the probability density function (PDF) for cross-set thicknesses and dune heights (Leclair and Bridge, 2001). The work by Leclair and Bridge (2001) has shown that the dune height (h_m) can be estimated from mean cross-set thickness (S_m) using a regression equation:

$$h_{\mathrm{m}} = 5.3\beta + 0.001\beta^{2} \tag{2}$$

$$\beta = S_{\mathrm{m}}/1.8 \tag{3}$$

which can be simplified as:

$$h_{\mathrm{m}} = 2.9\, S_{\mathrm{m}} \tag{4}$$

where h_m is the mean dune height, S_m is the mean cross-set thickness, β is the mean value of the exponential tail of the PDF for topographic height relative datum. The range of error in this empirical equation is ∼20% (Leclair and Bridge, 2001). Hence, the authors suggest the equation be used on data set with similar standard deviation. Based on the observation that the ratio of bankfull depth to dune height is common between 6 and 10 (Bridge and Mackey, 1993; Bridge and Tye, 2000), dune height (h_m) can be used to estimate channel bankfull flow depth (d):

$$6 < d/h_{\mathrm{m}} < 10 \tag{5}$$

Machine-Assisted Estimation of Channel Belt

A support vector machine regression algorithm was developed to generate a new empirical equation that relates preserved cross-set thickness to dune height to improve channel depth estimates from cross-set thickness. These relationships were established from measurements of dunes, and corresponding cross-set geometry produced under known hydrological conditions of a flume. First, multiple regression analysis using least squares elimination method was applied to the data set of Leclair (2002), which includes measurements of flow conditions and resulting bedform and cross-set heights, in order to determine the statistical relationship between dune heights and cross-set thicknesses.

Multiple regression analysis

This study employs multiple regression to highlight the relationship between all the variables measured in flume studies that were used to explain the relationship between cross-set thickness and dune height (Leclair, 2002). The equation used for multiple regression is given as:

$$Y = \beta_0 + \beta_1 X_1 + \beta_2 X_2 + \cdots + \beta_n X_n + \varepsilon \tag{6}$$

where Y is the dependent variable represented as cross-set thickness, β_0 is the intercept, β_n are the coefficients, X_n are the independent variables describing flow conditions and depositional products, and ε is the random error. The accuracy of the multivariate regression was scored using R^2. Then, SVR was applied to create and improve empirical relationships between the variables with the highest level of statistical significance as determined from the multiple regression analysis.

SVR analysis

Support vector regression is a type of supervised machine learning algorithm that fits as many instances in the model by taking into consideration the outliers in the dataset while developing an empirical relationship. The SVR machine

learning model was selected because it performs linear or non-linear regression in a higher-dimensional space using linear, polynomial, or Gaussian kernels. The kernels transform the data into a higher-dimensional space by creating a vector from the evaluation of the test positions of all the data and establishes a linear, polynomial, or Gaussian relationship among the variables in the data. The Gaussian kernel uses normal distribution curves around data points to try to establish a relationship with the variables being considered. The advantage of SVR over linear regression is that SVR allows the model to be less fitted to the training data but more flexible for predicting new data (Zhang et al., 2014). SVR can also be used for multivariate regression; hence, new variables can be added to try to improve predictions. The simplified equation for predicting the dependent variable (Y) using the SVR model (Bao and Liu, 2006; Awad and Khanna, 2015) is given by:

$$Y = w^T \phi(x) + b \tag{7}$$

where Y is the dependent variable, $w = (w_0, w_1, w_2, \ldots)^T$ is the fitting coefficient in the higher dimensional space, ϕ is the kernel function transforming the independent variable x (cross-set thickness in this paper) to a higher dimensional feature space, and b is the intercept. The model's performances compared to the previously used empirical equation (Eq. 2) were evaluated by testing the accuracy of the model's predictions using mean square errors (MSEs). Grid search algorithm was used to determine the best penalty parameter (C), fitting error (ξ), and the kernel line of best fit for the data. Details of the algorithm and selected parameters to develop the SVR model are in the **Supplementary Material**. Algorithms for the SVR was written using Python and scikit-learn libraries (Pedregosa et al., 2011; Python, 2019). The steps taken to derive the SVR model for predicting dune height from cross set thickness include data preprocessing, kernel and parameter selection, and model fitting (**Figure 4**).

Data preprocessing. This includes sorting of the independent variable from lowest to highest value and normalizing the data. The cross-set thickness was set as the independent variable, while the dune height was set as the dependent variable for the SVR model. The cross-set thickness data were sorted and both data set were normalized. Normalization removes any disparity in the model that may be due to different units of measurements and large variance between values in the data that might skew the regression model in favor of the data set with larger values. The normalization of the independent and dependent variables involved adjusting both data set to a common scale. The normalization method used was MinMaxScaler, which has the ability to scale the data set between any range of values stipulated. The data were scaled into values between 0 and 1 using methods described in Pedregosa et al. (2011).

Kernel and parameter selection. Grid search was used to cross-check all kernels and parameters until there was convergence, i.e., the ideal kernel and parameters that will give the best solution are determined. Kernel is a weighing factor between two sequences of linear and/or non-linear data, which enables the correlation of the data set in higher dimension space (Pedregosa et al., 2011). Three types of kernel considered are linear, polynomial, and Gaussian kernels. The parameters considered include gamma, C, and epsilon (ξ). The gamma parameter defines how far the influence of a single training example reaches and can be seen as the inverse of the radius of influence of samples selected by the model as support vectors (Pedregosa et al., 2011). The gamma range considered was from 0.5 to 0.8. The C parameter trades off correct classification of training examples against maximization of the decision function's margin; hence, the C parameter behaves as a regularization parameter in the SVM (Pedregosa et al., 2011). The range of C parameters considered was from 0.1 to 100. The epsilon defines a margin of tolerance where no penalty is given to errors (Pedregosa et al., 2011). The larger epsilon is, the larger errors you admit in your solution. The epsilon range considered was from 0.01 to 0.5. The gamma, C, and epsilon values, 0.8, 10, and 0.01, respectively, were selected because they produced the best SVR model. The accuracy of the SVR model, when using the Gaussian kernel and selected parameters 0.8, 10, and 0.01 for gamma, C, and epsilon values, respectively, is 84%.

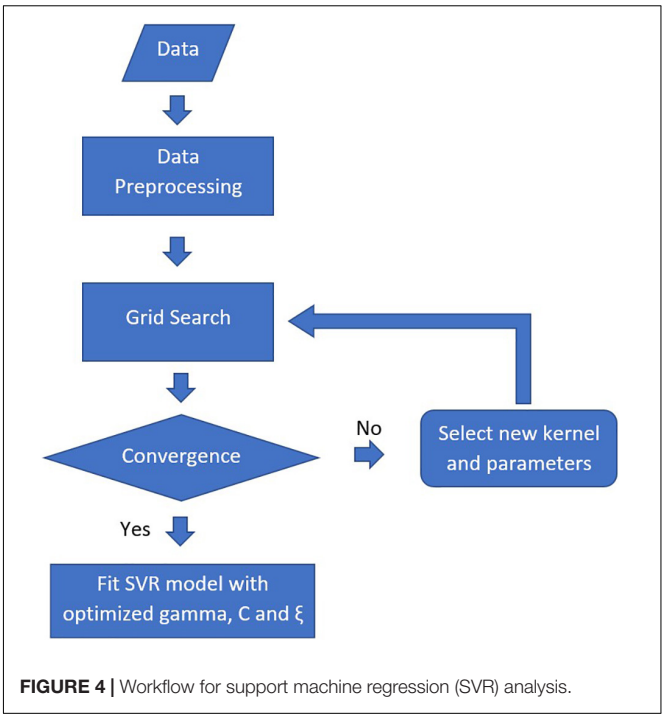

FIGURE 4 | Workflow for support machine regression (SVR) analysis.

SVR model fitting. Support vector regression model is fitted to the data set using the kernel and parameters from the grid search analysis. The model can be used to predict the dune height from cross-set thickness data inputted into the model. An inverse normalization is used to revert the normalized data and normalized model prediction.

Channel Width

Full channel widths were determined from Channel belt 1. Full channel belt widths could not be determined from the other channel belts because of the erosive nature of the channel boundaries. True channel width was derived from apparent channel widths measured from Channel belt 1 by correcting for

the orientation of the MPAF outcrop and paleoflow direction. Channel width was also estimated using published scaling relationships for channel geometry that takes into consideration the channel style as well as the tectonic and climatic setting of the fluvial systems (Gibling, 2006; Blum et al., 2013). The common range of channel width to depth scaling ratios selected from Gibling (2006) includes 5–50 for fixed river systems, which were used in Channel belt 1, 50–1000 for braided and low-sinuosity rivers used for Channel belts 2 and 3, and 30–250 for Channel belt 4.

Paleoslope

Paleoslope was estimated using grain size and density of sediment grains following the empirical equation of Holbrook and Wanas (2014):

$$\tau^{*}_{bf50} = (d_{m}S)/(RD_{50}) = \text{constant} \quad (8)$$

where S is the slope, τ^{*}_{bf50} is the bankfull Shields number for dimensionless shear stress, d_m is the mean bank full flow depth, R is the submerged dimensionless density of sand–gravel sediment (qs–qw), and D_{50} is the median grain size. τ^{*}_{bf50} is assumed to be 1.86 after Holbrook and Wanas (2014).

Grain size for this study was quantified from thin-section petrography, as well as estimated from observations of rocks in outcrop using a grain size card with graphical representation of Wentworth grain size classes. The error in grain size made from grain size cards has an error of about 1/2 phi (Lin and Bhattacharya, 2017). Four thin sections were selected that were representative of average flow in the four fluvial channel types interpreted in the lower MPAF. The thin-sections were acquired from above the scour deposits, which should be representative of deposits of moderate flow conditions. For each thin section, the maximum axis of at least 100 grains was measured and used to calculate median grain size (D_{50}) for use in the empirical equation to estimate the paleoslope for MPAF paleochannels (Holbrook and Wanas, 2014).

Paleohydrology

Channel dimensions and paleoslope combined with flow velocity permit paleohydrologic reconstruction of MPAF channels using channel width derived from scaling factors so as to account for variabilities in channel cross-sectional area due to the depositional environment. Paleodischarge was estimated using the continuity equation (Eq. 9):

$$Q = VA \quad (9)$$

where Q is the instantaneous discharge and A is the cross-section area, which is the product of channel width and depth. Flow velocity was estimated by using sedimentary structures to infer the bedform for comparison with the bedform phase diagram of Rubin and McCulloch (1980). The dominant bedform observed in the channel belts was used to estimate flow velocity under the assumption that the dominant bedform reflects dominant bedload transport conditions during flooding events (Bhattacharya et al., 2016; Lin and Bhattacharya, 2017). The cross-sectional area was derived from estimated depth using the SVR machine-assisted model and width from width to depth scaling the relationship of modern and ancient fluvial channels (Gibling, 2006). We elected to not use empirical equations to estimate channel width from channel depth estimates, as this approach does not consider channel style as a variable in constraining channel width.

RESULTS

MPAF Channel Belts

Facies and facies architectural analysis revealed nine lithofacies that represented fluvial channel deposits. The channel lithofacies include horizontally stratified sandstone, ripple-stratified sandstone, poorly sorted sandstone, planar cross-stratified sandstone, trough cross-stratified sandstone, massive sandstone, and low angle cross-bedded sandstone or convex upward sandstone, laminated mudrock, and massive mudrock facies (**Figure 5**). The coal beds overlie mudrocks and non-channel sandstones. We categorize the fluvial channel deposits into channel belts based on the channel planform.

Channel Belt 1: Low Sinuosity Fluvial System

Channel belt 1 is made up of multiple stories up to 10-m thick of tabular and lenticular, fine to medium-grained sandstones with sharp, sub-horizontal to horizontal, undulating erosional basal contact and sharp, curved erosional bounding surface above (**Figure 5**). Channel belt 1 overlies the No. 5 Block coal bed (**Figure 2**). Five stories were identified in Channel belt 1. Individual stories are characterized by multiple sandstone bed sets, which may be capped by mudrock, and are bounded above and below by an erosional surface. The two bottom stories are made up to 3-m thick lenticular sandstone separated by a sharp near-horizontal erosional surface. The lenticular sandstones comprise of convex upward, fine to medium-grained, massive (Sm), and trough cross-stratified (St) sandstone with sharp, curved bedding plane at the base. The massive and trough cross-stratified sandstone beds are overlain by horizontal laminated sandstone (Sh) beds with a sharp horizontal bedding plane. The Sh is either onlaped by Sm or St beds with sharp, horizontal, or curved bedding planes. The Sm, St, and onlaped Sh beds are overlain by St and Sp beds with sharp horizontal bedding plane. The Sh may be overlain by interlaminated claystone, siltstone, and poorly sorted, ripple laminated sandstone in some places. The Sh may be overlain by interlaminated claystone, siltstone, and poorly sorted, ripple laminated sandstone in some places.

The three upper stories are made up of up to 2-m thick tabular sandstone bounded below by near-horizontal erosional surfaces. The tabular sandstones are made of tabular, fine to medium-grained trough cross and planar cross-stratified (Sp) sandstones with sharp, horizontal bedding plane. The Sp overlies the St in the tabular sandstone. The Sp may be overlain by horizontal laminated sandstone beds in some places. The Sp beds are up to 1-m thick in some places. The uppermost tabular sandstone is erosionally truncated and overlain by sandstones from Channel belt 2. The sandstone of Channel belt 1 contains abundant coal and siderite intraclast, and fossilized plant fragments. Channel

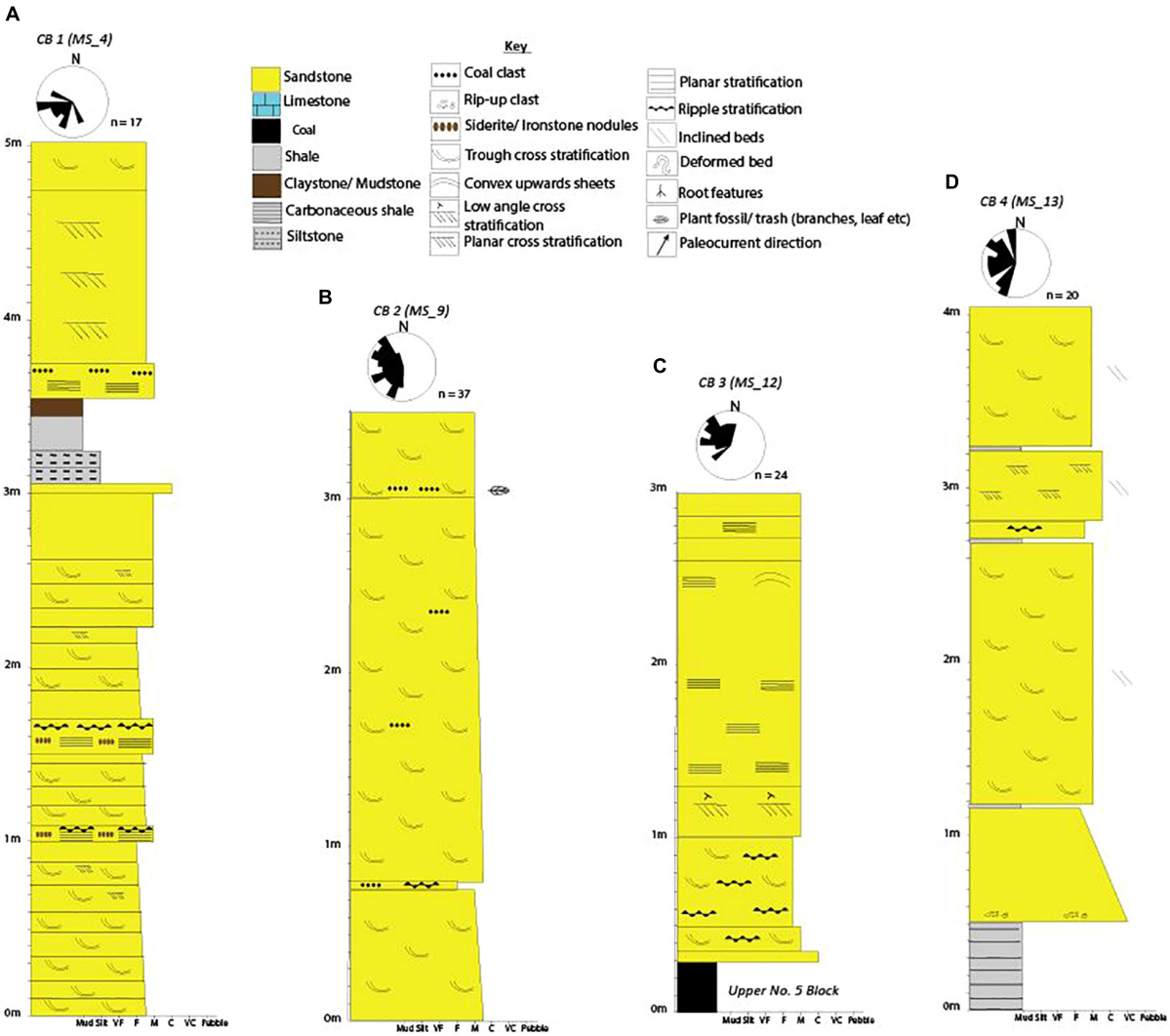

FIGURE 5 | Measured sections of channel belts 1–4 showing key depositional facies and paleocurrent data. **(A)** Channel belt 1 (CB 1) represents low sinuosity channel deposits. **(B)** Channel belt 2 (CB 2) represents braided channel deposits. **(C)** Channel belt 3 (CB 3) represents high-velocity channel deposits. **(D)** Channel belt 4 (CB 4) represents sinuous channel deposits.

belt 1 overlies the No. 5 Block coal bed. Paleocurrent data from trough cross-bedded sandstone indicate northeast to southwest direction of paleoflow. The lenticular sand bodies, which are overlain by Sh and onlaped by Sm and or St beds, are interpreted as mid-channel bar deposits while the tabular sand bodies are downstream accretion compound strata (Miall, 1996). The lack of a lateral accretion bar suggests low translation by channel. The abundance of coal and siderite intraclast suggest abundant vegetation and wet environment common in distal coastal plain depositional environments (Miall, 1996; Allen et al., 2014). Combined these features suggest Channel belt 1 are deposits of a distal, low sinuosity fluvial system.

Channel Belt 2: Braided Fluvial System

Channel belt 2 is made up of up to 5-m thick, multistory, amalgamated, medium-grained sandstone bounded above and below by sharp, undulating, horizontal, and curved erosional surfaces. Three stories were identified based on discontinuous, sub-horizontal, basal erosional surface, and channel lag deposits. Channel lag deposits, which comprise pebble size coal clast and iron-rich claystone clast and veins, were used to infer the base of the story where the basal erosional surfaces were not apparent. Individual stories are characterized by up to 0.3-m thick, amalgamated, medium-grained, compound through cross-stratified (St) sandstone beds with sharp or gradational, horizontal, or trough-shaped bedding plane. The St are rarely overlain by horizontal, fine-grained, ripple laminated sandstone (Sr) beds. Where the Sr is absent St may be overlain by up to 0.3-m thick, medium-grained, planar cross-stratified sandstone beds (Sp), or St. Channel belt 2 sandstones contain coal intraclast and petrified plant stems in places and is overlain by deltaic, lake, and well-drained floodplain deposits. The deltaic

deposits are characterized by coarsening upward, interlaminated shale, and very fine-grained sandstone, the lake deposits are characterized by laterally continuous, tabular, massive sandstone beds, while the well-drained floodplain deposits characterized by discontinuous, lens-shaped, coarsening upward ripple laminated sandstone beds and laterally continuous interlaminated siltstone, mudstone, and shale, which are overlain by the Upper No. 5 Block coal bed. Paleocurrent data from the trough cross-stratified beds indicate both northwest and southwest paleoflow direction. However, the dominant paleoflow is toward the northwest. Neither lateral nor downstream accretion macroforms were observed in Channel belt 2. The abundance of compound trough cross-bedded facies suggests the system was dominated by 3D dunes. The presence of bed sets bounded by curved and/or horizontal bedding planes and the absence of a clear macroform such as lateral or downstream accreting deposits suggest that Channel belt 2 is dominated by compound bars common in braided channel fills (Miall, 1996; Bridge, 2009; Allen et al., 2014). Combined all these features lead to the interpretation of Channel belt 2 as deposits of a braided fluvial channel.

Channel Belt 3: High-Velocity Channel

Channel belt 3 is characterized by a fine to medium-grained, single-story tabular sandstone body bounded above and below by erosional surfaces. The facies association of Channel belt 3 is made up of poorly sorted, planar cross-stratified, trough cross stratified, massive, horizontally stratified, low angle cross stratified, and convex upward sandstone strata (**Figure 5**). This channel belt is composed of two distinct sandstone units: A lower unit dominated by interbedded poorly sorted and ripple bedded sandstone that is 0.5–1-m thick, and an upper unit dominated by sandstones with upper flow regime structures (Allen, 1982) such as horizontal and low angle cross stratified and convex upward sandstone (Miall, 1996; Fielding et al., 2009). In some areas, the lower sandstone unit has some trough cross-bedded facies at the base, which transitions abruptly into the poorly sorted ripple laminated facies locally. The low angle cross-stratified and convex upward facies are the most dominant bedform in this channel belt. Channel belt 3 overlies the Upper No. 5 Block coal bed. The abundance deposits with upper flow regime structures and the abrupt transition in facies succession suggest deposits by a high velocity flooding event therefore Channel belt 3 deposits may be deposits of a high velocity channel. The presence of low angle cross-beds and convex upward strata suggest supercritical flow event (Bridge, 2009; Allen et al., 2014; Miall, 2014). The presence of very coarse horizontal, ripple, and poorly sorted bedded sandstone is indicative of a fluvial system with substantial erosive power.

Channel Belt 4: Sinuous Meandering Channel

Channel belt 4 is characterized by fine to coarse-grained, multi-story inclined tabular and lenticular sandstone bodies bounded by sharp and erosional surfaces. A typical Channel belt 4 story is composed of poorly sorted sandstone, ripple stratified sandstone, planar cross-stratified sandstone, trough cross-stratified sandstone, and massive sandstone facies (**Figure 5**). Each story has poorly sorted and massive sandstone beds overlying an erosional base. The poorly sorted and massive sandstone beds are overlain by inclined, trough cross, and planar cross strata, which may be draped by ripple stratified sandstone locally. The sandstone bodies of Channel belt 4 stack vertically and extend laterally to form lateral accretion bars. The lower bounding surface for this channel belt is undulating erosional. The upper bounding surface is covered by soil and vegetation in the study area. Three stories were identified in the study location. The deposits of the first story of Channel belt 4 are overlain by floodplain deposits characterized by laterally continuous carbonaceous shale and claystone. The floodplain shale and claystone are overlain by the LKC bed. The Channel belt 4 sandstones below the LKC are deformed and have abundant root traces. The second and third stories do not have coal beds and are not deformed. The inclined geometry, vertical and lateral succession of massive, trough cross-stratified, planar cross-stratified, and ripple laminated facies are lateral accretion (point bar) deposits, which are common in the sinuous meandering channel. This led to the interpretation of Channel belt 4 sandstone bodies as deposits of a sinuous meandering fluvial channel system. The deformed sinuous channels were interpreted as water escape features caused by the oversaturation of the sinuous channel deposits (Plink-Björklund, 2015).

Machine-Assisted Approach to Dune Height Estimation From Cross-Bed Height

Multiple Regression

The machine-assisted model was developed using multiple regression analysis and the SVR algorithm on the flume experiment data used by Leclair and Bridge (2001) to derive the empirical equations. A p-value of 0.005 was selected to test the significance of the statistical relationship (Davis and Sampson, 1986). Backward elimination showed that dune height (h_m), as well as the dune length (lm) (i.e., the dune wavelength), had a high level of significance relationship (i.e., p-value < 0.005) with the cross-set thickness (S_m). It is difficult to measure the length of dunes in ancient deposits; hence, the relationship between cross-set thickness and dune height was further analyzed using SVR with the goal of developing a more efficient model for predicting dune height from the cross-set thickness in ancient channel deposits. These results from the multiple regression analysis highlighted the statistical relationship between cross-set thickness and dune height.

Support Vector Regression vs. Polynomial Regression

Dune height was set as the variable to be predicted from cross-set thickness (**Figure 6**) in order to compare SVR dune height predictions with the predictions from the empirical equation derived from polynomial regression (Eq. 4; Leclair and Bridge, 2001). The SVR model was used to predict dune heights from cross-set thicknesses derived from the flume experiment that Leclair and Bridge (2001) used to develop a polynomial regression model for dune height prediction from cross-set thickness. The Gaussian kernel, which used normal

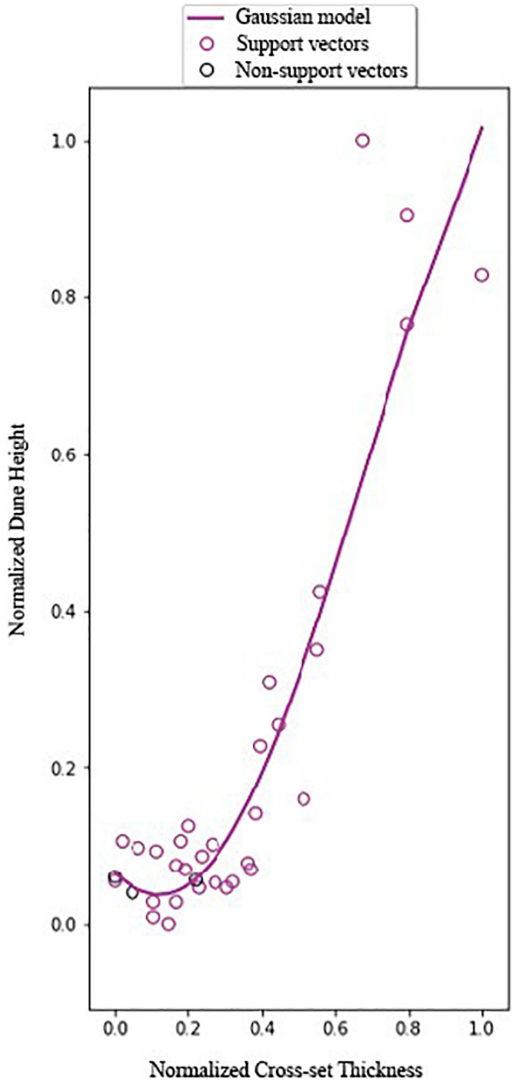

FIGURE 6 | Variation of mean dune height (hm) and cross-set thickness (Sm), with a Gaussian kernel hyperplane. The support vectors are the data points used by the Gaussian kernel for plotting the best-fitted hyperplane for the regression analysis. Data sourced from Leclair (2002).

distribution analysis on data points in order to highlight the best-fitted hyperplane in the dune heights and cross set thicknesses regression plot, produced the best predictions in the SVR model. The MSE and root MSE (RMSE) were used to compare the accuracy of predictions from both methods. The RMSE of predicted mean dune height from using the Leclair and Bridge (2001) model (Eq. 5) was 16.8 mm, whereas the RMSE of predicted mean dune height from the SVR model was 9.3 mm, indicating the SVR model estimates were closer to the actual dune height produced in the flume experiment.

Paleochannel Depth Estimates

Paleochannel depth was estimated from measured bar thickness corrected for compaction in Channel belts 1 and 4 using Eq. 1; however, only incomplete channel bars were observed in Channel belts 2 and 3. Measurements of these incomplete bars were recorded to constrain minimum paleochannel depth (**Table 1**). Paleochannel depths estimates were also determined from dune heights predicted from cross-set thicknesses for all of the MPAF channel belts using Eq. 5 (Bridge and Tye, 2000; **Tables 1, 2**). Paleochannel depth was estimated from the dune height (h_m) based on the observation that the ratio of bankfull depth to dune height is commonly between 6 and 10 (Bridge and Mackey, 1993; Bridge and Tye, 2000). Paleochannel depth estimated from cross-set thickness was recorded for individual channel stories in Channel belts 1 and 4 (**Table 2**). Channel stories were not identified in Channel belts 2 and 3 because of the amalgamated nature of deposit from Channel belt 2 and the absence of channel stories in Channel belt 3. Overall, depth estimated from cross-set thickness measurements is greater than those estimated from bar thickness, suggesting that the bars of the MPAF have been largely subjected to substantial erosional truncation (**Figure 7**).

Bar thicknesses for Channel belt 1 were acquired from two channel bar deposits with a roll-over top, which is indicative of non-eroded channel bar deposits (Chamberlin and Hajek, 2015). The bar thickness was acquired from story 4 of Channel belt 1 using the same method as shown in **Figure 8**. The uncompacted thicknesses of these bars are 2.2 and 4.4 m. The bankfull paleochannel depths estimated from cross-set thicknesses using the SVR model were determined from measurements of 32 cross-set thicknesses. Depth estimates range from 6.1 to 13.9 m (**Table 2**).

Depths could not be estimated from measured bar thicknesses for Channel belt 2 because of the compound nature of bars, erosional truncation, and partial preservation of the bar deposits. However, these partial bars can constrain minimum paleochannel to >0.83–2.2 m. The bankfull paleochannel depth estimated from the mean of 45 cross-set thicknesses ranges from 3.4 to 5.6 m.

Depths could not be determined from bar thickness for Channel belt 3 because of the lack of macroform scale sand bodies, which are used to interpret fluvial channel bars. Twenty-eight cross-set thicknesses were used to calculate the mean cross-set thicknesses used for SVR dune height prediction and paleochannel depth estimation. This yielded a depth estimate of 2.8–4.7 m.

Depth was estimated from bars with roll-over tops, which indicate they are fully preserved fluvial channel bar deposits (**Figure 8**; Chamberlin and Hajek, 2015). Bar thicknesses, which were measured from two bars in story 1 are 4.6 and 5.5 m, and one bar in story 2 of Channel belt 4 is 3.3 m. The bankfull paleochannel depth estimated from 37 cross-set thickness measurements from Channel belt 4 ranges from 3.6 to 9.6 m. The similarity in SVR predicted and bar thickness predicted bankfull paleochannel depths from stories 1 and 2 of Channel belt 4 indicates that Paleochannel depths predicted using SVR are accurate (**Tables 1**, **2**).

Paleochannel Width Estimates

The apparent width of the channel boundaries were measured from the boundaries of incised channel deposits. The incised paleochannel widths represent minimum channel widths as the

TABLE 1 | Results of estimated paleochannel geometry.

MPAF channels	Range of bar thickness (m), *n* = number of bars	Mean cross-set thickness (m), *n* = number of cross-sets	Depth range from pre-compaction bar thickness (m)	Depth range from SVR estimate of dune height for channel depth of 6–10 times dune height (m)	Width (*w*) from sand-body (m), *n* = number of channel widths	w/d_m from scaling relationships (Gibling, 2006 channel classification)
Channel belt 1 (multistory)	>2–4, *n* = 6	0.33, *n* = 23	>2.2–4.4	6.1–13.9	13.4–40.3, *n* = 5	5–50 (fixed Rivers)
Channel belt 2 (multistory)	>0.75–2, *n* = 3	0.21, *n* = 45	>0.83–2.2	3.4–5.6	>15.2–28.8, *n* = 2	50–1000 (braided and low sinuosity)
Channel belt 3 (single story)	NA	0.17, *n* = 28	NA	2.8–4.7	NA	50–1000 (braided and low sinuosity)
Channel belt 4 (multistory)	3–5, *n* = 3	0.25, *n* = 37	3.3–5.5	3.6–9.6	>17–27.6, *n* = 3	30–250 (meandering)

NA, insufficient data from field.

TABLE 2 | Results of estimated paleogeometry (channel depth and width), paleoslope, and paleodischarge.

Channel belt (CB)	Story	SVR d_m range (m)	Width range	Average grain size (mm)	Mean flow velocity*** (m/s)	Paleoslope gradient range	Paleodischarge range (m^3/s)
CB 1	1	NA	NA	0.20*	NA	NA	NA
	2	8.3–13.9	42–695	0.20*	1.175	0.00004–0.00007	409–11,351
	3	8.3–13.8	41–690	0.20**	1.175	0.00004–0.00007	403–11,188
	4	6.1–10.2	31–510	0.20*	1.1	0.0001–0.00006	206–5722
	5	NA	NA	0.20*	NA	NA	NA
CB 2	NA*	3.4–5.6	168–5600	0.3**	1.1	0.0002–0.0003	621–34,496
CB 3	NA*	2.8–4.7	141–4700	0.3**	1.75	0.0002–0.0003	696–38658
CB 4	1	4.1–6.8	122–1700	0.43**	1.1	0.0002–0.0003	549–12,716
	2	3.6–6	108–1500	0.43*	1.05	0.0004–0.0002	408–9450
	3	5.8–9.6	173–2400	0.43*	1.2	0.0003–0.0001	1194–27,648

*NA, not applicable due to insufficient data from outcrop; d_m, mean bankfull depth. ***Estimated using bed-form diagram. **Calculated using data from thin section and grainsize card. *Data from grain size card.*

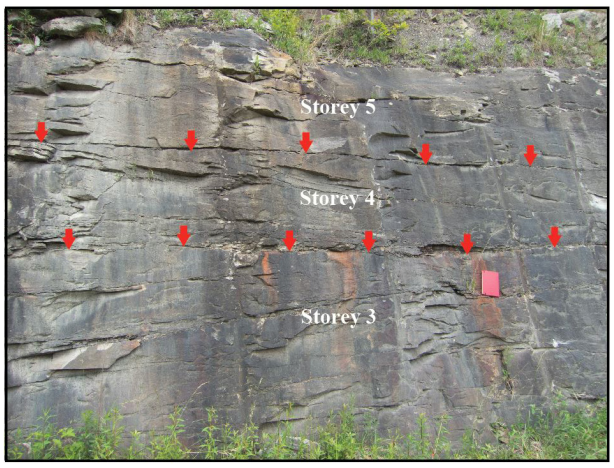

FIGURE 7 | Channel belt 1 outcrop. Arrows highlighting truncation of channel bar deposits in Channel belt 1. Notebook is 25 cm long.

FIGURE 8 | Example of how direct measurement of preserved bar is measured from outcrop data in Channel belt 4.

upper channel margins were commonly truncated. Channel widths were determined from nine sand bodies in the channel belts (**Table 1**). Apparent channel width was corrected for true width using paleocurrent direction. Paleocurrent direction was determined by 116 measurements of the orientation and dip of trough cross-beds. Measured channel width estimates range from values greater than the 13.4 to 40.3 m measured widths from the outcrop.

Channel widths were also estimated from the scaling relationships of channel width (w) to depth (d_m) ratio defined using modern systems by Gibling (2006). Estimated SVR channel depths were used to determine channel width. Channel width was estimated for individual stories in Channel belts 1 and 4 based on their interpreted channel styles. The paleochannel widths acquired from Channel belt 1 outcrop were from preserved channel boundaries, so the width was recorded as actual width. The paleochannel widths, which were determined from the measurement of five channel boundaries from Channel belt 1 deposits, are up to 40.3 m (**Table 1**). The measured paleochannel widths determined from the deposits of Channel belt 1 fall within the channel width ranges determined from the scaling

relationship. The width range determined from the scaling relationship is 31–695 m (**Table 2**). The width was determined by using the minimum and maximum *w*/*d* of 5 and 50, and SVR bankfull flow depth estimates of 6.1–13.9 m (**Tables 1**, **2**). The common *w*/*d* ratios for fixed channels in distal humid environments (Gibling, 2006) were used for widths analysis in Channel belt 1.

The measured paleochannel widths of the fluvial channel incision from Channel belt 2 are 15.2 and 28.28 m (**Table 1**). Two instances of channel incision were observed in Channel belt 2. The deposits of the incised channel were eroded therefore the upper boundaries of the paleochannels could not be determined. The *w*/*d* scaling relationship of 50–1000 for braided fluvial channels (Gibling, 2006) and mean flow depths estimated from the SVR were used for estimating widths for Channel belt 2. The paleochannel width range derived from *w*/*d* scaling relationship is 168–5600 m (**Table 2**).

Channel belt 3 does not have enough sedimentary features to determine channel width. It was difficult to measure any form of channel boundaries because deposits of Channel belt 3 did not have macroforms such as channel bars that could be used in identifying channel boundaries. The *w*/*d* scaling relationship of 50–1000, for braided and low sinuosity fluvial channels (Gibling, 2006) and mean flow depths estimated from the SVR were used for width estimate in channel belt 3. The paleochannel width range derived from *w*/*d* scaling relationship is 141–4700 m (**Table 2**).

The paleochannel incision widths measured from channel belt 4 are up to 27.6 m (**Table 1**). There were three instances of channel incision in Channel belt 4. The deposits in the channel incision were also eroded at the upper section, which made it impossible to estimate the true channel widths. The *w*/*d* scaling relationship of 30–250, for meandering fluvial channels (Gibling, 2006) were used for estimating widths in Channel belt 4. The paleochannel width range derived from *w*/*d* scaling relationship is 108–2400 m (**Table 2**).

Paleoslope Estimation

The paleoslope was estimated using grain size determined from thin-section petrography and a grain size card with a graphical representation of Wentworth grain size classes (grain size table in Channel Paleohydrology **Supplementary Material**). The overall grain sizes of the MPAF channels deposits range from pebble to clay sizes, which is common in fluvial channel deposits (**Table 2**). The clastic sediment of the MPAF fluvial channels are moderately sorted. The sediment grain sizes of Channel belt 1 ranges from coarse to fine-grained sand (0.5–0.17 mm) with the fine to medium-grained sand (∼0.25 mm) being the most dominant mode. The grain sizes of Channel belt 1 from thin section analysis yielded a D_{50} grain size value of 0.23 mm, categorized as fine-grained sandstone. The sediment grain sizes of Channel belt 2 vary from coarse to fine-grained sand (0.1–1.05 mm). Thin section analysis of Channel belt 2 resulted in a D_{50} grain size value of 0.33 mm, categorized as medium-grained sandstone. Channel belt 3 has sediment that varies from pebble to medium-grained sand (>2–0.25 mm). The D_{50} value of Channel belt 3 is 0.3 mm, categorized as medium-grained sandstone. Channel belt 4 sediment clast size varies from pebble to mud (>2 to <0.088 mm). Channel belt 4 grains have a D_{50} value of 0.4 mm, categorized as medium-grained sandstone.

Paleoslope of the MPAF channels estimated using Eq. 8 ranges from 0.00007 to 0.0004 (**Table 2**), which suggests a low paleoslope comparable to slope ranges for the Amazon, Mississippi and Niger Rivers (slope range ∼0.00002–0.0005; Blum et al., 2013). The estimated paleoslope for Channel belt 1 0.00007–0.0001. The estimated paleoslope for the other channels are: Channel belt 2 are 0.0002–0.0003, Channel belt 3 are 0.0002–0.0003, and Channel belt 4 are 0.0001–0.0004, which are an order of magnitude steeper than the estimated slope of the low sinuosity channel. The estimated lowest slope for Channel belt 1 agrees with the dominant fine grain size observed in the sand body.

Paleohydrology

The MPAF channel belt flow velocities, which were estimated using the bedform phase diagram, ranges from 0.6 to 2 m/s (**Figure 9** and **Table 2**). The flow velocity of Channel belt 1 is in the range of 0.85–1.5 m/s. The estimated flow velocity of Channel belt 1 was determined by using the bankfull depth range of 6.1–13.9 m, the dominant sedimentary structure, which is trough cross-stratification produced by dune bedforms, and the fine-grained sand bed form diagram. The estimated flow velocity of Channel belt 2 ranges from 0.6 to 1.6 m/s. The flow velocity of Channel belt 2 was determined using the bankfull depth range of 3.4–5.6 m, and plotting the chart area for the dominant sedimentary structure, which is dune scale cross-sets, on the medium-grained sand bedform phase diagram. Channel belt 3 deposits are dominated by lamination produced from low-amplitude, upper flow regime bedform; therefore, the bankfull depth range of 2.8–4.7 m was used to estimate a velocity range of 1.5–2 m/s. The velocity of Channel belt 4 was determined using the dominant sedimentary structure, which is the dune-scale cross-sets and the estimated channel depth range of 3.6–9.6 m to estimate the velocity, which ranges from 0.6000 to 1.7 m/s. Paleodischarge for the channel belts range from 206 to 38658 m^3/s. Channel belts 2 and 3 with paleodischarge values of 621–34,496 and 695–38,658 m^3/s are the highest paleodischarge. The other paleodischarge ranges are 206–11351 m^3/s for Channel belt 1 and 408 to 27648 m^3/s for Channel belt 4 (**Table 2**).

Errors and Uncertainties Associated With Numerical Analysis

Measurement of channel fill structures in the outcrop is subject to bias in interpretation sedimentary features from outcrop data, which represents an initial source of error. Detailed architectural analysis of outcrop aided the identification of channel bar (Bridge, 2009; Holbrook and Wanas, 2014). Other problems associated with measuring thickness data from channel bar include compaction and erosion. The degree of compaction is dependent on several factors such as original packing, original void ratio, shape of grains, degree of roundness of grains sand composition, and size grading (Ethridge and Schumm, 1977). Equation 1, which takes into account factors that affect the degree of compaction, was used to compensate for the 10% error due

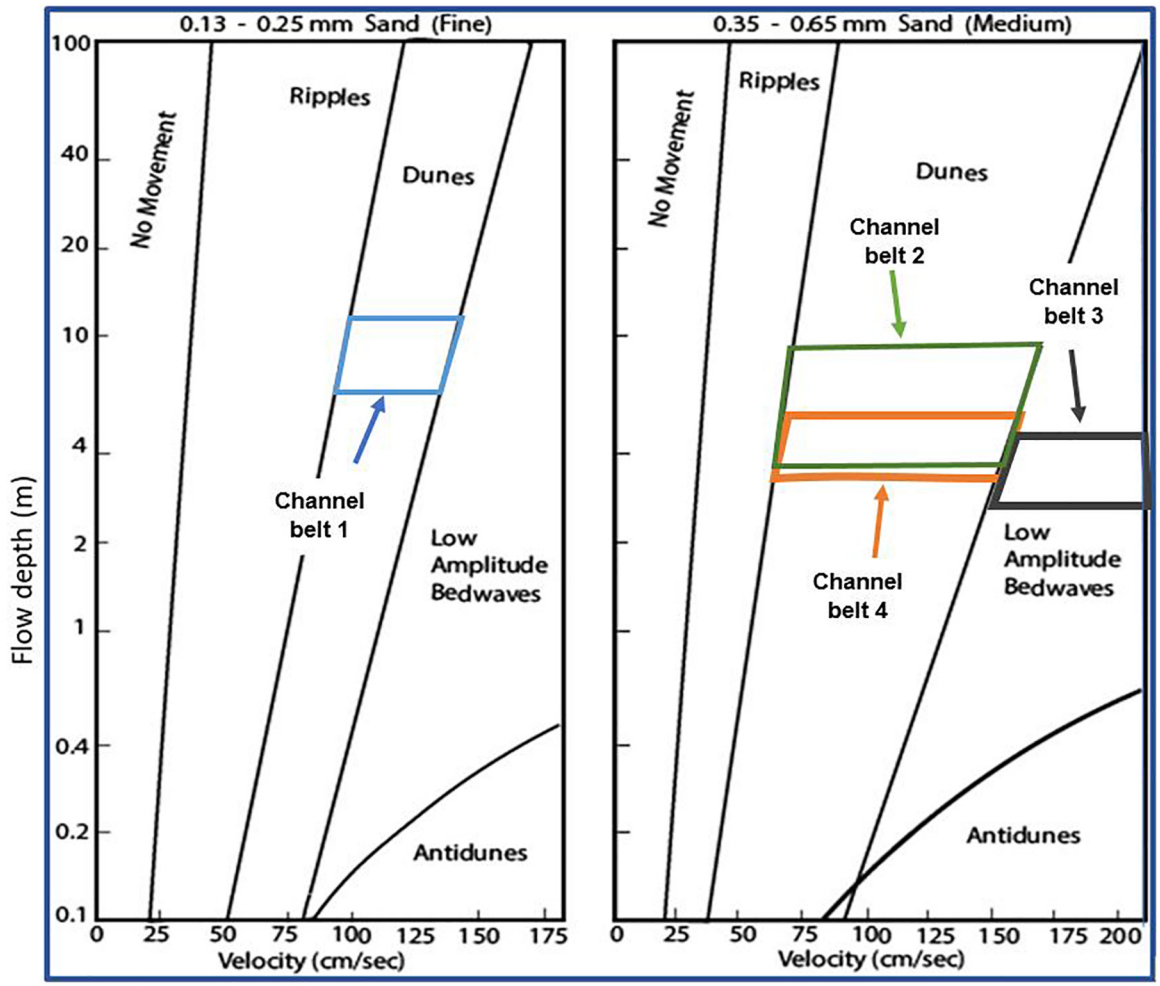

FIGURE 9 | Fine and medium-grained bedform phase diagrams of Rubin and McCulloch (1980). Estimated range of velocity for Channel belt 1 is 85–145 cm/s, Channel belt 2 is 6000–16,000 cm/s, Channel belt 3 is 150–200 cm/s, and Channel belt 4 is 6000–170 cm/s.

in measured bar thickness to compaction. It is impossible to estimate channel depth from an eroded bar; hence, data from eroded bar were recorded to give a minimum estimate of channel bar thickness. Errors associated with identifying and measuring channel bars can be up to 60% (Holbrook and Wanas, 2014). Errors identifying channel bar thickness using story thicknesses can be up to 25% (Holbrook and Wanas, 2014). Mean channel depth estimated from cross-set thickness is subject to the bias of preferential preservation of dunes during waning flow, which may not be representative of actual bankfull flow. This results in the estimation of mean dune heights that are not representative of actual flow conditions, which cause errors in the depth estimates. Mean channel depth estimated from dune height and cross-set thickness by using Eq. 5 have errors up to 25% if the depth range is averaged (Holbrook and Wanas, 2014). The accuracy of dune heights estimated using SVR is 84%. The score was calculated using the coefficient of R^2. Errors associated with estimating channel depth with Eq. 5 will also be encountered (Pedregosa et al., 2011). Measurement of channel width is also subject to the bias of interpretation, which may lead to errors in data acquired. Accuracy of channel width measurement is dependent on the identification of channel banks, which proved to be extremely difficult in the study outcrop. Channel width estimated form scaling factors have error ranges by a factor of ±4 (Blum et al., 2013). Channel dept and width estimated from the rock record are representative of extreme events, which may have resulted in extreme geomorphology and discharge than is normal to the depositional system (Gibling, 2006). Error associated with slope estimates is the assumption that bed shear stress required to move the sediment load is constant across the channel. The bankfull shield number used as a constant is for slope estimation varies by ±2 (Holbrook and Wanas, 2014). The grain size used for estimating slope is an average value and was measured with a Wentworth grain size calibrated card, which has errors of ∼1/2 phi (Lin and Bhattacharya, 2017). The errors associated with paleodischarge estimates are up to an order of magnitude (Holbrook and Wanas, 2014; Lin and Bhattacharya, 2017). The instantaneous paleodischarge estimates

are not representative of the annual or seasonal discharge in the paleochannel. The instantaneous discharge equation is a function of velocity of bankfull floodwaters, cross-sectional area of a channel, assuming the sediment supply is constant. The assumption of constant sediment supply adds more errors to the paleodischarge estimates as sediment type and sediment load varies. Another error associated with the paleodischarge estimate is based on the assumption that the cross-sectional area of a channel is the same, which is not so (Holbrook and Wanas, 2014). The cross-sectional area was also calculated using depth and width estimates, which means the errors from those numerical estimates are reflected in paleodischarge estimates. Additionally, the estimates from the instantaneous discharge have errors because the cross-sectional area for the paleochannels is estimated from mostly eroded channel deposits, which may not be representative of the actual sediment load.

DISCUSSION

Machine-Assisted Paleohydrological Analysis

The machine-assisted SVR analysis increased the accuracy of dune height prediction from cross-set thickness resulting in a higher accuracy of estimated channel depth. The results of the SVR analysis were compared to the widely used polynomial regression model developed by Leclair and Bridge (2001) using MSE and overall predictions showed comparable and in most cases better performance. The result from MSE analysis showed that the SVR model had a RMSE of 9 mm while the polynomial model had an RMSE of 16.8 mm.

Advantages of SVR Over Polynomial Regression

The SVR model considers outlier data when estimating dune cross-strata thickness. Furthermore, SVR analysis is done in a higher dimension so it allows for a comparison of additional variables that may improve prediction. For example, cross-set length may be added to the SVR model to improve the accuracy of predicted dune height. In geology, all data are important because they reflect the variability of the conditions during bed formation. The model of Leclair and Bridge (2001) was based on the data along the best line of fit. The predictions of the SVR model are non-linear due to the use of the Gaussian kernel, i.e., the model uses normal distribution to predict the zone of best fit. The result of utilizing outlier data and the Gaussian kernel is a more accurate prediction as evident by the RMSE of SVR compared to the previous model.

Channel Belt Evolution

Facies architecture, channel dimensions, paleoslope, and paleodischarge of the MPAF channel belts reveal an evolution of fluvial channel form in response to changing paleohydrological conditions. Of note, the channel depth shows variability among MPAF channels: 6.1–13.9 m for Channel belt 1, 3.4–5.6 m for Channel belt 2, 2.8–4.7 m for Channel belt 3, and 3.6–9.6 m for Channel belt 4. Channel width estimated from scaling relationships showed that the low sinuosity channels had a lower range of width, while the braided channels had the largest width range. The independently estimated paleoslope and paleodischarge, which were compared among the MPAF channel belts (**Table 2**), showed that all the channel belts at the study location had a low slope (0.00007–0.0004) and variable paleodischarge (**Figure 10**). The estimated paleoslope of the lower MPAF channel belts is similar to slope ranges for the Amazon, Mississippi, and Niger Rivers (slope range ∼0.00002–0.0005; Blum et al., 2013). This indicates that the paleoslope estimates obtained for the MPAF fluvial systems are consistent with physiographic models that suggest MPAF were deposited in low-gradient environments caused by unloading type relaxation of the foreland basin (Cecil, 1990; Cecil et al., 2003; Greb et al., 2008). Given the relatively low paleoslope estimated for all MPAF channel belt, the formation of upper plane beds and low amplitude bedforms from high-velocity flow is considered to reflect flooding events caused by intense precipitation (Kosanke and Cecil, 1996; Miall, 1996, 2014; Cecil and Dulong, 2003; Cecil et al., 2003).

Results indicate Channel belt 1 deposits formed from a low gradient, fine-grained, low-sinuosity channel form in an anastomosing fluvial system. Channel belt 1 has the thickest channel depth (6.1–13.9 m), which results in a relatively low w/d. This low w/d combined with the grain size, slope, and an abundance of coal intraclast and large plant fragments may reflect channel confinement due to bank stabilization by vegetation. The abundance of coal intraclasts and large plant fragments suggests abundant vegetation, which flourished in the humid climate, surrounded areas in the low sinuosity fluvial system (Cecil, 1990; Cecil et al., 2003; Allen et al., 2014). The estimated range for the paleoslope of the low-sinuosity channel of 0.00007–0.0001 is an order of magnitude lower than other MPAF channels in the study area. The low slope and high amount of fine-grained deposits may have contributed to Chanel belt 1 having the relatively highest channel depth and a low w/d (Gibling, 2006). The estimated paleodischarge for Channel belt 1 is 206–11351 m^3/s. This range of paleodischarge rate is the lowest of all the MPAF channel belts in the study area and is consistent with the abundance of fine-grained sediments deposited (**Figure 10**; Miall, 1996, 2014; Catuneanu, 2006).

Channel belt 2 directly overlies Channel belt 1 (**Figures 2**, **3**) and contains features that indicate deposition by a braided fluvial system in a humid climate, with low channel confinement, low paleoslope, and high paleodischarge. Channel belt 2 deposits are characterized by an abundance of trough cross-stratified, medium-grained sand, with a paleochannel depth range of 3.4–5.6 m. The abundance of trough cross-stratification suggests that the channel system was dominated by 3D dunes. The low paleochannel depth, higher slope values (0.0002–0.0003) and higher paleodischarge (621–34496 m^3/s) compared to other MPAF channel belts (**Figure 10**), suggests that the braided channel style of Channel belt 2 is due to mainly to an increased slope gradient. Channel belt 2 is interbedded with some plant trunk and coal clast, which suggests an abundance of vegetative material in the fluvial system; this suggests that the area was vegetated, but this vegetation wasn't sufficient for bank stabilization.

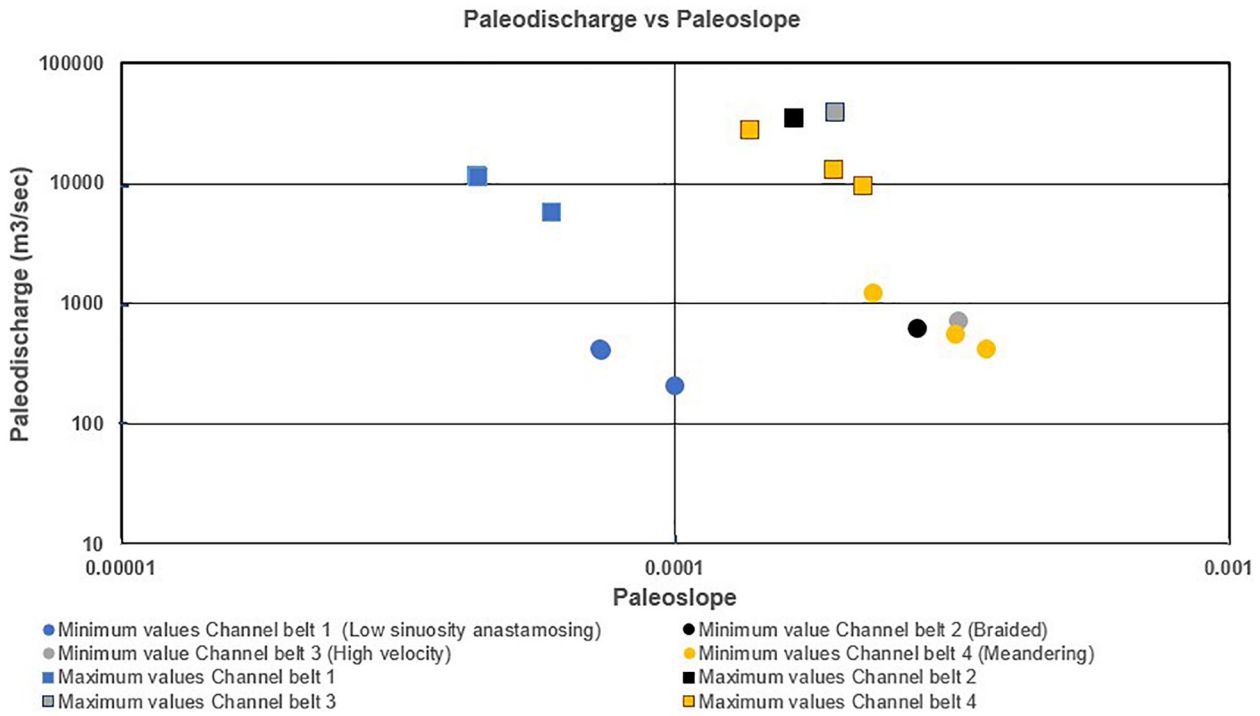

FIGURE 10 | Plot of paleodischarge versus paleoslope of MPAF channels at Birch River, WV.

Overlying the No. 5 block coal bed (**Figures 2**, **3**), Channel belt 3 sandstones were deposited by a low gradient, high-velocity fluvial system in a seasonal semi-arid climate. Channel belt 3 is characterized by an abundance of medium-grained, low amplitude bedforms and a relatively high width to depth ratio. The abundance of low amplitude bedforms in Channel belt 3 was attributed to high-velocity flooding event(s), which is supported by high paleodischarge values (695–38,658 m^3/s) compared to other MPAF channel belts. Channel belt 3 exhibits the shallowest paleochannel depths estimates compared to the other MPAF channels. This combined with the low paleoslope for Channel belt 3 (0.0002–0.0003) suggests that high-velocity flow resulted from a control other than paleoslope (Cecil et al., 2003; Cecil and Dulong, 2003; Plink-Björklund, 2015). The Burdekin River is an analog system developed in a seasonally wet-dry climate that experiences high velocity flows due to monsoonal precipitation events during wet seasons (Fielding and Alexander, 1996). The Burdekin River, just like CB 3, is dominated by upper plane beds and dunes, which represent fluctuating periods of extreme and moderate flow events.

Channel belt 4 directly overlies Channel belt 3 and contains features that indicate deposition by a low-gradient sinuous fluvial system. The high-velocity channel (Channel belt 3) is overlain by Story 1 of the sinuous channel (Channel belt 4). Story 1 is characterized by coarse to medium-grained, inclined sandstone beds with a channel depth range of 4.1–6.8 m (**Table 2**). The occurrence of convoluted beds and root structures in story 1 of the sinuous fluvial system may have been due to changes in water levels of the fluvial system brought about by seasonality in rainfall due to increasing aridity (Cecil et al., 2003; Cecil and Dulong, 2003; Fielding et al., 2009; Allen et al., 2014; Plink-Björklund, 2015). Overlying Story 1 is the LKC bed, which is overlain by Stories 2 and 3. Stories 2 and 3 are characterized by coarse to medium-grained, inclined sandstone beds with a channel depth range of 3.6–9.6 m (**Table 2**). The paleoslope (0.0001–0.0004) and paleodischarge (408–27,648 m^3/s) values of Channel belt 4 indicate an order of magnitude increase in the maximum paleodischarge rate despite the low channel gradient.

The effect of paleochannel geometry, paleoslope, and paleohydrology on the fluvial channel architecture and depositional style of the MPAF varies. The geometry of the MPAF channel varies in the study area. The channel width and depth, which has been used to compare fluvial channels of arid to humid differing climatic regimes (Fielding et al., 2009; Allen et al., 2014), was used to compare the MPAF channels. The depth ranges for the MPAF channels showed variability among MPAF channel belts: 6.1–13.9 m for Channel belt 1, 3.4–5.6 m for Channel belt 2, 2.8–4.7 m for Channel belt 3, and 3.6–9.6 m for Channel belt 4. The independently estimated paleoslope and paleohydrology, which were compared among the MPAF channel belts (**Table 2** and **Figure 10**), showed that the variation in channel depth of all the channel belts at the study location had developed on a low slope and with variable paleodischarge (**Table 2** and **Figure 10**). The low paleoslope observed in all MPAF channel belt also indicates that fast-flowing events that resulted in the formation of upper plane beds and low amplitude bedforms may have been due to flooding events caused by fluctuation in precipitation intensity

(Kosanke and Cecil, 1996; Cecil et al., 2003; Cecil and Dulong, 2003; Miall, 2014).

Possible Controls on Fluvial Channel Geometry and Paleohydrology

Eustatic rise and fall of sea level may have controlled paleoslope by changing fluvial base level (Blum and Törnqvist, 2000) across the basin in which a reduction in fluvial gradient due to sea-level rise should result in a reduction of channel flow velocity, while an increase in fluvial gradient should increase channel flow velocity. Glacio-eustatic models suggest fluvial channel sandstones are mainly deposited during glaciation when base-level is low in the basin and floodplain mudrocks are deposited during interglacial periods, when the base-level is high (Falcon-Lang, 2004; Greb et al., 2008; Haq and Schutter, 2008; Falcon-Lang and Dimichele, 2010). The effects of base-level rise and fall have a direct influence on the water levels and hence the flow depth of the fluvial channel. Sediment accommodation in a fluvial channel is limited by the water level and this is reflected in the thickness of preserved channel sand bodies of the MPAF (Shanley and McCabe, 1994; Currie, 1997; Blum and Törnqvist, 2000; Bhattacharya et al., 2016). The thicker channel depth observed in CB 1 and CB 4 may be due to eustatic base-level rise, while the lower thickness values of CB 2 and CB 4 may be due to eustatic base-level fall. However, the occurrence of water escape structures and rooting features in CB 4 sandstones suggests a variable water level in the fluvial system, which is not consistent with the eustatic base-level fluctuations. This suggests that glacio-eustasy played an important role in long-term accommodation succession of the fluvial system, but other factors overprinted the glacio-eustatic control.

Tectonic controls on accommodation and physiography of the Alleghenian foreland may have affected the evolution of MPAF channel belts. Tectonic subsidence and uplift may lead to the increase or decrease of slope and hence fluvial gradient. Relaxation and uplift of a subsided Alleghenian foreland basin would have resulted in an increase of slope (Holbrook and Schumm, 1999; Holbrook et al., 2006), which we interpret to have caused an increase of the fluvial gradient and change in fluvial styles reflected in the CBs 1–3 (**Table 2**). The effect of tectonic subsidence and uplift on the base level is similar to the eustatic effect on base level in a sedimentary basin. However, tectonic processes have third-order cycles (i.e., >1 my) which do not fit the higher frequency, fourth-order cycles (i.e., 0.1–1 my) of the MPAF channel belt (see MPAF age estimates, **Figure 2**). This implies that tectonic influence on MPAF geometry and paleohydrology has been masked by other controls. Additionally, tectonic uplifts which resulted in the formation of the Pangean Mountains may have resulted in the formation of a rainshadow zone, which led to extended periods without precipitation (Greb et al., 2008). However, the duration of tectonic processes does not match the higher frequency processes of the MPAF (DiMichele et al., 2010; Gibling et al., 2014).

Paleoclimatic control on precipitation and evapotranspiration rates and the abundance of vegetation may have influenced the geometry and hydrology of the MPAF fluvial system. An increase in or decrease in annual precipitation and evapotranspiration rates may have led to changes in the rate of discharge in the catchment area and fluvial system. The abundance of vegetation in different climatic conditions may also affect the geometry and hydrology of the fluvial system. The amount of vegetative cover influences the run-off in a fluvial catchment area and rooting increases the stability of channel banks (Schumm, 1968, 1981, 1988; Fielding et al., 2009). The amount of vegetative cover in the fluvial catchment area of ever-wet, humid fluvial systems have more vegetative cover and experience less erosion and water run-off compared to more arid catchment areas with less vegetative cover. Precipitation and evapotranspiration rates also vary in fluvial systems of humid and seasonally wet–dry climates (Cecil and Dulong, 2003; Cecil et al., 2004). The constant precipitation events and abundant vegetation cover in the fluvial depositional system of an ever-wet humid climate results in stable water input in the fluvial catchment area and constant paleodischarge rates in the fluvial system. Any fluctuation in the base level of the ever wet, humid fluvial system is driven by other factors such as eustasy. Also, erosion in the humid fluvial system will be limited to areas within the channel due to the stabilizing effects of abundant vegetation on the channel banks, which may lead to increased channel flow depth compared to channel width. The increased thicknesses of Channel belts 1 and 4 deposits above the LKC may be due to deposition in a humid climate characterized by constant precipitation, an abundance of vegetation and moderate paleodischarge. The sinuous channel belt (CB 4) and the low sinuosity channel belt (CB 1) have the lowest range of paleoslope and paleodischarge, except for the uniquely high paleodischarge range of the story 3 of the sinuous channel belt, which may be due to an increase in base level as a result of an increase in precipitation rates. Fluvial systems of seasonally wet–dry climates experience more evapotranspiration, which results in a reduction in water levels in the fluvial system. Precipitation events in the fluvial systems of seasonally wet–dry climates result in a sudden increase in water input to the fluvial catchment area, which results in increased paleoflow and paleodischarge (Cecil and Dulong, 2003; Fielding et al., 2009; Plink-Björklund, 2015). The relatively low thickness of the braided and high-velocity channel suggests that there was low accommodation, which may be due to the reduction of the stratigraphic base level during the periods of high evapotranspiration. The high range of paleodischarge values of the braided (CB 2) and high-velocity (CB 3) channel belts indicates a high paleoslope and fluvial gradient, which may have been due to onset of precipitation in a fluvial system previously experiencing low stratigraphic base level, which we interpret to have been caused by high evapotranspiration rates during dry season.

Paleoclimatic models developed from miospore composition of coal indicate wet–dry–wet MPAF depositional environment (**Figure 11**; Eble, 2002), which was attributed to fluctuations in paleoclimate of the Appalachian basin during the Middle Pennsylvanian (Eble, 2002; DiMichele et al., 2010; Falcon-Lang and Dimichele, 2010; Cecil, 2013). The miospore data show lycopsid, fern, calamites, and cordaites composition of MPAF coal beds at Birch River. The lycopsid indicates deposition in a wet, humid environment, while the ferns indicate deposition

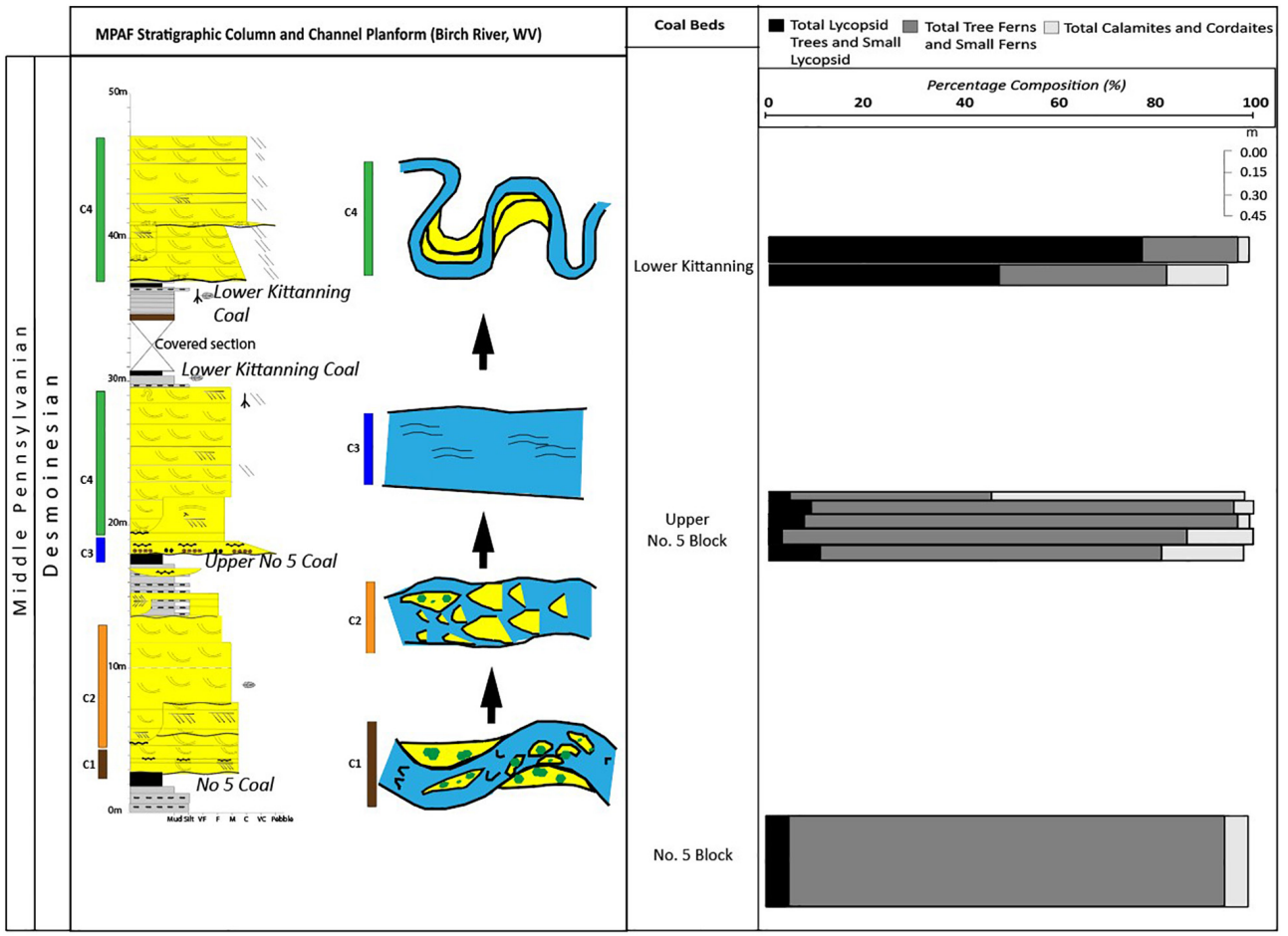

FIGURE 11 | MPAF channel belts and distribution of numerically significant miospore taxa through time, Birch River, West Virginia. Miospore data modified from Eble (2002). CB, channel belt.

in a dry, arid environment. A comparison of estimated paleoslope, paleodischarge, and geomorphology data with the miospore data highlights a relationship between MPAF channel depth, paleoslope and paleodischarge, and lycopsid and fern composition. Channel paleoslope and paleodischarge range increases with increasing fern content and while channel depth increases with increasing lycopsid content. This suggests that paleoclimate changes may have been controlling the MPAF channel belt geomorphology, paleoslope, and paleodischarge. The miospore data show a decrease in lycopsid and an increase in fern with time, as observed in the Little No. 5 Block coal bed, which underlies MPAF deposits of this study, to the No. 5 Block coal bed, which underlies the low sinuosity channel (**Figure 11**).

Therefore, we infer that the abundance of upper plane stage beds, low amplitude bedforms in Channel belt 3 is likely due to changes in precipitation and evapotranspiration. The fluvial depositional mechanisms of the Channel belt 3, such as paleoslope and paleohydrology, that resulted in the various bedforms of the high-velocity fluvial system may have been due to the humid to semi-arid paleoclimate change during the Pennsylvanian as modeled from Pennsylvanian paleobotany and Canadian fluvial systems (Cecil, 1990; Cecil et al., 2003; Greb et al., 2008; Allen et al., 2014). A seasonal wet–dry climate, which is common in semi-arid regions, usually results in an episodic influx of large volumes of water, which may have resulted in high-velocity floods forming the low amplitude bedforms observed in the high-velocity channel (Fielding et al., 2009; Plink-Björklund, 2015). The increase in channel depth of the sinuous channels above the LKC bed may be due to the reverse of paleoclimate to a wetter more humid climate, which is supported by the increase in lycopsid spores in the LKC beds that indicate a wet environment (Kosanke and Cecil, 1996; Eble, 2002).

CONCLUSION

This study used numerical modeling to highlight changes in fluvial channel geomorphology and hydrology that coincides with periods of paleoclimate change during the Middle Pennsylvanian. Measured and estimated paleochannel depth and width were used to determine changes in paleoslope and paleodischarge of

the MPAF channel belts. SVR machine-assisted algorithm was effective in improving the accuracy of estimating dune heights and channel depth, from cross-set thickness. Paleochannel depth decreases during periods of increasing paleoclimate dryness; and then starts to increase during periods of increasing paleoclimate wetness. The decrease in paleochannel depth may be due to a reduction in stratigraphic base level caused by low annual precipitation, which is common in fluvial systems of seasonal wet–dry, semi-arid/semi-humid climate. Paleodischarge varies across the MPAF however, MPAF zones that experienced an increase in paleodischarge coincides with periods of paleoclimate change from ever-wet humid to seasonal semi-arid climate. Paleoslope estimates indicate low gradient physiography for the MPAF depositional environment, which agrees with previous models of ancient coal forming environments in West Virginia. Further review of possible effects of eustatic, tectonic, and paleoclimatic effect on the geometry and hydrology of fluvial systems indicated that paleoclimate was a dominant control on MPAF channel belt geomorphology and hydrology. By highlighting qualitative and quantitative characteristics of MPAF fluvial channels, this research shows a way of identifying the effects of paleoclimatic forcing on the hydrology and geomorphology of fluvial systems.

DATA AVAILABILITY STATEMENT

All datasets generated for this study are included in the article/**Supplementary Material**.

AUTHOR CONTRIBUTIONS

All authors listed have made a substantial, direct and intellectual contribution to the work, and approved it for publication.

FUNDING

Field and laboratory work for this research was made possible by funds and grants from the American Association of Petroleum Geologist (AAPG), Shumaker Fund, and West Virginia University.

SUPPLEMENTARY MATERIAL

The Supplementary Material for this article can be found online at: https://www.frontiersin.org/articles/10.3389/feart.2019.00361/full#supplementary-material

REFERENCES

Allen, J. P., Fielding, C. R., Gibling, M. R., and Rygel, M. C. (2014). Recognizing products of palaeoclimate fluctuation in the fluvial stratigraphic record: an example from the Pennsylvanian to Lower Permian of Cape Breton Island, Nova Scotia. *Sedimentology* 61, 1332–1381. doi: 10.1111/sed.12102

Allen, J. R. (1982). *Sedimentary Structures, Their Character and Physical Basis*. Amsterdam: Elsevier Science & Technology.

Allen, J. R. L. (1970). A quantitative model of grain size and sedimentary structures in lateral deposits. *Geol. J.* 7, 129–146. doi: 10.1002/gj.3350070108

Archer, A. W., and Greb, S. F. (1995). An Amazon-scale drainage system in the early Pennsylvanian of central North America. *J. Geol.* 103, 611–627. doi: 10.1086/629784

Arkle, T. Jr., Beissel, D. R., Larese, R. E., Nuhfer, E. B., Patchen, D. G., Smosna, R. A., et al. (1979). Mississippian and Pennsylvanian (carboniferous) systems in the United States: West Virginia and Maryland. *U.S. Geol. Surv. Prof. Pap.* 1110D, 1110.

Awad, M., and Khanna, R. (2015). "Support vector regression," in *Efficient Learning Machines: Theories, Concepts, and Applications for Engineers and System Designers*, eds M. Awad, and R. Khanna, (Berkeley, CA: Apress), 67–80. doi: 10.1007/978-1-4302-5990-9_4

Bao, Y., and Liu, Z. (2006). "A fast grid search method in support vector regression forecasting time series," in *Intelligent Data Engineering and Automated Learning – IDEAL 2006 Lecture Notes in Computer Science*, eds E. Corchado, H. Yin, V. Botti, and C. Fyfe, (Berlin: Springer), 504–511. doi: 10.1007/11875581_61

Bhattacharya, J. P., Copeland, P., Lawton, T. F., and Holbrook, J. (2016). Estimation of source area, river paleo-discharge, paleoslope, and sediment budgets of linked deep-time depositional systems and implications for hydrocarbon potential. *Earth Sci. Rev.* 153, 77–110. doi: 10.1016/j.earscirev.2015.10.013

Blake, B. M., Cross, A. T., Eble, C., Gillespie, W. H., and Pfefferkorn, H. (2002). "Selected megafossils from the Carboniferous of the Appalachian region, eastern United States: geographic and stratigraphic distribution," in *Carboniferous and Permian of the World: Canadian Society of Petroleum Geologists Memoir 19*, eds L. Hills, C. M. Henderson, and E. W. Bamber, (Calgary, AB: Canadian Society of Petroleum Geologists).

Blum, M., Martin, J., Milliken, K., and Garvin, M. (2013). Paleovalley systems: insights from Quaternary analogs and experiments. *Earth Sci. Rev.* 116, 128–169. doi: 10.1016/j.earscirev.2012.09.003

Blum, M. D., and Törnqvist, T. E. (2000). Fluvial responses to climate and sea-level change: a review and look forward. *Sedimentology* 47, 2–48. doi: 10.1046/j.1365-3091.2000.00008.x

Bridge, J. S. (2009). *Rivers and Floodplains: Forms, Processes, and Sedimentary Record*. Hoboken, NJ: John Wiley & Sons.

Bridge, J. S., and Mackey, S. D. (1993). "A revised alluvial stratigraphy model," in *Alluvial Sedimentation*, eds M. Marzo, and C. Puigdefábregas, (International Association of Sedimentologists), 317–336. doi: 10.1002/9781444303995.ch22

Bridge, J. S., and Tye, R. S. (2000). Interpreting the dimensions of ancient fluvial channel bars, channels, and channel belts from wireline-logs and cores. *Am. Assoc. Pet. Geol. Bull.* 84, 1205–1228.

Catuneanu, O. (2006). *Principles of Sequence Stratigraphy*. Amsterdam: Elsevier.

Cecil, C. B. (1990). Paleoclimate controls on stratigraphic repetition of chemical and siliciclastic rocks. *Geology* 18, 533–536.

Cecil, C. B. (2013). An overview and interpretation of autocyclic and allocyclic processes and the accumulation of strata during the Pennsylvanian–Permian transition in the central Appalachian Basin, USA. *Int. J. Coal Geol.* 119, 21–31. doi: 10.1016/j.coal.2013.07.012

Cecil, C. B., Brezinski, D. K., and Dulong, F. (2004). The Paleozoic record of changes in global climate and sea level: central Appalachian basin. *U.S. Geol. Surv. Circ.* 1264, 77–133.

Cecil, C. B., and Dulong, F. T. (2003). "Precipitation models for sediment supply in warm climates," in *Climate Controls on Stratigraphy: Society for Sedimentary Geology (SEPM)*, Vol. 77, eds C. B. Cecil, and N. T. Edgar, (Tulsa, Ok: SEPM Society for Sedimentary Geology), 21–27. doi: 10.2110/pec.03.77.0021

Cecil, C. B., Dulong, F. T., West, R. R., Stamm, R., Wardlaw, B., and Edgar, N. T. (2003). "Climate controls on the stratigraphy of a Middle Pennsylvanian cyclothem in North America," in *Climate Controls on Stratigraphy*, eds C. B. Cecil, and N. T. Edgar (Tulsa, Ok: SEPM Society for Sedimentary Geology). doi: 10.2110/pec.03.77.0151

Cecil, C. B., Stanton, R. W., Neuzil, S. G., Dulong, F. T., Ruppert, L. F., and Pierce, B. S. (1985). Paleoclimate controls on late Paleozoic sedimentation and peat formation in the central Appalachian Basin (USA). *Int. J. Coal Geol.* 5, 195–230. doi: 10.1016/0166-5162(85)90014-x

Chamberlin, E. P., and Hajek, E. A. (2015). Interpreting paleo-avulsion dynamics from multistory sand bodies. *J. Sediment. Res.* 85, 82–94. doi: 10.2110/jsr.2015.09

Currie, B. S. (1997). Sequence stratigraphy of nonmarine Jurassic–Cretaceous rocks, central Cordilleran foreland-basin system. *GSA Bull.* 109, 1206–1222.

Davidson, S. K., and Hartley, A. J. (2010). Towards a quantitative method for estimating paleohydrology from clast size and comparison with modern rivers. *J. Sediment. Res.* 80, 688–702. doi: 10.2110/jsr.2010.062

Davis, J. C., and Sampson, R. J. (1986). *Statistics and Data Analysis in Geology*. New York, NY: Wiley.

DeCelles, P. G., Langford, R. P., and Schwartz, R. K. (1983). Two new methods of paleocurrent determination from trough cross-stratification. *J. Sediment. Res.* 53, 629–642.

DiMichele, W. A. (2013). Wetland-dryland vegetational dynamics in the Pennsylvanian ice age tropics. *Int. J. Plant Sci.* 175, 123–164. doi: 10.1086/675235

DiMichele, W. A., Cecil, C. B., Montañez, I. P., and Falcon-Lang, H. J. (2010). Cyclic changes in Pennsylvanian paleoclimate and effects on floristic dynamics in tropical Pangaea. *Int. J. Coal Geol.* 83, 329–344. doi: 10.1016/j.coal.2010.01.007

Donaldson, A. C., and Shumaker, R. C. (1981). "Late Paleozoic molasse of central Appalachians," in *Sedimentation and Tectonics in Alluvial Basins: Geological Association of Canada Special Paper 23*, ed. A. D. Miall, (St. John's, NL: Geological Association of Canada), 99–124.

Eble, C. F. (2002). Palynology of late Middle Pennsylvanian coal beds in the Appalachian Basin. *Int. J. Coal Geol.* 50, 73–88. doi: 10.1016/s0166-5162(02)00114-3

Ethridge, F. G., and Schumm, S. A. (1977). "Reconstructing paleochannel morphologic and flow characteristics: methodology, limitations, and assessment," in *Fluvial Sedimentology: Canadian Society of Petroleum Geologists Memoir*, Vol. 5, ed. A. D. Miall, (Calgary, AB: Canadian Society of Petroleum Geologists), 703–722.

Ettensohn, F. R. (2005). "5. The sedimentary record of foreland-basin, tectophase cycles: examples from the Appalachian Basin, USA," in *Developments in Sedimentology Cyclic Development of Sedimentary Basins*, eds J. M. Mabessoone, and V. H. Neumann, (Amsterdam: Elsevier), 139–172. doi: 10.1016/S0070-4571(05)80007-X

Ettensohn, F. R. (2008). "Chapter 4 the Appalachian foreland basin in Eastern United States," in *Sedimentary Basins of the World the Sedimentary Basins of the United States and Canada*, ed. A. D. Miall, (Amsterdam: Elsevier), 105–179. doi: 10.1016/s1874-5997(08)00004-x

Falcon-Lang, H. J. (2004). Pennsylvanian tropical rain forests responded to glacial-interglacial rhythms. *Geology* 32, 689–692. doi: 10.1130/G20523.1

Falcon-Lang, H. J., and Dimichele, W. A. (2010). What happened to the coal forests during Pennsylvanian glacial phases? *Palaios* 25, 611–617. doi: 10.2110/palo.2009.p09-162r

Fielding, C. R., and Alexander, J. (1996). Sedimentology of the upper Burdekin River of North Queensland, Australia—an example of a tropical, variable discharge river. *Terra Nova* 8, 447–457. doi: 10.1111/j.1365-3121.1996.tb00770.x

Fielding, C. R., Allen, J. P., Alexander, J., and Gibling, M. R. (2009). Facies model for fluvial systems in the seasonal tropics and subtropics. *Geology* 37, 623–626. doi: 10.1130/g25727a.1

Gibling, M. R. (2006). Width and thickness of fluvial channel bodies and valley fills in the geological record: a literature compilation and classification. *J. Sediment. Res.* 76, 731–770. doi: 10.2110/jsr.2006.060

Gibling, M. R., Davies, N. S., Falcon-Lang, H. J., Bashforth, A. R., DiMichele, W. A., Rygel, M. C., et al. (2014). Palaeozoic co-evolution of rivers and vegetation: a synthesis of current knowledge. *Proc. Geol.Assoc.* 125, 524–533.

Greb, S. F., Pashin, J. C., Martino, R. L., and Eble, C. F. (2008). "Appalachian sedimentary cycles during the Pennsylvanian: changing influences of sea level, climate, and tectonics," in Resolving the Late Paleozoic Gondwanan Ice Age in Time and Space, Vol. 441, eds C. F. Fielding, T. D. Frank, and J. L. Isbell (Tulsa, Ok: SEPM Society for Sedimentary Geology), 235–248. doi: 10.1130/2008.2441(16)

Haq, B. U., and Schutter, S. R. (2008). A chronology of Paleozoic sea-level changes. *Science* 322, 64–68. doi: 10.1126/science.1161648

Holbrook, J., and Schumm, S. A. (1999). Geomorphic and sedimentary response of rivers to tectonic deformation: a brief review and critique of a tool for recognizing subtle epeirogenic deformation in modern and ancient settings. *Tectonophysics* 305, 287–306. doi: 10.1016/s0040-1951(99)00011-6

Holbrook, J., Scott, R. W., and Oboh-Ikuenobe, F. E. (2006). Base-level buffers and buttresses: a model for upstream versus downstream control on fluvial geometry and architecture within sequences. *J. Sediment. Res.* 76, 162–174. doi: 10.2110/jsr.2005.10

Holbrook, J., and Wanas, H. (2014). A fulcrum approach to assessing source-to-sink mass balance using channel paleohydrologic paramaters derivable from common fluvial data sets with an example from the Cretaceous of Egypt. *J. Sediment. Res.* 84, 349–372. doi: 10.2110/jsr.2014.29

Kosanke, R. M., and Cecil, C. B. (1996). Late Pennsylvanian climate changes and palynomorph extinctions. *Rev. Palaeobot. Palynol.* 90, 113–140. doi: 10.1016/0034-6667(95)000275

Leclair, S. F. (2002). Preservation of cross-strata due to the migration of subaqueous dunes: an experimental investigation. *Sedimentology* 49, 1157–1180. doi: 10.1046/j.1365-3091.2002.00482.x

Leclair, S. F., and Bridge, J. S. (2001). Quantitative interpretation of sedimentary structures formed by river dunes. *J. Sediment. Res.* 71, 713–716. doi: 10.1306/2dc40962-0e47-11d7-8643000102c1865d

Leeder, M. R. (1993). *Tectonic Controls upon Drainage Basin Development, River Channel Migration and Alluvial Architecture: Implications for Hydrocarbon Reservoir Development and Characterization*, Vol. 73. London: Geological Society, 7–22. doi: 10.1144/GSL.SP.1993.073.01.02

Leeder, M. R. (2009). "On the interactions between turbulent flow, sediment transport and bedform mechanics in channelized flows," in *Modern and Ancient Fluvial Systems*, eds J. D. Collinson, and J. Lewin, (London: Wiley-Blackwell), 3–18. doi: 10.1002/9781444303773.ch1

Lin, W., and Bhattacharya, J. P. (2017). Estimation of Source-to-sink mass balance by a fulcrum approach using channel paleohydrologic parameters of the Cretaceous Dunvegan Formation, Canada. *J. Sediment. Res.* 87, 97–116. doi: 10.2110/jsr.2017.1

Miall, A. (2014). *Fluvial Depositional Systems*. Cham: Springer International Publishing. doi: 10.1007/978-3-319-006666

Miall, A. D. (1996). *The Geology of Fluvial Deposits*. Berlin: Springer.

Montañez, I. P., McElwain, J. C., Poulsen, C. J., White, J. D., DiMichele, W. A., Wilson, J. P., et al. (2016). Climate, pCO2 and terrestrial carbon cycle linkages during late Palaeozoic glacial–interglacial cycles. *Nat. Geosci.* 9, 824–828. doi: 10.1038/ngeo2822

Pedregosa, F., Varoquaux, G., Gramfort, A., Michel, V., Thirion, B., Grisel, O., et al. (2011). Scikit-learn: machine learning in Python. *J. Mach. Learn. Res.* 12, 2825–2830.

Peppers, R. A. (1996). *Palynological Correlation of Major Pennsylvanian (Middle and Upper Carboniferous) Chronostratigraphic Boundaries in the Illinois and other Coal Basins*. Boulder, CO: Geological Society of America.

Plink-Björklund, P. (2015). Morphodynamics of rivers strongly affected by monsoon precipitation: review of depositional style and forcing factors. *Sediment. Geol.* 323, 110–147. doi: 10.1016/j.sedgeo.2015.04.004

Python (2019). Python Software Foundation. *Python.Org*. Available at: https://www.python.org/ (accessed June 28, 2019).

Rubin, D. M., and McCulloch, D. S. (1980). Single and superimposed bedforms: a synthesis of San Francisco Bay and flume observations. *Sediment. Geol.* 26, 207–231. doi: 10.1016/0037-0738(80)90012-3

Sak, P. B., McQuarrie, N., Oliver, B. P., Lavdovsky, N., and Jackson, M. S. (2012). Unraveling the central Appalachian fold-thrust belt, Pennsylvania: the power of sequentially restored balanced cross sections for a blind fold-thrust belt. *Geosphere* 8, 685–702.

Schumm, S. A. (1968). *River Adjustment to Altered Hydrologic Regimen-Murrumbidgee River and Paleochannels, Australia*. Washington, DC: US Government Printing Office.

Schumm, S. A. (1981). "Evolution and response of the fluvial system, sedimentologic implications," in *Recent and Ancient Nonmarine Depositional Environments*, eds P. G. Ethridge, and K. M. Flores, (Tulsa, OK: Society for Sedimentary Geology).

Schumm, S. A. (1988). Variability of the fluvial system in space and time. *Scales Glob. Change* 35, 225–250.

Shanley, K. W., and McCabe, P. J. (1994). Perspectives on the sequence stratigraphy of continental strata. *Am. Assoc. Pet. Geol. Bull.* 78, 544–568.

Stubbs, D. G. (2018). *A Sequence Stratigraphic Analysis of the Allegheny Group (Middle Pennsylvanian), Southeast Ohio*. Masters thesis, Ohio University, Athens, OH.

Tabor, N. J., and Montanez, I. P. (2002). Shifts in late Paleozoic atmospheric circulation over western equatorial Pangea: insights from pedogenic mineral δ18O compositions. *Geology* 30, 1127–1130.

Tabor, N. J., and Poulsen, C. J. (2008). Palaeoclimate across the Late Pennsylvanian–Early Permian tropical palaeolatitudes: a review of climate indicators, their distribution, and relation to palaeophysiographic climate factors. *Palaeogeogr. Palaeoclimatol. Palaeoecol.* 268, 293–310. doi: 10.1016/j.palaeo.2008.03.052

Zhang, Y., Kimberg, D. Y., Coslett, H. B., Schwartz, M. F., and Wang, Z. (2014). "Support vector regression based multivariate lesion-symptom mapping," in *Proceedings of the 36th Annual International Conference of the IEEE Engineering in Medicine and Biology Society* (Chicago, IL: IEEE), 5599–5602.

Conflict of Interest: The authors declare that the research was conducted in the absence of any commercial or financial relationships that could be construed as a potential conflict of interest.

frontiers in Earth Science

ORIGINAL RESEARCH
published: 23 January 2020
doi: 10.3389/feart.2019.00358

Inherited Depositional Topography Control on Shelf-Margin Oversteepening, Readjustment, and Coarse-Grained Sediment Delivery to Deep Water, Magallanes Basin, Chile

Dustin B. Bauer[1,2], Stephen M. Hubbard[1], Jacob A. Covault[3] and Brian W. Romans[4]*

[1] Department of Geoscience, University of Calgary, Calgary, AB, Canada, [2] Chevron Canada Limited, Calgary, AB, Canada, [3] Bureau of Economic Geology, Jackson School of Geosciences, The University of Texas at Austin, Austin, TX, United States, [4] Department of Geosciences, Virginia Tech, Blacksburg, VA, United States

OPEN ACCESS

Edited by:
Amanda Owen, University of Glasgow, United Kingdom

Reviewed by:
Gary Hampson, Imperial College London, United Kingdom
Nicholas Perez, Texas A&M University, United States

***Correspondence:**
Stephen M. Hubbard
shubbard@ucalgary.ca

Specialty section:
This article was submitted to Sedimentology, Stratigraphy and Diagenesis, a section of the journal Frontiers in Earth Science

Received: *14 August 2019*
Accepted: *26 December 2019*
Published: *23 January 2020*

Citation:
Bauer DB, Hubbard SM, Covault JA and Romans BW (2020) Inherited Depositional Topography Control on Shelf-Margin Oversteepening, Readjustment, and Coarse-Grained Sediment Delivery to Deep Water, Magallanes Basin, Chile. Front. Earth Sci. 7:358. doi: 10.3389/feart.2019.00358

A shelf-margin depositional system is the stratigraphic product of terrigenous sediment delivery to the ocean, comprising a flat to low-gradient shelf, or topset, which transitions to a steeper deep-water slope, and, ultimately, a relatively flat basin floor, or bottomset. Erosional and depositional processes across these physiographic domains approximate a clinoform in the stratigraphic record. The shelf margin is a critical environment for terrigenous sediment dispersal because it is a process-regime boundary that links the shelf to deep water and is a marker of basin evolution through time. Additionally, the coarse-grained deposits of strata associated with the shelf-margin zone are important subsurface reservoirs or aquifers. Here, we characterize the shelf-margin and upper slope stratigraphy of the outcropping Upper Cretaceous Tres Pasos and Dorotea formations, Magallanes Basin, southern Chile. The Late Cretaceous Magallanes retroarc foreland basin was an elongate trough oriented parallel to the southern Andean arc and fold-and-thrust belt. The Tres Pasos and Dorotea formations record southward (basin axial) progradation of a high-relief shelf and slope system (>1000 m paleo-water depth) represented by a stratigraphic succession up to 3 km thick that is exposed for tens of kilometers along depositional dip. The character and distribution of deposits that define shelf margins contain evidence for a variety of processes related to deposition, erosion, sediment bypass, and mass wasting. The overall architecture of the Magallanes Basin strata is indicative of a graded shelf-margin system interrupted by periods of slope oversteepening and development of out-of-grade conditions. These punctuated periods are recognized by sedimentological evidence for enhanced bypass of coarse-grained sediment across the upper slope, and thick submarine fan successions in more distal segments. Development of oversteepened depositional topography is particularly significant as it instigated the only two major periods of coarse-grained sediment delivery to deep water over ~8 Myr during the Campanian. The controls on sediment dispersal beyond the shelf margin are commonly discussed in terms of allogenic forcings, such as tectonics, climate, eustasy, and receiving-basin geometry, as well as autogenic behavior,

such as delta-lobe switching. However, inherited depositional topography does not clearly fit within an allogenic/autogenic dichotomy. Depositional topography inherited from shelf-margin evolution influences the position of subsequent shelf margins, which can promote coarse-grained sediment delivery to deep water.

Keywords: stratigraphy, clinoform, basin evolution, clastic sedimentology, Magallanes Basin

INTRODUCTION

A shelf-margin is characterized in depositional-dip profile from shallow-dipping topset, across steeper foreset (clinoform), to shallow-dipping bottomset (**Figure 1**). Shelf-margin profiles that approximate clinoforms are generally considered to represent progradation of graded slopes (Hedberg, 1970; Ross et al., 1994; Steel and Olsen, 2002; Johannessen and Steel, 2005; Patruno et al., 2015; Hodgson et al., 2018). Graded margins are defined as margins where erosional and depositional processes are in equilibrium, resulting in topographically smooth slope profiles that prograde basinward (Hedberg, 1970; Ross et al., 1994). Conversely, Hedberg (1970) described out-of-grade slopes, wherein the shelf margin and upper slope are zones of net erosion, sediment bypass, and mass wasting, whereas the lower slope and basin are associated with substantial deposition. The shelf margin is a gateway for the transport of coarse-grained sediment into deep water, and it is commonly attributed to either external forcings (i.e., allogenic controls) promoting sediment supply (Carvajal and Steel, 2009; Kertznus and Kneller, 2009) or internal dynamics of the system (i.e., autogenic controls), such as compensational stacking as a result of delta-lobe switching (Olariu and Bhattacharya, 2006; Muto et al., 2007; Straub et al., 2009; Hajek and Straub, 2017). Ross et al. (1994) noted that inherited depositional topography can control the evolution of later shelf margins, potentially fostering development of oversteepened upper slopes and promoting mass wasting and/or coarse-grained sediment delivery to deep water (**Figure 1**). Inherited depositional topography does not clearly fit into the either/or, allogenic/autogenic dichotomy of controls on shelf-margin depositional evolution because underlying deposits might have been the product of a wholly distinct set of conditions.

Studies of shelf-margin depositional systems have commonly focused on the prediction of down-slope deep-water fans through stratigraphic analysis (Plink-Björklund et al., 2001; Prather et al., 2017), analysis of external controls (Carvajal and Steel, 2009), or investigation of shelf-edge deposits (i.e., wave-, tide-, or river-dominated process regime) (e.g., Dixon et al., 2012b; Cosgrove et al., 2018). The controls on transitions between slopes with a graded profile and out-of-grade configurations that promote coarse-grained sediment transfer to deep water have remained understudied (Gomis-Cartesio et al., 2018). Slope readjustment comprises the processes of erosion, sediment bypass, and marine onlap of submarine-fan deposits in response to changing basin physiography (Ross et al., 1994). However, the detailed sedimentology and stratigraphy of major shelf-margin readjustments, like those described by Ross et al. (1994) across a large-scale shelf-margin transect, have not been well documented. Furthermore, comparably little work has been focused on the sedimentologic record along the entirety of the transition from shallow-marine to deep-water depocenters along basin margins of high relief (>500 m) (Dixon et al., 2012a; Poyatos-Moré et al., 2019). Deciphering the details of siliciclastic basin margins is challenging as a result of their large scale (several hundreds of meters to kilometers of relief; McMillen, 1991; Helland-Hansen, 1992; Hubbard et al., 2010; Patruno et al., 2015). These high-relief shelf-margin systems are most commonly observed in seismic-reflection data, characterized by >10 m of vertical resolution (e.g., Pinous et al., 2001; Houseknecht et al., 2009), with important insight drawn from stratigraphic modeling (e.g., Uličný et al., 2002; Burgess et al., 2008; Gerber et al., 2008).

This study focuses on the characterization of outcropping shelf-margin stratigraphy, with an emphasis on the record of punctuated out-of-grade conditions related to inherited depositional topography in the Upper Cretaceous Tres Pasos and Dorotea formations, southern Chile. The unique outcrop perspective of seismic-scale clinoforms (i.e., >1000 m relief) provides the opportunity to investigate the stratigraphic architecture developed in response to shelf-margin oversteepening. This is augmented with documentation of the down-dip sedimentological variability along out-of-grade surfaces that were associated with significant coarse-grained sediment bypass to the deep basin.

GEOLOGIC SETTING

In this study, we examine deposits of the Upper Cretaceous Dorotea and Tres Pasos formations that crop out in southern Chile (**Figure 2**; Hubbard et al., 2010; Daniels et al., 2018). The units were deposited in the Cenomanian–Maastrichtian Magallanes retroarc foreland basin, located at the southern end of the 7000 km-long Andean Cordillera along the southwestern margin of the South American plate (**Figure 2A**; Dalziel, 1981; Wilson, 1991; Fildani and Hessler, 2005; Daniels et al., 2019).

The Magallanes Basin contains 3–5 km of Upper Cretaceous deep-water strata, deposited during a prolonged period of elevated subsidence (Romans et al., 2011; Bernhardt et al., 2012). The foreland basin is underlain by thinned continental crust, attributed to a precursor extensional back-arc basin (Rocas Verdes Basin; Romans et al., 2010; Fosdick et al., 2011). This attenuated continental crust promoted high subsidence during thrust loading and led to long-lived deep-water conditions in the retroarc setting (Natland et al., 1974; Hubbard et al., 2010; Fosdick et al., 2014). Deposition of unconfined turbidites of the Cenomanian-Turonian Punta Barrosa Formation marks the onset of deep-water sedimentation (Fildani et al., 2003; Malkowski et al., 2017), followed by the Coniacian-early

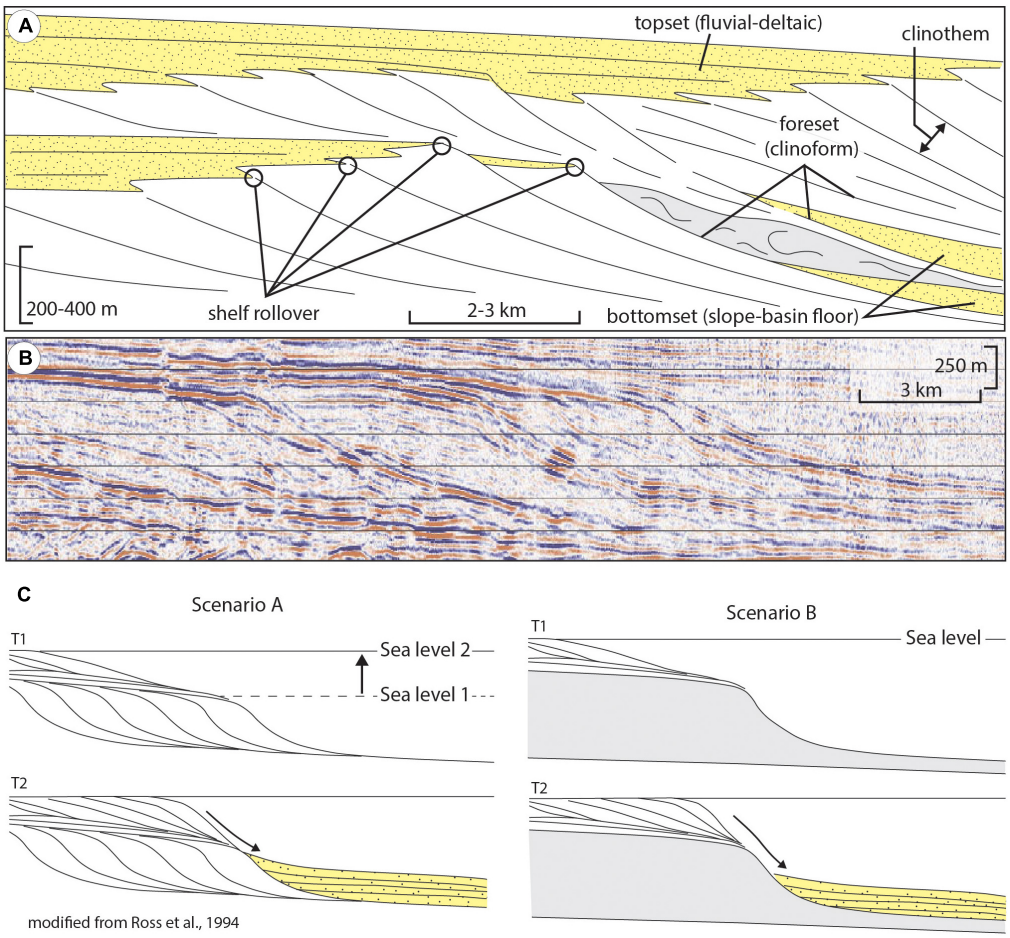

FIGURE 1 | (A) Schematic dip-oriented basin margin cross-section. Note the variety of clinoform scales indicated. **(B)** Seismic section from the Alaska North Slope showing clinoforms of moderate to high-relief; red = peak, black = trough, frequency ~36 Hz (United States Geological Survey Data accessed from www.sepmstrata.org). **(C)** Two scenarios of slope oversteepening that result in shelf-margin readjustment and phases of enhanced coarse-grained sediment delivery beyond the shelf margin. Scenario **(A)** results from a significant relative sea-level rise; after a substantial transgression, the slope profile becomes oversteep and unstable once it progrades back to the point where it reaches the former, drowned shelf margin. Scenario **(B)** results from the progradation of a shelf-margin system to the edge of an escarpment. In this instance, the slope also steepens and becomes more unstable, leading to onlap of basin floor fan deposits onto the slope (modified from Ross et al., 1994).

Campanian Cerro Toro Formation, a mudstone-dominated succession with a conglomeratic channel system situated along the length of the foredeep axis (**Figure 2D**; Crane and Lowe, 2008; Hubbard et al., 2008; Jobe et al., 2010). The subsidence rate waned and the basin underwent a ~2 Myr long period during which mass-failure processes dominated, presumably due to a change in hinterland dynamics and/or basin uplift (Daniels et al., 2018, 2019). Subsequently, the basin filled with the Campanian-Maastrichtian Tres Pasos and Dorotea formations, characterized by shelf-margin clinoforms that prograded along the basin axis, from north to south (Romans et al., 2009; Hubbard et al., 2010; Schwartz and Graham, 2015). The Tres Pasos Formation is a mudstone-dominated slope succession with intercalated sandy turbidite systems and mass-transport deposits (Smith, 1977; Shultz et al., 2005; Armitage et al., 2009; Auchter et al., 2016); these strata are overlain by genetically linked deltaic deposits of the Dorotea Formation (Arbe and Hechem, 1984; Macellari et al., 1989; Covault et al., 2009; Hubbard et al., 2010; Leppe et al., 2012; Schwartz and Graham, 2015; Schwartz et al., 2017; Manriquez et al., 2019). The deep-water basin (>1000 m relief) and basin axially oriented depositional systems (>40 km long slopes) promoted the development of shelf-margin clinoforms similar in scale to those of continental margins (**Figures 2E,F**; Carvajal and Steel, 2009; Hubbard et al., 2010; Romans et al., 2011).

METHODOLOGY

The study area is located at approximately 51° 00′ S and 72° 30′ W, adjacent to the Chile-Argentina border (**Figure 2**). We focus on a 15 km-long exposure of a high-relief shelf-margin depositional system at Cerro Cazador (**Figure 2C**). At this location, we record south-southeast paleoflow, which is

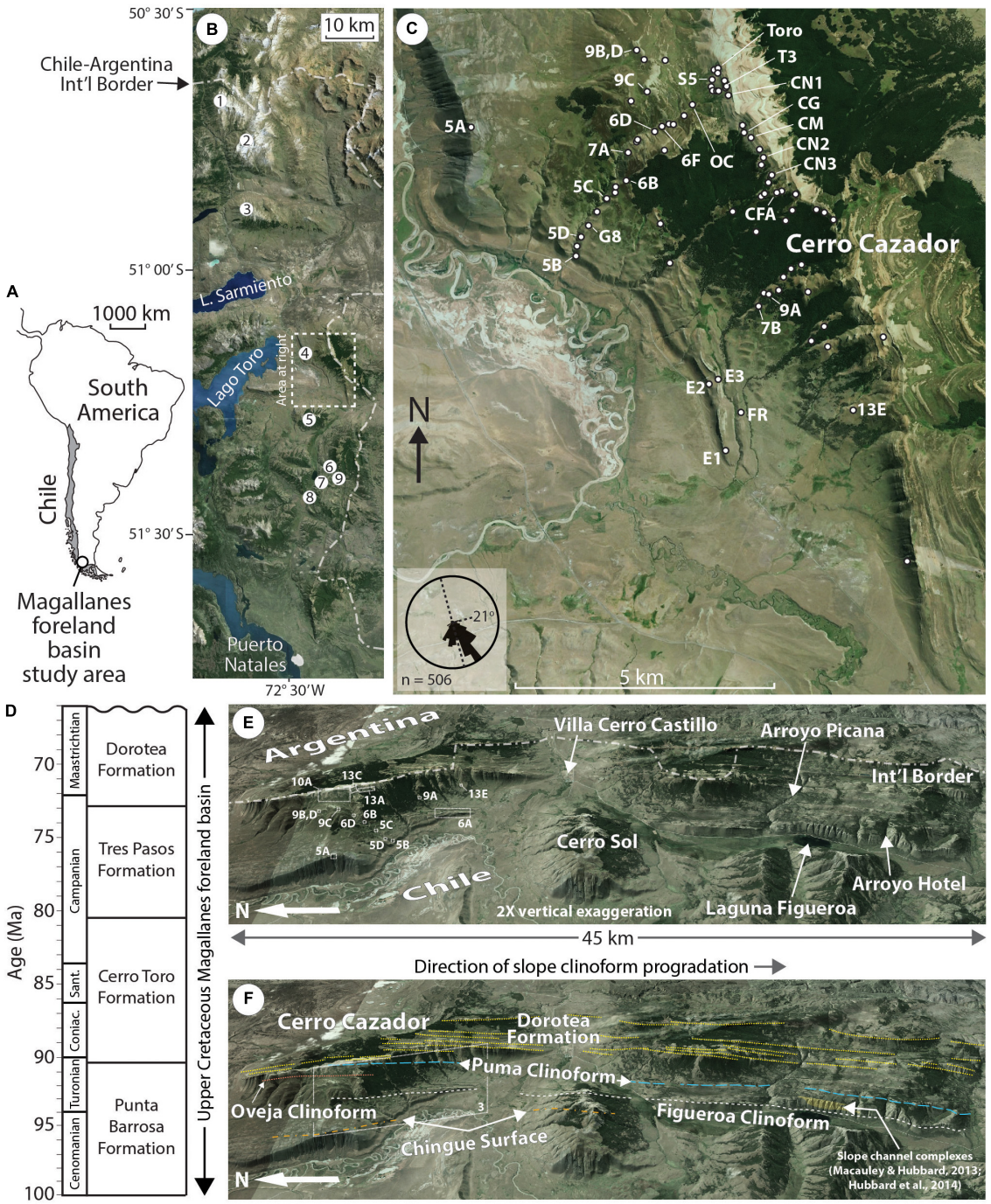

FIGURE 2 | Magallanes Basin stratigraphy and study context. **(A)** Continental-, **(B)** provincial- and **(C)** mountain- scale context for the study. Regional satellite image in **(B)** features previously studied Tres Pasos and Dorotea formation outcrops: (1) Cerro Divisadero, Romans et al., 2009; (2) Cerro Escondido, Covault et al., 2009; (3) Sierra Contreras, Armitage et al., 2009; (4) El Chingue Bluff, Shultz and Hubbard, 2005; (5) Cerro Sol, Hubbard et al., 2010; (6) Arroyo Picana, Pemberton et al., 2016; (7) Laguna Figueroa, Macauley and Hubbard, 2013; Hubbard et al., 2014; (8) Arroyo Hotel, Hubbard et al., 2010; and (9) Puma-Picana confluence, Reimchen et al., 2016. Paleoflow was orientated S-SE at 160°–170° on average, near parallel to the current structural orientation of the strata (strike = 165; dip = 21E) yielding a depositional dip perspective. White dots in **(C)** indicate outcrop locations studied. In instances where these are labeled with a preceding number, the label corresponds to the Figure number where this location is featured; labels with a preceding letter are locations that are featured within Figures. **(D)** Stratigraphic chart for the foreland basin in the vicinity of Cerro Cazador with the simplified stratigraphic architecture of the main lithostratigraphic units. The Tres Pasos and Dorotea formations are associated with the final fill of a long-lived deep-water seaway (modified from Daniels et al., 2019). **(E)** Eastward view of the area studied highlighting key geographical features and locations of areas featured in figures. **(F)** Same view as in Part **(E)** showing the stratigraphic framework of the area, featuring a dip-oriented cross-section of a high-relief clinoform system (cf. **Figure 1**). The Dorotea Formation consists of deltaic deposits whereas the underlying Tres Pasos Formation comprises genetically linked, southward-prograding clinoform strata. All satellite image data from Google, Landsat, Copernicus, 2016, http://google.com/earth/index.html.

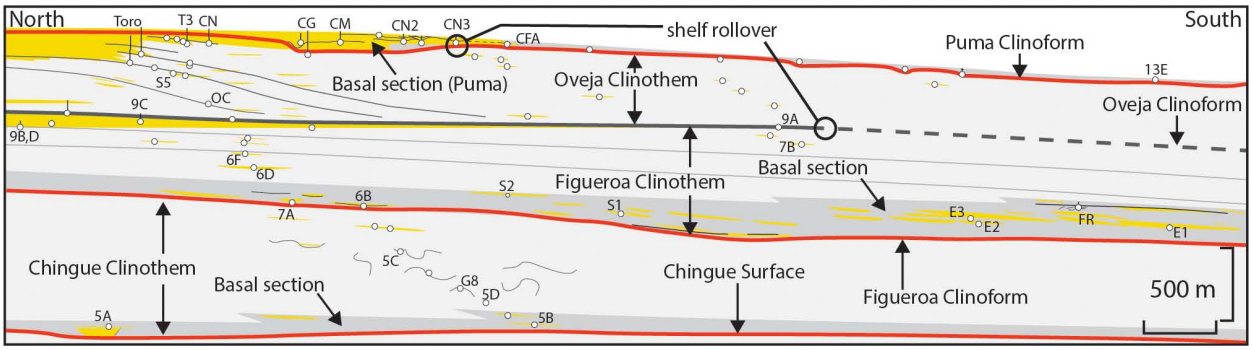

FIGURE 3 | Simplified depositional dip-oriented stratigraphic cross-section constructed from outcrop observations at Cerro Cazador (see **Figures 2E**, **4** for transect location). The main stratigraphic components and outcrop locations provide context for outcrop descriptions and interpretations. Note that thin vertical lines indicate locations of particularly long (>25 m) detailed measured sections. In general, sandstone-dominated strata are yellow and siltstone-dominated clinothem packages are gray; basal clinothem packages emphasized with a darker shade of gray. Thick, bold lines (red and dark gray) are interpreted clinoforms.

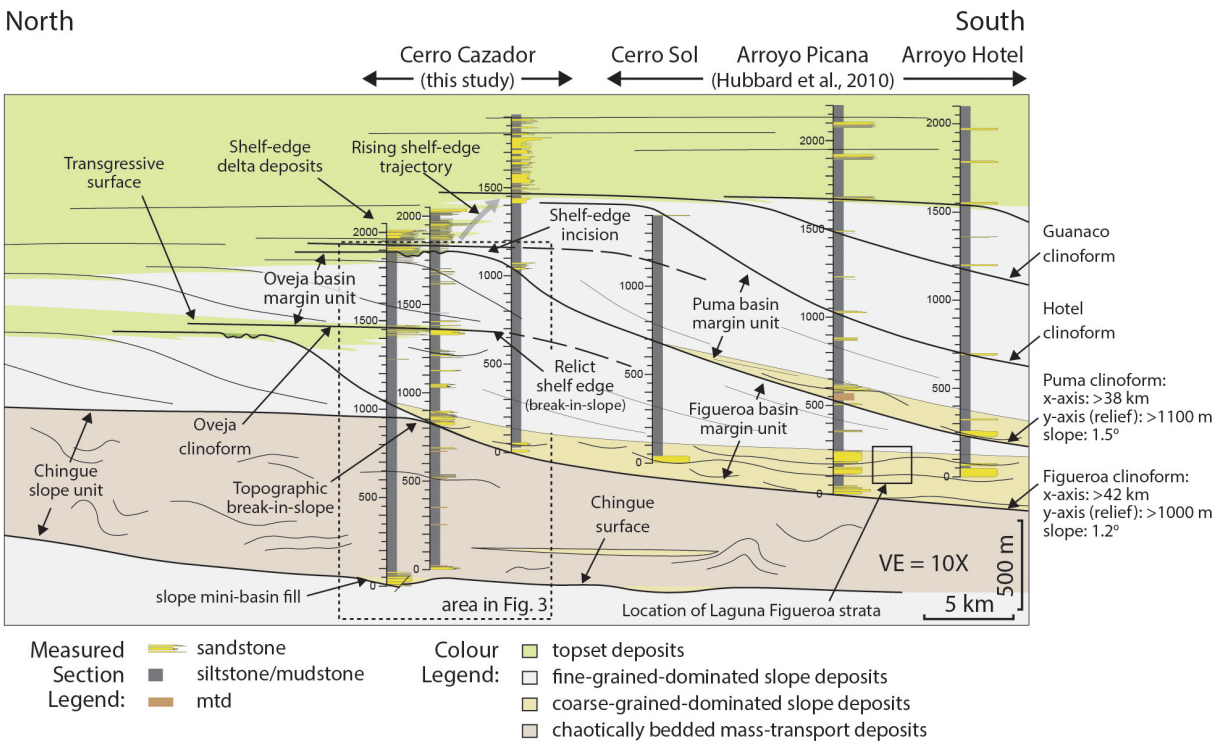

FIGURE 4 | Reconstructed dip-oriented regional cross-section of the Tres Pasos and Dorotea formations from Cerro Cazador to Arroyo Hotel, integrating data from this study, Hubbard et al. (2010), and Daniels et al. (2018) (**Figures 2E,F**). Note the presence of only two sandstone-prone stratigraphic intervals in the mudstone-dominated slope clinoform system, which immediately overlie the Figueroa and Puma clinoforms in the southern half of the transect.

approximately parallel to the N/NW-S/SE south trend of the outcrop (**Figure 2C**; Smith, 1977; Shultz and Hubbard, 2005; Bauer, 2012; Daniels et al., 2018). The correlation between deltaic and slope strata can be physically traced in the outcrop belt over several kilometers in many cases (**Figures 2F**, **3**, **4**). Relatively flat strata of the upper part of the Dorotea Formation at the top of the succession are preserved across the entire study area and are used as a datum, providing the basis for estimations of shelf-margin relief.

High-resolution satellite imagery draped on a digital elevation model was used to correlate the outcrop to the regional stratigraphic framework of Hubbard et al. (2010) to the south, which comprises a series of southward-prograding clinoforms and clinothems >35 km long and 900–1000 m thick (**Figures 2E,F**). Hubbard et al. (2010) were the first to interpret these clinoforms by tracing the base of thick (40–100 m), sandstone-rich packages exposed as prominent ridges 10–35 km long in the outcrop belt. These composite

sandy units are described as "basal clinothem packages" in this study, which directly overlie erosional surfaces that share characteristics of sequence boundaries (Mitchum et al., 1977; Houseknecht et al., 2009). Although clinoforms can be defined by relatively continuous shelf-margin mudstone-prone strata that potentially represent zones of maximum flooding (Galloway, 1989; Steel et al., 2008; Houseknecht et al., 2009), the large scale of the Tres Pasos-Dorotea clinoforms in the Magallanes Basin and sparse exposure of vegetated mudstone-prone strata make delineation of flooding surfaces unreliable over long distances. As such, it is likely that many more clinoforms are present in the outcrop belt than are detected and reported here; the identified clinoforms likely bound multiple clinothems (e.g., Patruno et al., 2015). Thus, these strata could be considered as clinothem sets or compound clinothems, but for simplicity we refer to them as clinothems throughout.

The dataset collected for this study includes 2980 m of measured stratigraphic section, which represents the foundation for facies analysis. Facies variations along individual clinoforms are documented from measurements of grain size, sedimentary structures, bed contacts, and trace fossils (summarized in **Table 1**). Detailed stratigraphic correlations are made by physically tracing surfaces as well as beds, and confirmed through the use of ground-based and aerial photo mosaics. Where tracing surfaces is not possible due to inaccessible topography, regional correlations (5–40 km) are made with high-resolution satellite data (<1 m resolution).

TRES PASOS AND DOROTEA STRATIGRAPHY AND SEDIMENTOLOGY

Regionally, the fill of the Magallanes Basin is characterized by southward prograding shelf-margin strata exposed for >100 km north-south distance (Romans et al., 2010; Daniels et al., 2018). We consider the clinoforms to be high relief, based on comparison to the compilation of Carvajal et al. (2009). In this section, we describe and interpret key characteristics of the Tres Pasos-Dorotea shelf-margin system, aspects of which were first broadly presented by Hubbard et al. (2010). Key components are the 40–100 m-thick basal clinothem packages (**Figure 3**), which variably extend at least tens of kilometers from Cerro Cazador (north) to Arroyo Hotel (south) (**Figure 4**). These sandstone-rich basal packages are overlain by fine-grained successions hundreds of meters thick, which compose the bulk of clinothem strata. Toward the north, clinothems are capped by resistant sandstone-rich (topset) deposits; these deposits generally pinch out southward (basinward).

The strata include a section of thick, mass-transport-deposit (MTD)-dominated strata (Chingue unit), and three shelf-margin units (i.e., Figueroa, Oveja, and Puma; **Figure 3**). The MTD-dominated Chingue unit and the progressively younger shelf-margin units (Figueroa through Puma) correspond to the four stages of basin evolution described by Daniels et al. (2018). Although the shelf-margin strata correlates farther to the south, our emphasis on clinothems associated with abundant slope sandstone focused our analysis on the Figueroa and Puma shelf-margin units (**Figure 4**). Due to the large scale of the shelf-margin strata and limited outcrop extent, only the youngest shelf-margin units (upper Figueroa, Oveja, and Puma) are exposed from topset through distal slope; the bases of the Figueroa and Chingue units are characterized exclusively by slope strata in the portion of the outcrop belt studied. There is a lack of evidence for unconfined submarine fan deposits at the distal end of the outcrop belt. It is plausible that unconfined deposits have not been encountered because a significant toe-of-slope break at the transition to the basin floor did not exist in the basin; both non- and deep-marine foreland basins commonly promote formation of long channel systems due to a preferred tectonic slope along their axes, as well as lateral confinement (e.g., Graham et al., 1975; Burbank, 1992; Malkowski et al., 2017; Sharman et al., 2018).

Like other outcrops of large-scale shelf-margin systems, the Tres Pasos-Dorotea deposits at Cerro Cazador provide primarily a two-dimensional (2-D) perspective of the ancient basin margin, limiting interpretations of stratigraphic evolution in 3-D. Considerable along-strike variability of continental margins on the modern seafloor (e.g., Olariu and Steel, 2009; Ryan W. B. et al., 2009) suggests that the same variation ought to be expected in the stratigraphic record of the Magallanes foreland basin margin (e.g., Martinsen and Helland-Hansen, 1995; Driscoll and Karner, 1999; Jones et al., 2015; Madof et al., 2016; Paumard et al., 2018; Poyatos-Moré et al., 2019).

The Chingue Unit

The Chingue deep-water unit is up to 900 m thick and exposed for 5 km along depositional dip (**Figure 4**). Due to the large thickness and areal extent of the stratigraphic unit, deposits of only a relatively short segment of the entire paleo-slope crop out at Cerro Cazador. A basal sandstone-rich Chingue stratigraphic package is 50–75 m thick (**Figure 3**) and consists of an upward coarsening and bed thickening succession (Facies F1, F3–5; **Figures 5A,B**) capped by a chaotically bedded deposit (Facies F2) and a sandstone-filled channel form (Facies F3; **Table 1**). The basal sandstone-rich Chingue stratigraphic package is lenticular in a depositional-dip perspective, and overlies a zone of growth faulting and abundant sandstone intrusions (**Figure 5A**). Overlying this basal package is ∼800 m of chaotically bedded strata (**Figure 4**).

Shultz and Hubbard (2005) attribute the basal sandstone-rich package of the Chingue deep-water unit to ponding in localized accommodation created by growth faulting on an unstable slope. The capping MTD and channel fill are interpreted to record healing of the accommodation and basinward stepping of a channel system down slope (cf. transient fan of Adeogba et al., 2005). Overlying this basal sandstone-rich section, the hundreds of meters of chaotically bedded deposits are attributed to long-lived mass wasting (Facies F2; **Figures 5C,D**; **Table 1**; Daniels et al., 2018). The propensity of MTDs is interpreted to record an extended period of out-of-grade slope processes, during which the upper slope was oversteepened and prone to regular failure (**Figure 4**; Ross et al., 1994; Prather et al., 2017). These MTD-dominated strata reach their maximum thickness at Cerro Cazador and thin southward (**Figure 4**).

TABLE 1 | Facies of the Tres Pasos and Dorotea formations at Cerro Cazador.

	Facies	Texture	Thickness	Physical structures	Grading	Sorting	Basal contact	Bed geometry	Lithological accessories	Trace fossils	BI	Trace fossil size and abundance	Interpretation
F1	Carbonaceous mudstone	siltstone and clay	3-400 cm	Planar laminae	None	Moderate-well	Gradational	Extensive 100's of meters	Organic detritus	*Th, Pl, Sk*	0–3	Small, rare	Low density gravity flow and suspension deposits
F2	Chaotically bedded sandstone and mudstone	fg ss, siltstone and clay	<10 m	Overturned and contorted beds, rare planar laminae	None	Poor-moderate	Discordant	Rafted siltstone blocks, lenticular sandstone beds, laterally extensive to locally contorted units	Organic detritus	np	0	np	Mass transport, including cohesive debris flow deposits
F3	Amalgamated sandstone	cg to mg ss with granules and pebbles	5–130 cm	Massive, planar laminae, asymmetrical ripple cross-stratification	Normal	Poor-moderate	Erosive 3–50 cm relief	Channelized 5–50 m	Mudstone intraclasts, rare shell molds	np	0	np	Traction deposits; high density turbulent flows
F4	Tabular non-amalgamated sandstone	cg to vfg ss with rare granules	1–105 cm	Planar stratification, asymmetrical ripple cross-stratification	Normal	moderate	Flat/sharp	Laterally extensive (up to 75 m) some beds thin laterally over 10–25 m	Rare mudstone intraclasts, organic detritus	*Sk, Th, Pl, Op*	0–2	Small to moderate, rare	Laterally extensive high to low density turbidites
F5	Lenticular non-amalgamated sandstone	cg to vfg ss with rare granules	1–150 cm	Planar stratification, asymmetrical ripple cross-stratification	Normal	moderate	Flat to erosive <5 cm relief	Beds thin over 10–75 m	Rare mudstone intraclasts, organic detritus	*Sk, Pl, Gy, Th, Op, He, CH, Ch*	0–2	Small to moderate, rare	Traction deposits; high density turbidites

(Continued)

TABLE 1 | Continued

	Facies	Texture	Thickness	Physical structures	Grading	Sorting	Basal contact	Bed geometry	Lithological accessories	Trace fossils	BI	Trace fossil size and abundance	Interpretation
F6	TCS lenticular sandstone	mg to fg	5–100 cm	trough cross-stratification, planar stratification, backset stratification	None to normal at very top	Poor-moderate	flat to erosive <5 cm relief	Lenticular 2–25 m	Rare mudstone intraclasts, organic detritus	*Sk, Pl, Op*	0–1	small, rare	Traction deposits; sustained unidirectional currents
F7	Lenticular sandstone	cg to mg ss with granules and pebbles, rare silt	10–120 cm	Trough cross-stratification, planar stratification, asymmetrical ripple cross-stratification	Normal	Poor-moderate	Erosive 5–100 cm relief	Channelized 10–40 m	Organic detritus, wood and plant debris), mudstone intraclasts	Np	0	np	Traction deposits; unidirectional channel flow
F8	TCS and planar laminated sandstone	cg to fg ss	10-100 cm	Planar stratification, tabular cross-stratification	None to slightly normal	Poor-moderate	Flat/sharp to slightly erosive 0–3 cm relief	Lenticular 10–70 m	Organic detritus, mudstone intraclasts	*Pl, Sk, Op, Gy, Pa, Te, fug*	0–2	Small - robust, rare	Sustained unidirectional flow, dune migration
F9	Hummocky cross-stratified sandstone	mg to fg ss	40–75 cm	Hummocky cross-stratification, symmetrical ripple cross stratification	Normal	Moderate-well	Wavy to flat	Lenticular 10–50 m	Minor organic detritus	np	0	np	Reworking of sediment through oscillatory currents
F10	Deformed sandstone	mg ss to siltstone	2–150 cm	Contorted layers, flames, ball and pillow	None to slightly normal	Moderate	Undulatory and irregular	Lenticular 5–20 m	Organic detritus	np	0	np	Water escape, slumping, loading
F11	Inversely graded sandstone	fg to mg ss	10–20 cm	Flames, ball and pillow	Reverse	Moderate	Flat/sharp	Lenticular 20–50 m	Organic detritus, rare mudstone intraclasts	np	0	np	Waxing gravity flow deposits, loading
F12	Organic rich mudstone and fine-grained sandstone	fg to vfg ss, siltstone and clay	1–100 cm	Planar laminations, asymmetrical ripple cross-stratification	Normal	Moderate	Gradational	Extensive 100's m's	Abundant organic detritus	*Pl, Th, Sk*	0–4	Small, rare to moderate	Low density turbidites and suspension deposits

(Continued)

TABLE 1 | Continued

	Facies	Texture	Thickness	Physical structures	Grading	Sorting	Basal contact	Bed geometry	Lithological accessories	Trace fossils	BI	Trace fossil size and abundance	Interpretation
F13	Normally graded sandstone	mg to vfg ss	1–50 cm	Planar stratification, asymmetrical ripple cross-stratification	Normal	Moderate-well	Flat/sharp	lenticular to tabular 10–100 m	Organic detritus	*Sk, Pl, Th, Op, Ch*	0–3	Small - moderate, rare to moderate	High density gravity flow deposits
F14	Carbonaceous mudstone and mudstone	siltstone and clay	1–500 cm	Planar laminae	None	Moderate	Gradational	Extensive 100's m's	Organic detritus	*Pl, Th, Sk*	0–3	Small, rare to moderate	Low density turbidites and suspension deposits

Bl, bioturbation index (cf. MacEachern and Bann, 2008); vfg, very fine-grained; fg, fine-grained; mg, medium-grained; cg, coarse-grained; ss, sandstone; Th, Thalassinoides; Pl, Planolites; Sk, Skolithos; Op, Ophiomorpha; Gy, Gyrolithes; He, Helminthopsis; Pa, Palaeophycus; Te, Teichichnus; Ch, Chondrites; fug, fugichnia; np, not present; TCS, trough cross-stratified.

The Figueroa Shelf-Margin Unit

The Figueroa shelf-margin unit is up to 600–700 m thick and exposed for >40 km along depositional dip (**Figure 4**). The basal Figueroa clinothem package is 75–125 m thick (**Figure 3**), primarily consisting of sandstone-filled channel forms (Facies F3-F4) encased in mudstone (Facies F1) and chaotically bedded deposits (Facies F2) (**Figures 6A–C**, **7A**). Channel forms are discontinuously exposed along the dip-oriented outcrop belt (**Figure 6A**). The base of this sandstone-rich succession defines the Figueroa clinoform, which has at least 900–1000 m of relief (**Figures 2F**, **4**; Hubbard et al., 2010; Daniels et al., 2018). Although the paleoslope gradient cannot be accurately measured in the uplifted stratigraphic succession, physical correlation in the outcrop belt demonstrates that it is steepest in the most proximal locations preserved (see Cerro Cazador locality in **Figure 4**). The topset deposit is not preserved in the outcrop belt for this clinoform segment.

The basal Figueroa clinothem package reflects a transition to increased sand delivery to the slope, supported by the presence of a 300 m-thick section of sandy slope turbidites at Laguna Figueroa (**Figures 4**, **8**; Hubbard et al., 2010). We postulate that a southward prograding delta reached the break-in-slope associated with the upper surface of MTD-dominated stratigraphy in the Chingue unit (**Figure 8**). The basin margin was oversteepened, and a prolonged period of coarse-grained sediment transfer off the shelf edge was initiated (cf. Ross et al., 1994; **Figure 1C**). A number of drivers for the sedimentation pattern in the basin could be drawn upon; however, the inherited basin topography evident from the stratigraphic analysis is suggestive that it was a dominant driver of off-shelf delivery of coarse-grained sediment.

The upper part of the Figueroa clinothem, stratigraphically overlying the sandstone-rich basal clinothem package (**Figure 3**), is 300–500 m thick at Cerro Cazador. To the north, it is capped by a series of upward-coarsening packages that are collectively up to 100–150 m thick (Facies F9–10, F12, F14) (**Figure 8** and **Table 1**). These packages pinch-out southward into widespread concordant fine-grained strata with isolated sandstone bodies (Facies F1, F4-F5) (**Figures 6D–F**) and localized MTDs (**Figure 7B**). The coarsening-upward packages are characterized by widespread evidence for shallow-marine conditions, including hummocky cross stratification, symmetrical ripples, abundant wood debris, and a low-diversity trace fossil suite (**Figure 9**; **Table 1**; MacEachern et al., 2005).

Upper Figueroa clinothem stratigraphy is interpreted to record the southward transition of deltaic topset deposits into mudstone-prone prodelta and slope strata (**Figures 3**, **4**).

The Oveja Shelf-Margin Unit

The Oveja shelf-margin unit is 300–400 m thick (**Figures 3**, **10A–C**), consisting of a 30–50 m thick upper section with 5–20 m thick upward-coarsening and bed-thickening successions with carbonaceous mudstone (F14), lenticular coarse-grained sandstone (F7), medium-grained sandstone (F10, F13), and hummocky cross-stratified sandstone (F9) (**Figures 7C**, **11**). This upper section transitions southward to laterally extensive

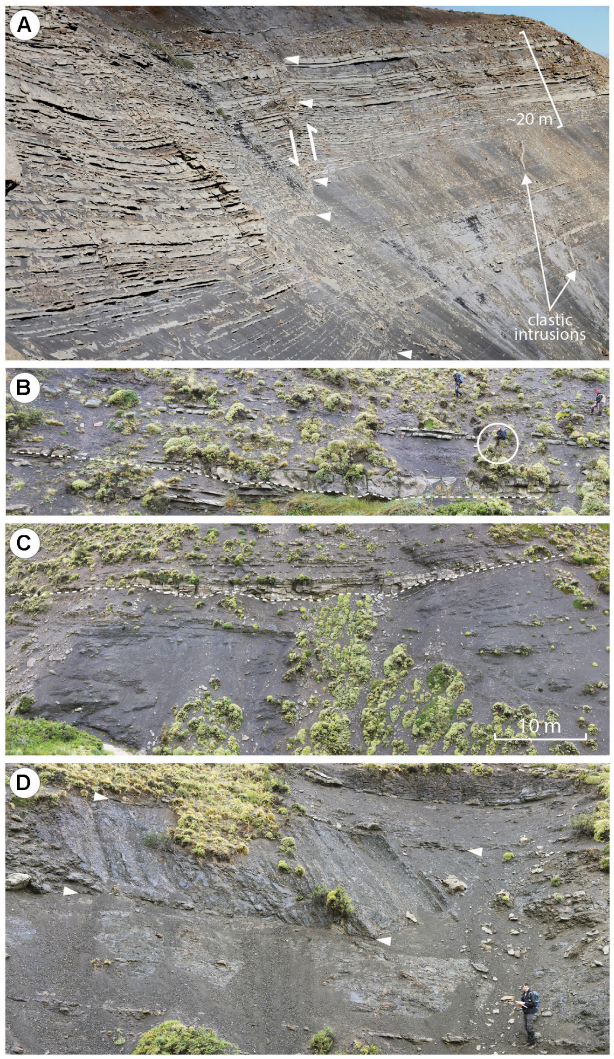

FIGURE 5 | Chingue slope unit stratigraphic architecture and facies. **(A)** Southward view of El Chingue Bluff (location 5A, **Figures 2C**, **3**) characterized by thin and thick bedded non-amalgamated turbidites (F4 and F5) within both the hanging wall and foot wall of a synthetic growth fault (indicated by white arrowheads); clastic intrusions are parallel or sub-parallel to the faults (cf. Shultz and Hubbard, 2005). **(B)** Interbedded mudstone (F1) and tabular non-amalgamated sandstone (F4), with lenticular scour-fill also present (F5) (base demarcated by thin dashed white line). Note person (circled) for scale. **(C)** Chaotically bedded fine-grained sandstone and mudstone deposits (F2) overlain by interbedded mudstone (F1) and sandstone (F4 and F5) (separated by white dashed line). The overlying facies are interpreted to have infilled rugose topography on top of the chaotically bedded deposits. **(D)** Slumped deposits (F2) encased in concordant mudstone (F1). The base and top of the slumped deposits are indicated with white arrowheads. Person at lower right for scale. All outcrop locations are denoted by Figure number within **Figures 2C**, **3**.

(km-scale), upward-coarsening and bed-thickening packages 20–60 m thick composed of interbedded fine-grained sandstone and mudstone (Facies F1, F4) (**Figures 10F,G**, **11**). The most distal deposits at the base, which make up most of the thickness of this unit, are primarily fine grained (Facies F1), punctuated by thin and lenticular sandstone-filled channel forms characterized by variably oriented stratification, including backsets (Facies F5-F6) (**Figures 10D,E** and **Table 1**). Notably, the upper half of this unit is exceptionally exposed along a series of unvegetated mountainside outcrops, which display seismic-scale stratal geometries characterized by basinward-dipping and basinward-thinning packages overlain by flatter units (i.e., apparent toplap) (**Figures 10A**, **11**). Collectively, these strata record the progradation of Oveja shelf-margin clinoforms.

We interpret the sharp lithologic change from deltaic sandstone of the upper Figueroa clinothem to overlying mudstone of the basal Oveja clinothem to reflect a backstep of the shelf (**Figure 8**; Houseknecht and Shank, 2004; Henriksen et al., 2011). The emplacement of distal slope facies on the proximal deltaic deposits (**Figures 3**, **4**, **10A–C**) indicates a landward shift of facies above the Figueroa clinothem. The magnitude of apparent backstep (i.e., >10 km) and landward shift of facies could represent a basin-wide event and reorganization of the shelf-slope system (**Figure 1C**; cf. Ross et al., 1994). Although the 3-D character of shelf-margin migration and its driving mechanism are speculative, orogenic activity in the adjacent Andean Cordillera and associated basin subsidence and transgression of the shoreline could have influenced stratigraphic sequence development (cf. Cant and Stockmal, 1989; Laskowski et al., 2013). Correlation between events in the fold-and-thrust belt (Fosdick et al., 2011) and the timing of this major landward retreat of facies cannot be constrained with current data. However, Daniels et al. (2018) showed that this transgression took place at ∼75 Ma, which corresponds to a time of significant global sea-level rise (Kominz et al., 2008).

We interpret that sustained sediment supply promoted progradation of the Oveja basin margin at Cerro Cazador (**Figures 8**, **11**). The 300–400 m-relief clinoforms prograded toward the abandoned, or relict shelf edge break-in-slope of the underlying high-relief Figueroa shelf-margin unit (**Figure 8E**). Regardless of potential external (e.g., Carvajal et al., 2009) or internal (e.g., Gerber et al., 2008) drivers on the accommodation/supply regime, as the relict shelf edge was encountered, a period of slope instability and failure (i.e., out-of-grade conditions) led to truncation of the Oveja clinothem topset and initiation of the Puma shelf-margin unit (**Figure 8F**).

The Puma Shelf-Margin Unit

The basal 20–100 m thick Puma basal clinothem package (**Figure 3**) is correlated for 35–40 km along paleoslope (**Figure 4**). In the most proximal location on Cerro Cazador (**Figures 11B**, **12**), sandstone-dominated strata (Facies F8, F10, F13) overlie undulatory surfaces with up to 4 m of relief. Basinward, upward-coarsening packages (F8, F10-F11, F13–14) are truncated by multiple concave-up surfaces with 5–60 m relief that are up to 150 m wide (minimum estimate based on partial strike view; **Figures 12**, **13A–D**). These surfaces define channel forms composed of mostly heterolithic deposits (F14) including lenticular sandstone beds with rare pebble lags (F7) (**Figures 7D**, **13C**). More distally, the basal Puma clinothem package largely comprises fine-grained deposits (F11, F13, F14) that are truncated

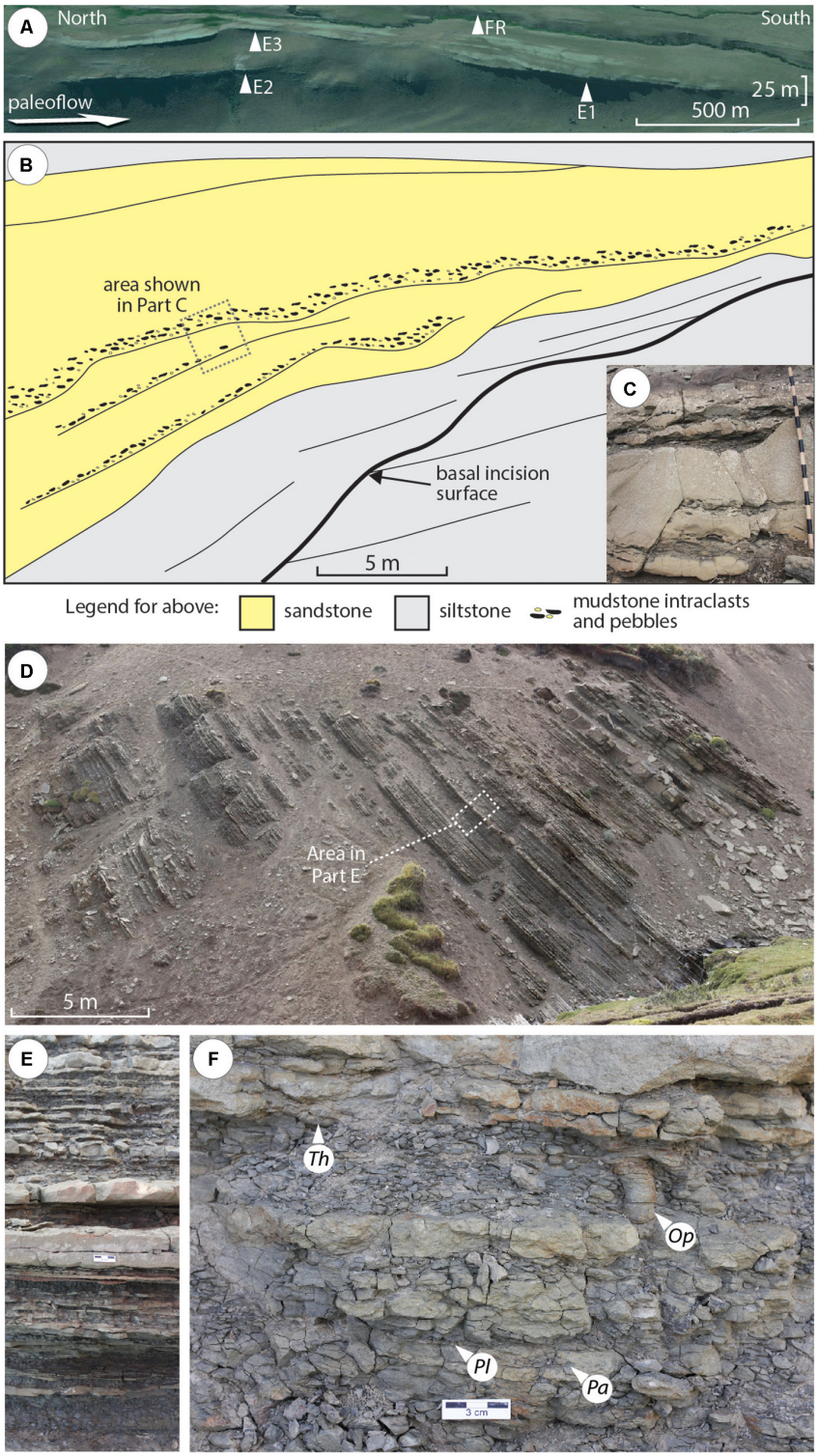

FIGURE 6 | Figueroa shelf-margin stratigraphic architecture and facies. **(A)** Depositional dip-oriented perspective satellite image featuring discontinuously resistant, along-slope channel sandstone deposits (white arrows; locations E1-E3 and FR in **Figures 2C**, **3**) (image data from Google, Landsat, Copernicus, 2016, http://google.com/earth/index.html). **(B)** Outcrop sketch of channel fill with the basal incision surface draped by mudstone-dominated turbidites, and subsequently overlain by amalgamated thick-bedded sandstone deposits (F3). **(C)** Variably amalgamated thick- to thin-bedded turbidites with common mudstone clasts; Jacob staff is 1.5 m in length. **(D)** Interbedded tabular, normally graded sandstone (F4) and carbonaceous mudstone (F1). **(E)** Interbedded tabular normally graded fine- to medium-grained sandstone (F4) and mudstone (F1) [location in **(D)**]. Scale bar in middle of photo is 3 cm long. **(F)** Bioturbated mudstone (F1) and fine- to medium-grained sandstone (F4) with rare *Thalassinoides* (Th), *Ophiomorpha* (Op), *Palaeophycus* (Pa) and *Planolites* (Pl). All outcrop locations are denoted by Figure number in **Figures 2C**, **3**.

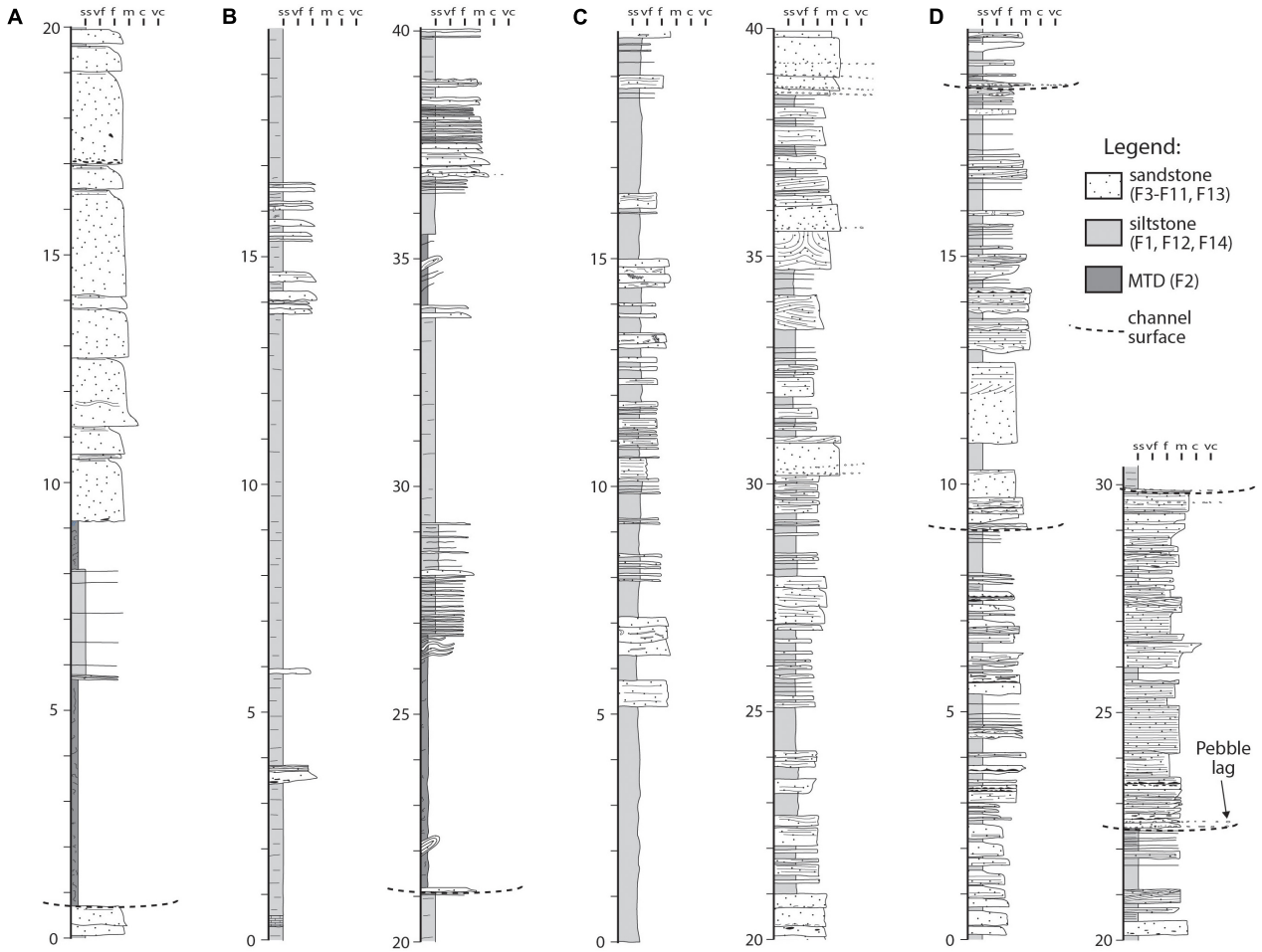

FIGURE 7 | Measured sections at selected outcrop locations, with locations of channelized erosion surfaces indicated. **(A)** Submarine channel fill in the basal Figueroa clinothem package (location 7A in **Figures 2C**, **3**). **(B)** Background slope deposits, including abundant fine-grained concordant strata as well as chaotically bedded MTD's in the upper Figueroa clinothem (location 7B in **Figures 2C**, **3**). **(C)** Overall upward coarsening succession of the Oveja shelf-margin topset (location Toro in **Figures 2C**, **3**). **(D)** Heterolithic channel fills at the Puma clinoform shelf margin; extrabasinal clast lags often mantle erosion surfaces (location CN2 in **Figures 2C**, **3**).

by concave surfaces with 1–5 m relief, which are overlain by similar interbedded facies (**Figures 13E,F**).

Evidence for mass wasting and slump-induced concave-up surfaces at the shelf margin at Cerro Cazador (**Figures 13A–D**) mark the position of the Puma shelf edge (**Figure 8**). As the Oveja basin margin prograded to the abandoned, relict shelf edge of the underlying Figueroa shelf margin unit (**Figure 8**), the shelf-margin relief increased and a period of slope readjustment ensued (**Figure 8E**). Regional mapping shows that just basinward of the associated shelf-edge delta, the paleoslope was at its steepest (**Figure 4**). The Puma margin records a basinward shift of facies and the introduction of abundant sand and gravel into the basin (e.g., Plink-Björklund and Steel, 2005; Houseknecht et al., 2009). Reimchen et al. (2016) demonstrated that 35 km basinward from the mapped shelf margin on Cerro Cazador, the Puma basal clinothem package is composed of conglomerate- and sandstone-dominated submarine channel deposits >60 m thick (**Figure 4**). After a period of enhanced coarse-grained sediment delivery to deep water, deposition of mudstone-prone slope facies ensued as the shelf-edge trajectory began to rise sharply (**Figure 4**). Slope strata are largely dominated by mudstone above the Puma clinoform across the Cerro Cazador study area.

The Stratigraphic Record of Sediment Transfer Along High-Relief Clinoforms

The outcropping stratigraphic record at Cerro Cazador shows evidence of net-depositional slope processes, including voluminous fine-grained strata that compose the Chingue unit, and the Figueroa, Oveja and Puma shelf-margin units (**Figure 4**). We interpret that a significant proportion of the slope strata is a result of hemipelagic or channel-overbank sedimentation of fine-grained material (Normark et al., 1993; Deptuck et al., 2003; Kane and Hodgson, 2011; Poyatos-Moré et al., 2016).

Shelf-edge to upper-slope conduit development directly overlying the Puma clinoform on Cerro Cazador, including

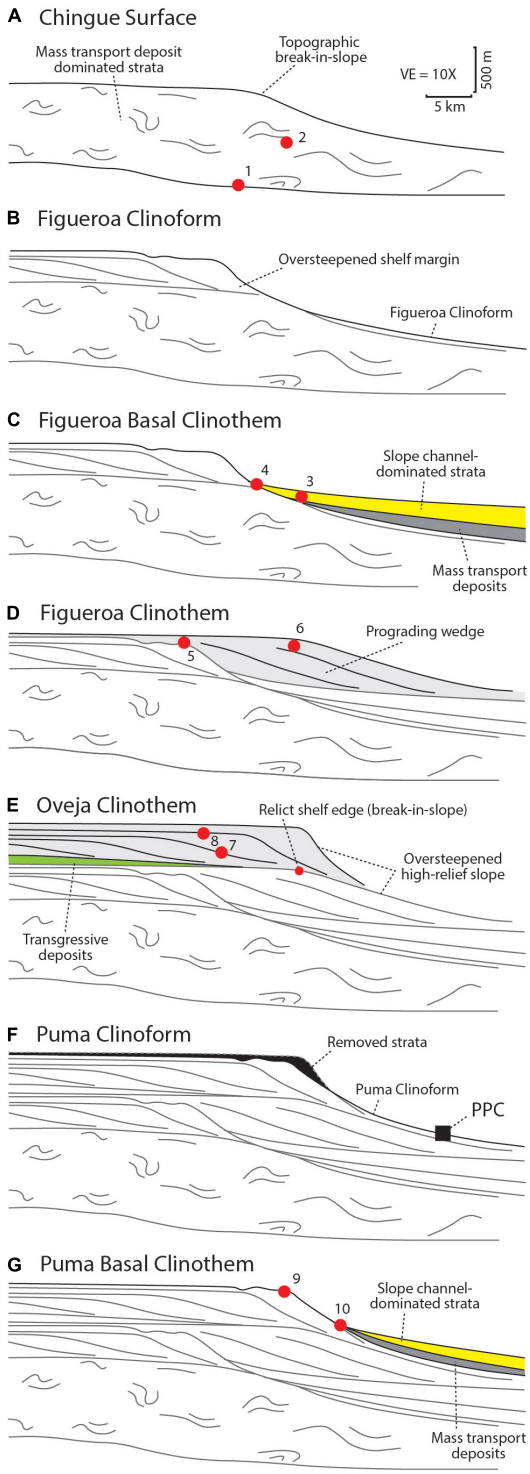

FIGURE 8 | Simplified depositional evolution of shelf-margin strata in the Magallanes Basin study area (from **Figure 4**). Part **(A)** is the first evolutionary stage through to part **(G)**, which is the last. Although at this scale clinoforms can only be drawn in a way that implies fairly straightforward correlation of simple surfaces over tens of kilometers, the results of detailed sedimentological and stratigraphic architecture analysis indicate that these surfaces are typically composite features that formed over a protracted period

(Continued)

FIGURE 8 | Continued

in many instances. In parts **(C,G)**, enhanced sediment bypass of the upper slope and sand/gravel deposition in the basin was facilitated. Red dots indicate approximate locations of features figured in the manuscript: 1 (**Figures 5A,B**); 2 (**Figures 5C,D**); 3 (**Figures 6A**, **14B**); 4 (**Figures 6B**, **7A**); 5 (**Figures 9B–D**); 6 (**Figures 7B**, **9A**); 7 (**Figures 10D,E**); 8 (**Figures 7C**, **11**); 9 (**Figures 7D**, **13A–D**); 10 (**Figure 13E**). Note that PPC = the confluence of the Puma Clinoform and Arroyo Picana.

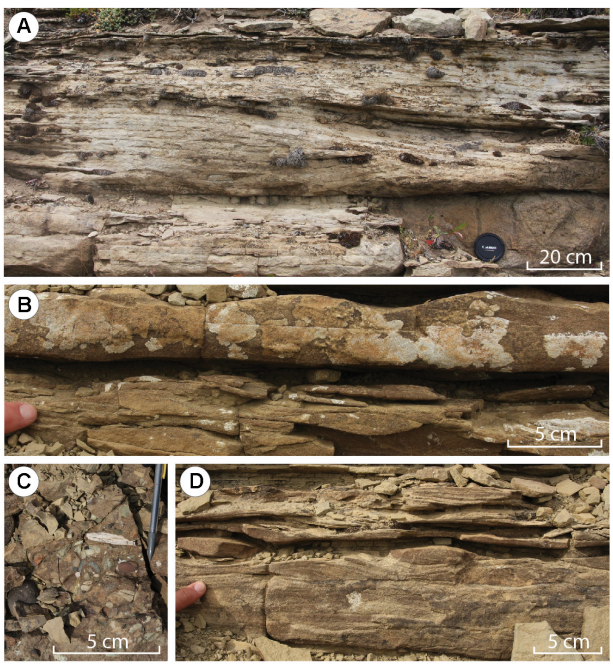

FIGURE 9 | Figueroa basin margin topset facies. **(A)** Hummocky cross-stratified (HCS) fine-grained sandstone (F9). **(B)** Symmetrical (top) and asymmetrical ripples (below) within fine-grained sandstone deposits (F9). **(C)** Coarse-grained sandstone with pebbles, granules, shell material, and woody debris (F7). **(D)** Planar laminae overlain by asymmetrical ripples in fine-grained sandstone deposits (F13). All outcrop locations are denoted by figure number within **Figures 2C,E**, **3**.

mass-wasting deposits overlain by channel forms up to 60 m thick, records initiation of a zone of predominantly coarse-grained sediment bypass (**Figures 13A–D**; cf. Nemec et al., 1988; Anderson et al., 1996; Jones et al., 2013). The channel fills are largely dominated by heterolithic thin- to thick-bedded strata with very thin sandstone and pebble lags that are among the coarsest deposits on the slope (**Figure 7D**). Such features are interpreted to provide a template for channelized sediment transfer to deep water (Mayall et al., 1992; Porebski and Steel, 2003; Ridente et al., 2007; Sylvester et al., 2012; Gomis-Cartesio et al., 2018; Gales et al., 2019).

Extensive tracts of basal clinothem packages, between the shelf edge and lower slope, are characterized by abundant cross-cutting erosional surfaces with >10 m of relief, as well as the complex superposition of channel fills, mass-wasting deposits, ponded sandstones and lag deposits (**Figure 14**). Collectively, these deposits highlight the protracted development of stratigraphic

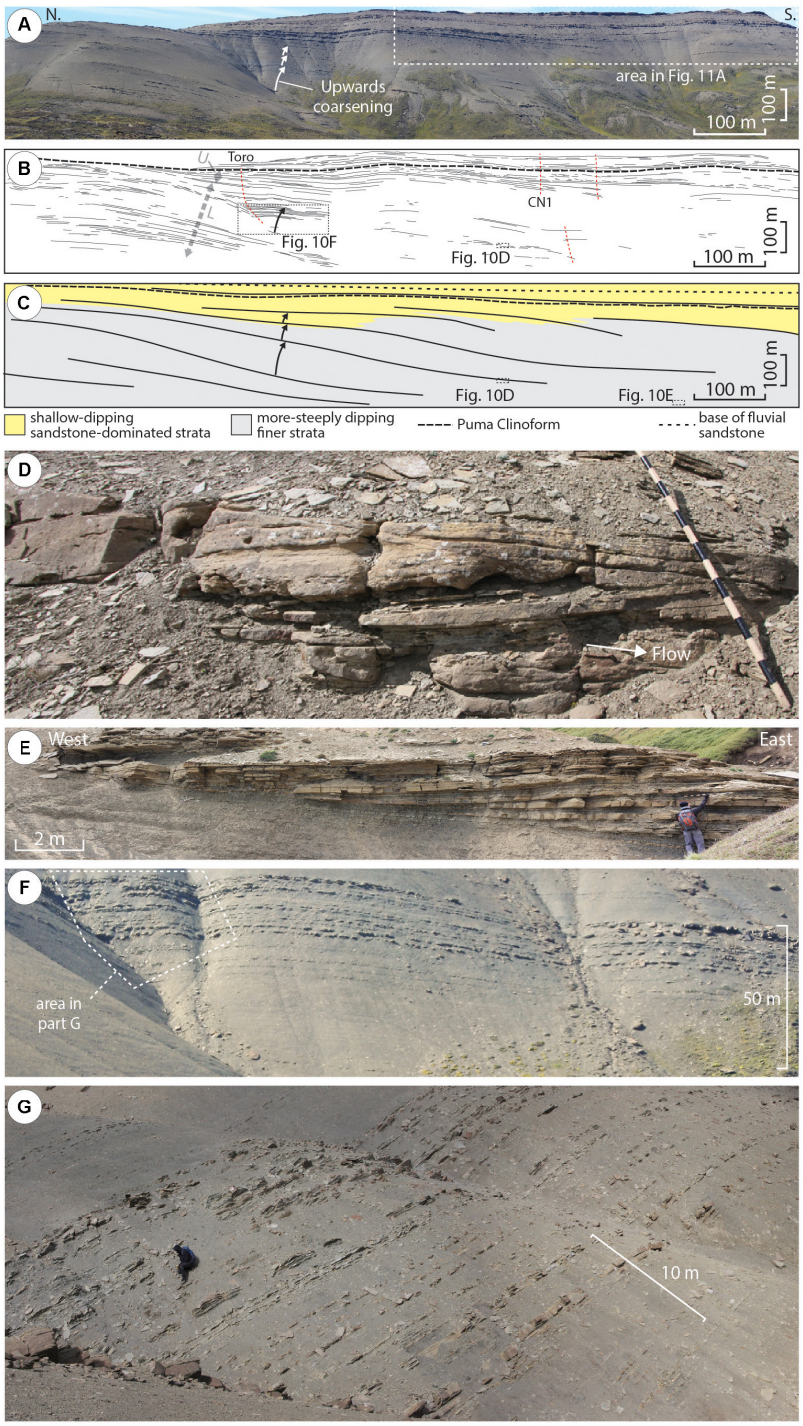

FIGURE 10 | Oveja shelf-margin stratigraphic architecture and facies. **(A)** Depositional dip perspective with an emphasis on coarsening upward packages (white arrows); the top of the section is dominated by sandy deposits (see **Figure 2E** for location). **(B)** Line-drawing trace of **(A)**, which enhances stratigraphic surfaces, including relatively shallow dipping topset strata (top of image) and more steeply dipping slope strata (middle to base of image). Gray dashed line approximates the boundary between lower (L), and upper (U) sections of the clinothem, as described. The black dashed black line demarcates the Puma clinoform. Selected measured section locations are shown with sub-vertical dashed red lines. **(C)** Schematic diagram showing the interpretation of stratigraphic architecture in **(A,B)**. **(D)** Non-amalgamated cross-bedded medium-grained sandstone (F6) within lenticular channel form [location shown on **(C)**]. Variably oriented cross-stratification, including backsets, suggest that these bodies formed during phases of high discharge (Ponce and Carmona, 2011; Hage et al., 2018). **(E)** Semi- to non-amalgamated wedge, in which the beds lap out or pinch out at the basal to marginal edge of a lenticular sedimentary body [location shown on Part **(C)**]. **(F)** Overall coarsening upward package [location shown on **(B)**]. **(G)** Interbedded normally graded planar-laminated sandstone (F13) and carbonaceous mudstone (F1) toward the top of a thick upward-coarsening section.

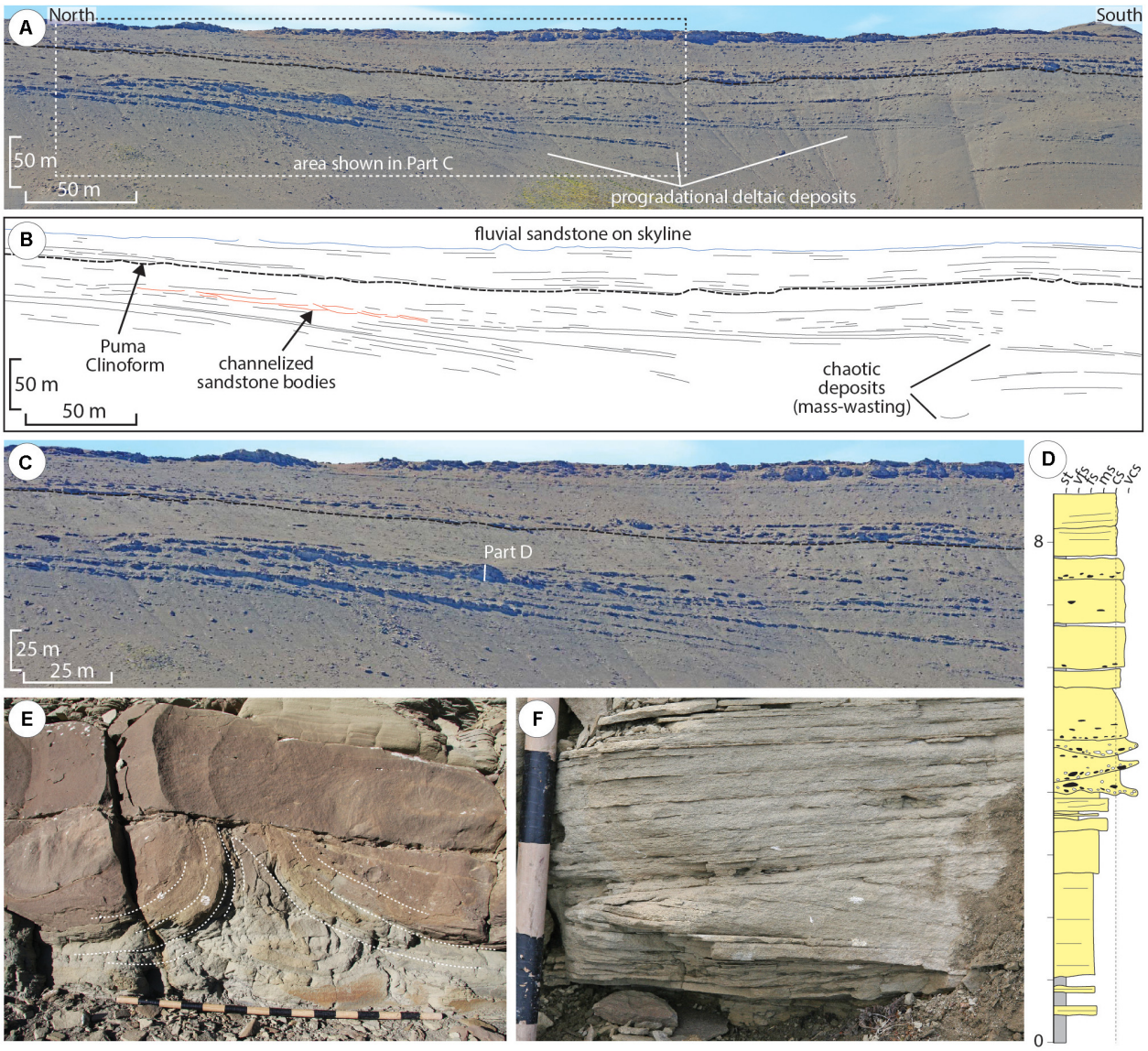

FIGURE 11 | (A) Photo-mosaic and **(B)** line-drawing trace of the upper portion of the Oveja shelf margin and the proximal deposits overlying the Puma clinoform showing river dominated deltaic clinoforms dipping basinward and transitioning into siltstone-dominated slope deposits. See **Figure 10A** for location. **(C)** Photo mosaic of deltaic clinoform topset highlighted in **(A)**. **(D–F)** Facies of the upper section of the Oveja clinothem, including: **(D)** Detailed stratigraphic section of typical sandstone-dominated coarsening upward package with interbedded carbonaceous mudstone (F14) and thin-bedded sandstone (F13) overlain by planar-laminated sandstone (F8) and coarse- to very coarse-grained lenticular sandstone (F7). Section location is shown in **(C)**. **(E)** Loading structure in medium-grained sandstone (F10); Jacob staff at base of photo is 1.5 m long (outcrop location is top of Toro section; **Figure 3**). See bed in measured section (**Figure 7C**) at 35 m for stratigraphic context. **(F)** Planar and trough cross-stratified medium-grained sandstone (F7); 10 cm intervals indicated on Jacob staff. Location is section CN (**Figure 3**).

surfaces in response to a variety of processes including erosion, sediment bypass, mass-wasting and deposition from gravity flows (Hodgson et al., 2016). Bed-scale evidence for high-energy currents that bypassed a portion of their sediment load along the basal sections of the Figueroa and Puma clinothems include: (1) conglomeratic lag deposits; (2) cross bedding; and (3) mudstone drapes that mantle erosion surfaces, which are interpreted to record deposition from the tails of largely bypassing turbidity currents (**Table 1**; cf. Mutti and Normark, 1987; Stevenson et al., 2015). Sedimentary body-scale evidence for prolonged sediment transfer across the Magallanes Basin slopes are represented by mass-wasting deposits (F2) including large rafted sediment blocks (**Figure 13B**), channel forms with evidence for a polyphase history of multiple cut-and-fill events (5–20 m thick) (**Figures 6A–C**, **7A**), and channel forms filled primarily with thinly interbedded turbidites (**Figures 13E,F**; cf. Hubbard et al., 2014; Stevenson et al., 2015).

Perhaps the most significant record of sediment bypass along the Figueroa and Puma basal clinothem packages in the Cerro Cazador study area is the increase in overall proportion of

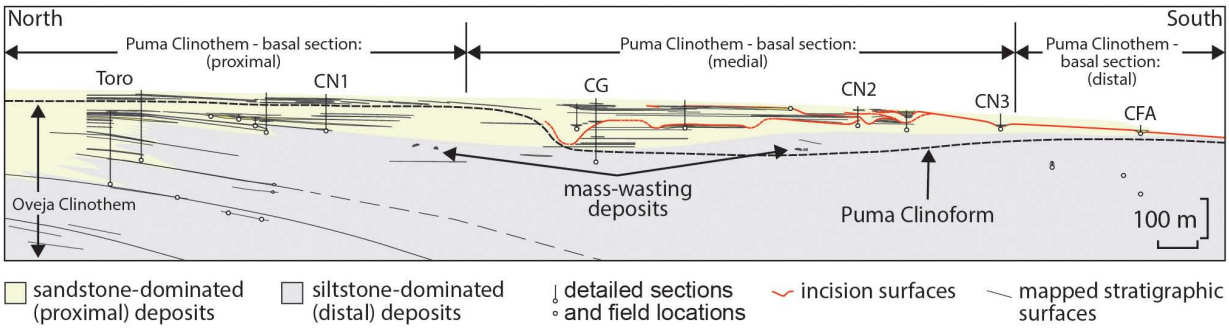

FIGURE 12 | Depositional dip-oriented cross-section (no vertical exaggeration) of the proximal through distal Puma basal clinothem package. Main incision surfaces and mapped stratigraphic surfaces, as well as measured section locations, are indicated (key section locations shown in **Figure 3**).

sandstone and conglomerate deposits from upper slope strata downslope 30–40 km to the south, in the vicinity of Arroyo Picana and Laguna Figueroa (**Figures 4**, **8**; Macauley and Hubbard, 2013; Hubbard et al., 2014; Pemberton et al., 2016; Reimchen et al., 2016). Coarse-grained lower-slope to basin-floor deposits are commonly linked to laterally extensive (kilometers), deep (10's of meters) incisions and canyons developed along the coeval shelf margin (e.g., Anderson et al., 1996; Johannessen and Steel, 2005; Ryan M. C. et al., 2009; Henriksen et al., 2011; Sylvester et al., 2012).

DISCUSSION: DEPOSITIONAL TOPOGRAPHY CONTROL ON SLOPE READJUSTMENT

The Campanian shelf-margin to slope depositional system at Cerro Cazador is dominated by mudstone across the 2-2.5 km thick and >60 km long transect (**Figures 2F**, **4**). Two prominent sandstone-rich packages mantle clinoform surfaces (i.e., Figueroa and Puma basal clinothem packages), standing out amongst the fine-grained stratigraphic backdrop. As such, they represent an opportunity to investigate the topographic controls on coarse-grained sediment delivery across a high-relief basin margin in the context of well-defined stratigraphic architecture, sediment-routing history, and source-area evolution (Romans et al., 2010, 2011; Fosdick et al., 2011; Bernhardt et al., 2012; Daniels et al., 2018).

We document ∼8 Myr of coarse-grained sediment transfer beyond the shelf margin in the deep-water Magallanes Basin (Daniels et al., 2019). Ross et al. (1994) proposed a series of mechanisms associated with shelf-margin readjustment that lead to enhanced coarse-grained sediment delivery beyond the shelf margin (**Figure 1**); however, the predicted stratigraphic architecture has yet to be widely linked to an outcrop record.

At Cerro Cazador, an early phase of instability is recorded by the Chingue unit, which comprises growth faults, extensive sandstone intrusions, and chaotically bedded deposits indicative of unstable slope conditions (**Figures 4**, **5**). These strata accumulated over 2-2.5 Myr and are mapped beyond the study area for up to 100 km north-south along depositional dip (Daniels et al., 2018). The extensive period of mass wasting resulted in a southward-thinning wedge of dominantly MTDs up to 900 m thick at Cerro Cazador, where it then thins to <500 m southward over a distance of only ∼20 km. We speculate that the thickest composite slope sandstone accumulation (∼300 m) in the basin resulted from progradation of the Figueroa basin margin to the break-in-slope at the top of the Chingue interval where MTDs begin to thin rapidly to the south (**Figure 8**). This observed change in basin margin architecture associated with prominent antecedent topography combined with the introduction of voluminous sand and gravel to the basin is consistent with the interpretation that the clinoform slope oversteepened, initiating the long-lived (up to >2 Myr; Daniels et al., 2018) Figueora channel system. Up slope, the Figueroa system is characterized by substantial erosion and sediment bypass, which transitions down slope to hundreds of meters of submarine channel strata that is comparable to channel deposits in continental margin strata (Macauley and Hubbard, 2013; Fowler and Novakovic, 2018; Pemberton et al., 2018; Jackson et al., 2019). The generation of this oversteepened slope is similar to a mechanism proposed by Ross et al. (1994), wherein steep slopes develop as a result of fluctuating carbonate and siliciclastic deposition and/or tectonic deformation. In mixed siliciclastic and carbonate systems, following carbonate platform development, deltas reach the relict carbonate platform edge and the oversteepened slope leads to prolonged coarse-grained sediment delivery to deep water (see Scenario B; **Figure 1C**). Using a modeling approach, Uličný et al. (2002) showed that 2-D stacking patterns of shelf-slope-basin clinoform systems are highly sensitive to initial depth (i.e., water depth at onset of deposition). Their study focused on tectonic (fault) inheritance whereas we emphasize topography inherited from the previous depositional phase. In the Chilean basin, instead of development of a break in slope at a relict carbonate platform edge, a morphologically similar scenario was established through the emplacement of mass-transport deposits prior to development of the Figueroa shelf-margin (**Figure 8A**).

The large-magnitude backstep on top of the Figueroa basin margin set the stage for an additional, protracted phase of slope instability and submarine-fan development

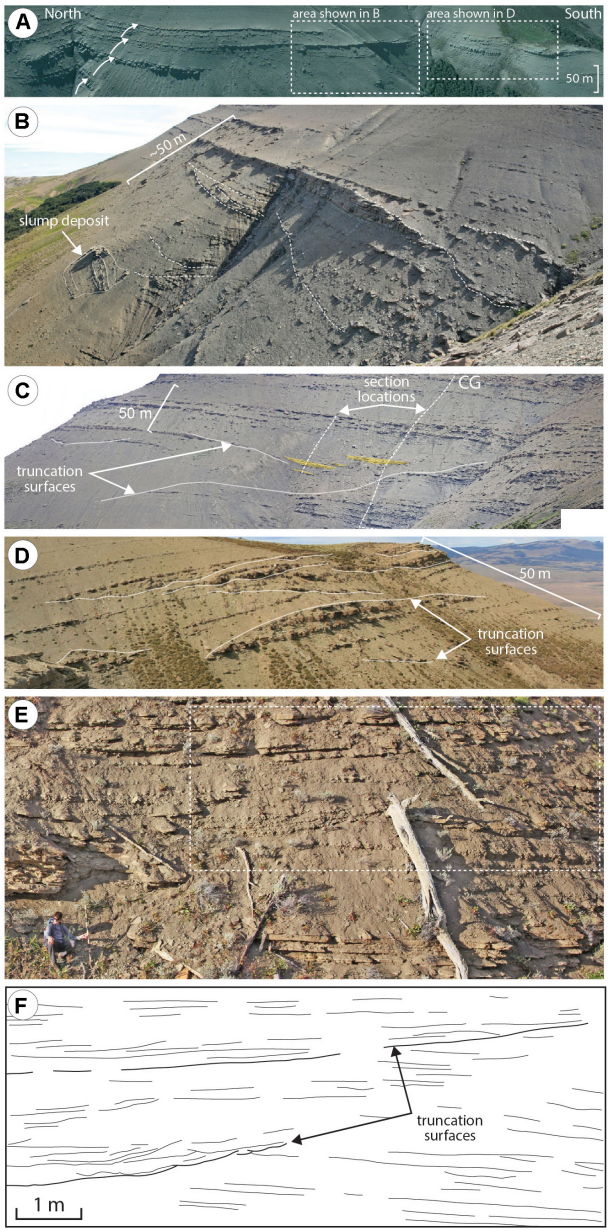

FIGURE 13 | Puma basal clinothem package stratigraphic architecture and facies. **(A)** Dip-oriented satellite image of Cerro Cazador near the interpreted Puma clinoform shelf margin (refer to **Figure 2E** for location). White arrows highlight coarsening upward packages (image data: Google, Landsat, Copernicus, 2016, http://google.com/earth/index.html). **(B)** Incision surfaces (dashed white lines) cutting deltaic strata at the shelf margin. Location shown in **(A)**. **(C)** Strike perspective of a significant incision surface (lowest example), which truncates interbedded mudstone and sandstone, and is infilled with comparable facies as well as channelized sandstone (yellow). Paleoflow is approximately out of the page; sub-vertical white lines indicate the location of measured sections (**Figure 2E** for location). **(D)** Multiple erosion surfaces (white lines) that truncate deltaic deposits in proximity to the shelf edge rollover. Location shown in **(A)**. **(E)** Photograph and **(F)** line drawing trace of fine-grained sandstone and mudstone at a distal location of the Puma basal clinothem package. Truncation surfaces are apparent, and erosional relief is in-filled with facies similar to that which was incised. Outcrop location denoted on **Figures 2C,E**, **3**.

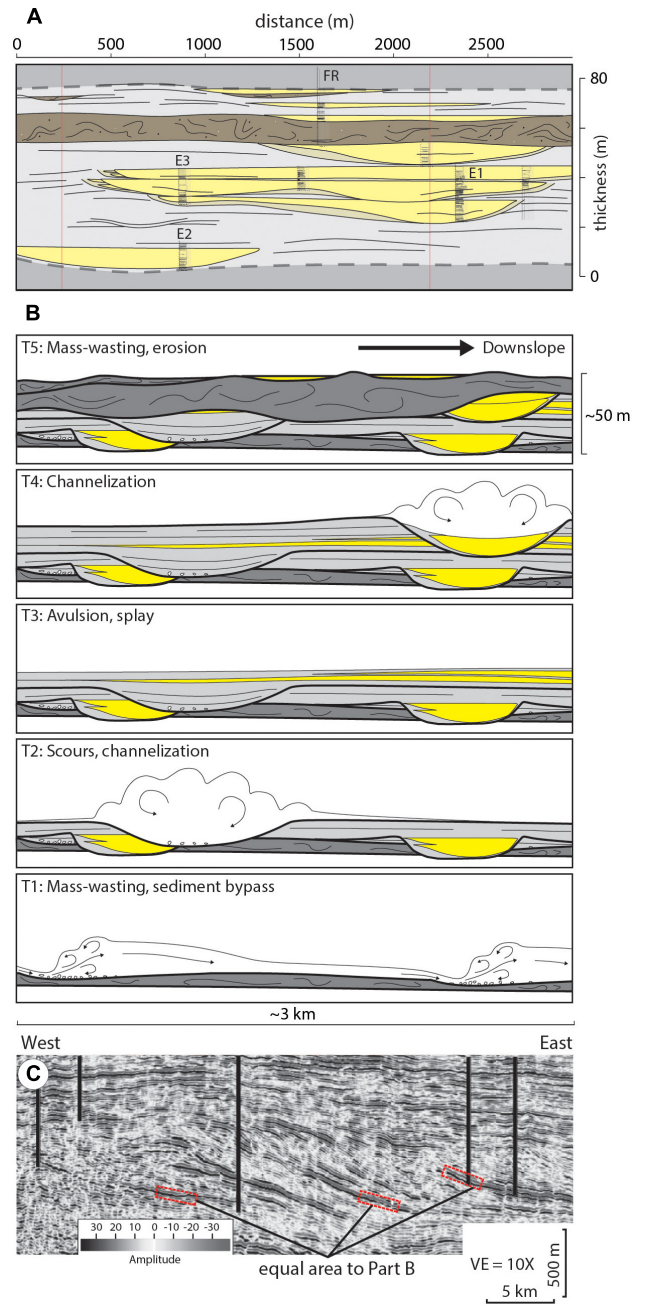

FIGURE 14 | (A) Dip-oriented schematic cross-section of channelized strata that compose a segment of the basal Figueroa clinothem package (see **Figure 6A** for outcrop overview). A similarly scaled perspective to this section is presented at various locations in **(C)** (red outlined boxes). **(B)** Schematic evolution of the sandstone-prone basal clinoform package in **(A)**. The area featured is comparable in scale and character to that featured in **(A)**. A sustained period of elevated off-shelf coarse-grained sediment transfer results in a composite sedimentary package defined by deposits that record erosion, mass-wasting, sediment bypass and deposition. **(C)** Vertical seismic section from the Magallanes Basin highlighting prograding clinothems up to 600–800 m thick, providing context for the basal clinothem segment featured in **(A)** (modified from Gallardo, 2014). The Late Eocene-Early Miocene strata record the infilling of the deep-water basin approximately 150 km south of the Cerro Cazador study area along the foreland basin axis.

(**Figure 8E**). This backstep is followed by the progradation of the Oveja basin margin to the abandoned, relict shelf edge of the Figuoera basin margin. The corresponding change in shelf-margin physiography led to a period of oversteepening that resulted in erosion of Oveja shelf-margin strata and initiation of the coarse-grained basal Puma clinoform package (**Figures 8F,G**). Similar to Figueroa strata, submarine-channel systems that are compositionally and architecturally similar to examples documented from continental margins are mapped along the system (Reimchen et al., 2016). The observed stratigraphic architecture at Cerro Cazador is consistent with scenario A of Ross et al. (1994), as shown in **Figure 1C**.

The erosional Figueroa and Puma clinoforms mark the disruption of a graded shelf-margin profile (**Figure 4**). Antecedent topography inherited from preceding phases significantly influenced the development of subsequent shelf margins including oversteepened upper slopes, and the transfer of coarse-grained sediment to deep water. Whether the inherited topography was a result of initial configuration (e.g., tectonic) or from predecessor clinoform shelf-margin position, the break in the slope profile caused the system to reach a disequilibrium state.

An important goal of sedimentary geoscientists is to gain insights into the controls on sedimentation and the creation of the depositional record for prediction in analogous settings. In an effort to communicate to colleagues and the broader geoscience community, we commonly attempt to place our interpretations in the context of allogenic versus autogenic controls (e.g., Beerbower, 1964; Paola et al., 2009). Allogenic controls are external to the sediment-routing and depositional system, including changes in eustatic sea level, tectonics, climate, and initial geometry of the receiving basin, whereas autogenic controls are internal to the sedimentary system, including intermittent sediment storage producing episodic, spatially discontinuous sedimentation (Romans et al., 2016; Hajek and Straub, 2017) and landward retreat of deltaic prisms in response to changing area and slope during deposition (Muto and Steel, 2002). However, some controls do not clearly fit into an either/or, allogenic/autogenic dichotomy. The disruption of graded shelf-margin profiles in response to inherited depositional topography during basin evolution is one such control. For example, although receiving-basin geometry can be considered an allogenic control governed by underlying tectonic configuration (Nelson and Kulm, 1973; Mutti and Normark, 1987), subsequent basin filling creates the depositional topography across which sediment transport and deposition occur to create stratigraphic architecture (e.g., Burgess et al., 2008). In this way, both external tectonic underpinning and internal dynamics of sedimentation govern resultant topography, which, in turn, influences the occurrence and position of shelf margins prone to deliver coarse sediment to the basin. Beyond understanding controls on margin evolution through major slope readjustments, there are implications for reservoir prediction associated with hydrocarbon exploration or carbon storage (see Ross et al., 1994); for example, the thickest, coarsest turbidite accumulations onlap erosional shelf-margin clinoforms and develop downstream of paleotopographic escarpments (**Figures 8C,G**). Additionally, with sufficient data coverage (outcrop or subsurface) the prediction of stacking patterns and facies in the context of inherited topography has the advantage of such features being potentially preserved and identified in the physical stratigraphic record without invoking assumptions about external forcings that are difficult or, in some cases, impossible to constrain.

CONCLUSION

A large-scale shelf-to-slope depositional system featuring basin margins with >1000 m paleobathymetric relief and slope lengths >40 km is preserved in outcropping Cretaceous strata of Chilean Patagonia. The depositional architecture observed in these outcrops is analogous to seismically imaged clinoforms of slope systems worldwide. The strata are characterized by evidence for the development of two key coarse-grained sediment-delivery systems that resulted in fairways of sandstone-dominated submarine-channel deposits >100 m thick in the deep-water basin: the Figueroa and Puma clinoforms. The stratigraphic position and architecture of each leads to an interpretation that they formed during major slope readjustments, across initially oversteepened depositional topography, which resulted in transient out-of-grade slope conditions. Strata directly overlying the Figueroa and Puma clinoforms (i.e., basal clinothem packages) are sandstone-rich, recording phases of enhanced coarse-grained sediment delivery to the deep-water basin. The 35 km long and up to 2.5 km thick stratigraphic section represented by the two slope systems was largely associated with mudstone, deposited over 3–4 Ma. The only two large-scale sandstone accumulations in the 2-D outcrop belt are recorded by the Figueroa and Puma basal clinothem packages, demonstrating the importance of major slope readjustments in margin evolution. Pre-existing depositional topography controls the locations of subsequent shelf margins and coarse-grained sediment delivery to deep water. Understanding this control has predictive value in analogous settings that were subjected to intermittent oversteepening and transient phases of coarse-grained sediment bypass to deep water.

DATA AVAILABILITY STATEMENT

All datasets generated for this study are included in the article/supplementary material.

AUTHOR CONTRIBUTIONS

DB did the fieldwork as a graduate student and wrote the initial draft. SH envisioned the project, secured the funding, assisted with fieldwork, and edited the manuscript. JC and BR assisted in the field and with manuscript preparation, including formulating the purpose, and organization of the manuscript.

FUNDING

Support for this research was provided by the Chile Slope Systems Joint Industry Project, members of which include Anadarko, BG Group, BHP Billiton, BP, Chevron, ConocoPhillips, Equinor, Hess, Maersk, Marathon, Nexen-CNOOC, Shell, and Repsol. Additional financial support was provided by the Natural Sciences and Engineering Research Council (Grant number RGPIN/341715-2013 to SH).

ACKNOWLEDGMENTS

The results presented benefited substantially from discussions with Andrea Fildani (Deep Time Institute), who first visited Cerro Cazador in 2008. Andrew Madof (Chevron USA) provided insightful input that shaped some of the ideas presented in this work. Fieldwork was assisted by Ryan Macauley, Sean Fletcher, Kerrie Bann, Keegan Raines, Erin Pemberton, and Kirt Campion. We thank Mr. Mauricio Alvarez Kusanovic and Ms. Hella Roerhs Jeppesen for graciously allowing us to access their land. The comments from Frontiers reviewers GH and NP improved the clarity of the manuscript immensely and are much appreciated. Reviews of an earlier version of this manuscript by Drs. Sverre Henriksen (Equinor), Ron Steel (UT Austin), and Chris Jackson (Imperial College London) significantly improved the focus of the manuscript – we appreciate their significant efforts on our behalf. JC acknowledges support of the Quantitative Clastics Laboratory sponsors.

REFERENCES

Adeogba, A., McHargue, T. R., and Graham, S. A. (2005). Transient fan architecture and depositional controls from near-surface 3-D seismic data, Niger Delta continental slope. *AAPG Bull.* 89, 627–643. doi: 10.1306/11200404025

Anderson, J. B., Abdulah, K., and Sazalejo, S. (1996). "Late quaternary sedimentation and high-resolution sequence stratigraphy of the east Texas shelf," in *Geology of Siliciclastic Shelf Seas*, eds M. de Batist, and P. Jacobs, (London: Geol. Soc. Special Publication), 95–124. doi: 10.1144/gsl.sp.1996.117.01.06

Arbe, H. A., and Hechem, J. J. (1984). Estratigrafı'a y facies de depo′sitos marinos profundos del Creta′cico Superior, Lago Argentino, Provincia de Santa Cruz (Stratigraphy and deep marine deposition facies of the Upper Cretaceous, Lago Argentino, Santa Cruz). *Congreso Geologico Argentino* 9, 7–41.

Armitage, D. A., Romans, B. W., Covault, J. A., and Graham, S. A. (2009). The influence of mass-transport deposit surface topography on the evolution of turbidite architecture: the sierra contreras, tres pasos formation (Cretaceous), southern Chile. *J. Sed. Res.* 79, 287–301. doi: 10.2110/jsr.2009.035

Auchter, N. C., Romans, B. W., and Hubbard, S. M. (2016). Influence of deposit architecture on intrastratal deformation, slope deposits of the Tres Pasos Formation. *Chile. Sed. Geol.* 341, 13–26. doi: 10.1016/j.sedgeo.2016.05.005

Bauer, D. B. (2012). *Stratigraphic Evolution of a High-Relief Slope Clinoform System, Magallanes Basin, Chilean Patagonia*. M.Sc. Thesis, University of Calgary, Calgary.

Beerbower, J. R. (1964). Cyclothem and cyclic depositional mechanisms in alluvial plain sedimentation. *Kansas Geol. Surv. Bull.* 169, 31–42.

Bernhardt, A., Jobe, J. R., Grove, M., and Lowe, D. R. (2012). Palaeogeography and diachronous infill of an ancient deep-marine foreland basin, Upper Cretaceous Cerro Toro Formation, Magallanes Basin. *Basin Res.* 24, 269–294. doi: 10.1111/j.1365-2117.2011.00528.x

Burbank, D. W. (1992). Causes of recent Himalayan uplift deduced from deposited patterns in the Ganges basin. *Nature* 357, 680–683. doi: 10.1038/357680a0

Burgess, P. M., Steel, R. J., and Granjeon, D. (2008). "Stratigraphic forward modeling of basin-margin clinooform systems: implications for controls on topset and shelf width and timing of formation of shelf-edge deltas," in *Recent Advances in Models of Siliciclastic Shallow-Marine Stratigraphy*, Vol. 90, eds G. J. Hampson, R. J. Steel, P. M. Burgess, and R. W. Dalrymple (Tulsa: Society for Sedimentary Geology Special Publication), 35–45.

Cant, D. J., and Stockmal, G. S. (1989). The Alberta foreland basin: relationship between stratigraphy and Cordilleran terrane-accretion events. *Can. J. Earth Sci.* 26, 1964–1975. doi: 10.1139/e89-166

Carvajal, C., Steel, R., and Petter, A. (2009). Sediment supply: the main driver of shelf-margin growth. *Earth Sci. Rev.* 79, 221–248. doi: 10.1016/j.earscirev.2009.06.008

Carvajal, C. R., and Steel, R. J. (2009). Shelf-edge architecture and bypass of sand to deep water: influence of shelf-edge processes, sea level, and sediment supply. *J. Sed. Res.* 79, 652–672. doi: 10.2110/jsr.2009.074

Cosgrove, G. I. E., Hodgson, D. M., Poyatos-More, M., Mountney, N. P., and McCaffrey, W. D. (2018). Filter or conveyor? Establishing relationships between clinoform rollover trajectory, sedimentary process regime, and grain character within intrashelf clinothems, Offshore New Jersey, U.S.A. *J. Sed. Res.* 88, 917–941. doi: 10.2110/jsr.2018.44

Covault, J. A., Romans, B. W., and Graham, S. A. (2009). Outcrop expression of a continental-margin shelf-edge delta from the Cretaceous Magallanes Basin. *Chile. J. Sed. Res.* 79, 523–539. doi: 10.2110/jsr.2009.053

Crane, W. H., and Lowe, D. R. (2008). Architecture and evolution of the Paine channel complex, Cerro Toro Formation (Upper Cretaceous), Silla Syncline, Magallanes Basin, Chile. *Sedimentology* 55, 979–1009. doi: 10.1111/j.1365-3091.2007.00933.x

Dalziel, I. W. D. (1981). Back-arc extension in the southern andes: a review and critical reappraisal. *Roy. Soc. Lon. Philosoph. Trans. ser. A* 300, 319–335. doi: 10.1098/rsta.1981.0067

Daniels, B. G., Auchter, N. C., Hubbard, S. M., Romans, B. W., Matthews, W. A., and Stright, L. (2018). Timing of deep-water slope evolution constrained by large-n detrital zircon and volcanic ash geochronology, Cretaceous Magallanes Basin, Chile. *Bull. Geol. Soc. Am.* 130, 438–454. doi: 10.1130/b31757.1

Daniels, B. G., Hubbard, S. M., Romans, B. W., Malkowski, M. A., Matthews, W. A., Bernhardt, A., et al. (2019). Revised chronostratigraphic framework for the Cretaceous Magallanes-Austral Basin, Ultima Esperanza Province, Chile. *J. South. Am. Earth. Sci.* 94:102209. doi: 10.1016/j.jsames.2019.05.025

Deptuck, M. E., Steffens, G. S., Barton, M., and Pirmez, C. (2003). Architecture and evoltion of upper fan channel-belts on the Niger Delta slope and in the Arabian Sea. *Mar. Pet. Geol.* 20, 649–676. doi: 10.1016/j.marpetgeo.2003.01.004

Dixon, J. F., Steel, R. J., and Olariu, C. (2012a). River-dominated, shelf-edge deltas: delivery of sand across the shelf break in the absence of slope incision. *Sedimentology* 59, 1133–1157. doi: 10.1111/j.1365-3091.2011.01298.x

Dixon, J. F., Steel, R. J., and Olariu, C. (2012b). Shelf-edge delta regime as a predictor of deep-water deposition. *J. Sed. Res.* 82, 681–687. doi: 10.2110/jsr.2012.59

Driscoll, N. W., and Karner, G. D. (1999). Three-dimensional quantitative modeling of clinoform development. *Mar. Geol.* 154, 383–398. doi: 10.1016/s0025-3227(98)00125-x

Fildani, A., Cope, T. D., Graham, S. A., and Wooden, J. L. (2003). Initiation of the Magallanes foreland basin: Timing of the southernmost Patagonian Andes orogeny revised by detrital zircon provenance analysis. *Geology* 31, 1081–1084.

Fildani, A., and Hessler, A. M. (2005). Stratigraphic record across a retroarc basin inversion: Rocas Verdes–Magallanes Basin. Patagonian Andes. *Geol. Soc. Am. Bull.* 117, 1596–1614.

Fosdick, J. C., Graham, S. A., and Hilley, G. E. (2014). Influence of attenuated lithosphere and sediment loading on flexure of the deep-water Magallanes retroarc foreland basin, southern Andes. *Tectonics* 33, 2505–2525. doi: 10.1002/2014tc003684

Fosdick, J. C., Romans, B. W., Fildani, A., Bernhardt, A., Calderon, M., and Graham, S. A. (2011). Kinematic evolution of the Patagonian retroarc fold-and-thrust belt and Magallanes foreland basin, Chile and Argentina, 51°30'S. *Geol. Soc. Am. Bull.* 123, 1679–1698. doi: 10.1130/b30242.1

Fowler, J. N., and Novakovic, L. (2018). Deepwater slope valley reservoir architecture and connectivity. Brazil. *Lead. Edge* 37, 276–282. doi: 10.1190/tle37040276.1

Gales, J. A., Talling, P. J., Cartigny, M. J. B., Hughes Clarke, J., Lintern, G., Stacey, C., et al. (2019). What controls submarine channel development and morphology of deltas entering deep-water fjords? *Earth. Surf. Pro. Landforms* 44, 535–551. doi: 10.1002/esp.4515

Gallardo, R. E. (2014). Seismic sequence stratigraphy of a foreland unit in the Magallanes-Austral basin, Dorado Riquelme Block, Chile: implications for deep-marine reservoirs. *Lat. Am. J. Sed. Basin Anal.* 21, 49–64.

Galloway, W. E. (1989). Genetic stratigraphic sequences in basin analysis 1. Architecture and genesis of flooding-surface bounded depositional units. *AAPG Bull.* 73, 125–142.

Gerber, T. P., Pratson, L. F., Wolinsky, M. A., Steel, R., Mohr, J., Swenson, J. B., et al. (2008). Clinoform progradation by turbidity currents: modeling and experiments. *J. Sed. Res.* 78, 220–238. doi: 10.2110/jsr.2008.023

Gomis-Cartesio, L. E., Pyatotos-More, M., Hodgson, D. M., and Flint, S. S. (2018). Shelf-margin clinothem progradation, degradation and readjustment: Tanqua Depocentre, Karoo Basin (South Africa). *Sedimentology* 65, 809–841. doi: 10.1111/sed.12406

Graham, S. A., Dickinson, W. R., and Ingersoll, R. V. (1975). Himalayan-Bengal model for flysch dispersal in the Appalachian-Ouachita system. *Bull. Geol. Soc. Am.* 86, 273–286.

Hage, S., Cartigny, M. J. B., Clare, M. A., Sumner, E. J., Vendettuoli, D., Hughes Clarke, J. E., et al. (2018). How to recognize crescentic bedforms formed by supercritical turbidity currents in the geologic record: insights from active submarine channels. *Geology* 46, 563–566. doi: 10.1130/g40095.1

Hajek, E. A., and Straub, K. M. (2017). Autogenic sedimentation in clastic stratigraphy. *Ann. Rev. Earth Plan. Sci.* 45, 681–709. doi: 10.1146/annurev-earth-063016-015935

Hedberg, H. D. (1970). Continental margins from viewpoint of the petroleum geologist. *AAPG Bull.* 54, 3–43.

Helland-Hansen, W. (1992). Geometry and facies of Tertiary clinothems, Spitsbergen. *Sedimentology* 39, 1013–1029. doi: 10.1111/j.1365-3091.1992.tb01994.x

Henriksen, S., Helland-Hansen, W., and Bullimore, S. (2011). Relationships between shelf-edge trajectories and sediment dispersal along depositional dip and strike: a different approach to sequence stratigraphy. *Basin Res.* 23, 3–21. doi: 10.1111/j.1365-2117.2010.00463.x

Hodgson, D. M., Browning, J. V., Miller, K. G., Hesselbo, S. P., Poyatos-More, M., Mountain, G. S., et al. (2018). Sedimentology, stratigraphic context, and implications of intrashelf bottomset deposits, offshore New Jersey. *Geosphere* 14, 95–114. doi: 10.1130/ges01530.1

Hodgson, D. M., Kane, I. A., Flint, S. S., Brunt, R. L., and Ortiz-Karpf, A. (2016). Time-transgressive confinement on the slope and the progradation of basin-floor fans: implications for the sequence stratigraphy of deep-water deposits. *J. Sed. Res.* 86, 73–86. doi: 10.2110/jsr.2016.3

Houseknecht, D. W., Bird, K. J., and Schenk, C. J. (2009). Seismic analysis of clinoform depositional sequences and shelf–margin trajectories in Lower Cretaceous (Albian) strata, Alaska North Slope. *Basin Res.* 21, 644–654. doi: 10.1111/j.1365-2117.2008.00392.x

Houseknecht, D. W., and Shank, C. J. (2004). "Sedimentology and Sequence Stratigraphy of the Cretaceous Nanushuk, Seabee, and Tuluvak Formations exposed on Uniat Mountain, north-central Alaska," in *U.S. Geological Survey Professional Paper 1709-B*, (North-Central Alaska: USGS).

Hubbard, S. M., Covault, J. A., Fildani, A., and Romans, B. W. (2014). Sediment transfer and deposition in slope channels: deciphering the record of enigmatic deep-sea processes from outcrop. *Bull. Geol. Soc. Am.* 126, 857–871. doi: 10.1130/b30996.1

Hubbard, S. M., Fildani, A., Romans, B. W., Covault, J. A., and McHargue, T. R. (2010). High-relief slope clinoform development: insights from outcrop, Magallanes Basin, Chile. *J. Sed. Res.* 80, 357–375. doi: 10.2110/jsr.2010.042

Hubbard, S. M., Romans, B. W., and Graham, S. A. (2008). Deep-water foreland basin deposits of the Cerro Toro Formation, Magallanes Basin, Chile: architectural elements of a sinuous basin axial channel belt. *Sedimentology* 55, 1333–1359. doi: 10.1111/j.1365-3091.2007.00948.x

Jackson, A., Stright, L., Hubbard, S. M., and Romans, B. W. (2019). Static connectivity of stacked deep-water channel elements constrained by high-resolution digital outcrop models. *AAPG Bull.* 103, 2943–2973. doi: 10.1306/03061917346

Jobe, Z. R., Bernhardt, A., and Lowe, D. R. (2010). Facies and architectural asymmetry in a conglomerate-rich submarine channel fill, Cerro Toro Formation, Sierra Del Toro, Magallanes Basin, Chile. *J. Sed. Res.* 80, 1085–1108. doi: 10.2110/jsr.2010.092

Johannessen, E. P., and Steel, R. J. (2005). Shelf-margin clinoforms and prediction of deepwater sands. *Basin Res.* 17, 521–550. doi: 10.1111/j.1365-2117.2005.00278.x

Jones, G. E. D., Hodgson, D. M., and Flint, S. S. (2013). Contrast in the process response of stacked clinothems to the shelf-slope rollover. *Geosphere* 9, 299–316. doi: 10.1130/ges00796.1

Jones, G. E. D., Hodgson, D. M., and Flint, S. S. (2015). Lateral variability in clinoform trajectory, process regime, and sediment dispersal patterns beyond the shelf-edge rollover in exhumed basin margin-scale clinothems. *Basin Res.* 27, 657–680. doi: 10.1111/bre.12092

Kane, I. A., and Hodgson, D. M. (2011). Sedimentological criteria to differentiate submarine channel levee subenvironments: exhumed examples from the Rosario Fm. (Upper Cretaceous) of Baja California, Mexico, and the Fort Brown Fm. (Permian), Karoo basin, S. Africa. *Mar. Pet. Geo.* 28, 807–823. doi: 10.1016/j.marpetgeo.2010.05.009

Kertznus, V., and Kneller, B. (2009). Clinoform quantification for assessing the effects of external forcing on continental margin development. *Basin Res.* 21, 738–758. doi: 10.1111/j.1365-2117.2009.00411.x

Kominz, M. A., Browning, J. V., Miller, K. G., Sugarman, P. J., Mizintseva, S., and Scotese, C. R. (2008). Late Cretaceous to Miocene sea-level estimates from the New Jersey and Delaware coastal plain coreholes: an error analysis. *Basin Res.* 20, 211–226. doi: 10.1111/j.1365-2117.2008.00354.x

Laskowski, A. K., DeCelles, P. G., and Gehrels, G. E. (2013). Detrital zircon geochronology of Cordilleran retroarc foreland basin strata, western Canada. *Tectonics* 32, 1–22.

Leppe, M., Mihoc, M., Varela, N., Stinnesbeck, W., Mansilla, H., Bierma, H., et al. (2012). Evolution of the Austral-Antarctic flora during the Cretaceous: new insights from a paleobiogeographic perspective. *Rev. Chile. De hist. Nat.* 85, 369–392. doi: 10.4067/s0716-078x2012000400002

Macauley, R. V., and Hubbard, S. M. (2013). Slope channel sedimentary processes and stratigraphic stacking, Cretaceous Tres Pasos Formation slope system, Chilean Patagonia. *Mar. Petrol. Geol.* 41, 146–162. doi: 10.1016/j.marpetgeo.2012.02.004

MacEachern, J. A., and Bann, K. L. (2008). "The role of ichnology in refining shallow marine facies models," in *Recent Advances in Models of Siliciclastic Shallow-Marine Stratigraphy*, Vol. 90, eds G. J. Hampson, R. J. Steel, P. M. Burgess, and R. W. Dalrymple, (Tulsa: Society for Sedimentary Geology Special Publication), 73–116. doi: 10.2110/pec.08.90.0073

MacEachern, J. A., Bann, K. L., Bhattacharya, J. P., and Howell, C. D. (2005). "Ichnology of deltas: Organism responses to the dynamic interplay of rivers, waves, storms, and tides," in *River Deltas – Concepts, Models, and Examples*, Vol. 83, eds L. Giosan, and J. P. Bhattacharya, (Tulsa, PA: Society for Sedimentary Geology Special Publication), 49–85. doi: 10.2110/pec.05.83.0049

Macellari, C. E., Barrio, C. A., and Manassero, M. J. (1989). Upper Cretaceous to Paleocene depositional sequences and sandstone petrography of southwestern Patagonia (Argentina and Chile). *J. S. Am. Earth Sci.* 2, 223–239. doi: 10.1016/0895-9811(89)90031-x

Madof, A. S., Harris, A. D., and Connell, S. D. (2016). Nearshore along-strike variability: is the concept of the systems tract unhinged? *Geology* 44, 315–318. doi: 10.1130/g37613.1

Malkowski, M. A., Schwartz, T. M., Sharman, G. R., Sickmann, Z. T., and Graham, S. A. (2017). Stratigraphic and provenance variations in the early evolution of the Magallanes-Austral foreland basin: implications for the role of longitudinal versus transverse sediment dispersal during arc-continent collision. *Bull. Geol. Soc. Am.* 129, 349–371. doi: 10.1130/b31549.1

Manriquez, L. M. E., Lavina, E. L. C., Fernandez, R. A., Trevisan, C., and Leppe, M. A. (2019). Campanian-Maastrichtian and Eocene stratigraphic architecture, facies analysis, and paleoenvironmental evolution of the northern Magallanes

Basin (Chilean Patagonia). *J. S. Am. Earth Sci.* 93, 102–118. doi: 10.1016/j.jsames.2019.04.010

Martinsen, O. J., and Helland-Hansen, W. (1995). Strike variability of clastic depositional systems: does it matter for sequence-stratigraphic analysis? *Geology* 23, 439–442.

Mayall, M. J., Yielding, C. A., Oldroyd, J. D., Pulham, A. J., and Sakurai, S. (1992). Facies in a shelf-edge delta – An example from the subsurface of the Gulf of Mexico, middle Pliocene, Mississippi Canyon, Block 1091. *AAPG Bull.* 76, 435–448.

McMillen, K. J. (1991). "Seismic stratigraphy of Lower Cretaceous foreland basin submarine fans in the North Slope, Alaska," in *Seismic Facies and Sedimentary Processes of Submarine Fans and Turbidite Systems*, eds P. Weimer, and M. H. Link, (New York: Springer-Verlag), 289–302. doi: 10.1007/978-1-4684-8276-8_15

Mitchum, R. M., Vail, P. R., and Thompson, S. III (1977). "Seismic stratigraphy and global changes of sea level; Part 2, The depositional sequence as a basic unit for stratigraphic analysis," in *Seismic Stratigraphy; Applications to Hydrocarbon Exploration*, Vol. 26, ed. C. E. Payton, (Tulsa, PA: AAPG), 53–62.

Muto, T., and Steel, R. J. (2002). Role of autoretreat and *A/S* changes in the understanding of deltaic shoreline trajectory: a semi-quantitative approach. *Basin Res.* 14, 303–318. doi: 10.1046/j.1365-2117.2002.00179.x

Muto, T., Steel, R. J., and Swenson, J. B. (2007). Autostratigraphy: a framework norm for genetic stratigraphy. *J. Sed. Res.* 77, 2–12. doi: 10.2110/jsr.2007.005

Mutti, E., and Normark, W. R. (1987). "Comparing examples of modern and ancient turbidite systems: problems and concepts," in *Deep Water Clastic Deposits: Models and Case Histories*, eds J. K. Legget, and G. G. Zuffa, (London: Graham and Trotman), 1–38. doi: 10.1007/978-94-009-3241-8_1

Natland, M. L., Gonzalez, E., Canon, A., and Ernst, M. (1974). A system of stages for correlation of Magallanes Basin sediments. *Mem. Geol. Soc. Am.* 139:126.

Nelson, C. H., and Kulm, L. D. (1973). "Submarine fans and channels," in *Turbidites and Deep-Water Sedimentation*, eds G. V. Middleton, and A. J. Bouma, (Tulsa, PA: Society for Sedimentary Geology), 39–70.

Nemec, W., Steel, R. J., Gjelberg, J., Collinson, J. D., Prestholm, E., and Øxnevad, I. E. (1988). Anatomy of collapsed and re-established delta front in Lower Cretaceous of eastern Spitsbergen: gravitational sliding and sedimentation processes. *AAPG Bull.* 72, 454–476.

Normark, W. R., Posamentier, H., and Mutti, E. (1993). Turbidite systems: state of the art and future directions. *Rev. Geoph.* 31, 91–116. doi: 10.1029/92rg02832

Olariu, C., and Bhattacharya, J. P. (2006). Terminal distributary channels and delta front architecture of river-dominated delta systems. *J. Sed. Res.* 76, 212–233. doi: 10.2110/jsr.2006.026

Olariu, C., and Steel, R. J. (2009). Influence of point-source sediment-supply on modern shelf-slope morphology: implications for interpretation of ancient margins. *Basin Res.* 21, 484–501. doi: 10.1111/j.1365-2117.2009.00420.x

Paola, C., Straub, K., Mohrig, D., and Reinhardt, L. (2009). The "unreasonable effectiveness" of stratigraphic and geomorphic experiments. *Earth Sci. Rev.* 97, 1–43. doi: 10.1016/j.earscirev.2009.05.003

Patruno, S., Hampson, G. J., and Jackson, C. A.-L. (2015). Quantitative characterization of deltaic and subaqueous clinoforms. *Earth Sci. Rev.* 142, 79–119. doi: 10.1016/j.earscirev.2015.01.004

Paumard, V., Bourget, J., Payenberg, T., Ainsworth, R. B., George, A. D., Lang, S., et al. (2018). Controls on shelf-margin architecture and sediment partitioning during a syn-rift to post-rift transition: insights from the Barrow Group (Northern Carnarvon Basin, North West Shelf, Australia). *Earth Sci. Rev.* 177, 643–677. doi: 10.1016/j.earscirev.2017.11.026

Pemberton, E. A. L., Hubbard, S. M., Fildani, A., Romans, B. W., and Stright, L. (2016). The stratigraphic expression of decreasing confinement along a deep-water sediment-routing system: outcrop example from southern Chile. *Geosphere* 12, 1–21.

Pemberton, E. A. L., Stright, L., Fletcher, S., and Hubbard, S. M. (2018). The influence of stratigraphic architecture on seismic response: reflectivity modeling of outcropping deepwater channel units. *Interpretation* 6, T783–T808.

Pinous, O. V., Levchuk, M. A., and Sahagian, D. L. (2001). Regional synthesis of the productive Neocomian complex of West Siberia: sequence stratigraphic framework. *AAPG Bull.* 85, 1713–1730.

Plink-Björklund, P., Mellere, D., and Steel, R. J. (2001). Turbidite variability and architecture of sand-prone, deep-water slopes: eocene clinoforms in the central Spitsbergen. *J. Sed. Res.* 71, 895–912. doi: 10.1306/030501710895

Plink-Björklund, P., and Steel, R. J. (2005). "Deltas on falling-stage and lowstand shelf-margins, the eocene central basin of spitsbergen: importance of sediment supply," in *River Deltas–Concepts, Models, and Examples*, Vol. 83, eds L. Giosan, and J. P. Bhattacharya, (Tulsa, PA: Society for Sedimentary Geology Special Publication), 179–206. doi: 10.2110/pec.05.83.0179

Ponce, J. J., and Carmona, N. (2011). Coarse-grained sediment waves in hyperpycnal clinoform systems, Miocene of the Austral foreland basin, Argentina. *Geology* 39, 763–766. doi: 10.1130/g31939.1

Porebski, S. J., and Steel, R. J. (2003). Shelf-margin deltas: their stratigraphic significance and relation to deepwater sands. *Earth Sci. Rev.* 62, 283–326. doi: 10.1016/s0012-8252(02)00161-7

Poyatos-Moré, M., Jones, G. D., Brunt, R. L., Hodgson, D. M., Wild, R. J., and Flint, S. S. (2016). Mud-dominated basin margin progradation: processes and implications. *J. Sed. Res.* 86, 863–878.

Poyatos-Moré, M., Jones, G. D., Brunt, R. L., Tek, D., Hodgson, D. M., and Flint, S. S. (2019). Clinoform architecture and along-strike variability through an exhumed erosional to accretionary basin margin transition. *Basin Res* 31, 920–947. doi: 10.1111/bre.12351

Prather, B. E., O'Byrne, C., Pirmez, C., and Sylvester, Z. (2017). Sediment partitioning, continental slopes and base-of-slope systems. *Basin Res.* 29, 394–416.

Reimchen, A., Hubbard, S. M., Stright, L., and Romans, B. W. (2016). Using seafloor morphometrics to constrain stratigraphic models of sinuous submarine channel systems. *Mar. Petrol. Geol.* 77, 92–115.

Ridente, D., Foglini, F., Minisini, D., Trincardi, F., and Verdicchio, G. (2007). Shelf-edge erosion, sediment failure and inception of Bari Canyon on the Southwest Adriatic Margin (Central Mediterranean). *Mar. Geol.* 246, 208–230.

Romans, B. W., Castelltort, S., Covault, J. A., Fildani, A., and Walsh, J. P. (2016). Environmental signal propagation in sedimentary systems across timescales. *Earth Sci. Rev.* 153, 7–29.

Romans, B. W., Fildani, A., Graham, S. A., Hubbard, S. M., and Covault, J. A. (2010). Importance of predecessor basin history on the sedimentary fill of a retroarc foreland basin: provenance analysis of the Cretaceous Magallanes Basin, Chile (50-52°). *Basin Res.* 22, 640–658.

Romans, B. W., Fildani, A., Hubbard, S. M., Covault, J. A., Fosdick, J. C., and Graham, S. A. (2011). Evolution of deep-water stratigraphic architecture, Magallanes Basin, Chile. *Mar. Petrol. Geol.* 28, 612–628.

Romans, B. W., Hubbard, S. M., and Graham, S. A. (2009). Stratigraphic evolution of an outcropping continental slope system, Tres Pasos Formation at Cerro Divisadero, Chile. *Sedimentology* 56, 737–764.

Ross, W. C., Halliwel, B. A., May, J. A., Watts, D. E., and Syvitski, J. P. M. (1994). Slope readjustment: a new model for the development of submarine fans and aprons. *Geology* 22, 511–514.

Ryan, M. C., Helland-Hansen, W., Johannessen, E. P., and Steel, R. J. (2009). Erosional vs. accretionary shelf margins: the influence of margin type on deepwater sedimentation: an example from the Porcupine basin, offshore western Ireland. *Basin Res.* 21, 676–703.

Ryan, W. B., Carbotte, S. M., Coplan, J. O., O'Hara, S., Melkonian, A., Arko, R., et al. (2009). Global multi-resolution topography synthesis. *Geochem. Geoph. Geosyst* 10:Q03014. doi: 10.1029/2008GC002332

Schwartz, T. M., Fosdick, J. C., and Graham, S. A. (2017). Using detrital zircon U-Pb ages to calculate Late Cretaceous sedimentation rates in the Magallanes-Austral basin, Patagonia. *Basin Res.* 29, 725–746.

Schwartz, T. M., and Graham, S. A. (2015). Stratigraphic architecture of a tide-influenced shelf-edge delta, Upper Cretaceous Dorotea Formation, Magallanes-Austral basin, Patagonia. *Sedimentology* 62, 1039–1077.

Sharman, G. R., Hubbard, S. M., Covault, J. A., Hinsch, R., Linzer, H.-G., and Graham, S. A. (2018). Sediment routing evolution in the North Alpine Foreland Basin, Austria: interplay of transverse and longitudinal sediment dispersal. *Basin Res.* 30, 426–447.

Shultz, M. R., Fildani, A., Cope, T. D., and Graham, S. A. (2005). "Deposition and stratigraphic architecture of an outcropping ancient slope system: Tres Pasos Formation, Magallanes Basin, southern Chile," in *Submarine Slope Systems: Processes and Products*, Vol. 244, eds D. M. Hodgson, and S. S. Flint, (London: Geological Society Special Publication), 27–50.

Shultz, M. R., and Hubbard, S. M. (2005). Sedimentology, stratigraphic architecture, and ichnology of gravity-flow deposits partially ponded in a

growth-fault-controlled slope minibasin, Tres Pasos Formation (Cretaceous), southern Chile. *J. Sed. Res.* 75, 440–453.

Smith, C. H. L. (1977). *Sedimentology of the Late Cretaceous (Santonian–Maastrichtian) Tres Pasos Formation, Ultima Esperanza District, southern Chile*. M.Sc Thesis, University of Wisconsin, Madison, WI.

Steel, R. J., Carvajal, C., Petter, A. L., and Uroza, C. (2008). "Shelf and shelf-margin growth in scenarios of rising and falling sea level," in *Recent Advances in Models of Siliciclastic Shallow-Marine Stratigraphy*, Vol. 90, eds G. J. Hampson, R. J. Steel, P. M. Burgess, and R. W. Dalrymple, (Tulsa, PA: Society for Sedimentary Geology Special Publication), 47–71.

Steel, R. J., and Olsen, T. (2002). "Clinoforms, clinoform trajectory and deepwater sands," in *Sequence Stratigraphic Models for Exploration and Production: Evolving Methodology, Emerging Models and Application Histories*, eds J. M. Armentrout, and N. C. Rosen, (Tulsa, PA: Society for Sedimentary Geology Special Publication), 367–381.

Stevenson, C. J., Jackson, C. A.-L., Hodgson, D. M., Hubbard, S. M., and Eggenhuisen, J. T. (2015). Deep-water sediment bypass. *J. Sed. Res.* 85, 1058–1081.

Straub, K. M., Paola, C., Mohrig, D., Wolinsky, M. A., and George, T. (2009). Compensational stacking of channelized sedimentary deposits. *J. Sed. Res.* 79, 673–688.

Sylvester, Z., Deptuck, M. E., Prather, B. E., Pirmez, C., and O'Byrne, C. (2012). "Seismic stratigraphy of a shelf-edge delta and linked submarine channels in the northeastern Gulf of Mexico," in *Application of the Principles of Seismic Geomorphology to Continental-Slope and Base-of-Slope Systems: Case Studies from Seafloor and Near-Seafloor Analogues*, Vol. 99, eds B. E. Prather, M. E. Deptuck, D. Mohrig, B. Van Hoorn, and R. B. Wynn, (Tulsa, PA: Society for Sedimentary Geology Special Publication), 31–59.

Uličný, D., Nichols, G., and Waltham, D. (2002). Role of initial depth at basin margins in sequence architecture: field examples and computer models. *Basin Res.* 14, 347–360. doi: 10.1046/j.1365-2117.2002.00183.x

Wilson, T. J. (1991). Transition from back-arc to foreland basin development in southernmost Andes: stratigraphic record from the Ultima Esperanza District. *Chile. Bull. Geol. Soc. Am.* 103, 98–111.

Conflict of Interest: DB was employed by company Chevron Canada Limited.

The remaining authors declare that the research was conducted in the absence of any commercial or financial relationships that could be construed as a potential conflict of interest.

frontiers in Earth Science

ORIGINAL RESEARCH
published: 28 January 2020
doi: 10.3389/feart.2019.00353

Erosional and Tectonic Evolution of a Retroarc Orogenic Wedge as Revealed by Sedimentary Provenance: Case of the Oligocene – Miocene Patagonian Andes

Joel S. Leonard[1,2], Julie C. Fosdick[3] and Rebecca A. VanderLeest[3]*

[1] School of Earth and Space Exploration, Arizona State University, Tempe, AZ, United States, [2] Department of Earth and Atmospheric Sciences, Indiana University, Bloomington, IN, United States, [3] Department of Geosciences, University of Connecticut, Storrs, CT, United States

OPEN ACCESS

Edited by:
David Mark Hodgson, University of Leeds, United Kingdom

Reviewed by:
Joel Saylor, The University of British Columbia, Canada
Brian K. Horton, The University of Texas at Austin, United States
Emily Finzel, The University of Iowa, United States

***Correspondence:**
Joel S. Leonard
joel.leonard@asu.edu

Specialty section:
This article was submitted to Sedimentology, Stratigraphy, and Diagenesis, a section of the journal Frontiers in Earth Science

Received: *16 August 2019*
Accepted: *18 December 2019*
Published: *28 January 2020*

Citation:
Leonard JS, Fosdick JC and VanderLeest RA (2020) Erosional and Tectonic Evolution of a Retroarc Orogenic Wedge as Revealed by Sedimentary Provenance: Case of the Oligocene – Miocene Patagonian Andes. Front. Earth Sci. 7:353. doi: 10.3389/feart.2019.00353

Sedimentary provenance techniques have been widely applied in foreland basin settings to understand tectonic and magmatic processes by tracking the exposure and erosion of distinct sediment source areas through time. We present a case example from the Magallanes-Austral retroarc foreland basin of Chile and Argentina (51°30'S), where modal sandstone and conglomerate compositional data, detrital zircon U-Pb geochronology, and sedimentology data from the Oligocene-Miocene Río Guillermo Formation document a change in source areas during an important stage of orogenic development. In particular, our results from the ∼24.3–21.7 Ma Río Guillermo Formation record an abrupt shift from transitional to undissected arc provenance that indicate rejuvenated magmatism within the contemporary arc. Minor components of lithic grains suggest a subordinate source of recycled sediments that we interpret may have been derived from the intervening external fold-and-thrust belt, rather than directly from sources in the hinterland thrust domain. Detrital zircon U-Pb geochronology data show mostly Neogene (∼20–40 Ma) and Cretaceous (∼70–110 Ma) age groups, with minor amounts of Jurassic (∼145–155 Ma), and Paleozoic (∼260–540 Ma) age groups, which are consistent with a syndepositional arc and recycled external fold-and-thrust belt sources. Stratigraphic data suggest a vegetated, channelized braidplain environment developed above an erosional unconformity with the underlying shallow-marine Río Turbio Formation. Upsection, the Río Guillermo Formation locally transitions to a low-energy, organic-rich floodplain setting located within the upper reaches of a fluvial-tidal transition zone of the coastal plain, and the uppermost part of the formation is characterized by a coarse-grained sandy channelized braidplain environment along the foreland basin margin. Moderate sediment accumulation rates and coastal plain

progradation during this period is consistent with sustained sediment flux from the Patagonian Andes and tectonic subsidence along the basin margin. Taken collectively, we propose that the abrupt provenance shift dominantly records erosion of the rejuvenated mafic volcanic arc, despite coeval changes in orogenic wedge dynamics brought about by increased plate convergence rates that drove uplift of the intervening external-fold-and-thrust belt along reactivated deep-seated high-angle basin structures.

Keywords: foreland basins, sedimentary provenance, patagonian andes, magallanes-austral basin, cenozoic

INTRODUCTION

In Cordilleran systems, crustal thickening caused by retroarc upper plate shortening, batholith emplacement, and arc volcanism build topography, while surface processes act to erode and redistribute sediments to the foreland basin. The surface evolution of convergent orogens is archived in the sedimentary deposits of their companion foreland basins, but unlocking this archive requires discerning tectonic signals from climatic or eustatic signals that control the depositional environments and composition of basin infill. Thus, considerable research has been devoted to identifying diagnostic signals of tectonics, climate, and eustasy in sedimentary deposits (e.g., Posamentier et al., 1988; Jordan and Flemings, 1991; Heller et al., 1993, 2001; Paola, 2000; Armitage et al., 2011; Romans et al., 2016). The location and magnitude of upper plate shortening and rock uplift will dictate the lithology of potential source areas within the orogen. The development of orogenic wedges may follow Coulomb wedge theory as phases of internal deformation or self-similar growth in response to changes in the frictional properties and physical characteristics of the wedge over time, such as pore pressure, depth and geometry of basal detachment, and surface slope (Davis et al., 1983; Dahlen, 1984; DeCelles and Mitra, 1995; Horton, 1999; Willett, 1999). However, in orogens with reactivated high-angle structures (e.g., Hilley et al., 2005; Mora et al., 2006; Saylor et al., 2012), the patterns of deformation and erosion may reflect vertical uplift and exhumation rather than high rates of internal shortening across the orogenic wedge.

In the absence of direct measurements of deformation, sediment provenance can shed light on erosion of different source areas that may respond to changes in orogenic wedge behavior. Pulses of coarse-grained sediments in foreland basins are commonly interpreted within the context of increased sediment supply from thrust-generated topography, and/or increased precipitation and erosion (Burbank et al., 1988; Heller et al., 1988; Paola et al., 1992; Garcia-Castellanos et al., 2002; Allen and Heller, 2011; Armitage et al., 2011). Abrupt shifts in sediment provenance at geologic timescales can be an indication of tectonic reconfiguration of upland source areas (Horton et al., 2004). Thus, the timing, duration, and sedimentary character of the progradational units bear on the tectonic history of an orogenic system.

We explore the sedimentary provenance and sedimentology of the latest Oligocene-early Miocene basin record in the Southern Patagonian Andes (**Figure 1**), which preserves coarse-grained deposition during the early stages of a regionally important phase of mountain-building and changes in orogenic wedge dynamics. The Magallanes–Austral retroarc foreland basin lies on the eastern flank of the Patagonian Andes at the southern tip of the South American continent (**Figure 1**). This foreland basin and fold-and-thrust belt records a long-lived orogenic system with a major phase of mountain-building in the Late Cretaceous (∼100–88 Ma) following closure and inversion of the Rocas Verdes Basin and arc-continent collision (Calderón et al., 2016). At the latitude of our study area, this depocenter was a predominantly longitudinal marine depositional system that derived much of its sediment from the continental Patagonian and Fuegian Andes (Fildani et al., 2008; Romans et al., 2011). Thrust front advancement during Paleogene time and progressive deepening of the basal sole-out detachment depth in latest Oligocene – early Miocene time (Fosdick et al., 2011) promoted an eastward shift of the foreland deposition and a transition to transverse sediment routing (Biddle et al., 1986; Fosdick et al., 2011). These younger phases of Cenozoic orogenesis are broadly coeval with major mountain building, crustal shortening, and basin subsidence in the Central and Northern Andes (e.g., Horton, 2018); however, the magnitude of shortening and preserved basin record is considerably less in the Magallanes-Austral Basin (Fosdick et al., 2011).

Here, we investigate the Chattian-Aquitanian Río Guillermo Formation from the Magallanes-Austral Basin (**Figure 1**), and by comparison with potential source areas and provenance studies from underlying basin strata, answer the following questions: (1) What were the primary sediment sources of the Río Guillermo Formation? (2) How are the coarse-grained progradational deposits linked to the thrusting history and changes in upland sediment-source paleogeography? Our findings constrain the sources of sediment and stratigraphic stacking patterns during reactivation of deep-seated faulting and regional uplift of the Patagonian fold-and-thrust belt. These findings capitalize on new age constraints for the timing of Cenozoic (Maastrichtian through early Miocene) sedimentation in the Magallanes-Austral Basin (Fosdick et al., 2011, 2019), and reinforce causal linkages between changes in sediment routing and a structural reorganization of the Patagonian fold-and-thrust belt (**Figure 1B**). Our work on the Río Guillermo Formation, specifically, provides new detailed sedimentology and provenance data that add further context for regional exhumation and magmatic evolution histories that, taken

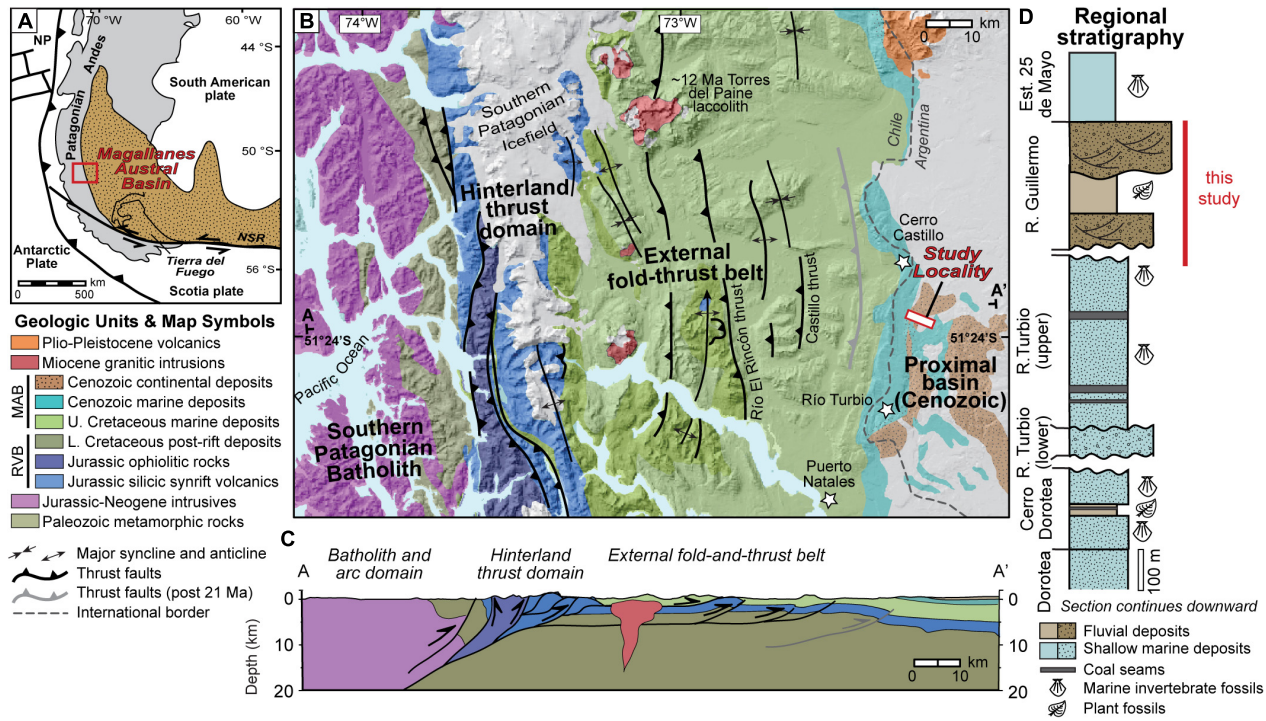

FIGURE 1 | (A) Location of the Patagonian Andes retroarc orogenic belt and foreland basin system. NP, Nazca plate; NSR, North Scotia Ridge. **(B)** Geologic map compiled from Malumián et al. (2000), SERNAGEOMIN (2003), and Fosdick et al. (2011). The hinterland thrust domain includes faulted and folded rocks of Jurassic Sarmiento Ophiolitic Complex and Tobífera Formation. The external fold-and-thrust belt comprises the Zapata, Punta Barrosa, Cerro Toro, Tres Pasos, and Dorotea formations. MAB, Magallanes-Austral Basin; RVB, Rocas Verdes Basin. **(C)** Simplified regional cross-section showing major structural features of the Patagonian Andes (modified from Fosdick et al., 2011, 2013). **(D)** Regional stratigraphy of the study area showing Upper Cretaceous – Neogene strata (adapted from Fosdick et al., 2019). See text for discussion.

together, contribute to a better understanding of coupled foreland basin and orogenic processes.

GEOLOGIC SETTING AND PREVIOUS WORK

Tectonic and Sedimentary History of the Magallanes-Austral Basin

The Magallanes-Austral retroarc foreland basin of Chile and Argentina is situated at the southernmost tip of South America adjacent to the Patagonian and Fuegian Andes orogenic belt (Ghiglione et al., 2016; **Figure 1A**). Prior to its transition to foreland depocenter in the Early Cretaceous, this region was occupied by the Rocas Verdes backarc basin that formed in the Jurassic as a result of the tectonic break-up of Gondwana (Dalziel et al., 1974; Wilson, 1991; Fildani and Hessler, 2005; Calderón et al., 2016). Backarc spreading culminated in the genesis of attenuated pseudo-oceanic crust and deep marine sedimentary conditions (Dalziel et al., 1974; de Wit and Stern, 1981; Fildani and Hessler, 2005). Initiation of subduction of the Farallon-Nazca plate beneath South America and compression from the west in the Early Cretaceous led to closure of the Rocas Verdes backarc and the conclusion of this pre-foreland extensional phase (Calderón et al., 2012, 2016). However, pre-foreland structural remnants and weakened crust produced during this time are thought to be important factors controlling sedimentation patterns in the basin during the Late Cretaceous and the opening of the South Atlantic Ocean (Romans et al., 2010; Malkowski et al., 2017).

Extensive research over several decades has characterized early foreland development of a narrow foredeep trough and protracted deep marine sedimentary conditions, followed by southward axial progradation and infilling by slope-shelf and deltaic systems from the Late Cretaceous through early Cenozoic (Macellari et al., 1989; Fildani and Hessler, 2005; Hubbard et al., 2008; Romans et al., 2011; Malkowski et al., 2017; Sickmann et al., 2019). Crustal shortening estimates suggest that at least 20–27 km of shortening across the narrow fold-and-thrust belt occurred during this time (Fosdick et al., 2011). Shallow to marginal marine, deltaic, and estuarine sedimentary environments persisted in the basin through the Paleogene (Malumián and Caramés, 1997; Rodríguez Raising, 2010; Schwartz and Graham, 2015), and by Eocene – Oligocene time growth and encroachment of the Patagonian external fold-and-thrust belt resulted in consistent eastward (i.e., transverse) sediment dispersal (Biddle et al., 1986). Few constraints on the timing and magnitude of Paleogene crustal shortening are available, but estimates based on cross-cutting relationships

suggest ∼6.5 km of shortening occurred prior to 29 Ma (Fosdick et al., 2011). Early Eocene subduction of the Aluk-Farallon spreading ridge (Cande and Leslie, 1986; Breitsprecher and Thorkelson, 2009) resulted in a hiatus of arc volcanism that lasted from middle Eocene – latest Oligocene time (Ramos, 1989; Hervé et al., 2007), but produced regionally extensive plateau basalts (Ramos and Kay, 1992), and may have caused broad regional uplift that enhanced a basin-wide Paleogene unconformity within the foreland succession (Biddle et al., 1986; Fosdick et al., 2015; Schwartz et al., 2016; George et al., 2019).

Late Oligocene time marked a switch in the characteristic style of foreland deformation, from dominantly thin-skinned to high-angle basement-cored thrusting with less retroarc shortening (∼3–4 km) across the fold-and-thrust belt (Fosdick et al., 2011), that is followed closely by deposition of the first exclusively terrestrial and fluvial systems at this latitude in the earliest Miocene (Fosdick et al., 2019). The switch to basement-cored thrusting (**Figure 1C**) is generally attributed to more rapid and trench-normal convergence on the western margin of South America ∼27 Ma (Fosdick et al., 2011; Somoza and Ghidella, 2012; Ghiglione et al., 2016), although other authors suggest that far-field effects relating to growth of the North Scotia Ridge, and Tierra del Fuego to the south ∼23 Ma (Cunningham et al., 1995; Eagles and Jokat, 2014) may have also played a role (Lagabrielle et al., 2009; Fosdick et al., 2013). The seismically imaged basement thrusts are interpreted to be reactivated high-angle extensional structures inherited from the predecessor Rocas Verdes Basin (Fosdick et al., 2011). Terrestrial sedimentary conditions are succeeded by a brief, but regionally extensive marine incursion and return to shallow marine conditions across much of the basin in early Miocene time (Malumián and Caramés, 1997). Recently, the dominant control on the extent and magnitude of basin flooding has been interpreted as propagation of the Patagonian Andean thrust front and associated increase in flexural subsidence (Fosdick et al., 2019). Key to this interpretation is revised chronology of the upper part of the Río Turbio Formation and overlying Río Guillermo Formation, which are as young as latest Priabonian through middle Chattian (36.6–26.6 Ma), and latest Chattian through Aquitanian (24.3–21.7 Ma), respectively (Fosdick et al., 2011, 2019). Finally, deposition of the synorogenic Santa Cruz Formation (∼18–14) Ma record coeval coarse-grained sedimentation, surface uplift, and continental sedimentation across the Patagonian foreland (e.g., Blisniuk et al., 2005; Ramos and Ghiglione, 2008) prior to passage of the Chile Triple Junction at this latitude (Gorring et al., 2003; Kay et al., 2004; Breitsprecher and Thorkelson, 2009). Opening of a slab window resulting from this later ridge collision is associated with regional uplift of the Patagonian foreland and inversion of the Magallanes-Austral Basin (Guillaume et al., 2009, 2013; Fosdick et al., 2011).

Previous Work on Río Guillermo Formation

The Río Guillermo Formation is the first exclusively terrestrial sedimentary unit at this latitude (∼51°S) (Hünicken, 1955; Malumián and Caramés, 1997; Rodríguez Raising, 2010), but is scarcely exposed at the surface and has been the subject of widely varying interpretations of both its age and significance relating to the greater basin development. The base of the Río Guillermo Formation in the study region is characterized by an erosional unconformity with ∼20–30 cm of channelized pebble-to-cobble conglomerate scoured into the underlying mudstone beds of the Río Turbio Formation (**Figure 1D**). It is generally composed of conglomerate, sandstone, and mudstone interpreted to be fluvial in origin, minor coal horizons, and notably containing abundant silicified tree trunks (Malumián and Caramés, 1997). Sandstones are composed largely of volcanic detritus, suggesting the potential for arc-related provenance (Manassero, 1990). Early work correlated this unit with the coeval Río Leona Formation that has similar characteristics and is more regionally exposed, and suggested an Oligocene – Miocene age (Riccardi and Rolleri, 1980; Russo et al., 1980). However, later work assigns early Eocene – early Oligocene ages on the basis of paleontological assemblages (Malumián and Caramés, 1997; Malumián et al., 2000; Rodríguez Raising, 2010; Malumián and Náñez, 2011; Pearson et al., 2012). This discrepancy in age assignments had led to disperate associations with Eocene – Oligocene marine transgressions and climatic optima (Malumián and Caramés, 1997; Malumián et al., 2000; Malumián and Náñez, 2011). Rodríguez Raising (2010) conducted a sequence stratigraphic analysis and documented an overall upward increase in rate of basin accommodation generation, superimposed by cyclic phases of aggradation, and erosion linked generally to phases of deformation.

As part of a regional study on the kinematic history of faulting and sedimentaton across the Patagonian Andes, Fosdick et al. (2011) reported a zircon U-Pb SHRIMP age from an interbeded tuff at the top of the Río Guillermo Formation, suggesting the top of the unit was as young as 21.7 Ma. More recently, Fosdick et al. (2019) provided new estimates on the timing of sedimentaton for the whole Cenozoic basin succession in our study area – including the lower formationnal boundary of the Río Guillermo Formation – based on detrital zircon U-Pb geochronological data. These data establish a latest Chattian through Aquitanian age (∼24.3–21.7 Ma) for the Río Guillermo Formation and support the interpretation of contemporaneous deposition with previously recongnized faulting stages within the fold-and-thrust belt (later Stage IV and early Stage V faulting of Fosdick et al., 2011, 2019). This work provides detailed sedimentology, sandstone petrography, modal clast analysis, and additional detrital zircon U-Pb geochronology of the Río Guillermo Formation.

Characteristic Source Areas in the Patagonian Andes

New provenance data from the upper Eocene - lower Miocene Magallanes-Austral basinfill at ∼51°S capture changes in sediment composition and interpreted changes in source areas. Here we summarize the age, lithology, and tectonic association of potential sources [see Romans et al. (2010), Fosdick et al. (2015),

Schwartz et al. (2016), Daniels et al. (2017), George et al. (2019), Sickmann et al. (2019)] for recent work of the detrital zircon geochronology from the Cretaceous basin fill).

(1) The Patagonian continental basement comprises Paleozoic metamorphic units exposed as wall rocks to the Mesozoic-Neogene batholith and within thrust slices in the hinterland thrust domain (**Figure 1B**). At the latitude of the study area, these rocks include the Paleozoic Eastern Andean Metamorphic Complex (EAMC), a variably deformed and metamorphosed complex of greenschist grade turbiditic and minor intercalated marl successions and metabasite flows, and localized areas of higher metamorphic grade rocks (Hervé et al., 2003, 2008; Calderón et al., 2016).

(2) Generally east of the Paleozoic metamorphic basement, the hinterland thrust domain is characterized by Upper Jurassic (∼140–160 Ma) metarhyolitic Tobífera Formation and ophiolitic rocks of the Rocas Verdes Basin (**Figure 1B**). These rocks represent the quasi-oceanic and attenuated continental lithosphere of the backarc basin floor, prior to closure of the basin during arc-continent collision and inversion of the retroarc basin during initiation of the Magallanes-Austral foreland basin phase. Today, the modern drainage divide resides along the Tobífera duplex structures constructed from thrust stacks of the Tobífera Formation (**Figure 1C**). Post-rifting thermal sag and incipient foreland basin sedimentation are preserved in the upper Jurassic – lower Cretaceous Zapata Formation.

(3) The Paleozoic basement and Jurassic hinterland thrust domain is intruded by the Late Jurassic – Neogene Southern Patagonian Batholith (SPB), which preserves the root of the Late Jurassic – Neogene magmatic arc system (**Figures 1B,C**). There are three primary recognized Cretaceous episodes of plutonic emplacement (144–137, 136–127, and 126–75 Ma), followed by early Paleogene (67–40 Ma), and Neogene (25–15 Ma) episodes (Hervé et al., 2007). Some of the Miocene granitic intrusions locally intrude the external fold-and-thrust belt (described below), including the ∼26 Ma Cerro Donoso pluton, ∼15.4 Ma Cerro Balmaceda pluton, and ∼12.5 Ma Torres del Paine Intrusive Complex (Michel et al., 2008; Sánchez et al., 2008; Ramírez de Arellano et al., 2012). Rocks are generally composed of granodiorite, tonalite, and granite, with minor isolated gabbroic intrusions.

(4) East of the Paleozoic-Jurassic basement thrust domain, the Cretaceous – Neogene external fold-and-thrust belt consists of Cenomanian-Paleocene retroarc foreland basin marine mudstone, siltstone, and sandstone deposited in submarine channel-fill deposits of the Punta Barossa, Cerro Toro, Tres Pasos, and Dorotea Formations (**Figure 1B**). In general, these rocks are characterized by *dissected arc* provenance, with dominant sources from the SPB, hinterland thrust domain, and Paleozoic metamorphic basement (Fildani and Hessler, 2005; Hubbard et al., 2008; Romans et al., 2010; Schwartz et al., 2016). Structural style includes both thin-skinned and thick-skinned deformation. Importantly, the eastern leading edge of the external thrust belt (i.e., the Río El Rincon and Castillo thrust sheets) sedimentary succession would have constituted the deformation front during deposition of the upper Río Turbio and Río Guillermo formations (Fosdick et al., 2011; **Figure 1C**).

Based on structural style and characteristic domains of deformation (Ghiglione et al., 2010; Fosdick et al., 2011), we refer separately to these source areas as the basement domain (Paleozoic basement and Mesozoic SPB), the hinterland thrust domain (Rocas Verdes Basin floor, high-angle shear zones, and thin-skinned detachments within the basal Tobífera metavolcanic units), and the external fold-and-thrust belt (thin-skinned deformation superimposed by reactivated basement faults).

METHODS AND RESULTS

Our analysis consists of a stratigraphic section of the Río Guillermo Formation that records detailed provenance during incipient terrestrial sedimentation at this latitude. Sample details including geographic locations, position in measured sections, and type of analysis are summarized in **Table 1**.

Oligocene-Miocene Sedimentology and Stratigraphy

We focused on the outcrop exposures of the Río Guillermo Formation and underlying Río Turbio Formation in the Estancia Cancha Carrera, east of the Chile-Argentina international border (**Figure 1B**). Here, the outcrops are variably well-exposed in the stream valley of the modern Río Guillermo and form a series of gently east-dipping exposures along the incised river valley (**Figures 2A,E**). Locally, the Neogene deposits are disconformably overlain by Pleistocene glaciofluvial deposits and have deep soil horizons developed at the top of hillslope outcrops, thus limiting exposure to valley walls. The limited extent of high-quality rock exposure along the Patagonian foothills precludes a more extensive three-dimensional analysis of stratigraphic architecture, so we leverage high-resolution vertical information and sampling from this type locality of this stratigraphic level (Hünicken, 1955; Malumián et al., 2000). We measured approximately 340 m, locally constituting the full stratigraphic thickness of the fluvial Río Guillermo Formation. Paleocurrent measurements were taken from imbricated clasts, limbs of trough cross-beds, and orientations of petrified tree logs preserved in channel deposits, then corrected for 15°E regional dip. We characterize three subunits based on distinct changes in sedimentary facies assemblages (**Figure 3**). Sedimentary facies codes (**Table 2**) in the following unit descriptions are from Miall (1978, 2006). We make a distinction between "coarse-grained" and "fine-grained" depositional intervals such that coarse-grained refers to sand grain-sizes and larger, which in most cases herein is inferred to represent bedload deposition in an active channel.

Unit 1 is ∼95 m thick and consists of cliff-forming medium- to thick-bedded, trough cross-stratified, granule-to-cobble conglomerate (*Gt* and *Gh*). The base of the unit

TABLE 1 | Locality information for clast counts, sandstone petrography, and detrital zircon U-Pb LA-ICPMS samples.

Sample type	Sample	Formation	Latitude (°S)	Longitude (°W)	Elevation (m)	Stratigraphic Height (m)	Calculated MDA (Ma ± 2σ)
Conglomerate clast count	CCS3-PC2	Río Guillermo	51.30992	72.20304	405	271.5	
	CCS3-PC1	Río Guillermo	51.31000	72.20271	371	258	
	CCS2-PC2	Río Guillermo	51.31316	72.21686	379	91	
	CCS1-PC3	Río Guillermo	51.31308	72.22132	393	68	
	CCS1-PC1	Río Guillermo	51.31260	72.22176	358	17.5	
Sandstone petrography	15CCS307	Río Guillermo	51.30823	72.19668	403	336	
	15CCS305	Río Guillermo	51.30820	72.19702	391	321	
	15CCS304	Río Guillermo	51.30989	72.20073	381	300	
	15CCS303	Río Guillermo	51.30974	72.20173	386	276	
	15CCS302	Río Guillermo	51.31009	72.20272	395	270	
	15CCS301	Río Guillermo	51.31002	72.20271	375	263.5	
	15CCS212	Río Guillermo	51.31335	72.21058	348	119	
	15CCS108	Río Guillermo	51.31356	72.22148	389	69.5	
	15CCS107	Río Guillermo	51.31300	72.22132	406	65	
	15CCS106	Río Guillermo	51.31298	72.22125	371	52	
	15CCS104	Río Guillermo	51.31270	72.22145	377	31.5	
	15CCS102	Río Guillermo	51.31261	72.22161	355	17.5	
	15CCS101	Río Guillermo	51.31249	72.22168	348	3.5	
	15RTDZ01*	Río Turbio (upper)	51.30919	72.21978	334	−30	
	14RTDZ-7*	Río Turbio (upper)	51.29761	72.23581	349	−60	
	14RTDZ-8*	Río Turbio (upper)	51.29667	72.23819	282	−90	
Detrital Zircon	JCF09-237B‡	Río Guillermo	51.30338	72.18670	389	343	22.8 ± 0.2 (*n* = 65)
	15CCS306	Río Guillermo	51.30816	72.19702	381	321	23.0 ± 0.3 (*n* = 11)
	15CCS302	Río Guillermo	51.31009	72.20272	395	270	22.7 ± 0.3 (*n* = 16)
	15CCS210	Río Guillermo	51.31315	72.21645	380	94	24.6 ± 0.5 (*n* = 7)
	15CCS105	Río Guillermo	51.31296	72.22133	383	41.5	
	RT28DZ6‡	Río Guillermo	51.31163	72.22042	323	1	24.3 ± 0.6 (*n* = 8)
	RT28DZ5‡	Río Turbio (upper)	51.31373	72.21932	349	−1	26.6 ± 0.2 (*n* = 5)
	RT28DZ7‡*	Río Turbio (upper)	51.29761	72.23581	349	−60	35.4 ± 0.2 (*n* = 45)
	RT28DZ8‡*	Río Turbio (upper)	51.29667	72.23819	282	−90	36.6 ± 0.3 (*n* = 65)

‡*Samples from Fosdick et al. (2019).* **Approximate stratigraphic position in measured section.*

is the erosional contact with the underlying fine-grained Río Turbio Formation. Channelized bases are moderately erosive and marked by imbricated basal lag deposits, meter-scale, sand-filled channel cuts, and abundant petrified wood fragments (**Figures 2A–D**, **3**). Coarse-grained intervals increase in abundance and thickness upsection from ∼6–8 m to ∼12 m thick at the top of the unit (**Figure 3**). These coarse-grained strata are interbedded with thin-bedded, organic rich fine-grained sandstone and siltstone, with rare lignite horizons (*St, Fl,* and *C)*. Fossil plant debris (leaf impressions, twigs) and burrows, predominantly vertical, are common in fine-grained beds. We interpret these deposits to record conglomeratic fluvial bedload and overbank deposition of gravel bars and bedforms in a vegetated braidplain environment. Basal contacts of the fine-grained intervals are generally sharp, with little or no evidence of upward-fining that would reflect waning flow in the bedload deposition (e.g., Miall, 2006), consistent with an avulsive fluvial system. Abundant and well-preserved fossilized wood and tree stumps in life position suggest high sedimentation rates, subsidence, and burial of the floodplain (**Figures 2C**, **3**).

Unit 2 is ∼160 m thick and consists dominantly of poorly exposed, weakly stratified, interbedded organic-rich mudstone and siltstone (**Figures 2E,G,H**, **3**). The deposits are fissile with crude lamination and range in color from yellow to brown, gray, and orange (*Fl)* (**Figure 2F**). Where preserved, bedding style within organic-rich mudstone and siltstone ranges from horizontal lamination to lenticular bedding (**Figures 2G,H**). Rare thin beds of very fine- to fine-grained, horizontally laminated or structureless sandstone (*Fl*), and trough cross-stratified granule conglomerate (*Gt*) are present, and have erosive or sharp basal contacts, interpreted as localized splay deposits (**Figure 3**). Fossilized leaf impressions and other floral elements are present, though we note the lack of observed marine invertebrate fauna compared to those observed in the underlying upper Río Turbio Formation (Sequence 9 of Rodríguez Raising, 2010). Our observations are limited to the exposures of the lower part of Unit 2, and we estimate an additional ∼75 m of covered section within the fine-grained, recessive interval, based on regional dip and basal contact of overlying coarse-grained deposits of Unit 3. This interval is correlated across the Cancha Carrera study area, suggesting lateral continuity of this depositional facies. We

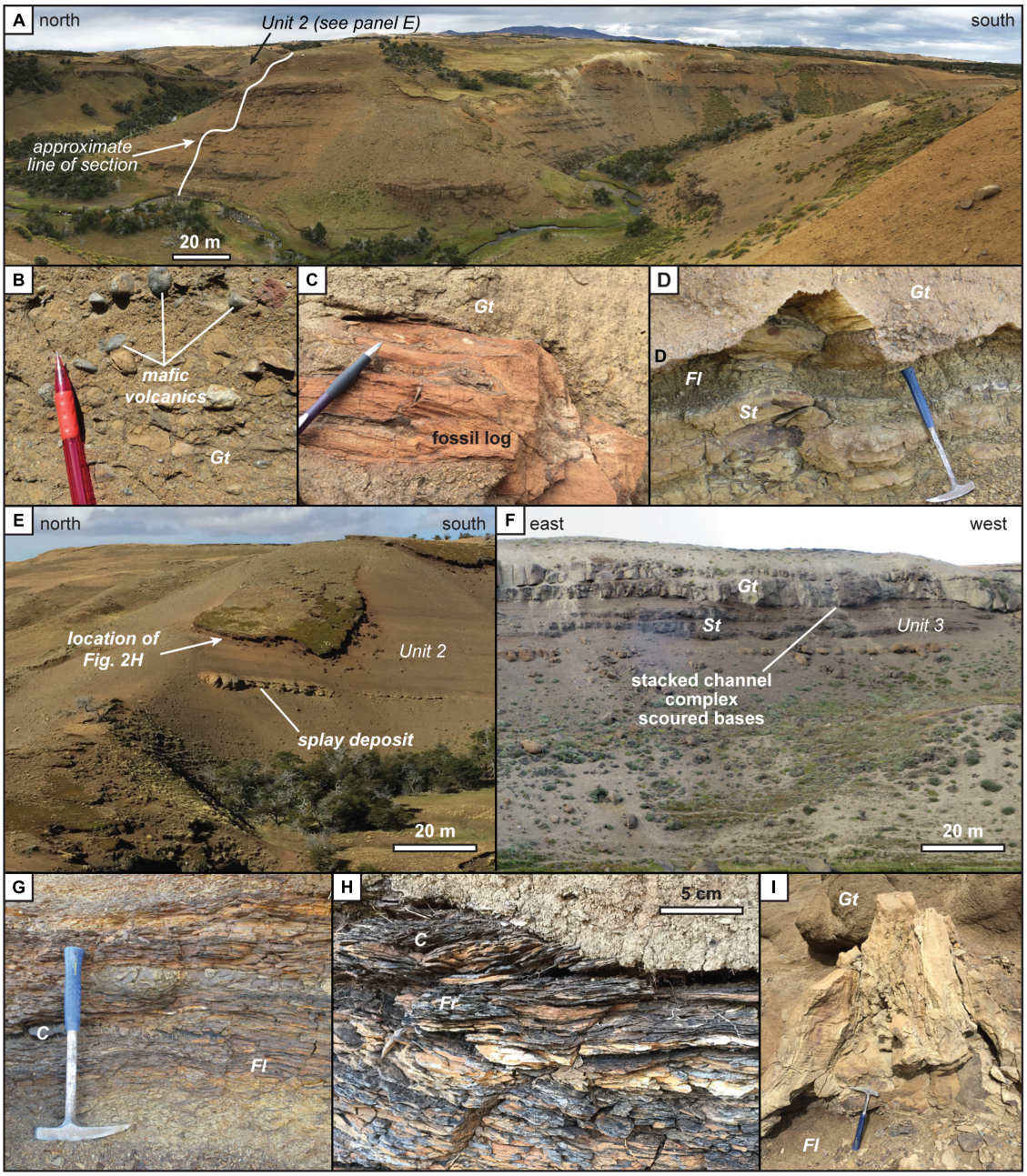

FIGURE 2 | Representative outcrops of the Río Guillermo Formation at the Cancha Carrera study area. **(A)** Panoramic basinward view of Unit 1 showing channelized *Gt* conglomerate and *St* sandstone and fine-grained, slope-forming strata (*Fl, C*). White line depicts location of part of the measured section in **Figure 3**. **(B)** Representative clasts from a *Gt* bed from Unit 1. **(C)** Petrified wood encased within *Gt* conglomerate in Unit 1. **(D)** Erosive base of channelized *Gt* strata into underlying fine-grained strata in Unit 1. **(E)** Panoramic basinward view of Unit 2 showing mostly interbedded mudstone and siltstone with sparse channelized *Gt*, *Gh*, *Gt* deposits. White line depicts location of part of the measured section. **(F)** Panoramic view of Unit 2 showing channelized *Gt* and *St* beds and recessive slope-forming *St* and *Sl* strata. **(G,H)** Fine-grained *St*, *Fl*, and *C* of Unit 2. **(I)** Fossilized tree trunk in life position, rooted in fine-grained *St and Fl* and buried by channel *Gt* deposits of Unit 3. See **Table 2** for lithofacies codes.

interpret deposits of Unit 2 to represent a sustained interval of low-energy, organic-rich floodplain deposition within the upper reaches of a fluvial-tidal transition zone of the coastal plain.

Unit 3 is ∼85 m thick and consists of sandstone, conglomerate, siltstone, mudstone, and minor lignite (**Figures 2F**, **3**). Conglomerate beds are generally trough cross-stratified with highly erosive basal contacts and occasionally have imbricate basal lags (*Gt, Gh,* and *St*), similar to Unit 1 (**Figures 2F**, **3**). Similar to the fine-grained depositional intervals within Unit 1, the siltstone and mudstone deposits are generally horizontally or

crudely ripple cross-laminated with sparse sandstone lenses (*Fl*) and rare lignite horizons (*C*). The distinguishing characteristic of Unit 3 is abundant thick-bedded, low angle trough cross-stratified sandstone that ranges in grain-size from very fine- to very coarse-grained. Planar cross-stratification and massive bedding are also present (*Sp, Sm)*, although are less abundant than trough cross-stratified bedding (**Figure 3**). Erosive or sharp basal contacts are most common between coarse- and fine-grained intervals, but upward fining bar forms are also present and are unique to Unit 3. Fossil logs and tree stumps in life position are present in both conglomerate and sandstone beds (**Figure 2I**). We interpret Unit 3 strata to have been deposited in a channelized, sandy fluvial braidplain environment. Preservation of bar forms and erosive conglomerate and sandstone deposits are consistent with channelized flow conditions, but the sharp depositional contacts between fine-grained overbank facies and underlying bedload deposits suggest an avulsive character to the fluvial system.

Taken together, increasing rates of vertical aggradation is apparent throughout the Río Guillermo Formation, as evidenced by distinct upsection changes in the character of active channel facies that either reflect increasing accommodation and/or sediment flux. Alternating coarse- and fine-grained intervals characteristic of the basal ∼100 m (Unit 1, **Figure 3**) are consistent with fluvial aggradation under accommodation limited conditions where preservation of sandstone in active channel deposits is poor (Miall, 2006). In contrast, active channel deposits in the uppermost ∼90 m (Unit 3, **Figure 3**) contain sandstone beds as well as similar fining-upward bar forms that indicate the rate of aggradation was relatively higher. Therefore, we interpret that a more continuous and expanded stratigraphy is represented higher in the section (Unit 3) than lower in the section (Unit 1), but both fundamentally reflect the same type of depositional system under differing accommodation or sediment flux conditions. The transition between these two depositional units is obscured by the thick accumulation of tidally influenced floodplain deposits (Unit 2) that we interpret reflect a combination of river avulsion and deepening along the basin margin coastal plain. The limited outcrop extent of the Río Guillermo Formation precludes evidence for any correlative in-channel deposits of equivalent age to Unit 2. Abundant tree trunks fossilized in life position, rooted in fine-grained floodplain deposits, and preserved by in-channel deposits suggests sedimentation rates were high throughout deposition of the full stratigraphic thickness (**Figure 3**), and more quantitative constraints on internal variations in sediment flux are not possible within the resolution of our data.

Modal Analysis of Conglomerate and Sandstone Compositions

We collected modal sandstone petrographic and conglomerate lithologic data from the Río Guillermo Formation and underlying upper Río Turbio Formation to track upsection changes in lithic grain compositions and diagnostic clast lithology that could be linked to potential source areas (**Figures 4**, **5**). Petrographic thin sections from 16 sandstone samples from the upper part of the Río Turbio and Río Guillermo formations were analyzed for quartz-feldspar-lithics framework mineralogy (QFL), lithic grain types (LmLvLs), single crystal phases, and cement composition (see **Figure 3** for sample locations in section). The three samples from the upper Río Turbio Formation were collected from Sequence 9 of Rodríguez Raising (2010). Samples were point-counted (for 400 grains) using the Gazzi-Dickinson method (after Ingersoll et al., 1984; Dickinson, 1985) using a Pelcon automated point counting system and a Leica DMZ2700 petrographic light microscope at Indiana University Bloomington. Grain parameters identified in these point counts are listed in the **Supplementary Table S1**, and recalculated data are provided in **Table 3**. Recalculated framework modal compositions were used to determine tectonic provenance (Dickinson and Suczek, 1979; Dickinson, 1985). Quartz-Feldspar-Lithics (i.e., QtFL and QmFLt) data from the upper Río Turbio and Río Guillermo formations were compared with published sandstone petrographic analyses of lower stratigraphic intervals and plotted on ternary diagrams, with tectonic fields as defined by Dickinson (1985). Refer to **Supplementary Table S1** for point counting grain classifications and **Supplementary Table S2** for raw point count data.

Ternary QFL, QmFLt, and LmLvLs plots of modal sandstone compositions from this study are shown in **Figure 4** accompanied by previously published samples from the underlying Punta Barrosa, Cerro Toro, Tres Pasos, and Dorotea formations (Fildani and Hessler, 2005; Valenzuela, 2006; Romans et al., 2010). These data reveal a long-term trend toward increasingly lithic-rich compositions upsection. In detail, the Punta Barrosa Formation records substantial contributions from metamorphic lithics, interpreted as incipient topographic uplift of the nascent orogen, and the Cerro Toro Formation records an increase in intermediate-to-felsic volcanic lithics, interpreted as unroofing of the Tobífera Formation in the hinterland thrust domain. Our data show a continuation of increasing lithic trend in the upper Río Turbio Formation culminating in a distinctly volcanic lithic-rich Río Guillermo Formation (**Figure 4**).

Detailed compositional data recorded from point counts are presented in **Figure 5**. In general, the upper Río Turbio Formation has an immature lithic-rich composition, particularly volcanic lithics. Relative abundances of quartz and lithic grains steadily increase upsection at the expense of feldspar and accessory minerals (**Figure 5B**). The Río Guillermo Formation is characterized by extreme compositional and textural immaturity, reflected in higher concentrations of labile mafic accessory minerals and volcanic lithic grains (**Figures 5B,C**). Quartz is sparse throughout, as is the proportion of metamorphic lithic grains relative to the upper Río Turbio Formation. Pyroxene also appears as an important mineral component. Finally, we note a consistent lack of sedimentary lithic grains in both units (**Figure 4**), but acknowledge this observation may be biased by preferential weathering. Notably, the upper Río Turbio Formation has a higher abundance of Lm compared to the Río Guillermo Formation (**Figure 4**).

Conglomerate compositions were determined by conducting *in situ* clast counts from five counting stations through the measured section of the Río Guillermo Formation, where

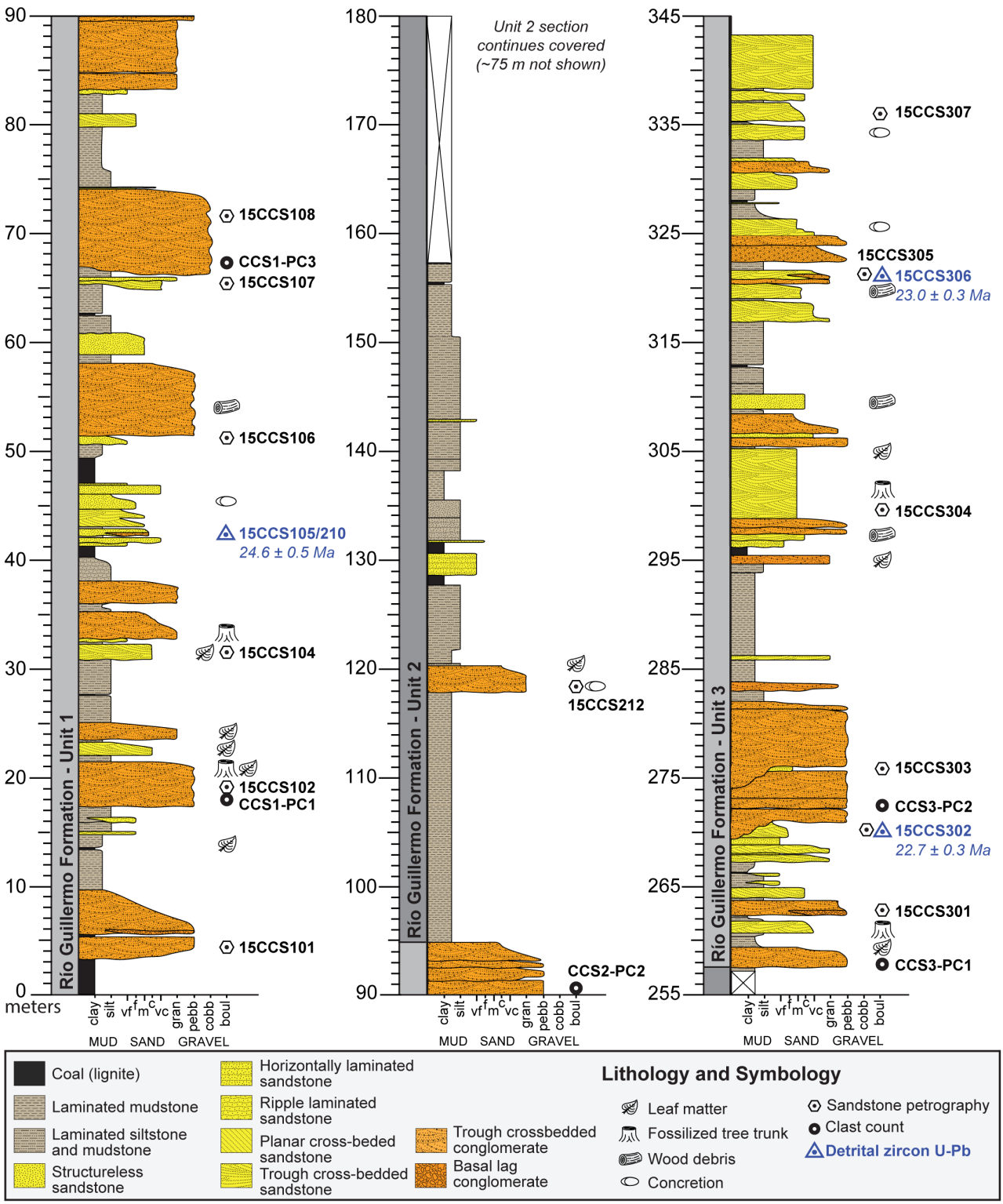

FIGURE 3 | Measured stratigraphic section of the Río Guillermo Formation at Cancha Carrera, Argentina, with sample locations for sandstone petrography, modal clast analysis, and detrital zircon U-Pb geochronology. We subdivide the formation into three major units based on sedimentology and stratigraphic architecture. Maximum depositional ages (blue triangles) interpreted from the detrital zircon U-Pb data are reported at 2σ. See text for detailed descriptions. Locations of measured section: Base 51.31259°S, 72.22169°W; Top 51.30823°S, 72.19668°W.

TABLE 2 | Lithofacies codes, sedimentary structures, and interpretations used in this study (modified after Miall, 1978).

Lithofacies code	Description	Interpretation
Gt	Matrix-supported granule to cobble conglomerate, trough cross-stratification	Channel fill deposits
Gh	Clast-supported granule to cobble conglomerate, crudely or horizontally bedded, imbrication	Longitudinal bedforms, lag deposits, sieve deposits
St	Fine- to very coarse-grained pebbly sandstone, solitary or grouped trough cross-stratification	Sinuous crested or isolated dunes
Sp	Fine- to very coarse-grained pebbly sandstone, solitary or grouped planar cross-stratification	Straight crested dunes
Sh	Fine- to very coarse-grained pebbly sandstone, horizontal and ripple laminations	Plane-bed flow (critical flow)
Sl	Fine- to very coarse-grained pebbly sandstone, angle cross-stratification	Scour fills, humpback or washed-out dunes, antidunes
Fl	Fine sandstone, siltstone and mudstone, horizontal and ripple laminations	Overbank, abandoned channel or waning flood deposits
C	Coal, carbonaceous mud, plant debris, and mud films	Vegetated swamp deposits

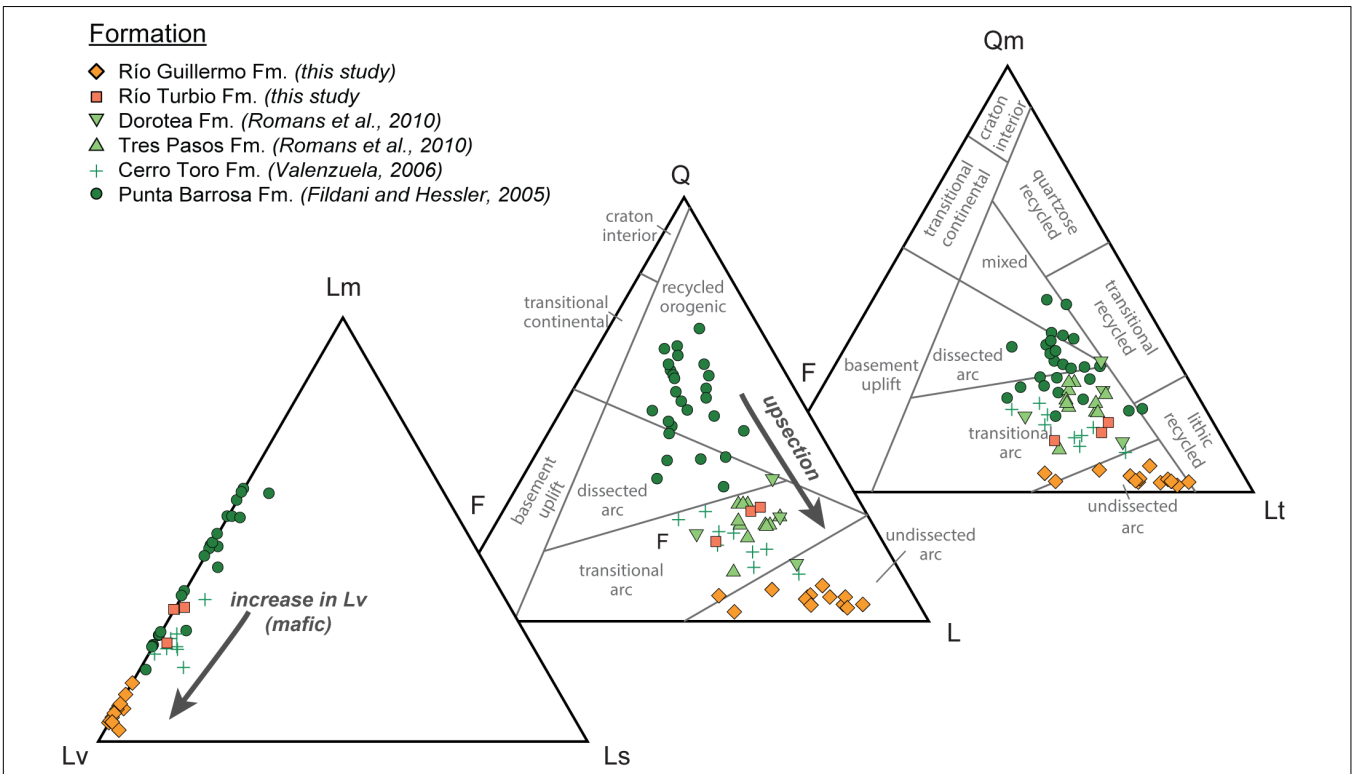

FIGURE 4 | Sandstone modal petrographic data from the Río Turbio Formation (red squares) and Río Guillermo Formation (orange diamonds) shown in comparison to published petrographic data from the Magallanes-Austral Basin. Refer to **Table 3** for parameters. Tectonic provenance fields are from Dickinson (1985). QFL (Quartz-Feldspar-Lithics) and QmFLt (Monocrystalline quartz-Feldspar-Lithic total) data show an upsection trend of decreasing in compositional maturity toward *undissected arc* source areas. LmLvLs data show a shift from Lm toward Lv, suggesting that the influx of mafic volcanic arc sediment is swamping any other recycled orogenic sources. Published datasets from the Upper Cretaceous basin infill are compiled from Fildani and Hessler (2005), Valenzuela (2006), and Romans et al. (2010).

conglomerate beds consisted of sufficiently large clasts (coarse pebbles and small cobbles) to allow for petrological identification in the field. To minimize bias toward more durable clast types, we used the area counting technique (Howard, 1993) for all pebble- and cobble-sized clasts until 60 counts were reached for four of five stations, while the stratigraphically highest count was limited by the fine grain-size. We report normalized compositions from seven diagnostic clast lithologic compositions: pale green metavolcanic, white quartz, mafic volcanic, mudstone, dark schist, granitoid, and intermediate-felsic volcanic (**Figure 5D**). Recalculated data are shown in **Table 4**.

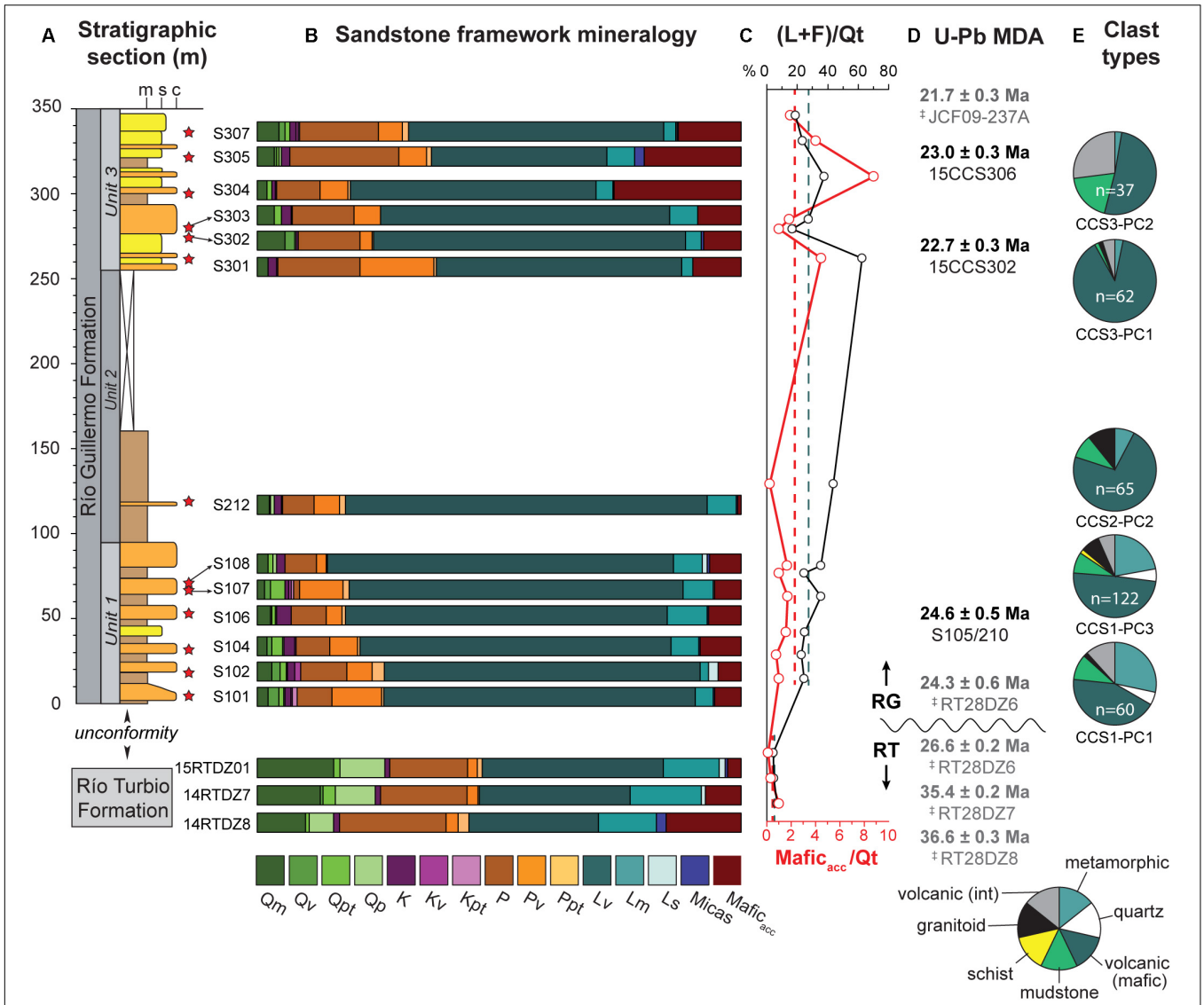

FIGURE 5 | Summary of modal sandstone petrography, clast compositions, and MDA from the Río Guillermo Formation at Cancha Carrera. Data from the underlying upper Río Turbio Formation are shown for comparison (stratigraphic positions approximated). **(A)** Simplified stratigraphic column. **(B)** Sandstone framework mineralogy. See **Table 4** caption for mineralogic abbreviations and section "Upper Oligocene-Lower Miocene Tectonics and Sedimentation History" for detailed discussion of trends. **(C)** (L + F)/Qt and $Mafic_{acc}$/Qt plots show relative immaturity (in %) of Río Guillermo Formation vs. upper Río Turbio Formation Dashed line represents the average of data for respective formations. **(D)** Relative contributions of clasts shown approximately in stratigraphic position – see **Figure 3** for sample locations. **(E)** Maximum depositional ages (MDA) interpreted from detrital zircon U-Pb geochronology. For comparison, ‡ denotes samples from Fosdick et al. (2019).

Conglomerate compositions throughout the Río Guillermo Formation are dominated (up to ∼90%) by mafic volcanic clasts (**Figure 5E**). There is an upsection decrease in pale green metavolcanic clasts and white quartz pebbles; we do not find white quartz pebbles in the upper part of the section (Units 2 and 3). Intermediate-felsic volcanic clasts are abundant at the base and top of the section. Granitoid clasts steadily increase in relative abundance through the lower part of the section, but become sparse upsection. Persistent, but subordinate, amounts of mudstone are also present, and rare biotite schist clasts were found in the bottom of the section.

Detrital Zircon U-Pb LA-ICP-MS Geochronology

Standard 5–6 kg samples were collected at regular intervals within the Río Guillermo Formation (**Figure 3** and **Table 1**). Mineral separations were performed by ZirChron, LLC using standard crushing, grinding, density, and heavy liquid procedures. Samples from the lower Río Guillermo Formation yielded very few zircon, and samples collected higher in the section were only modestly more zircon fertile. We re-processed our mineral concentrates to capture all available zircon; however, the zircon yield was limited by the sample volume. All extracted

TABLE 3 | Recalculated modal sandstone composition data.

Sample	Counts	Qm	Qv	Qpt	Qp	K	Kv	Kpt	P	Pv	Ppt	Lv	Lm	Ls	Micas	Mafic Acc.
	n	(%)	(%)	(%)	(%)	(%)	(%)	(%)	(%)	(%)	(%)	(%)	(%)	(%)	(%)	(%)
14RTDZ-8	400	10	0	0.8	5	1.3	0	0	22	2.5	2.3	26.8	12	0	2	15.5
14RTDZ-7	353	13	0.6	2.5	8.2	1.1	0	0	17.8	2.3	0.3	31.2	14.7	0.8	0	7.4
15RTDZ01	400	15.8	0	1.3	9.8	1	0	0	16	2	1	37.3	11.5	1.3	0.5	2.8
15CCS101	401	2.2	2.2	1	0.2	1.2	0.2	1	7.2	10.2	0.5	64.3	3.7	0	0.2	5.5
15CCS102	400	3	1.8	1.3	0.3	1.5	1.3	0	9.5	5.3	2.5	65.3	1.8	2	0	4.8
15CCS104	400	2	1	2.3	0.3	2.3	0.3	0	7	5.8	0.5	64.3	5.8	0	0.3	8.5
15CCS106	400	2.8	0.3	0.8	0.3	3	0	0	7.3	3.3	0.8	66.5	8.3	0	0.3	6.8
15CCS107	400	1.5	1.3	3	0	0.8	0.5	0.5	1.3	9	1.3	69	6.3	0.3	0	5.5
15CCS108	400	2.3	0	1	0.8	1.8	0	0	6.5	2	0.3	71.5	6	1	0.5	6.5
15CCS212	400	2.5	0	0.3	0.8	1.5	0.3	0	6.5	5.3	1.3	74.8	6	0	0.3	0.8
15CCS301	400	2.3	0	0	0	1.8	0.3	0	17	16.5	0.5	49.5	2.3	0	0	10
15CCS302	400	5.8	2	0	0.3	0.5	0	0	12.8	2.5	0.3	64.5	3.3	0	0.5	7.8
15CCS303	400	3.5	0	1.5	0	2	0.3	0	12.8	5.5	0	59.8	5.8	0	0	9
15CCS304	400	2	0	1	0	0.8	0.3	0	9	5.8	0.5	50.8	3.5	0	0.3	26.3
15CCS305	400	4.5	1.3	1	0	1.3	0.5	0.3	16.3	5	1.3	52.8	2.5	0.3	0.3	13
15CCS307	400	3.5	0.5	0.5	0.5	1.8	0	0	22.5	5.8	1	36.3	5.8	0	2	20

Qm, monocrystalline quartz; Qv, volcanic quartz; Qpt, plutonic quartz; Qp, polycrystalline quartz; K, mono-crystalline K-feldspar; Kv, volcanic K-feldspar; Kpt, plutonic K-feldspar; P, monocrystalline plagioclase feldspar; Pv, volcanic plagioclase feldspar; Ppt, plutonic plagioclase feldspar; Lv, volcanic lithic; Lm, metamorphic lithic; Ls, sedimentary lithic; Micas, Bt + Chl + Mu; Mafic$_{acc}$, Amphibole + Pyroxene (cpx) + Ol.

TABLE 4 | Recalculated modal clast composition data.

Count name	Clasts counted	Pale green metavolcanic	White quartz	Mafic volcanic	Mudstone	Schist (dark)	Granitoid	Intermediate volcanic
	(*n*)	(%)	(%)	(%)	(%)	(%)	(%)	(%)
CCS1-PC1	60	28.3	5	43.3	10	0	1.7	11.7
CCS1-PC3	122	22.1	4.9	49.2	8.2	1.6	7.4	6.6
CCS2-PC2	65	7.7	0	72.3	9.2	0	10.8	0
CCS3-PC1	62	3.2	0	88.7	1.6	0	1.6	4.8
CCS3-PC2	37	2.7	0	51.4	18.9	0	0	27

individual zircons from each sample were hand-picked and mounted on double-sided tape to make them available for future (U-Th)/He double dating. Zircon U-Pb LA-ICPMS analyses were conducted at University of Arizona LaserChron Center following analytical procedures of Gehrels (2012). Grains were analyzed at random to avoid bias in detrital age distributions. A very small percentage of grains have anomalously high analytical uncertainty (>20%, 1σ) in $^{207}Pb/^{235}U$ and were excluded from final age distributions. However, inclusion of these grains does not substantively affect any interpretations put forward. Given the low zircon yield of these samples, our data interpretations are largely summarized for the formation in general, rather than detailed upsection changes in age spectra. Maximum depositional ages (MDA) (**Table 1**) are calculated based on youngest age populations defined by three or more overlapping zircon ages (2σ). Refer to **Supplementary Table S3** for detrital zircon LA-ICPMS data.

Detrital zircon analyses from both the upper Río Turbio Formation and Río Guillermo Formation are characterized by bimodal distributions of Cenozoic and Cretaceous populations with very few Paleozoic and older grains (**Figure 6**). Cretaceous ages from both formations are characterized by bimodal distributions; however, the youngest of these modes (67–78 Ma) is a new association that does not correspond with known bedrock geochronology (Hervé et al., 2007). A prominent Eocene peak (30–40 Ma) is an exclusive feature of the upper Río Turbio Formation, while Neogene ages characterize Cenozoic populations in the Río Guillermo Formation This Eocene peak is also a new association and post-dates known Paleogene magmatism in the Southern Patagonian Batholith (Hervé et al., 2007).

Sample 15CCS105/210 is a composite from stratigraphically adjacent locations in the lower part of the section, both with poor zircon yields, 24 and 57 grains, respectively. Ages range from *ca.* 24 to 503 Ma, with a single significant Cenozoic peak centered at *ca.* 25 Ma populated by the 10 youngest grains, a broadly bimodal Cretaceous age group with peaks at (74, 79, and 83 Ma) defining the younger mode and (100, 105, and 108 Ma) defining the older mode, and a minor Late Jurassic age peak. An error-weighted mean of the youngest coherent zircon population ($n = 7$) yields a calculated MDA of 24.6 ± 0.5 Ma (2σ). This age overlaps with the calculated MDA of 24.3 ± 0.6 Ma (2σ) from the stratigraphically

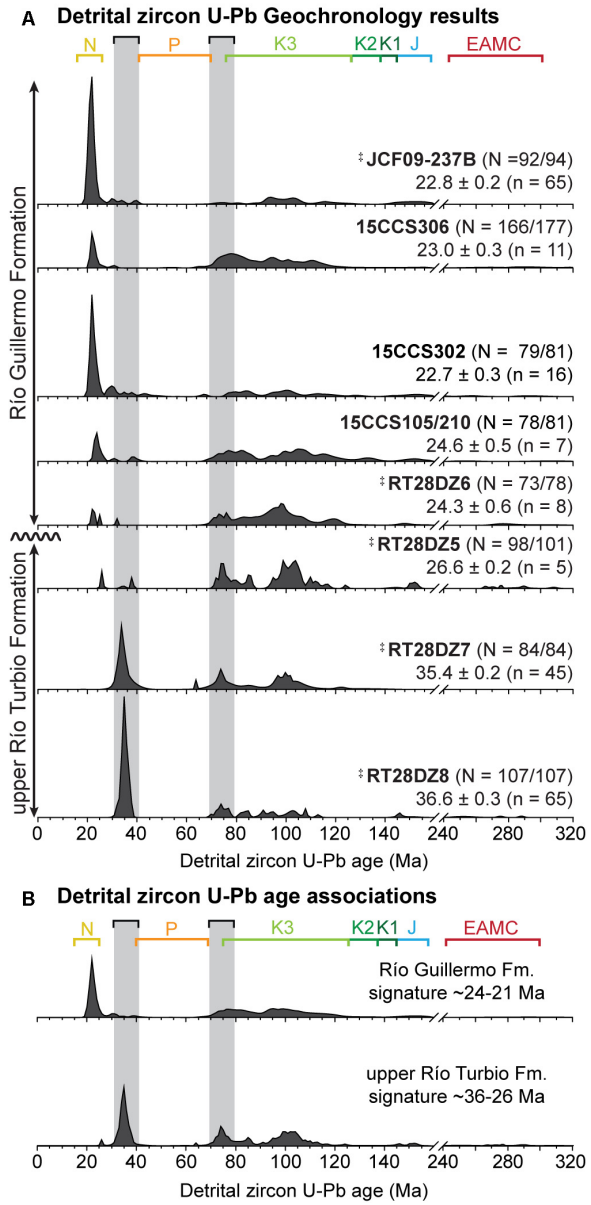

FIGURE 6 | Detrital zircon U-Pb LA-ICP-MS data showing upsection changes in provenance. **(A)** Normalized probability age distributions from the Río Guillermo and upper Río Turbio formations. Note the change in scale at 160 Ma. Ages of igneous sources as reported from Hervé et al. (2007) are Neogene (N), Paleogene (P), Cretaceous I (K1), Cretaceous II (K2), and Cretaceous III (K3), Jurassic (J), and Eastern Andean Metamorphic Complex (EAMC). **(B)** Combined detrital zircon age associations for the pre-tectonic and post-tectonic sediment sources, showing a loss of a predominant 30–40 Ma source prior to 24 Ma. ‡ denotes samples from Fosdick et al. (2019).

lower RT28DZ6 from Fosdick et al. (2019) at the base of the Río Guillermo Formation, which does not suffer from similarly low zircon fertility.

Sample 15CCS302 had a relatively higher zircon yield of 108 grains but contained a significant number of grains excluded due to high (>20%) analytical uncertainty. The age distribution is characterized by a strong *ca.* 23 Ma peak populated by the 33 youngest grains, a minor Eocene peak at 32 Ma, and minor Late and middle Cretaceous modes defined by peaks at 81, 85, and 101 Ma, respectively. An error-weighted mean of the youngest coherent zircon population (n = 16) yields a calculated MDA of 22.7 ± 0.3 Ma (2σ).

Sample 15CCS306 had a moderate zircon yield producing 198 grains, with 177 of those analyses within threshold uncertainty. Age distributions show a well-defined *ca.* 23 Ma early Miocene peak, and significant Late – Early Cretaceous age groups with peaks at (75, 79, 89, 96, and 106 Ma). An error-weighted mean of the youngest coherent zircon population (n = 11) yields a calculated MDA of 23.0 ± 0.3 Ma (2σ).

DISCUSSION

Integrated sedimentary provenance and sedimentology from the Río Guillermo Formation capture the drainage configuration during latest Oligocene – early Miocene development of the southern Patagonian Andes. Here, we discuss the detailed provenance signatures within the context of the kinematic history of the Patagonian fold-and-thrust belt and the long-term foreland basin record. Specifically, this synthesis explores the regional driving factors and chronologic progression of the structural and topographic development of an orogenic wedge during forced adjustment to incorporation of inherited basin structures (Fosdick et al., 2011) and migration of the locus of exhumation (Thomson et al., 2001; Fosdick et al., 2013).

Interpreted Provenance of the Upper Oligocene – Lower Miocene Basin Fill

We interpret the collective provenance datasets of modal sandstone, conglomerate compositions, and detrital zircon geochronology across the transition from proximal upper Oligocene to middle Miocene deposits preserved in the basin at this latitude. Below we outline distinct provenance trends observed within the upper Río Turbio Formation and overlying Río Guillermo Formation that support (1) a shift from transitional to undissected arc source areas, (2) persistent connectivity to the syndepositional volcanic arc, (3) waning sediment contribution from internal fold-thrust belt (Jurassic and Paleozoic), and (4) a pronounced loss of the late Eocene (~40–30 Ma) zircon source areas in earliest Oligocene time.

Sandstone provenance of the upper Río Turbio Formation is consistent with a *transitional arc* source (c.f. Dickinson, 1985), and has similar compositional character to the underlying Dorotea, Tres Pasos, and Cerro Toro formations of the external fold-and-thrust belt (**Figures 1B**, **4**). We interpret this consistency to suggest either (1) a stable source area despite substantial unconformities, changes in sedimentation style, and depositional environments contained within that stratigraphic succession during this time interval, and/or (2) recycling of these underlying units where they are exposed in thrust sheet hanging-wall blocks to the west of our study area (**Figure 1**). Locally, upsection trends within the upper Río Turbio Formation include

a progressive loss of labile minerals (i.e., amphibole, pyroxene, olivine) and increase in quartz grains (**Figure 5B**), which could be due to winnowing effects during recycling and higher rates of weathering in the source areas (e.g., Johnsson, 1993; Cox et al., 1995). The Upper Cretaceous basin infill, and in particular the Punta Barrosa Formation, contains abundant metamorphic lithics representative of the EAMC and hinterland thrust domain (**Figure 4**). Therefore, within the upper Río Turbio Formation, the maturation of sandstone compositions and comparable or lesser relative abundance of L_m lithics may record recycled provenance from these external fold-and-thrust belt sources. The lack of Paleocene zircons precludes the underlying Cerro Dorotea Formation (Fosdick et al., 2019) as a source, suggesting these strata were not yet exposed during deposition of the Río Turbio and Río Guillermo formations.

Provenance data from the overlying Río Guillermo Formation suggest a distinct shift in the sediment source areas to a mafic volcanic arc, and lesser contributions from the hinterland thrust domain or external fold-and-thrust belt (**Figures 4**, **5B,C,E**). Sandstones are texturally and compositionally extremely immature throughout, as evidenced by high relative abundance of volcanic lithic grains and mafic minerals, and dearth of quartz (**Figure 4**). These data also preclude any significant recycling from Río Turbio Formation equivalent or older foreland basin strata as a significant potential sediment source. Rather, the abundance of chemically and physically susceptible sandstone grains (e.g., volcanic lithics and mafic minerals and/or those dominant cleavage planes) is consistent with direct sourcing from the active magmatic arc. Whole rock $^{40}Ar/^{39}Ar$ ages and major and trace element geochemistry from the mafic volcanic clasts indicate Miocene (25–22 Ma) eruptive ages with arc geochemistry (VanderLeest et al., 2018). The prominent Miocene zircon U-Pb age peak generally youngs upsection within the Río Guillermo Formation and supports direct connectivity with the magmatic arc (**Figure 6**).

Maintenance of a direct sediment routing pathway from the magmatic arc to the proximal foredeep through Oligocene-Miocene sedimentation is supported by younging of youngest detrital age populations from ∼33 Ma to ∼21 Ma upsection (**Figure 6A**). We note, however, the abrupt loss of the prominent Eocene zircon U-Pb age peak (40–30 Ma) at the top of the upper Río Turbio Formation (between samples RT28DZ7 and RT28DZ5; **Figure 6A**). This Eocene peak is not a previously recognized phase of arc magmatism identified within the SPB or associated volcanic rocks (Hervé et al., 2007), suggesting limited original extent of Eocene magmatism and/or underrepresentative sampling due to remote access of the fjords. The loss of the Eocene arc source during Río Guillermo deposition may be interpreted as either isolation of the Eocene source by Oligocene-Miocene volcanic cover or intervening thrust sheets, or erosional removal. The "reappearance" of the Eocene age peak in younger overlying strata may indicate recycling of Paleogene deposits (Fosdick et al., 2015), or drainage reorganization with directly sourced remnants of the Eocene arc.

In addition to the syndepositional volcanic arc primary source area to the Río Guillermo Formation, we evaluate direct or recycled sediment sources from other orogenic source areas. Evidence of subordinate sediment contribution from the hinterland thrust domain or external fold-and-thrust belt include the pale green metavolcanic and white quartz clasts (∼20%), diagnostic of the Upper Jurassic Tobífera Formation, and biotite schist clasts (<5%) that are likely derived from EAMC basement rocks (**Figure 5E**). Additionally, well-indurated extrabasinal mudstone clasts (6–18%), which are least diagnostic in terms of potential source areas, but point to either the hinterland thrust domain and/or external fold-and-thrust belt source areas (e.g., Zapata Formation and/or mudstone-rich facies of the Cerro Toro Formation). These sediment types are challenging to interpret because they could be derived directly from the hinterland thrust domain (**Figure 1**), or recycled from the external fold-and-thrust belt, which includes similar hinterland and batholith derived provenance signatures. Specifically, SPB-derived granitoid clasts and metarhyolite clasts from the Tobífera Formation are abundant in the Cenomanian Cerro Toro Formation (Crane, 2004; Valenzuela, 2006), which comprises part of the external fold-and-thrust belt. The Late Cretaceous detrital zircon U-Pb age clusters reflect either direct sourcing from the eroded batholith or recycled zircons from the external fold-and-thrust belt (e.g., Romans et al., 2010; Fosdick et al., 2015). The decrease in relative abundance of metarhyolite clasts and substantial lack of Late Jurassic zircon U-Pb ages may indicate dilution of the Tobífera Formation clasts as the syndepositional arc source areas became dominant.

Due to the paucity of Jurassic and Paleozoic U-Pb zircon ages or sediment types (metamorphic lithics, SPB granitoids) characteristic of the hinterland thrust domain, we prefer an interpretation for the Río Guillermo Formation as (1) direct sourcing of the active Miocene arc, with (2) lesser recycled sediment input from the external fold-thrust-belt. In this scenario, the headwaters of the ancestral Río Guillermo resided in the extensive Miocene volcanic highlands, but the drainage network largely bypassed the hinterland thrust domain. This scenario may be analogous to the changes in basin configuration interpreted for the Neogene Bermejo Basin in the Central Andes, where uplift of the Precordillera caused river drainage reorganization that shifted from a mixture of Precordillera and hinterland-derived source areas, to a regional point-source within the hinterland Frontal Cordillera (Jordan et al., 1993).

Upper Oligocene-Lower Miocene Tectonics and Sedimentation History

Our new provenance interpretations from the upper Oligocene through lower Miocene Magallanes-Austral Basin at Estancia Cancha Carrera indicate a major shift in source areas that is consistent with rejuvenation of arc magmatism and a tectonic reorganization of the hinterland and fold-and-thrust belt. This shift in sedimentary provenance between ∼27 and 24 Ma that predates a basin margin change in depositional environment and transition from shallow marine to fluvial sedimentation, as recorded by the Río Guillermo Formation. Here, we compare the timing of eustatic sea level variations, retroarc deformation, and plate convergence rates, to understand the geologic context

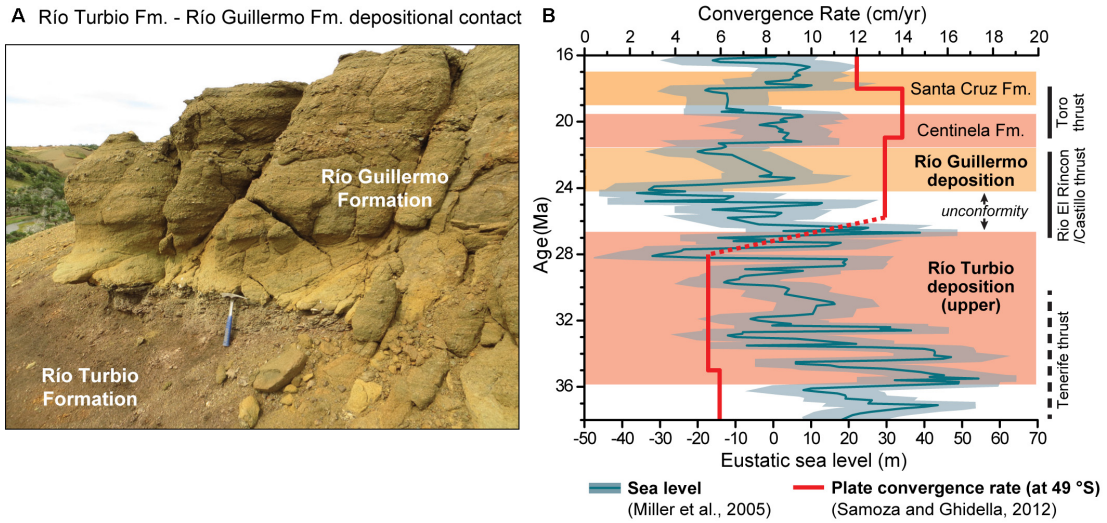

FIGURE 7 | (A) Outcrop photograph of the disconformable contact between the Río Guillermo Formation and underlying upper Río Turbio Formation at the Cancha Carrera study locality. **(B)** Changes in eustatic sea level during deposition of the foreland basin deposits in our study area. Sea level data from Miller et al. (2005). Convergence rates between the South America and Farallon plates for 49°S from Somoza and Ghidella (2012). Timing of faulting in the external fold-and-thrust belt from Fosdick et al. (2011). Depositional ages from Fosdick et al. (2015, 2019), and references therein. The erosional unconformity between the Río Turbio and Río Guillermo formations corresponds in time and duration to a long-term drop in eustatic sea level.

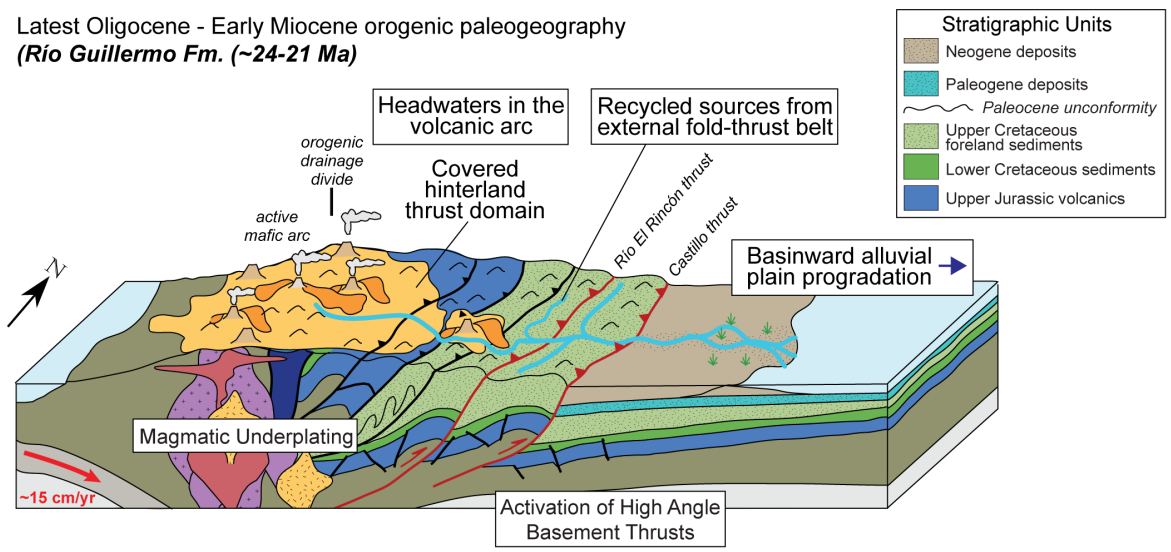

FIGURE 8 | Schematic paleogeographic cartoon of the late Oligocene – early Miocene orogenic configuration during deposition of the Río Guillermo Formation. Modified from Fosdick et al. (2015) with new learnings specifically to this time interval.

for these changes in sediment source areas in Patagonia, with implications for orogenic and basin sedimentation processes.

The ~2 Myr disconformable contact between the uppermost Río Turbio Formation and Río Guillermo Formation reflects a change from marginal marine to fluvial depositional environments (**Figure 7A**) that we suggest is at least partially influenced by a global regression across this time interval. By ~24 Ma, eastward directed fluvial sedimentation was established, representing a basin margin shallowing to non-marine conditions. Sedimentation of the entire ~350 m compacted thickness of the Río Guillermo Formation at Estancia Cancha Carrera is tightly constrained to ~2.5 Myr. This requires sufficient basin accommodation and sediment flux to produce a modest sedimentation rate (~0.14 km/Myr) over this time interval, on par with Neogene rates observed elsewhere in the Andean foreland basin systems (e.g., Goddard and Carrapa, 2018). Over that corresponding time interval, eustatic sea level is characterized by an abrupt 30–50 m rise and relative highstand (Miller et al., 2005; **Figure 7B**). This transgression is well-recorded in the more distal reaches of the basin, as recorded

in coeval shallow marine deposits of the San Julián Formation along the present-day Atlantic coast (Parras et al., 2008, 2012).

The kinematic development of the Patagonian fold-and-thrust belt records a decrease in upper crustal shortening since Late Cretaceous time, along with a deepening of the basal detachment in at least two stages of Cenozoic deformation (Fosdick et al., 2011). Based on structural mapping, seismic-reflection data, cross-cutting relationships, and available chronology of synorogenic foreland basin deposits, Fosdick et al. (2011) documented two phases of Cenozoic deformation characterized by basement-involved shortening and deepening of the decollement: Stage IV (∼27–21 Ma), with faulting of the Río Rincon and Castillo faults along a reconstructed decollement depth of ∼8–10 km; and Stage V (∼21–18 Ma), with further deepening of the decollement to ∼16–18 km along the Toro thrust. The little crustal shortening represented by these deformational phases (∼3–4 km) are consistent with high-angle fault geometries, several km of vertical rock uplift, and regional exhumation across the external fold-and-thrust belt (Fosdick et al., 2011, 2013). Both basement faulting stages are interpreted as inverted Mesozoic normal faults based on outcrop and subsurface data. Revised chronology of the Cenozoic foreland basin deposits (Fosdick et al., 2019), specifically the uppermost upper Río Turbio Formation (∼26 Ma) and Río Guillermo Formation (∼24–21 Ma), correspond in time to Stage IV, and perhaps the earliest part of Stage V. Our provenance interpretations from these deposits record a shift from *transitional arc* to *undissected arc* sources by between ∼27 and ∼24 Ma that was coeval with the widening of the orogenic wedge via forward propagation of reactivated basement faulting during Stage IV faulting (**Figure 8**).

Within the upper Río Turbio Formation, the maturation of sandstone compositions and persistent presence of L_m and L_s lithics may record continued sourcing from the hinterland prior to the major shift toward volcanic highland topography by 24 Ma. Starting ∼24 Ma at the base of Río Guillermo Formation, generation of volcanic highland topography due to rejuvenated magmatic arc provided volcanic sediment to the foreland basin margin (**Figure 8**). The relative paucity of sediment derived directly from the hinterland thrust domain may be explained by trunk rivers connected to the upland and arc, thereby routing around the retroarc foreland topography (**Figure 8**).

Previous workers have linked the Stage IV Río El Rincón-Castillo faulting to more rapid and orthogonal plate convergence between the Nazca and South American plates (Fosdick et al., 2013) and potential increase in retroforeland convergence due to transpressive development of the North Scotia Ridge (Bry et al., 2004; Lagabrielle et al., 2009; Fosdick et al., 2011). As the thrust front migrated cratonward, deformation along the Río El Rincón-Castillo faults (**Figure 8**) may have been localized by pre-existing basement structures beneath the foreland (Fosdick et al., 2011). Re-activation of these basement structures may have had the effect of changing the stress state of the orogenic wedge by activating a deeper sole-out depth (e.g., Hilley et al., 2005) and promoting vertical topographic uplift across the external fold-and-thrust belt. We posit that, although this phase of deformation caused foreland basin subsidence and sedimentation of the lower Miocene Río Guillermo Formation, headwaters located within the volcanic highlands, rather than the thrust sheets, provided the primary sediment flux to the basin margin (**Figure 8**).

The rejuvenation of the Miocene volcanic arc is consistent with an acceleration in plate convergence rates that occurred between 28 and 25 Ma prior to the breakup of the Farallon plate (Somoza and Ghidella, 2012; **Figure 7B**), which may have driven enhanced hydration melting and retroarc deformation. This scenario is consistent both with the uptick in early Miocene arc volcanism (VanderLeest et al., 2018) and provenance data reported here. Although this episode of orogenesis in Patagonia was limited in the magnitude of deformation and basin subsidence compared to elsewhere along the Andes (e.g., see Horton, 2018 for a recent synthesis), our data characterize the orogen-to-basin connection during this brief phase of retroarc deformation in Patagonia.

Lastly, the thermochronologic record from the Patagonian Andes suggests a post late Oligocene eastward migration of the locus of maximum denudation that we discuss briefly within the context of the Río Guillermo foreland basin history. Apatite fission track cooling ages from the Southern Patagonian Batholith document accelerated cooling and inferred denudation from ∼30 to 23 Ma (Thomson et al., 2001). Subsequently, this locus of maximum denudation shifted to the eastern margin of the batholith (**Figure 1**) until ∼18–14 Ma, which has been interpreted as an eastward migration in the topographic crest during that time (Thomson et al., 2001). Thus, the locus of maximum denudation during Río Guillermo deposition would have likely corresponded to the Miocene volcanic arc highlands (since eroded away) constructed within the Mesozoic batholith (**Figure 8**). We interpret the lack of substantial thrust belt provenance in the Río Guillermo Formation to be explained by a point-source routing system in the volcanic arc. Farther east, thermal history modeling of zircon (U-Th)/He thermochronology data suggest focused denudation between ∼17 and 16 Ma within the external fold-and-thrust belt, suggesting exhumation of at least 5 km since that time (Fosdick et al., 2013; Goddard and Fosdick, 2019). This sediment sourced from the more recently, deeply exhumed external-fold-and-thrust belt was likely shed into the offshore basins (Ghiglione et al., 2016), possibly in response to subduction of the Chile Ridge spreading ridge (Goddard and Fosdick, 2019).

CONCLUSION

Integration of sedimentary provenance analysis from the uppermost Río Turbio and Río Guillermo formations highlight the abrupt transition between ∼27 and 24 Ma from dissected/transitional arc to undissected arc that represents erosion of the mafic volcanic highlands. The Oligocene upper Río Turbio Formation likely records early uplift and erosion of the proximal Río El Rincón-Castillo thrusts of the external fold-and-thrust belt, prior to rejuvenated arc activity. Between

∼24 and 21 Ma deposition of the Río Guillermo Formation, the active arc provided most of the sediment supply to the retroarc foreland basin, despite coeval changes in orogenic wedge dynamics and uplift and exhumation of the intervening external-fold-and-thrust belt along a deeper detachment and reactivation of high-angle basin structures (**Figure 8**). These structures originated as high-angle normal faults related to the predecessor Rocas Verdes Basin extensional history that were reactivated during advancement of the foreland deformational front. This provenance record provides additional context for inferred migrations of the paleotopographic crest and magmatic arc based on low-temperature thermochronology datasets. These findings have important implications for interpreting paleogeographic changes and tectonic signals from provenance data in retroarc settings dominated by volcanic sources (Varela et al., 2013), where sustained arc activity may overwhelm the signal of late-stage deformation. In the case of the Magallanes-Austral Basin, the Río Guillermo Formation tracks one of the final phases of Cordilleran orogenesis prior to plate reorganization and subduction of the impinging Chile Ridge spreading center.

DATA AVAILABILITY STATEMENT

All datasets generated for this study are included in the article/**Supplementary Material**.

AUTHOR CONTRIBUTIONS

JL and JF participated in project fieldwork, collection of clast count and stratigraphic data, and sampling for geochronology and sandstone petrography. JL performed zircon LA-ICPMS geochronology, sandstone petrographic analyses, and preliminary interpretations. JL, JF, and RV contributed to data synthesis, interpretations, and manuscript preparation. JF developed the project idea and secured financial support.

FUNDING

This research was supported by the U.S. National Science Foundation Award EAR-1649585 to JF, the Robert R. Shrock Foundation at Indiana University, and the Geological Society of America Graduate Research Grant Program.

ACKNOWLEDGMENTS

We acknowledge B. Romans, T. Schwartz, E. Bostelmann, R. Ugalde, M. Griffin, A. Parras, M. Ghiglione, and M. Hren for insightful discussions on Patagonian geology. J. L. Oyarzún and N. Raffer graciously provided logistical support. We thank S. F. Alvarez for permission to conduct fieldwork at the Estancia Cancha Carrera. The Arizona LaserChron Center (NSF Award EAR-1338583) provided expert analytical assistance. Reviews by EF, BH, JS, and editor DH greatly improved the scope and clarity of this manuscript.

SUPPLEMENTARY MATERIAL

The Supplementary Material for this article can be found online at: https://www.frontiersin.org/articles/10.3389/feart.2019.00353/full#supplementary-material

REFERENCES

Allen, P. A., and Heller, P. L. (2011). "Dispersal and preservation of tectonically generated alluvial gravels in sedimentary basins," in *Tectonics of Sedimentary Basins: Recent Advances*, eds C. Busby, and A. Azor, (Oxford, UK: Blackwell Publishing Ltd.), 111–130. doi: 10.1002/9781444347166.ch6

Armitage, J. J., Duller, R. A., Whittaker, A. C., and Allen, P. A. (2011). Transformation of tectonic and climatic signals from source to sedimentary archive. *Nat. Geosci.* 4, 231–235. doi: 10.1038/NGEO1087

Biddle, K. T., Uliana, M. A., Mitchum, R. M., Fitzgerald, M. G., and Wright, R. C. (1986). "The stratigraphic and structural evolution of the central and eastern Magallanes Basin, southern South America," in *Foreland Basins*, eds P. A. Allen, and P. Homewood, (Oxford, UK: Blackwell Publishing), 41–61. doi: 10.1002/9781444303810.ch2

Blisniuk, P. M., Stern, L. A., Chamberlain, C. P., Idleman, B., and Zeitler, P. K. (2005). Climatic and evologic changes during Miocene surface uplift in the Southern Patagonian Andes. *Earth Planet. Sci. Lett.* 230, 125–142. doi: 10.1016/j.epsl.2004.11.015

Breitsprecher, K., and Thorkelson, D. J. (2009). Neogene kinematic history of Nazca-Antarctic-Phoenix slab windows beneath Patagonia and the Antarctic Peninsula. *Tectonophysics* 464, 10–20. doi: 10.1016/j.tecto.2008.02.013

Bry, M., White, N., Singh, S., England, R., and Trowell, C. (2004). Anatomy and formation of oblique continental collision: South Falkland basin. *Tectonics* 23, 1–20. doi: 10.1029/2002TC001482

Burbank, D. W., Beck, R. A., Raynolds, R. G. H., Hobbs, R., and Tahirkheli, R. A. K. (1988). Thrusting and gravel progradation in foreland basins: a test of post-thrusting gravel dispersal. *Geology* 16, 1143–1146.

Calderón, M., Fosdick, J. C., Warren, C., Massonne, H.-J., Fanning, C. M., Fadel Cury, L., et al. (2012). The low-grade Canal de las Montañas Shear Zone and its role on the tectonic emplacement of the sarmiento ophiolitic complex and late cretaceous Patagonian Andes orogeny, Chile. *Tectonophysics* 524, 165–185. doi: 10.1016/j.tecto.2011.12.034

Calderón, M., Hervé, F., Fuentes, F., and Fosdick, J. C. (2016). "Tectonic evolution of Paleozoic and mesozoic andean metamorphic complexes and the Rocas Verdes ophiolites in southern Patagonia," in *Geodynamic Evolution of the Southernmost Andes*, ed. M. Ghiglione, (Berlin: Springer-Verlag), 7–36. doi: 10.1007/978-3-319-39727-6_2

Cande, S. C., and Leslie, R. B. (1986). Late Cenozoic tectonics of the Southern Chile trench. *J. Geophys. Res. Solid Earth* 91, 471–496.

Cox, R., Lowe, D. R., and Cullers, R. L. (1995). The influence of sediment recycling and basement composition on evolution of mudrock chemistry in the southwestern United States. *Geochim. Cosmochim. Acta* 59, 2919–2940. doi: 10.1016/0016-7037(95)00185-9

Crane, W. H. (2004). *Depositional History of the Upper Cretaceous Cerro Toro Formation, Silla Syncline, Magallanes Basin, Chile*. Ph.D. thesis, Stanford University, Stanford, CA.

Cunningham, W. D., Dalziel, I. W. D., Lee, T.-Y., and Lawver, L. A. (1995). Southernmost South America-Antarctic Peninsula relative plate motions since 84 Ma: implications for the tectonic evolution of the Scotia Arc region. *J. Geophys. Res.* 100, 8257–8266. doi: 10.1029/95jb00033

Dahlen, F. A. (1984). Noncohesive critical Coulomb wedges: an exact solution. *J. Geophys. Res.* 89, 10125–10133. doi: 10.1029/jb089ib12p10125

Dalziel, I. W. D., de Wit, M. J., and Palmer, K. F. (1974). Fossil marginal basin in the southern Andes. *Nature* 250, 291–294. doi: 10.1038/250291a0

Daniels, B. G., Auchter, N. C., Hubbard, S. M., Romans, B. W., Matthews, W. A., and Stright, L. (2017). Timing of deep-water slope evolution constrained by large-n detrital and volcanic ash zircon geochronology, Cretaceous Magallanes Basin, Chile. *Bull. Geol. Soc. Am.* 130, 438–454. doi: 10.1130/B31757.1

Davis, D., Suppe, J., and Dahlen, F. A. (1983). Mechanics of fold-and-thrust belts and accretionary wedges. *J. Geophys. Res.* 88, 1153–1172.

de Wit, M. J., and Stern, C. R. (1981). Variations in the degree of crustal extension during formation of a back-arc basin. *Tectonophysics* 72, 229–260. doi: 10.1016/0040-1951(81)90240-7

DeCelles, P. G., and Mitra, G. (1995). History of the Sevier orogenic wedge in terms of critical taper models, northeast Utah and southwest Wyoming. *Geol. Soc. Am. Bull.* 107, 454–462. doi: 10.1130/0016-76061995107<0454

Dickinson, W. R. (1985). "Provenance relations from detrital modes of sandstones," in *Provenance of Arenites, NATO Advanced Science Institutes Series*, ed. G. G. Zuffa, (Washington, D.C: NATO), 333–362.

Dickinson, W. R., and Suczek, C. A. (1979). Plate tectonics and sandstone compositions. *Am. Assoc. Petrol. Geol. Bull.* 63, 2164–2182.

Eagles, G., and Jokat, W. (2014). Tectonic reconstructions for paleobathymetry in Drake Passage. *Tectonophysics* 611, 28–50. doi: 10.1016/j.tecto.2013.11.021

Fildani, A., and Hessler, A. M. (2005). Stratigraphic record across a retroarc basin inversion: rocas verdes–magallanes Basin, Patagonian Andes, Chile. *Geol. Soc. Am. Bull.* 117, 1596–1614. doi: 10.1130/B25708.1

Fildani, A., Romans, B. W., Fosdick, J. C., Crane, W. H., and Hubbard, S. M. (2008). "Orogenesis of the Patagonian Andes as reflected by basin evolution in southernmost South America," in *Ores and Orogenesis: Circum-Pacific Tectonics, Geologic Evolution, and Ore Deposits*, eds J. E. Spencer, and S. R. Titley, (Tucson: Arizona Geological Society), 259–268.

Fosdick, J., VanderLeest, R., Bostelmann, E., Leonard, J., Ugalde, R., Oyarzún, J., et al. (2019). Revised timing of Cenozoic Atlantic incursions and changing hinterland sediment sources during southern Patagonian orogenesis. *EarthArXiv* [Preprint]. doi: 10.31223/osf.io/vqkds

Fosdick, J. C., Grove, M. J., Graham, S. A., Hourigan, J. K., Lovera, O., and Romans, B. W. (2015). Detrital thermochonologic record of burial heating and sediment recycling in the Magallanes foreland basin, Patagonian Andes. *Basin Res.* 27, 546–572. doi: 10.111/bre.12088

Fosdick, J. C., Grove, M. J., Hourigan, J. K., and Calderón, M. L. (2013). Retroarc deformation and exhumation near the end of the Andes, southern Patagonia. *Earth Planet. Sci. Lett.* 361, 504–517. doi: 10.1016/j.epsl.2012.12.007

Fosdick, J. C., Romans, B. W., Fildani, A., Bernhardt, A., Calderón, M., and Graham, S. A. (2011). Kinematic evolution of the Patagonian retroarc fold-and-thrust belt and Magallanes foreland basin, Chile and Argentina, 51°30'S. *Geol. Soc. Am. Bull.* 123, 1679–1698. doi: 10.1130/B30242.1

Garcia-Castellanos, D., Fernandez, M., and Torne, M. (2002). Modeling the evolution of the Guadalquivir foreland basin (southern Spain). *Tectonics* 21, 9.1–9.17. doi: 10.1029/2001TC001339

Gehrels, G. (2012). "Detrital Zircon U-Pb geochronology: current methods and new opportunities," in *Tectonics of Sedimentary Basins: Recent Advances*, eds C. Busby, and A. Azor, (Oxford, UK: Blackwell Publishing Ltd.), 45–62. doi: 10.1002/9781444347166.ch2

George, S. W. M., Davis, S. N., Fernández, R. A., Manríquez, L. M. E., Leppe, M. A., Horton, B. K., et al. (2019). Chronology of deposition and unconformity development across the cretaceous–paleogene boundary, Magallanes-Austral Basin, Patagonian Andes. *J. South Am. Earth Sci.* 97:102237. doi: 10.1016/j.jsames.2019.102237

Ghiglione, M. C., Quinteros, J., Yagupsky, D., Bonillo-Martínez, P., Hlebzevtich, J., Ramos, V. A., et al. (2010). Structure and tectonic history of the foreland basins of southernmost South America. *J. South Am. Earth Sci.* 29, 262–277. doi: 10.1016/j.jsames.2009.07.2006

Ghiglione, M. C., Ramos, V., Cuitiño, J., and Barberón, V. (2016). "Growth of the Southern Patagonian Andes (46-53°S) and its relation with subduction processes," in *Growth of the Southern Andes*, eds A. Folguera, M. Naipauer, L. Sagripanty, M. C. Ghiglione, D. Orts, and L. B. Giambiagi, (Berlin: Springer), 201–240. doi: 10.1007/978-3-319-23060-3_10

Goddard, A. L. S., and Fosdick, J. C. (2019). Multichronometer thermochronologic modeling of migrating spreading ridge subduction in southern Patagonia. *Geology* 47, 555–558. doi: 10.1130/G46091.1/4678798/g46091.pdf

Goddard, A. S., and Carrapa, B. (2018). Effects of Miocene-Pliocene global climate changes on continental sedimentation: a case study from the southern Central Andes. *Geology* 46, 647–650. doi: 10.1130/G40280.1

Gorring, M., Singer, B., Gowers, J., and Kay, S. M. (2003). Plio–Pleistocene basalts from the Meseta del Lago Buenos Aires, Argentina: evidence for asthenosphere–lithosphere interactions during slab window magmatism. *Chem. Geol.* 193, 215–235. doi: 10.1016/s0009-2541(02)00249-8

Guillaume, B., Gautheron, C., Simon-Labric, T., Martinod, J., Roddaz, M., and Douville, E. (2013). Dynamic topography control on Patagonian relief evolution as inferred from low temperature thermochronology. *Earth Planet. Sci. Lett.* 364, 157–167. doi: 10.1016/j.epsl.2012.12.036

Guillaume, B., Martinod, J., Husson, L., Roddaz, M., and Riquelme, R. (2009). Neogene uplift of central eastern Patagonia: dynamic response to active spreading ridge subduction? *Tectonics* 28:55.

Heller, P. L., Angevine, C. L., Winslow, N. S., and Paola, C. (1988). Two-phase stratigraphie model of foreland-basin sequences. *Geology* 16, 501–504.

Heller, P. L., Burns, B., and Marzo, M. (1993). Stratographic solution sets for determining the roles of sediment supply, subsidence, and sea-level on transgressions and regressions. *Geology* 21, 747–750.

Heller, P. L., Paola, C., Hwang, I., John, B., and Steel, R. (2001). Geomorphology and sequence stratigraphy due to slow and rapid base-level changes in an experimental subsiding Basin (XES 96-1). *Am. Assoc. Petrol. Geol. Bull.* 85, 817–838. doi: 10.1306/8626CA0F-173B-11D7-8645000102C1865D

Hervé, F., Calderón, M., and Faúndez, V. (2008). The metamorphic complexes of the Patagonian and Fuegian Andes. *Geol. Acta* 6, 43–53.

Hervé, F., Fanning, C. M., and Pankhurst, R. J. (2003). Detrital zircon age patterns and provenance of the metamorphic complexes of southern Chile. *J. South Am. Earth Sci.* 16, 107–123. doi: 10.1016/S0895-9811(03)00022-1

Hervé, F., Pankhurst, R. J., Fanning, C. M., Calderón, M., and Yaxley, G. M. (2007). The South Patagonian batholith: 150 my of granite magmatism on a plate margin. *Lithos* 97, 373–394. doi: 10.1016/j.lithos.2007.01.007

Hilley, G. E., Blisniuk, P. M., and Strecker, M. R. (2005). Mechanics and erosion of basement-cored uplift provinces. *J. Geophys. Res.* 110, 1–22. doi: 10.1029/2005JB003704

Horton, B. K. (1999). Erosional control on the geometry and kinematics of thrust belt development in the central Andes. *Tectonics* 18, 1292–1304. doi: 10.1029/1999TC900051

Horton, B. K. (2018). Sedimentary record of Andean mountain building. *Earth Sci. Rev.* 178, 279–309. doi: 10.1016/j.earscirev.2017.11.025

Horton, B. K., Constenius, K. N., and DeCelles, P. G. (2004). Tectonic control on coarse-grained foreland-basin sequences: an example from the Cordilleran foreland basin, Utah. *Geology* 32, 637–640. doi: 10.1130/G20407.1

Howard, J. L. (1993). The statistics of counting clasts in rudites: a review, with examples from the upper Palaeogene of southern California, USA. *Sedimentology* 40, 157–174. doi: 10.1111/j.1365-3091.1993.tb01759.x

Hubbard, S. M., Romans, B. W., and Graham, S. A. (2008). Deep-water foreland basin deposits of the cerro toro formation, Magallanes basin, Chile: architectural elements of a sinuous basin axial channel belt. *Sedimentology* 55, 1333–1359. doi: 10.1111/j.1365-3091.2007.00948.x

Hünicken, M. (1955). Depósitos neocretácicos y terciarios del extremo S.S.W. de Santa Cruz. Cuenca Carbonífera de Río Turbio. *Rev. Instit. Nacl. Invest. Cienc. Nat.* 4, 1–161.

Ingersoll, R. V., Bullard, T. F., Ford, R. L., Grimm, J. P., Pickle, J. D., and Sares, S. W. (1984). The effect of grain size of detrital modes: a test of the Gazzi-Dickinson point-counting method. *J. Sediment. Res.* 54, 103–116. doi: 10.1306/212F83B9-2B24-11D7-8648000102C1865D

Johnsson, M. J. (1993). The system controlling the composition of clastic sediments. *Geol. Soc. Am. Special Pap.* 284, 1–19.

Jordan, T., Allmendinger, R., Damanti, J., and Drake, R. (1993). Chronology of motion in a complete thrust belt: the Precordillera, 30-31°S, Andes Mountains. *J. Geol.* 101, 135–156. doi: 10.1086/648213

Jordan, T. E., and Flemings, P. B. (1991). Large-scale stratigraphic architecture, eustatic variation, and unsteady tectonism: a theoretical evaluation. *J. Geophys. Res.* 96, 6681–6699. doi: 10.1038/ncomms11427

Kay, S. M., Gorring, M., and Ramos, V. A. (2004). Magmatic sources, setting and causes of Eocene to Recent Patagonian plateau magmatism (36°S to 52 °S latitude). *Rev. Asoc. Geol. Argent.* 59, 556–568.

Lagabrielle, Y., Goddéris, Y., Donnadieu, Y., Malavieille, J., and Suarez, M. (2009). The tectonic history of Drake Passage and its possible impacts on global climate.

Earth and Planetary Science Letters 279, 197–211. doi: 10.1016/j.epsl.2008.12.037

Macellari, C. E., Barrio, C. A., and Manassero, M. J. (1989). Upper Cretaceous to Paleocene depositional sequences and standstone petrography of southwestern Patagonia (Argentina and Chile). *J. South Am. Earth Sci.* 2, 223–239. doi: 10.1016/0895-9811(89)90031-x

Malkowski, M. A., Sharman, G. R., Graham, S. A., and Fildani, A. (2017). Characterization and diachronous initiation of coarse clastic deposition in the Magallanes–Austral foreland basin, Patagonian Andes. *Basin Res.* 29, 298–326. doi: 10.1111/bre.12150

Malumián, N., and Caramés, A. (1997). Upper Campanian-Paleogene from the Río Turbio coal measures in southern Argentina: micropaleontology and the Paleocene/Eocene boundary. *J. South Am. Earth Sci.* 10, 189–201. doi: 10.1016/s0895-9811(97)00015-1

Malumián, N., and Náñez, C. (2011). Late Cretaceous-Cenozoic transgressions in Patagonia and the Fuegian Andes: foraminifera, paleoecology, and paleogeography. *Biol. J. Linnean Soc.* 103, 269–288. doi: 10.1111/j.1095-8312.2011.01649.x

Malumián, N., Panza, J. L., Parisi, C., Naňez, C., Caramés, A., and Torre, A. (2000). Hoja Geológica 5172-III, Yacimiento Río Turbio (1:250,000). *Serv. Geol. Minero Argent. Boletin* 247, 180.

Manassero, M. J. (1990). *Composición y procedencia de la Formación Río Turbio en el sector occidental del Valle Homónimo, Provincia de Santa Cruz: III Reunión Argentina de Sedimentología* (San Juan: Resúmenes), 181–186.

Miall, A. D. (1978). "Lithofacies types and vertical profile models in braided river deposits: a summary," in *Fluvial Sedimentology*, ed. A. D. Miall, (Calgary: Canadian Society of Petroleum Geology), 597–604.

Miall, A. D. (2006). *The Geology of Fluvial Deposits: Sedimentary Facies, Analysis and Petroleum Geology*. New York, NY: Spring-Verlag.

Michel, J., Baumgartner, L., Putlitz, B., Schaltegger, U., and Ovtcharova, M. (2008). Incremental growth of the Patagonian Torres del Paine laccolith over 90 k.y. *Geology* 36, 459–462. doi: 10.1130/G24546A.1

Miller, K. G., Kominz, M. A., Browning, J. V., Wright, J. D., Mountain, G. S., Katz, M. E., et al. (2005). The Phanerozoic record of global sea-level change. *Science* 310, 1293–1298. doi: 10.1126/science.1116412

Mora, A., Parra, M., Strecker, M. R., Kammer, A., Dimaté, C., and Rodríguez, F. (2006). Cenozoic contractional reactivation of Mesozoic extensional structures in the Eastern Cordillera of Colombia. *Tectonics* 25, 1–19. doi: 10.1029/2005TC001854

Paola, C. (2000). Quantitative models of sedimentary basin filling. *Sedimentology* 41, 121–178. doi: 10.1046/j.1365-3091.2000.00006.x

Paola, C., Heller, P. L., and Angevine, C. L. (1992). The large-scale dynamics of grain-size variation in alluvial basins, 1: theory. *Basin Res.* 4, 73–90. doi: 10.1111/j.1365-2117.1992.tb00145.x

Parras, A., Dix, G. R., and Griffin, M. (2012). Sr-isotope chronostratigraphy of Paleogene-Neogene marine deposits: Austral Basin, southern Patagonia (Argentina). *J. South Am. Earth Sci.* 37, 122–135. doi: 10.1016/j.jsames.2012.02.007

Parras, A., Griffin, M., Feldmann, R., Casadío, S., Schweitzer, C., and Marenssi, S. (2008). Journal of South American Earth Sciences Correlation of marine beds based on Sr- and Ar-date determinations and faunal affinities across the Paleogene/Neogene boundary in southern Patagonia, Argentina. *J. South Am. Earth Sci.* 26, 204–216. doi: 10.1016/j.jsames.2008.03.006

Pearson, N. J., Mángano, M. G., Buatois, L. A., Casadío, S., and Rodríguez Raising, M. (2012). Ichnology, sedimentology, and sequence stratigraphy of out-estuarine and coastal-plain deposits: implications for the distinction between allogenic and autogenic expressions of the Glossifungites Ichnofacies. *Paleogeogr. Paleoclimatol. Paleoecol.* 333, 192–217. doi: 10.1016/j.paleo.2012.03.031

Posamentier, H. W., Jervey, M. T., and Vail, P. R. (1988). "Eustatic controls on clastic deposition I - conceptual framework," in *Sea Level Changes - An Integrated Approach, Special Publication*, eds C. K. Wilgus, B. S. Hastings, C.G. St. C. Kendall, H. W. Posamentier, C. A. Ross, and J. C. Van Wagoner, (Tulsa: Society of Economic Paleontologists and Minerologists), 110–124.

Ramírez de Arellano, C., Putlitz, B., Müntener, O., and Ovtcharova, M. (2012). High precision U/Pb zircon dating of the Chaltén Plutonic Complex (Cerro Fitz Roy, Patagonia) and its relationship to arc migration in the southernmost Andes. *Tectonics* 31:C003048.

Ramos, V. A. (1989). Andean foothills structures in Northern Magallanes Basin, Argentina. *Am. Assoc. Petrol. Geol. Bull.* 73, 887–903.

Ramos, V. A., and Kay, S. M. (1992). Southern Patagonian plateau basalts and deformation: backarc testimony of ridge collisions. *Tectonophysics* 205, 261–282. doi: 10.1016/0040-1951(92)90430-E

Ramos, V. R., and Ghiglione, M. C. (2008). Tectonic evolution of the Patagonian Andes. *Dev. Quat. Sci.* 11, 57–71. doi: 10.1016/s1571-0866(07)10004-x

Riccardi, A. C., and Rolleri, E. O. (1980). *Cordillera Patagonica Austral, Segundo Simosio Geología Regional Argentina*. La Paz: Acadmia Nacional de Ciencias, 1174–1306.

Rodríguez Raising, M. (2010). *Estratigrafía Secuencial de los Depósitos Marinos y Continentales del Eoceno – Oligoceno Temprano de la Cuenca Austral, Suroeste de la Provincia de Santa Cruz*. Ph.D. thesis, Cuenca austral, Santa Cruz.

Romans, B. W., Castelltort, S., Covault, J. A., Fildani, A., and Walsh, J. P. (2016). Environmental signal propagation in sedimentary systems across timescales. *Earth Sci. Rev.* 153, 7–29. doi: 10.1016/j.earscirev.2015.07.012

Romans, B. W., Fildani, A., Graham, S. A., Hubbard, S. M., and Covault, J. A. (2010). Importance of predecessor basin history on the sedimentary fill of a retroarc foreland basin: provenance analysis of the Cretaceous Magallanes. *Basin Res.* 22, 640–658. doi: 10.1111/j.1365-2117.2009.00443.x

Romans, B. W., Fildani, A., Hubbard, S. M., Covault, J. A., Fosdick, J. C., and Graham, S. A. (2011). Evolution of deep-water stratigraphic architecture, Magallanes Basin, Chile. *Mar. Petrol. Geol.* 28, 612–628. doi: 10.1016/j.marpetgeo.2010.05.002

Russo, A., Flores, M. A., and Di Benedetto, H. (1980). *Patagonia Austral Extraandina: Segundo Simosio Geología Regional Argentina* (La Paz: Acadmia Nacional de Ciencias), 1431–1462.

Sánchez, A., Hervé, F., and de Saint-blanquat, M. (2008). "Relations between plutonism in the back-arc region in southern Patagonia and Chile Rise subduction: a geochronological review," in *Proceddings of the 7th international Symposium on Andean Geodynamics (ISAG 2008, Nice)*, (Oxford: John Wiley & Sons), 485–488.

Saylor, J. E., Horton, B. K., Stockli, D. F., Mora, A., and Corredor, J. (2012). Structural and thermochronological evidence for Paleogene basement-involved shortening in the axial Eastern Cordillera, Colombia. *J. South Am. Earth Sci.* 39, 202–215. doi: 10.1016/j.jsames.2012.04.009

Schwartz, T. M., Fosdick, J. C., and Graham, S. A. (2016). Using detrital zircon U-Pb ages to calculate Late Cretaceous sedimentation rates in the Magallanes-Austral basin, Patagonia. *Basin Res.* 29, 725–746. doi: 10.1111/bre.12198

Schwartz, T. M., and Graham, S. A. (2015). Stratigraphic architecture of a tide-influenced shelf-edge delta, Upper Cretaceous Dorotea Formation, Magallanes-Austral Basin, Patagonia. *Sedimentology* 62, 1039–1077. doi: 10.1111/sed.12176

SERNAGEOMIN (2003). *Mapa Geológico de Chile: Version Digital. Publicación Geológica Digital, No. 4, 2003. CDROM, version 1.0, 2003. Base Geológica escala 1:1.000.000*. Santiago: Servicio Nacional de Geología y Minería.

Sickmann, Z. T., Schwartz, T. M., Malkowski, M. A., Dobbs, S. C., and Graham, S. A. (2019). Interpreting large detrital geochronology data sets in retroarc foreland basins: an example from the Magallanes-Austral Basin, southernmost Patagonia. *Lithosphere2* 11, 620–642. doi: 10.1130/L1060.1/4792995/l1060.pdf

Somoza, R., and Ghidella, M. E. (2012). Late Cretaceous to recent plate motions in western South America revisited. *Earth Planet. Sci. Lett.* 331, 152–163. doi: 10.1016/j.epsl.2012.03.003

Thomson, S. N., Hervé, F., and Stöckhert, B. (2001). Mesozoic-Cenozoic denudation history of the Patagonian Andes (southern Chile) and its correlation to different subduction precesses. *Tectonics* 20, 693–711. doi: 10.1029/2001TC900013

VanderLeest, R. A., Fosdick, J. C., Leonard, J. S., and Morgan, L. E. (2018). "Early miocene mafic arc volcanism of the patagonian andes revealed with detrital multi-chronometer and trace element geochemistry from the Magallanes Basin 50-52°," in *Proceedings of the American Geophysical Union Fall Meeting 2018*, (Washington, D.C: American Geophysical Union).

Varela, A. N., Gomez-Peral, L. E., Richiano, S., and Poiré, D. G. (2013). Distinguishing similar volcanic source areas from an integrated provenance analysis: implications for foreland Andean basins. *J. Sedimentary Res.* 83, 258–276. doi: 10.2110/jsr.2013.22

Valenzuela, A. (2006). *Provenienca Sedimentaria de Estratos de Cabo Nariz y Formacion Cerro Toro, Cretacico Tardio - Paleoceno, Magallanes, Chile*. Ph.D. thesis, Universidad de Chile, Santiago.

Willett, S. D. (1999). Orogeny and orography: the effects of erosion on the structure of mountain belts. *J. Geophys. Res.* 104, 28957–28987. doi: 10.1029/1999JB900248

Wilson, T. J. (1991). Transition from back-arc to foreland basin development in the southernmost andes - stratigraphic record from the Ultima-Esperanza-District, Chile. *Geol. Soc. Am. Bull.* 103, 98–111. doi: 10.1130/0016-7606(1991)103<0098:tfbatf>2.3.co;2

Conflict of Interest: The authors declare that the research was conducted in the absence of any commercial or financial relationships that could be construed as a potential conflict of interest.

frontiers in Earth Science

ORIGINAL RESEARCH
published: 03 March 2020
doi: 10.3389/feart.2020.00051

Strike-Slip Transpressional Uplift Offshore San Onofre, California Inhibits Sediment Delivery to the Deep Sea

Emily A. Wei, James J. Holmes and Neal W. Driscoll*

Scripps Institution of Oceanography, University of California, San Diego, San Diego, CA, United States

The Inner California Borderlands is a complex margin where sediment delivery to the basin floor is largely routed through canyon-channel-gully systems. Using nested geophysical surveys, piston and gravity cores from the Eastern Gulf of Santa Catalina, this study compares two canyon systems and investigates how tectonics, shelf width, gradient, and autogenic processes influence turbidite emplacement timing and grain size. One end-member canyon is the Dana Point Canyon, which is ∼2 km from the San Juan Creek drainage and has a concave-up channel profile. The other end-member system consists of the San Onofre North and South (SON and SOS) canyons that are detached from San Mateo Creek by a wide 10 km shelf and they traverse a tectonically deformed slope with multiple ponded basins. Radiocarbon ages sampled from eight cores reveal that turbidite deposition at Dana Point persists during the sea-level lowstand of Marine Isotope Stage (MIS) 2 through the subsequent transgression and highstand. On the contrary, turbidite emplacement adjacent to the SON and SOS canyons occurs mostly during MIS 2 and ceases around 8 ka. The main regional control on turbidite timing is the wide shelf adjacent to the SON and SOS canyons that is formed by a broad uplifted anticline. This anticline separates the SON and SOS canyons from a riverine source during the sea-level transgression. Much of the tectonic deformation offshore of San Onofre was created by transpression along the right-lateral Newport Inglewood-Rose Canyon Fault Zone. Second-order controls on local turbidite emplacement include small synclines and anticlines that form ponded basins and accommodate deformation on the San Mateo Fault Zone. These basins engender deposition and intervening steep slopes promote sediment bypass. Complex bathymetry offshore San Onofre also affects channel gradient by either accelerating or decelerating flow. Turbidity flow dynamics modified by gradient changes offshore of San Onofre have the ability to modulate channel architecture and grain size. The implications of this work are that tectonically deformed morphology complicates the timing of turbidite emplacement throughout a sea-level cycle and the interpretation of turbidites as paleoseismic records in such regions.

Keywords: seismic stratigraphy, sequence stratigraphy, California (USA), submarine canyon, continental slope

OPEN ACCESS

Edited by:
Julie Fosdick, University of Connecticut, United States

Reviewed by:
Tiago M. Alves, Cardiff University, United Kingdom
Ángel Puga-Bernabéu, University of Granada, Spain

****Correspondence:***
Emily A. Wei
eawei@ucsd.edu

Specialty section:
This article was submitted to Sedimentology, Stratigraphy and Diagenesis, a section of the journal Frontiers in Earth Science

Received: *02 September 2019*
Accepted: *13 February 2020*
Published: *03 March 2020*

Citation:
Wei EA, Holmes JJ and Driscoll NW (2020) Strike-Slip Transpressional Uplift Offshore San Onofre, California Inhibits Sediment Delivery to the Deep Sea. Front. Earth Sci. 8:51. doi: 10.3389/feart.2020.00051

INTRODUCTION

Studying submarine canyons has both societal and scientific relevance. Not only do submarine canyons serve as conduits for terrigenous material across margins to the deep sea (Allen, 2008), but fan deposits at the base of submarine canyons can also serve as significant hydrocarbon reservoirs when filled with sand- or silt-prone sequences (Mayall and Stewart, 2000; Stow and Mayall, 2000; Pettingill and Weimer, 2002; Mayall et al., 2006). Large catastrophic flows through channels in the eastern Gulf of Santa Catalina (GoSC) can be a significant geohazard to marine infrastructure (Paull et al., 2002; Xu et al., 2010). For these reasons, it is important to understand the evolutionary processes that shape canyon morphology and stacking patterns through time in sedimentary basins.

The Inner California Borderlands (ICB) is a complex, tectonically active margin that is characterized by narrow continental shelves dissected by numerous canyon-channel systems (Normark et al., 2009). As distances between river mouths and canyon heads are short, the ICB is an ideal place to study source-to-sink processes and sediment routing (Normark et al., 2009; Covault et al., 2010; Romans et al., 2016). Sediment flux to submarine canyons can occur either as particles that settle out of suspension or sediment gravity flows that move downslope. Hereafter we will refer to sediment gravity flows as turbidity currents, as the deposits we observe are graded. Turbidity currents can transport large quantities of sediment (Talling et al., 2015); nevertheless, they have not been observed to traverse entire submarine canyon-channel systems (Fildani, 2017; Symons et al., 2017). Plausible triggers for turbidity currents include river floods, storm events, tsunami wave loading, sediment loading, internal tides, and earthquakes (Goldfinger et al., 2007; Xu et al., 2010; Talling et al., 2013). Storm waves can rework shelf sediment and advect it to canyon heads as a turbid layer (Xu et al., 2010). Since multiple mechanisms are capable of producing turbidity currents, it can be difficult to distinguish seismo-turbidites from those produced by tsunamis, storms, and sediment loading. Some studies have argued that seismo-turbidites can be distinguished by wide areal extent, multiple coarse-fraction pulses, variable mineralogical provenance, greater depositional mass, and coarser texture than the storm-generated events (Nakajima and Kanai, 2000; Goldfinger et al., 2007; Goldfinger, 2011). Other studies cite concerns for using turbidites as records of paleoseismic activity, as geologic dating lacks the time resolution to determine whether a fault ruptured as a whole or whether it ruptured in segments over a time period of days, years, or even decades (Nelson et al., 1995; Atwater et al., 2014). Furthermore, Sumner et al. (2013) and Atwater et al. (2014) have discussed uncertainties with methods used to evaluate paleoseismic deposits, such as the confluence test (Goldfinger et al., 2003), synchronous turbidite deposition in multiple basins (Gràcià et al., 2010), large turbidite volumes (Talling et al., 2015), and correlating turbidites to historically recorded earthquakes (Sumner et al., 2013). As such, there is still debate as to whether deep-sea turbidites are reliable paleo-seismometers (Sumner et al., 2013; Atwater et al., 2014).

Morphologic factors such as bathymetry and shelf width may also exert important controls on sediment flux to canyons (Xu et al., 2010; Damuth and Olson, 2015). Distance from a river source and shelf width may change throughout sea-level cycles. Sequence stratigraphic models predict that the greatest delivery of sediment to canyons and basin floor occurs during falling stages in sea-level and sea-level lowstands when rivers deposit directly into the canyon-channel system (e.g., Vail et al., 1977; Mitchum, 1985; Posamentier et al., 1991). Nonetheless, recent studies have proposed that sea-level is subordinate to the distance between the canyon head and shoreline (Covault et al., 2010; Blum et al., 2013; Gamberi et al., 2015) and proposed that distances < 5 km result in canyons characterized by active sand transport (Sweet and Blum, 2016). Secondary factors can exert controls on sediment flux to the deep sea, including ponded basins, which may serve as local depocenters that trap flow deposits (Prather et al., 1998; Damuth and Olson, 2015). Intraslope basins formed by diapirs or tectonic deformation may influence trends in bathymetry and subsequently the morphology of submarine canyons (Damuth, 1994; Damuth and Olson, 2015; Qin et al., 2019).

Recent research on submarine canyons in the Eastern GoSC (e.g., Covault et al., 2007, 2011; Normark et al., 2009) used cores from submarine fans and channel thalwegs to propose that shelf width and sea-level exert the largest controls on the timing of turbidite emplacement. Nevertheless, these studies did not conduct in-depth analyses on local deformation and gradient changes that may influence gravity flows. Comparisons between the San Onofre North (SON), South (SOS), and Dana Point canyons present an opportunity to study the interplay of tectonically controlled wide shelves and local ponded basins on the timing of turbidite emplacement. The shelf offshore of San Onofre has a maximum width of ∼10 km that deviates from narrower (∼2 km) shelves offshore of much of the ICB and Dana Point (**Figure 1C**). By comparing the Dana Point to the SON and SOS canyon-channel systems, the overarching goal of this research is to test the hypothesis that the wide shelf exerts broad controls on the timing of turbidite emplacement to the deep basins. The highly deformed slope offshore of San Onofre presents an opportunity to examine how ponded basins and gradients cause variances in depositional timing downslope.

GEOLOGIC SETTING

Geomorphology of the Inner California Borderlands

The Inner California Borderlands is a complex seismically active region off Southern California that is highly deformed (Ehlig, 1977; Crouch, 1979; Legg, 1991; Crouch and Suppe, 1993; Magistrale, 1993; Nicholson et al., 1994; Bohannon and Geist, 1998; Meade and Hager, 2005; Ryan et al., 2009, 2012; Maloney et al., 2016). Such deformation is responsible for the characteristic basin and ridge basement structure observed in the ICB bathymetry. The main basins within the ICB are the GoSC and the San Diego Trough (SDT). Our coring locations focus on the Eastern GoSC (**Figure 1**).

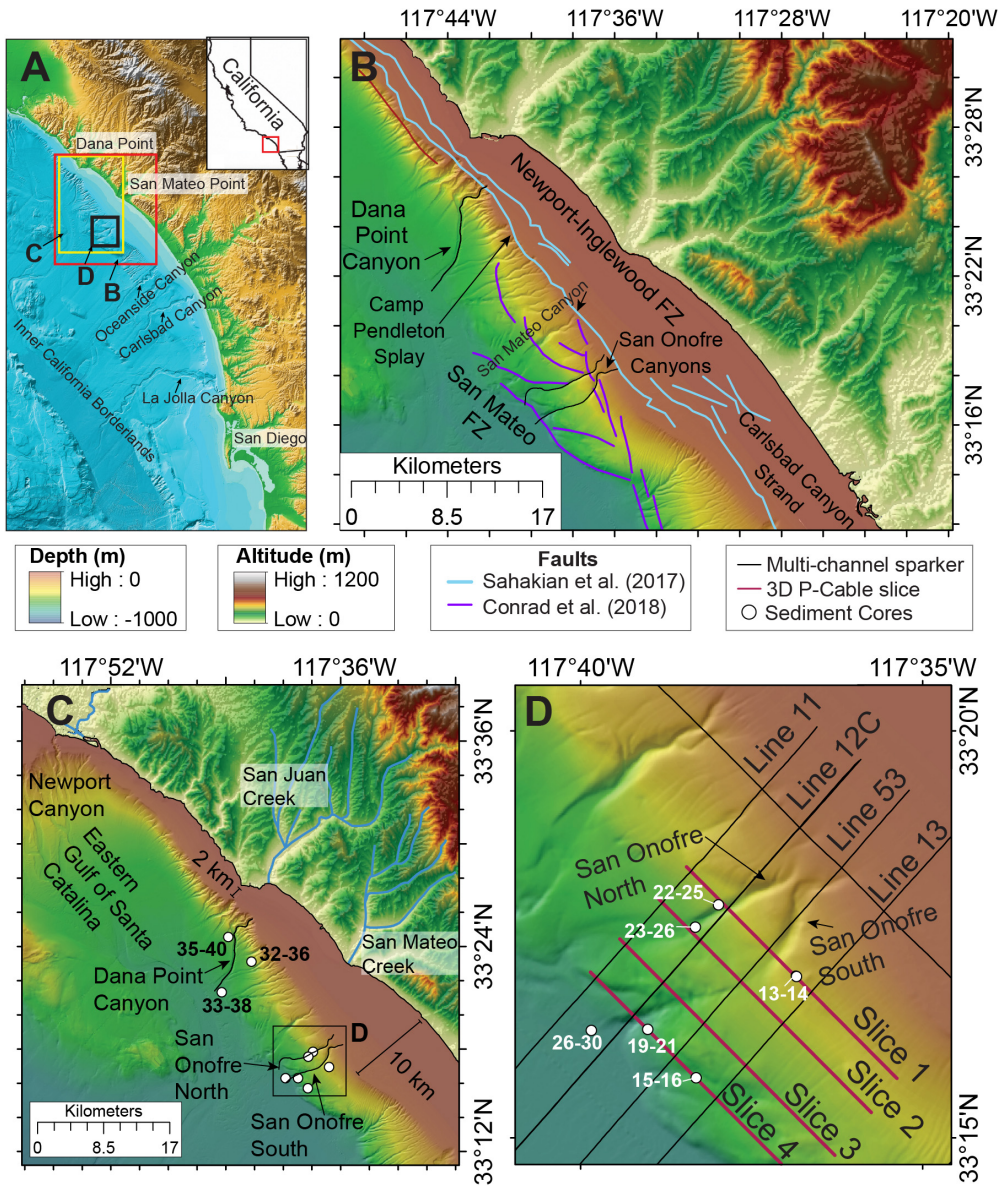

FIGURE 1 | (A) The Inner California Borderlands (ICB) is a tectonically active region located offshore of Southern California. This study focuses on the portion of the margin with the wide continental shelf. The locations of insets B, C, and D are shown. **(B)** Previously mapped active faults within the study area are shown. Blue faults are from Sahakian et al. (2017) and purple faults are from Conrad et al. (2018). FZ = Fault Zone. **(C)** Location of Dana Point and San Onofre North and South canyons. The area shown in inset D is outlined by the black box. **(D)** The study area offshore of San Onofre. This study uses 2D Sparker Multi-channel seismics shown by the black lines and slices of 3D P-cable Sparker seismics shown by the red lines. Gravity Cores (GC) and Jumbo Piston Cores (JPC) are labeled with white circles. Bathymetry from Dartnell et al. (2015).

Strike-Slip Tectonics Offshore San Onofre

Much of the complex tectonic deformation in the ICB occurred during the Oligocene to the late Miocene, when the ICB underwent block rotation, extension, and transcurrent faulting associated with microplate capture and formation of the Transverse Ranges (Lonsdale, 1991; Nicholson et al., 1994; ten Brink et al., 2000). As plate motion became more northerly during the late Miocene, deformation of this region created a vast system of basins and ridges that dominates ICB bathymetry (Atwater and Stock, 1998; Maloney et al., 2016). After the late Miocene, deformation in the ICB decreased dramatically and changed in style (Maloney et al., 2016).

Sediment dispersal in the study area is affected most by the active Newport-Inglewood Fault, which is part of the Newport-Inglewood/Rose-Canyon (NIRC) Fault (**Figure 1B**; Klotsko et al., 2015; Sahakian et al., 2017). The right-lateral strike-slip NIRC Fault trends northwest-southeast, has been active since at least

the Miocene in the north, and it is estimated to accommodate 0.5–2 mm a^{-1} of Pacific-North American plate boundary motion (Freeman et al., 1992). The NIRC fault exhibits much variability from south to north. The NIRC Fault Zone is characterized by compression offshore of San Onofre and to the south near La Jolla, whereas it is characterized by extensional deformation and divergence near Carlsbad (Maloney et al., 2016). Where the shelf is wide, two segments of the NIRC fault are separated by a stepover of 1 km (**Figure 1B**). The left lateral jog between these two segments engenders transpression and forms an anticlinal feature responsible for the widening of the shelf in this region (Sahakian et al., 2017). The anticlinal feature is onlapped by younger sediment (Sahakian et al., 2017). Deformation offshore San Onofre is older than at other locations to the north or south on the NIRC fault (Sahakian et al., 2017), as the transgressive surface is not displaced (Klotsko et al., 2015). It is estimated that fault activity pre-dates 100 ka (Sahakian et al., 2017). Furthermore, it is possible that the central section of the NIRC fault has not experienced surface rupture from recent historical events such as the 1933 M 6.4 Long Beach earthquake (Sahakian et al., 2017). The slope offshore San Onofre is deformed by the San Mateo (SM) Fault Zone, which consists of steeply to moderately northeast-dipping fault strands (Maloney et al., 2016; Conrad et al., 2018). Deformation within the SM Fault Zone includes strike-slip, normal, and reverse offset, with the greatest amount of deformation on the lower slope (Conrad et al., 2018). Many of these faults exhibit cross-cutting relationships and are difficult to resolve, which explains multiple interpretations of faults across this region (Conrad et al., 2018).

Canyon Systems in the ICB

The Dana Point and San Onofre canyons are detached from small creeks that may be primary sediment sources to the canyons. South of Dana Point, the San Juan Creek has an annual sediment discharge of 98 Mt a^{-1} (Warrick and Farnsworth, 2009) and contributes to the Dana Point Canyon. Just north of San Onofre, the San Mateo Creek discharges 2.7 Mt a^{-1} of sediment (Warrick and Farnsworth, 2009) and is detached from the head of San Mateo Canyon. Previous studies speculate that sediment discharge from the San Mateo Creek was higher in the past, as evidenced by the creek's construction of a subaerial delta (Kennedy and Tan, 2007).

Main canyons in the Eastern Gulf of Santa Catalina include the Newport, Oceanside, Carlsbad, San Mateo, and La Jolla canyon-channel systems as well as numerous small gullies (Prins and Postma, 2000; Covault et al., 2007; Covault and Romans, 2009; Normark et al., 2009; Covault and Graham, 2010). It is estimated that about half of the canyons and most of the small gullies were active during the LGM and became inactive during the post-glacial transgression when canyon heads were stranded on the upper slope (Normark et al., 2009). The Newport Canyon remains active in the present day, as it is fed directly by the Santa Ana River, the San Diego Creek, and indirectly by littoral drift from other rivers (Normark et al., 2009; Warrick and Farnsworth, 2009). Another canyon that is presently active is the La Jolla Canyon, which is sourced by littoral drift (Normark et al., 2009). The La Jolla Canyon represents the end of the littoral cell, as it is bounded to the south by resistant Cretaceous rocks that trap sediment (Inman and Brush, 1973; Normark et al., 2009; Le Dantec et al., 2010). Both the Oceanside and Carlsbad canyons are not presently active, as they were drowned during the post-glacial transgression (Normark et al., 2009). Gullies on the margin are not necessarily connected to rivers and creeks onshore (Piper et al., 1990) and it is proposed that they could form where coastal geomorphology focuses rip currents during storms (Normark et al., 2009).

MATERIALS AND METHODS

2D multi-channel seismic reflection data were collected in August 2013 on the R/V New Horizon and R/V Melville using a 2 kJ three-tip EG&G sparker source and 48-channel streamer. Group spacing of 6.25 m and 6.25 m shot spacing allows reflectors to be resolved to approximately 1.5 s two-way travel time (Sahakian et al., 2017). Data were stacked at 1500 m/s and processing included poststack f-k migration using a water velocity of 1500 m/s (Driscoll et al., 2013; Sahakian et al., 2017). Based on observations from the 2D dataset, a high-resolution 3D data set was acquired using a 3D P-Cable system with 14 streamers with 8 channels per streamer, 6.25 m group spacing, 3.125 m shot spacing, and a 2 kJ three-tip EG&G sparker source. This study uses a data grid of 39 km^2 collected over the continental slope and the 2D seismic data are published in Driscoll et al. (2013) and Sahakian et al. (2017). 3D data were processed by Geotrace Technologies.

High-resolution bathymetry from Dartnell et al. (2015) was visualized in ArcMap 10 to examine canyon geomorphology. Gradient maps were constructed and used to delineate thalwegs of the canyon-channel systems. Two-dimensional profiles starting at the canyon head were taken through the canyon-channel thalwegs using the 3D analyst tool. At intervals of 0.5 km from the canyon head, across-channel profiles were oriented perpendicular to the channel in order to calculate channel relief.

In January 2016, 64 Gravity (GC) and Jumbo-piston cores (JPC) were collected onboard the R/V Thompson. Additionally, 546 km of Compressed High Intensity Radar Pulse (CHIRP) data were collected near coring targets. The survey and coring targets were designed to image faults and paleochannels that could potentially serve as piercing points. Trigger cores were deployed with the JPCs. GC and JPC targets were selected from previously collected Sparker and Boomer Multichannel as well as CHIRP seismic profiles. In some cases, drift in ship position caused the cores to be offset from the profiles, in which case the core locations were projected orthogonally onto the profile. On board, whole intact cores were scanned for magnetic susceptibility, gamma density, P-wave velocity, and resistivity using a GeoTek Core-logger. Cores were split and observations of color, grain size, sediment structures, and general lithology were recorded.

54 samples were collected for radiocarbon dating, preferentially from planktonic foraminifera (**Table 1**). As some samples did not contain sufficient planktonic foraminifera for age dating, benthic foraminifera were used in these samples. Fragmented foraminifera and foraminifera that showed signs

TABLE 1 | Radiocarbon ages used in this study.

Core	Depth (m)	Calibrated age	Uncalibrated age	Age error	Type of foraminifera
GC 13–14	0.19	42860	40000	960	Planktonic
	0.19	45880	44600	1700	Benthic
GC 22–25	1.35	23250	21050	50	Benthic
	2.58	40660	38300	880	Benthic
	2.58	41880	38700	910	Planktonic
GC 23–26	1.29	12810	13100	40	Benthic
	1.29	9460	9180	25	Planktonic
	2.12	8850	10050	30	Benthic
	2.12	10300	9480	30	Planktonic
JPC 15–16	1.87	13400	13700	45	Benthic
	2.04	13360	13650	55	Benthic
	2.10	37560	35500	620	Benthic
	2.10	16530	14800	60	Planktonic
	2.16	14270	14450	45	Benthic
	2.30	13880	14150	60	Benthic
	3.18	17670	15600	55	Planktonic
	3.18	17670	16650	65	Benthic
	3.32	18170	17100	65	Benthic
	3.32	18060	15950	60	Planktonic
	4.09	17480	16500	50	Benthic
JPC 19–21	3.48	13450	13750	45	Benthic
	3.59	13880	14150	40	Benthic
	5.32	18890	17800	80	Benthic
	5.48	19300	18150	75	Benthic
	7.29	25830	23700	150	Benthic
	7.39	26270	24200	160	Benthic
	7.68	27620	25600	140	Benthic
	7.74	27840	25900	200	Benthic
	7.74	33140	30100	320	Planktonic
JPC 26–30	2.10	13160	13015	40	Benthic
	4.30	20260	18540	60	Benthic
	7.20	27500	25400	140	Benthic
	7.38	28780	26900	150	Benthic
	7.38	28930	26000	130	Planktonic
	8.43	33870	31900	390	Benthic
	8.51	34200	32300	410	Benthic
	9.15	35450	33700	490	Benthic
GC 35–40	0.78	570	2730	20	Benthic
	0.96	820	3030	20	Benthic
	1.41	1680	3850	20	Benthic
	1.94	2790	4760	20	Benthic
	2.13	3180	5080	25	Benthic
	2.83	5260	6680	30	Benthic
	2.98	5760	7140	25	Benthic
JPC 32–36	0.44	1030	3230	20	Benthic
	5.22	15540	15150	45	Benthic
	5.37	15990	15450	50	Benthic
	7.94	18890	17800	85	Benthic
JPC 33–38	4.00	10770	10230	25	Planktonic
	6.10	13960	13180	45	Planktonic
	7.22	18010	16950	210	Benthic
	7.60	16320	15700	70	Benthic
	7.77	15860	15350	60	Benthic

of diagenesis were avoided. For 9 samples, both planktonic and benthic samples were collected in order to define a reservoir age. 48 samples were analyzed at the National Ocean Sciences Accelerator Mass Spectrometry facility at the Woods Hole Oceanographic Institution and produced an age using the Libby half-life of 5568 years and following the convention of Stuiver and Pollach (1977). The remaining samples were analyzed at the WM Keck Carbon Cycle Accelerator Mass Spectrometry facility at the University of California Irvine following the same conventions. The ^{14}C ages were converted using the CALIB program version 7.0.4 (Stuiver and Reimer, 1993) with a reservoir age of 800 for planktonic foraminifera < 12,000 year and a reservoir age of 1100 for planktonic foraminifera > 12,000 year (Southon et al., 1990; Kienast and McKay, 2001; Kovanen and Easterbrook, 2002). Based on the 9 samples that acquired ages for both benthic and planktonic foraminifera, we calculated an average difference in reservoir age of 900 years. For this difference in reservoir age, benthic foraminifera < 12,000 year would have a reservoir age of 1700 year, which is comparable to the reservoir age of 1750 for benthic foraminifera used by Mix et al. (1999), Covault et al. (2010), Brothers et al. (2015), and others. Thus, we used this value of 1750 years for a benthic reservoir age. Age-depth models for cores containing more than two dates were constructed using the Bacon software version 2.3.3 (Blaauw and Christen, 2011) using the reservoir ages as mentioned above and calibrated using the Marine 13 curve (**Supplementary Figure S1**). The Bacon software divided each core into 20 cm thick vertical sections and estimated accumulation rates for each section through millions of Markov Chain Monte Carlo iterations (Blaauw and Christen, 2011). This version of the Bacon software allows users to input abrupt events of sedimentation such as slumps and turbidites (Blaauw and Christen, 2011). Nevertheless, the software assumes that there are no hiatuses between these rapid sedimentation events (Blaauw and Christen, 2011) and does not account for sediment reworking in cores. The bounding depths of sand layers with abrupt basal contacts were inputted into the software as rapid periods of deposition in the age-depth models. If sand layers were bound by radiocarbon dates, the date of the sand layer was taken as an average of the corrected dates. If the sand layers were lacking bracketing radiocarbon ages, the age of the base of the sand layer was determined using the age-depth model produced by the Bacon software. In sections where turbidites are amalgamated, turbidites were distinguished by their erosive basal boundary and the age of the center of each turbidite was extrapolated using the age-depth model.

RESULTS

San Onofre North and South (SON and SOS) Canyon-Channel Geomorphology

The SON and SOS canyon-channel have respective lengths of 9.61 and 9.74 km and sinuosities of 1.15 and 1.10. Bathymetric profiles through the SON, SOS, and Dana Point canyons reveal marked variability in gradient (**Figures 2A–C**). The upper, middle, and lower slopes of each canyon are defined by changes in gradient. The SON Canyon-channel is characterized by a

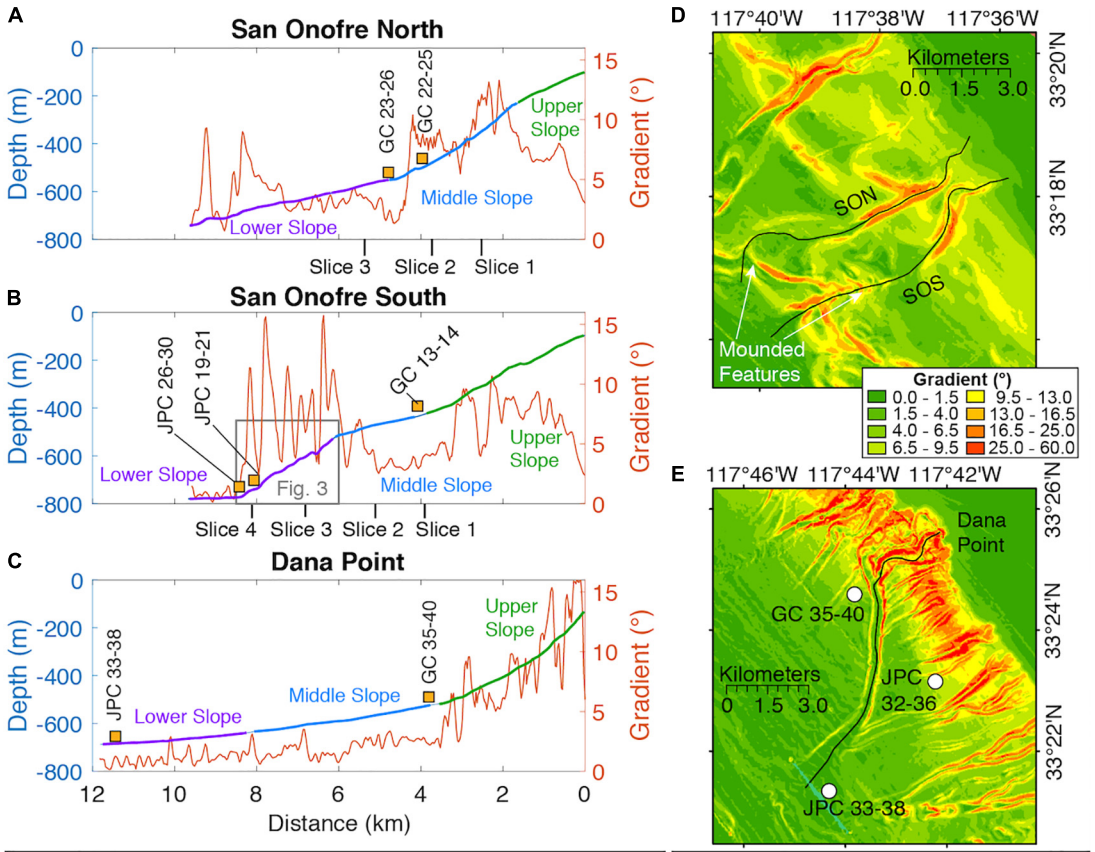

FIGURE 2 | (A–C) Bathymetric profiles of the San Onofre North, San Onofre South, and Dana Point Canyons are plotted with channel gradient. The channel profiles are subdivided into the Upper, Middle, and Lower slope. The locations of sediment cores are projected onto profiles as yellow squares. The intersections of Sparker 3D seismic slices are shown by the vertical black lines. In **(B)**, the location of **Figure 3** is highlighted. **(D,E)** Gradient maps offshore of San Onofre and Dana Point. SON = San Onofre North, SOS = San Onofre South. Green colors represent gentler gradients and red colors represent steeper gradients. The bathymetric profile through the channel is shown by the black line.

steep concave-up profile (maximum of ∼13°) in the middle slope between the depths of 240 and 680 m (**Figure 2A**). The characteristic feature of the SOS Canyon-channel is the gently sloping and smooth terraced feature (average ∼4.5°) in the middle slope between the depths of 430 and 480 m, above and below which the average gradient increases to ∼7° (**Figure 2B**). The lower slope has higher rugosity than the upper or middle slopes due to mounded features between 500 and 800 m that increase channel gradient for short distances (**Figures 2B**, **3**). On the slope map, these mounded features are crescentic in plan-view, are perpendicular to the SOS canyon, and exhibit steeper gradients (**Figure 2D**). We fit a linear regression to the morphology and subtracted the average slope from the bathymetric profile to reveal five mounded features, with three low-amplitude mounds with wavelengths ranging from 260 to 307 m and two larger mounds with longer wavelengths of 613 and 641 m (**Figure 3**).

We examined cross-sections of the SON and SOS canyons to calculate channel relief (**Figures 4A,B**). In both the SON and SOS canyon-channels, deeper channel depths are spatially coincident with steeper channel gradients (**Figure 4B**). The SON and SOS canyon-channels are narrow and v-shaped in the middle slope and widen in the lower slope (**Figures 4C,D**), consistent with other canyon-channel systems on the California margin and worldwide (e.g., Menard, 1955; Normark, 1970; Covault et al., 2011). The SON channel exhibits the greatest relief of 70 m between Slices 1 and 2 at approximately 3 km on the channel profile (**Figure 4B**) and this maximum incision is spatially coincident with a decrease in channel gradient. Where the channel has greatest relief, it is characterized by a v-shape in cross-section 4 (**Figure 4C**). Maximum relief of the SOS channel is farther downslope, between Slices 3 and 4 (**Figure 4B**), where the channel widens and has an asymmetrical v-shape near cross-section 8 (**Figure 4D**).

The head of the SON channel, shown in cross-section 1, exhibits minimum width (302 m), depth (3.7 m), and cross-sectional area (708 m^2; **Figure 4C**). While the SON channel exhibits maximum width (1185 m) and cross-sectional area (18650 m^2) in cross-section 8, SON channel depth reaches a maximum at cross-section 3 (68 m; **Figures 4B,C**). In contrast to the SON channel, minimum width (492 m), depth (5.5 m), and cross-sectional area (1216 m^2) are located in the middle

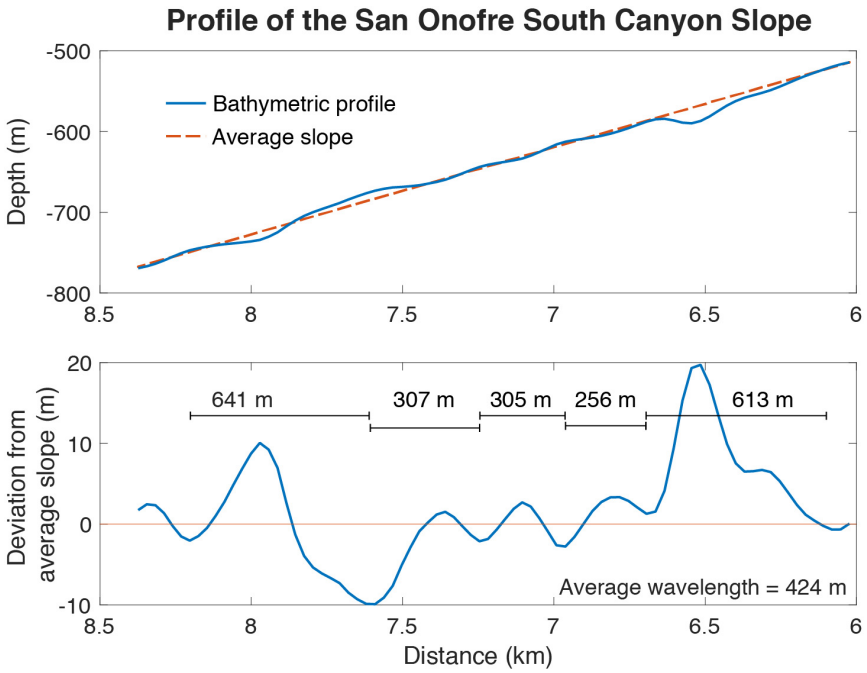

FIGURE 3 | (Top) The bathymetric profile from the lower slope of the San Onofre South Canyon is plotted in blue and has undulatory features. The dashed orange line is the average slope for this length of the canyon. **(Bottom)** Subtracting the average slope from the bathymetric profile reveals undulatory features with amplitudes ranging from 2 to 15 m and wavelengths ranging from 256 to 641 m.

slope cross-section 5 (**Figures 4B,D**). Like the SON channel, width, depth, and cross-sectional area reach maximums in cross-sections 7 and 9, with widths of 3412 m, depths of 83 m, and cross-sectional areas of 87270 m^2 (**Figures 4B,D**).

Stratigraphy of the San Onofre Slope and Canyons

Sparker dip profiles through the study area reveal the internal structure of sediment packages along the slope. Four sediment units were delineated based on sequence stratigraphic principles (e.g., Mitchum et al., 1977; Vail et al., 1977; Christie-Blick and Driscoll, 1995). The upper boundaries of many of the packages can be defined by toplapping reflectors against the base of the overlying unit. The uppermost sediment package on the slope is the Pink Unit that infills local bathymetric lows in all dip profiles and pinches out where there are local bathymetric highs (**Figure 5**). In strike profiles, the Pink Unit exhibits continuous high-amplitude reflectors that distinguish it from the underlying Blue Unit (**Figures 6A,B**). In dip profiles, the underlying Blue Unit also infills local bathymetric lows and is not present everywhere on the slope (**Figure 5**). Low-amplitude reflectors within the Blue Unit exhibit toplap in strike profiles, especially over bathymetric highs (**Figures 6A,B**). Orange Unit reflectors exhibit toplap in dip Line 11 against the Blue Unit (**Figure 5A**), and in dip Line 53, flat-lying reflectors in the Blue Unit terminate against the Orange Unit (**Figure 5C**). Green Unit reflectors exhibit some toplap against the overlying Orange Unit around 5 km in dip Line 53 and around 7 km in dip Line 13 (**Figures 5C,D**). The lower boundary of the Green Unit is delineated by a high amplitude reflector in strike Slice 1 and the northwest portion of Slice 3 (**Figures 6A,C**) and this lower boundary truncates underlying reflectors in Slice 4 (**Figure 6D**). Sediment packages below the Green Unit were not interpreted.

Dip profiles through the survey area (**Figure 5**) reveal that in general, portions of the slope with steep gradients are along anticline limbs. Conversely, portions of the slope with gentler gradients correspond to infilled synclines. Upper slope synclines appear only in the two northern dip profiles (**Figures 5A,B**). Some faults bounding the upper-slope syncline appear to offset reflectors just below the seafloor (**Figure 5A**). The upper-slope syncline is separated from a mid-slope syncline by an anticline that is cross-cut by a recent fault and obscured by gas-wipeout (**Figures 5A,B**). In contrast to the upper-slope syncline, the mid-slope syncline is observed in all dip profiles (**Figure 5**). Note that the local mid-slope and upper-slope synclines are completely infilled by sediment (**Figure 5**). Deformation within the mid-slope syncline appears to have along-margin variability. Faults at the syncline boundaries in lines 12C, 53, and 13 appear to deform the uppermost reflectors; nevertheless, faults cross-cutting the mid-slope syncline appear to have deformed only the Green and Orange units (**Figures 5A–C**). In these three lines, only Green and Orange units exhibit sediment thickening toward cross-cutting faults in the mid-slope syncline (**Figures 5A–C**). At the slope-basin transition, recent sediment onlaps slope deposits (**Figure 5B**). This recent sediment has an undulatory bathymetric expression and appears to step northeast

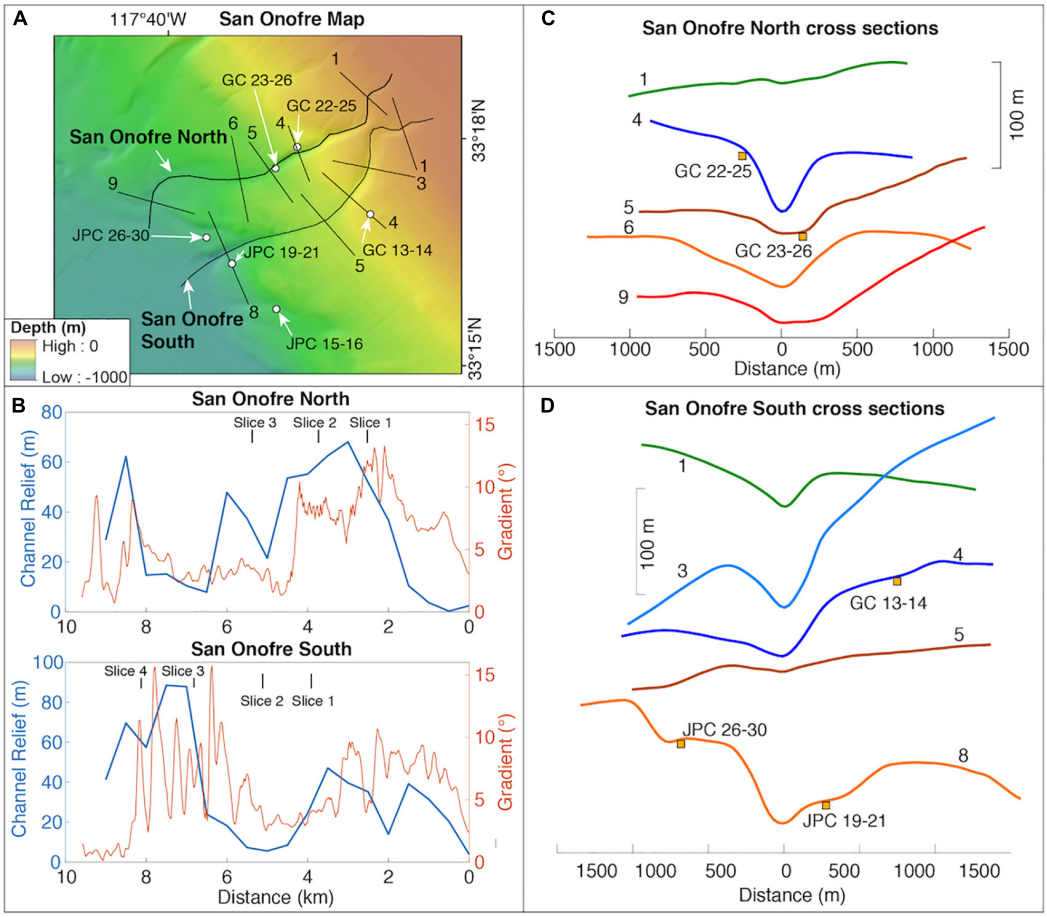

FIGURE 4 | (A) Bathymetry of the San Onofre North (SON) and South (SOS) Canyons. Cross-sections numbers correspond to their distance (in km) from the start of the bathymetric profile and are shown in panels **C** and **D**. Sediment cores are labeled. **(B)** Channel relief is plotted relative to channel slope for the two canyons. The intersections of the 3D Multichannel Sparker slices with the canyons are indicated at the top of the plots. **(C,D)** Cross sections through the SON and SOS canyon-channels are plotted. Horizontal and vertical scales are shown. Sediment cores were projected onto cross-sections and are indicated by yellow boxes.

through time (**Figure 5A**). The most seaward undulatory feature is onlapped by aggrading reflectors (**Figure 5A**). Four slices from 3D P-Cable data oriented along-strike to the margin reveal that the most prominent feature shaping the slope offshore of San Onofre is a prominent anticline that is clearly imaged in Slice 2 (**Figure 6B**). Sediment thins across the anticline crest and thicken away from the crest (**Figure 6B**).

Channel and overbank deposit geometry appear to correspond to variations in channel gradient. Pink Unit deposits adjacent to the SON channel have aggradational reflector character in Slices 1, 2, and 4 (**Figures 6A,B,D**). The SON channel incises into 16 m of aggradational Pink Unit deposits in Slice 1 (**Figure 6A**). In Slice 2, the SON channel incises into 18 m of Pink Unit deposits, above which a u-shaped feature is infilled with discontinuous, wavy reflectors (**Figure 6B**). Overbank deposits with gull-wing geometries that converge away from the channel are defined as channel levees, after Qin et al. (2016). Modern Pink Unit levees to the northwest of SON have maximum thicknesses of 82 m in Slice 1 and 87 m in Slice 2 (**Figure 6B**). Modern levees to the southeast of SOS are thick in Slice 1 and thin in Slice 2 (**Figures 6A,B**), whereas Pink Unit levees in between the SON and SOS channels are complicated by cross-cutting relationships. In Slice 2, the relict SOS channel may have truncated relict levee deposits from the SON canyon. Broadening in Slice 3, the SON channel is partially infilled with a Pink Unit deposit that unconformably aggrades into a NW-SE trending synform (**Figure 6C**). The SON channel is not present in Slice 4 (**Figure 6D**). Levees bounding the SOS channel exhibit more variability. In Slice 1, the SOS channel has an asymmetric v-shape that is adjacent to dipping wavy reflectors in the northwest levee and conformable reflectors in the southeast levee (**Figure 6A**). In Slice 2, the SOS channel is extremely narrow and shallow, and is bordered to the northwest by discontinuous, wavy reflectors (**Figure 6B**). The SOS channel in Slice 3 appears to be located in a local syncline and truncates reflectors in the Orange Unit (**Figure 6C**). In Slice 3, note the lack of Pink Unit channel levees. In the lower slope Slice 4, the SOS channel exhibits asymmetry, with thick levees to the northwest and thinner levees to the southeast that form a bench-like feature (**Figure 6D**).

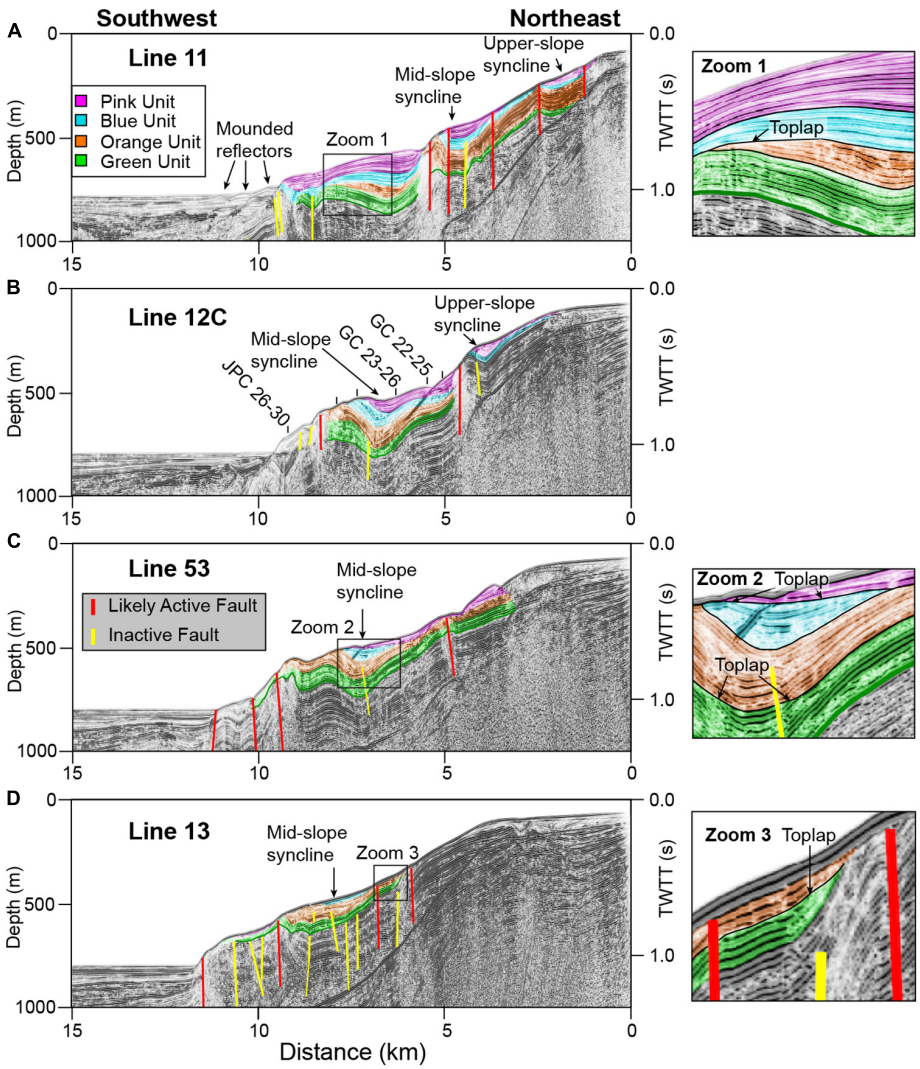

FIGURE 5 | Sparker seismic dip profiles offshore San Onofre reveal the internal structure of the slope and are organized with the northernmost profile at the top and southernmost profile at the bottom. **(A)** Line 11 is located northwest of the SON canyon, **(B)** Line 12C intersects the SON canyon, **(C)** Line 53 intersects the SOS canyon, and **(D)** Line 13 is southeast of the SOS canyon. The continental slope is characterized by a mid-slope syncline that decreases gradient that is bound by anticlines that increase gradient. Lines 11 and 12C contain upper slope synclines. The mid- and upper-slope synclines act as ponded basins that trap sediment. Mounded features are shown at the slope-basin transition in Line 11. Colors of Units are shown in panel **A**. Active faults offset reflectors just below the seafloor are shown in red. Inactive faults offset deeper reflectors and are shown in yellow. Sediment cores are projected onto seismic lines. Locations of lines are shown in **Figure 1**. At right are enlargements of areas that show toplapping relationships. Vertical Exaggeration = 5.6. For uninterpreted seismic profiles, see **Supplementary Figure S2**.

Deformation on this margin is complex, as evidenced by the multiple synclines imaged in dip profiles that create local accommodation (**Figure 5**), anticlines imaged in dip profiles that increase gradient (**Figure 5**), and a prominent anticline imaged in strike slices that appears to exert control on SON and SOS locations as well as Pink Unit levee thickness (**Figure 6**). 3-dimensional seismic fence diagrams provide an unprecedented view of the synclines and anticlines (**Figure 7**). Overall, the SON and SOS channels are located on the flank of the broad antiform in Slices 1 and 2 in the middle slope (**Figures 6A,B**, 7). The SON channel thalweg is located at deeper depths than the SOS channel thalweg (**Figures 6A,B**, 7), since accommodation for the SOS channel is limited, as it is located proximal to the antiform. The lack of accumulation adjacent to the SOS channel in Slices 1–2 is coincident with its v-shape and as the SOS channel moves into a synform in Slices 3–4, channel width increases (**Figures 6A,B**, 7).

San Onofre Sediment Core Lithology and Chronology

Cores offshore of San Onofre can be grouped by their depth on the middle slope (300–600 m) or on the lower slope (600–1000 m). With the exception of JPC 15–16, the upper portions

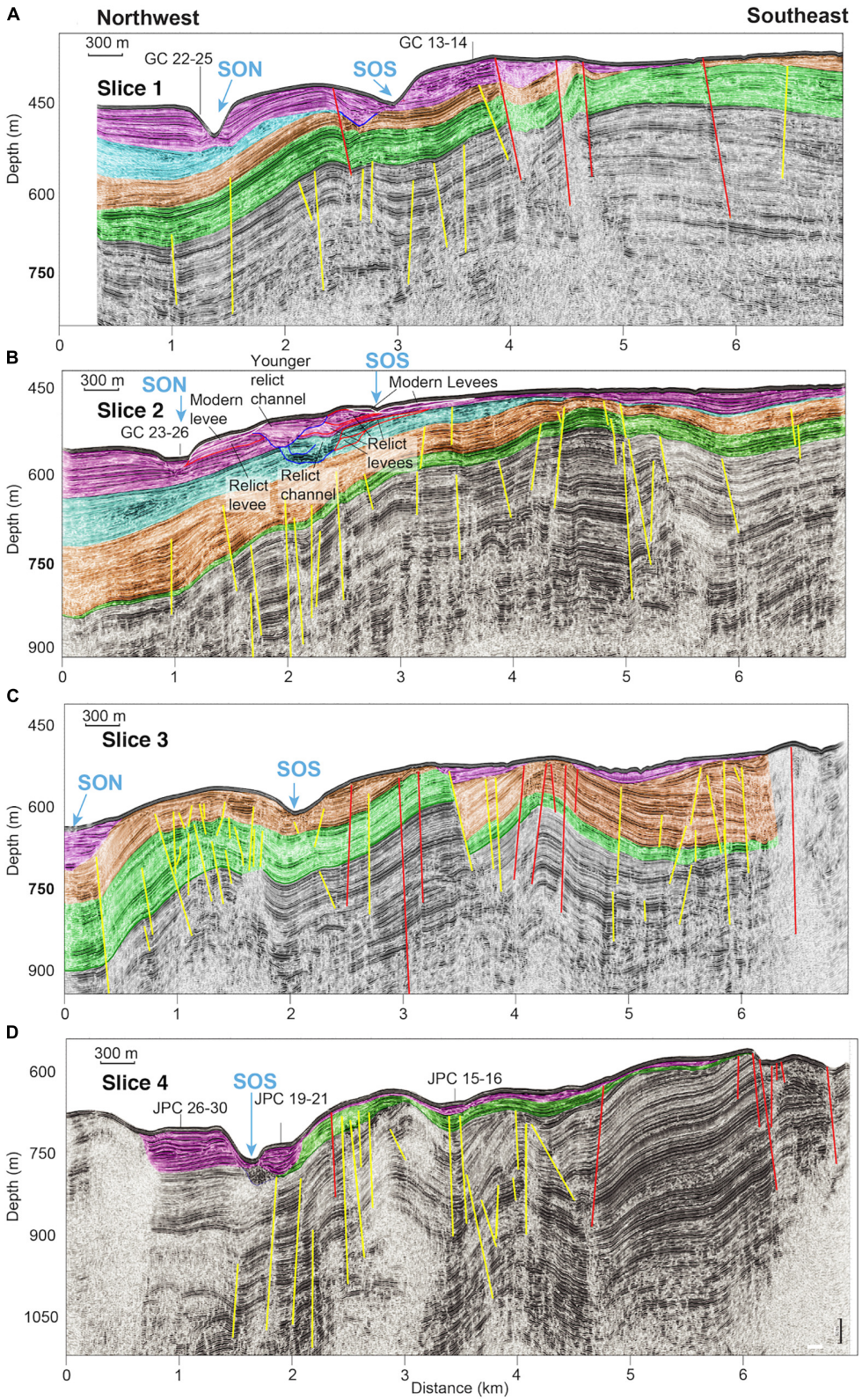

FIGURE 6 | Strike slices along the San Onofre margin reveal the internal architecture of the slope and channel elements. **(A)** Slice 1 and **(B)** slice 2 are located on the middle slope. **(C)** Slice 3 and **(D)** slice 4 are located on the lower slope. This anticline controls the location of the SON and SOS canyons ad well as the thickness of Pink, Blue, Orange, and Green units. The shallowest (easternmost) slice is at the top and the deepest slice (westernmost) is at the bottom. Sediment cores are projected onto seismic slices. Locations of lines are shown in **Figure 1**. Vertical Exaggeration = 5.1. For uninterpreted seismic profiles, see **Supplementary Figure S3**.

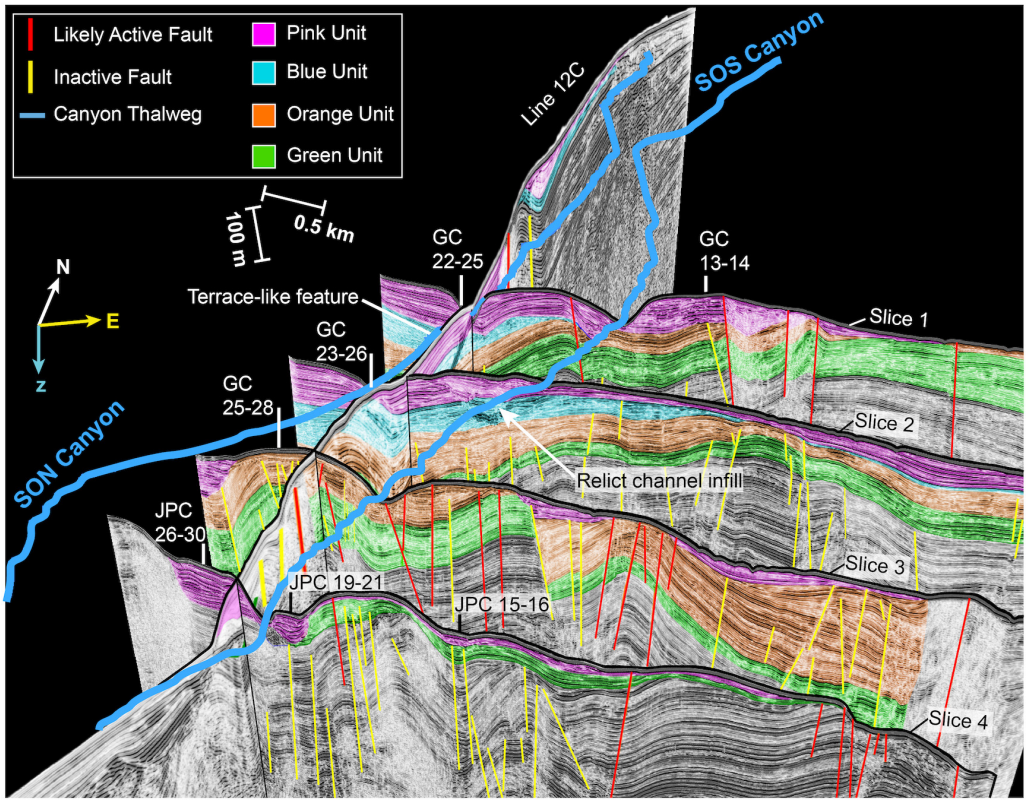

FIGURE 7 | A 3D seismic fence diagram with Sparker 2-D seismic line 12C and Sparker 3D slices. The locations of the two canyons are traced in blue. Colors denote sediment units, with the Pink unit as the youngest and the Green unit as the oldest. Likely active faults are shown in red and inactive faults are shown in yellow. Locations of cores are plotted as white or black lines. Vertical Exaggeration = 6.

of most of the cores offshore of San Onofre are capped by tens of cm to meters of clay or silty clay (**Figure 8**). This clay cap is commonly homogenous and bioturbated. In JPC 26–30, the base of the upper clay section is dated to approximately 13.2 kyr, 23.3 kyr in GC 22–25, and 44.4 kyr in GC 13–14 (**Figure 8**). Below this cap, silty clay or silt layers are interbedded with thin (< 1 cm) to thick (10's of cm) sand layers. Many of these sand layers fine upward. Sand layers are commonly observed to have sharp, erosive basal boundaries and gradational upper boundaries; however, basal boundaries are occasionally diffuse. Often, sand layers are characterized by color changes, as noted by the change from olive green to tan in the photo of JPC 19–21 (**Figure 8** photo inset). Nevertheless, some of the sand layers, such as those shown in the photo inset of JPC 15–16, exhibit only slight color changes. Some of the sand layers also contained shell hash in GCs 22–25 and 23–26 from the middle slope (**Figure 8**).

GC 13–14 was recovered from the southeast end of a channel levee on the middle slope and it contains only one sand layer (**Figures 6**, **8**). This layer has a sharp basal boundary and is composed of a mud matrix with unsorted medium sand, gravel, and shell hash (**Figure 8** photo inset). The middle portion of GC 22–25 contains 5 sand layers that fine upward with grain sizes ranging from fine to coarse sand. Radiocarbon dates bracketing the five sand layers suggest that they were deposited between 23.3 and 41.9 ka (**Figure 8**). GC 23–26, recovered from the SOS channel thalweg (**Figure 5B**), is composed of an upper silt cap, two sand layers composed of fine sand that are separated by 40 cm of clay, and blocky silt with shell hash in the lower sections of the core. Shell hash is interbedded with silt in GC 23–26 and the concentration of shell hash decreases downsection beginning at 1.4 m (**Figure 8** photo inset).

JPCs 15–16, 26–30, and 19–21 were recovered from the lower slope (**Figures 6D**, **8**) and are longer cores that contain 13, 14, and 23 sand layers respectively. The upper 30 cm of JPC 15–16 contains an upward-fining sand layer with coarse sand at the base. The lower 2.5 m of JPC 15–16 is characterized by sand layers with fine to medium sand that are interbedded with silt and clay. Sand layers increase in frequency and thickness in the lower 1.5 m in the core with ages ranging between 17.7 to 18.1 ka. Constraining the exact timing of sand layer deposition is difficult in this core, as ages are inverted. As such, dating of the layers was conducted using age models calculated by the R Bacon package (**Supplementary Figure S1**). In the lower portion of JPC 26–30, sand layers are less frequent than those in JPCs 15–16 or 19–21 and these sand layers predate the LGM. Overall, sand layers within JPC 19–21 at 5.3 m depth have a lighter color than the surrounding silt and exhibit sharp basal and upper contacts (**Figure 8** photo inset). Around 6 m, sand layers are closer

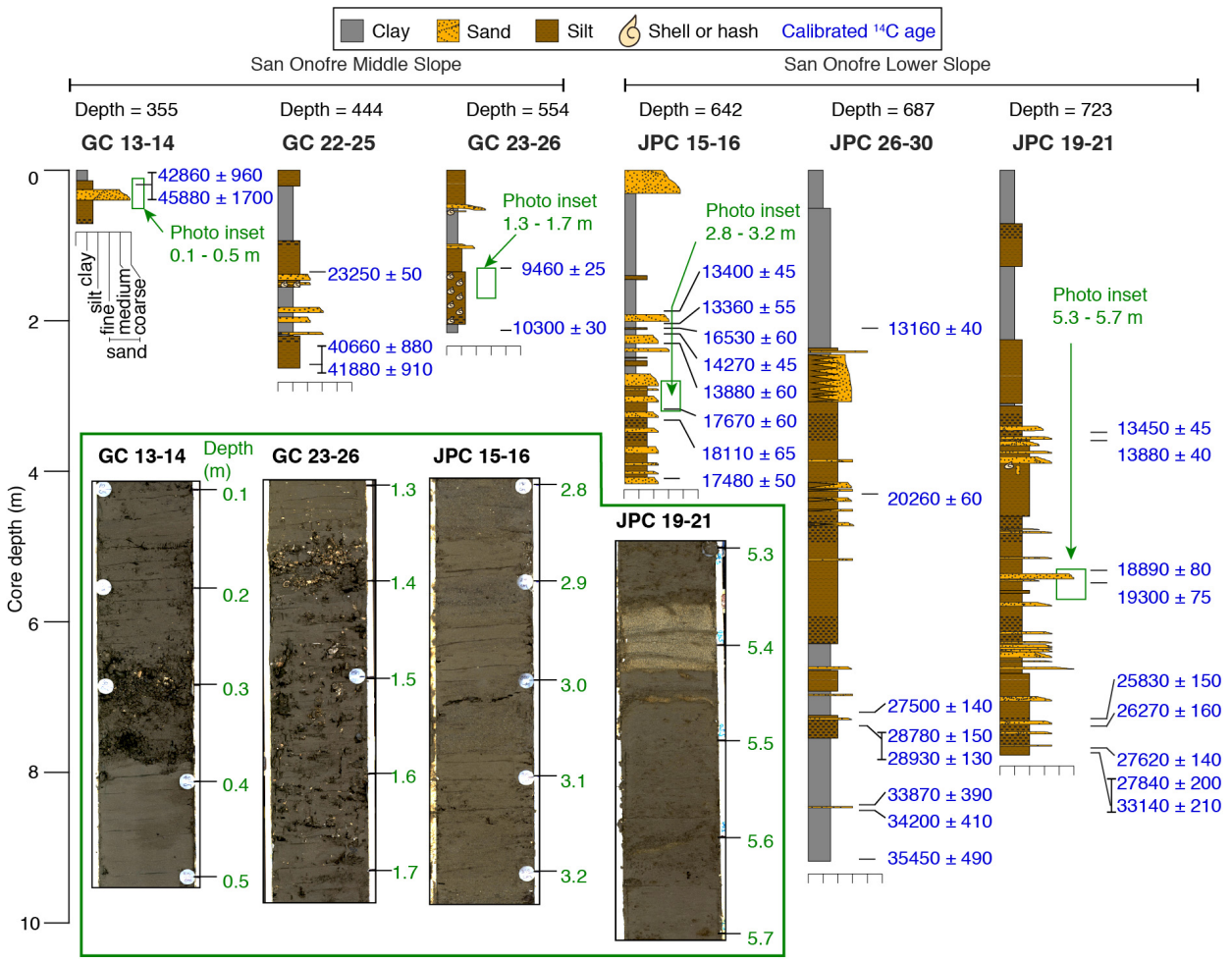

FIGURE 8 | Schematic diagrams of San Onofre cores. Labeled grain size scale is shown under GC 13–14 and unlabeled scales are shown under all other cores. Calibrated radiocarbon ages are shown to the right of the cores. At the bottom left, photo insets of select cores are plotted with their depth. The locations of the photo insets are shown relative to core diagrams by the outlined green rectangles.

together and thicken until the bottom of JPC 19–21, where sand layers are spaced farther apart and consist of fine sand (**Figure 8**).

Dana Point Canyon-Channel and Core Stratigraphy

The narrow shelf (∼2 km) offshore of Dana Point separates the head of Dana Point Canyon from San Juan Creek (**Figure 1C**). Dana Point Canyon has two branches at the head and one broad meander, resulting in a low sinuosity of 1.13 (**Figures 2E**, **9A**). Three cores, GCs 35–40, and JPCs 32–36 and 33–38 were collected adjacent to the Dana Point Canyon (**Figures 1C**, **9A**). Sparker seismic surveys do not extend into this area and therefore, most of our interpretations on geomorphology are based off limited CHIRP seismic coverage and multibeam bathymetry.

The bathymetric profile of the Dana Point Canyon is generally concave-up with a steep upper slope (5–15°), and gentler gradients on the middle and lower slopes (0–3°; **Figure 2C**). Steep gradients in the upper slope coincide with greater channel relief and canyon-channel depth dramatically decreases between 3 and 4 km as gradient decreases (**Figure 9B**). This transition occurs at the intersection of the canyon head branches and at the inner bend of the canyon's meander (**Figures 9A,B**). A CHIRP seismic profile through this transition and bathymetric cross-sections at 3 and 4 kilometers reveal that the canyon has higher walls to the east (**Figures 9C,D**). Unlike the SON and SOS canyons, the Dana Point Canyon maintains a u-shaped channel with a wide valley floor throughout the slope (**Figure 9D**). Depth and cross-sectional area are greatest at 1 km and lowest at 8 km (**Figure 9B**). Like the SON and SOS canyon-channels, maximum widths of the DP channel are at 9–10 km (**Figure 9D**).

JPC 32–36 and GC 35–40 are located on the middle slope at depths of 500 and 510 m, whereas JPC 33–38 is located on the lower slope at depths of 688 m. GC 35–40 was recovered from the Dana Point channel flank and is located at the transition from higher to lower channel gradient (**Figures 9B,C**).

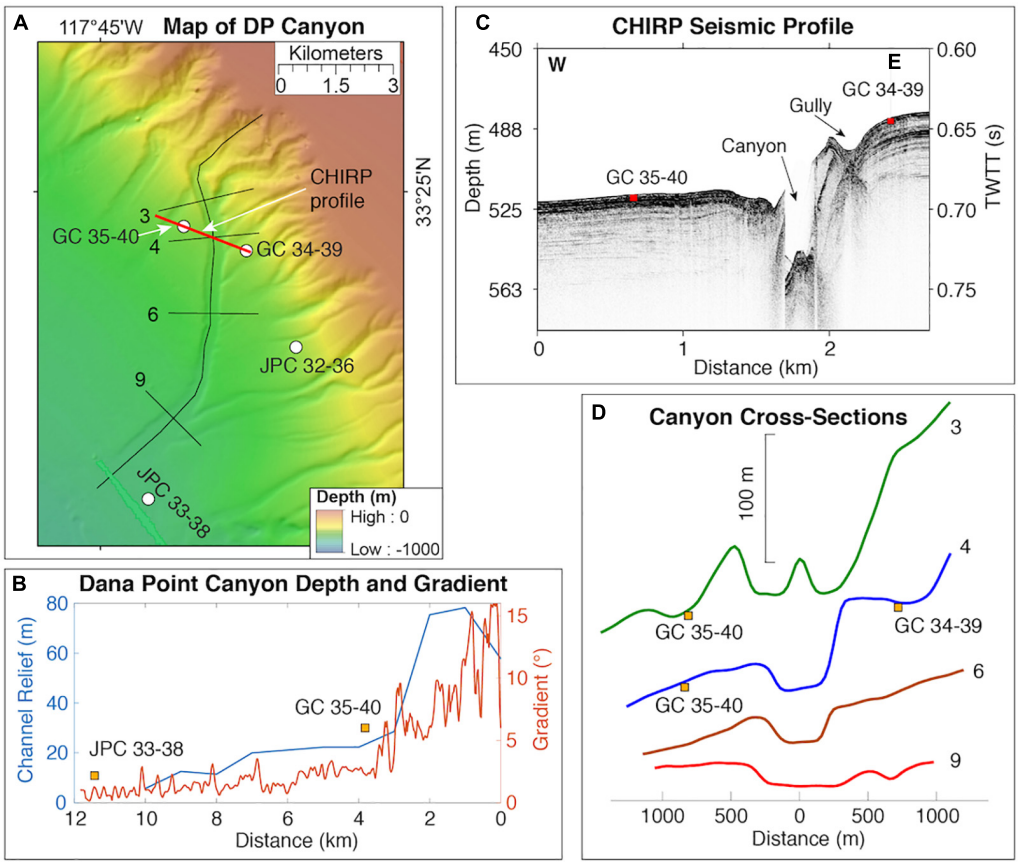

FIGURE 9 | (A) Bathymetry of the Dana Point Canyon. The location of the CHIRP profile shown in panel **B** is highlighted in red. Cross-sections numbers correspond to their distance (in km) from the start of the bathymetric profile and are shown in panel **D**. Sediment cores used in this study are also labeled. **(B)** Channel relief is plotted relative to channel gradient. Yellow boxes indicate the location of sediment cores along the bathymetric profile. **(C)** CHIRP seismic profile through GCs 35–40 and 34–39. **(D)** Cross sections through the DP canyon-channel are plotted. Numbers at right correspond to the distance along the bathymetric profile. Horizontal and vertical scales are shown. Sediment cores were projected onto cross-sections and are indicated by yellow boxes.

JPC 33–38 is located at the slope-basin transition where the canyon widens (**Figure 9A**). Cores in Dana Point are capped by an upper layer of clay and silt that varies from < 1 to 4 m thick (**Figure 10**). In GC 35–40, the age of the clay and silt cap is < 570 years BP, < 10.8 ka in JPC 33–38, and cannot be constrained by available ages in JPC 32–36 (**Figure 10**). Below this, silty clay and sandy silt are interbedded with fine sand. Sand layers in GC 35–40 are a few cm's thick, whereas sand layers in JPC 32–36 are thin and most are < 1 cm (**Figure 10**). The 12 sand layers in GC 35–40 exhibit ages between 570 and 5760 years BP and this range of ages is limited by the short core recovery. JPC 32–36, which is farthest core from the Dana Point Canyon, has the thinnest and fewest sand layers (7) that are dated between 15.5 and 18.9 ka (**Figure 10**). Thick and thin sand layers in JPC 33–38 are amalgamated and can be distinguished by erosive lower boundaries (**Figure 10**). JPC 33–38 has the most abundant (37) and thickest sand layers that range in age from 10.7 to 15.9 ka (**Figure 10**). Sand color ranges from olive-gray in the photo of GC 35–40 to light tan in the photo of JPC 33–38 (**Figure 10**). Some sand layers in JPC 33–38 contain shell hash, which can be observed between 5.6 and 5.7 m in this core's photo inset (**Figure 10**).

DISCUSSION

Turbidite Chronology and Uncertainties

Deposition on the continental slope predominantly occurs by two main modes: gravity-driven turbidity flows during intervals with high terrigenous supply or hemipelagic sedimentation when terrigenous supply is low (Stow and Piper, 1984; Walsh and Nittrouer, 2003; Maier et al., 2017). Turbidites were identified in sediment cores by fining-upward sand layers (i.e., graded beds) with erosional bases (Stow and Piper, 1984). While many of the turbidites have sharp, erosive basal contacts and gradational upper contacts, some basal boundaries are occasionally diffuse. The homogenous, upper clay section observed in most cores (**Figures 8**, **10**) is interpreted as hemipelagic sediment drapes that accumulate more slowly. Most of the cores in the study, with the exception of GC 23–26 and JPC 15–16, recovered turbidite deposits from channel

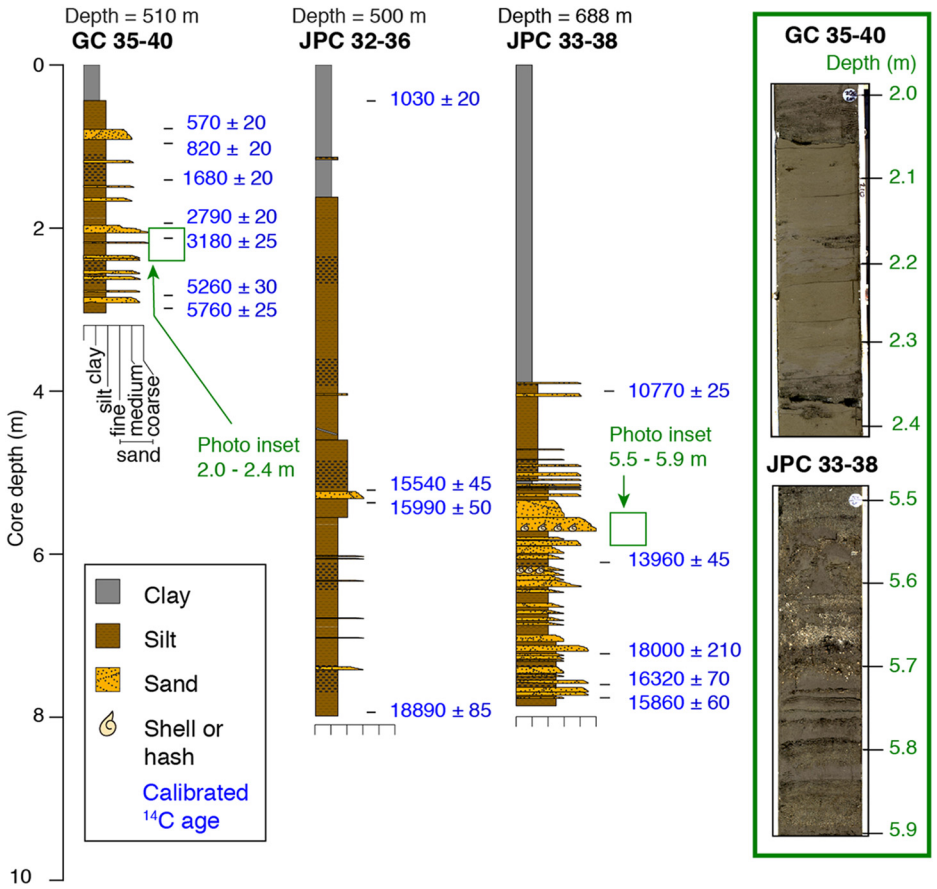

FIGURE 10 | Schematic diagrams of Dana Point cores. Grain size scale is shown under GC 35–40. Unlabeled grain size scales are shown below all other cores. Calibrated radiocarbon ages are shown to the right of the cores. At right, photo insets of select cores are plotted with their depth. The location of the photo insets are shown relative to core diagrams by the outlined green rectangles.

levee deposits. Thus, the channel levee cores record higher-volume turbidity currents and it is possible that additional cores from the channel thalweg could preserve younger lower-volume turbidites.

Broad patterns in the histogram reveal that turbidites from high-volume gravity flows are emplaced to the Dana Point slope throughout lowstands and highstands in sea-level (**Figure 11**). Conversely, turbidites from high-volume gravity flows are emplaced offshore San Onofre predominantly during MIS 2 and exhibit a marked decreased around 12–13 ka with the youngest turbidites deposited at approximately 8 ka (**Figure 11**).

Offshore Dana Point, turbidites were emplaced in GC 35–40 from 1 to 6 ka, in JPC 33–38 from 13 to 18 ka, and in JPC 32–36 from 15 to 19 ka (**Figures 10**, **11**). Recent turbidite emplacement at GC 35–40 suggests that the upper portion of Dana Point Canyon had high-volume turbidity currents during the sea-level falling stage, lowstand, transgression, and highstand. High-volume turbidity currents may not have reached the lower portion of Dana Point Canyon, the sites of JPCs 32–36 and 33–38, to emplace turbidites after 13 ka. This difference may be related to sediment supply, as recent studies question whether turbidity currents can traverse entire submarine canyon-channel systems (Fildani, 2017; Symons et al., 2017). Thus, presently active turbidity flows in Dana Point Canyon may be restricted to the upper slope.

The paucity of turbidites offshore San Onofre that are younger than 8 ka suggests that the most favorable conditions for turbidite deposition offshore of San Onofre were during the MIS 2 and 3 lowstands and the early transgression (**Figure 11**). Older turbidites within the San Onofre cores dating back to 40 ka may have a high potential for recovery within JPCs because sedimentation rates are lower offshore San Onofre than in Dana Point and cores offshore San Onofre are condensed. It appears that the shallowest cores offshore San Onofre, GC 13–14 and GC 22–25, have the oldest turbidite ages whereas cores on the middle and lower slopes have slightly younger turbidite ages (**Figure 11**). GC 23–26 from the channel levee records the youngest turbidite deposits (**Figures 8**, **11A**); nevertheless, it is possible that turbidity currents may have reworked and eroded thalweg deposits. This process may be related to ponded basins, channel gradient, and geomorphology, as discussed in Sections "Across-Margin Deformation Controls Local Turbidite Emplacement" and "Channel Gradient Controls on Morphology and Turbidite Emplacement."

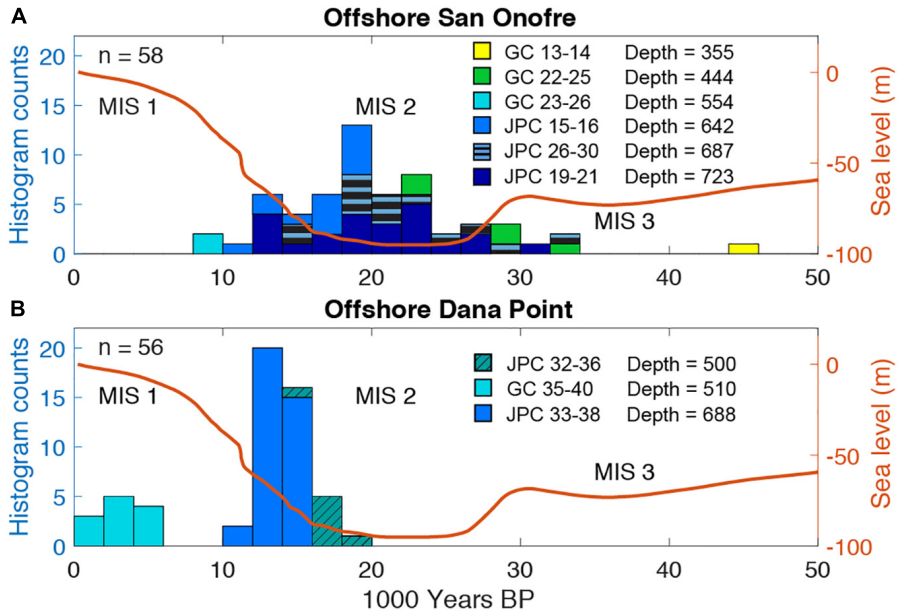

FIGURE 11 | (A) Histograms of sand layer depositional timing offshore San Onofre and Dana Point have bins of 2000 years. **(A)** The number of sand layers recovered from cores offshore San Onofre. **(B)** The number of sand layers recovered from cores offshore Dana Point. In orange, the Southern California sea-level curve from Muhs et al. (2012) versus time.

Reservoir ages for foraminifera vary with depth; ages range from 1000 to 2000 years and have errors as large as 40‰ $\Delta^{14}C$ (~320 years) along the Southern California margin (Roach et al., 2013; C. Charles, pers. comm.). As a result, uncertainties exist and precise age estimates for turbidites are not feasible. Such uncertainties for radiocarbon dating on the Southern California margin are associated with the effects of vertical ocean mixing and migration of benthic foraminifera species from the depth of calcification to the depth of deposition (Roach et al., 2013). Furthermore, Bayesian constructions of age-depth models have limitations, as these models do not consider hiatuses or sediment reworking (Blaauw and Christen, 2011). In some sections of JPCs 15–16 and 33–38, inverted radiocarbon ages are within 1000-year error windows found by Roach et al. (2013). When the inverted ages are outside of the 1000-year error window, we hypothesize that inverted ages may be caused by turbidity currents or mass wasting events that mobilize sediment with older foraminifera re-deposited downslope. As such, we examined broad patterns in turbidite depositional timing, such as MIS 3, MIS 2, the post-LGM transgression, and MIS 1. Histograms for turbidite ages offshore of San Onofre and Dana Point employ a 2000-year bin in order to account for large uncertainties in radiocarbon dating (**Figure 11**).

The hemipelagic mud cap observed in the upper section of most cores is interpreted to have been deposited after terrigenous supply to the canyon-channel declined. Such hemipelagic deposits are also observed draping inactive canyons that halted deposition ~15–20 kyr ago (Sweet and Blum, 2016), such as the Mississippi (Normark et al., 1986), Amazon (Milliman et al., 1975; Normark et al., 1997), and Nile (Ducassou et al., 2009). While recent papers in the ICB have interpreted mud deposits interbedded with turbidites as hemipelagic background sedimentation (e.g., Maier et al., 2017), some studies in the Gulf of Mexico interpret gray-brown muds interbedded with turbidites as hemiturbidites, or thin fluid-mud flows moving continuously downslope (Damuth, 1977; Damuth and Olson, 2015). It is difficult for us to discern their exact origin, as laminations are obscured by bioturbation. As such, we treated mud interlayers in the age model as constant-rate deposition.

Shelf Width Controls Turbidite Deposition

The San Onofre and Dana Point canyons have four main differences that may affect the emplacement of turbidites, namely (i) shelf width is ~10 km offshore San Onofre versus ~2 km offshore of Dana Point (**Figure 1C**); (ii) Dana Point canyons were likely attached to San Juan Creek during falling stages in sea-level, the lowstand, and the ensuing transgression, whereas the San Onofre canyons were likely not attached to a creek source during the post-glacial transgression; (iii) the Dana Point channel profile is relatively smooth and concave-up in comparison to a more rugose SON and SOS channel profiles; and (iv) sediment discharge to Dana Point Canyon from San Juan Creek is an order of magnitude larger than sediment discharge from San Mateo Creek to the San Onofre canyons. As shelf width is known to be an important control on sediment supply to the slope and basin, widening of the shelf caused by the anticline may contribute to decreased sediment delivery to the slope in that region (Covault et al., 2007, 2010). We propose that broad tectonic and structural controls influence the timing of turbidite deposition regionally (San Onofre versus Dana Point).

Large-scale features such as shelf width and slope gradient are controlled by tectonic deformation. The broad anticline along the outer shelf imaged by Sahakian et al. (2017) is a first-order tectonic feature that has increased shelf width offshore of San Onofre. Second-order features include the anticlines and synclines imaged in dip and strike profiles along the slope (**Figures 5**, **6**). The ponded basins and anticlines are related to transpression and transtension along faults in the SM Fault Zone (Maloney et al., 2016; Conrad et al., 2018). Third-order features such as channel levees are influenced by properties of turbidity flows, such as flow velocity and entrainment.

Comparisons of the SON and SOS canyons to the Dana Point Canyon draw similarities to studies that contrast coast-disconnected canyons versus connected canyons along the same active margin (*sensu* Gamberi et al., 2015). A study on the Sicilian margin observed that canyons with heads close to the coast are active during the present highstand and are sourced by hyperpycnal flows or longshore currents that rework shelf sands (Gamberi et al., 2015). In contrast, sediment supply to coast-disconnected canyons ceased during the post-glacial transgression (Gamberi et al., 2015). Our comparison suggests that Dana Point may maintain more connectivity to a larger sediment source, whereas the San Onofre Canyons may be farther from the San Mateo Creek with comparatively lower sediment supply.

Deformation on the Slope Controls Turbidite Emplacement

Deformation across the San Onofre slope exerts three main influences on turbidite emplacement: (i) anticlines and synclines form ponded basins that either trap sediment or cause bypass across the slope (**Figures 5**, **7**), (ii) anticlines and synclines dictate the morphology of SON and SOS channel levees along the slope, and (iii) structural controls influence slope gradient, which in turn affect canyon-channel dynamics and geomorphology. Models predict that ponded basins exert controls on grain size, as these basins are predicted to fill with thick, sand-rich deposits, whereas slope deposits tend to contain less sand (Prather, 2000). This model may explain why GCs 22–25 and 23–26 recovered ∼4–5 turbidites from the mid-slope syncline/ponded basin (**Figures 7**, **8**).

On the slope, the only mechanism of generating basins/synclines may be tectonic deformation (Covault et al., 2012) such as right jogs on the right-lateral strike-slip NIRC and SM Fault Zone that form transtensional basins (Ryan et al., 2009; Maloney et al., 2016; Conrad et al., 2018). Recent deformation of the middle slope ponded basin may be observed in Line 11 (**Figure 5A**); however, recent deformation of Blue and Pink unit sediment is not observed south of Line 11 (**Figure 5**). Thus, it appears that deformation within the ICB occurred on timescales much longer than the timescales of recent deposition; on this margin, there was no recent renewal of accommodation in local ponded basins. Thick Pink, Blue, and Orange units infilling the mid-slope ponded basin have diminished relief on the continental slope in dip profiles (Line 12C; **Figure 5B**) as well as SON and SOS channel relief on the intersecting Slice 2 (Slice 2; **Figures 6B**, **7**). Nested U-shaped bodies that truncate underlying deposits and are infilled with aggrading Blue and Pink units are suggestive of relict channels (**Figure 6B**). As these nested U-shaped bodies are bound by gull-wing shaped levees, we interpret these U-shaped bodies as relict channels rather than localized deformation or draping infill. The older and deeper relict channel was infilled and this aggradational sediment was subsequently truncated by a younger relict channel located to the northwest with shallower channel depths (**Figure 6B**). After the complete infilling of the younger relict channel, the present-day SOS channel is deflected to the southeast of the relict channels and maintains a shallow depth (**Figure 6B**). The infilled relict channels serve as an example of how the formation of such ponded basins affect the flow dynamics of channels and channel element architecture.

When ponded basins in the upper, middle, and lower San Onofre slope became completely infilled, sediment likely bypassed these basins and deposited turbidites on the lower slope and basin floor (**Figures 5–7**). The radiocarbon age below the mud cap in GC 22–25 could imply that turbidite emplacement in the ponded basin ceased before 23.25 ka as the basin infilled. Shortly after, bypass of the ponded basin and pelagic sedimentation may have commenced. This hypothesis is supported by abundant turbidites on lower slope JPCs 15–16, 19–21, and 26–30 that post-date 23 ka (**Figure 11**).

The anticlines and synclines imaged in the dip and strike profiles (**Figures 5**, **6**) exert controls on the levee morphology adjacent to the SON and SOS canyon-channels. On the middle slope, levees thin toward the anticline crest adjacent to the SOS canyon-channel and thicken away from the anticline crest (**Figures 6A,B**). Levees located closer to the anticline crest may have less frequent deposition than those located at deeper depths away from the anticline. For example, GC 13–14 has one turbidite that is ∼20 kyr older than multiple turbidites in GC 22–25. While GC 13–14 is located on a shallower levee close to the anticline crest, GC 22–25 is located in deeper water away from the anticline crest. On the lower slope, the SOS channel migrates into a syncline as the channel widens (**Figures 6C,D**). Thus, deformation on the San Mateo Fault Zone appears to influence turbidite emplacement and timing over lateral distances < 1 km by creating ponded basins that trap sediment, forming anticlines that cause sediment bypass in the cross-margin direction, and affecting levee architecture in the along-margin direction.

Channel Gradient Controls on Morphology and Turbidite Emplacement

Channel gradient exerts controls on turbidity flow behavior, as the velocity of turbidity flows is proportional to gradient (McHargue et al., 2011). Steep gradients along broader scales are often related to greater incision, whereas gentler gradients are related to deposition (Prather, 2000; McHargue et al., 2011; Brothers et al., 2015; Maier et al., 2017). Breaks in channel gradient can emplace turbidites and steep gradients can cause bypass of turbidity currents; as a result, gradient can influence the frequency and timing of turbidite emplacement. Without tectonic deformation, canyon-channel systems on a continental

slope would trend toward an equilibrium profile just like fluvial systems (McHargue et al., 2011). A smooth concave-up profile is observed through the Dana Point Canyon, whereas tectonic deformation offshore of San Onofre has created bathymetric irregularities that disrupt the equilibrium profile for the SON and SOS canyons (**Figure 2**). In this manner, the SON and SOS canyons exhibit similarities to the Palos Verdes Channel, where strike-slip tectonics that create local uplift or pull-apart basins that have inhibited channels from developing an equilibrium profile (Maier et al., 2017). Such variability in turbidity current flow over the SON, SOS, and Dana Point canyons may further overprint the influence of shelf width on turbidite emplacement. While we attempt to address the overlapping influences of shelf width and current dynamics on the turbidite record, these signals cannot be unambiguously teased out, as multiple processes can form similar deposits (Talling et al., 2012).

The concave-up bathymetric profile of the Dana Point Canyon suggests less tectonic deformation in this area than the SON and SOS canyon-channels; nevertheless, depth and changes in downslope gradient may cause local variances in the timing of turbidite emplacement. The gradient changes from 5 to 15° in the upper slope to < 5° in the middle slope (**Figure 2C**); GC 35–40 is located at this break in gradient and here deposition may be favored over bypass. As a result, it records recent turbidites within the past 600 years (**Figure 10**). We hypothesize that the presence of older turbidites in JPC 32–36 could be due to its lower slope location and its location farther from the channel axis (**Figure 9A**).

Turbidite age and the SON and SOS channel gradient do not exhibit a one-to-one relationship. Breaks, or abrupt changes in channel gradient (*sensu* Maier et al., 2017) are observed at the transitions from the upper to middle and middle to lower slopes (**Figure 2**) and may further influence localized turbidite emplacement by decelerating flow. Where these breaks occur, thick, aggradational channel levees flank the SON and SOS channels (**Figure 7**). Such a break on the mid-slope and the core's thalweg location may explain turbidite emplacement in GC 23–26 as recent as 8 ka (**Figures 2A**), whereas other cores on the San Onofre slope have older turbidites emplaced after 10 ka (**Figure 8**).

Conversely, steep gradients in the lower slope facilitate faster turbidity currents that potentially caused bypass, thinning sediment cover, and older turbidite emplacement. In Slice 3, a small NE-SW trending anticline separating the SON and SOS canyons appears to have no Pink or Blue unit sediment cover and the SOS channel appears to incise the southwest flank of the anticline (**Figures 6C**, **7**). The only core recovered from a portion of the slope with a steep gradient is GC 22–25, and a lack of turbidites younger than 23.3 ka in this core (**Figures 8**, **11**) may be indicative of either bypass due to steep channel gradient or sediment starvation caused by infilling of the upslope ponded basin.

On the lower slope, deformation on short length scales (< 1 km) may favor hydraulic jumps that produce the mounded bathymetry shown in **Figure 3** and also observed in the slope map in **Figure 2D**. The northern extent of these mounds was imaged by dip Line 11 (**Figure 5A**) as landward-migrating mounded reflectors (**Figure 5A**). Note that the landward-migrating mounds are observed just landward of the basin deposits. These mounds are similar to crescentic bedforms located at the channel-lobe transition zone in the adjacent San Mateo Canyon and have been interpreted as cyclic steps (Kostic, 2011; Covault et al., 2014, 2017). Cyclic steps are large-scale, upstream-migrating, wave-like bedforms with wavelengths of 100's to 1000's of m (Covault et al., 2017). In the San Mateo Canyon (Covault et al., 2014) and in model simulations (Kostic, 2011), cyclic steps are located at the decrease in gradient at the channel-lobe transition zone (Covault et al., 2017). Cyclic steps that are oriented orthogonal to the canyon, such as the ones observed here, are typically initiated by large turbidity currents (Normark et al., 2002; Covault et al., 2017). Offshore San Onofre, cyclic steps are observed in the lower kilometer of the SON profile (**Figure 2A**), as the SON channel widens (**Figure 2D**) and throughout the steep lower slope in the SOS profile (**Figures 2B**, **3**). In a manner similar to the San Mateo Canyon, subsurface folding observed in dip Line 12C (**Figure 5B**) caused by deformation along the San Mateo Fault Zone (Conrad et al., 2018) may create rugose bathymetry that causes turbidity currents to undergo hydraulic jumps necessary for the formation of cyclic steps (e.g., Ryan et al., 2009; Covault et al., 2017). The increased bathymetric rugosity caused by deformation and cyclic steps may play an important role in deposition along submarine channels, as has been documented in Brazil (Gamboa and Alves, 2015; Qin et al., 2016).

Implications for Paleoseismic Studies

When autogenic processes such as flow filtering are complicated by allogenic elements such as gradient, ponded basins, and wide shelves, the record of turbidite emplacement becomes increasingly difficult to disentangle. As such, paleoseismology studies that rely on turbidite emplacement records (e.g., Goldfinger et al., 2003, 2007) should be approached with caution. The most conclusive results of this study confirm findings of regional scales from Covault et al. (2007, 2010) and Normark et al. (2009) and the effects of local ponded basins *sensu* Prather et al. (1998) and Damuth and Olson (2015). The wide shelf offshore San Onofre likely prevents terrigenous supply to the deep sea during the post-glacial transgression and highstand, whereas the narrow shelf offshore Dana Point remains connected to sediment sources and has allowed for the recent emplacement of turbidites within the past 1000 years. On scales finer than 1 km, the dynamics of tectonic deformation and gradient can explain variances in depositional timing from individual cores.

Despite recent advances in linking modern flow processes to their deposits (e.g., Xu et al., 2010; Symons et al., 2017; Maier et al., 2019), we still do not completely understand down-canyon variability in turbidity current flow and the preservation of facies adjacent to canyons. Even though the margin offshore of Dana Point has likely experienced less deformation than offshore San Onofre, the record of turbidite emplacement is difficult to disentangle due to channel gradient and autogenic processes. As such, individual core records from the much more complex margin offshore of San Onofre are affected not only by breaks in channel gradient, but also by tectonically

controlled ponded basins. Turbidites offshore this tectonically active margin could theoretically record recent deformation. Nevertheless, turbidites offshore of San Onofre are > 8 ka and fail to record historical earthquakes such as the 1933 Long Beach earthquake. This also supports the hypothesis of Sahakian et al. (2017) that the San Onofre segment has been inactive for much longer (> 10 ka) than other segments the NIRC Fault Zone.

The large uncertainties for radiocarbon dating turbidite deposits in Southern California with ^{14}C makes using turbidites to reconstruct paleoseismicity difficult. Some studies have argued that seismically triggered turbidites can be distinguished by synchronous turbidites emplaced over a wide area (Goldfinger, 2011; Sumner et al., 2013). Many of these studies, such as Goldfinger et al. (2007), aim to use seismoturbidites to constrain earthquake recurrence intervals on the order of 100's of years; nevertheless, constraining turbidite ages to 100's of years has much uncertainty along the Southern California margin. Depending on deposit depth, $\Delta^{14}C$ could exhibit wide variability and may be influenced by El Niño Southern Oscillation patterns (Roach et al., 2013). Radiocarbon dating lacks the time resolution to constrain whether a fault ruptured over days or even decades (Nelson et al., 1995; Atwater et al., 2014). In Southern California, uncertainties with radiocarbon ages preclude the required accuracy for events spaced by 100's of years, let alone for a single earthquake event. Sumner et al. (2013) suggested that the most reliable records of seismoturbidites were recovered within a few years of a major earthquake event and could be dated using multiple methods, such as ^{14}C and ^{210}Pb.

A disconnect persists between the ages of the cores, the recovered length of the cores, and the resolution of the Sparker 2D and 3D profiles. Despite advances in coring technology, piston cores and gravity cores are still not able to recover cores long enough to resolve sediment packages older than the Pink Unit or sediment offset by faulting. Without deeper cores, it is difficult to constrain margin evolution on the timescales imaged in the seismic reflection data.

CONCLUSION

This study draws comparisons between small end-member canyons within the ICB. Dana Point Canyon can be considered a shore-proximal canyon with minimal tectonic deformation on the continental slope. As evidenced from dated turbidite deposits, this canyon has remained active during the most recent sea-level lowstand, transgression, and highstand. In contrast, the San Onofre North and South canyons are separated from the coast by a wide ∼10 km shelf that is characterized by extensive deformation. Shelf widening offshore of San Onofre is caused by a left step along the right-lateral Newport Inglewood/Rose Canyon Fault (Maloney et al., 2016; Sahakian et al., 2017). This broad feature inhibits sand supply to the SON and SOS canyons after 8 ka and these canyons are predominantly active during MIS 2. Over lateral distances < 1 km, variability in turbidite emplacement timing can be attributed to ponded basins, small anticlines that promote bypass, and increases in gradient. These basins were likely formed by cross-cutting faults in the San Mateo Fault Zone. Gradient and autogenic processes of turbidity flows may play an important role controlling the grain size of turbidites. Thus, allogenic processes acting on a range of scales muddies interpretations of the turbidite record as paleoseismic indicators.

DATA AVAILABILITY STATEMENT

Multi-channel seismic data are published by Driscoll et al. (2013) and are available online at doi: 10.1594/IEDA/500041. The datasets generated for this study are available on request to the corresponding author.

AUTHOR CONTRIBUTIONS

EW wrote the manuscript, made figures, and analyzed data. JH processed 2D and 3D seismic data and generated seismic profiles for figures. JH also was co-chief scientist on the cruise that acquired sediment cores and contributed scientific insight into the manuscript. ND was the PI on the seismic and coring cruises and provided guidance for the figures and manuscript.

FUNDING

This project was funded by the California Public Utilities Commission through Southern California Edison. Funding for six radiocarbon ages was provided by the Scripps Institution of Oceanography Department Graduate Student Excellence Research Award.

ACKNOWLEDGMENTS

Many thanks to the crew of the R/V Thompson and core technicians at Oregon State University for assisting with the collection of these cores, the crew of the R/V New Horizon and R/V Melville for assisting with the acquisition of seismic profiles and swath bathymetry, Geotrace Technologies and NCS Subsea Inc., for processing seismic data, and Alex Hangsterfer at Scripps for aiding with core curation. Leanne Hirsch, Mackenzie Roberts, and Lana Graves processed the cores and sampled benthic and planktonic foraminifera for radiocarbon age dating. The two reviewers provided helpful insight that improved this manuscript.

SUPPLEMENTARY MATERIAL

The Supplementary Material for this article can be found online at: https://www.frontiersin.org/articles/10.3389/feart.2020.00051/full#supplementary-material

FIGURE S1 | Age-depth models of all cores. Plotted are the median age, the 95% confidence interval, and the probability density function of the calibrated age. Sand layers are shown in horizontal gray bars.

FIGURE S2 | Sparker seismic dip profiles offshore of San Onofre. Profiles are organized with the northernmost profile at the top and southernmost profile at the bottom. Locations of lines are shown in **Figure 1**. For interpreted seismic profiles, see **Figure 5**.

FIGURE S3 | Strike slices along the San Onofre margin. The shallowest slice is at the top and the deepest slice is at the bottom. Locations of lines are shown in **Figure 1**. For interpreted seismic profiles, see **Figure 6**.

REFERENCES

Allen, P. A. (2008). Time scales of tectonic landscapes and their sediment routing systems. *Geol. Soc. Lond. Spec. Publ.* 296, 7–28. doi: 10.1144/sp296.2

Atwater, B. F., Carson, B., Griggs, G. B., Johnson, H. P., and Salmi, M. S. (2014). Rethinking turbidite paleoseismology along the Cascadia subduction zone. *Geology* 42, 827–830. doi: 10.1130/g35902.1

Atwater, T., and Stock, J. (1998). Pacific-North America plate tectonics of the Neogene southwestern United States: an update. *Int. Geol. Rev.* 40, 375–402. doi: 10.1080/00206819809465216

Blaauw, M., and Christen, J. A. (2011). Flexible paleoclimate age-depth models using an autoregressive gamma process. *Bayesian Anal.* 6, 457–474. doi: 10.1214/11-ba618

Blum, M., Martin, J., Milliken, K., and Garvin, M. (2013). Paleovalley systems: insights from Quaternary analogs and experiments. *Earth Sci. Rev.* 116, 128–169. doi: 10.1016/j.earscirev.2012.09.003

Bohannon, R. G., and Geist, E. (1998). Upper crustal structure and Neogene tectonic development of the California continental borderland. *Geol. Soc. Am. Bull.* 110, 779–800. doi: 10.1130/0016-7606(1998)110<0779:ucsant>2.3.co;2

Brothers, D. S., Conrad, J. E., Maier, K. L., Paull, C. K., McGann, M., and Caress, D. W. (2015). The Palos Verdes fault offshore southern California: late Pleistocene to present tectonic geomorphology, seascape evolution, and slip rate estimate based on AUV and ROV surveys. *J. Geophys. Res. Solid Earth* 120, 4734–4758. doi: 10.1002/2015jb011938

Christie-Blick, N., and Driscoll, N. W. (1995). Sequence stratigraphy. *Annu. Rev. Earth and Planet. Sci.* 23, 451–478.

Conrad, J. E., Brothers, D. S., Maier, K. L., Ryan, H. F., Dartnell, P., et al. (2018). *Right-Lateral Fault Motion Along the Slope-Basin Transition, Gulf of Santa Catalina, Southern California. From the Mountains to the Abyss: The California Borderland as an Archive of Southern California Geologic Evolution, Special Publication*, Vol. 110. Broken Arrow, OK: Society for Sedimentary Geology, California, 110–117.

Covault, J. A., and Graham, S. A. (2010). Submarine fans at all sea-level stands: tectono-morphologic and climatic controls on terrigenous sediment delivery to the deep sea. *Geology* 38, 939–942. doi: 10.1130/g31081.1

Covault, J. A., Kostic, S., Paull, C. K., Ryan, H. F., and Fildani, A. (2014). Submarine channel initiation, filling and maintenance from sea−floor geomorphology and morphodynamic modelling of cyclic steps. *Sedimentology* 61, 1031–1054. doi: 10.1111/sed.12084

Covault, J. A., Kostic, S., Paull, C. K., Sylvester, Z., and Fildani, A. (2017). Cyclic steps and related supercritical bedforms: building blocks of deep-water depositional systems, western North America. *Mar. Geol.* 393, 4–20. doi: 10.1016/j.margeo.2016.12.009

Covault, J. A., Normark, W. R., Romans, B. W., and Graham, S. A. (2007). Highstand fans in the California borderland: the overlooked deep-water depositional systems. *Geology* 35, 783–786.

Covault, J. A., and Romans, B. W. (2009). Growth patterns of deep-sea fans revisited: turbidite-system morphology in confined basins, examples from the California Borderland. *Mar. Geol.* 265, 51–66. doi: 10.1016/j.margeo.2009.06.016

Covault, J. A., Romans, B. W., Fildani, A., McGann, M., and Graham, S. A. (2010). Rapid climatic signal propagation from source to sink in a southern California sediment-routing system. *J. Geol.* 118, 247–259. doi: 10.1086/651539

Covault, J. A., Romans, B. W., Graham, S. A., Fildani, A., and Hilley, G. E. (2011). Terrestrial source to deep-sea sink sediment budgets at high and low sea levels: insights from tectonically active Southern California. *Geology* 39, 619–622. doi: 10.1130/g31801.1

Covault, J. A., Shelef, E., Traer, M., Hubbard, S. M., Romans, B. W., and Fildani, A. (2012). Deep-water channel run-out length: insights from seafloor geomorphology. *J. Sediment. Res.* 82, 21–36. doi: 10.2110/jsr.2012.2

Crouch, J. (1979). Neogene tectonic evolution of the western Transverse Ranges and the California Continental Borderland. *Geol. Soc. Am. Bull.* 90, 338–345.

Crouch, J. K., and Suppe, J. (1993). Late Cenozoic tectonic evolution of the Los Angeles basin and inner California borderland: a model for core complex-like crustal extension. *Geol. Soc. Am. Bull.* 105, 1415–1434. doi: 10.1130/0016-7606(1993)105<1415:lcteot>2.3.co;2

Damuth, J. E. (1977). Late Quaternary sedimentation in the western Equatorial Atlantic. *Geol. Soc. Am. Bull.* 88, 695–710.

Damuth, J. E. (1994). Neogene gravity tectonics and depositional processes on the deep Niger Delta continental margin. *Mar. Petrol. Geol.* 11, 320–346. doi: 10.1016/0264-8172(94)90053-1

Damuth, J. E., and Olson, H. C. (2015). Latest Quaternary sedimentation in the northern Gulf of Mexico intraslope basin province: I. Sediment facies and depositional processes. *Geosphere* 11, 1689–1718. doi: 10.1130/ges01090.1

Dartnell, P., Driscoll, N. W., Brothers, D., Conrad, J. E., Kluesner, J., and Kent, G. M. (2015). *Colored Shaded-Relief Bathymetry, Acoustic Backscatter, and Selected Perspective Views of the Inner Continental Borderland, Southern California*, U.S. Geological Survey Scientific Investigations Map 3324, 3 sheets, Southern California, U.S. Available online at: https://dx.doi.org/10.3133/sim3324 (accessed December 01, 2016).

Driscoll, N., Kent, G., and Bormann, J. (2013). *Processed Multi-Channel Seismic Data (Stacks and Migrations) Offshore California Acquired During the R/V New Horizon Expedition NH1320 (2013) Using a Sparker Source*. Palisades, NY: Academic Seismic Portal at UTIG, Marine Geoscience Data System, doi: 10.1594/IEDA/500041

Ducassou, E., Migeon, S., Mulder, T., Murat, A., Capotondi, L., Bernasconi, S. M., et al. (2009). Evolution of the Nile deep−sea turbidite system during the Late Quaternary: influence of climate change on fan sedimentation. *Sedimentology* 56, 2061–2090. doi: 10.1111/j.1365-3091.2009.01070.x

Ehlig, P. (1977). *Geologic Report on the Area Adjacent to the San Onofre Nuclear Generating Station, Northwestern San Diego County, California. Neotectonics and Coastal Instability: Orange and Northern San Diego Counties, California*. Long Beach, CA: AAPG Pacific Section, 113–132.

Fildani, A. (2017). Submarine canyons: a brief review looking forward. *Geology* 45, 383–384. doi: 10.1130/focus042017.1

Freeman, S. T., Heath, E. G., Guptill, P. D., and Waggoner, J. T. (1992). "Seismic hazard assessment, newport-inglewood fault zone," in *Engineering Geology Practice in Southern California*, Vol. 4, eds B. W. Pipkin and R. J. Proctor (Reston, VA: U.S. Geological Survey), 211–231.

Gamberi, F., Rovere, M., Marani, M. P., and Dykstra, M. (2015). Modern submarine canyon feeder-system and deep-sea fan growth in a tectonically active margin (northern Sicily). *Geosphere* 11, 307–319. doi: 10.1130/ges01030.1

Gamboa, D., and Alves, T. M. (2015). Spatial and dimensional relationships of submarine slope architectural elements: a seismic-scale analysis from the Espírito Santo Basin (SE Brazil). *Mar. Petrol. Geol.* 64, 43–57. doi: 10.1016/j.marpetgeo.2015.02.035

Goldfinger, C. (2011). Submarine paleoseismology based on turbidite records. *Annu. Rev. Mar. Sci.* 3, 35–66. doi: 10.1146/annurev-marine-120709-142852

Goldfinger, C., Morey, A. E., Nelson, C. H., Gutiérrez-Pastor, J., Johnson, J. E., Karabanov, E., et al. (2007). Rupture lengths and temporal history of significant earthquakes on the offshore and north coast segments of the Northern San Andreas fault based on turbidite stratigraphy. *Earth Planet. Sci. Lett.* 254, 9–27. doi: 10.1016/j.epsl.2006.11.017

Goldfinger, C., Nelson, C. H., Johnson, J. E., and Party, S. S. (2003). Holocene earthquake records from the Cascadia subduction zone and northern San

Andreas fault based on precise dating of offshore turbidites. *Annu. Rev. Earth Planet. Sci.* 31, 555–577.

Gràcià, E., Vizcaino, A., Estucia, C., Asiolic, A., Ro-dés, Á, Pallàs, R., et al. (2010). Holocene earth- quake record offshore Portugal (SW Iberia): testing turbidite paleoseismology in a slow-con- vergence margin. *Quat. Sci. Rev.* 29, 1156–1172. doi: 10.1016/j.quascirev.2010.01.010

Inman, D. L., and Brush, B. M. (1973). The coastal challenge. *Science* 181, 20–32.

Kennedy, M. P., and Tan, S. S. (2007). *Geologic Map of the Oceanside 30'x60'Quadrangle, California. Department of Conservation, California Geological Survey*. Reston, VA: U.S. Geological Survey.

Kienast, S. S., and McKay, J. L. (2001). Sea surface temperatures in the subarctic northeast Pacific reflect millennial−scale climate oscillations during the last 16 kyrs. *Geophys. Res. Lett.* 28, 1563–1566. doi: 10.1029/2000gl012543

Klotsko, S., Driscoll, N., Kent, G., and Brothers, D. (2015). Continental shelf morphology and stratigraphy offshore San Onofre, California: the interplay between rates of eustatic change and sediment supply. *Mar. Geol.* 369, 116–126. doi: 10.1016/j.margeo.2015.08.003

Kostic, S. (2011). Modeling of submarine cyclic steps: controls on their formation, migration, and architecture. *Geosphere* 7, 294–304. doi: 10.1130/ges00601.1

Kovanen, D. J., and Easterbrook, D. J. (2002). Paleodeviations of radiocarbon marine reservoir values for the northeast Pacific. *Geology* 30, 243–246.

Le Dantec, N., Hogarth, L. J., Driscoll, N. W., Babcock, J. M., Barnhardt, W. A., and Schwab, W. C. (2010). Tectonic controls on nearshore sediment accumulation and submarine canyon morphology offshore La Jolla, Southern California. *Mar. Geol.* 268, 115–128. doi: 10.1016/j.margeo.2009.10.026

Legg, M. R. (1991). "Developments in understanding the tectonic evolution of the California Continental Borderland," in *Society of Economic Paleontologists and Mineralogists Special Publication*, Vol. 46, ed. R. H. Osbourne (Broken Arrow, OK: Society for Sedimentary Geology), 291–312.

Lonsdale, P. (1991). *Structural Patterns of the Pacific Floor Offshore of Peninsular California, Chapter 7: Part III. Regional Geophysics and Geology, AAPG Memoir 47*. Tulsa, OK: American Association of Petroleum Geologists, 87–125.

Magistrale, H. (1993). Seismicity of the Rose Canyon fault zone near San Diego, California. *Bull. Seismol. Soc. Am.* 83, 1971–1978.

Maier, K. L., Brothers, D. S., Paull, C. K., McGann, M., Caress, D. W., and Conrada, J. E. (2017). Records of continental slope sediment flow morphodynamic responses to gradient and active faulting from integrated AUV and ROV data, offshore Palos Verdes, southern California Borderland. *Mar. Geol.* 393, 47–66. doi: 10.1016/j.margeo.2016.10.001

Maier, K. L., Gales, J., Paull, C. K., Rosenberger, K., Talling, P. J., Simmons, S. M., et al. (2019). Linking direct measurements of turbidity currents to submarine canyon-floor deposits. *Front. Earth Sci.* 7:144. doi: 10.3389/feart.2019.00144

Maloney, J. M., Driscoll, N., Kent, G., Duke, S., Freeman, T., Bormann, J., et al. (2016). Segmentation and step−overs along strike−slip fault systems in the inner California borderlands: implications for fault architecture and basin formation. *Appl. Geol. Calif. Environ. Eng. Geol.* 26, 655–677.

Mayall, M., Jones, E., and Casey, M. (2006). Turbidite channel reservoirs—key elements in facies prediction and effective development. *Mar. Pet. Geol.* 23, 821–841. doi: 10.1016/j.marpetgeo.2006.08.001

Mayall, M., and Stewart, I. (2000). "The architecture of turbidite slope channels," in *Proceedings of the 20th Annual Research Conference, Deep-Water Reservoirs of the World: SEPM, Gulf Coast Section*, (McLean, VA: GeoScienceWorld), 586.

McHargue, T., Pyrcz, M. J., Sullivan, M. D., Clark, J., Fildani, A., Romans, B., et al. (2011). Architecture of turbidite channel systems on the continental slope: patterns and predictions. *Mar. Pet. Geol.* 28, 728–743. doi: 10.1016/j.marpetgeo.2010.07.008

Meade, B. J., and Hager, B. H. (2005). Block models of crustal motion in southern California constrained by GPS measurements. *J. Geophys. Res. Solid Earth* 110, 1–19.

Menard, H. W. Jr. (1955). Deep-sea channels, topography, and sedimentation. *AAPG Bull.* 39, 236–255.

Milliman, J. D., Summerhayes, C. P., and Barretto, H. T. (1975). Quaternary sedimentation on the Amazon continental margin: a model. *Geol. Soc. Am. Bull.* 86, 610–614.

Mitchum, R. Jr., Vail, P., and Thompson, S. III (1977). "Seismic stratigraphy and global changes of sea level: part 2. The depositional sequence as a basic unit for stratigraphic analysis: section 2. Application of seismic reflection configuration to stratigraphic interpretation," in *Seismic Stratigraphy: Applications to Hydrocarbon Exploration. Memoir 26*, ed. C. E. Payton (Tulsa, OK: American Association of Petroleum Geologists), 53–62.

Mitchum, R. M. Jr. (1985). "Seismic stratigraphic expression of submarine fans," in *Seismic Stratigraphy II: American Association of Petroleum Geologists Memoir*, Vol. 39, eds O. R. Berg and D. G. Wolverton (New York, NY: Springer), 117–138.

Mix, A. C., Lund, D. C., Pisias, N. G., Bodén, P., Bornmalm, L., Lyle, M., et al. (1999). "Rapid climate oscillations in the northeast Pacific during the last deglaciation reflect Northern and Southern Hemisphere sources," in *Mechanisms for Global Climate Change at Millennial Time Scales. Geophysical Monograph Series 112*, eds P. Clark, R. S. Webb, and L. D. Keigwin (Washington, DC: American Geophysical Union), 127–148. doi: 10.1029/gm112p0127

Muhs, D. R., Simmons, K. R., Schumann, R. R., Groves, L. T., Mitrovica, J. X., and Laurel, D. (2012). Sea-level history during the last interglacial complex on San Nicolas Island, California: implications for glacial isostatic adjustment processes, paleozoogeography and tectonics. *Quat. Sci. Rev.* 37, 1–25. doi: 10.1016/j.quascirev.2012.01.010

Nakajima, T., and Kanai, Y. (2000). Sedimentary features of seismoturbidites triggered by the 1983 and older historical earthquakes in the eastern margin of the Japan Sea. *Sediment. Geol.* 135, 1–19. doi: 10.1016/s0037-0738(00)00059-2

Nelson, A. R., Atwater, B. F., Bobrowsky, P. T., Bradley, L.-A., Clague, J. J., Carver, G. A., et al. (1995). Radiocarbon evidence for extensive plate-boundary rupture about 300 years ago at the Cascadia subduction zone. *Nature* 378:371. doi: 10.1038/378371a0

Nicholson, C., Sorlien, C. C., Atwater, T., Crowell, J. C., and Luyendyk, B. P. (1994). Microplate capture, rotation of the western Transverse Ranges, and initiation of the San Andreas transform as a low-angle fault system. *Geology* 22, 491–495.

Normark, W. R. (1970). Growth patterns of deep-sea fans. *AAPG Bull.* 54, 2170–2195.

Normark, W. R., Damuth, J. E., and Leg 155 Sedimentology Group. (1997). "Sedimentary facies and associated depositional elements of the Amazon Fan," in *Proceedings of the Ocean Drilling Program, Scientific Results*, Vol. 155, eds R. D. Flood, D. J. W. Piper, A. Klaus, and L. C. Peterson (College Station, TX: Ocean Drilling Program), 611–652.

Normark, W. R., Meyer, A. W., Cremer, M., Droz, L., Pickering, K. T., Stelting, C. E., et al. (1986). "Summary of drilling results for the Mississippi Fan and considerations for application to other turbidite systems," in *Initial Reports of the Deep Sea Drilling Program 96*, eds A. H. Bouma, J. M. Coleman, and A. W. Meyer (Washington DC: U.S. Government Printing Office), 425–436.

Normark, W. R., Piper, D. J., Posamentier, H., Pirmez, C., and Migeon, S. (2002). Variability in form and growth of sediment waves on turbidite channel levees. *Mar. Geol.* 192, 23–58. doi: 10.1016/s0025-3227(02)00548-0

Normark, W. R., Piper, D. J., Romans, B. W., Covault, J. A., Dartnell, P., Sliter, R. W., et al. (2009). *Submarine canyon and fan systems of the California Continental Borderland. Earth Science in the Urban Ocean: The Southern California Continental Borderland: Geological Society of America, Special Paper* 454. McLean, VA: GeoScienceWorld, 141–168.

Paull, C., Ussler, W., Greene, H., Keaten, R., Mitts, P., and Barry, J. (2002). Caught in the act: the 20 December 2001 gravity flow event in Monterey Canyon. *Geo Mar. Lett.* 22, 227–232. doi: 10.1007/s00367-003-0117-2

Pettingill, H. S., and Weimer, P. (2002). Worlwide deepwater exploration and production: past, present, and future. *Lead. Edge* 21, 371–376. doi: 10.1190/1.1471600

Piper, D. J., Kontopoulos, N., Anagnostou, C., Chronis, G., and Panagos, A. (1990). Modern fan deltas in the western Gulf of Corinth, Greece. *Geo Mar. Lett.* 10, 5–12. doi: 10.1007/bf02431016

Posamentier, H., Erskine, R., and Mitchum, R. (1991). "Models for submarine-fan deposition within a sequence-stratigraphic framework," in *Seismic Facies and Sedimentary Processes of Submarine Fans and Turbidite Systems*, eds P. Weimer and M. H. Link (New York, NY: Springer), 127–136. doi: 10.1007/978-1-4684-8276-8_6

Prather, B. (2000). Calibration and visualization of depositional process models for above-grade slopes: a case study from the Gulf of Mexico. *Mar. Pet. Geol.* 17, 619–638. doi: 10.1016/s0264-8172(00)00015-5

Prather, B. E., Booth, J. R., Steffens, G. S., and Craig, P. A. (1998). Classification, lithologic calibration and stratigraphic succession of seismic facies from intraslope basins, deep water Gulf of Mexico, USA. *AAPG Bull.* 82, 701–728.

Prins, M. A., and Postma, G. (2000). Effects of climate, sea level, and tectonics unraveled for last deglaciation turbidite records of the Arabian Sea. *Geology* 28, 375–378. doi: 10.1130/0091-7613(2000)028<0375:eocsla>2.3.co;2

Qin, Y., Alves, T. M., Constantine, J., and Gamboa, D. (2016). Quantitative seismic geomorphology of a submarine channel system in SE Brazil (Espírito Santo Basin): scale comparison with other submarine channel systems. *Mar. Petrol. Geol.* 78, 455–473. doi: 10.1016/j.marpetgeo.2016.09.024

Qin, Y., Alves, T. M., Constantine, J. A., Gamboa, D., and Wu, S. (2019). Effect of channel tributaries on the evolution of submarine channel confluences (Espírito Santo Basin, SE Brazil). *Bulletin* 132, 263–272. doi: 10.1130/b35082.1

Roach, L. D., Charles, C. D., Field, D. B., and Guilderson, T. P. (2013). Foraminiferal radiocarbon record of northeast Pacific decadal subsurface variability. *J. Geophys. Res. Oceans* 118, 4317–4333. doi: 10.1002/jgrc.20274

Romans, B. W., Castelltort, S., Covault, J. A., Fildani, A., and Walsh, J. (2016). Environmental signal propagation in sedimentary systems across timescales. *Earth Sci. Rev.* 153, 7–29. doi: 10.1016/j.earscirev.2015.07.012

Ryan, H. F., Conrad, J. E., Paull, C., and McGann, M. (2012). Slip rate on the San Diego trough fault zone, inner California Borderland, and the 1986 Oceanside earthquake swarm revisited. *Bull. Seismol. Soc. Am.* 102, 2300–2312. doi: 10.1785/0120110317

Ryan, H. F., Legg, M. R., Conrad, J. E., Sliter, R. W., Lee, H., et al. (2009). *Recent Faulting in the Gulf of Santa Catalina: San Diego to Dana Point. Earth Science in the Urban Ocean: The Southern California Continental Borderland: Geological Society of America Special Paper* 454. McLean, VA: GeoScienceWorld, 291–315.

Sahakian, V., Bormann, J., Driscoll, N., Harding, A., Kent, G., and Wesnousky, S. (2017). Seismic constraints on the architecture of the Newport−Inglewood/Rose Canyon fault: Implications for the length and magnitude of future earthquake ruptures. *J. Geophys. Res. Solid Earth* 122, 2085–2105.

Southon, J. R., Nelson, D. E., and Vogel, J. S. (1990). A record of past ocean−atmosphere radiocarbon differences from the northeast Pacific. *Paleoceanography* 5, 197–206. doi: 10.1029/pa005i002p00197

Stow, D. A., and Mayall, M. (2000). Deep-water sedimentary systems: new models for the 21st century. *Mar. Pet. Geol.* 17, 125–135. doi: 10.1016/s0264-8172(99)00064-1

Stow, D. A. V., and Piper, D. J. W. (1984). Deep-water fine-grained sediments; history, methodology and terminology. *Geol. Soc. Spec. Publ.* 15, 611–646.

Stuiver, M., and Pollach, H. (1977). On the reporting of 14C ages. *Radiocarbon* 19, 355–359.

Stuiver, M., and Reimer, P. J. (1993). Extended 14 C data base and revised CALIB 3.0 14 C age calibration program. *Radiocarbon* 35, 215–230. doi: 10.1017/s0033822200013904

Sumner, E. J., Siti, M. I., McNeill, L. C., Talling, P. J., Henstock, T. J., Wynn, R. B., et al. (2013). Can turbidites be used to reconstruct a paleoearthquake record for the central Sumatran margin? *Geology* 41, 763–766. doi: 10.1130/g34298.1

Sweet, M. L., and Blum, M. D. (2016). Connections between fluvial to shallow marine environments and submarine canyons: implications for sediment transfer to deep water. *J. Sediment. Res.* 86, 1147–1162. doi: 10.2110/jsr.2016.64

Symons, W. O., Sumner, E. J., Paull, C. K., Cartigny, M. J., Xu, J., Maier, K. L., et al. (2017). A new model for turbidity current behavior based on integration of flow monitoring and precision coring in a submarine canyon. *Geology* 45, 367–370. doi: 10.1130/g38764.1

Talling, P. J., Allin, J., Armitage, D. A., Arnott, R. W., Cartigny, M. J., Clare, M. A., et al. (2015). Key future directions for research on turbidity currents and their deposits. *J. Sediment. Res.* 85, 153–169.

Talling, P. J., Masson, D. G., Sumner, E. J., and Malgesini, G. (2012). Subaqueous sediment density flows: Depositional processes and deposit types. *Sedimentology* 59, 1937–2003. doi: 10.1111/j.1365-3091.2012.01353.x

Talling, P. J., Paull, C. K., and Piper, D. J. (2013). How are subaqueous sediment density flows triggered, what is their internal structure and how does it evolve? Direct observations from monitoring of active flows. *Earth Sci. Rev.* 125, 244–287. doi: 10.1016/j.earscirev.2013.07.005

ten Brink, U. S., Zhang, J., Brocher, T. M., Okaya, D. A., Klitgord, K. D., and Fuis, G. S. (2000). Geophysical evidence for the evolution of the California Inner Continental Borderland as a metamorphic core complex. *J. Geophys. Res. Solid Earth* 105, 5835–5857. doi: 10.1029/1999jb900318

Vail, P. R., Mitchum, Jr, and Thompson, S. III (1977). "Seismic stratigraphy and global changes of sea level: Part 3. Relative changes of sea level from Coastal Onlap," in *Seismic Stratigraphy: Applications to Hydrocarbon Exploration: AAPG Memoir 26*, ed. C. E. Payton (Tulsa, OK: American Association of Petroleum Geologists), 63–81.

Walsh, J. P., and Nittrouer, C. A. (2003). Contrasting styles of off-shelf sediment accumulation in New Guinea. *Mar. Geol.* 196, 105–125. doi: 10.1016/S0025-3227(03)00069-0

Warrick, J. A., and Farnsworth, K. L. (2009). Sources of sediment to the coastal waters of the Southern California Bight. *Geol. Soc. Am. Special Pap.* 454, 39–52.

Xu, J., Swarzenski, P. W., Noble, M., and Li, A.-C. (2010). Event-driven sediment flux in Hueneme and Mugu submarine canyons, southern California. *Mar. Geol.* 269, 74–88. doi: 10.1016/j.margeo.2009.12.007

Conflict of Interest: The authors declare that the research was conducted in the absence of any commercial or financial relationships that could be construed as a potential conflict of interest.

frontiers in Earth Science

ORIGINAL RESEARCH
published: 24 June 2020
doi: 10.3389/feart.2020.00215

Recognizing Allogenic Controls on the Stratigraphic Architecture of Ancient Alluvial Fans in the Western US

Scott R. Meek, Barbara Carrapa and Peter G. DeCelles*

Department of Geosciences, The University of Arizona, Tucson, AZ, United States

Alluvial fans are a significant part of the sediment routing system, forming distinctive steep, fan-shaped deposits of coarse-grained detritus where rivers lose flow velocity after exiting confined mountain drainages. Processes on the fan are influenced by both internal (autogenic) feedback cycles like channel avulsion and by external (allogenic) conditions such as climate and tectonics. These conditions in turn influence the stratigraphic architecture (i.e., the pattern of channel stacking and sizes) within the fan. Studying stratigraphic architecture of alluvial fans can, therefore, provide insight into controls on fan deposition. We employ UAV-based photogrammetric models to analyze the stratigraphic architecture of two well-exposed ancient alluvial fans in the western US – the Eocene Richards Mountain Conglomerate and the Cretaceous Echo Canyon Conglomerate. Both fans were deposited under relatively warm, wet climates and compressional tectonic regimes. We use a seven-fold hierarchy of bounding surfaces and associated lithosomes to describe alluvial fan architecture. First- through fourth-order surfaces and lithosomes represent bedform to channel-scale features influenced primarily by autogenic processes on the fan. Controls on fifth-order surfaces/lithosomes have historically been poorly understood, but probably represent fanhead trench migration and lobe construction. Sixth-order surfaces bound individual alluvial fans and seventh-order surfaces correspond to formation boundaries. These are controlled primarily by tectonics. The fifth-order architectural style of the deposits in our two study areas is significantly different and we use this difference to try to isolate a primary control on fifth-order alluvial architecture. Average width:height ratios of fifth-order lithosomes are nearly twice as high for Echo Canyon (112:1) than for Richards Mountain (64:1). This indicates that active channels on the Echo Canyon fan were more mobile than those on the Richards Mountain fan. We attribute this to a more seasonal climate and less vegetation during the deposition of the Echo Canyon Conglomerate (relative to Richards Mountain). This would have increased lateral migration by destabilizing channels through increased sediment flux and flood events. Our results imply that fifth-order stratigraphic architecture of ancient alluvial fans may provide insight into allogenic processes related to paleoclimate. They also indicate risk of increased geologic hazards on alluvial fans where anthropogenic climate change increases future climate variability.

Keywords: stratigraphic architecture, alluvial fan, allogenic, autogenic, paleoclimate, fan dynamics, Western US

OPEN ACCESS

Edited by:
Miquel Poyatos Moré, University of Oslo, Norway

Reviewed by:
Stuart Clarke, Keele University, United Kingdom
Nicholas Perez, Texas A&M University, United States

****Correspondence:***
Scott R. Meek
scottrmeek@gmail.com

Specialty section:
This article was submitted to Sedimentology, Stratigraphy and Diagenesis, a section of the journal Frontiers in Earth Science

Received: *16 August 2019*
Accepted: *22 May 2020*
Published: *24 June 2020*

Citation:
Meek SR, Carrapa B and DeCelles PG (2020) Recognizing Allogenic Controls on the Stratigraphic Architecture of Ancient Alluvial Fans in the Western US. Front. Earth Sci. 8:215. doi: 10.3389/feart.2020.00215

INTRODUCTION

Stratigraphic Architecture of Alluvial Fans

Alluvial fans are a significant part of the sediment routing system in areas of high relief. They form as rivers lose flow velocity after exiting confined mountain drainages (Bull, 1964). This promotes deposition of coarse-grained sediments which form a characteristic fan shape as the location of active deposition migrates back and forth over time (Bull, 1977; Leeder et al., 1998; Harvey et al., 2005; Blair and McPherson, 2009). Because alluvial fans necessarily occur in tectonically active regions they have the potential to preserve stratigraphic records of local tectonic events as well as climate (e.g., Dade and Verdeyen, 2007). Processes operating on the fan influence the distribution of various facies and the stratigraphic architecture (i.e., the pattern of channel stacking and sizes) within the fan. Studying stratigraphic architecture can therefore help reveal the tectonic and climatic conditions under which a fan was deposited and a wealth of studies exist which attempt to do just this (e.g., Gunster and Skowronek, 2001; Bettis, 2003; Harvey et al., 2003, 2005; Klinger et al., 2003). In practice, it is difficult to obtain detailed information on high-frequency climate and tectonic events from fan sedimentology due to difficulties with high-resolution dating of alluvial fan deposits, high temporal variability in fan sedimentation rates and lack of control in field-based studies (Dorn, 2009). However, general predictions of tectonic and climatic conditions over larger time scales of thousands to millions of years from stratigraphic architecture (as we attempt in this study) are more feasible.

Alluvial fan architecture may be controlled by different processes (Crews, 1985; DeCelles et al., 1991; Heller and Paola, 1996; Whipple et al., 1998; Allen et al., 2013) including allogenic processes such as tectonics (e.g., gross basin geometry, rates of subsidence, control of sediment supply via uplift and erosion of source terrain), climate (e.g., discharge controlled by precipitation levels, arid vs. humid settings, vegetation cover), or base level changes (which may be related to changes in climate or tectonic activity). Autogenic processes can also act as an important control on alluvial architecture (e.g., Bull, 1991; Parker et al., 1998; Clarke et al., 2010; Hofmann et al., 2011; Hajek et al., 2012; Miller et al., 2014; Ventra and Clarke, 2018; Bowman, 2019). Common autogenic processes on alluvial fans include failure of oversteepened slopes (resulting in debris flows), channel avulsion and lobe switching in response to sediment accumulation, incision and backfilling of fanhead trenches, sheet flow, and migration of channels, bars, and bedforms.

Stratigraphic architecture has been extensively studied in fluvial systems (e.g., Miall, 1985; Heller and Paola, 1996; Nichols and Fisher, 2007; Straub et al., 2009) but has been historically understudied in alluvial fans. Previous work has concluded that small-scale architecture (channel-scale and smaller) is controlled largely by autogenic processes, whereas large-scale architecture (fan-scale and above) is predominantly a result of long-term tectonic activity (DeCelles et al., 1991). Our study seeks to improve understanding of which processes are most important in controlling the style of intermediate-scale (channel complex) alluvial fan architecture by examining the intermediate-scale architecture of two ancient alluvial fan deposits in the western US that were deposited under similar tectonic and climatic settings. We use the architectural hierarchy established by DeCelles et al. (1991) as a starting point for this comparative study. DeCelles et al. (1991) created a seven-fold hierarchy of lithosomes (genetically related bodies of rock) to describe the internal organization of the Beartooth Conglomerate (**Table 1** and **Figure 1**). The Beartooth Conglomerate is an informally named unit of upper Paleocene conglomerates exposed along the eastern flank of the Beartooth Range on the Montana/Wyoming border (**Figure 2**). The tectonic and climatic conditions (e.g., a compressional tectonic setting and relatively warm, humid climate) under which the Beartooth Conglomerate was deposited were similar to the conditions under which the Echo Canyon and Richards Mountain Conglomerates were deposited (DeCelles et al., 1991; **Table 2**).

The real importance of better understanding alluvial architecture is the potential to link depositional conditions to fan dynamics. Alluvial fans are complex systems that have historically been poorly understood (e.g., Bull, 1977; Lecce, 1990) and alluvial architecture can be a powerful tool for interpreting the rock record and the path sediment follows from source to sink (Armitage et al., 2011; Michael et al., 2014; Romans et al., 2016; D'Arcy et al., 2017). Alluvial deposits commonly form important aquifers (Neton et al., 1994; Zhu et al., 2017) and occasionally serve as hydrocarbon reservoirs (Shepherd, 2009) where their internal structure could affect fluid flow paths. They also commonly occur in highly developed areas, and because they are associated with mountainous terrain and debris flows (Larsen et al., 2001), understanding how they function is important for geologic hazard mitigation. This study is particularly relevant in addressing the question of how processes operating on alluvial fans will change in response to climatic variation, considering the rapid climate change occurring at present across the globe.

Study Areas

Two field sites were examined for this study: Echo Canyon, UT and Richards Mountain, WY (**Figures 2**, **3**). Both locations have well-exposed ancient alluvial fan deposits, known as the Echo Canyon Conglomerate and Richards Mountain Conglomerate, respectively (**Figure 3**). These fans were deposited under similar tectonic and climatic settings (e.g., Crawford, 1979; Crews and Ethridge, 1993; DeCelles, 1994) which are summarized in **Table 2** (along with the depositional conditions for the Beartooth Conglomerate). In theory, we would expect this to result in similar architectural styles. Differences in architectural style would indicate that at least one of a number of controlling factors differed between the two sites. We compare the two study areas by quantitatively describing the alluvial architecture (specifically, the width:height ratios of fifth-order lithosomes, which represent channel complexes) at both sites.

Eocene Richards Mountain Conglomerate (Wyoming)

The Richards Mountain Conglomerate is a widely used informal name for a coarse-grained alluvial fan deposited between ca. 56

TABLE 1 | Summary of the hierarchy of lithosomes and bounding surfaces in alluvial fans.

Lithosome order	Bounding surfaces	Bounding surface and lithosome characteristics	Interpreted processes
1	1	Erosional, trough cross-set boundaries	Migration of subaqueous dunes
		Erosional or accretionary	Hyperconcentrated flows and debris flows
2	2	Erosional surfaces	Minor erosion during changing flow-stage
3	3	Large-scale planar cross-strata	Migration of macroforms in trenches and shallow braided channels
4	4e	Erosional bases of large lenticular lithosomes; commonly stepped and terraced; enclose complex packages of channel facies up to several meters thick and tens to hundreds of meters wide	Erosion and migration of shallow (several meters) channels
	4a	Accretionary upper surfaces of packages of channel facies; usually convex upward or nearly flat	Accretion and burial of large macroforms in channels
5	5e	Major erosional surfaces at bases of thick (tens of meters) packages of 4th order lithosomes; commonly erode into paleosol caps on underlying lithosomes	Lateral migration of trenches on inner part of fan
	5a	Flat upper surfaces of thick (tens of meters) packages of 4th order lithosomes; hundreds to thousands of meters wide; commonly capped by paleosols	Backfilling and abandonment of trenches on inner fan
6	6	Boundaries of individual alluvial fans; usually ragged between adjacent fans and/or axial fluvial deposits; often truncated by faults toward source area; enclosed lithosomes are hundreds of meters thick and several kilometers wide	Deposition of individual alluvial fan
7	7	Boundary of entire alluvial fan complex; may be an angular unconformity or a conformable transition to basinal fluvial or lacustrine facies	Deposition and lateral coalescence of multiple fans

After DeCelles et al., 1991. Modified for general use in describing variable alluvial fan deposits. Bounding surfaces followed by an "e" are erosional in nature, while those followed by an "a" are accretionary.

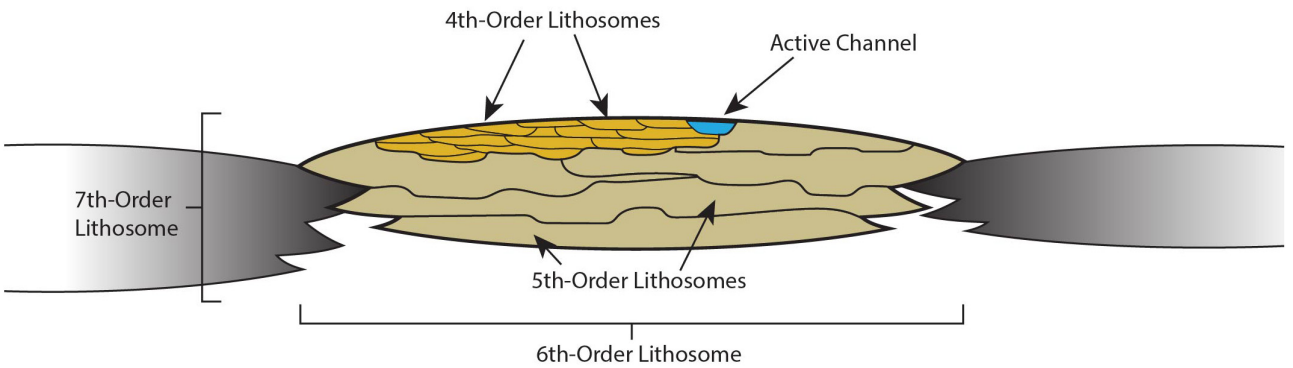

FIGURE 1 | Simplified representation of the lithosomal hierarchy described in DeCelles et al. (1991). First- through third-order lithosomes and bounding surfaces represent bedforms, scour surfaces, and large-scale cross-strata (generally at sub-meter scale) and combine to form channel-filling fourth-order lithosomes (up to several meters thick and tens to hundreds of meters wide). As channels migrate across the fan, they leave fifth-order lithosomes composed of amalgamated fourth order lithosomes (tens of meters thick and hundreds to thousands of meters wide). Sixth- and seventh-order lithosomes correspond to individual alluvial fans and laterally amalgamated fans respectively (several hundred meters thick and several thousand meters wide). See **Table 2** for details of the lithosomal hierarchy.

and 53 Ma within the Eocene Wasatch Formation (Culbertson, 1969; Crews, 1985; Crews and Ethridge, 1993). The Richards Mountain Conglomerate holds up an approximately 13 km hogback that forms Richards Mountain in southern Wyoming (**Figures 2**, **3**). The southern face of the mountain exposes a strike-parallel cross-section through a single alluvial fan shed into a foreland basin on the northern flank of the Laramide Uinta Arch (from which the fan sediments were sourced). Average paleoflow direction was to the north (Crews, 1985). The Richards Mountain fan conformably overlies fluvial rocks of the main body of the Wasatch Formation. The top of the conglomerate is a fan-delta and grades upward into lacustrine facies of the Wasatch and Green River formations. Basinward (north) the fan rapidly fines and interfingers with lacustrine and fluvial facies of the main body of the Wasatch Formation (Crews, 1985; Crews and Ethridge, 1993). The fan itself is notable for its abundant paleosols and pervasive pedogenic alteration (**Figures 4**, **5**), as well as a distinct lack of the debris-flow facies (Crews and Ethridge, 1993) common to alluvial fans (Shultz, 1984; Larsen et al., 2001; Blair and McPherson, 2009). Climate at the time of deposition (shortly after the PETM) was warm and humid (Brooks, 1949; Frakes, 1979; Wolfe, 1980; Thrasher and Sloan, 2009). Evidence

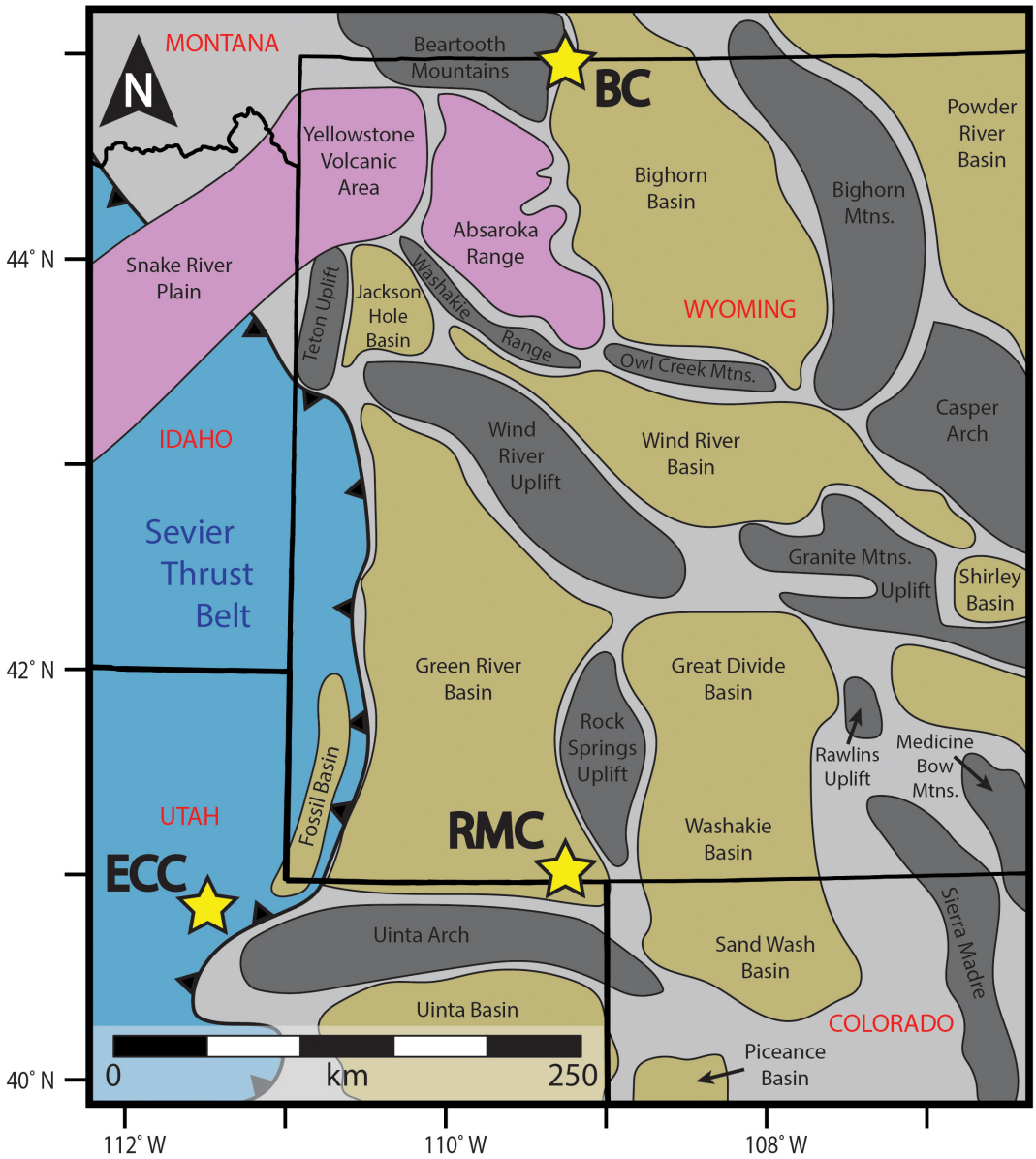

FIGURE 2 | Surface locations of major structural features in the region surrounding the study areas. Locations of the Echo Canyon Conglomerate (ECC), Richards Mountain Conglomerate (RMC), and Beartooth Conglomerate (BC) are marked by stars. The Echo Canyon Conglomerate was shed from the Sevier Thrust Belt while the Richards Mountain Conglomerate and Beartooth Conglomerates were sourced from the Uinta and Beartooth Ranges respectively (both Laramide structures). Modified from Lamerson (1982), Roehler (1992), Smith et al. (2008), and Törö et al. (2015).

for a humid climate (**Table 2**) comes from the abundant paleosol development and the stream-flow dominated nature of the fan as well as from fossil plants characteristic of a warm, rainy forest or jungle (Crews and Ethridge, 1993).

Cretaceous Echo Canyon Conglomerate (Utah)

The Echo Canyon Conglomerate has been palynologically dated as Coniacian-Santonian in age (Jacobson and Nichols, 1982) and was deposited between ca. 87 and 85 Ma (Jacobson and Nichols, 1982; DeCelles, 1994; Painter et al., 2014). The unit crops out along Interstate Highway 80 over about 11 km of Echo Canyon in northeastern Utah (**Figures 2**, **3**), where it is spectacularly exposed (particularly on the northwest side of the canyon). The outcrop cuts obliquely through the fan relative to paleoflow direction, which was predominantly eastward (DeCelles, 1994). It was deposited by multiple, coalesced alluvial fans in the proximal foreland basin or wedgetop of the Utah-Idaho-Wyoming salient of the Sevier Thrust Belt and sourced mainly from the Willard Thrust Sheet (DeCelles, 1988). The Echo Canyon Conglomerate conformably overlays fluvial to shallow marine deposits of the Henefer Formation (interpreted as a progradational fan-delta-front sequences) and is overlain by an

TABLE 2 | Summary of study areas.

	Beartooth Conglomerate	Richards Mountain Conglomerate	Echo Canyon Conglomerate
Age	Late Paleocene	Early Eocene	Late Cretaceous
Climate	Warm	Warm/humid	Warm/arid-subhumid
Tectonic Setting	Compressional (Laramide/thick-skinned style)	Compressional (Laramide/thick-skinned style)	Compressional (Sevier/thin-skinned style)
Fan locations represented in outcrop	Proximal to distal	Proximal	Proximal to medial
Facies	Debris-flow/ steam flow	Stream-flow	Debris-flow/ stream-flow

Beartooth Conglomerate information from DeCelles et al. (1991). Richards Mountain Conglomerate information from Crews (1985) and Crews and Ethridge (1993). Echo Canyon Conglomerate information from Crawford (1979); Jacobson and Nichols (1982), and DeCelles (1994).

angular unconformity with alluvial deposits of the Evanston Formation (DeCelles, 1994; **Figure 6**). Lateral facies changes in the Echo Canyon Conglomerate are largely unknown, as the margins of the fan have been lost to synorogenic erosion. The Echo Canyon Conglomerate has been interpreted to have been deposited during warm, subhumid-humid climate typical of western North America during the Late Cretaceous Epoch (Crawford, 1979; Crawford and Dott, 1979; Franczyk et al., 1992; Burgener et al., 2019). This is further supported by abundant plant fossils, paleosol development, and mudstones that may have been deposited in standing bodies of water (Crawford, 1979). It is important to note however, that, unlike the Richards Mountain Conglomerate, debris-flow facies are present at Echo Canyon (Crawford, 1979; DeCelles, 1994), although they are a relatively minor component of the section (**Figures 4**, **5**).

MATERIALS AND METHODS

Data on alluvial architecture was obtained from digital outcrop models generated using photogrammetry. These models are available in the data repository. Photogrammetric modeling is a process by which photos of an object taken from multiple vantage points can be combined into a spatially accurate three-dimensional model of that object. Though a relatively new technique, the use of digital outcrop models built using photogrammetric techniques has been well established as an effective tool for the geosciences (e.g., Fabuel-Perez et al., 2010;

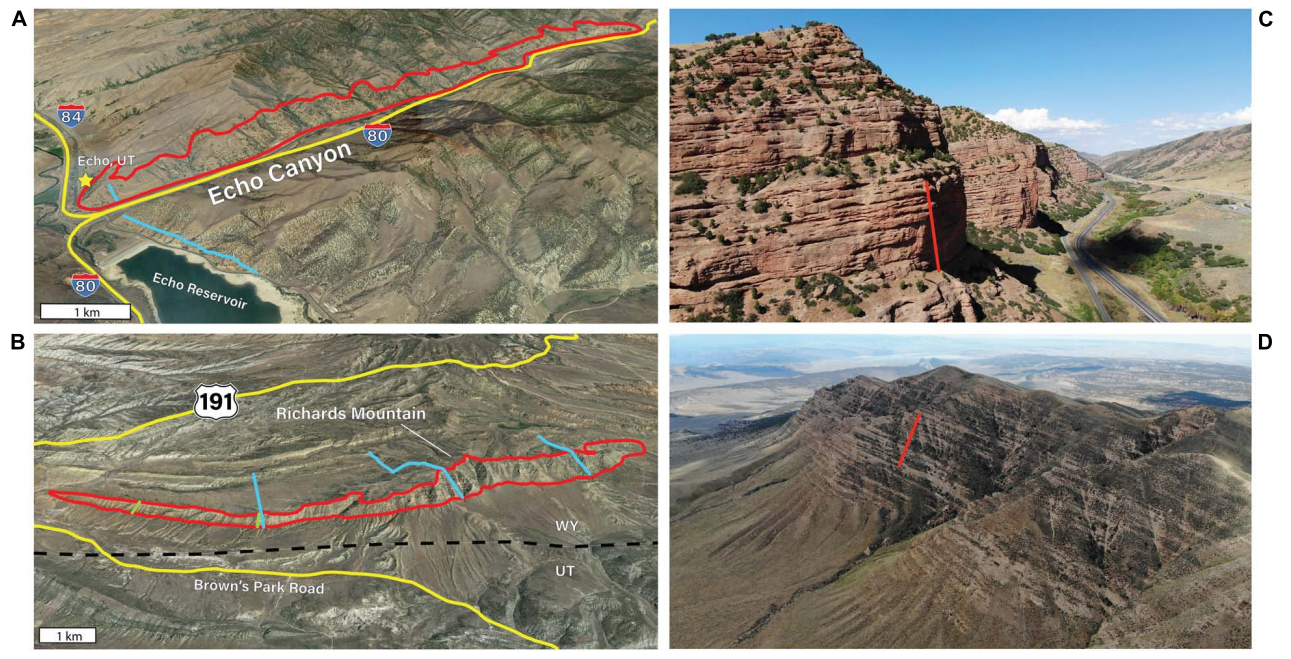

FIGURE 3 | Overview of study areas. For **(A)** and **(B)**, areas outlined in red indicate approximate extent of digital outcrop models. Blue lines indicate locations of sedimentary logs from previous workers. Green lines indicate locations of sedimentary logs measured by the authors. Roads are shown in yellow. Satellite imagery modified from Google Earth (2019). **(A)** Oblique view (looking north) of Echo Canyon study area. Outcrops are exposed along the north side of Echo Canyon, immediately northeast of the town of Echo, UT. Area outlined in red is approximately 11 km long. Sedimentary log from DeCelles (1994). **(B)** Oblique view (looking north) of the Richards Mountain study area. Richards Mountain is located in southwestern Wyoming, just north of the UT-WY border and east of the intersection of US 191 and Brown's Park Road. Sedimentary logs in blue are from Crews (1985). Logs in green measured by S. Meek. Area outlined in red is approximately 13 km long. **(C)** The Echo Canyon Conglomerate crops out in sheer red cliffs over the first 11 km of Echo Canyon in northeastern Utah. View is to the northeast. Red line is approximately 60 m long. Red cliffs are predominantly clast-supported massive conglomerate with interbedded sandstone. Slope covered sections generally correspond to paleosols and/or mudstones. **(D)** The Richards Mountain Conglomerate is exposed in the 13 km hogback that forms Richards Mountain in southern Wyoming, just north of the Uinta Mountains. View is to the west. Red line is approximately 200 m long. Light colored bands are thick conglomerate beds. Vegetation-covered areas largely correspond with paleosols.

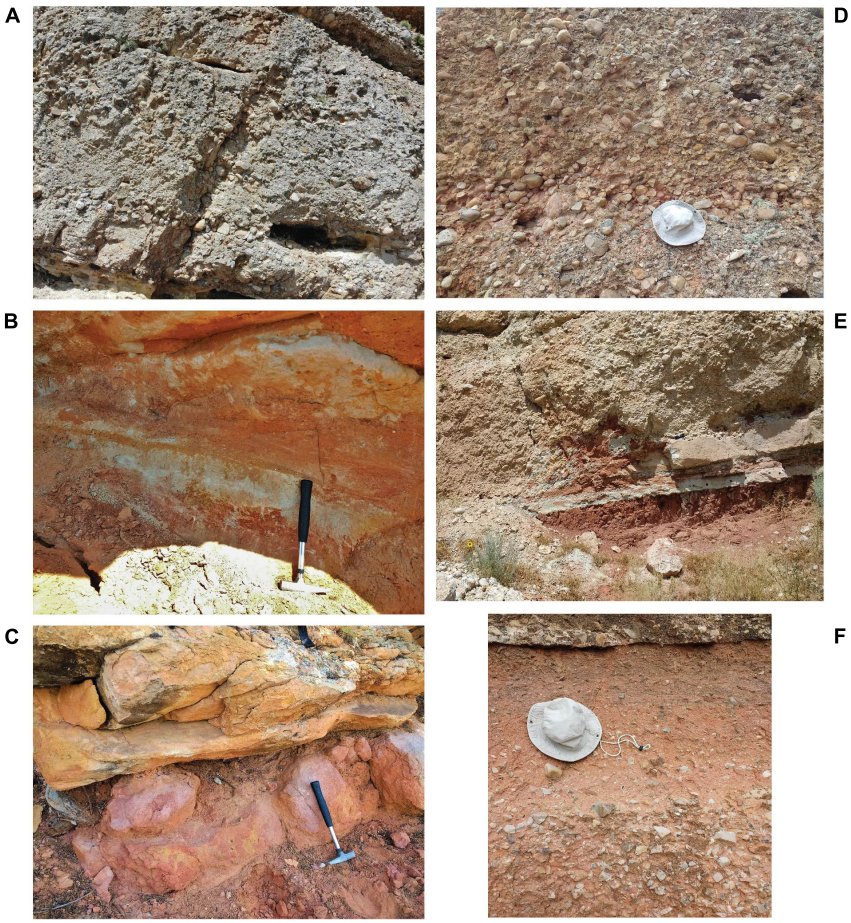

FIGURE 4 | Key facies found in the Richards Mountain Conglomerate **(A–C)** and Echo Canyon Conglomerate **(D–F)**. **(A)** Clast-supported structureless to poorly stratified cobble and boulder conglomerates. Interpreted as channel deposits on a streamflow-dominated alluvial fan. **(B)** Fine-grained sandstone with mottled red and yellow colors and ripple/trough-cross-stratification or structureless texture. Rhizoliths are abundant (light-colored, linear features near handle of hammer). Interpreted as sandy channel deposits that have undergone early pedogenesis. **(C)** Fine-grained, structureless mudstones (lower pink bed) with abundant rhizoliths and red and yellow mottling. Interpreted as mature paleosols which frequently cap the conglomerate and sandstone channel complexes that make up the bulk of fifth-order lithosomes. **(D)** Clast-supported, structureless cobble conglomerates. Interpreted as channel deposits probably emplaced in high-intensity, short-duration flows or possibly as debris flows. **(E)** Largely, structureless red mudstones with rhizoliths and some mottling of color at bottom of image. Interpreted as paleosols formed on inactive fan segments; frequently scoured away by overlying channel conglomerates (as also seen in this image). **(F)** Clast-supported, angular pebble to cobble conglomerate grading upward into matrix-supported angular pebble conglomerate. Interpreted as deposits from debris-flows or highly concentrated flows due to matrix-support and highly angular clasts.

Bemis et al., 2014; García-Sellés et al., 2014; Smith et al., 2015; Carrivick et al., 2016). Key outcrops were photographed using a GPS-enabled quadcopter drone (DJI Mavic Air) which enables quick, cost-effective data collection over large areas, including inaccessible cliff faces. Photos were taken from distances of around 100–300 m from the outcrop. With a 12-megapixel camera on the drone this gives pixel sizes (and thus model resolution) of <10 cm. Images of each portion of the outcrop were taken from multiple angles and with significant overlap in order to provide the modeling software with sufficient data to match key points in the imagery and stitch together a model with full outcrop coverage. This required roughly 1,000–2,000 images at each study site. Digital outcrop models were built using the standard workflow in the Agisoft Metashape software package. Models were built in several individual sections, referred to in the Metashape software as "chunks." While not required, building the model in these pieces is helpful when working with a large number of images, as each chunk uses only around 50–300 images. This allows for faster processing and avoids some issues with correlating images that were, for example, taken on different days under slightly different lighting conditions. The chunks can later be merged to produce a complete model of the outcrop. Building the model involves first uploading images to the individual chunks, then cropping images to remove unwanted portions (like the sky or distant mountains). 40,000 key points are then automatically identified on each image. 4,000 of these are used on each image to align it with overlapping images. Once tie points are in place, they are used to create a sparse point cloud which can be manually or automatically edited to remove misplaced points. A dense point cloud can then be generated at

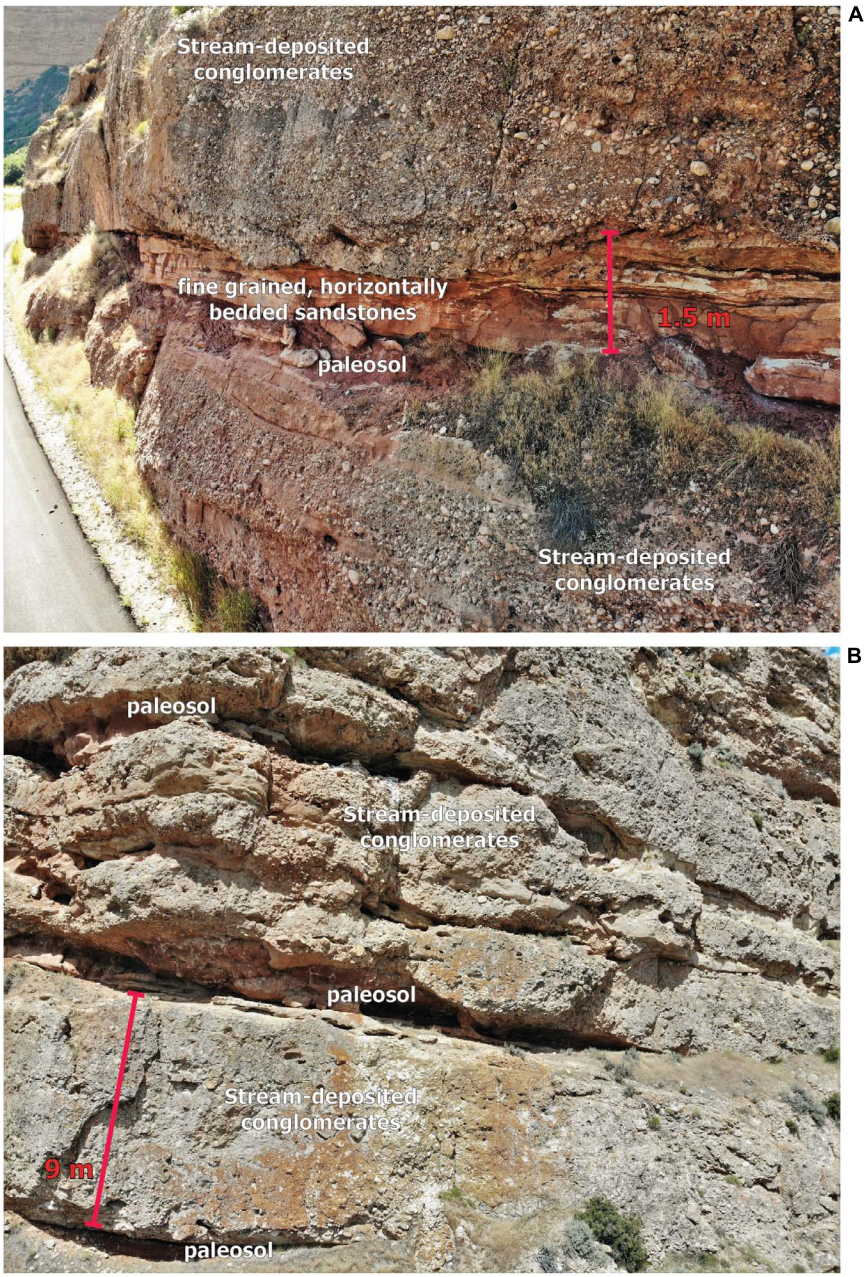

FIGURE 5 | Representative outcrops showing common facies associations in study areas. Coarse-grained conglomeratic units representing channel deposits are usually capped by paleosol horizons, which are in turn scoured into by overlying conglomerates. **(A)** The Echo Canyon Conglomerate. Shown in this image are clast-supported, cobble conglomerates above and below a relatively fine-grained interval containing paleosols and thin-bedded sandstones. While these conglomerates are interpreted as having been deposited by streamflow due to imbrication and trough-cross-stratification, structureless clast-supported conglomerates are quite common in the Echo Canyon Conglomerate and are interpreted as debris-flow deposits. Clast- to matrix- supported very angular conglomerates are rare (but present) and are also interpreted as deposits from debris-flows or highly concentrated flows. **(B)** The Richards Mountain Conglomerate. Common facies shown here are clast-supported, cobble to boulder conglomerates (interpreted as streamflow deposits) and fine-grained paleosol intervals. Notice the mottled, reddish coloration of paleosol intervals. Rhizoliths are visible in the central paleosol as light-colored lines in the red unit.

the desired resolution. High quality point clouds are generally better for detailed interpretation; however, lower quality point clouds are easier to manipulate for large areas. We created both low- and high-resolution point clouds for these purposes. Our high-resolution models contain around 70 million points per thousand images used. The final steps in model creation involve automatically generating a triangular mesh based on the dense point cloud and overlaying imagery onto this mesh as a "textured surface." Again, both of these steps can be performed at either high- or low-resolution.

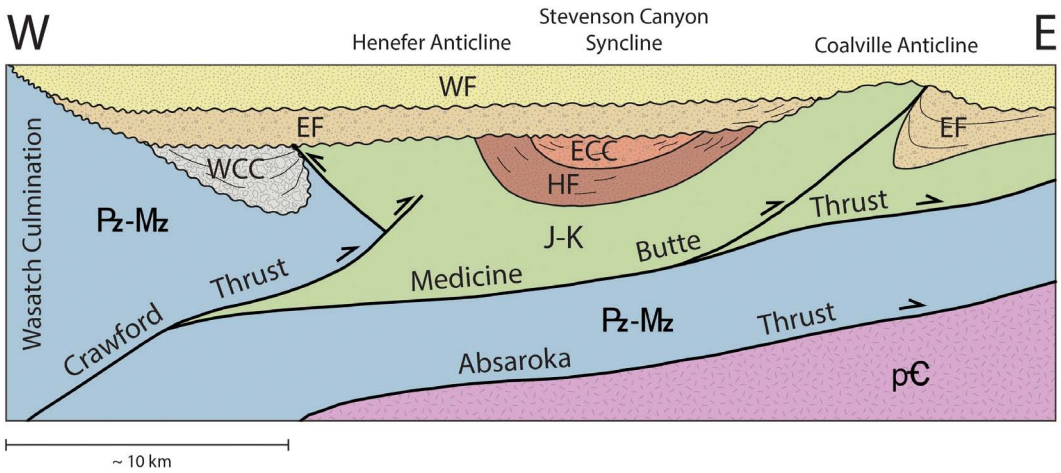

FIGURE 6 | Schematic cross-section showing key structural elements and stratigraphic relationships of the synorogenic sediments near the Echo Canyon study area. There is no vertical exaggeration; however, relative formation thicknesses are only roughly to scale. The Echo Canyon Conglomerate (ECC) is confined to the Stevenson Canyon Syncline where conformably overlies the fluvial Henefer Formation (HF). The ECC is truncated above by an angular unconformity with conglomerates of the Evanston Formation (EF). Also represented here are conglomerates of the Wasatch Formation (WF) and the Weber Canyon Conglomerate (WCC), the Paleozoic to Mesozoic (|-}) rocks of the Crawford and Absaroka thrust sheets, the Jurassic to Cretaceous (J-K) rocks of the Medicine Butte Thrust sheet, and the underlying Precambrian crystalline basement rocks (=). Modified from DeCelles (1994).

The final result of this process is a 3D, georeferenced digital model of the outcrop. These digital outcrop models provide high-resolution (features <10 cm are clearly visible) 2D and 3D outcrop data that would be difficult to accurately represent using sedimentary logs alone (models are available in the data repository). This level of coverage allows comprehensive analysis of alluvial architecture over the 10 + km exposures in this study, rather than just isolated outcrops. It should be noted that while exposure is excellent perpendicular to depositional dip in both study areas, there is essentially no downdip exposure of the Richards Mountain Conglomerate, and only limited downdip exposure of the Echo Canyon Conglomerate. We will therefore focus on architectural patterns and lithesome measurements only in a strike-parallel direction. Lithosome dimensions (summary in **Table 3**) were measured directly from the photogrammetric models by using the measure tool in Metashape. These measurements have sub-meter accuracy. Alluvial architecture of the study areas was described by qualitatively describing stacking patterns and quantifying dimensions (width and height, i.e., thickness) of lithosomes. We emphasize width:height ratios of fifth-order lithosomes as the forcing mechanisms behind these intermediate-scale architectural elements are poorly understood. Not all fifth-order lithosomes were measured due to poor exposure and/or incompleteness due to erosion of outcrops. Attempts were made, however, to measure as many of the most complete lithosomes as possible and to draw these measurements from all exposed portions of the fans in order to have a truly representative sample. A total of 41 fifth-order lithosomes were measured – 18 in Echo Canyon and 23 at Richards Mountain (all measurements available in **Supplementary Table S1**).

Interpretations of the digital outcrop models were informed by detailed sedimentary logs at each field site. Sections measured by the authors (**Figure 7**) were used in combination with sections measured by Crews (1985) and DeCelles (1994). These detailed sections were compared to the photogrammetric models to ensure accurate characterization of the facies within each formation (**Figure 8**), which is critical to correctly interpreting physical processes. Bounding surfaces of fifth-order lithosomes in outcrop are marked by the presence of major erosional surfaces at the base of thick packages of fourth-order lithosomes (**Table 1**). These frequently consist of conglomerates scouring into fine-grained paleosol caps on the underlying fifth-order lithosome (**Figure 9**). On a large scale (e.g., on the photogrammetric models) these surfaces can generally be recognized by the presence of a laterally extensive, thin and recessive boundary between packages of fourth order lithosomes. This recessive boundary corresponds to the paleosol caps on fifth-order lithsomes. These surfaces were identified and interpreted in Metashape (examples in **Figure 10**). Thickness can vary significantly across the fifth-order lithosomes due to scouring, pinching out of lithosomes and/or a lensoidal geometries. Heights for fifth-order lithosomes were therefore measured at the point of maximum thickness in order to provide a minimum estimate for the true maximum thickness of the lithosome (**Table 3** and **Supplementary Table S1**).

It should be noted that the measured widths of fifth-order lithosomes are in all cases minimum estimates. At Richards Mountain this was due largely to outcrop quality – in many cases the edges of the channel complexes were poorly exposed as the conglomeratic and sandy units thinned. In Echo Canyon the reported widths are probably significantly more underestimated; nearly all of the measured lithosomes were truncated on one or both ends by normal faulting (which makes it difficult to correlate the strata within about 1 km of the canyon mouth) or by the angular unconformity with the overlying Evanston Formation (which has removed an unknown amount of the

TABLE 3 | Fifth-order lithosome dimensions and width:height ratios.

	Echo Canyon Conglomerate (*n* = 18)			Richards Mountain Conglomerate (*n* = 23)		
	Width (m)	**Height/thickness (m)**	**Width:height ratio**	**Width (m)**	**Height/thickness (m)**	**Width:height ratio**
Max	3,786	33	179	5,073	43	181
Min	1,151	14	57	297	13	13
Average	2,505	23	**112**	1,742	26	**64**
Median	2,623	24	104	1,224	27	46
SD	796	6	37	1,534	8	48

Lithosome widths were corrected where necessary for oblique exposure angles. Height was measured at the point of maximum observed thickness. Note that average width:height ratios for fifth-order lithosomes (bolded) in the Echo Canyon Conglomerate are nearly twice those observed in the Richards Mountain Conglomerate.

original depositional width of the channel complexes). Due to oblique exposure angles, apparent lithosome width was often far greater than the actual width; these widths were corrected for oblique exposure where necessary using the method outlined in Fabuel-Perez (2009), with the assumption of an average paleoflow direction to the east for Echo Canyon (DeCelles, 1994) and to the north for Richards Mountain (Crews and Ethridge, 1993). Average paleoflow direction was used in place of specific paleocurrent measurements from individual lithosomes due to the relative inaccessibility of many outcrops and the significant time savings involved. In smaller study areas, study areas where outcrops are readily accessible, and/or where ample time is available, individual paleocurrents would certainly be preferable to increase accuracy of width corrections. These paleocurrents would probably best be collected after identification of lithosomes from digital outcrop models when possible.

RESULTS

First- Through Fourth-Order Lithosomes

Architectural styles of first-order through fourth-order lithosomes (**Table 1**) are predominantly shaped by autogenic sedimentary processes (DeCelles et al., 1991). Detailed measurements of these small-scale lithosomes were not made for this study; however, it is worth noting that observations in the field did not reveal any obvious differences in the average dimensions of these lithosomes between the two study areas. Major differences between the small-scale lithosomes of the two fans were mostly confined to lithology – for example, in the presence of debris-flow facies in Echo Canyon and the extensive pedogenic alteration to much of the Richards Mountain section.

Fifth-Order Lithosomes

Fifth-order lithosomes represent the deposits of channel complexes that migrate across alluvial fans (**Table 1**). The proximal parts of these channel complexes are formed by fanhead trenches, while the distal portions consist of depositional lobes (DeCelles et al., 1991). A total of 41 fifth-order lithosomes were measured; 23 at Richards Mountain and 18 in Echo Canyon (see **Table 3** and **Figure 11**). At Richards Mountain, these ranged from approximately 300–5,000 m in width (averaging 1,742 m) and 13–43 m in height (averaging 26 m). Width:height ratio ranged from 13:1 to 181:1 and averaged 64:1. At Echo Canyon, fifth-order lithosomes ranged from approximately 1,150–3,800 m wide (averaging 2,505 m) and 14–33 m high (averaging 23 m). Width:height ratio in Echo Canyon ranged from 57:1 to 179:1 and averaged 112:1 (nearly twice the average at Richards Mountain). A two-sample *t*-test (one-tailed) showed that these values were truly significantly larger at Echo Canyon (M = 112, SD = 37) than at Richards Mountain (M = 64, SD = 37), $t(39) = 3.46$, $p = 0.0007$. Neither study area showed any obvious vertical trends in width:height ratios of fifth-order lithosomes. Width:height ratios did tend to be larger in the axial portion of the Richards Mountain fan than on the fan margins. The Echo Canyon fan did not have any clear trends in lateral variation of width:height ratios.

Stacking patterns and qualitative descriptions also varied between the two study areas. The fifth-order lithosomes in the Echo Canyon Conglomerate tend to have a tabular shape in cross-section, continue across the vast majority of the sixth-order lithosomes that contain them and have scoured away most of the paleosol caps on underlying channel complexes (although partial paleosol caps are common). In contrast, the fifth-order lithosomes of the Richards Mountain Conglomerate are more lenticular in shape, never traverse the entire fan and show a greater tendency toward compensational stacking patterns (i.e., axes of channel complexes are offset from one another). **Figure 12** depicts a simplified version of the observed geometries and architectural styles. Additionally, the preservation of a thick and laterally continuous paleosol cap on fifth-order lithosomes is more common in the Richards Mountain fan relative to Echo Canyon.

Sixth- and Seventh-Order Lithosomes

Sixth- and seventh-order lithosomes (**Table 1**) were also not quantitatively analyzed for this study, but a few qualitative observations are informative, as they provide insights into the tectonic histories of the study areas. The Richards Mountain Conglomerate consists of a single sixth-order lithosome (an individual alluvial fan). The sixth-order surfaces bounding this lithosome consist of gradational contacts with fluvial and lacustrine facies of the Wasatch Formation above and below, respectively (Crews, 1985; Crews and Ethridge, 1993). These sixth-order surfaces coincide with the seventh-order surfaces that bound the entire Richards Mountain Conglomerate (since the entire section contains only one sixth-order lithosome). Other minor sixth-order lithosomes do exist along strike at

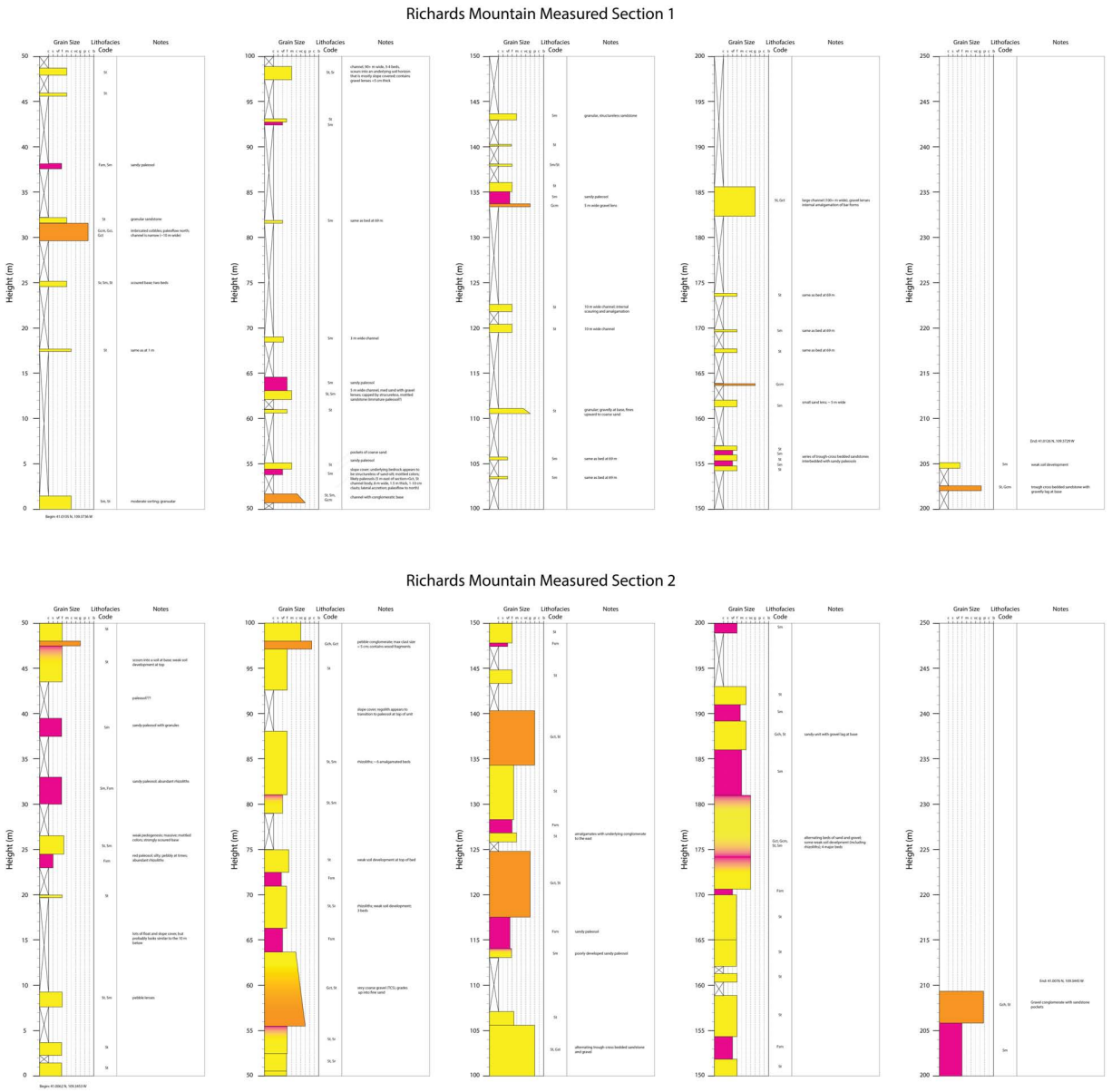

FIGURE 7 | Details of sedimentary logs measured at Richards Mountain by the authors. Additional sedimentary logs used for interpreting the deposits at Richards Mountain can be found in Crews (1985). Facies codes represent the following: Fsm = Fine-grained, massive/structureless. Usually paleosols. Sm = massive/structureless sandstone. Usually indicates bioturbation and early pedogenesis in these logs. St = trough-cross-stratified sandstone. Sr = ripple-cross-stratified sandstone. Gcm = clast-supported massive/structureless conglomerates. Gct = clast-supported trough-cross-stratified conglomerates. Gci = clast-supported, imbricated conglomerates, Gch = clast-supported, horizontally bedded conglomerates.

the same stratigraphic interval within the Wasatch Formation (Crews, 1985; Crews and Ethridge, 1993); however, these do not overlap with the fan exposed on Richards Mountain.

The Echo Canyon Conglomerate displays quite a different large-scale architectural style. Here, the formation is composed of at least two overlapping fans (sixth-order lithosomes). Whether others existed along strike at the time of deposition is not known, although it seems likely. The sixth-order bounding surfaces are erosional contacts between the various fans. In Echo Canyon, the seventh-order bounding surfaces that encompass the formation consist of the transitional contact with the underlying fluvial Henefer Formation and an angular unconformity with the overlying Hams Fork Conglomerate of the Evanston Formation.

DISCUSSION

Perhaps the most striking and intriguing of our results is the great difference in average width:height ratios of the fifth-order lithosomes in these two ancient alluvial fans.

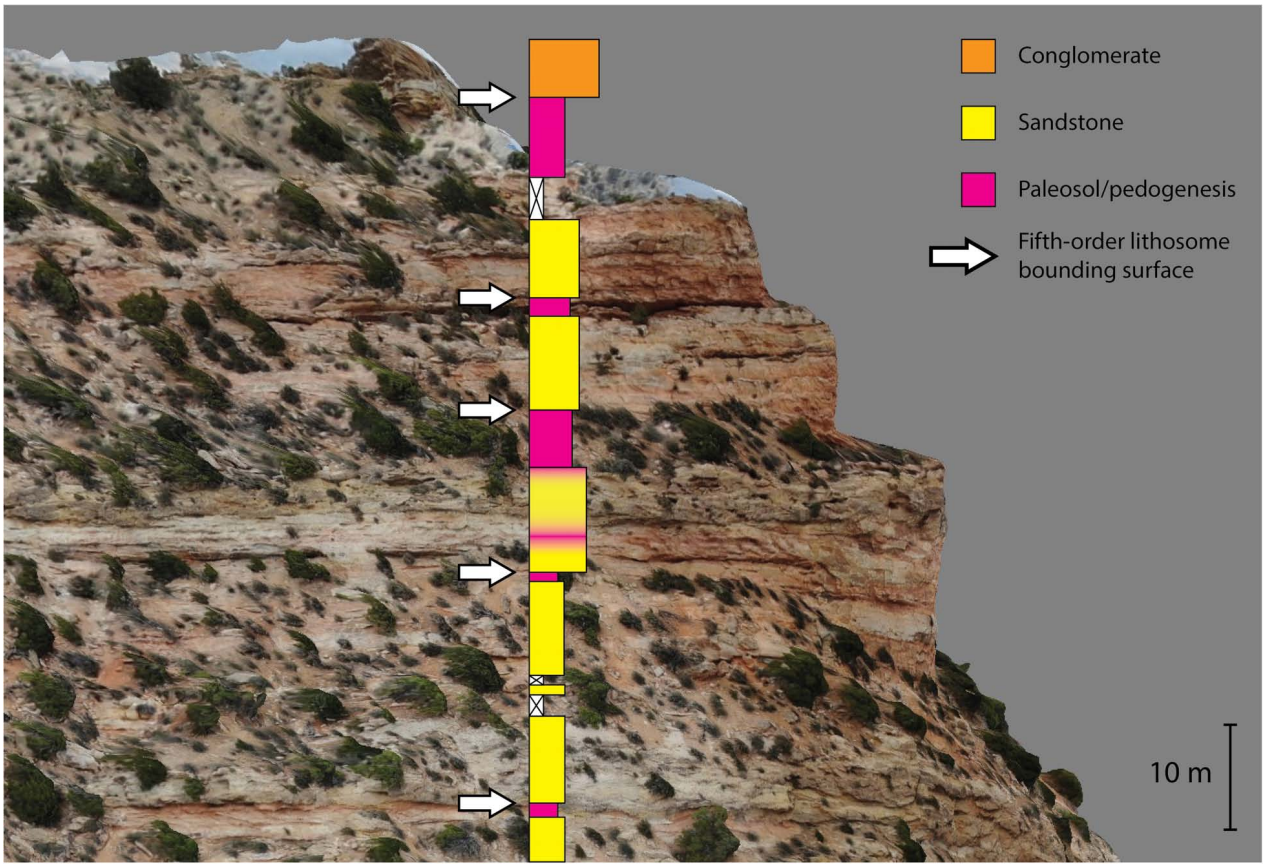

FIGURE 8 | Small portion of the digital outcrop model from the western end of Richards Mountain with a simplified portion of the Richards Mountain Measured Section 2 (**Figure 7B**) overlain for facies correlation. Fifth-order bounding surfaces are marked by white arrows. These bounding surfaces can generally be recognized by their lateral continuity and the frequent presence of a recessive paleosol cap on the underlying lithosome. The boundary between lithosomes is placed at the top of this paleosol cap, where channel-filling sandstones or conglomerates of the overlying lithosome scour into the paleosols. Note that each fifth-order bounding surface corresponds with the top of a paleosol on the sedimentary log.

Fifth-order lithosomes of a given thickness in the Echo Canyon Conglomerate average nearly twice the width of their counterparts in the Richards Mountain Conglomerate (**Figures 11**, **12** and **Table 3**). In order to interpret the meaning of this disparity in width:height ratios, we must first understand what process controls the width of fifth-order lithosomes. We interpret this to be a function of the efficiency of the migration of channels across the fan. Essentially, the channels (and it follows, channel complexes) of the Echo Canyon Conglomerate were more effective at sweeping across those alluvial fans than were the channel complexes of the fan at Richards Mountain. Many conditions, both allogenic and autogenic, can influence the rate of channel migration in fluvial or alluvial systems. The number of factors that can play a role make determining the dominant processes and factors controlling a complex and challenging task. We examine below the likelihood of four different major processes/conditions having contributed to the observed difference in width:height ratios between the study areas: (1) the nature of the source material and resulting sediment on the fan, (2) the position (proximal vs. distal) on the fan at which dimensions are measured, (3) tectonic influences such as rates of uplift and subsidence, and (4) climatic controls on efficiency of channel migration.

Discussion of Key Facies

Correctly interpreting environment of deposition and identifying lithosomal bounding surfaces in alluvial fan deposits requires recognition of key facies and the spatial relationships between facies. Key facies in each study area (**Figure 4**) are similar, but important differences exist. Key facies of the Richards Mountain Conglomerate include clast-supported, structureless to poorly stratified or imbricated cobble and boulder conglomerates and fine-grained sandstones with ripple and/or trough-cross-stratification interpreted as channel deposits on a streamflow-dominated alluvial fan. Debris flow deposits are conspicuously absent. This raises questions about whether the Richards Mountain Conglomerate should be classified as an alluvial fan at all rather than just a coarse braid plain deposit (Crews and Ethridge, 1993). However, given the large clast size (up to 1.5 m), the plano-convex cross-sectional shape of the deposit, and the rapid disappearance of coarse material basinward (pinching out from a maximum thickness of 750 m over just a few km) we feel

FIGURE 9 | Close-up view the "Detailed Section" digital outcrop model from Echo Canyon (available in the data repository). Fourth-order lithosomes can be clearly seen as individual beds in the conglomerates at the top and bottom of the image. In the middle of the image is a light-colored, recessive unit that consists of green and red fine-grained, thinly bedded sandstones as well as structureless mudstones interpreted as paleosols. The top of this recessive unit corresponds to a fifth-order bounding surface. See juniper trees for scale.

it is still appropriate to characterize this deposit as an alluvial fan in agreement with previous interpretations (Crews and Ethridge, 1993). The sandstones frequently exhibit mottled red and yellow colors, rhizoliths, and a structureless texture. These are interpreted as sandy channel deposits that have undergone early pedogenesis. Structureless, mottled mudstones are also common and are interpreted as mature paleosols.

In the Echo Canyon Conglomerate clast-supported cobble conglomerates are the most common facies. Some of the conglomerate beds in Echo Canyon show imbrication and/or stratification and likely represent stream-flow deposits. However, most are structureless and are interpreted as channel deposits probably emplaced in high-intensity, short-duration flows or possibly as debris flows. Rare beds of clast-supported, angular pebble to cobble conglomerate grading upward into matrix-supported angular pebble conglomerate also exist and are interpreted as deposits from debris-flows or highly concentrated flows due to their matrix-support and highly angular clasts. Structureless red or mottled mudstones with rhizoliths are common (though not as common as at Richards Mountain) and are interpreted as paleosols. Facies in both study areas follow a consistent pattern of spatial organization (**Figures 5**, **8**, **9**). One or more beds of channel-fill conglomerates are overlain by finer-grained intervals of thin-bedded or structureless sandstones and mudstones that represent sheet-flow deposits and pedogenesis on inactive fan segments. Overlying conglomerates representing renewed channel deposition scour into the fine-grained paleosol caps (which are frequently completely removed by the channel scour). The erosional surface between the fine-grained caps and the overlying conglomerates represents the bounding surface between fifth-order lithosomes.

Significance of Small- and Large-Scale Alluvial Architecture

Small-scale alluvial architecture (first- to fourth-order lithosomes; **Figure 1** and **Table 1**) in these ancient alluvial fans is probably most important in helping to reveal how autogenic processes were operating during deposition. While we did not examine the architecture of these smaller features in detail for this study, in-depth examination could yield further insight into paleoclimate (specifically precipitation) through examination of flow conditions. Large-scale (sixth- and seventh-order) lithosomes were also not analyzed in detail, but they do provide some important insight into the general tectonic histories of these synorogenic alluvial fans. For example, the synclinal structure of the Echo Canyon Conglomerate along with its erosional truncation in an angular unconformity with the overlying Hams Fork Conglomerate of the Evanston Formation are a clear record of its incorporation into the wedge-top of the Sevier thrust belt. By comparison, the Richards Mountain Conglomerate lacks any of this post-depositional deformation

and truncation, indicating it existed only within the foredeep of the Uinta Mountain uplift.

Possible Causes of Variability in Width:Height Ratios of Fifth-Order Lithosomes

Position on Fan, Grain Size, and Source Area Lithology

Alluvial architecture will change downstream based on the interactions between basin geometry, sediment supply, subsidence rate and avulsion type/frequency (Heller and Paola, 1996; Allen et al., 2013). The downstream position on an alluvial fan at which dimensions of channel complexes are exposed (**Table 2**) will therefore likely affect what the observed width:height ratios of those channel complexes are. Heller and Paola (1996) used numerical models to demonstrate the wide range of possible changes in downstream alluvial architecture based on the interaction of these factors. Based on their work and assuming typical foreland basin geometries (greatest accommodation toward the hinterland) we would expect to see fifth-order lithosomes thinning and stacking more densely in our study areas as accommodation decreases. Furthermore, assuming channels remain relatively straight as is common on alluvial fans, the rate of channel migration should increase downfan, since a small adjustment in channel trajectory at the fan apex would translate to a much larger adjustment in position several kilometers downstream. Both effects should combine to produce a larger width:height ratio of fifth-order lithosomes in the more distal portions of these alluvial fans.

Additionally, the decrease in grain-size that occurs between proximal and distal portions of alluvial fans could impact channel mobility and alluvial architecture. Several studies (e.g., Nanson and Hickin, 1986; Constantine et al., 2008) have demonstrated that grain-size of channel bank material is tied to bank erodibility and, thus, channel migration rates. In general, these studies have found that erodibility and migration rates increase with decreasing grain size down to silt-sized material after which cohesion in clay-sized particles decreases erodibility and channel migration. It does seem plausible that downstream position of the outcrop exposures in the study areas could account for at least part of the increase in width:height ratios observed in the Echo Canyon Conglomerate relative to the Richards Mountain Conglomerate as a result of changes in either accommodation or grain size. Maximum clast sizes at Richards Mountain (over 100 cm) are considerably greater than those in Echo Canyon (about 40 cm; **Supplementary Figure S1**). This may suggest that the Richards Mountain outcrops represent more proximal deposits than Echo Canyon, though there are many other factors that could be affecting grain size, such as lithology of the sediment source area or length of sediment routing system (e.g., Blair, 1999; Michael et al., 2014; D'Arcy et al., 2017). For example, a source area dominated by poorly resistant mudstones should tend toward finer-grained sediment than a source area dominated by resistant limestones and quartzites. In the case of these two study areas, source lithology is unlikely to be a strong control on the observed differences in maximum grain size. Detailed clast composition data is available for both the Echo Canyon Conglomerate (Crawford, 1979; DeCelles, 1988, 1994) and the Richards Mountain Conglomerate (Crews, 1985; Crews and Ethridge, 1993). Both alluvial fans were sourced from equivalent stratigraphic sections and contain

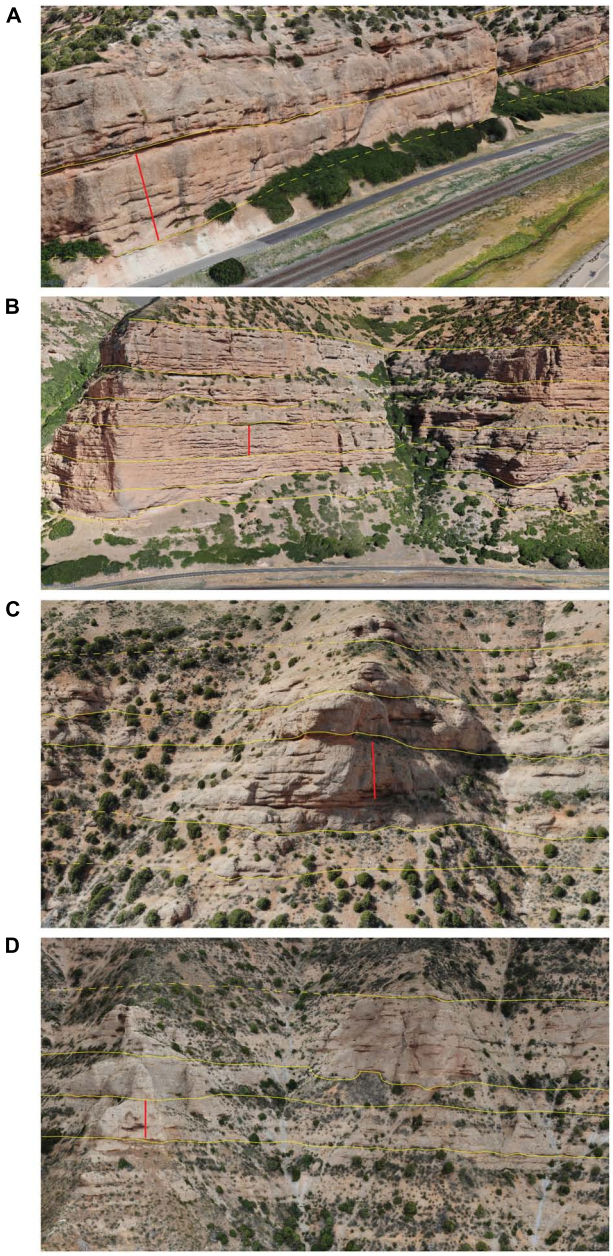

FIGURE 10 | Interpreted selections from digital outcrop models. Fifth-order bounding surfaces are marked by yellow lines (dashed where uncertain or covered). These bounding surfaces can generally be recognized by their lateral continuity and the frequent presence of a paleosol cap on the underlying lithosome (though this is often removed by scouring from the overlying lithosome). Red lines on each images are approximately 25 m long. **(A)** and **(B)** are from the Echo Canyon model. **(C)** and **(D)** are from the Richards Mountain model.

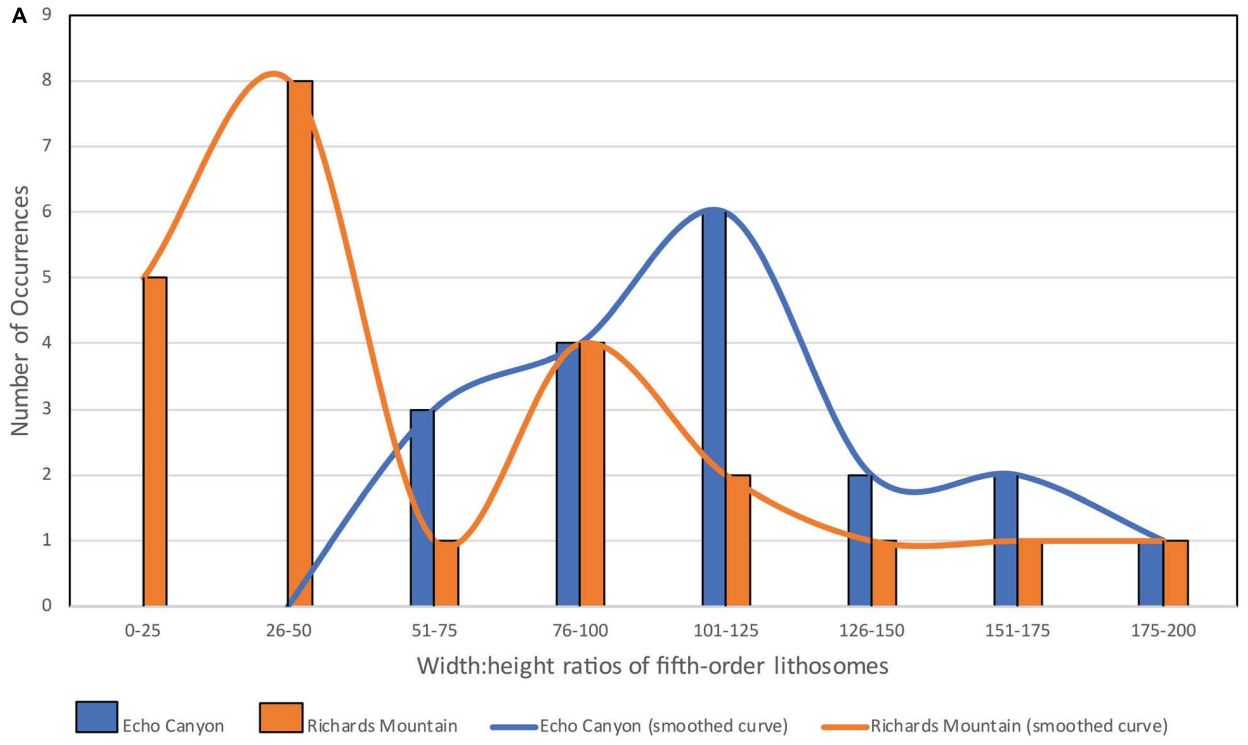

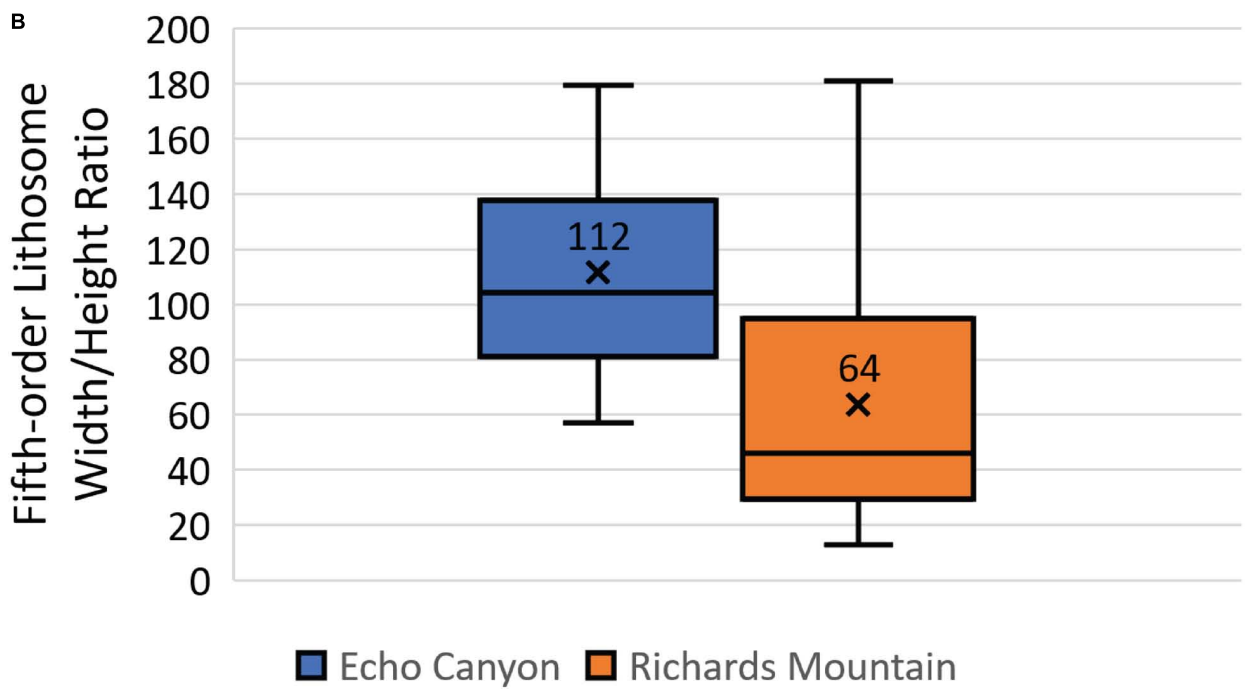

FIGURE 11 | Statistical summary of width:height ratios of fifth-order lithosomes in the Echo Canyon Conglomerate and the Richards Mountain Conglomerate. Lithosome widths were corrected where necessary for oblique exposure angles. Height was measured at the point of maximum observed thickness. A two-sample *t*-test (one-tailed) showed that these ratios were significantly larger at Echo Canyon (M = 112, SD = 37) than at Richards Mountain (M = 64, SD = 37), $t(39) = 3.46$, $p = 0.0007$. **(A)** Distribution of fifth-order width:height ratios. Lines represent a smoothed curve of the distributions. Note that Echo Canyon width:height ratios tend to be larger than those at Richards Mountain. **(B)** Box-and-whisker plots showing range of width:height ratios for fifth-order lithosomes in the Echo Canyon and Richards Mountain Conglomerates. "X" indicates average. Note that average width:height ratios for fifth-order lithosomes in the Echo Canyon Conglomerate are nearly twice those observed in the Richards Mountain Conglomerate.

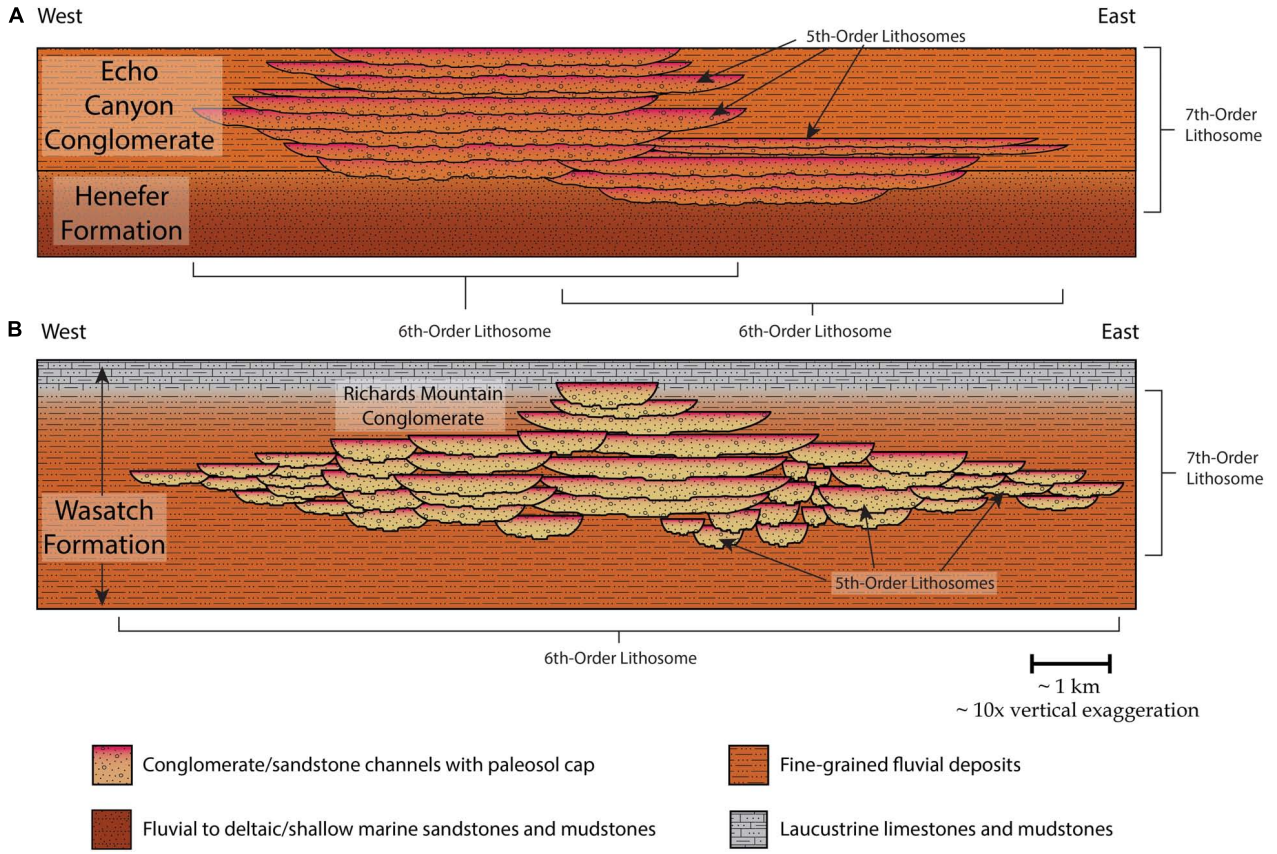

FIGURE 12 | Simplified representation of the architectural styles of the Echo Canyon Conglomerate **(A)** and the Richards Mountain Conglomerate **(B)**. Width:height ratios of fifth-order lithosomes are represented at their correct relative sizes between the two fans (with approximately10× vertical exaggeration). Stacking patterns of fifth-order lithosomes are represented schematically for both fans. While the dimensions, placement, and number of fifth-order lithosomes do not exactly match the actual deposits, general trends in the dimensions and placement of lithosomes do accurately represent the real study areas. Note that in the Echo Canyon Conglomerate, fifth-order lithosomes are organized into multiple sixth-order lithosomes (individual alluvial fans). Contrast this with the Richards Mountain Conglomerate, where the fifth-order lithosomes comprise only one, larger sixth-order lithosome. Note also that at Echo Canyon, the fifth-order lithosomes extend laterally across essentially the entire sixth-order lithosome that contains them, while at Richards Mountain the fifth-order lithosomes extend laterally across only a relatively small portion of their sixth-order lithosome.

resistant Mesozoic and Paleozoic sandstones and limestones and Proterozoic quartzites. It seems more likely then that differences in grain size between the two fans are due to other factors, including downfan position, size and gradient of the fan, or distance of the fan apex from the source area. Regardless of the exact control on clast size, finer-grained conglomerates could have allowed for more erodible channel banks on the Echo Canyon Fan and, therefore, more mobile channels and higher width:height ratios for fifth-order lithosomes.

There are problems, however, with using fan position alone to explain the observed differences in alluvial architecture. If the major differences in architecture between Echo Canyon and Richards Mountain are due primarily to fan position, we would expect to see comparable differences between proximal and distal sediments within each individual fan. These relationships are not observed, however. The largest width:height ratios observed at Richards Mountain actually occurred in the axial, most proximal portion of the fan where clast sizes are at a maximum. Sandy channel complexes on the margins of the fan had smaller width:height ratios than some of these more proximal channel complexes, opposite of what would have been expected. At Echo Canyon, no clear differences in architectural style were evident in a downstream direction. Due to the lack of a clear relationship between fan position and architectural style, even within the individual fans, we also believe that fan position is not an adequate explanation for the significant differences observed between width:height ratios of fifth-order lithosomes in the two study areas, though it cannot be ruled out entirely.

Tectonics

Alluvial fans require high relief source terrains in order to form and so by necessity exist in intimate association with areas of active tectonism. Tectonic conditions in turn have the potential to exert a strong control on alluvial architectural style. Changes in architecture may result from different basin geometries, variable rates of uplift and/or changes in the balance between sediment supply and rate of creation of accommodation via basin subsidence (Heller and Paola, 1996; Allen et al., 2013).

Both the Uinta Uplift and the Sevier Thrust Belt are the result of compressional tectonics. The Uinta Uplift was produced by "thick-skinned" Laramide-style deformation (basement-cored uplifts) while the Sevier Thrust Belt resulted from "thin-skinned" deformation mostly involving sedimentary cover rocks. Despite these differences in structural style, both source terrains were tectonically active during fan deposition and basin geometries were not significantly different (i.e., both were deposited in flexural foredeeps), removing these major factors in the different architectural styles of the two study areas.

The balance between sediment supply and subsidence has been recognized by many workers (e.g., Leeder, 1978; Knox, 1983; Heller and Paola, 1996; Allen et al., 2013) as a controlling factor on alluvial and fluvial architecture. Assuming sediment supply is constant, increased subsidence rates should allow for more effective trapping of sediment and lead to greater rates of aggradation. Increased aggradation will in turn increase the preservation potential of fine-grained overbank deposits and lead to more isolated channel bodies (Leeder, 1978; Knox, 1983). Alternatively, reduced rates of subsidence and aggradation provide relatively more time for lateral migration of channels while also allowing for increased winnowing and bypass of fine-grained sediments. So, for a given thickness of sediment (all else being held equal), the active channel on an alluvial fan should be able to migrate across a greater portion of the fan and remove more of the fine material (including paleosol caps on fifth-order lithosomes) from the underlying fan surface in a slowly subsiding basin than it could in a rapidly subsiding and aggrading basin.

With this concept in mind, tectonically controlled differences in subsidence rates seem like an attractive way to explain the differences in architectural style between the Echo Canyon and Richards Mountain Conglomerates. If rates of subsidence and sediment accumulation were greater during deposition of the Richards Mountain Conglomerate than at Echo Canyon, it could nicely explain the greater preservation of paleosols and other fine-grained material at Richards Mountain and the increased effectiveness of lateral channel migration at Echo Canyon. However, when subsidence rates at both study areas are calculated from existing subsidence curves (Palmer, 1983; Crews and Ethridge, 1993; DeCelles, 1994), it appears that the Richards Mountain Conglomerate was not accumulating significantly (if at all) faster than the Echo Canyon Conglomerate (approximately 0.1–0.25 mm/year at Richards Mountain vs. 0.18–0.23 mm/year at Echo Canyon). Admittedly, these are very rough estimates given the lack of high-resolution age data in the study areas. The minimal difference in estimated subsidence rates between the study areas does suggest, however, that tectonic controls alone are unlikely to explain the difference in architectural styles we observe. Better resolution for depositional ages on the two fans would aid significantly in resolving to exactly what degree tectonics may have played a role in shaping architectural style.

Climate

Variation in climatic factors, including mean annual precipitation and seasonality of precipitation, can function as strong controls on stratigraphic architecture and lateral channel migration. Review of previous work on the paleoclimate of our study areas (e.g., Crawford, 1979; Crews, 1985; Fricke et al., 2009; Foreman et al., 2012) indicates that the most significant difference in the two climates was probably their amount and style of precipitation. Precipitation strongly influences vegetation cover and sediment supply and directly controls discharge, all of which may affect architectural style. Greater mean annual precipitation (i.e., a wetter climate) supports greater vegetation cover. Vegetation exerts a primary control on channel migration by increasing the cohesiveness of channel margins, which decreases erosion and lateral migration. Increased vegetation also secondarily stabilizes channels by limiting erosion in the catchment area and thereby decreasing sediment flux (Smith, 1994; Gran and Paola, 2001; Giardino and Lee, 2011; Wickert et al., 2013). High sediment flux destabilizes channels by overwhelming the transport capacity of the stream and causing frequent, small avulsions and increased rates of lateral migration (Salcher et al., 2010; Wickert et al., 2013; Legg and Olson, 2014), a phenomenon that is readily observable in sediment-choked braided rivers (Ashworth et al., 2004).

Interestingly, sediment flux does not increase linearly with increasing precipitation. Instead, sediment flux peaks in semiarid-subhumid climates at around 30 cm mean annual precipitation. Sediment supply is limited by vegetation cover in wetter climates and by lack of runoff in dryer climates (Langbein and Schtjmm, 1958; Smith, 1994). Increased variability in precipitation also increases sediment flux; both field studies and numerical models have shown spikes in sediment flux where precipitation and discharge are highly variable and/or seasonal (e.g., Smith, 1994; Cecil and Terence Edgar, 2003; Pelletier et al., unpublished). Strong seasonality and variability in precipitation, such as in monsoonal climates, is therefore another contributor to channel mobility because it destabilizes channels through increased sediment flux as well through large-scale flood events (Starkel, 1979). This may be observed occurring on fluvial megafans in monsoonal climates (Leier et al., 2005), which exhibit some of the most mobile channels on the planet. The opposite has also been documented after the construction of reservoirs; the river channels downstream of new reservoirs usually experience decreased lateral migration due to regulation of flow and trapping of sediment upstream (Shields et al., 2000; Larsen et al., 2006).

Several lines of evidence support the interpretation that the Echo Canyon Conglomerate was deposited in a more seasonal climate than was the Richards Mountain Conglomerate and thus may have had greater rates of lateral channel migration due to increased sediment flux, more variable discharge, and decreased vegetation. While both fans were streamflow dominated (Crawford, 1979; Crews and Ethridge, 1993; DeCelles, 1994), debris flows are present only at Echo Canyon (Crawford, 1979; DeCelles, 1994) and are conspicuously lacking at Richards Mountain (Crews, 1985; Crews and Ethridge, 1993). High-intensity or long-duration precipitation is generally required to form a debris flow (Caine, 1980), and the rainfall threshold for debris flow initiation is generally higher in areas with year-round wet climates (Wilson, 2000; Giannecchini, 2006). Debris flows are therefore favored in areas with highly variable precipitation

and commonly occur after infrequent but strong and brief storms where only minimal infiltration occurs (Starkel, 1979; Pierson, 1980; Radbruch-Hall et al., 1982). Debris flows at Echo Canyon therefore suggest that these conditions were at least occurring on occasion. Crawford (1979) also interpreted the common occurrence of soft sediment deformation features and extremely poorly sorted and somewhat chaotic conglomerates in Echo Canyon as an indicator that much of that fan was deposited by short, intense flows. Furthermore, climate models, stable isotope data, and the fossil record strongly suggest that a North American monsoon, fueled by moisture from the Western Interior Seaway, was active on the eastern flank of the Sevier Orogenic belt (i.e., at the location of the Echo Canyon fan) during the late Cretaceous (Fricke et al., 2009). No such monsoonal conditions are known to have existed in western North America during the time that the Richards Mountain Conglomerate was being deposited. Most evidence suggests that the Richards Mountain fan was active under year-round wet conditions. Again, debris flows have not been observed on this fan, signs of pedogenic alteration are pervasive throughout the fan (even in sandy and gravelly channel deposits), and signs of vegetation (including rhizoliths, woody material, and leaves that probably came from a jungle) are abundant (Crews, 1985; Crews and Ethridge, 1993; **Figures 4**, **5**). The interfingering of the Richards Mountain Conglomerate downdip with the lacustrine Green River Formation and its transition to a fan delta at the top of the section also show that conditions were wet enough (at least at times) to support large lakes. All these characteristics suggest a relatively stable and wet climate that would have contributed to channel stability through steady flow, dense vegetation, and reduced sediment flux. Monsoonal conditions and increased sediment fluxes are speculated to have occurred during the PETM and the PETM appears to have influenced stratigraphic architecture of fluvial deposits (Foreman et al., 2012) to produce a similar architectural style to that observed in Echo Canyon. It is possible that the Richards Mountain Conglomerate avoided these effects because it was deposited several million years after the peak of the PETM.

In summary, lithologic evidence and indications of a late Cretaceous North American monsoon support the interpretation of the Echo Canyon Conglomerate as having been deposited under a strongly seasonal, subhumid climate, while the Richards Mountain Conglomerate appears to have been deposited in a relatively more stable and humid climate. This would have led to relatively higher rates of lateral channel migration on the Echo Canyon fan due to flashier discharge, higher sediment flux, and possibly sparser vegetation cover. It is also possible that the increased sediment supply at Echo Canyon could have overwhelmed creation of accommodation and allowed for increased winnowing of overbank deposits and paleosols and larger width:height ratios of fifth-order lithosomes as discussed previously.

Potential Sources of Error

Sources of error in this study were primarily minor flaws in the photogrammetric models including misalignments of up to several meters between model chunks (caused by changing lighting conditions between photos) or accidental incomplete coverage of some outcrops. Further error was likely introduced by using general paleoflow directions to correct for apparent lithosome widths (**Table 3** and **Supplementary Table S1**). While using general paleoflow directions certainly saves an immense amount of time in the field (one of the main advantages of the method we employ in this study), it does introduce a potentially significant source of error depending on the variability of individual paleocurrent directions. These challenges, along with difficulty in correlation of some fifth-order lithosomes due to faulting, erosion, or slope cover meant that measurements of fifth-order lithosome widths in particular were subject to errors of several meters (due to lack of exposure of thin beds on the margins of lithosomes). This was compensated for by measuring as many lithosomes as possible from all parts of the study areas with adequate exposure. We should note again though, that width:height ratios of fifth-order lithosomes (particularly at Echo Canyon) are minimum estimates. Fortunately, because underestimation of width:height ratios are probably greater at Echo Canyon, this should not change our primary observation that fifth-order lithosomes there have significantly larger width:height ratios as compared to those observed on Richards Mountain.

Lack of data is, of course, always of concern and this study was no exception. Downfan position, subsidence rates and local climate all had to be roughly estimated due to limited outcrop extent and the lack of detailed age and geochemical paleoclimate data at our particular study sites. This introduces uncertainty into our discussion of possible contributing factors to variations in alluvial architecture, but again the evidence that does exist is overwhelmingly in support of climate as the main driver of architectural style.

Implications

Given the evidence to support increased channel mobility through a dryer and more seasonal climate at Echo Canyon than found at Richards Mountain (and the lack of strong evidence to explain increased lateral migration due to source material lithology, position on the fan, or subsidence rates) we propose that the differences observed in width:height ratios of fifth-order lithosomes between the study areas are primarily due to differences in climate. Other studies (e.g., Smith, 1994; Ritter et al., 1995; D'Arcy et al., 2017) have reached similar conclusions about climate being the dominant driver behind changes in alluvial fan development. Our interpretation has two major implications. First, providing other allogenic and autogenic factors can be reasonably eliminated as causal mechanisms, stratigraphic architecture of fifth-order lithosomes in alluvial fans may provide insight into paleoclimate, specifically seasonality. Secondly, as anthropogenic climate change continues to affect modern and future climates, we might expect to observe increased lateral migration of channel complexes on alluvial fans in regions where precipitation is becoming more variable. Climate studies predict that large portions of the globe (including areas such as California, northern Venezuela, etc. already at risk from debris flow events and other alluvial processes) will experience more extreme precipitation events in coming decades

(e.g., Kunkel et al., 2013), meaning that this effect has the potential to be widespread. While this statement assumes that other factors are held constant (an admittedly questionable assumption given the great uncertainties associated with climate change) it may still hold true in a general sense. The time scale over which fan processes may respond to changing climate is somewhat uncertain due to lack of high-resolution temporal data from alluvial fan deposits; however, at the least this insight allows for increased awareness of the potential for future changes and increases in geological hazards associated with alluvial fan dynamics.

CONCLUSION

We find that the width:height ratios of fifth-order lithosomes in the alluvial fan deposits of the Cretaceous Echo Canyon Conglomerate are nearly twice those of their counterparts in the Eocene Richards Mountain Conglomerate. This indicates that some mechanism was allowing the channel complexes on the Echo Canyon fan to more effectively sweep across the alluvial fan surface. Most evidence points toward climate being the main driver behind this enhanced lateral migration, though other factors such as subsidence rates may have played minor roles. A more seasonal and warmer climate during the deposition of the Echo Canyon Conglomerate in the late Cretaceous allowed channel to migrate more effectively across the fan by destabilizing channels through increased sediment flux, flood events, and possibly decreased vegetation as compared to the wetter, more consistent climate during Richards Mountain deposition.

Our results imply that the architectural styles (specifically with/height ratios of fifth-order lithosomes) of ancient alluvial fans may be cautiously used to provide insight into allogenic controls related to paleoclimate where sufficient evidence exists to eliminate other causal mechanisms. They also suggest that in regions where anthropogenic climate change results in more variable patterns of precipitation, alluvial fans may show decreased channel stability and, hence, greater risk to human activity and development on alluvial fans.

DATA AVAILABILITY STATEMENT

All datasets generated for this study are included in the article/**Supplementary Material**.

AUTHOR CONTRIBUTIONS

BC and SM contributed to the conception and design of the study. BC and PD provided background information, an introduction to the study areas, and mentoring, reviewed and provided feedback and editing on the manuscript. SM collected field data, built and analyzed photogrammetric models, performed statistical analysis, drafted figures and tables, and wrote the manuscript. All authors contributed to the article and approved the submitted version.

FUNDING

Funding for this project was provided to SM by the 2018 AAPG Grants-in-Aid Program (Alexander and Geraldine Wanek Memorial Grant) and the University of Arizona Department of Geosciences.

ACKNOWLEDGMENTS

We are grateful to those at the AAPG and the University of Arizona who provided financial assistance for this project, to the faculty in the University of Arizona Department of Geosciences for their input and suggestions, and to Samantha Meek for her assistance with field work.

SUPPLEMENTARY MATERIAL

The Supplementary Material for this article can be found online at: https://www.frontiersin.org/articles/10.3389/feart.2020.00215/full#supplementary-material

REFERENCES

Allen, P. A., Armitage, J. J., Carter, A., Duller, R. A., Michael, N. A., Sinclair, H. D., et al. (2013). The Qs problem: sediment volumetric balance of proximal foreland basin systems. *Sedimentology* 60, 102–130. doi: 10.1111/sed.12015

Armitage, J. J., Duller, R. A., Whittaker, A. C., and Allen, P. A. (2011). Transformation of tectonic and climatic signals from source to sedimentary archive. *Nat. Geosci.* 4, 231–235. doi: 10.1038/ngeo1087

Ashworth, P. J., Best, J. L., and Jones, M. (2004). Relationship between sediment supply and avulsion frequency in braided rivers. *Geology* 32, 21–24. doi: 10.1130/G19919.1

Bemis, S. P., Micklethwaite, S., Turner, D., James, M. R., Akciz, S., Thiele, T., et al. (2014). Ground-based and UAV-based photogrammetry: a multi-scale, high-resolution mapping tool for structural geology and paleoseismology. *J. Struct. Geol.* 69, 163–178. doi: 10.1016/j.jsg.2014.10.007

Bettis, E. A. III (2003). Patterns in holocene colluvium and alluvial fans across the prairie-forest transition in the midcontinent USA. *Geoarcheol. An Int. J.* 18, 779–797. doi: 10.1002/gea.10087

Blair, T. C. (1999). Cause of dominance by sheetflood vs. debris-flow processes on two adjoining alluvial fans, Death Valley, California. *Sedimentology* 46, 1015–1028. doi: 10.1046/j.1365-3091.1999.00261.x

Blair, T. C., and McPherson, J. G. (2009). "Processes and forms of alluvial fans," in *Geomorphology of Desert Environments*, eds A. J. Parsons and A. D. Abrahams (Berlin: Springer Science+Business Media), 413–466.

Bowman, D. (2019). *Principles of Alluvial Fan Morphology*. Cham: Springer.

Brooks, C. E. P. (1949). *Climate Through the Ages*, 2nd Edn. London: Ernest Benn, Ltd.

Bull, W. B. (1964). Alluvial fans and near-surface subsidence in western Fresno County, California. *Paper Presented at United States Geological Survey Professional Paper 437-A*. Reston: United States Geological Survey.

Bull, W. B. (1977). The alluvial-fan environment. *Prog. Phys. Geogr. Earth Environ.* 1, 222–270. doi: 10.1177/030913337700100202

Bull, W. B. (1991). *Geomorphic Responses to Climatic Change*. Oxford: Oxford Press.

Burgener, L., Hyland, E., Huntington, K. W., Kelson, J. R., and Sewall, J. O. (2019). Revisiting the equable climate problem during the Late Cretaceous greenhouse

using paleosol carbonate clumped isotope temperatures from the Campanian of the Western Interior Basin, USA. *Palaeogeogr. Palaeoclimatol. Palaeoecol.* 516, 244–267. doi: 10.1016/j.palaeo.2018.12.004

Caine, N. (1980). The rainfall intensity:duration control of shallow landslides and debris flows. *Geogr. Ann. Ser. A, Phys. Geogr.* 62, 23–27. doi: 10.1080/04353676.1980.11879996

Carrivick, J. L., Smith, M. W., and Quincey, D. J. (2016). *Structure from Motion in the Geosciences*. Chichester, UK: John Wiley & Sons, Ltd.

Cecil, C. B., and Terence Edgar, N. (2003). *Climate Controls on Stratigraphy: SEPM Special Publication No.77*. Available online at: http://www.sepm.org.downloadedfromhttps://pubs.geoscienceworld.org/books/chapter-pdf/3798282/9781565762145_frontmatter.pdf (accessed February 4, 2019).

Clarke, L., Quine, T. A., and Nicholas, A. (2010). An experimental investigation of autogenic behaviour during alluvial fan evolution. *Geomorphology* 115, 278–285. doi: 10.1016/j.geomorph.2009.06.033

Constantine, C. R., Dunne, T., and Hanson, G. J. (2008). Examining the physical meaning of the bank erosion coefficient used in meander migration modeling. *Geomorphology* 106, 242–252. doi: 10.1016/j.geomorph.2008.11.002

Crawford, G. A., and Dott, R. H. (1979). *Alluvial-Fan Deposition and Tectonic Significance of Two Late Cretaceous-Paleocene Conglomerates in North-Central Utah Thrust Belt*. Available online at: http://archives.datapages.com.erl.lib.byu.edu/data/bulletns/1977-79/images/pg/00630003/0400/04370.pdf (accessed April 11, 2018).

Crawford, K. A. (1979). *Sedimentology and Tectonic Significance of the Late Cretaceous-Paleocene Echo Canyon and Evanston Synorogenic Conglomerates of the North-Central Utah Thrust Belt*. Madison, WI: University of Wisconsin.

Crews, S. G. (1985). *Response of Basin-Margin Depositional Sytems to Laramide Uplift of the Northeastern Uinta Mountains*, M.S. thesis, Colorado State University, Colorado.

Crews, S. G., and Ethridge, F. G. (1993). Laramide tectonics and humid alluvial fan sedimentation, NE Uinta Uplift, Utah and Wyoming. *J. Sediment. Petrol.* 63, 420–436.

Culbertson, W. C. (1969). *Facies Changes in the Eocene Rocks in the Southeastern Part of the Green River Basin, Wyoming*. Available online at: http://archives.datapages.com.erl.lib.byu.edu/data/uga/data/016/016001/pdfs/205.pdf (accessed April 11, 2018).

Dade, B. W., and Verdeyen, M. E. (2007). Tectonic and climatic controls of alluvial-fan size and source-catchment relief. *J. Geol. Soc. Lond.* 164, 353–358. doi: 10.1144/0016-76492006-039

D'Arcy, M., Whittaker, A. C., and Roda-Boluda, D. C. (2017). Measuring alluvial fan sensitivity to past climate changes using a self-similarity approach to grain-size fining, Death Valley, California. *Sedimentology* 64, 388–424. doi: 10.1007/978-1-4614-7495-1_23

DeCelles, P. G. (1988). Lithologic provenance modeling applied to the Late Cretaceous synorogenic Echo Canyon Conglomerate, Utah: a case of multiple source areas. *Geology* 16, 1039–1043.

DeCelles, P. G. (1994). Late cretaceous-paleocene synorogenic sedimentation and kinematic history of the sevier thrust belt, Northeast Utah and Southwest Wyoming. *Geol. Soc. Am. Bull.* 106, 32–56. doi: 10.1130/0016-7606(1994)106<0032:lcpssa>2.3.co;2

DeCelles, P. G., Gray, M. B., Ridgeway, K. D., Cole, R. B., Pivnik, D. A., Pequera, N., et al. (1991). Controls on synorogenic alluvial-fan architecture, beartooth conglomerate (Palaeocene), wyoming and montana. *Sedimentology* 38, 567–590. doi: 10.1111/j.1365-3091.1991.tb01009.x

Dorn, R. I. (2009). "The role of climatic change in alluvial fan development the persistence of climatic change in alluvial-fan studies," in *Geomorphology of Desert Environments*, eds A. J. Parsons and A. D. Abrahams (Cham: Springer Science+Business Media), 723–742. doi: 10.1007/978-1-4020-5719-9_24

Fabuel-Perez (2009). *A New Approach for Outcrop Characterization and Geostatistical Analysis of a Low-Sinuosity Fluvial -Dominated Succession Using Digital Outcrop Models*. Available online at: https://watermark-silverchair-com.ezproxy1.library.arizona.edu/bltn08102.pdf (accessed February 11, 2019).

Fabuel-Perez, I., Hodgetts, D., and Redfern, J. (2010). Integration of digital outcrop models (DOMs) and high resolution sedimentology - workflow and implications for geological modelling: oukaimeden sandstone formation, High Atlas (Morocco). *Pet. Geosci.* 16, 133–154. doi: 10.1144/1354-079309-820

Foreman, B. Z., Heller, P. L., and Clementz, M. T. (2012). Fluvial response to abrupt global warming at the Palaeocene/Eocene boundary. *Nature* 491, 92–95. doi: 10.1038/nature11513

Frakes, L. A. (1979). *Climates Throughout Geologic Time*. Amsterdam: Elsevier.

Franczyk, K. J., Fouch, T. D., Johnson, R. C., Molenaar, C. M., and Cobban, W. A. (1992). "Cretaceous and tertiary paleogeographic reconstructions for the uinta-piceance basin," in *Proceedings of the U.S. Geological Survey Bulletin 1787: Evolution of Sedimentary Basins - Uinta and Piceance Basins*. Reston: United States Geological Survey.

Fricke, H. C., Foreman, B. Z., and Sewall, J. O. (2009). Integrated climate model-oxygen isotope evidence for a North American monsoon during the Late Cretaceous. *Earth Planet. Sci. Lett.* 289, 11–21. doi: 10.1016/j.epsl.2009.10.018

García-Sellés, D., Granado, P., Gratacos, O., Carrera, N., and Arbues, P. (2014). "Capture and geological data extraction: tools for a better analysis and digital modelling," in *Proceedings of the Vertical Geology Conference*. Lausanne: University of Lausanne.

Giannecchini, R. (2006). *Natural Hazards and Earth System Sciences Relationship between Rainfall and Shallow Landslides in the Southern Apuan Alps (Italy)*. Available online at: http://www.nat-hazards-earth-syst-sci.net/6/357/2006/ (accessed June 29, 2019).

Giardino, J. R., and Lee, A. A. (2011). *Rates of Channel Migration on the Brazos River*. Available online at: http://www.twdb.texas.gov/publications/reports/contracted_reports/doc/0904830898_Brazos.pdf (accessed July 20, 2019).

Google Earth (2019). *Satellite Imagery of Echo Canyon, Utah and Richards Mountain, Wyoming*. Images Acquired by Landsat/Copernicus, Maxar Technologies, USDA Farm Service Agency, and State of Utah. Available online at: earth.google.com/web/ (accessed December 16, 2019).

Gran, K., and Paola, C. (2001). Riparian vegetation controls on braided stream dynamics. *Water Resour. Res.* 37, 3275–3283. doi: 10.1029/2000WR000203

Gunster, N., and Skowronek, A. (2001). Sediment-soil sequences in the Granada Basin as evidence for long-and short-term climatic changes during the Pliocene and Quaternary in the Western Mediterranean. *Quat. Int.* 78, 17–32. doi: 10.1016/s1040-6182(00)00112-9

Hajek, E. A., Heller, P. L., and Schur, E. L. (2012). Field test of autogenic control on alluvial stratrigraphy (Ferris Formation, Upper Cretaceous - Paleogene, Wyoming). *Geol. Soc. Am. Bull.* 124, 1898–1912. doi: 10.1130/B30526.1

Harvey, A. M., Foster, G., Hannam, J., and Mather, A. E. (2003). The Tabernas alluvial fan and lake system, southeast Spain: applications of mineral magnetic and pedogenic iron oxide analyses towards clarifying the Quaternary sediment sequences. *Geomorphology* 50, 151–171. doi: 10.1016/s0169-555x(02)00212-x

Harvey, A. M., Mather, A. E., and Stokes, M. (2005). *Alluvial Fans: Geomorphology, Sedimentology, Dynamics (Geological Society Special Publication No. 251)*. Available online at: https://sudartomas.files.wordpress.com/2012/11/alluvialfans_geomorphologysedimentologydynamics.pdf (accessed April 12, 2018).

Heller, P. L., and Paola, C. (1996). Downstream changes in alluvial architecture: an exploration of controls on channel-stacking patterns. *J. Sediment. Res.* 66, 297–306.

Hofmann, M. H., Wroblewski, A., and Boyd, R. (2011). Mechanisms controlling the clustering of fluvial channels and the compensational stacking of cluster belts. *J. Sediment. Res.* 81, 670–685. doi: 10.2110/jsr.2011.54

Jacobson, S. R., and Nichols, D. J. (1982). Palynological dating of syntectonic units in the Utah-Wyoming Thrust belt: the evanston formation, echo canyon conglomerate, and little muddy creek conglomerate. *Geol. Stud. Cordilleran Thrust Belt* 2, 735–750.

Klinger, Y., Avouac, J. P., Bourles, D., and Tisnerat, N. (2003). Alluvial deposition and lake-level fluctuations forced by Late Quaternary climate change: the Dead Sea case example. *Sediment. Geol.* 162, 119–139. doi: 10.1016/j.sedgeo.2003.07.001

Knox, J. C. (1983). "Responses of river systems to Holocene climates," in *Late Quaternary Environments of the United States, Vol. 2, the Holocene*, eds H. E. Wright and S. C. Porter (Minneapolis: University of Minnesota Press), 26–41. doi: 10.5749/j.ctttt09b.8

Kunkel, K. E., Karl, T. R., Easterling, D. R., Redmond, K., Young, J., Yin, X., et al. (2013). Probable maximum precipitation and climate change. *Geophys. Res. Lett.* 40, 1402–1408. doi: 10.1002/grl.50334

Lamerson, P. R. (1982). *The Fossil Basin and Its Relationship to the Absaroka Thrust System, Wyoming and Utah*. Denver: Rocky Mountain Association of Geologists, 279–340.

Langbein, W. B., and Schtjmm, S. A. (1958). Yield of sediment in relation to mean annual precipitation. *Transactions* 39, 1076–1084.

Larsen, E. W., Fremier, A. K., and Girvetz, E. H. (2006). Modeling the effeccts of variable annual flow on river channel meansder migration patterns, Sacramento River, California, USA. *J. Am. Water Resour. Assoc.* 42, 1063–1075. doi: 10.1111/j.1752-1688.2006.tb04514.x

Larsen, M. C., Wieczorek, G. F., Eaton, L. S., Morgan, B. A., and Torres- Sierra, H. (2001). Venezuelan debris flow and flash flood disaster of 1999 studied. *EOS* 82, 572–573.

Lecce, S. A. (1990). "The alluvial fan problem," in *Alluvial Fans: A Field Approach*, eds A. H. Rachocki and M. Church (Hoboken, NJ: John Wiley & Sons Ltd), 3–24.

Leeder, M. R. (1978). "A quantitative stratigraphic model for alluvium, with special reference to channel deposit density and interconnectedness," in *Fluvial Sedimentology: Canadian Society of Petroluem Geologists Memoir*, Vol. 5, ed. A. D. Miall (Calgary, AB: CSPG), 587–596.

Leeder, M. R., Harris, T., and Kirkby, M. J. (1998). Sediment supply and climate change: implications for basin stratigraphy. *Basin Res.* 10, 7–18. doi: 10.1046/j.1365-2117.1998.00054.x

Legg, N. T., and Olson, P. L. (2014). *Channel Migration Processes and Patterns in Western Washington: A Synthesis for Floodplain Management and Restoration*. Available online at: https://fortress.wa.gov/ecy/publications/SummaryPages/1406028.html (accessed July 9, 2019).

Leier, A. L., DeCelles, P. G., and Pelletier, J. D. (2005). Mountains, monsoons, and megafans. *Geology* 33, 289–292. doi: 10.1130/G21228.1

Miall, A. D. (1985). Architectural-element analysis: a new method of facies analysis applied to fluvial deposits. *Earth Sci. Rev.* 22, 261–308. doi: 10.1016/0012-8252(85)90001-7

Michael, N. A., Whittaker, A. C., Carter, A., and Allen, P. A. (2014). Volumetric budget and grain-size fractionation of a geological sediment routing system: eocene escanilla formation, south-central Pyrenees. *Bull. Geol. Soc. Am.* 126, 585–599. doi: 10.1130/B30954.1

Miller, K. L., Reitz, M. D., and Jerolmack, D. J. (2014). Generalized sorting profile of alluvial fans. *Geophys. Res. Lett.* 41, 7191–7199. doi: 10.1002/2014GL060991

Nanson, G. C., and Hickin, E. J. (1986). A statistical analysis of bank erosion and channel migration in western Canada. *Geol. Soc. Am. Bull.* 97, 497–504.

Neton, M. J., Dorsch, J., Olson, C. D., and Young, S. C. (1994). Architecture and directional scales of heterogeneity in alluvial-fan aquifers. *J. Sediment. Res. Sect. B Stratigr. Glob. Stud.* 64, 245–257. doi: 10.1306/D4267FA0-2B26-11D7-8648000102C1865D

Nichols, G. J., and Fisher, J. A. (2007). Processes, facies and architecture of fluvial distributary system deposits. *Sediment. Geol.* 195, 75–90. doi: 10.1016/j.sedgeo.2006.07.004

Painter, C. S., Carrapa, B., Decelles, P. G., Gehrels, G. E., and Thomson, S. N. (2014). Exhumation of the North American Cordillera revealed by multi-dating of Upper Jurassic-Upper Cretaceous foreland basin deposits. *Geol. Soc. Am. Bull.* 126, 1439–1464. doi: 10.1130/B30999.1

Palmer, A. R. (1983). The decade of north american geology 1983 geologic time scale. *Geology* 11, 503–504.

Parker, G., Paola, C., Whipple, K. X., and Mohrig, D. (1998). Alluvial fans formed by channelized fluvial and sheet flow. I: theory. *J. Hydraul. Eng.* 124, 985–995. doi: 10.1061/(asce)0733-9429(1998)124:10(985)

Pierson, T. C. (1980). Erosion and deposition by debris flows at Mt Thomas, North Canterbury, New Zealand. *Earth Surf. Process.* 5, 227–247. doi: 10.1002/esp.3760050302

Radbruch-Hall, D. H., Colton, R. B., Davies, W. E., Lucchitta, I., Skipp, B. A., and Varnes, D. J. (1982). Landslide overview map of the conterminous United States. *Paper Presented at Geological Survey Professional Paper 1183* (Washington, D.C: Geological Survey).

Ritter, J. B., Miller, J. R., Enzel, Y., and Wells, S. G. (1995). Reconciling the roles of tectonism and climate in Quaternary alluvial fan evolution. *Geology* 23, 245–248.

Roehler, H. W. (1992). *Introduction to Greater Green River Basin Geology, Physiography, and History of Investigations*. Washington, D.C: Geological Survey, A1–A14.

Romans, B. W., Castelltort, S., Covault, J. A., Fildani, A., and Walsh, J. P. (2016). Environmental signal propagation in sedimentary systems across timescales. *Earth Sci. Rev.* 153, 7–29. doi: 10.1016/j.earscirev.2015.07.012

Salcher, B. C., Faber, R., and Wagreich, M. (2010). Climate as main factor controlling the sequence development of two Pleistocene alluvial fans in the Vienna Basin (eastern Austria) - A numerical modelling approach. *Geomorphology* 115, 215–227. doi: 10.1016/j.geomorph.2009.06.030

Shepherd, M. (2009). "Less common reservoir types," in *Oil field production geology: AAPG Memoir 91*, ed. M. Shepherd (Tulsa: American Association of Petroleum Geologists), 311–312. doi: 10.1306/13161227m913372

Shields, F. D. Jr., Simon, A., and Steffen, L. J. (2000). *Reservoir Effects on Downstream River Channel Migration*. Available online at: https://pubag.nal.usda.gov/download/4055/PDF (accessed July 13, 2019).

Shultz, A. W. (1984). Subaerial debris-flow deposition in the Upper Paleozoic Cutler Formation, Western Colorado. *J. Sediment. Petrol.* 54, 759–772.

Smith, G. A. (1994). Climatic influences on continental deposition during late-stage filling of an extensional basin, southeastern Arizona. *Geol. Soc. Am. Bull.* 106, 1212–1228. doi: 10.1130/0016-7606(1994)106<1212:ciocdd>2.3.co;2

Smith, M. E., Carroll, A. R., and Singer, B. S. (2008). Synoptic reconstruction of a major ancient lake system: eocene green river formation, Western United States. *Bull. Geol. Soc. Am.* 120, 54–84. doi: 10.1130/B26073.1

Smith, M. W., Carrivick, J. L., and Quincey, D. J. (2015). Structure from motion photogrammetry in physical geography. *Prog. Phys. Geogr.* 40, 247–275. doi: 10.1177/0309133315615805

Starkel, L. (1979). The role of extreme meteorological events in the shaping of mountain relief. *Geogr. Pol.* 41, 13–20.

Straub, K. M., Paola, C., Mohrig, D., Wolinsky, M. A., and George, T. (2009). Compensational stacking of channelized sedimentary deposits. *J. Sediment. Res.* 79, 673–688. doi: 10.2110/jsr.2009.070

Thrasher, B. L., and Sloan, L. C. (2009). Carbon dioxide and the early Eocene climate of western North America. *Geology* 37, 807–810. doi: 10.1130/G30090A.1

Törö, B., Pratt, B. R., and Renaut, R. W. (2015). Tectonically Induced Change in Lake Evolution Recorded by Seismites in the Eocene Green River Formation, Wyoming. *Terra* 27, 218–224. doi: 10.1111/ter.12150

Ventra, D., and Clarke, L. E. (2018). "Geology and geomorphology of alluvial and fluvial fans: current progress and research perspectives," in *Geology and Geomorphology ofAlluvial and Fluvial Fans: Terrestrial and Planetary Perspectives*, eds D. Ventra and L. E. Clarke (London: Geology and Geomorphology ofAlluvial and Fluvial Fans: Terrestrial and Planetary Perspectives), 1–21. doi: 10.1144/sp440.16

Whipple, K. X., Parker, G., Paola, C., and Mohrig, D. (1998). Channel dynamics, sediment transport, and the slope of alluvial fans: experimental study. *J. Geol.* 106, 677–693.

Wickert, A. D., Martin, J. M., Tal, M., Kim, W., Sheets, B., and Paola, C. (2013). River channel lateral mobility: metrics, time scales, and controls. *J. Geophys. Res. Earth Surf.* 118, 396–412. doi: 10.1029/2012JF002386

Wilson, R. C. (2000). "Climatic variations in rainfall thresholds for debris-flow activity," in *Proceedings of the 1st Plinius Conf. on Mediterranean Storms*, eds P. Claps and F. Siccardi (Maratea: United States Geological Survey), 415–424.

Wolfe, J. A. (1980). Tertiary climates and floristic relationships at high latitudes in the northern hemisphere. *Palaeogeogr. Palaeoclimatol. Palaeoecol.* 30, 313–323. doi: 10.1016/0031-0182(80)90063-2

Zhu, L., Gong, H., Dai, Z., Guo, G., and Teatini, P. (2017). Modeling 3-D permeability distribution in alluvial fans using facies architecture and geophysical acquisitions. *Hydrol. Earth Syst. Sci.* 21, 721–733. doi: 10.5194/hess-21-721-2017

Conflict of Interest: The authors declare that the research was conducted in the absence of any commercial or financial relationships that could be construed as a potential conflict of interest.

Advantages of publishing in Frontiers

OPEN ACCESS
Articles are free to read for greatest visibility and readership

FAST PUBLICATION
Around 90 days from submission to decision

HIGH QUALITY PEER-REVIEW
Rigorous, collaborative, and constructive peer-review

TRANSPARENT PEER-REVIEW
Editors and reviewers acknowledged by name on published articles

Frontiers
Avenue du Tribunal-Fédéral 34
1005 Lausanne | Switzerland

Visit us: www.frontiersin.org
Contact us: info@frontiersin.org | +41 21 510 17 00

REPRODUCIBILITY OF RESEARCH
Support open data and methods to enhance research reproducibility

DIGITAL PUBLISHING
Articles designed for optimal readership across devices

FOLLOW US
@frontiersin

IMPACT METRICS
Advanced article metrics track visibility across digital media

EXTENSIVE PROMOTION
Marketing and promotion of impactful research

LOOP RESEARCH NETWORK
Our network increases your article's readership